

# Microstructure and Texture in Steels and Other Materials





Arunansu Haldar • Satyam Suwas  
Debashish Bhattacharjee  
Editors

Proceedings of the International Conference on

# Microstructure and Texture in Steels

and Other Materials

February 5–7, 2008, Jamshedpur, India



Springer



*Editors*

Arunansu Haldar, Dr.  
Tata Steel Ltd.  
Jamshedpur-831001  
India  
arunansuhalدار@tatasteel.com

Debashish Bhattacharjee, Dr.  
Tata Steel Ltd.  
Jamshedpur-831001  
India  
dbhattac@tatasteel.com

Satyam Suwas, Asst. Prof.  
Indian Institute of Science  
Department of Materials Engineering  
Bangalore-560012  
India  
satyamsuwas@materials.iisc.ernet.in

ISBN 978-1-84882-453-9

e-ISBN 978-1-84882-454-6

DOI 10.1007/978-1-84882-454-6

Springer Dordrecht Heidelberg London New York

British Library Cataloguing in Publication Data

A catalogue record for this book is available from the British Library

Library of Congress Control Number: 2009931372

© Springer-Verlag London Limited 2009

Apart from any fair dealing for the purposes of research or private study, or criticism or review, as permitted under the Copyright, Designs and Patents Act 1988, this publication may only be reproduced, stored or transmitted, in any form or by any means, with the prior permission in writing of the publishers, or in the case of reprographic reproduction in accordance with the terms of licences issued by the Copyright Licensing Agency. Enquiries concerning reproduction outside those terms should be sent to the publishers.

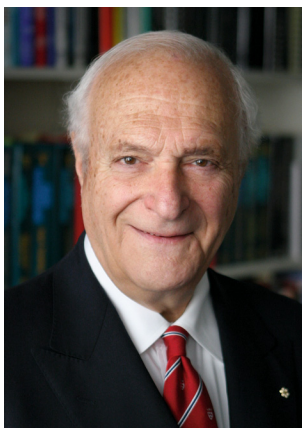
The use of registered names, trademarks, etc. in this publication does not imply, even in the absence of a specific statement, that such names are exempt from the relevant laws and regulations and therefore free for general use.

The publisher makes no representation, express or implied, with regard to the accuracy of the information contained in this book and cannot accept any legal responsibility or liability for any errors or omissions that may be made.

*Cover design:* eStudioCalamar, Figueres/Berlin

Printed on acid-free paper

Springer is part of Springer Science+Business Media ([www.springer.com](http://www.springer.com))



Department of Mining & Materials Engineering  
**McGill University**  
M.H. Wong Building  
3610 University Street  
Montreal, Quebec, Canada  
H3A 2B2

**Professor John J. Jonas, OC, CQ, FRSC**  
Birks Professor of Metallurgy Emeritus  
Tel: (514) 398-1649  
Fax: (514) 398-4492  
e-mail: john.jonas@mcgill.ca

## Foreword

I am sometimes asked, when presenting a paper on “Recent advances in steel processing”, whether, after a century and a half of research on steels, there is anything left to discover. “Hasn’t everything there is to know been determined by now?” they say. My usual answer is to quote Albert Einstein’s reply on such occasions. This great scientist would simply say: “When the radius of knowledge expands, so does the circumference of ignorance”. In fact, because of the linear relationship between radius and circumference, he was actually understating the extent to which the boundary between the ‘known’ and the ‘unknown’ expands with the progress of science. Perhaps he should have used the radius of a *sphere* to typify what is known or even that of a 4- or 5-dimensional sphere! Then the area of the interface would have increased much more rapidly.

This is made clearly evident when we turn to the papers presented at the Jamshedpur *International Conference on Microstructure and Texture in Steels 2008 (MATS2008)*.

In this case, the twenty three invited papers and eleven contributory papers, which are collected in these proceedings, display an impressive depth and novelty that would have intrigued old Albert, if he could be with us. Although swords have been made for centuries, with age-old lore about effective quenching methods, we are still learning fascinating things about martensite, its properties, and how to produce it. When it comes to deformation, we have now entered into the realm of “severe plastic deformation”, and are uncovering hitherto unimagined

properties and characteristics of our strained samples. I wonder whether asymmetric rolling will become a process that can be employed in industry. Similarly, are we likely to be able to develop practical and useful methods for making ultrafine grain steels?

There is so much going on in the field of textures. Some of the remarkable advances in 3D x-ray diffraction have been described here. With the progress that continues to be made in the power and speed of computers, the simulations carried out using the methods of crystal plasticity are leading to greater and greater insights into the behaviour of metals. The widespread availability of electron back-scattered diffraction (EBSD) attachments in electron microscopes has taken metallography to previously unattainable new heights! We can now obtain simultaneous, detailed topological and crystallographic information and even perform *in situ* tests (both mechanical and thermal) in such equipment! Details of some of these approaches have been presented at this conference and are included in the proceedings.

Part of the fascination of steel research lies in the complexities of the microstructures involved. In addition to austenite, ferrite and martensite, we must also be able to take into account effects arising from the presence of pearlite, bainite, various precipitates, inclusions, grain boundary segregants, and more recently, even twins! And then there are the nanocrystalline structures, which have distinct properties of their own. There is almost no limit to the number of microstructures we can study.

Examination of the papers in this volume will convince even the sceptic that the radius of our sphere of knowledge has been considerably extended during the recent past and that, as a result, the interface with the unknown has been stretched even further.

McGill University  
August 14, 2008

*John J. Jonas*

A handwritten signature in black ink, reading "John J. Jonas". The signature is stylized with large, sweeping loops for the first and last names, and a more compact, cursive script for the middle initial "J".

# Preface

This volume is a collection of papers presented at the International Conference in “Microstructure and Texture in Steels” held in Jamshedpur between 5–7th of February 2008.

Texture and microstructure, besides chemistry, are key factors that control properties of engineering materials. The design of any engineering product needs proper knowledge of these two parameters. Texture and Microstructure evolve during thermo-mechanical processing of materials. These processes constitute the most important steps in product fabrication schedule, especially for steels for automotive application. It is, therefore, quite natural that they should be the subject of intensive research. Hence the theme selected for this international conference was microstructure and texture in steels. This conference was organized jointly by R&D, Tata Steel and the Indian Institute of Metals, Jamshedpur Chapter, on the occasion of centenary celebration of Tata Steel and 70 years of the company’s Research & Development Division.

In recent times, the science of processing of steels has acquired new dimensions. The quest for stronger and more formable steels has led to new approaches towards optimal design of material and components. Effect of steel processing on evolution of texture and microstructure are being studied with renewed interest. In particular, the advent of new techniques such as orientation imaging microscopy, local texture determination by synchrotron radiation and new approaches in modelling and simulation of microstructure and texture have led to deeper understanding of this subject. In this conference, each of these aspects was covered at length by experts in these fields.

This conference also covered new developments such as production of ultra-fine grains or nanostructured materials. Also covered was research on materials other than steels, as they highlighted the mechanisms and use of modern characterisation tools.

The contents of this volume have been structured to suit the convenience of the readers. Papers in the introductory section are on fundamentals of texture and

microstructure of steels. These also include emerging fields such as grain boundary engineering.

The second section deals with topics on applied research on microstructure and texture control in steels. This section includes bulk as well as surface characteristics, such as coating and design of new steels for specialised applications and new concepts of microstructure design.

The third section is dedicated to modelling of texture and microstructure. This is followed by a section on specialized characterisation techniques for microstructure and texture examination.

The next section contains papers on special processes and materials. Some papers on the exotic materials like iron aluminium have also been included.

In addition to the invited papers, this volume also includes papers contributed by research scholars from various countries.

Since materials covered in the book are non-steel as well, the book has been named as 'Texture and Microstructure of steels and other materials'.

We hope that the reader will find in this collection an up-to-date account of current issues, concepts, techniques and thoughts related to the science of texture and microstructure.

We are indebted to all the speakers who had accepted our invitation and have taken the pain of traveling from different parts of the globe to attend and share their knowledge with us. We are thankful to the delegates as well as their sponsoring organisations for showing their interest and to the sponsors of this conference for encouraging the efforts. We are indeed grateful to the Indian Institute of Metals, for jointly organising this conference and to the publishers, Springer Link Pvt. Ltd., for kindly agreeing to publish the proceedings. Last but not the least, thanks to all those who worked in the background to make the conference a great success.

The editors wish to thank the Management of Tata Steel for their encouragement and support.

# Contents

## Part I Introduction

<b>1</b>	<b>Transformation Textures Associated with Steel Processing .....</b>	<b>3</b>
	<i>John J. Jonas</i>	
1.1	Introduction .....	3
1.2	Hot Band Textures.....	6
1.2.1	General Features .....	6
1.2.2	Effects of Austenite Rolling and Recrystallization on the Texture .....	8
1.3	The Bain, Kurdjumov-Sachs, and Nishiyama-Wassermann Correspondence Relationships .....	8
1.4	Transformation Behavior of Recrystallized Austenite .....	10
1.5	Transformation Behavior of Deformed Austenite .....	11
1.6	Variant Selection .....	12
1.7	Overall Summary of the Rolling and Transformation Behavior .....	14
	References.....	16
<b>2</b>	<b>Mathematics of Crystallographic Texture in Martensitic and Related Transformations .....</b>	<b>19</b>
	<i>H.K.D.H. Bhadeshia, S. Kundu, and H. Abreu</i>	
2.1	Introduction .....	19
2.2	Crystallographic Theory of Martensite.....	20
2.2.1	Structure of the Interface.....	20
2.2.2	The Shape Deformation .....	20
2.2.3	The Bain Strain .....	21
2.2.4	Phenomenological Solution .....	23
2.2.5	The Crystallographic Set.....	25



2.3	Variant Selection .....	26
2.4	Transformation Plasticity .....	28
2.5	The Intensity of the Texture .....	29
2.6	Summary .....	30
	References.....	30
<b>3</b>	<b>Structure and Strength of IF Steel</b>	
	<b>After Large Strain Deformation</b> .....	33
	<i>Niels Hansen, Xiaoxu Huang, and Naoya Kamikawa</i>	
3.1	Introduction .....	33
3.2	Universal Pattern of Structural Evolution.....	34
3.2.1	Cold Rolling.....	34
3.2.2	Accumulative Roll-Bonding (ARB).....	37
3.2.3	Rolling of Lath Martensite.....	38
3.2.4	Summary: Structural Observations .....	38
3.3	Microstructural Parameters and Flow Stress .....	39
3.3.1	Summary: Structure-Property Relationships.....	41
3.4	Concluding Remarks .....	41
	References.....	42
<b>4</b>	<b>The Coming of Grain Boundary Engineering in the 21st Century ....</b>	43
	<i>Tadao Watanabe, Sadahiro Tsurekawa, Xiang Zhao, and Liang Zuo</i>	
4.1	Introduction .....	44
4.1.1	Material-Assisted Civilization and Development .....	44
4.1.2	Requirements for High Performance Materials.....	44
4.1.3	Importance of Grain Boundaries in Engineering Materials.....	46
4.2	Grain Boundary Microstructures in Polycrystalline Materials .....	46
4.2.1	Versatility of Grain Boundary Microstructure .....	46
4.2.2	Structure-Dependent Boundary Properties.....	48
4.2.3	Structure-Dependent Grain Boundary Fracture .....	49
4.2.4	Observations of Grain Boundary-Related Fracture of Polycrystalline Materials .....	50
4.3	Grain Boundary Engineering (GBE) for High Performance Materials .....	52
4.3.1	Basic Concept of Grain Boundary Engineering .....	52
4.3.2	Possible Processing Methods for Grain Boundary Engineering.....	53
4.4	The Characterization of Grain Boundary Microstructures by OIM .....	54
4.4.1	Quantitative Analysis of Grain Boundary Microstructures .....	54
4.4.2	Grain Boundary Character Distribution (GBCD) .....	56
4.4.3	Grain Boundary Connectivity .....	57

4.5	Metallurgical Factors Affecting GBCD.....	57
4.5.1	Relation Between GBCD and Grain Size .....	57
4.5.2	Relation Between GBCD and Texture .....	59
4.5.3	Relation Between GBCD and Material Purity/Composition .....	61
4.6	Prediction of GBCD-Controlled Brittle-Ductile Transition and Fracture Toughness.....	62
4.7	The Control of Intergranular Brittleness by Grain Boundary Engineering.....	64
4.7.1	The Control of Intrinsic Intergranular Brittleness.....	64
4.7.2	The Control of Oxidation-Induced Intergranular Brittleness.....	67
4.8	Grain Boundary Engineering by Magnetic Field Application .....	70
4.8.1	The Control of Segregation-Induced Brittleness.....	70
4.8.2	The Control of Abnormal Grain Growth and Heterogeneous Microstructure .....	72
4.8.3	Microstructure Control by Magnetic Phase Transformation.....	74
4.9	Grain Boundary Engineering for Photovoltaic Polysilicon .....	75
4.10	Summary and Prospect .....	77
	References.....	79

## Part II Control of Texture and Microstructure in Steels

<b>5</b>	<b>Texture Development in Low Carbon Sheet Steels for Automotive Application .....</b>	<b>85</b>
	<i>Jun-Yun Kang, Dong-Ik Kim, and Hu-Chul Lee</i>	
5.1	Introduction .....	86
5.2	Texture Development in Low Carbon Sheet Steels.....	87
5.2.1	Development of Cold Rolled Microstructure and Texture .....	88
5.2.2	Development of Recrystallization Texture .....	90
5.2.3	Mechanism of the Recrystallization Texture Formation.....	93
5.3	Effect of Austenite Transformation on the Recrystallization Texture of DP Steel .....	98
5.4	Summary .....	99
	References.....	100
<b>6</b>	<b>Texture and Microstructure Evolution at the Metal-Vapour Interface During Transformation Annealing in a Mn and Al Alloyed Ultra Low Carbon Steel .....</b>	<b>103</b>
	<i>Leo A.I. Kestens, Jai Gautam, and Roumen Petrov</i>	
6.1	Introduction .....	103

6.2	Experimental Procedure .....	104
6.3	Results .....	105
6.3.1	Surface Texture and Through Thickness Microstructure Before Annealing .....	105
6.3.2	Surface Texture at Different Temperatures During Interrupted Annealing .....	106
6.3.3	Through Thickness Grain Morphology .....	107
6.4	Discussion .....	107
6.5	Conclusions .....	108
	References .....	109
<b>7</b>	<b>Precipitation Behavior and Textural Evolution in Interstitial Free High Strength (IFHS) Steels .....</b>	<b>111</b>
	<i>R.K. Ray and P. Ghosh</i>	
7.1	Introduction .....	111
7.2	Precipitation in Batch Annealed (BA) IFHS Steels .....	112
7.3	Precipitation in Continuous Annealed (CA) IFHS Steels .....	115
7.4	Precipitation of FeTiP .....	117
7.4.1	Structure and Constitution of FeTiP .....	118
7.4.2	FeTiP Formation in Cold Rolled and Annealed Steels ....	119
7.4.3	Prevention of FeTiP Formation in BA-IFHS Steels .....	122
7.5	Conclusions .....	123
	References .....	123
<b>8</b>	<b>Texture, Microstructure and Properties of Coatings on a few Industrially Produced Galvanized and Galvannealed Interstitial Free Steels .....</b>	<b>125</b>
	<i>D. Bhattacharjee, A. Chakraborty, R. Pais, and R.K. Ray</i>	
8.1	Introduction .....	125
8.2	Experimental Procedure .....	127
8.3	Experimental Results .....	129
8.4	Discussion .....	140
8.5	Conclusions .....	142
	References .....	143
<b>9</b>	<b>Effects of Microalloying in Multi Phase Steels for Car Body Manufacture .....</b>	<b>145</b>
	<i>Wolfgang Bleck and Kriangyut Phiu-on</i>	
9.1	Introduction .....	145
9.2	Definition .....	146
9.3	Alloy Concepts .....	149
9.4	Processing .....	153
9.5	Properties .....	160
9.6	Conclusion .....	162
	References .....	162

<b>10 State-of-the-Science of High Manganese TWIP Steels for Automotive Applications</b> .....	165
<i>B.C. De Cooman, L. Chen, Han S. Kim, Y. Estrin, S.K. Kim, and H. Voswinckel</i>	
10.1 Introduction .....	166
10.2 Experimental .....	169
10.3 Results .....	169
10.4 Microstructural Analysis .....	175
10.5 Discussion .....	177
10.6 Conclusion.....	180
References.....	182
<b>11 Third Generation of AHSS: Microstructure Design Concepts</b> .....	185
<i>David K. Matlock and John G. Speer</i>	
11.1 Introduction .....	186
11.2 Analysis of Strengthening in AHSS Steels.....	188
11.3 Predictions of AHSS Microstructures and Properties.....	194
11.4 Evaluation of Methodologies to Produce Third Generation AHSS .....	199
11.5 Summary .....	202
References.....	203

### Part III Modeling

<b>12 Crystal Plasticity Based Modelling of Deformation Textures</b> .....	209
<i>P. Van Houtte</i>	
12.1 Introduction .....	209
12.2 Crystal Plasticity Based Models .....	210
12.2.1 General.....	210
12.2.2 Full Constraint (FC) Taylor Theory.....	212
12.2.3 LAMEL Model .....	213
12.2.4 Grain Interaction (GIA) Model.....	214
12.2.5 Advanced Lamel Model (ALAMEL).....	215
12.2.6 Crystal Plasticity Finite Element Models (CPFEM) .....	216
12.3 Model Validation.....	216
12.4 Discussion and Conclusions .....	222
References.....	223
<b>13 Simulation of Persistence Characteristics of Textures During Plastic Deformation</b> .....	225
<i>László S. Tóth</i>	
13.1 Introduction .....	225

13.2	Principles of Orientation Stability .....	226
13.2.1	Stability Condition .....	226
13.2.2	Evolution of Orientation Density .....	227
13.2.3	Role of Rigid Body Rotation.....	228
13.3	How to Identify Ideal Orientations? .....	232
13.3.1	The Persistence Parameter .....	232
13.3.2	Examples for Persistence Maps .....	233
13.3.3	The Role of Strain Rate Sensitivity in the Persistence of Shear Textures .....	239
13.4	The Role of the Divergence Quantity in the Formation of Textures .....	240
13.5	Summary and Conclusions .....	244
	References.....	245
<b>14</b>	<b>DXRD and Its Applications Leading to New Modelling.....</b>	<b>247</b>
	<i>D. Juul Jensen</i>	
14.1	Introduction .....	247
14.2	3DXRD.....	248
14.3	Growth During Recrystallization.....	249
14.3.1	Growth Rate Distributions .....	249
14.3.2	Anisotropic Growth.....	251
14.4	Distribution of Nucleation Sites .....	252
14.5	Discussion and Conclusion.....	253
	References.....	254
<b>15</b>	<b>3D Image-Based Viscoplastic Response with Crystal Plasticity .....</b>	<b>255</b>
	<i>Anthony D. Rollett, Sukbin Lee, and Ricardo A. Lebensohn</i>	
15.1	Introduction .....	255
15.2	FFT Method.....	256
15.3	3D Image of Nickel Alloy .....	257
15.4	Results and Discussion .....	258
15.5	Summary .....	263
	References.....	263

## Part IV Specialized Characterization Techniques

<b>16</b>	<b>Diffraction Techniques in Steel Research: An Overview .....</b>	<b>267</b>
	<i>Stefan Melzer and Jaap Moerman</i>	
16.1	Introduction .....	268
16.2	Experimental Details .....	268
16.2.1	Equipment .....	268
16.2.2	Techniques .....	268

16.3	Characterisation of Advanced High-Strength Steels .....	269
16.3.1	Texture Measurement of Ferrite and Austenite Phase .....	269
16.3.2	Retained Austenite .....	271
16.3.3	Detection of Complex Microstructures .....	273
16.3.4	Welds .....	275
16.4	Characterisation of Nickel Plated Battery Steels .....	277
16.5	In situ Real-Time Measurement Techniques .....	280
16.6	Summary .....	283
	References.....	283
<b>17</b>	<b>Non-Contact Non-Destructive Measurement of Texture Using an Electro-Magnetic Acoustic Transducer (EMAT) Sensor .....</b>	<b>285</b>
	<i>C.L. Davis</i>	
17.1	Introduction .....	286
17.2	Materials and Experimental Method .....	289
17.3	Results and Discussion .....	291
17.4	Conclusions .....	304
	References.....	305
<b>18</b>	<b>Texture Transition in Steel ST37K, in situ Measurement at High Temperatures Using High-Energy X-rays .....</b>	<b>307</b>
	<i>H.-G. Brokmeier, S.B. Yi, and J. Homeyer</i>	
18.1	Synchrotron Radiation.....	308
18.1.1	Hard X-ray Instrumentation .....	310
18.1.2	Texture Measurements by High Energy Synchrotron Radiation .....	311
18.2	High Temperature Measurements by High-Energy Synchrotron Radiation.....	313
18.2.1	Sample Description and Experimental Conditions .....	313
18.2.2	In situ High-Temperature Phase Analysis of ST37K.....	315
18.2.3	In situ High-Temperature Texture Analysis of ST37K....	317
18.3	Conclusion.....	319
	References.....	320

## **Part V Texture and Microstructure Development During Special Processes and Materials**

<b>19</b>	<b>Ultra-fine Grain Materials by Severe Plastic Deformation: Application to Steels .....</b>	<b>325</b>
	<i>Satyam Suwas, Ayan Bhowmik, and Somjeet Biswas</i>	
19.1	Introduction .....	325
19.2	General Characteristics of Severe Plastic Deformation.....	327
19.2.1	Equal Channel Angular Extrusion .....	329
19.2.2	Accumulative Roll Bonding.....	332

19.3	Severe Plastic Deformation Processes as Applied to Steels .....	333
19.3.1	Equal Channel Angular Extrusion .....	333
19.3.2	Accumulative Roll Bonding.....	340
19.4	Summary and Perspective .....	340
	References.....	341
<b>20</b>	<b>Development of Texture from the HAZ to Weldmetal</b>	
	<b>Across the Fusion Boundary .....</b>	<b>345</b>
	<i>Martin Strangwood and Claire Davis</i>	
20.1	Introduction .....	345
20.2	Experimental .....	346
20.3	Results and Discussion .....	347
20.3.1	Fe-3 wt% Si Steel.....	347
20.3.2	430 Stainless Steel .....	348
20.3.3	AA5182 Spot Weld.....	353
20.3.4	AA5251 MIG Weld .....	355
20.4	Conclusions and Further Work.....	358
	References.....	358
<b>21</b>	<b>Evolution of Recrystallization Texture in AISI300 Series</b>	
	<b>Austenitic Stainless Steels After Cold Rolling to Large Strain .....</b>	<b>361</b>
	<i>Sandip Ghosh Chowdhury, P. Sahu, B. Mahato, and P.K. De</i>	
21.1	Introduction .....	361
21.2	Experimental Procedure .....	362
21.3	Results .....	363
21.3.1	Deformation Texture.....	363
21.3.2	Microstructure.....	367
21.3.3	Recrystallization .....	369
21.4	Discussion .....	373
21.5	Conclusions .....	377
	References.....	378
<b>22</b>	<b>Deformation and Recrystallization Textures in Iron Aluminides .....</b>	<b>379</b>
	<i>W. Skrotzki, R. Tamm, K. Kegler, and C.-G. Oertel</i>	
22.1	Introduction .....	379
22.2	Experimental .....	381
22.3	Results and Discussion .....	382
22.4	Conclusions .....	389
	References.....	390
<b>23</b>	<b>Effect of Nanocrystallization on the Phase Stability of Al-Cu-Ti</b>	
	<b>and Al-Cu-Nb Metallic Systems .....</b>	<b>393</b>
	<i>S. Bera and I. Manna</i>	
23.1	Introduction .....	393
23.2	Thermodynamic Model .....	394

23.3	Results and Discussion .....	396
23.4	Conclusion .....	404
	References .....	404

## Part VI Contributory Papers

<b>24</b>	<b>Investigation of Microstructure Development During <math>\alpha</math>-<math>\gamma</math>-<math>\alpha</math> Phase Transformation in Steel by Using High Temperature in situ EBSD .....</b>	<b>409</b>
	<i>I. Lischewski, D.M. Kirch, A. Ziemons, and G. Gottstein</i>	
24.1	Introduction .....	409
24.2	Experimental Results .....	410
24.3	Discussion .....	412
24.4	Summary .....	413
	References .....	413
<b>25</b>	<b>A New Flow Function to Model Texture Evolution in Symmetric and Asymmetric Rolling .....</b>	<b>415</b>
	<i>Benoît Beausir and László S. Tóth</i>	
25.1	Introduction .....	415
25.2	Flow Modelling .....	416
25.3	Velocity Field, Velocity Gradient and Texture Results .....	418
25.4	Conclusion .....	420
	References .....	420
<b>26</b>	<b>Microstructure and Texture Evolution During the Accumulative Roll Bonding of Pure Ni .....</b>	<b>421</b>
	<i>P.P. Bhattacharjee, D. Terada, and N. Tsuji</i>	
26.1	Introduction .....	421
26.2	Experimental .....	422
	26.2.1 ARB Process .....	422
	26.2.2 Microstructural Investigation .....	422
26.3	Results and Discussion .....	423
26.4	Conclusions .....	429
	References .....	429
<b>27</b>	<b>Microstructure of the Rust Formed on Si-Al Bearing Ultrafine-Grained Weathering Steel .....</b>	<b>431</b>
	<i>V. Raman and T. Nishimura</i>	
27.1	Introduction .....	431
27.2	Experiments .....	432
27.3	Results and Discussions .....	433
27.4	Conclusions .....	437
	References .....	437



<b>28</b>	<b>Microstructure Evolution in Three FCC Materials During Limited Dome Height Test</b> .....	439
	<i>S. Mishra, P. Pant, K. Narasimhan, and I. Samajdar</i>	
28.1	Introduction .....	439
28.2	Experimental Details .....	440
28.3	Results and Discussions.....	441
28.4	Conclusions .....	443
	References.....	443
<b>29</b>	<b>The Facet Method for the Description of Yield Loci of Textured Materials</b> .....	445
	<i>Sampath Kumar Yerra, Albert Van Bael, and Paul Van Houtte</i>	
29.1	Introduction .....	446
29.2	The Facet Method.....	446
29.3	Results and Discussion .....	447
	References.....	449
<b>30</b>	<b>The Hall-Petch Relationship in Interstitial-Free Steel Processed by Equal Channel Angular Extrusion</b> .....	451
	<i>Azdiar A. Gazder, Christopher H.J. Davies, and Elena V. Pereloma</i>	
30.1	Introduction .....	451
30.2	Experimental Procedure .....	453
30.3	Results and Discussion .....	453
30.4	Conclusions .....	455
	References.....	456
<b>31</b>	<b>Evolution of Crystallographic Texture During Equal Channel Angular Extrusion (ECAE) of (<math>\alpha</math>+<math>\beta</math>) Brass</b> .....	457
	<i>Satyaveer Singh D., Ayan Bhowmik, Somjeet Biswas, Satyam Suwas, and K. Chattopadhyay</i>	
31.1	Introduction .....	457
31.2	Experimental Procedures.....	458
31.3	Results and Discussions.....	459
31.4	Conclusions .....	464
	References.....	464
<b>32</b>	<b>Grain Growth in ECAE Processed Pure Magnesium</b> .....	465
	<i>Somjeet Biswas, Satyaveer Singh D., and Satyam Suwas</i>	
32.1	Introduction .....	465
32.2	Experimental Methods.....	466
32.3	Results and Discussions.....	466
32.3.1	Grain Growth Statistics .....	468
32.3.2	Activation Energy .....	468
32.3.3	Texture Analysis .....	469

32.4	Conclusions .....	472
	References.....	473
<b>33</b>	<b>Solidification Microstructure and Texture in Grain-Refined Titanium Alloys.....</b>	<b>475</b>
	<i>Segolene de Waziers, Shibayan Roy, Satyam Suwas, S. Tamirisakandala, R. Srinivasan, and D.B. Miracle</i>	
33.1	Introduction .....	475
33.2	Experimental .....	477
33.3	Results and Discussions.....	477
33.4	Conclusion.....	481
	References.....	482
<b>34</b>	<b>Effect of Intercritical Heat Treatment on the Abrasive Wear Behaviour of Plain Carbon Dual Phase Steel.....</b>	<b>483</b>
	<i>M.K. Manoj, V. Pancholi, and S.K. Nath</i>	
34.1	Introduction .....	483
34.2	Experimental .....	484
34.3	Results and Discussion .....	485
34.4	Conclusion.....	487
	References.....	488



# **Part I**

## **Introduction**



# Chapter 1

## Transformation Textures Associated with Steel Processing

John J. Jonas

**Abstract.** The effects on texture formation of rolling above and below the  $T_{nr}$  (no-recrystallization temperature) are considered. Rolling above the  $T_{nr}$  leads to the appearance of the ‘cube’ component, while the absence of recrystallization accompanied by strain accumulation is responsible for the appearance of the fcc ‘rolling fibre’. The latter consists of the Cu (copper), S, Br (brass) and Goss (as well as intermediate) components. On transformation, the cube is converted into the rotated cube, Goss, and rotated Goss. After lower temperature finishing, the Cu and Br are converted into the ‘transformed Cu’ and ‘transformed Br’, respectively. Some attention is paid to the Kurdjumov-Sachs and Nishiyama-Wassermann correspondence relations and the importance of variant selection (departure from these relations) is discussed. Finally, the effect of operating parameters such as cooling rate, grain size and solute level are also considered.

### 1.1 Introduction

The processing of steel involves five distinct sets of texture development mechanisms:

- i) austenite (face-centered cubic, or fcc) deformation (during hot rolling);
- ii) austenite recrystallization (during and after hot rolling);
- iii) the gamma-to-alpha transformation (on cooling after rolling);
- iv) ferrite (body-centered cubic, or bcc) deformation (during warm or cold rolling);  
and
- v) static recrystallization during annealing after cold rolling.

---

J.J. Jonas

Materials Engineering, McGill University, 3610 University Street, Montreal, H3A 2B2, QC, Canada

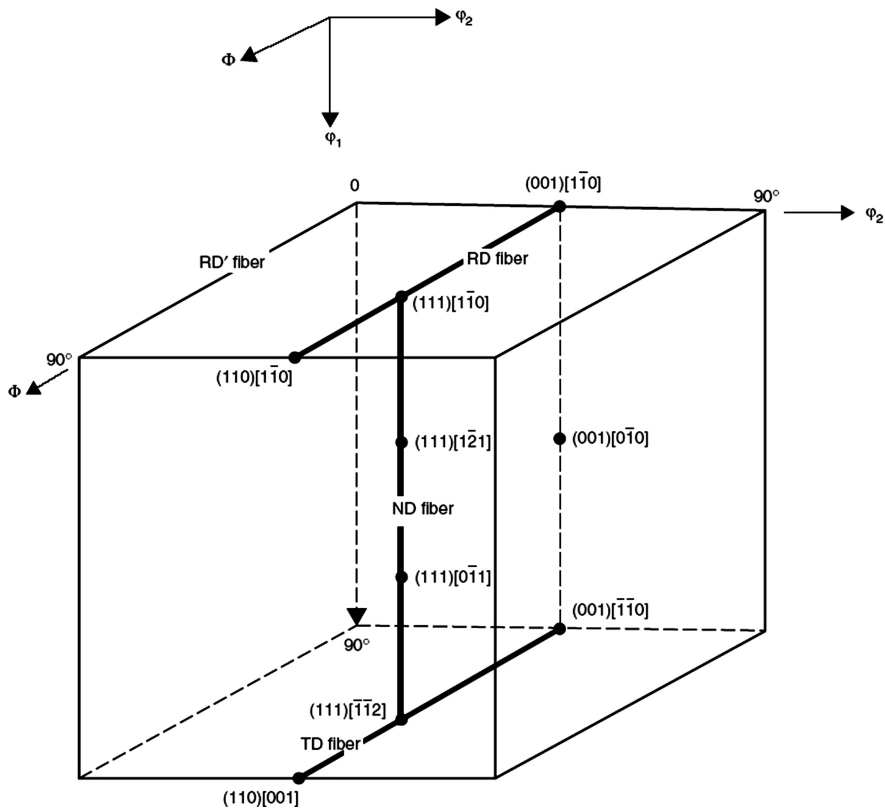


**Fig. 1.1** Three-dimensional view of Euler space (Bunge notation). The “horizontal H” lying in the  $\phi_2 = 45^\circ$  cross section and which is of particular importance in the processing of steel is shown in bold.

This article focuses on items i), ii), and iii), i.e. on the factors that determine the hot band texture.

The results obtained by various workers are presented here in the form of cross-sections of Euler space, using the notation developed by Bunge [1]. Pole figures are only employed where they facilitate the understanding of the basic mechanisms involved. A three-dimensional view of the Euler space applicable to cubic materials subjected to plane strain (and which therefore possess orthorhombic symmetry) is displayed in Fig. 1.1, where the origins of the axes for the variables  $\phi_1$ ,  $\Phi$ , and  $\phi_2$  can be seen. This cube has dimensions of  $90^\circ$  by  $90^\circ$  by  $90^\circ$ . Of particular interest is the cross-section of this figure located at  $\phi_2 = 45^\circ$  (containing an “H” with a vertical crossbar delineated in bold). Because of the importance of this cross-section in the interpretation of bcc (ferrite/bainite/martensite) textures, this section is presented in greater detail in Fig. 1.2 (a), where the most important ideal orientations associated with the plane-strain processing of such materials are identified. As discussed in greater detail below, both the deformation as well as the recrystallization compo-

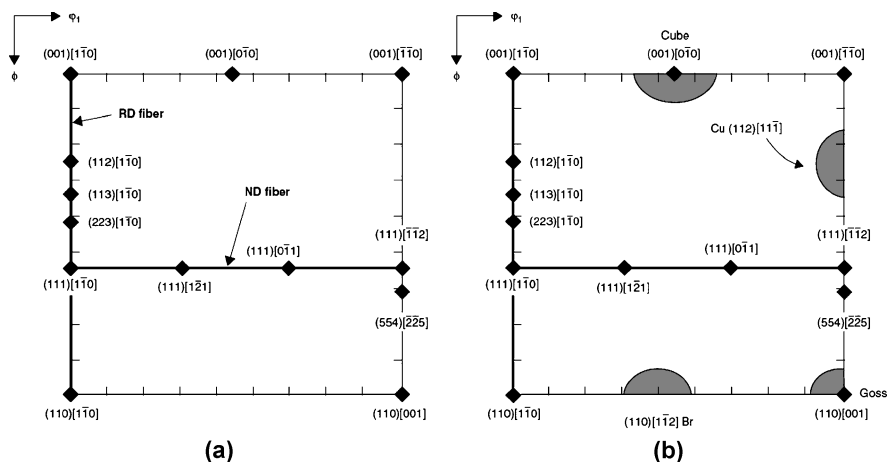


**Fig. 1.2** Plan views of the  $\phi_2 = 45^\circ$  section of Fig. 1.1 (a) The principal ideal orientations playing significant roles in the processing of bcc steel are shown. Rolling reinforces the rolling-direction (RD) fiber (and to a lesser extent, the normal-direction, or ND fiber), while recrystallization reinforces the ND fiber. (b) Plan view of the  $\phi_2 = 45^\circ$  section of Fig. 1.1. The principal ideal orientations that play significant roles during the processing of austenite (face-centered cubic, or fcc, steel) are shown. Rolling introduces the copper (Cu), brass (Br), and Goss, together with the S (not shown); recrystallization converts these into the cube.

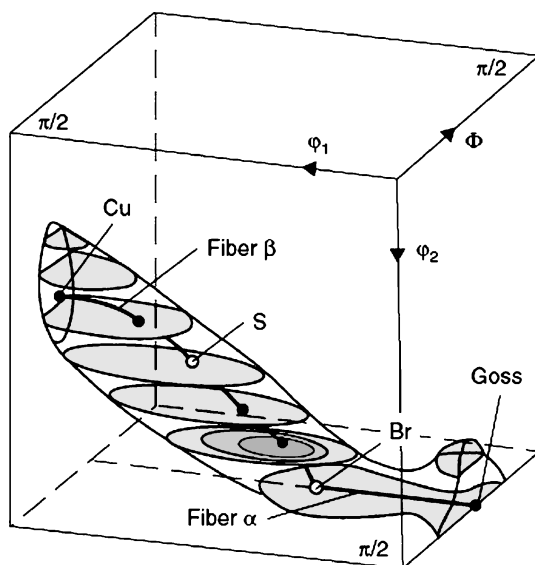
nents are shown here. A similar diagram is reproduced in Fig. 1.2 (b) for the case of fcc processing, where once again both the deformation as well as the recrystallization components are identified.

The textures developed during rod and bar (long product) rolling, and during subsequent transformation, are not covered here; nevertheless, the principles and basic phenomena involved are similar. Returning to the plane strain deformation of steel, it should be pointed out that, despite the difference in temperature, the preferred orientations produced during hot rolling do not differ (except in minor details) from those observed after cold deformation. Similarly, the textures developed during the hot rolling of steel are similar to those observed after the plane strain rolling of fcc metals such as Al, Cu, Ni, Ag, Au, Pt, etc. The two hot rolling fcc “fibers” are illustrated in Fig. 1.3, where the “ $\alpha$ ” fiber can be seen to consist of all orientations lying between the Goss  $\{110\} \langle 001 \rangle$  ( $\phi_1 = 0^\circ$ ,  $\Phi = 45^\circ$ ,  $\phi_2 = 90^\circ$ ) and the brass or Br  $\{110\} \langle 112 \rangle$  ( $\phi_1 = 35.3^\circ$ ,  $\Phi = 45^\circ$ ,  $\phi_2 = 90^\circ$ ) and defined by  $\langle 110 \rangle$  being parallel to the sheet plane normal.<sup>1</sup>

<sup>1</sup> Note that, because of the multiplicities inherent in Euler space, individual orientations appear two or three times in the  $90^\circ$  by  $90^\circ$  by  $90^\circ$  cube presented in Figs. 1.1 and 1.3. Thus the Goss component is shown as being located at ( $\phi_1 = 90^\circ$ ,  $\Phi = 90^\circ$ ,  $\phi_2 = 45^\circ$ ) in Fig. 1.1, whereas it is illustrated as situated at ( $\phi_1 = 0^\circ$ ,  $\Phi = 45^\circ$ ,  $\phi_2 = 90^\circ$ ) in Fig. 1.3. Similar remarks apply to the Cu, Br, and other components. These features of the geometry of Euler space are beyond the scope of the present brief survey.



**Fig. 1.3** Three-dimensional view of the face-centered cubic (fcc) (austenite) rolling fiber, illustrating the main texture components.



The second fiber, known as the  $\beta$ , consists of the copper or Cu  $\{112\} \langle 111 \rangle$  ( $\phi_1 = 90^\circ$ ,  $\Phi = 35.3^\circ$ ,  $\phi_2 = 45^\circ$ ), S  $\{123\} \langle 634 \rangle$  ( $\phi_1 = 59.0^\circ$ ,  $\Phi = 36.7^\circ$ ,  $\phi_2 = 63.4^\circ$ ), and brass or Br orientations, as well as all the intermediate components located on the fiber. During rolling, orientations that are initially distributed nearly randomly within the cube are gradually drawn into the “tube” that is shown. The extent to which grain orientations are concentrated within as opposed to outside the tube (and therefore the texture “intensity”) increases with the amount of rolling reduction. Following each rolling pass, the material may either recrystallize or the work hardening may be retained, leading to “strain” (stored-energy) accumulation. The former and latter events lead to the formation of the recrystallization and deformation textures, respectively, which are considered in more detail below.

## 1.2 Hot Band Textures

### 1.2.1 General Features

The microstructural processes that control the five texture formation mechanisms listed above are illustrated schematically in Fig. 1.4. Here it can be seen that, at temperatures above the  $T_{nr}$  (the “no-recrystallization temperature” identified as  $950^\circ\text{C}$  in the diagram), the deformed grains (containing fcc deformation textures) are regularly converted into equiaxed grains (containing the “cube” or fcc recrystallization texture, together with some of the retained rolling compo-

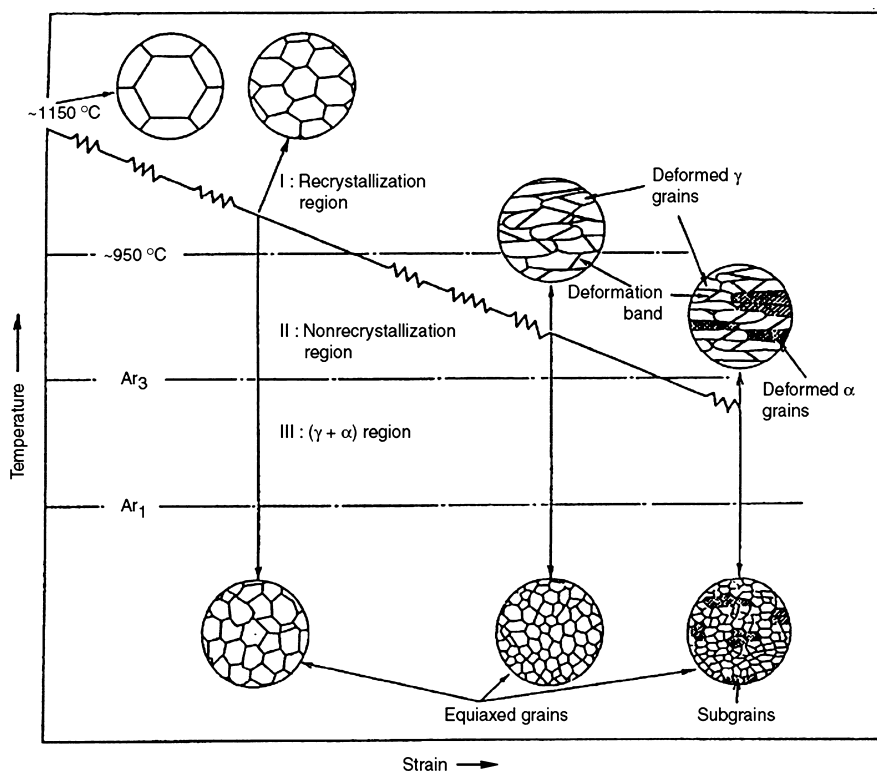


Fig. 1.4 The three stages of controlled rolling and of the associated changes in microstructure.

ment). The intensity of the cube component generally increases (and that of the retained rolling component decreases) with the accumulated strain prior to recrystallization. The  $\gamma$ -to- $\alpha$  phase transformation takes place in the temperature range between the  $A_{r3}$  (the “upper critical”) and  $A_{r1}$  (the “lower critical”). Its effect on the texture is considered in detail below. The  $T_{nr}$  in Fig. 1.4 refers to a microalloyed steel containing niobium and can be as high as 1000°C, depending on the alloy composition. The retardation of recrystallization between rolling passes can also be caused by solute elements such as chromium, nickel, molybdenum, and even manganese, but to a lesser degree, and depends on the length of the interpass interval. When it comes to plain carbon steels, the  $T_{nr}$  drops down to about 900°C. As a result, in the latter materials, the austenite is generally recrystallized prior to transformation. Nevertheless, even plain carbon steels can contain some of the retained rolling fiber prior to transformation and therefore the transformed copper and transformed Br components after transformation, particularly when finish rolling is completed at sufficiently low temperatures.

### 1.2.2 *Effects of Austenite Rolling and Recrystallization on the Texture*

The austenite hot-rolling texture has already been illustrated in Fig. 1.3, and three of the main components (the Cu, Br, and Goss) have been identified in Fig. 1.2 (b). (Note that the S component is located outside this plane of section, as are all the intermediate orientations belonging to the  $\beta$  fiber, such as the Cu/S and S/Br that lie between the Cu and Br.) Once recrystallization takes place, the rolling components are largely replaced by the recrystallization or cube component, which is identified as the  $\{001\} \langle 010 \rangle$  in Fig. 1.2 (b). The physical mechanisms involved in the formation of the cube texture are discussed in Ref. 2 and are also reviewed briefly below. If a pole figure or Euler diagram contains both the cube as well as the rolling components (i.e., the Cu, S, Br, and Goss), this either indicates that only partial recrystallization took place or that only moderate reductions were applied to the material between cycles of recrystallization.

## 1.3 The Bain, Kurdjumov-Sachs, and Nishiyama-Wassermann Correspondence Relationships

Before considering the details of the transformation of recrystallized or alternatively unrecrystallized (i.e., deformed) austenite, it is useful to review the so-called “correspondence relationships” briefly. The three most commonly considered are the Bain, Kurdjumov-Sachs (K-S), and Nishiyama-Wassermann (N-W). These are illustrated in Fig. 1.5 [3]. For further information regarding this topic, the reader is referred to Ref. 4 and 5. From Fig. 1.5, it can be seen that an austenite grain obeying the Bain transformation relationship will be ‘rotated’ by  $45^\circ$  around each of the three  $\langle 100 \rangle$  axes in turn, leading to the three alternate bcc “variants”. That is, 99  $\gamma$  grains can be expected to transform into 33 of each of the three variants with equal probability. Here the correspondence relations state that  $\{001\}_\gamma \parallel \{001\}_\alpha$  and that  $\langle 100 \rangle_\gamma \parallel \langle 110 \rangle_\alpha$ .

This “transformation” is essentially never observed and is only useful as an approximation and a point of reference. The K-S relations (Fig. 1.5 (a)) correspond to “rotations” of  $90^\circ$  about each of the 24  $\langle 112 \rangle$  axes in turn, leading to 24 variants in this case (instead of 3). (The reader should note that no physical rotations are involved here; it is the unit cells of the two phases that are related in this way as a result of very minor atomic movements.) Similar remarks apply to the Bain and N-W “rotations”. Here the correspondence relations are the following:  $\{111\}_\gamma \parallel \{110\}_\alpha$  and  $\langle 011 \rangle_\gamma \parallel \langle 111 \rangle_\alpha$  (Fig. 1.5 (b)). By inspection of Fig. 1.5, it can be seen that each Bain variant is surrounded by eight K-S variants as well as by four N-W variants. In this way, given the dispersions about ideal orientations in actual samples, a Bain “variant” is a reasonable approximation of the physical effects taking place within materials obeying the K-S relationship.

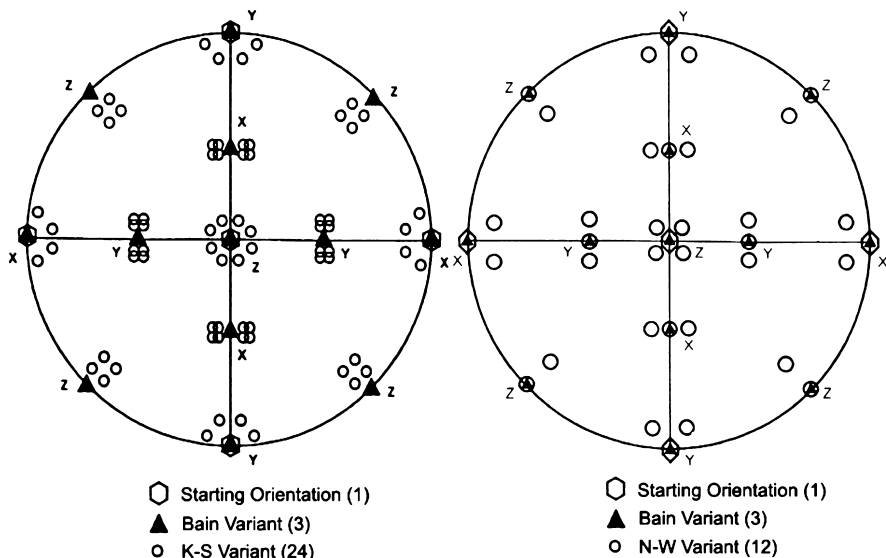


**Fig. 1.5** Schematic (002) pole figures of all variants of bcc  $\alpha$  phase formed from (001) [100] oriented fcc  $\gamma$  crystal following, respectively, the Bain and K-S relationships and the Bain and N-W relationships.

Similar remarks apply to the N-W correspondence relations. In this case, the plane correspondence condition is the same:  $\{111\}_{\gamma} \parallel \{110\}_{\alpha}$  and only the direction condition is different:  $\langle 112 \rangle_{\gamma} \parallel \langle 110 \rangle_{\alpha}$ . When the N-W relations are obeyed, there are only 12 variants, each of which is located exactly midway between two particular K-S variants. Again, the three Bain orientations provide good “averages” or approximate representations of the effects of the N-W transformation and are useful for this purpose, even if they do not represent actual physical events. Further information concerning this description of the transformation is provided in [6].

Recent work [7–9] indicates that both the K-S and the N-W relations are followed in industrial as well as model materials. Moreover, there is a continuous spread of orientations running from the exact K-S to the exact N-W position. These observations have been obtained from detailed orientation imaging microscopy (OIM) (electron backscattering diffraction, or EBSD) studies [7, 9], as well as by using other techniques, such as synchrotron radiation [8]. What they indicate is that the plane relation  $\{111\}_{\gamma} \parallel \{110\}_{\alpha}$  is universally respected, while there is considerable flexibility regarding the direction condition. One explanation of this observation has been proposed by Nagano and Enomoto [10], who used a molecular dynamics model to show that the energy of the  $\gamma/\alpha$  boundary depends critically on the plane of the interface. In most cases, the K-S relation provides the lowest energy, while for other orientations of this plane, it is the N-W. Still another explanation relies on the presence and influence of both perfect and partial dislocations [11]. This interpretation is described in more detail below.

So far, it has been assumed that all 24 K-S or all 12 N-W variants have an equal probability of being observed. While this is generally valid when recrystallized materials are being transformed, it does not apply to deformed (i.e., unrecrystallized) steels. The effects and importance of variant selection are considered below after an examination of the behavior of recrystallized austenite.

## 1.4 Transformation Behavior of Recrystallized Austenite

As indicated in Fig. 1.2 (b), the principal component present in recrystallized fcc materials, such as austenite, is the cube or  $\{001\} \langle 010 \rangle$  orientation. During transformation, although in fact 24 K-S (or 12 N-W) products are expected to be formed, their locations can be readily represented by their “averages”, that is, by the three Bain products of the cube parent. Given that  $45^\circ \langle 100 \rangle$  rotations are involved, inspection of Fig. 1.5 indicates that these are the Goss  $\{110\} \langle 001 \rangle$ , the rotated Goss  $\{110\} \langle 110 \rangle$  and the rotated cube  $\{001\} \langle 110 \rangle$ . Thus, the presence of the first two of these orientations in transformed steels (i.e., in ferrite or bainite) is a sign that the austenite was recrystallized prior to transformation. As the rotated cube can also be formed from the Br (i.e., from deformed austenite), see below, its presence is not an infallible sign of prior austenite recrystallization. A schematic illustration of this pattern of events is provided in Fig. 1.6, in which the cube can be seen at the center-top of the diagram. After transformation, it is replaced by the Goss (lower right-hand or RH corner), rotated Goss (lower left-hand or LH corner) and the rotated cube (upper LH and RH corners). Note that

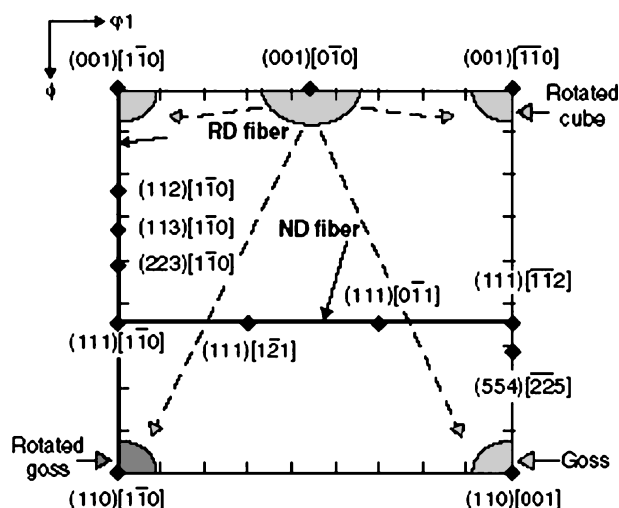
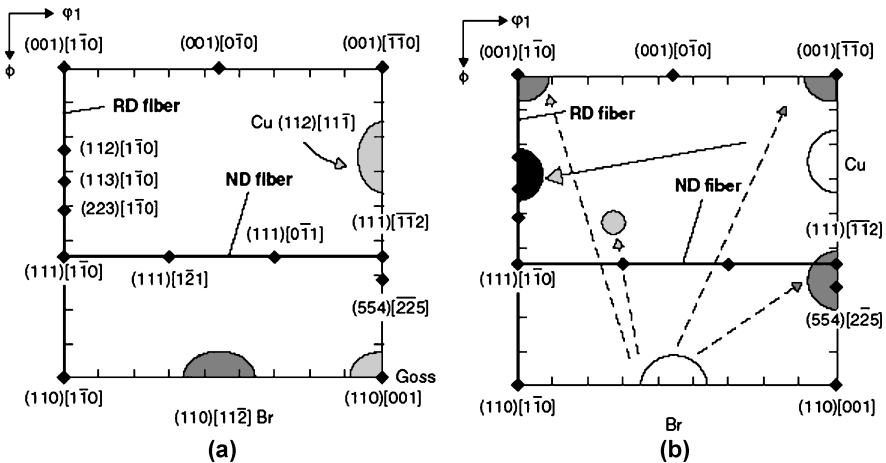


Fig. 1.6  $\phi_2 = 45^\circ$  section of Euler space showing the bcc texture components formed from the fcc cube component.

because of the multiplicities inherent in Euler space referred to previously, the rotated cube appear twice in this diagram. Because the cube is replaced by three components, the intensity of each is about one-third that of the original cube. This is a general feature of transformation textures, in that product textures are usually much less intense than parent textures.

## 1.5 Transformation Behavior of Deformed Austenite

The transformation behavior of *deformed* austenite is considerably more complex for two reasons. One is that many more parent orientations (all those of Fig. 1.3) are present than the single cube considered previously. Each of these can be expected to be responsible for a number of products. The other is the occurrence of variant selection, which is discussed below. Because of these complications, it has been a considerable challenge to unravel the physical events occurring during the transformation and therefore to predict the texture of such materials in a reliable way. The principal features of the texture changes taking place during transformation are summarized in Fig. 1.7. Here, the dominant Cu, Br, and Goss components of the parent rolling texture can be readily identified in the  $\phi_2=45^\circ$  cross-section. The components between Cu and Br, including the S, cannot be seen in this section as they are out of the plane of the diagram. The figure shows how the Cu is replaced by what is known as the “transformed Cu” or  $\{113\}\langle 110\rangle$  to  $\{112\}\langle 110\rangle$  on the LH side of the diagram. The Br transforms into the following components, which are also identified in the illustration: the “transformed Br” or  $\{554\}\langle 255\rangle$  to  $\{332\}\langle 113\rangle$  on the RH side, the rotated cube or  $\{001\}\langle 110\rangle$



**Fig. 1.7**  $\phi_2=45^\circ$  section of Euler space showing (a) two of the face-centered cubic (fcc) rolling texture components (copper, or Cu, and brass, or Br) and (b) the body-centered cubic (bcc) components formed from the Cu and Br.

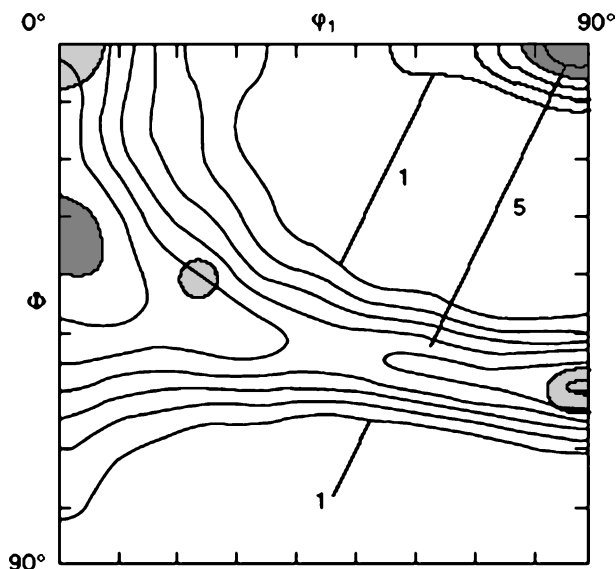


**Fig. 1.8** Transformation texture ( $\phi_2 = 45^\circ$  section) of a 0.02%Nb-0.02%Ti interstitial-free steel hot rolled to 90% reduction and finish rolled at  $820^\circ\text{C}$  ( $1510^\circ\text{F}$ ); maximum intensity = 7.6.

at the top LH and RH corners, and a further variant, located approximately at  $\{112\} \langle 131 \rangle$ . The numerous products resulting from the transformation of the Goss and S components are not shown here for simplicity; however, these lie between the Cu and Br products, as discussed below in more detail.

The transformed Cu and transformed Br orientations are shown again in Fig. 1.8, where they are compared with an industrial transformation texture pertaining to a niobium-titanium microalloyed interstitial-free (IF) steel. The experimental “transformation fiber” can be seen to run from the ideal transformed Cu position on the LH side to the ideal transformed Br location on the RH side. The intermediate positions along this fiber consist of the transformed Goss and transformed S product components referred to previously. Worthy of note in this diagram is the absence of any significant intensity near the cube  $\{001\} \langle 010 \rangle$  and rotated Goss  $\{110\} \langle 110 \rangle$  positions. These would normally be expected to be present according to the K-S and N-W relationships, if all 24 and all 12 products, respectively, were being formed. Their absence introduces the topic of variant selection, described next.

## 1.6 Variant Selection

If all 24 K-S (and all 12 N-W) variants were to appear after transformation then the product orientations would be fairly widely distributed in Euler space and the texture that forms would be relatively homogeneous; that is, no sharp intensities would be observed. However, such is not the case, and numerous workers have

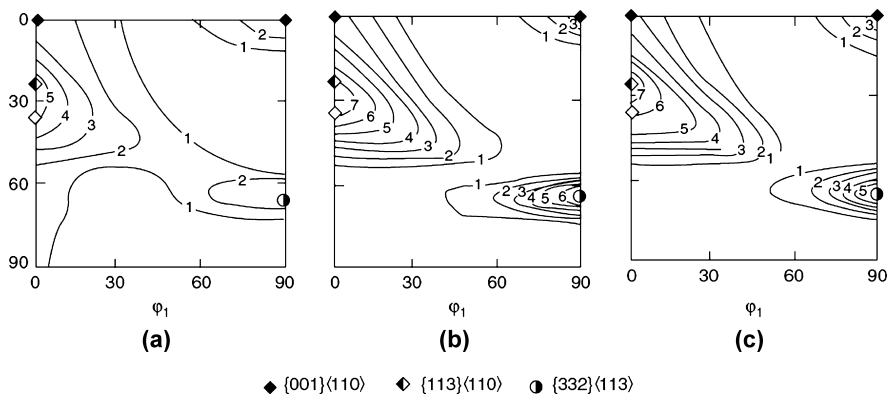


**Fig. 1.9**  $\phi_2 = 45^\circ$  sections of controlled-rolled steels containing the following transformation products. (a) Polygonal ferrite-pearlite, (b) Acicular ferrite, (c) Martensite.

studied the features and causes of variant selection (Ref. 4). For the present purpose, it is sufficient to recognize that only about one-third to one-half of the “expected” products are actually observed, so that the transformation produces less “randomization” of the texture (and therefore less of an intensity decrease) than predicted from a strict application of the K-S and N-W correspondence relations.

This effect has been attributed to the presence of dislocations in the deformed material, which assist in producing the shear that must accompany the transformation [12]. Each type of slip dislocation (i.e., each Burgers vector produced by the prior deformation) is responsible for a particular variant. In addition, there is evidence for the occurrence of reactions between coplanar glide dislocations [13]. These “product” dislocations can also be responsible for the appearance of variants. It has been shown that the rotation axis linking the parent and product crystals in the K-S relation is given by the cross product of the respective Burgers vector and the  $\{111\}$  slip plane normal [12, 13]. The above description linking the appearance of individual K-S variants to the presence of particular perfect dislocations has its counterpart in the link between individual N-W variants and the presence of particular partial dislocations [11]. The K-S correspondence relations (see above) are based on terms of the following general form:  $\{111\} \langle 110 \rangle_\gamma \parallel$  to ..., where the indices not only refer to particular fcc planes and close-packed directions, but to specific Burgers vectors lying on specific slip planes. In the N-W case (see above), the general form is:  $\{111\} \langle 112 \rangle_\gamma \parallel$  to ..., where the various  $\langle 112 \rangle$  indices refer to the Burgers vectors of specific partial dislocations.

An attractive feature of this model is that it can account for differences in the volume fractions of the K-S and N-W components in materials of different stacking-fault energies. It has also been shown to provide a physical explanation for the presence of some hitherto unexpected transformation variants [11]. When the cooling rate and hardenability are high enough to permit bainite and/or martensite to form, variant selection generally takes place and is even accentuated. Nevertheless, the general features of transformation textures are similar, as shown in Fig. 1.9, in



which the textures associated with polygonal ferrite, acicular ferrite (bainite), and martensite are displayed [14]. Here it is readily evident that the highest intensities in each case are situated at the “transformed Cu” and “transformed Br” locations and that the “transformation fiber” links these two ideal orientations. Furthermore, the rotated Goss and cube orientations that are expected in the absence of variant selection are absent. It is also of interest that the K-S and N-W relations are of much less importance with respect to ferrite formation than transformation into bainite or martensite.

## 1.7 Overall Summary of the Rolling and Transformation Behavior

The various observations summarized above and presented in more detail in the literature are collected for easy reference in Fig. 1.10. In this diagram, it can be seen that the Br component (No. 1) is converted into the  $\{332\} \langle 113 \rangle$  and then progressively into the  $\{554\} \langle 225 \rangle$  as the finishing temperature is decreased. It is also sharpened by the addition of substitutional solutes to the steel [15], see Fig. 1.11, which may be a stacking fault energy effect. Similar trends can be attributed to decreasing the grain size [16] (decreasing the reheat temperature), see Fig. 1.12, and to increasing the cooling rate [14]. With regard to the Cu (No. 2, Fig. 1.10), it transforms into the  $\{113\} \langle 110 \rangle$ , a product that moves toward the  $\{112\} \langle 110 \rangle$  and then the  $\{223\} \langle 110 \rangle$  as the finishing temperature is decreased [4, 5]. For reasons that are not yet known, the intensity of the transformed Cu component is relatively insensitive to the grain size, cooling rate, and presence of substitutional solutes.

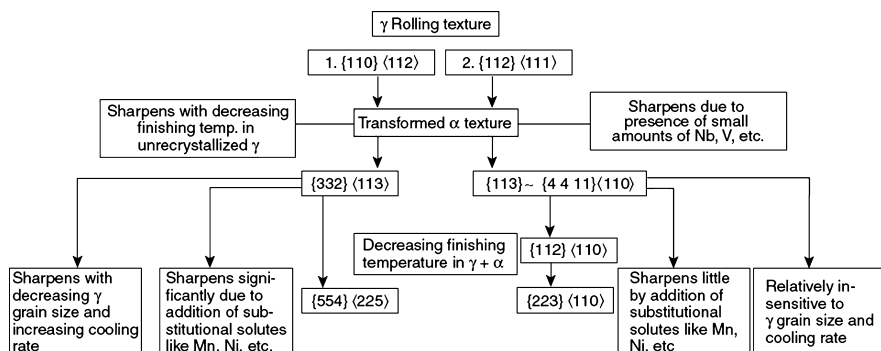


**Fig. 1.10** The effect of compositional and processing variables on the two major components of the transformation texture in steel.

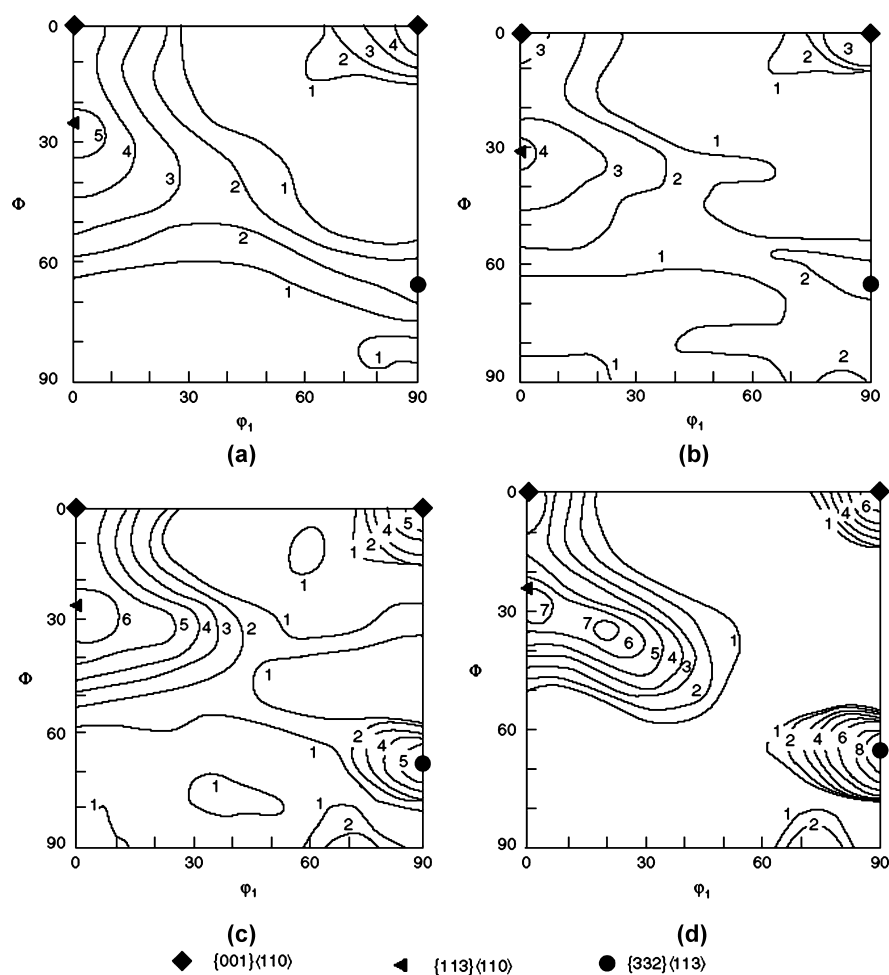


**Fig. 1.11**  $\varphi_2 = 45^\circ$  sections representing transformation textures in steels of basic composition 0.1%C-0.4% Si-0.05% Nb as a function of manganese content. (a) 1.28% Mn, (b) 1.78% Mn, (c) 2.06% Mn, (d) 2.48% Mn.

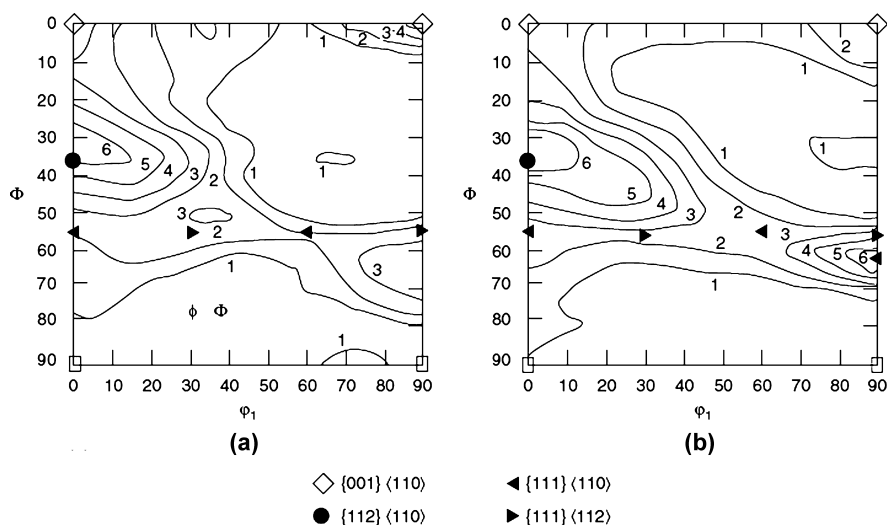
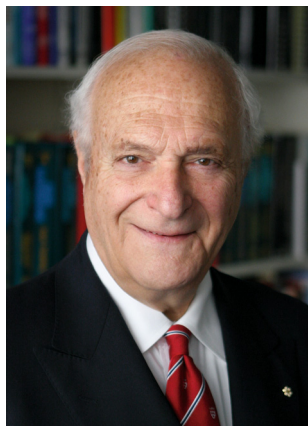


**Fig. 1.12**  $\varphi_2=45^\circ$  sections of a niobium-vanadium microalloyed steel that was quenched after controlled rolling from soaking temperatures of (a) 1250°C (2280°F) and (b) 1050°C (1920°F).

## References

1. H.-J. Bunge, *Texture Analysis in Materials Science*, Butterworths, 1982
2. D. Juul Jensen, *Acta Metall.*, Vol 43, 1995 p 4117
3. E. Furubayashi, H. Miyaji, and M. Nobuki, *Trans. ISIJ*, Vol 27, 1987, p 513
4. R.K. Ray and J.J. Jonas: *Transformation Textures in Steels*, *Int. Mater. Rev.*, Vol 35 1990, p 1–36
5. R.K. Ray, J.J. Jonas, M.P. Butron-Guillen, and J. Savoie, *Transformation Textures in Steels*, *ISIJ Int.*, Vol 34, 1994 p 927–942
6. Y. He, S. Godet, and J.J. Jonas: Representation of Misorientations in Rodrigues-Frank Space: Application to the Bain, Kurdjumov-Sachs and Nishiyama-Wassermann Orientation Relationships in the Gibeon Meteorite; *Acta Materialia*, 53, (2005), pp. 1179–1190.
7. Y. He, S. Godet, P.J. Jacques and J.J. Jonas: Crystallographic Features of the  $\gamma$ -to- $\alpha$  Transformation in a Nb-Added Transformation-Induced Plasticity Steel; *Metall. and Mater. Trans. A*, 37, (2006), pp. 2641–2653.
8. H.J. Bunge, W. Weiss, H. Klein, L. Weislak, U. Garbe, and J.R. Schneider, *J. Appl. Crystallogr.*, Vol 36, 2003, p 137
9. Y. He, S. Godet, P.J. Jacques and J.J. Jonas: Crystallographic Relations between Face- and Body-Centred Cubic Crystals Formed under Near-Equilibrium Conditions: Observations from the Gibeon Meteorite; *Acta Materialia*, vol. 54, (2006), pp. 1323–1334.
10. T. Nagano and M. Enomoto, Calculation of the Interfacial Energies and Equilibrium Shape of Ferrite in Austenite, *Metall. and Mater. Trans. A*, 2004, in press.
11. J. Jonas, Y. He, and S. Godet: The Possible Role of Partial Dislocations in Facilitating Transformations of the Nishiyama-Wassermann Type, *Scr. Mater.*, Vol 52, 2005, p 175–179
12. N.J. Wittridge, J.J. Jonas, and J.H. Root, A Dislocation-Based Model for Variant Selection During the  $\gamma$ -to- $\alpha$  Transformation, *Metall. Mater. Trans.*, Vol 32A, 2001, p 889–901

13. M. Sum and J.J. Jonas, A Dislocation Reaction Model for Variant Selection During the Austenite-to-Martensite Transformation, Textures Microstruct., Vol 31, 1999, p 187–215
- Transformations in Metals and Alloys, Van Nostrand Reinhold, 1981, p 382
14. T. Yutori and R. Ogawa, Tetsu-to-Hagane', Vol 65, 1979, p 1747
15. H. Inagaki, Proc. Sixth International Conference on Textures of Materials, Vol 1, ISIJ, Tokyo, 1981, p 149
16. H. Inagaki and M. Kodama, Tetsu-to-Hagane', Vol 67, 1981, p S640



John J. Jonas  
Professor  
McGill University  
Montreal  
Canada



## Chapter 2

# Mathematics of Crystallographic Texture in Martensitic and Related Transformations

H.K.D.H. Bhadeshia, S. Kundu, and H. Abreu

**Abstract.** This paper is an introduction to the mathematical estimation of the crystallographic texture and microstructure resulting from the displacive transformation of austenite in steels, under the influence of an externally applied system of stresses. It begins with an introduction to the problem, a description of the phenomenological theory of martensite crystallography, and the application of this theory along with a variant selection criterion to determine the texture due to solid-state, displacive transformation. It is demonstrated that there remain difficulties which make a complete closure between theory and experiment unlikely. Progress is needed in relating the chemical and mechanical driving forces for phase transformation to the evolution of overall volume fractions of different crystallographic variants.

## 2.1 Introduction

In general usage the term *texture* refers to the feel of a material or object, due to some sort of a pattern within the material. *Crystallographic texture* is said to exist in a polycrystalline material when the distribution of crystal orientations is not random relative to some frame of reference. An understanding of texture can help relate single-crystal properties to those of aggregates of crystals [1, 2]. The texture can also be used to engineer the properties of grain boundaries to optimise them for corrosion resistance, magnetic anisotropy etc.

---

H.K.D.H. Bhadeshia  
University of Cambridge, Materials Science and Metallurgy, Cambridge, U.K.

S. Kundu  
TATA Steel, Research and Development Division, Jamshedpur, India

H. Abreu  
Universidade Federal do Ceará, Engenharia Metalúrgica e de Materiais, Fortaleza, Brasil

In a displacive transformation, the crystal structure of the parent is deformed into that of the product without the need for any diffusion. Since this involves the coordinated motion of atoms, the product phase is confined within the boundaries of the original austenite grain in which it nucleated; there is always therefore a fixed orientation relationship between the parent and the product phases. In this simplified scenario, it becomes possible in principle to rigorously calculate the transformation texture. To do this requires an understanding of the classical theory of martensite crystallography [3, 4]. We begin therefore with an introduction to this theory.

## 2.2 Crystallographic Theory of Martensite

### 2.2.1 *Structure of the Interface*

Any process which contributes to the formation of martensite cannot rely on assistance from thermal activation. There must therefore exist a high level of continuity across the interface, which must either be coherent or semi-coherent. A stress-free fully coherent interface is impossible for the austenite ( $\gamma$ ) to martensite ( $\alpha'$ ) transformation since the lattice deformation  $\mathbf{B}\mathbf{R}$  is an invariant-line strain. The semi-coherent interface must be such that the interfacial dislocations can glide as the interface moves (climb is not permitted). It follows that the Burgers vectors of the interface dislocations must not lie in the interface plane unless the dislocations are screw in character.

There is an additional condition for a semi-coherent interface to be glissile. The line vectors of the interfacial dislocations must lie along an *invariant-line*, i.e., a line which joins the parent and product crystals without any rotation or distortion. Why is that? If there is any distortion along the dislocation line, then other dislocations are needed to accommodate that misfit. It will then be necessary to have more than one set of non-parallel dislocations in the interface. These non-parallel dislocations can intersect to form jogs which render the interface sessile.

It follows that for martensitic transformation to be possible, the deformation which changes the parent into the product must leave one or more lines invariant (unrotated, undistorted). A deformation which leaves one line invariant is called an *invariant-line strain*.

### 2.2.2 *The Shape Deformation*

The passage of a slip dislocation through a crystal causes the formation of a step where the glide plane intersects the free surface (Fig. 2.1 (a),(b)). The passage of many such dislocations on parallel slip planes causes macroscopic shear (Fig. 2.1 (c), (d)). Slip causes a change in shape but not a change in the crystal structure, because the Burgers vectors of the dislocations are also lattice vectors.

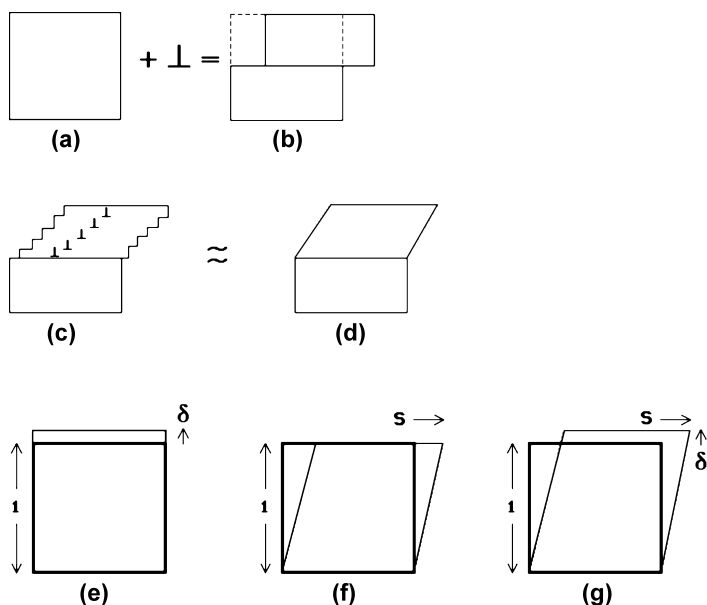


**Fig. 2.1** (a, b) Step caused by the passage of a slip dislocation. (c, d) Many slip dislocations, causing a macroscopic shear. (e) An invariant-plane strain with a uniaxial dilatation. (f) An invariant-plane strain which is a simple shear. (g) An invariant-plane strain which is the combined effect of a uniaxial dilatation and a simple shear.

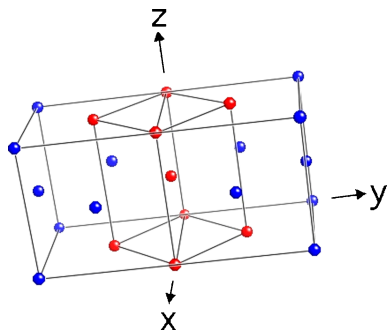
During martensitic transformation, the pattern in which the atoms in the parent crystal are arranged is *deformed* into that appropriate for martensite, there must be a corresponding change in the macroscopic shape of the crystal undergoing transformation. The dislocations responsible for the deformation are in the  $\alpha'/\gamma$  interface, with Burgers vectors such that in addition to deformation they also cause the change in crystal structure. The deformation is such that an initially flat surface becomes uniformly tilted about the line formed by the intersection of the interface plane with the free surface. Any scratch traversing the transformed region is similarly deflected though the scratch remains connected at the  $\alpha'/\gamma$  interface. These observations, and others, confirm that the measured shape deformation is an invariant-plane strain (Fig. 2.1 (e)–(g)) with a large shear component ( $\approx 0.22$ ) and a small dilatational strain ( $\approx 0.03$ ) directed normal to the habit plane.

### 2.2.3 The Bain Strain

Consider the displacive transformation of austenite (cubic-close packed crystal structure) to martensite (body-centred cubic or body-centred tetragonal). The change in



**Fig. 2.2** Two face-centred cubic unit cells of austenite, together with a body-centred tetragonal cell of austenite. The Bain strain (not illustrated here) involves a compression of the body-centred tetragonal cell of austenite along  $z$  and a uniform expansion on the  $x$ - $y$  plane.



crystal structure is achieved by a homogeneous deformation known as the Bain strain  $\mathbf{B}$ , which although proposed in 1924 [5] has stood the test of time as the pure deformation which achieves the desired change with the smallest strains [6]. The diagonal terms of the  $3 \times 3$  matrix  $\mathbf{B}$  are given by  $a_{\alpha'}/a_{\gamma}$ ,  $\sqrt{2}a_{\alpha'}/a_{\gamma}$  and  $\sqrt{2}a_{\alpha'}/a_{\gamma}$ , whereas the remaining terms are zero when  $\mathbf{B}$  is defined relative to the principal axes.  $a_{\alpha'}$  and  $a_{\gamma}$  are the lattice parameters of martensite and austenite, respectively. The Bain correspondence is illustrated in Fig. 2.2 and implies the orientation relationship:

$$\begin{aligned} [0\ 0\ 1]_{\gamma} & \parallel [0\ 0\ 1]_{\alpha'} \\ [1\ -1\ 0]_{\gamma} & \parallel [1\ 0\ 0]_{\alpha'} \\ [1\ 1\ 0]_{\gamma} & \parallel [0\ 1\ 0]_{\alpha'} \end{aligned}$$

This orientation is not observed experimentally because the strain energy associated with  $\mathbf{B}$  would be too large, several  $\text{kJ mol}^{-1}$  [7], which is far in excess of the chemical driving force for transformation [8].

Furthermore, the Bain strain does not satisfy the minimum requirement of martensitic transformation, that the deformation must leave one line invariant in order to ensure sufficient coherency in the  $\gamma/\alpha'$  interface to enable it to move without diffusion [3, 4, 9–11]. This can be seen in Figs. 2.3 (a), (b); the austenite is represented as a sphere which, as a result of the Bain strain  $\mathbf{B}$ , is deformed into an ellipsoid of revolution which represents the martensite. There are no lines which are left undistorted or unrotated by  $\mathbf{B}$ . There are no lines in the  $(0\ 0\ 1)_{\gamma}$  plane which are undistorted. The lines  $ab$  and  $cd$  are undistorted but are rotated to the new positions  $a'b'$  and  $c'd'$ . Such rotated lines are not invariant. However, the combined effect of the Bain strain  $\mathbf{B}$  and the rigid body rotation  $\mathbf{R}$  is indeed an invariant-line strain (ILS) because it brings  $cd$  and  $c'd'$  into coincidence (Fig. 2.3 (c)). This is the reason why the observed irrational orientation relationship differs from that implied by the Bain strain. Indeed, the rotation required to convert  $\mathbf{B}$  into an invariant line strain precisely corrects the Bain orientation into that which is observed experimentally.

It is now possible to reach some conclusions regarding orientation relationships in relation to transformation textures, whether these are for displacive or reconstructive phase change [12, 13].

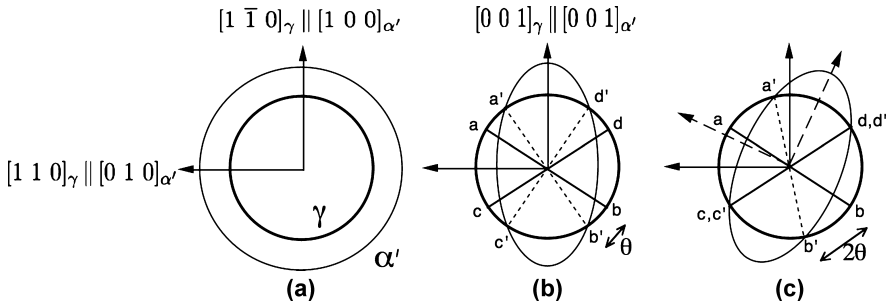


**Fig. 2.3** (a) and (b) show the effect of the Bain strain on austenite, which when undeformed is represented as a sphere in three-dimensions. The strain transforms it to an ellipsoid of revolution. (c) shows the ILS obtained by combining the Bain strain with a rigid body rotation through an angle  $\theta$ .

- The Bain orientation relationship does not exist. It is not appropriate to use this in calculating transformation texture. Any favourable conclusions reached based on the Bain orientation [14, 15] must be regarded as fortuitous (Hutchinson 2005).
- The Bain deformation is an incomplete description of the transformation strain and hence should not form the basis for variant selection [16].

As stated above, the combination **BR** predicts the exact orientation relationship which is irrational. However, it is often assumed in texture analysis that the orientation relationship between the austenite and martensite is that due to Kurdjumov-Sachs (KS) or Nishiyama-Wasserman (NW) [13, 17–19], but it has been known for some time that the true relation must be irrational [3, 4, 9, 11]. Although the difference between this irrational and assumed orientation may seem less than a few degrees, it is vital because the assumed orientations do not in general lead to an invariant-line between the parent and product lattices. The existence of an invariant line is an essential requirement for martensitic transformation to occur. It is not surprising therefore, that Nolze [20] in his experimental study of several hundred thousand  $\gamma/\alpha'$  orientation relations, found detailed deviations from assumed Kurdjumov-Sachs etc. orientations.

Much is often made of the fact that there are 24 variants of KS and only 12 of NW. However, if the actual irrational orientation is used then there will always be 24 variants.

## 2.2.4 Phenomenological Solution

We have seen that there is no rotation which can make **B** into an invariant-plane strain since this would require two non-parallel invariant-lines. It follows that austenite cannot be transformed into martensite by a homogeneous strain which is

an IPS. And yet, the observed shape deformation leaves the habit plane undistorted and unrotated, i.e., it is an invariant-plane strain.

The phenomenological theory of martensite crystallography solves this remaining problem (Fig. 2.4). The Bain strain converts the structure of the parent phase into that of the product phase. When combined with an appropriate rigid body rotation, the net homogeneous lattice deformation  $\mathbf{RB}$  is an invariant-line strain (step  $a$  to  $c$  in Fig. 2.4). However, the observed shape deformation is an invariant-plane strain  $\mathbf{P}_1$  (step  $a$  to  $b$  in Fig. 2.4), but this gives the wrong crystal structure. If a second homogeneous shear  $\mathbf{P}_2$  is combined with  $\mathbf{P}_1$  (step  $b$  to  $c$ ), then the correct structure is obtained but the wrong shape since

$$\mathbf{P}_1 \mathbf{P}_2 = \mathbf{RB}$$

These discrepancies are all resolved if the shape changing effect of  $\mathbf{P}_2$  is cancelled macroscopically by an inhomogeneous lattice-invariant deformation, which may be slip or twinning as illustrated in Fig. 2.4.

The theory explains all the observed features of the martensite crystallography. The orientation relationship is predicted by deducing the rotation needed to change the Bain strain into an invariant-line strain. The habit plane does not have rational indices because the amount of lattice-invariant deformation needed to recover the correct the macroscopic shape is not usually rational. The theory predicts a sub-

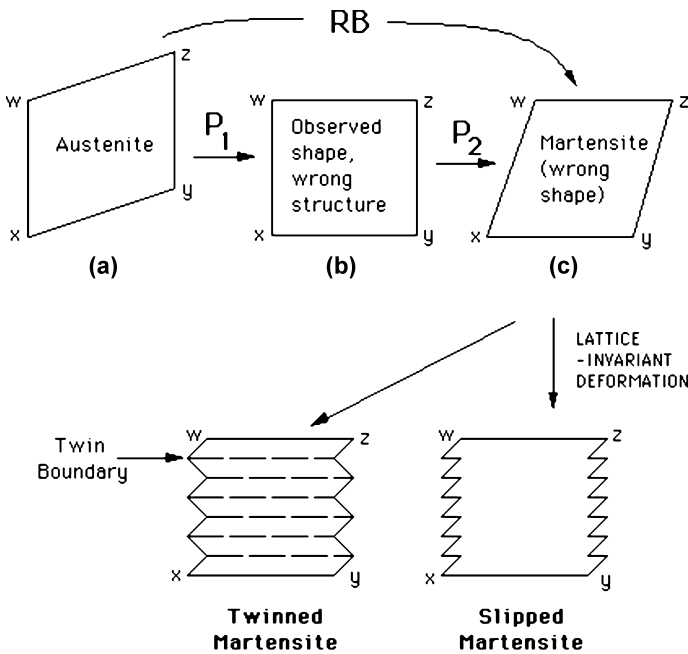


Fig. 2.4 The phenomenological theory of martensite crystallography.

structure in plates of martensite (either twins or slip steps) as is observed experimentally. The transformation goes to all the trouble of ensuring that the shape deformation is macroscopically an invariant-plane strain because this reduces the strain energy when compared with the case where the shape deformation might be an invariant-line strain.

### 2.2.5 The Crystallographic Set

In order to understand how to use the crystallographic theory of martensite in estimating texture, it is important to realise that the transformation is dominated by strain energy due to the shape deformation and hence many of the crystallographic variables cannot be varied independently. Figure 2.5 illustrates two crystals separated by an interface. The relative orientation of the two crystals can be described in terms of an axis-angle pair so that there are three degrees of freedom associated with the orientation relationship. One of these is the right-handed angle of rotation and the other two are independent direction cosines of the rotation axis. The interface plane, which is identified by its normal, itself can be varied whilst keeping the orientation relationship fixed. This adds another two degrees of freedom, making a total of five independent ways in which the properties of the bicrystal can be varied.

This conventional description of the degrees of freedom is severely constrained in the case of displacive transformations where the orientation relationship, interface plane (habit plane), lattice-invariant deformation and shape deformation are mathematically connected by the single equation of the crystallographic theory. Changing any one of these necessarily alters all the others in this *crystallographic set*, an example of which is given in Fig. 2.6. It is not rigorous to assign an orientation and then use independent data for the shape deformation, as is sometimes done [12, 19, 21]. Similarly, the use of shears which are consistent with an assumed orientation relationship but not with the habit plane [22] contradicts the need for a self-consistent mathematical set. In recent work it has been incorrectly proposed

#### Degrees of freedom

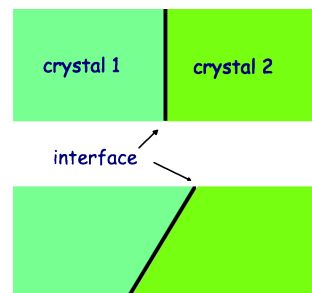


**Fig. 2.5** The conventional degrees of freedom associated with a bicrystal containing an interface. Translations in the plane of the interface are neglected here.

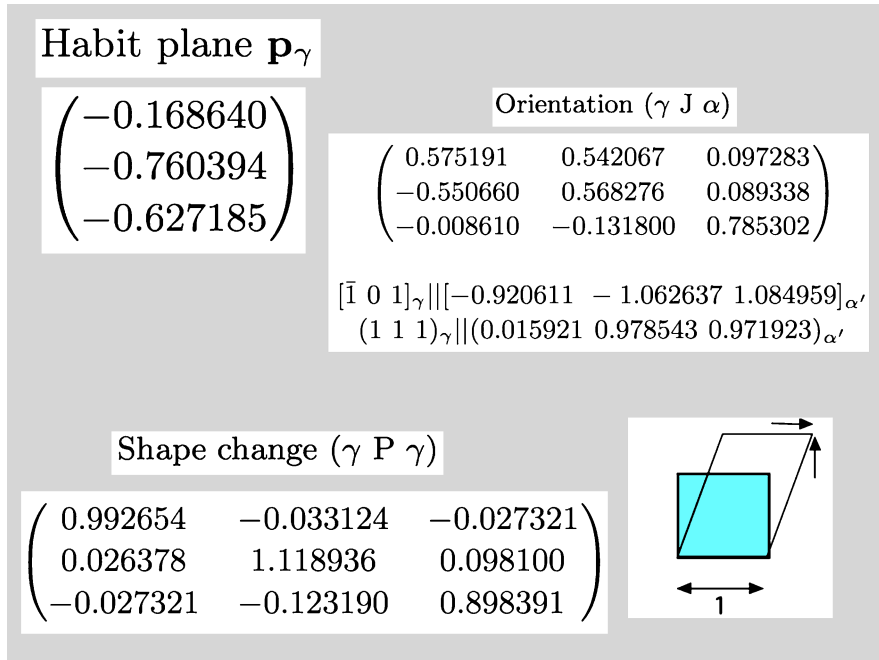


**Fig. 2.6** An example of a complete crystallographic set describing a single plate of martensite, including the habit plane, the shape deformation and the orientation relationship (and implicitly the lattice-invariant deformation). All of these quantities are mathematically connected and cannot in general be varied independently.

that the amount of lattice-invariant shear (in the form of twin fraction) can be independently varied while keeping all the other characteristics constant [23].

## 2.3 Variant Selection

Displacive transformations are best regarded as deformation mechanisms which at the same time alter the crystal structure. The variant selection problem then reduces to issues similar to the selection of slip systems out of all the possibilities available during single-crystal deformation [1]. A slip system consists of a slip plane and slip direction, for example,  $(1 \ 1 \ 1)[1 \ 0 \ -1]$  is one of 12 crystallographically equivalent systems in austenite. An applied stress is resolved on to each of the slip systems, and that which has the highest resolved shear stress is said to be activated.

By analogy, the deformation due to martensitic transformation occurs on the habit plane (unit normal  $\mathbf{p}$ ) in a displacement direction (unit vector  $\mathbf{d}$ ). The latter will not lie precisely in the habit plane because the dilatational strain due to the volume change of transformation is directed normal to the habit plane. The domi-

nating strain is the shear parallel to the habit plane at about 0.26. The total deformation is expressed as a  $3 \times 3$  matrix  $\mathbf{P}$ :

$$(\gamma \mathbf{P} \gamma) = \mathbf{I} + m[\gamma; \mathbf{d}](\mathbf{p}; \gamma^*)$$

where  $m$  is the magnitude of the shape deformation and  $\gamma$  and  $\gamma^*$  represent the real and reciprocal bases of the austenite.  $\mathbf{P}$  thus completely defines the deformation system, and there will in general be 24 different variants.

The shape deformation  $\mathbf{P}$  is an invariant-plane strain and is the experimentally observed permanent shape change caused when martensite forms.

When calculating the favoured system during slip deformation, it is the macroscopic shear on the slip plane and slip direction which determines selection through interaction with the applied stress. The detailed atomic motions (e.g. in surmounting Peierls barriers) or microscopic heterogeneities (due to the discrete nature of atoms) are irrelevant in the selection of the system. In a similar way, it is the interaction of the applied stress with  $\mathbf{P}$  which determines variant selection.  $\mathbf{B}$  and  $\mathbf{R}$  or other factorisations of the shape deformation are incomplete descriptions of the relevant strain. The interaction energy which provides the mechanical driving force for transformation [24]:

$$U = \sigma_N \delta + \tau s$$

where  $\sigma_N$  is the stress component normal to the habit plane,  $\tau$  is the shear stress resolved on the habit plane in the direction of shear.  $\delta$  and  $s$  are the respective normal and shear strains associated with transformation. The energy  $U$  can be used as a rigorous variant selection criterion when the stresses applied are less than those required to cause plasticity in the austenite prior to its transformation or when the plastic strain is not the dominant effect in variant selection [25].

The conclusions that can be reached from the discussion in this section are:

- In calculating transformation texture it is necessary to use a self-consistent crystallographic set, rather than make independent assumptions about the orientation relationship and shape deformation as is sometimes done. The set must be such that the lattice deformation  $\mathbf{B}\mathbf{R}$  is an invariant-line strain; the analysis in [21] does not satisfy this criterion.
- The deformation due to martensitic transformation is an invariant-plane strain  $\mathbf{P}$ . It is this which should be used to calculate the interaction energy (variant selection) rather than, for example, the Bain strain [26].

The Patel and Cohen derivation of the interaction energy  $U$  can be generalised to an arbitrary stress tensor as follows [27]. Assuming that the summation convention applies,

$$\begin{aligned} \sigma_N &= (\sigma_{ij} p_i p_j) \mathbf{p} \\ \tau &= (\sigma_i - \sigma_N) \cdot \mathbf{e} = \sigma_{ij} p_j \mathbf{e}_i \\ U &= [\delta \sigma_{ij} p_i p_j + s \sigma_{ij} \mathbf{e}_i p_j] = \sigma_{ij} p_j [\delta p_i + s \mathbf{e}_i] \\ &= \sigma_{ij} p_j m d_i \\ &\equiv \sigma_{ij} \epsilon_{ij} \end{aligned}$$

where  $\sigma_t$  is the traction on the plane defined by the unit habit plane normal  $\mathbf{p}$  (components  $p_1, p_2, p_3$ ), and  $\mathbf{e}$  (components  $e_1, e_2, e_3$ ), is the unit direction on the habit plane along which the shear component of the shape deformation is directed;  $\epsilon_{ij}$  is

$$\epsilon_{ij} = \frac{(\gamma P \gamma) + (\gamma P' \gamma)}{2} - I$$

As with Patel and Cohen, these equation recognise the fact that the transformation strain is plastic.

## 2.4 Transformation Plasticity

Consider an arbitrary vector  $\mathbf{u}$  traversing a grain of austenite prior to transformation. This vector makes an intercept  $\Delta \mathbf{u}$  with a domain of austenite that eventually ends up as a plate of the displacive transformation product. It follows that the new vector  $\mathbf{v}$  is given by:

$$\mathbf{v} = \mathbf{P} \Delta \mathbf{u} + (\mathbf{u} - \Delta \mathbf{u})$$

This is generalised for a large number of plates in many austenite grains as follows:

$$\mathbf{v} = \sum_{k=1}^n \sum_{j=1}^{24} \mathbf{P}_j^k \Delta \mathbf{u}_j^k + \left( \mathbf{u} - \sum_{k=1}^n \sum_{j=1}^{24} \Delta \mathbf{u}_j^k \right)$$

where  $j=1 \dots 24$  represents the 24 crystallographic variants possible in each austenite grain, and  $k=1 \dots n$  represents the  $n$  austenite grains traversed by the

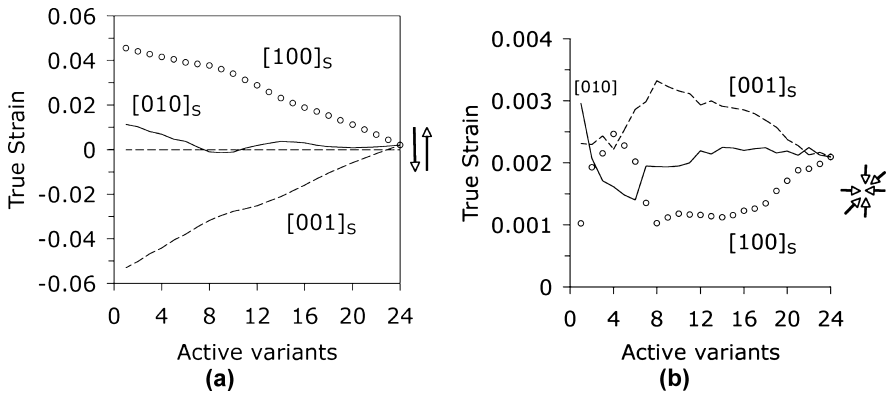


**Fig. 2.7** (a) Transformation strain along the sample axes when a polycrystalline sample is subjected to pure shear; (b) much small strains when subjected to hydrostatic compression. After Kundu et al. [25].

vector  $\mathbf{u}$ . In this scenario of a large number of plates, the various intercepts can be approximated by  $f_j^k \mathbf{u}$  where  $f_j^k$  is the fraction of sample transformed by variant  $j$  in austenite grain  $k$ .

The deformation caused by a particular plate  $j$  in austenite grain  $k$ , i.e.,  $(\gamma_k \mathbf{P}_j \gamma_k) \equiv \mathbf{P}_j^k$ . The remaining 23 such matrices for grain 1 of austenite can be deduced using symmetry operations and expressed in the reference frame of the sample using a similarity transformation.

Some calculations illustrating the anisotropy of strains as a function of the number of crystallographic variants of martensite allowed are illustrated in Fig. 2.7 for uniaxial tension and compression. That displacive transformations produce highly anisotropic strains when variant selection is significant has been demonstrated experimentally [28–30].

*An important outcome of the fact that transformation strains can be calculated using the crystallographic set of martensite is that such strains can be exploited as an alternative or supplemental method of assessing texture.*

## 2.5 The Intensity of the Texture

The analysis of texture as described above and in the published literature, leaves open the question of the degree of variant selection as a function of the magnitude of the applied stress.

The total free energy available for transformation is the sum of chemical and mechanical components, the latter being zero in the absence of an applied stress during transformation [28]:

$$\Delta G = \Delta G_{\text{CHEM}} + \Delta G_{\text{MECH}}$$

where  $\Delta G_{\text{MECH}} \equiv U$ .

It would be reasonable to assume that there is strong variant selection when the ratio of  $\Delta G_{\text{MECH}}/\Delta G$  is large [29]. This turns out to be the case as illustrated in Fig. 2.8. There is a strong, albeit empirical, linear correlation between the ratio  $\Delta G_{\text{MECH}}/\Delta G$  and the number of most favoured variants allowed to form in each of the austenite grains [25]. This is an important observation in that it allows the extent of variant selection, and hence the transformation strains to be calculated as a function of stress for any steel as long as the thermodynamic quantities can be estimated. Nevertheless, this clearly is an area where progress is needed from a fundamental point of view.

An additional point to emerge from this analysis is the way in which the energy  $U$  is calculated. Most publications treat the problem using elasticity but the strain due to transformation is plastic so the elastic calculations underestimate  $U$  by a factor of 2. This is important when calculating the ratio of mechanical to total driving force [27].



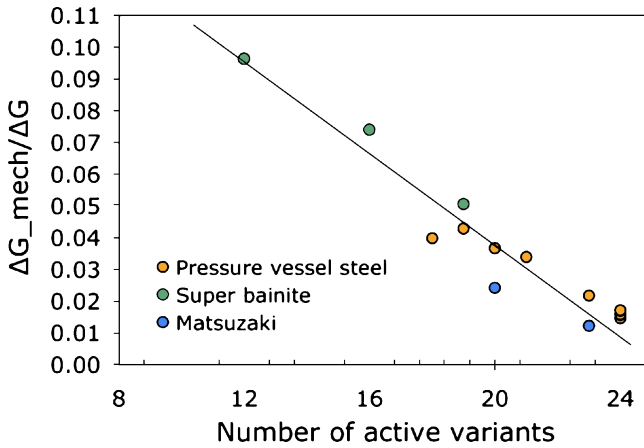


**Fig. 2.8** The ratio of the mechanical to total driving force for transformation as a function of the number of active variants for a variety of steels [25].

## 2.6 Summary

We have seen that there are significant advantages in dealing with the crystallographic texture due to displacive transformations using the crystallographic theory of martensite along with a variant selection criterion based on the classical interaction of stress with the shape deformation. The calculation of texture at the same time leads to the estimation of the net transformation strain in any direction. This strain may be highly anisotropic depending both on the strength of the texture of the parent austenite and of the extent of variant selection. The latter in turn depends on the ratio of the mechanical driving force to the total driving force for transformation. Variant selection is minimised when the chemical driving force dominates the total. Further work is needed to develop a quantitative understanding of the intensity of the transformation texture as a function of the variant selection criterion.

## References

- [1] E. Schmid, W. Boas: *Plasticity of Crystals* (translated from the 1935 edition of *Kristallplastizität*): F. A. Hughes and Co., London, U.K., 1950.
- [2] D. Dörner, S. Zaeferrer, L. Lahn, D. Raabe: *Journal of Magnetism and Magnetic Materials* 304 (2006) 183–186.
- [3] J.K. Mackenzie, J.S. Bowles: *Acta Metallurgica* 2 (1954) 138–147.
- [4] M.S. Wechsler, D.S. Lieberman, T.A. Read: *Trans. AIME Journal of Metals* 197 (1953) 1503–1515.
- [5] E.C. Bain: *Trans. AIME* 70 (1924) 25–46.

- [6] J.S. Bowles, C.M. Wayman: *Metallurgical Transactions* 3 (1972) 1113–1121.
- [7] M. Suezawa: *Materials Science and Engineering* 48 (1981) 255–260.
- [8] J.W. Christian: Thermodynamics and kinetics of martensite: in: G.B. Olson, M. Cohen (Eds.), *International Conference on Martensitic Transformations {ICOMAT} '79*: 1979: pp. 220–234.
- [9] J.S. Bowles, J. K. MacKenzie: *Acta Metallurgica* 2 (1954) 129–137.
- [10] J.W. Christian: *Metallurgical Transactions A* 13 (1982) 509–538.
- [11] H.K.D.H. Bhadeshia: *Geometry of Crystals*: 2nd edition, Institute of Materials, 2001.
- [12] W.B. Hutchinson, L. Ryde, P.S. Bate: *Materials Science Forum* 495–497 (2005) 1141–1149.
- [13] S. Kundu, H.K.D.H. Bhadeshia: *Scripta Materialia* 55 (2006) 779–781.
- [14] H. Miyaji, E.-I. Furubayashi: *Textures and Microstructure* 12 (1990) 189–197.
- [15] L. Kestens, R. Decocker, R. Petro: *Materials Science Forum* 408–412 (2002) 1173–1178.
- [16] E.-I. Furubayashi, H. Miyaji, M. Nobuki: *Trans. Iron Steel Institute of Japan* 27 (1987) 513–519.
- [17] R.P.L. Kestens, Y. Houbaert: *ISIJ International* 43 (2003) 1444–1452.
- [18] B. Bruckner, G. Gottstein: *ISIJ International* 41 (2001) 468–477.
- [19] P. Bate, B. Hutchinson: *Acta Materialia* 48 (2000) 3183–3192.
- [20] G. Nolze: *Zeitschrift für Metallkunde* 95 (2004) 744–755.
- [21] D.W. Suh, H.N. Han, S.J. Kim: *ISIJ International* 46 (2006) 341–343.
- [22] Y. Higo, F. Lécroisey, T. Mori: *Acta Metallurgica* 22 (1974) 313–323.
- [23] T. Mori, E.C. Oliver, M.R. Daymond and P.J. Withers, *Materials Science and Engineering A*: Volume 378, Issues 1–2, 25 July 2004, Pages 479–483.
- [24] J.R. Patel, M. Cohen: *Acta Metallurgica* 1 (1953) 531–538.
- [25] S. Kundu, K. Hase, H.K.D.H. Bhadeshia: *Proceedings of the Royal Society A* 463 (2007) 2309–2328.
- [26] H.N. Han, D.W. Suh: *Acta Materialia* 51 (2003) 4907–4917.
- [27] S. Kundu, H.K.D.H. Bhadeshia: *Scripta Materialia* 57 (2007) 869–872.
- [28] H.K.D.H. Bhadeshia: Possible effects of stress on steel weld microstructures: in: H. Cerjak, H.K.D.H. Bhadeshia (Eds.), *Mathematical Modelling of Weld Phenomena – II*: Institute of Materials, London, U.K., 1995: pp. 71–118.
- [29] H.K.D.H. Bhadeshia, S.A. David, J.M. Vitek, R.W. Reed: *Materials Science and Technology* 7 (1991) 686–698.
- [30] A. Matsuzaki, H.K.D.H. Bhadeshia, H. Harada: *Acta Metallurgica and Materialia* 42 (1994) 1081–1090.
- [31] J.W. Stewart, R.C. Thomson, H.K.D.H. Bhadeshia: *Journal of Materials Science* 29 (1994) 6079–6084.



Harshad Kumar Dharamshi Hansraj Bhadeshia  
Professor of Physical Metallurgy,  
Department of Materials Science  
and Metallurgy,  
University of Cambridge  
UK



# Chapter 3

## Structure and Strength of IF Steel After Large Strain Deformation

Niels Hansen, Xiaoxu Huang, and Naoya Kamikawa

**Abstract.** Interstitial free (IF) steel with an ultrafine microstructure has been produced by three different routes: (i) cold rolling, (ii) accumulative roll-bonding (ARB) and (iii) martensitic transformation followed by cold rolling. The microstructure refines with increasing strain without saturation to a value of about 100 nm at an equivalent strain ( $\epsilon_{VM}$ ) of 8, which is the maximum strain investigated. At all strains a microscopic analysis by transmission electron microscopy (TEM) and electron backscatter diffraction (EBSD) shows that the microstructure is subdivided by dislocation boundaries and high-angle boundaries. For both cold rolled samples and ARB samples the flow stress increases as the boundary spacing decreases. For the finest structures this leads to a flow stress at room temperature in the range 900–1000 MPa. Finally structure-property relationships are discussed especially the effect of post-processing treatments by annealing and by low strain deformation.

### 3.1 Introduction

The finer the structure the stronger the metal is a guiding principle for material scientists and technologists. This principle is the basis for the current interest in new and advanced materials with fine scale structures down to the nanometer dimension. This has led to the development of new processes and to characterization and modelling of relationships between processing, structure and properties of materials with extremely fine microstructures of the order of tens to hundreds of

---

N. Hansen, X. Huang, and N. Kamikawa  
Center for Fundamental Research: Metal Structures in Four Dimensions, Materials Research  
Department, Risø National Laboratory – Technical University of Denmark (Risø DTU),  
DK-4000 Roskilde, Denmark

**Table 3.1** Chemical composition of IF steels (wt%).

Condition	C	N	Si	Mn	S	P	Ti	Al	Cu	B
Cold rolled (CR)	0.0031	0.0018	<0.01	0.15	0.005	0.01	0.049	0.054	–	<0.0001
ARB	0.002	0.003	0.01	0.17	–	0.012	0.072	–	0.01	–
Quenched + CR										
steel A	0.0026	0.0024	<0.01	1.48	0.005	0.008	0.046	0.015	–	0.0026
steel B	0.0049	0.0011	0.14	3.14	0.001	<0.001	0.021	0.009	–	0.0025

nanometers. This research and development has covered a wide range of metallic materials where the structural refinement has been obtained by thermomechanical processing.

In the following the structural refinement by plastic deformation will be discussed in general and exemplified by the structural evolution during rolling of interstitial free (IF) steel. In order to cover a large strain range three different processes have been investigated: (i) traditional rolling, (ii) accumulative roll-bonding (ARB) and (iii) martensitic transformation followed by rolling. For the chemical composition of the IF steels see Table 3.1. An increase in strain is followed by a decrease in the scale of the structure down to approximately 100 nm without saturation. The reduction in the structural scale is followed by an increase in strength which is determined in tension and related to characteristic strengthening parameters determined by electron microscopy. The research and development has been successful as samples with a high strength have been produced. However, the ductility is low and optimization of properties has been sought through post-process treatments which are described and discussed.

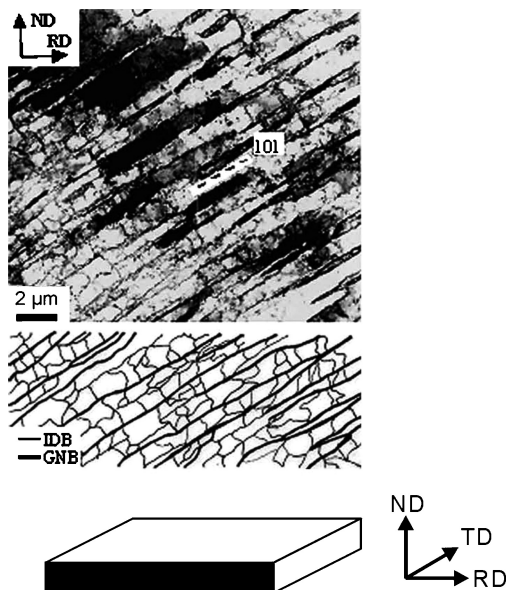
The present paper is an overview based mainly on research carried out at Risoe in collaboration with scientists abroad.

## 3.2 Universal Pattern of Structural Evolution

### 3.2.1 Cold Rolling

Plastic deformation of a metals requires mechanical energy where a large part is transformed into heat during processing. Only a small amount of energy of the order of few percent or less is stored in the metal mainly as dislocations. These dislocations arrange in different configurations, dependent on material and process parameters. It has however been found that the patterning follows general principles and the evolution of many different structures and their characteristics can therefore be described within a common framework [1, 2]. Such principles are for example that the structures minimize their energy per unit length of dislocation line

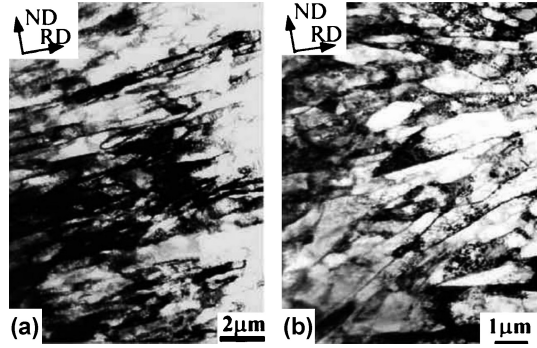
**Fig. 3.1** Deformation micro-structure after 10% cold rolling of IF steel (TEM image). The micro-structure is subdivided by extended planar dislocation boundaries (GNBs), parallel to the slip plane trace (101) and forming an angle of  $40^\circ$  with the rolling direction. Between the extended boundaries short interconnecting dislocation boundaries (IDBs) are seen. The sketch below the micrograph illustrates the grain subdivision into a cell block structure composed of GNBs and IDBs. Longitudinal (ND-RD) section [10].



[3] and that the grain orientation through the slip pattern significantly affects the evolution of the deformation microstructure [4, 5].

The microstructural evolution during cold rolling has been studied extensively in fcc metals as Al [6], Ni [7] and Cu [8] and to a lesser extent in bcc metals as iron and steel [9, 10]. However, the structural evolution with increasing strain has been found to be alike and will therefore be illustrated in the following for IF steel cold-rolled from 10 to 90% reduction in thickness [10]. At small strains a cell block structure forms where cell blocks are delineated by extended planar dislocation boundaries (geometrically necessary boundaries, GNBs). The cell blocks are further subdivided into cells by cell boundaries (incidental dislocation boundaries, IDBs) [1, 2]. A typical structure is shown in Fig. 3.1. As the strain is increased the spacing between the cell block boundaries and the cell boundaries decreases and the angle of misorientation across the boundaries increases. At large rolling reduction the structure is a typical lamellar structure, with nearly planar boundaries and short interconnecting boundaries forming a bamboo structure (see Fig. 3.2). The lamellar boundaries are high-angle boundaries ( $\theta \geq 15^\circ$ ) or dislocation boundaries ( $\theta \leq 15^\circ$ ) whereas the interconnecting boundaries are typically low-angle boundaries. Between the boundaries dislocation tangles can be observed. The microstructural evolution during warm rolling ( $800^\circ\text{C}$ ) has also been followed microscopically [11, 12]. As shown in Fig. 3.3, the microstructural evolution follows the general pattern of a structural subdivision by extended boundaries and short interconnecting boundaries forming a cell block structure [12]. Note however that the structural scale is much larger in Fig. 3.3 than in Fig. 3.1.

**Fig. 3.2** Deformation microstructure after 90% cold rolling of IF steel (TEM image). The microstructure is subdivided by (a) lamellar boundaries nearly parallel to the rolling direction and (b) a lamellar structure with microshear bands. Longitudinal (ND-RD) section [10].

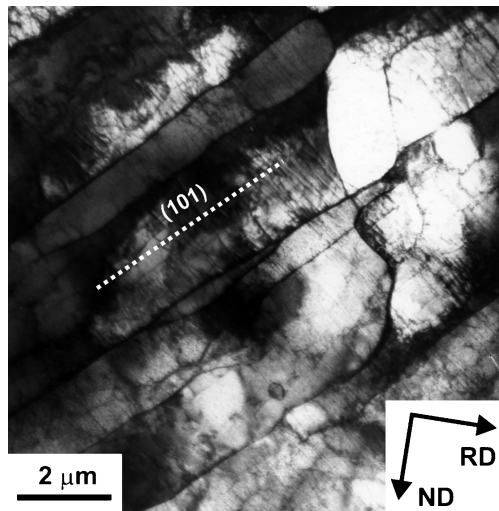


A qualitative description of the microstructural evolution must be followed by a quantification of microstructural parameters, where emphasis in the following will be put in the spacing between boundaries, the angle across boundaries and the dislocation density. The specific parameters are:

- Spacing between boundaries: (i) perpendicular to the rolling plane ( $d_t$ ), (ii) parallel to the rolling direction ( $d_l$ ) and (iii) random intercept spacing ( $d_R$ )
- Misorientation angle across the boundaries: (i) average angle for all boundaries, (ii) distribution of angles and (iii) frequency of high-angle boundaries ( $\theta \geq 15^\circ$ ) and low-angle boundaries ( $\theta \leq 15^\circ$ ).
- Density of dislocations present in low-angle boundaries and in the volumes between the different types of boundaries. For low-angle boundaries the dislocation density is proportional to the misorientation angle and to the area per unit volume of boundaries.

During cold rolling the microstructure subdivides on a finer and finer scale as the rolling strain is increased. At a rolling reduction of 90% ( $\epsilon_{VM} = 2.7$ ) the spac-

**Fig. 3.3** Deformation microstructure after 10% warm rolling of IF steel (TEM image). The microstructure is subdivided by extended planar dislocation boundaries (GNBs), parallel to the slip plane trace (101) and forming an angle of  $46^\circ$  with the rolling direction. Between the extended boundaries short interconnecting dislocation boundaries (IDBs) are seen. Longitudinal (ND-RD) section [12].



ing in the ND has decreased to about 0.22  $\mu\text{m}$  [10], and no saturation in boundary spacing has been observed. This has given an incentive to explore the structural evolution as the strain is further increased, to be discussed in the following.

3.2.2 Accumulative Roll-Bonding (ARB)

In order to introduce a high plastic strain in a sample without a reduction in sample thickness, the ARB process has been applied. This process differs from cold rolling as it consists of sheet rolling, cutting, surface degreasing, wire-brushing and finally roll bonding in one pass (one cycle) [13, 14]. The reduction in thickness per cycle is 50% corresponding to  $\epsilon_{VM}=0.8$ . The ARB process has been carried out with lubrication at room temperature and without lubrication at 500°C. For samples rolled without lubrication an additional shear strain is introduced together with the conventional rolling strain. Figure 3.4 shows that a typical lamellar structure evolves at large strain similar to the structure formed by rolling as shown in Fig. 3.2 [15]. Spacing data for ARB samples of IF steel is shown in Table 3.2 and Fig. 3.5 [10, 15–18]. This figure includes samples deformed under different conditions, and it illustrates that a fairly similar structural refinement

**Table 3.2** Average spacing between boundaries along the normal direction ( $d_t$ ) and along the rolling direction ( $d_l$ ).

Treatment	$\epsilon_{VM}$	$d_t$ ( $\mu\text{m}$ )	$d_l$ ( $\mu\text{m}$ )	Reference
Cold rolled 80%	1.9	0.29	0.76	10
Cold rolled 90%	2.7	0.22	0.72	10
ARB (7 cycles)*	5.6	0.21	0.93	16
ARB (10 cycles)**	8.0	0.09	not measured	17
Quenched + rolled 80%	1.9	0.22	0.36	18

\* at 500°C

\*\* at room temperature with lubrication

**Fig. 3.4** Deformation microstructure of 6-cycle ARB processed IF steel (TEM image). The microstructure is subdivided by lamellar boundaries nearly parallel to the rolling direction [15].

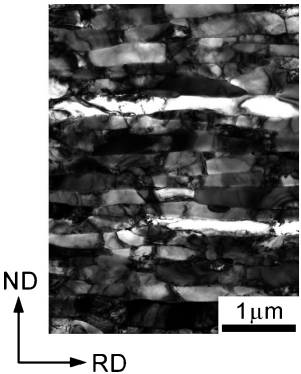
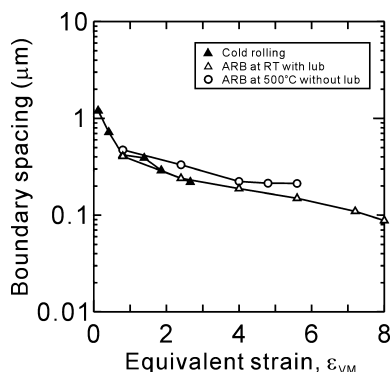




**Fig. 3.5** Boundary spacing measured along the normal direction (ND) as a function of the rolling strain ( $\epsilon_{VM}$ ) for IF steel deformed by cold rolling [10] and by ARB under two different conditions (see text) [15–17].



from low to medium strains can be obtained by cold rolling and by ARB. It is seen that the structure continues to refine with increasing strain without saturation. At the largest strain ( $\epsilon_{VM}=8$ ) the spacing between the lamellar boundaries has decreased to about 100 nm. The misorientation angle across the boundaries in the sample increases with increasing strain and the frequency of high-angle boundaries increases to about 70% at very large strain [19].

### 3.2.3 Rolling of Lath Martensite

By austenitizing and quenching of a low alloyed IF steel, a lath martensite structure can be formed. This structure is subdivided by dislocation boundaries and high-angle boundaries on a relatively fine scale [18, 20], i.e. it resembles the structure obtained by plastic deformation of a recrystallized structure. By cold-rolling the martensite structure transforms into a typical lamellar structure as illustrated in Fig. 3.6 for a sample cold rolled to a reduction of 80% ( $\epsilon_{VM}=1.9$ ) [18]. The scale of this structure is finer than the structure which can be obtained by cold rolling of recrystallized IF steel to the same reduction (see Table 3.2). The austenitizing and quenching may therefore be considered as a predeformation step raising the total strain significantly above the strain introduced during the subsequent rolling step.

### 3.2.4 Summary: Structural Observations

Independent of the deformation mode and the initial structure, the lamellar structure characterizes the samples deformed to a large rolling strain. The scale of the lamellar structure decreases as the strain is increased without saturation. At the largest strain examined ( $\epsilon_{VM}=8$ ), the lamellar spacing is about 100 nm. The deformed structure is subdivided into dislocation boundaries and high-angle boundaries where the frequency of the latter increases with increasing strain.

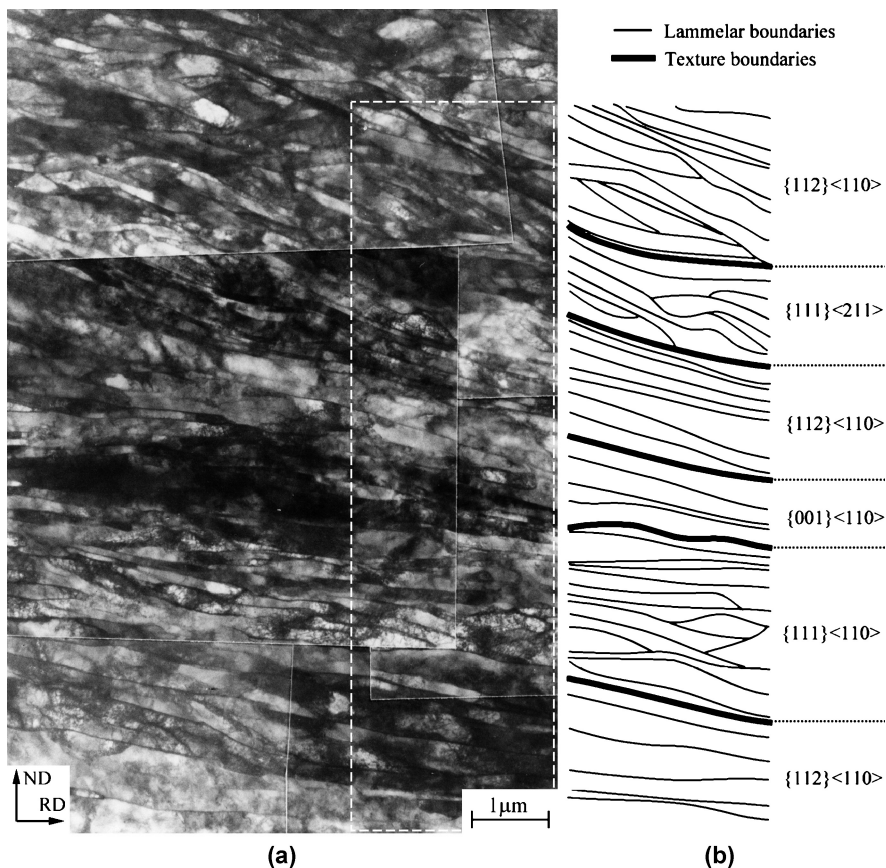


**Fig. 3.6** Deformation microstructure of lath martensite in IF steel after 80% cold rolling. (a) TEM image. (b) Sketch with texture components in the area marked by white broken lines in the TEM image (steel A) [18].

### 3.3 Microstructural Parameters and Flow Stress

It is a general observation that the flow stress of the deformed IF samples increases with increasing strain without saturation. The dominating structural feature is the subdividing boundaries which are dislocation boundaries and high angle boundaries. However, some dislocations are also present in the volume between the boundaries. In general the contribution to the flow stress of dislocations is proportional to the square root of the dislocation density and the contribution from high-angle boundaries is inverse proportional to the square root of their spacing. On the assumption of linear additivity of strength contributions, good agreement between calculation and experiment has been found for the flow stress of IF steel [10], nickel [7] and aluminum [6] and for the flow stress anisotropy in IF steel, aluminum and copper [21].

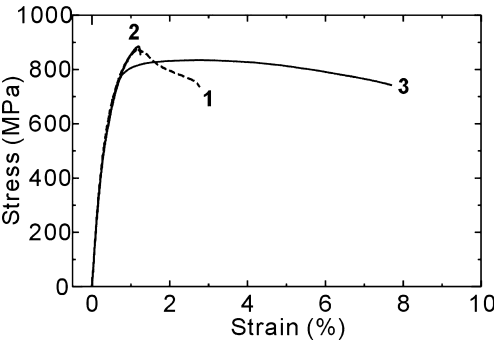
**Table 3.3** Mechanical properties.

Treatment	$\sigma_{0.2}$ (MPa)	UTS (MPa)
Cold rolled 80%	435	530
Cold rolled 90%	470	554
ARB (7 cycles)*	711	913
ARB (10 cycles)**	874	1032
Quenched + rolled 80%	–	~800***

\* at 500°C  
\*\* at room temperature with lubrication  
\*\*\* 3 × Vickers dardness

For the IF steel materials examined in the present work the yield stress (0.2% offset) and the ultimate tensile strength are given in Table 3.3. Both for the cold rolled samples and for the ARB samples an increase in strength follows a reduction in the structural scale. This behavior agrees with the general principle that the finer the structure the stronger the metal. However, when comparing the cold rolled and the ARB samples, the latter shows much higher strength for almost identical boundary spacings, see Table 3.2. This has led to more detailed investigations of various strengthening mechanisms for example interaction between glide dislocations and low- and high-angle boundaries, respectively. This research is inspired by an unexpected result of an annealing treatment at low temperature which was introduced to raise the low ductility characterizing samples in the deformed state. An increase in ductility and a decrease in strength was expected but the opposite was found [22]. This atypical behavior has been related to a removal of glide dislocation during annealing caused by the presence of closely spaced high-angle boundaries which can act as sinks for dislocations [22]. This assumption has been tested by giving a recovered sample a small reduction by cold rolling, which restored the properties of the unannealed sample, see Fig. 3.7 [23]. Qualitatively the assumption of dislocation recovery by annealing and reintroduction by deformation agrees with TEM observations of the microstructure in the different stages, see Fig. 3.8 [19]. The effect of easy dislocation annihilation due to a large fraction of high-angle boundaries may also significantly reduce the

**Fig. 3.7** Engineering stress-strain curves at room temperature for 6-cycle ARB processed IF steel. Strain rate:  $8.3 \times 10^{-4} \text{ s}^{-1}$ . Sample 1: As ARB processed, sample 2: sample 1 and annealed at 400°C for 0.5 h and sample 3: sample 2 plus cold rolling to 15% reduction [23].



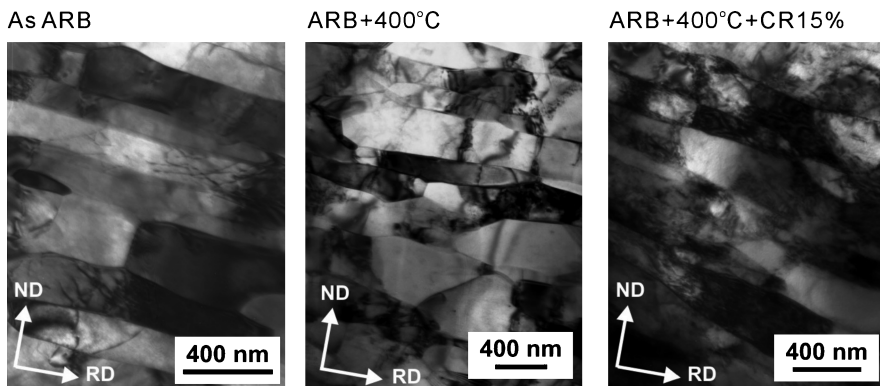


**Fig. 3.8** TEM images of IF steel processed under different conditions [19].

thermal stability of deformation induced nanostructures by increasing the recovery rate of samples deformed to large strains [24, 25].

### 3.3.1 Summary: Structure-Property Relationships

Independent of the deformation mode the flow stress of IF steel increases as the structural scale decreases. Strengthening mechanisms are boundary strengthening and dislocation strengthening, which are superimposed. Strengthening parameters have been quantified by electron microscopy and good agreement between model predictions and experiments has been found [26].

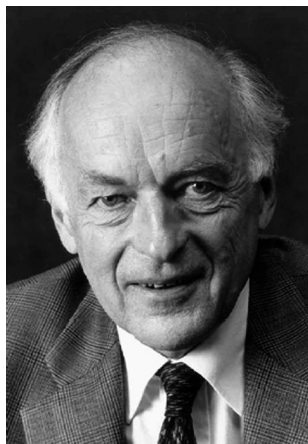
## 3.4 Concluding Remarks

The high strength of nanostructured metals produced by plastic deformation is caused by dislocation strengthening and boundary strengthening. Experimental and theoretical investigations of these mechanisms are therefore important steps in both process and property optimization of nanometals. An important part of this effort will be the development of advanced, automated characterization techniques on different length scales down to the nanometer dimension. It follows that future work must combine “blue sky” research and focused research with application of nanometals as a common goal.

**Acknowledgement** The authors gratefully acknowledge the Danish National Research Foundation for supporting the Center for Fundamental Research: Metal Structures in Four Dimensions, within which this work was performed.

## References

- [1] N. Hansen: *Metall. Mater. Trans. A*, 32A (2001), 2917.
- [2] D.A. Hughes and N. Hansen: *Plastic deformation structures*, ASM Handbook, ASM International, Materials Park, Ohio, USA, (2004), 192.
- [3] D. Kuhlmann-Wilsdorf: *Mater. Sci. Eng.*, A113 (1989), 1.
- [4] X. Huang and G. Winther: *Phil. Mag.*, 87 (2007), 5189.
- [5] G. Winther and X. Huang: *Phil. Mag.*, 87 (2007), 5215.
- [6] Q. Liu, X. Huang, D.J. Lloyd and N. Hansen: *Acta Mater.*, 50 (2002), 3789.
- [7] D.A. Hughes and N. Hansen: *Acta Mater.*, 48 (2000), 2985.
- [8] V.S. Ananthan, T. Leffers and N. Hansen: *Mater. Sci. Tech.*, 7 (1991), 1069.
- [9] R.A. Jago and N. Hansen: *Acta Metall.*, 34 (1986), 1711.
- [10] B.L. Li, A. Godfrey, Q.C. Meng, Q. Liu and N. Hansen: *Acta Mater.*, 52 (2004), 1069.
- [11] G.H. Akbari, C.M. Sellars and J.A. Whiteman: *Acta Mater.*, 45 (1997), 5047.
- [12] A. Haldar, X. Huang, T. Leffers, N. Hansen and R.K. Ray: *Acta Mater.*, 52 (2004), 5405.
- [13] Y. Saito, N. Tsuji, H. Utsunomiya, T. Sakai and R.G. Hong: *Scripta Mater.*, 39 (1998), 1221.
- [14] N. Tsuji, Y. Saito, S.H. Lee and Y. Minamino: *Adv. Eng. Mater.*, 5 (2003), 338.
- [15] X. Huang, N. Kamikawa, S. Morito, N. Hansen and N. Tsuji: *Proc. of Inter. Symp. on Ultrafine Grained Steels (ISUGS-2007)*, ISIJ, (2007), in press.
- [16] N. Kamikawa, N. Tsuji and Y. Minamino: *Sci. Tech. Adv. Mater.*, 5 (2004), 163.
- [17] N. Kamikawa: PhD thesis, Osaka University, Japan, (2006).
- [18] S. Morito, X. Huang, T. Furuhashi, T. Maki and N. Hansen: *Proc. of the 25th Risø Inter. Symp. on Mater. Sci.*, Risø National Laboratory, Roskilde, Denmark, (2004), 453.
- [19] X. Huang, N. Kamikawa and N. Hansen: *Mater. Sci. Eng. A*, (2008), in press.
- [20] S. Morito, X. Huang, T. Furuhashi, T. Maki and N. Hansen: *Acta Mater.*, 54 (2006), 5323.
- [21] Z.J. Li, G. Winther and N. Hansen: *Acta Mater.*, 54 (2006), 401.
- [22] X. Huang, N. Hansen and N. Tsuji: *Science*, 312 (2006), 249.
- [23] N. Kamikawa, H. Zhang, X. Huang and N. Hansen: to be published in *Mater. Sci. Forum* special volume "Advances in Nanostructured Materials Processed by Severe Plastic Deformation", (2008).
- [24] N. Kamikawa, N. Tsuji, X. Huang and N. Hansen: *Acta Mater.*, 54 (2006), 3055.
- [25] W.Q. Cao, A. Godfrey, N. Hansen and Q. Liu: submitted for publication.
- [26] X. Huang, S. Morito, T. Maki and N. Hansen: to be submitted for publication.



Niels Hansen  
 Center for Fundamental Research  
 Metal Structures in Four Dimensions  
 Materials Research Department  
 Risø National Laboratory  
 DK-4000 Roskilde  
 Denmark

## Chapter 4

# The Coming of Grain Boundary Engineering in the 21st Century

Tadao Watanabe, Sadahiro Tsurekawa, Xiang Zhao, and Liang Zuo

**Abstract.** This paper will discuss the background and the basic concept of the grain boundary engineering (GBE) proposed by one of the present authors in the early 1980s. It is shown that the grain boundary microstructure which can be quantitatively described by newly introduced microstructural parameters, i.e. the grain boundary character distribution (GBCD) and the grain boundary connectivity, can bridge the gap between structure-dependent properties of individual grain boundaries and bulk properties of polycrystalline materials. In order to prove the importance of GBCD and its applicability to GBE, we overview basic studies of GBE performed in the last two decades, showing the GBCD-controlled bulk properties and possible factors affecting GBCD, such as the grain size, texture, material purity/composition, for various kinds of materials including ferrous and non-ferrous materials. Recent achievements of GBE for structural materials are discussed paying a particular attention to the control of intrinsic and extrinsic brittleness caused by structure-dependent intergranular fracture. As the most recent successful achievements, GBE by high magnetic field applications is intro-

---

T. Watanabe

Visiting Professor, Key Laboratory of Anisotropy and Texture of Materials, Northeastern University, Shenyang, 110004, China, formerly Laboratory of Materials Design and Interface Engineering, Department of Nanomechanics, Graduate School of Engineering, Tohoku University, Sendai, Japan

S. Tsurekawa

Faculty of Engineering, Kumamoto University, Kumamoto, Japan

X. Zhao

Key Laboratory of Anisotropy and Texture of Materials, Northeastern University, Shenyang, 110004, China

L. Zuo

Key Laboratory of Anisotropy and Texture of Materials, Northeastern University, Shenyang, 110004, China

duced. Finally an example of GBE for functional materials is given taking the most recent study on polysilicon for high performance solar cells.

**Keywords:** Grain boundary engineering (GBE), Grain boundary microstructure, Texture control, Brittle fracture control, Grain boundary Character Distribution, Grain boundary structure

## 4.1 Introduction

### 4.1.1 *Material-Assisted Civilization and Development*

In the history of our human society, the advent of a new age of civilization and its rapid progress were always brought about by obtaining a new material and its extensive usage. We see this from “the Stone age, Bronze age, Iron age” which could meet man’s requirements for ever increasing performance, particularly the strength and toughness for structural materials. In the 20th century, the advent of semiconductor and its application to development of many kinds electronic devices have drastically changed our ways of daily life and activities, by starting a new age of computer-assisted systems based on Information Technology (IT) and global “Internet” communication. The advent of a new material and its extensive use can give our human society many opportunities to realize desirable and expected development and progress in our civilization on the bright side, but sometimes undesirable change with unexpected tragedy to the society, on the dark side.

Up to now, the most popular metal iron, its alloys and steels have been serving as important engineering structural and functional materials, since the iron age back to BC1500. Enormous efforts have been made in the last century by devoted pioneers, materials scientists and engineers in order to develop a new material, based on iron, steel and other non-ferrous materials, to meet ever increasing demand for higher performance materials to be used for high technology [1, 2].

### 4.1.2 *Requirements for High Performance Materials*

Any type of engineering materials should meet general requirements associated with the stability and reliability of material performance to be used for their services as components of large scale structures, ordinary scale machines, and small scale devices in various environments. Conventionally we classify engineering materials into two groups: structural materials and functional materials. To the former, excellent mechanical properties for machining and subsequent service are

always required, when used to construct large scale structure and ordinary scale machines. Functional materials must meet some special requirements to serve as component part providing a special and unique function with higher performance, for instance as magnetic, electric, optical material. Of course, a certain level of good mechanical performance is also required for even functional materials for keeping the original shape and size of a machine or device to stand their long service life. Another important requirement comes from a large variety of service environments and conditions where structural and functional materials are used, a wide range of temperature from cryo- to high-temperature, and from vacuum to detrimental gas atmosphere ranging from low to high pressure, under stress condition from static to dynamic and cyclic, under external fields such as electric or magnetic field or irradiation. However, we can specify several minimum requirements for structural and functional materials. Firstly for structural materials, the following requirements are usually made. (1) high strength and high fracture toughness, (2) good workability and machinability, (3) high corrosion and stress-corrosion resistance, (4) high oxidation resistance, (5) high creep resistance, (6) high damping capacity.

The discipline of the modern “Materials Science and Engineering” which emerged some time in the early 1950s [3], has been serving as a powerful tool for materials design and development for many years. However, we should recognize an important change of the situation in which structural and functional materials have been used. That is the size of machine parts composed of structural materials. Nowadays the size of parts spreads in a extremely wide range from meter (m) to micron meter ( $\mu\text{m}$ ) scale covering at least 6 orders in magnitude, as can be easily imagined from nuclear reactor and space shuttle on one side and micromachines on the other side. Now we are discussing the design and development of even nanomachines for various purposes in our human society. There is a simple question, “Can we use the same material for structures and machines with such a large difference of part size?”. It is not difficult to recognize that we cannot use the same material from the view point of safety and reliability, if we carefully consider the heterogeneity of microstructure in existing engineering materials. As the size of machine parts decreases, the effect of the heterogeneity of microstructure in a material may become more significant and seriously affect the performance, reliability and safety of it. So called “size effect” is one of important issues to be solved for future materials design and development, in connection with microstructure control for high performance materials. The stability and reliability of material properties and performance are known to be closely related to the stability and homogeneity of microstructure in materials [4]. It is well known that the original microstructure existing changes during service, particularly at high temperature and under stress condition, or irradiation. As a result of this, microstructure-controlled properties and performance often degrade, sometimes unexpectedly resulting in a serious accident and disaster in activities of our society. So we materials scientists and engineers must solve these problems which remain unsolved so far.



### ***4.1.3 Importance of Grain Boundaries in Engineering Materials***

From our basic knowledge of Materials Science and Engineering, it is a general recognition that most of engineering materials (metallic, ceramic and semiconductor materials) are polycrystalline so that existing grain boundaries can affect their bulk mechanical/physical/chemical properties of polycrystalline materials, different from those of single crystal and amorphous state of even the same material. Until recently the effect of grain boundaries has been studied only through the effect of the average grain size, i.e. the density of grain boundaries, tacitly assuming that all existing grain boundaries have the same character and structure. The flow stress and the fracture stress are formulated as a function of the average grain size by the Hall-Petch relationship, having served for many years as an important characteristic feature of mechanical properties [5]. Now we should have a new insight based on important findings from recent studies of grain boundary structures and properties [6–11]. It has been well established that grain boundary structure can differently affect almost all properties of individual grain boundaries depending on their atomistic structures so that we need to know what kinds of grain boundary structure exist and to what extent grain boundary structure can affect boundary properties, and how these existing grain boundaries can affect metallurgical phenomena in real polycrystalline materials. As for mechanical properties of polycrystalline materials, there remains a long pending unsolved problem that polycrystalline materials have a general tendency to become more brittle when their strength is increased. This has been the dilemma which material scientists and engineers have experienced in development of high performance structural materials [12–14]. The origin of a loss of the ductility and fracture toughness of polycrystalline materials was found to be primarily due to grain boundary (intergranular) fracture. When intergranular fracture occurs predominantly, polycrystalline materials show a severe brittleness and poor ductility, irrespective of being metallic, intermetallic or ceramic.

## **4.2 Grain Boundary Microstructures in Polycrystalline Materials**

### ***4.2.1 Versatility of Grain Boundary Microstructure***

Grain boundaries and interphase boundaries are important defects and microstructural components which can generally exist in almost all type of polycrystalline materials whether being metallic or non-metallic and irrespective of crystal structure (cubic or non-cubic). The grain boundaries (hereafter including interphase boundary) are two-dimensional (2D) lattice defect or interface where two neighboring grains are contacting and joining on atomistic scale. In a polycrystalline material, the orientation of individual grains can vary from grain to grain,

showing a specific distribution depending on material processing and condition. The character of grain boundary is geometrically defined by the relative orientation relationship between two adjoining grains, as has been discussed in detail [7, 8]. Let us look at some examples of the characterization of grain boundary in real material. Figures 4.1 (a) and 4.1 (b) show, respectively SEM and SEM-ECP micrographs for a  $\langle 100 \rangle$ -tilt-type boundary, and Fig. 4.1 (c) for  $\langle 100 \rangle$ -twist-type boundary observed in iron-6.5mass%Si ribbon [15, 16]. We can intuitively understand the type of the observed grain boundaries from the orientation of component crystals and common rotation axis lying along or normal to the trace of the grain boundary in SEM or ECP image. The common rotation axis is parallel to the grain boundary plane trace for the tilt-type boundary and normal for the twist-type boundary. In real polycrystalline materials, more general mixed-type grain boundaries with tilt and twist components occur more frequently. In a study of grain boundary structure and properties, conventionally we simply classify all existing grain boundaries into the following three groups [16]; low-angle boundaries (L) with the misorientation angle smaller than  $15^\circ$ , high-angle special boundaries with some ordered and periodic structure such as coincidence-site lattice (CSL/ $\Sigma$ ) boundaries with low- $\Sigma$  ( $<29$ ), and high-angle general random (R) boundaries without any ordered and periodic structure. The first two groups are considered to be of low-energy type and the third group of high-energy. Thus the character of individual grain boundaries existing in a polycrystal can be defined rather precisely. Moreover, the detail of geometrical configuration, shape and dimension and connectivity of grain boundaries in the two-dimensional (2D) and three-dimensional (3D) network should be described quantitatively. The structural and geometrical versatility and flexibility of the grain boundary microstructures can exert a large variety of their influence on bulk properties of polycrystalline materi-

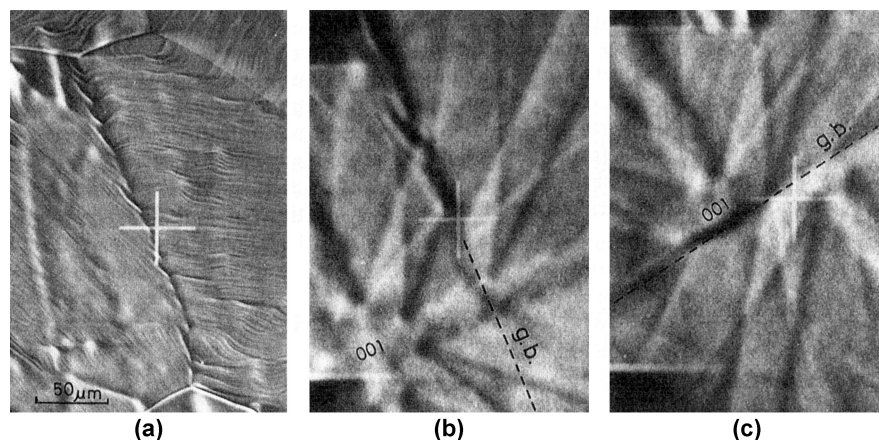


**Fig. 4.1** SEM-ECP micrographs taken at a tilt boundary and a twist boundary in Fe-6.5mass%Si alloy ribbon rapidly solidified and annealed at 1363 K for 3.6 ks. (a) SEM and (b) ECP micrographs taken from the same  $\langle 100 \rangle$ -tilt boundary and (c) ECP micrograph from a  $\langle 100 \rangle$ -twist boundary [15, 16].

als. In order to fully understand possible effects of grain boundaries we need to clarify, firstly, the relationship between grain boundary structures and properties, and secondly, the relationship between the grain boundary microstructure, bulk properties and processing method/conditions, as our basic knowledge of the grain boundary engineering. Fortunately the former relationship has been extensively studied and established since 1980s, and the literature has become available [6–11]. On the other hand, it is only recently that the importance of the latter relation was pointed out by Aust and Palumbo's group and the present authors', starting serious consideration into bulk properties based on structure-dependent boundary properties from the viewpoint of the grain boundary engineering [16–21].

### 4.2.2 *Structure-Dependent Boundary Properties*

It is well known that grain boundaries can be preferential sites for metallurgical phenomena such as segregation, precipitation, corrosion, deformation and fracture. Let us begin with an interesting finding on grain boundary corrosion behavior observed on a specimen with  $\langle 100 \rangle$  columnar grain structure cut out from a large cast ingot of Fe-15mass %Cr -0.55%Sn alloy [23]. Figure 4.2 clearly shows that the extent of intergranular corrosion evaluated from the width of corroded region is quite different among the three observed boundaries denoted by the number 1, 2, and 3. Namely GB.1 was most heavily corroded, GB.2 to lesser extent and GB.3 not at all. It is not difficult to understand that the propensity to intergranular corrosion is related to the grain boundary structure or the grain boundary energy which is expected to decrease in the order of GB.1, GB.2 and GB.3 corresponding to the dihedral angle of  $100^\circ$ ,  $110^\circ$ , and  $150^\circ$  respectively. Probably GB.3 has the lowest boundary energy and the highest resistance to intergranular corrosion. One more example of structure-

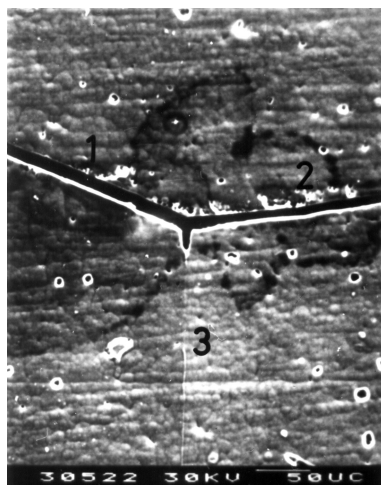


**Fig. 4.2** Observation on structure-dependent grain boundary corrosion occurring at the three grain boundaries meeting at a triple junction in a  $\langle 001 \rangle$  textured columnar grained specimen of Fe-17mass%Cr-0.55Sn alloy cast from the melt [23].

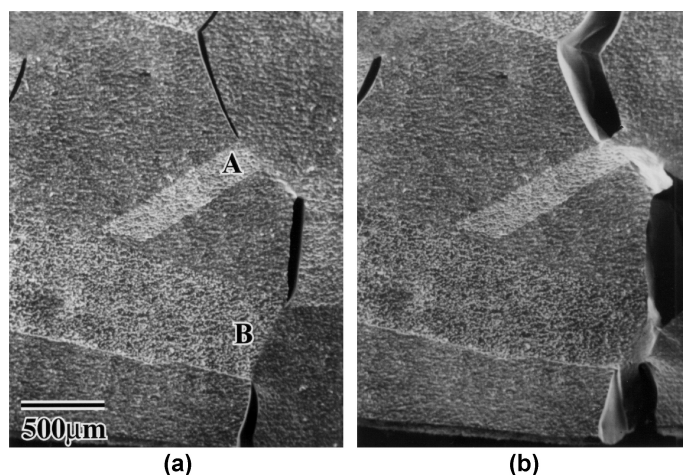


**Fig. 4.3** Successive observations (a), (b) of intergranular fracture in a polycrystal of copper-bismuth alloy at an SEM tensile stage [17]. Fracture would not occur at the portions of intersection of the boundaries with twins A and B.

dependent grain boundary property is taken from the early work by the authors [17] and shown in Fig. 4.3 (a)–(b). A set of two SEM micrographs were taken during in situ observation of fracture process of Bi-doped copper polycrystal specimen at a SEM tensile stage. It is evident that normally very ductile high purity copper polycrystal showed predominant intergranular fracture, probably due to segregation of embrittling element Bi. Moreover, the propagation of intergranular fracture was completely restricted at the positions A and B where the long weak grain boundaries interacted with annealing twins. Intergranular fracture could not propagate beyond the twin portion along the original boundary, probably because of a change of the grain boundary character and structure into that of a strong boundary. Thus it is evident that intergranular fracture occurs very heterogeneously in a polycrystal, as observed in extrinsically embrittled polycrystalline copper specimen. Now we can get an insight into structure-dependent intergranular fracture, i.e. how strongly grain boundary properties can be affected by the boundary character and structure. That is our basis of the grain boundary engineering by controlling the grain boundary microstructure so efficiently to be optimum for maximum desirable bulk properties and/or for minimizing detrimental effect as more as possible.

### 4.2.3 *Structure-Dependent Grain Boundary Fracture*

Since intergranular fracture and brittleness is a key issue of structural materials, let us discuss the origin of structure-dependent intergranular fracture, focusing on some possible change of the fracture energy. Structure-dependent fracture stress can be explained in terms of the energy change associated with intergranular frac-

ture as observed for metal bicrystals [21, 28, 29]. When intergranular fracture ideally occurs in the absence of plastic deformation or near the grain boundary, the fracture energy  $\gamma^*$  is given by the following equation:

$$\gamma^* = 2\gamma_s - \gamma_b \quad (4.1)$$

where  $\gamma_s$  is the surface energy of the exposed grain boundary and  $\gamma_b$  the pre-existing grain boundary energy. Since the grain boundary energy,  $\gamma_b$  has been well established to strongly depend on the boundary structure [6–9], we can expect some dependence of the intergranular fracture energy,  $\gamma^*$  on the grain boundary structure, assuming that the surface energy,  $\gamma_s$  does not depend on crystallographic orientation as much as  $\gamma_b$ . Lawn and Wilshaw have exactly pointed out the possibility of structure-dependent intergranular fracture [25]. For low-energy boundaries,  $\gamma^*$  will be large and intergranular fracture will be more difficult than at high-energy boundaries. If plastic deformation is involved in intergranular fracture, the fracture energy,  $\gamma^*$ , is written as follows:

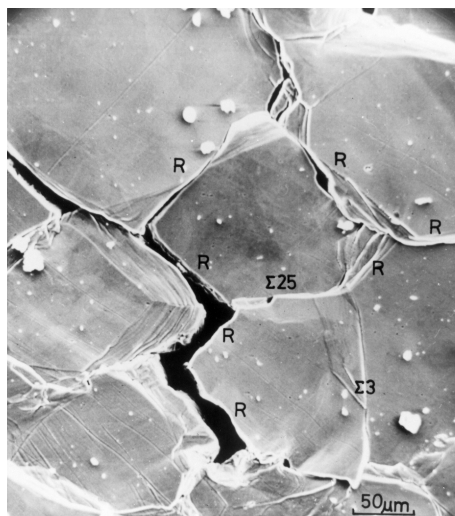
$$\gamma^* = 2\gamma_s - \gamma_b + \gamma_p \quad (4.2)$$

where  $\gamma_p$  is plastic work associated with the propagation of the microcrack. It is known that roughly speaking,  $\gamma_s = 3\gamma_b$  for metals and alloys [26]. McMahon and Vitek [27] have shown that  $\gamma_p$  can have a large portion of  $\gamma^*$  ( $\gamma_p = 15\gamma_s$ ). By simply comparing Eq. 4.1 with Eq. 4.2, we may consider that the fracture energy,  $\gamma^*$ , in the case of ideal intergranular fracture without plastic deformation, is generally smaller than that in the case where plastic deformation is involved in intergranular fracture. Namely we expect a stronger dependence of intergranular fracture on the grain boundary structure when  $\gamma_p$  makes a smaller contribution to the fracture energy,  $\gamma^*$ . In fact, it has been proved by experiments that the intergranular fracture stress strongly depends on the grain boundary type and the misorientation angle, as revealed by experimental studies on metal bicrystals containing the boundaries whose character and misorientation angle were systematically controlled [21, 24, 28]. Low-energy special boundaries (low-angle or low- $\Sigma$  coincidence boundaries) showed higher fracture stress, while high-energy random boundaries showed much lower fracture stress, smaller than 1/2 or 1/3 of the fracture stress of low-energy special boundaries. Hence, as intergranular fracture occurs more predominantly and ideally, the effect of grain boundary structure would be increasingly important to the fracture process of polycrystals. Namely, brittle intergranular fracture has intrinsically strong sensitivity to grain boundary structure in all situations.

#### **4.2.4 Observations of Grain Boundary-Related Fracture of Polycrystalline Materials**

In order to confirm structure-dependent intergranular fracture actually occurring in a polycrystal, let us visit some early experimental work [29]. Figure 4.4 shows

**Fig. 4.4** Structure-dependent intergranular creep fracture observed in Fe-0.8 at.%Sn alloy specimen crept at  $T = 973\text{ K}$  and  $\sigma = 29.4\text{ MPa}$  [29]. Note that high-angle random (R) boundaries are preferential sites for crack nucleation and propagation, but  $\Sigma 3$  boundary is extremely resistant to fracture.



a SEM micrograph which evidences structure-dependent intergranular creep fracture observed on the specimen of Fe-0.8 at.% Sn alloy crept at 973 K. The character of observed grain boundaries was determined by SEM-ECP technique before creep fracture testing. We see clearly that random boundaries (R) preferentially fractured due to easy grain boundary sliding during high temperature creep, while coincidence boundaries ( $\Sigma$ ) would not break at all, particularly at the  $\Sigma 3$  boundary which was aligned even perpendicular to the tensile axis (in the horizontal direction) and subjected the maximum normal stress to the boundary plane in the specimen. In situ observations on fracture processes in polycrystalline specimens of metals and alloys embrittled by doping or liquid metal, were also made with a SEM-tensile stage [17]. It was found that intergranular cracks formed initially at random boundaries propagated to the connecting random boundaries which fractured more easily due to sliding under favorable geometrical arrangement and stress condition. A summary of in situ observations on brittle fracture processes controlled by structure-dependent intergranular fracture is schematically shown in Fig. 4.5. When weak random boundaries are connecting with other random boundaries passing triple junctions, a polycrystal fractures in a typical brittle intergranular fracture mode as indicated by the fracture Path B. On the other hand, when low-energy strong boundaries and high-energy weak random boundaries are connecting to each other, a mixture of intergranular and transgranular fracture occurs, as indicated by the fracture Path A. Thus it is self-evident that the connectivity of grain boundaries with different characters and structures is also another key factor controlling the overall fracture processes, as well as the grain boundary character distribution (GBCD). Finally, let us keep in mind that much stronger structure-dependent intergranular fracture can be expected in high temperature deformation, because more grain boundary phenomena, (such as sliding, migration, segregation, precipitation and oxidation) can be involved in fracture processes at higher tempera-

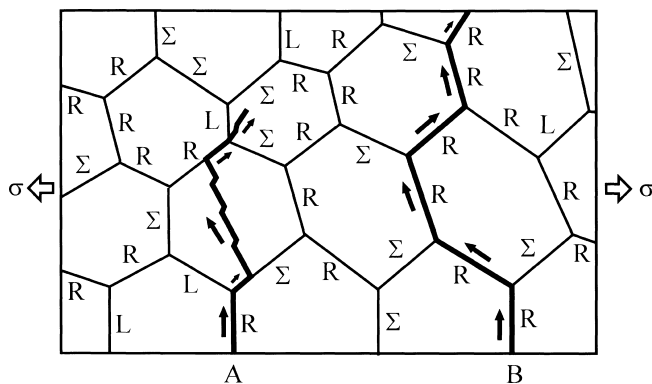


**Fig. 4.5** Schematic representation of grain boundary structure-dependent fracture processes in polycrystal [17]. Path A: combined process of intergranular and transgranular fractures occurring at different types of boundaries, Path B: typical intergranular fracture occurring continuously at connecting random boundaries.

tures, so that this may result in the amplification of their possible structure-dependent effects and contributions [29, 30].

### 4.3 Grain Boundary Engineering (GBE) for High Performance Materials

Now the time has come when we can more efficiently utilize our basic knowledge of structure-dependent grain boundary properties in designing and developing a new structural or functional material. This is a historical background behind our recent work on GBE overviewed in this paper. It seems timely that we overview the coming of “Grain Boundary Engineering (GBE)”, first proposed by one of the present authors in the early 1980s [17], has been increasingly accepted world-wide and being applied as a new approach to materials design and development of high performance materials [31–33]. In this paper, many recent successful achievements of GBE are introduced for ferrous and non ferrous materials, including even semiconductor for solar cells. Furthermore, some new attempts of GBE by high magnetic field application are introduced which the present authors and coworkers have recently made.

#### 4.3.1 Basic Concept of Grain Boundary Engineering

The effects of grain boundaries on bulk properties of polycrystalline materials are simply classified into two categories. One is such that the presence of grain boundaries exerts a “beneficial effect” on bulk properties, leading to some improvement or enhancement of performance of the materials, even to the generation

of a new function. The other is such that the presence of grain boundaries affects a “detrimental effect” on bulk properties, causing some degradation of material performance. Thus grain boundaries can exert both “beneficial effect” and “detrimental effect” on bulk properties. If it was possible to suppress the “detrimental effect” and conversely to increase the “beneficial effect” as much as possible in the course of material fabrication, we could endow polycrystalline materials of ordinary composition with much better material performance than original materials. Since, as we have already discussed, individual grain boundaries have their own boundary structural, geometrical and topological versatilities, in addition to their generality and applicability for all kinds of polycrystalline materials with any crystal structure. There is a huge potential of the control of grain boundaries on macro-, micro- and atomistic levels, so called the grain boundary microstructure in the two-dimensional (2D) and three-dimensional (3D) grain boundary networks. If it would be possible to maximize “beneficial effect” and minimize “detrimental effects” of grain boundaries, by designing and producing their optimum structure, morphology, geometry and arrangement of grain boundaries on the basis of the concept of grain boundary engineering, we could provide Materials Science and Engineering with a new breakthrough for its future progress. This is the basic concept of so called “Grain Boundary Engineering (GBE)”, originally “Grain Boundary Design and Control” [17, 34]. Aust and Palumbo’s group [18, 20, 35, 36], has eagerly applied the concept and successfully achieved GBE for high performance structural and functional materials, together with our group [17, 21, 32, 37] and other active colleagues [38–40] approaching this highly potential goal, up to now.

### ***4.3.2 Possible Processing Methods for Grain Boundary Engineering***

There are several key issues that should be clarified one by one, to establish the discipline of grain boundary engineering (GBE) for advanced materials and to develop a actual processing method for GBE well designed and programmed; (1) basic knowledge about the relation between grain boundary structure and properties, (2) experimental techniques for quantitative characterization and evaluation of the grain boundary atomistic, chemical, electronic-structures in real polycrystalline materials, (3) the relationship of the grain boundary microstructure with bulk properties in real polycrystalline materials, (4) modeling and prediction of boundary-controlled desirable bulk properties in connection with well-defined grain boundary microstructures, (5) development of possible processing methods of manipulating desirable and optimum grain boundary microstructures in a given material, and (6) to establish some theoretical basis of the prediction and evaluation of bulk properties of specific polycrystalline materials with a well designed and precisely controlled grain boundary microstructure. Some previous and recent works based on percolation approach may be useful and very promising [41–44]. The issue (6) is the subject related to the Chap. 6.



In order to discuss possible processing methods for manipulation of the grain boundary microstructures in polycrystalline materials, we should confirm what microstructural parameters associated with the grain boundary microstructure can be used for actual processing. The following are considered as possible parameters quantitatively determined by experiment.

- (1) Grain geometry and structures: Grain shape, size and aspect ratio, Grain orientation distribution, Grain size distribution, Texture type and sharpness, Mixing of different textures, Heterogeneity or homogeneity of grain structure, in 2D and 3D polycrystals.
- (2) Grain boundary (GB) geometry, morphology and topology: GB density, GB plane/inclination, GB inclination distribution, Triple junctions character/distribution.
- (3) Grain boundary structure: Atomic structure, GB character, Triple junction character.
- (4) Boundary chemistry: GB composition, Segregation level and local variation, Binding energy, GB energy, Electronic structure of GB.
- (5) Grain boundary properties: Intrinsic and extrinsic properties, structure-dependence, collective properties, beneficial or detrimental effect on a given bulk property.
- (6) Micro and Macrostructure relationship: Grain boundary character distribution (GBCD), GB connectivity, Relationship between GBCD and texture, Heterogeneity or homogeneity of GB microstructure, Grain boundary network (2D, 3D).

First, thermomechanical processing which is based on deformation and subsequent annealing, has been extensively and widely used for microstructural control until presently. So this processing method will be still used in future. Here it is worth thinking that the application of some external fields are also very useful and powerful for precise control of microstructures [45, 46]. Unidirectional solidification and unidirectional annealing under temperature gradient, magnetic field application, electric field application, static or cyclic stress application have been attempted up to now and successfully achieved GBE. In particular, the magnetic field application is a very promising, as recently introduced by the present authors [37] and will be discussed later in some detail.

## 4.4 The Characterization of Grain Boundary Microstructures by OIM

### 4.4.1 *Quantitative Analysis of Grain Boundary Microstructures*

Until 1982 before a new microstructural parameter termed “the grain boundary character distribution (GBCD)” was proposed [47], we could not characterize the

microstructure associated with grain boundaries, except the grain size, i.e. the density of grain boundaries in unit volume of a polycrystalline specimen. Strictly speaking, the term “grain size” provides no information about the character and structure of individual grain boundaries existing in a real polycrystal. As already mentioned, since the character of a grain boundary is defined by the relative orientation relationship between adjoining two grains on the basis of crystallographic geometry, we can characterize the grain boundary microstructure by modern methods of crystallographic diffraction analysis such as TEM, SEM-ECP and more recently SEM-EBSD/Orientation Imaging Microscopy (OIM) technique. The recent advent of computer-assisted SEM-EBSD/OIM technique developed by Brandt et al. [48], has drastically changed the situation and the capability of microstructure and texture analyses of polycrystalline materials. Nowadays, the characterization of the grain boundary microstructure and the determination of grain orientation distribution are not tedious and time consuming anymore as before. SEM-EBSD/OIM is now being increasingly used as a standard technique for quantitative analysis of the microstructure in polycrystalline materials, serving as a powerful tool for the grain boundary engineering. Let us look at an example of actual characterization of grain boundary microstructure and the determination of the grain boundary character distribution (GBCD).

Figure 4.6 (a) and 4.6 (b) show SEM image and OIM map redrawn from observation of the grain boundary microstructure of a polycrystalline molybdenum produced by annealing deformed single crystal [49]. Here it should be mentioned how much OIM technique is precise in analyzing the grain boundary microstructure, when we observe grain or grain boundary structure by optical microscopy or

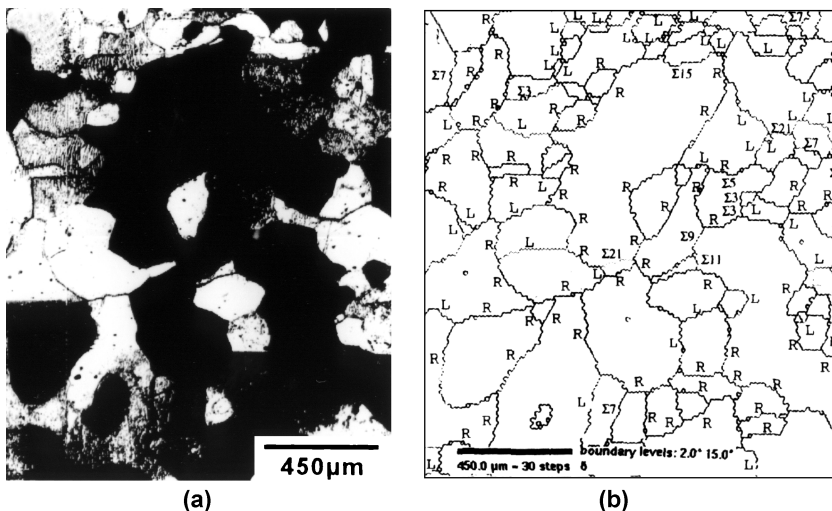


**Fig. 4.6** The characterization of grain boundary microstructure by SEM-EBSD/OIM system for molybdenum polycrystal produced by thermomechanical processing of single crystal [21]. (a) Optical micrograph, (b) grain boundary character distribution (GBCD) by OIM.

SEM-ECC contrast which can produce different contrasts dependent on the orientation of grains appearing at specimen surface. Since the contrast changes across a grain boundary, we can recognize the presence of a grain boundary and also the shape and size of individual grains in a polycrystal. However, when the surface orientation normal to grain surface is similar between adjoining grains, irrespective of large difference of orientation in surface plane, it is difficult to recognize the presence of a grain boundary, as clearly demonstrated in Fig. 4.6 (b). Thus, the computer-assisted SEM-EBSD/OIM technique brought about a new age of our quantitative evaluation of grain boundary microstructure. This technique has enabled us to make both microstructural and crystallographic analyses on microscale (even some tens of nanometer-scale grain size by using a FE-SEM) on a bulky specimen without much difficulty of specimen preparation. Now there will be no problem to bridge between local- and micro-scale grain boundary microstructure and macroscale ordinary microstructure of optical microscopic image level. We can efficiently use this powerful technique for GBE.

#### ***4.4.2 Grain Boundary Character Distribution (GBCD)***

The grain boundary character distribution (GBCD) was introduced by Watanabe [17] and it is now ordinarily used as a new microstructural parameter to describe the grain boundary microstructure. Indeed, this parameter can bridge the gap between structure-dependent properties of individual grain boundaries and bulk properties of polycrystalline materials, and also provides a statistical information of the overall grain boundary microstructure quantitatively characterized by OIM. As mentioned above, GBCD provides such important information as the type of observed boundaries and the frequency of occurrence of specific types of grain boundaries in a real polycrystalline material. It has been reported that GBCD can shows a large variety with systematical change depending on processing condition and metallurgical factors affecting the grain boundary microstructure [16, 49]. The magnitude of such an effect that GBCD can affect bulk properties, may be simply the summation of all grain boundaries included in statistical analysis, or more complicatedly some collective behavior of structure-dependent grain boundary properties of individual grain boundaries existing in a polycrystal. In fact, it is very likely that most of boundary-related metallurgical phenomena may occur and show collective behavior, as a result of strong structure-dependent grain boundary properties in a polycrystal. However, unfortunately at present, basic knowledge of collective behavior of grain boundary-related phenomena is very scarce [41–44]. Anyway, GBCD-controlled bulk properties can be modelled by using some theoretical basis to predict possible effects of microstructural and experimental parameters. Quite recently increasing numbers of experimental evidence for GBCD-controlled bulk properties have been reported in connection with the grain boundary engineering, as shown later. Thus the importance and usefulness of GBCD have been proved through challenging attempts at grain boundary engineering for

enhancement of performance or control of degradation of performance. Although effects of grain boundary microstructure on bulk properties and performance of polycrystalline materials, have not been fully understood yet, but structural and geometrical versatilities of grain boundaries must be a key for the generation of high performance and even a new function, as demonstrated by Positive Temperature Coefficient Resistor, (PTCR) electroceramics [50].

#### ***4.4.3 Grain Boundary Connectivity***

When grain boundary-related phenomena occur as collective behavior of many boundaries, the connectivity of grain boundaries with different characters and structures becomes important. Simply speaking, if the character and structure of all grain boundaries are similar, the situation will become much simpler. However, boundary-related bulk properties of real materials is not such case. For instance, structure-dependent intergranular fracture processes in a polycrystal must be discussed in consideration of the fact that the path of crack propagation must be always kept in random grain boundaries, namely, weak random boundaries should be connected to each other more frequently as already shown in Fig. 4.5. We need to know how inactive/low-energy and active/high energy boundaries are connected to form 2D or 3D grain boundary network in a polycrystal. The grain boundary connectivity is defined by the type of triple junction. It is not difficult to imagine that the important of triple junction may depend on the number of weak or strong boundaries meeting at the junction. So we can define the type of triple junction, by simply counting how many random boundaries are joining at a given triple junction [43, 51]; one random and other two low-energy/strong boundaries, one strong and two weak random boundaries, or three weak random boundaries. This is the reason why structure-dependent boundary-related metallurgical phenomena should be considered as the percolation process and collective behavior in a polycrystal.

### **4.5 Metallurgical Factors Affecting GBCD**

#### ***4.5.1 Relation Between GBCD and Grain Size***

Here, we discuss important features associated with the grain boundary character distribution (GBCD) which can play a key role in Grain Boundary Engineering. Unfortunately we have not yet fully understood what metallurgical factors can affect GBCD. Accordingly, it is interesting to reveal whether or how GBCD can be related to the grain size. Until recently the grain size was the only grain boundary-related parameter generally used in discussions of the effect of microstructure

on bulk properties of polycrystalline materials in the last half century. It is well known that the Hall-Petch relationship can well describe the relation between bulk mechanical properties and the grain size [52]. However, in the authors' opinion, the time of reconsideration of the Hall-Petch relationship has come, in connection with recent findings of structure-dependent boundary related bulk properties.

Since the early 1980s, several workers including us have studied the relation between the grain size and GBCD in several pure metals and alloys, by using TEM and SEM-ECP, SEM-EBSD/OIM techniques. One of the results obtained by summarizing the experimental data on GBCD is shown in Fig. 4.7 for various polycrystalline metallic materials produced mostly by thermomechanical processing which has been most widely and extensively applied to the production of metallic engineering materials. The frequency of occurrence of special grain boundaries, typically low- $\Sigma$  coincidence boundaries ( $\Sigma < 29$ ) is plotted as a function of the grain size for some pure metals (Al, Fe, Mo, W) and iron alloys. We can recognize several interesting features of the plot in this figure: Firstly we can recognize the tendency that the frequency of low- $\Sigma$  coincidence boundaries (including low-angle ( $\Sigma 1$ ) boundary) decreases with increasing the grain size, although there is a large scatter of data points for different materials within the band. The second interesting feature is that the frequency of low- $\Sigma$  coincidence boundaries for very fine

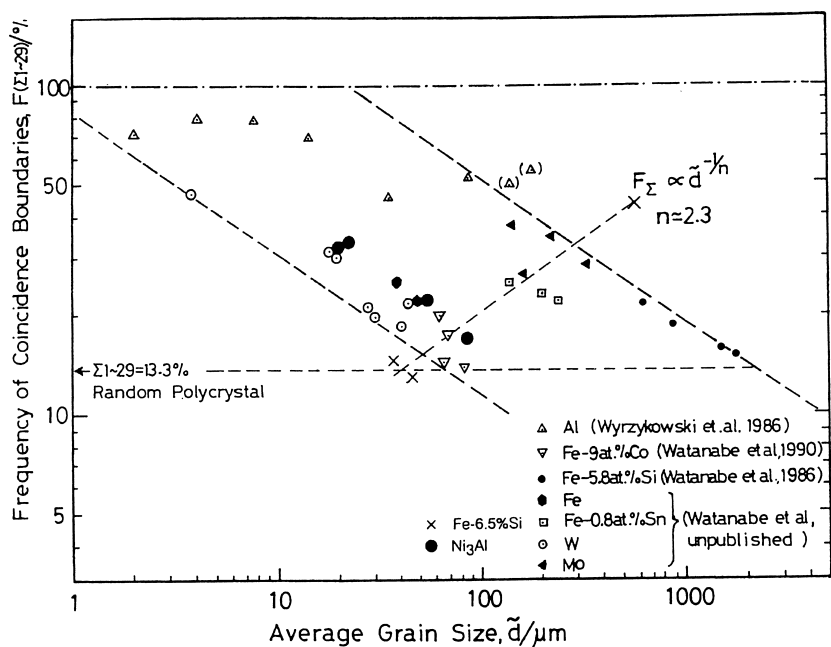


**Fig. 4.7** The frequency of low- $\Sigma$  coincidence boundaries ( $\Sigma = 1 \sim 29$ ) as a function of the mean grain size for thermomechanically processed bulk polycrystalline specimens of metals and alloys [16]. The data on rapidly solidified and annealed Fe-6.5mass%Si are also plotted in the figure, but showing the inverse relationship.

grained specimens, is higher than 50%, particularly for materials with the grain size smaller than  $10\text{ }\mu\text{m}$ . This may suggest the origin of unique or excellent properties which are often observed for ultrafine-grained materials. In fact, the above mentioned features have been more clearly evidenced by recent experimental studies on nanocrystalline materials like ECAP processed nickel [53], not in the case of electrodeposited nickel [54]. Finally the third interesting feature is that the data plot for the rapidly solidified and subsequently annealed Fe-6.5mass%Si alloy ribbons, indicated by a dotted line, shows the quite opposite relationship between the frequency of low- $\Sigma$  coincidence boundaries and the grain size in comparison with those for bulky specimens indicated by the band. In fact, this is due to the difference in the origin of the driving force for grain growth during annealing. Abnormal grain growth in the thin ribbons of the alloy can be driven by the surface energy which strongly depends on surface orientation of growing grain and annealing temperature [15]. Thus it has been revealed that the relationship between GBCD and the grain size can be quite different, depending on the mechanism of grain growth during annealing and original microstructures produced by different processing methods. This gives us an insight that GBCD can be largely controlled by some means in order to produce desirable bulk properties in polycrystalline materials, focusing the grain size, crystal structure (bcc, fcc, hcp, etc.), processing method and condition.

#### 4.5.2 *Relation Between GBCD and Texture*

Next let us look at the relation between GBCD and texture studied on rapidly solidified and subsequently annealed ribbon specimens of Fe-6.5mass%Si alloy [15, 55]. Figure 4.8 (a) shows the grain orientation distributions for the specimens differently annealed at different temperature for different times. The grain orientation distribution on as-solidified and slightly annealed ribbons A and B had “random texture”, while the specimens C and D, fully annealed at 1363 K and 1473 K for 3.6 ks, had sharp  $\langle 100 \rangle$  and  $\langle 110 \rangle$  texture, respectively. As a result of the evolution of such specific type of sharp texture, GBCD for  $\langle 100 \rangle$  and  $\langle 110 \rangle$  textured ribbons, shows quite different features as indicated in Fig. 4.8 (b). It was found that a higher frequency of low- $\Sigma$  coincidence boundaries can occur in the descending order of  $\Sigma$  value. Of particular interest and importance is the values of  $\Sigma$  of coincidence boundaries which actually occurred in the studied specimens; they are  $\Sigma 1, 5, 3, 25$  for  $\langle 100 \rangle$ -textured specimen, and  $\Sigma 1, 3, 9, 11, 17, 19$  for  $\langle 110 \rangle$ -textured specimen, as almost exactly predicted as possible coincidence orientations for  $\langle 100 \rangle$  and  $\langle 110 \rangle$  rotation axis respectively, by the coincidence-site lattice (CSL) theory of grain boundary structure [56]. It is reasonable to consider that the more ordered atomistic structure of grain boundary can occur for the lower- $\Sigma$  coincidence boundary, even if the boundary inclination can be another parameter affecting the grain boundary atomic structure and the grain boundary energy. In fact, it was experimentally evidenced that several lower- $\Sigma$  coincidence

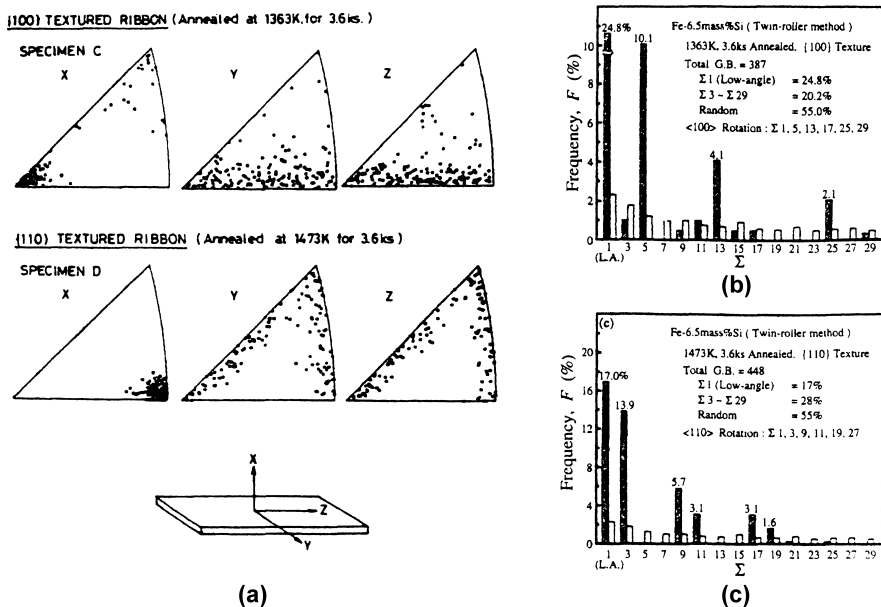


**Fig. 4.8** (a) Grain orientation distribution in {100}- and {110}-textured Fe-6.5mass%Si ribbons produced by rapid solidification and subsequent annealing for 3.6ks at 1363 K and 1473K, respectively [55]. (b) and (c) The frequency of low- $\Sigma$  coincidence boundaries as a function of  $\Sigma$  for {100}- and {110}-textured Fe-6.5mass%Si ribbons, respectively.

boundaries such as  $\Sigma 3$  and  $\Sigma 9$  have lower values of the grain boundary energy in comparison with random/general boundaries without any special relative orientation for the same sharply  $\langle 110 \rangle$  textured Fe-6.5mass%Si alloy ribbon with bcc structure [57]. Some slight difference ( $<10\%$ ) of the relative boundary energy observed for the  $\Sigma 3$  and  $\Sigma 9$  boundaries with different misorientation angles, may be due to the difference of the boundary inclination. Several groups have predicted [58–62] the close relationship between GBCD and the type and sharpness of texture by modelling textured polycrystals and the results were in good agreement with the observations on the Fe-6.5mass%Si alloy ribbons mentioned above. When the sharpness of a specific  $\langle hkl \rangle$  type of texture is increased, the level of the frequency of low- $\Sigma$  (including low-angle  $\Sigma 1$ ) systematically increases and it goes down in the descending order of  $\Sigma$  values given by the CSL orientation relationship for the  $\langle hkl \rangle$  rotation axis.

Here it is worth-while noting whether the relationship between GBCD and the type and sharpness of texture in polycrystals can be affected by crystal structure, for instance between bcc and fcc. It is well known that there is a large difference of microstructure and grain structure in polycrystals, in connection with the stacking fault energy. In particular fcc metals and alloys with low stacking fault energies like copper-base alloys, and austenitic stainless steels, have a high density of twins introduced during fabrication processing and subsequent annealing after deformation, but not in bcc metals and alloys with high stacking fault energies. As

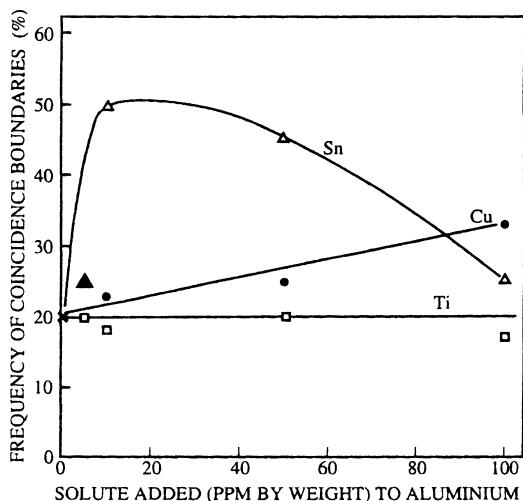
a result of this, multiple twinning can occur during annealing and thermomechanical processing, resulting in the evolution of “random texture” due to grain division and the occurrence of a higher frequency of  $\Sigma 3$ -related coincidence boundaries with  $\Sigma 3^n$  ( $n$  is the order of twinning, taking 1, 2, 3 for the first, second, third order twinning). This characteristic feature has been effectively utilized in grain boundary engineering for fcc materials with low-stacking fault energies, for example in order to improve the resistance to corrosion and stress-corrosion cracking in nickel-base-alloys [19, 35] and austenitic stainless steels [38, 39] and high temperature creep strength of nickel base-alloys [35, 40]. As discussed later, this is currently prevailing basis of GBE for fcc materials with low stacking fault energies, not applicable to bcc materials with high stacking fault energy. On the other hand, it is also known that unidirectional solidification or unidirectional annealing under a steep thermal gradient can introduce a sharp texture associated with columnar grain structure and a high frequency of low- $\Sigma$ /low-energy boundaries into polycrystalline materials, particularly in bcc materials without twin formation even during rapid solidification. In such case, the anisotropy of crystal structure and physical properties (e.g. thermal conductivity, orientation-dependent surface energy) can be the origin of the evolution of a sharp texture;  $\langle 100 \rangle$  textured columnar grain structure is often formed by solidification of cubic materials, although the sharpness of texture depends on the temperature gradient and solidification rate.

#### **4.5.3 Relation Between GBCD and Material Purity/Composition**

Grain boundaries inevitably play important roles in the evolution of a microstructure through their formation and migration occurring in a polycrystal, during solidification, recrystallization, phase transformation associated with actual materials fabrication processing. It is not difficult to consider that the formation and migration of grain boundaries are structure-dependent phenomena based on the interfacial dynamics so that these processes must be affected by the grain boundary energy. From current basic knowledge of grain boundary structure and migration [63], the material purity and composition are well known to greatly affect the migration of grain boundaries and resultant grain growth through segregation of impurity or solvent elements to moving boundaries, leading the evolution of a large variety of the microstructure even in the same condition of processing. Possible effect of the material purity and composition on GBCD was first studied systematically by Belluz and Aust [64] using zone refined aluminium polycrystals with systematically controlled amount of tin, copper and titanium. As seen in Fig. 4.9, by 10 ppm addition of tin was found to drastically increase the frequency of low- $\Sigma$  coincidence boundaries from 20% to 50%, while no change of the frequency was observed by addition of titanium and slight increase by copper addition. In fact, the GBCD is a measure of the grain boundary microstructure which was finally formed, as a result of the involvement of a number of boundary-related phenom-



**Fig. 4.9** Effects of micro-alloying of Sn, Cu and Ti on the frequency of low- $\Sigma$  coincidence boundaries in recrystallized zone-refined aluminium polycrystals (after Belluz and Aust, [64]).



ena. Understanding of observed effects of material purity/composition on GBCD needs systematic investigation and careful consideration into each of related phenomena involved in the evolution of studied grain boundary microstructures. Unfortunately, only a little is known about this kind of important issue of microstructure control, although extensive work has been performed by try and error, called “Microalloying” so far. Much remains to be studied in order to establish basic knowledge associated with GBCD and related factors, even for engineering metallic materials based on popular metals like iron, copper, aluminium, and nickel, although some basic studies were performed early by Aust’s group [18,20] and Watanabe’s group [15,16,65]. In the present authors’ opinion, it is strongly required to perform such a basic experimental study of the effect of the material composition/purity on grain boundary properties and GBCD, because structure-dependent grain boundary migration can be drastically affected by the level of the purity, sometimes showing quite opposite feature caused by impurity effects [63].

#### 4.6 Prediction of GBCD-Controlled Brittle-Ductile Transition and Fracture Toughness

It is important to study how and to what extent the fraction of strong or weak boundaries, GBCD and the grain boundary connectivity can affect the fracture processes and fracture characteristics in polycrystalline materials. Lim and Watanabe performed a modelling of GBCD-controlled fracture processes and predicted the fracture toughness as a function of strong low-energy boundaries, for the two-dimensional (2D) polycrystals with hexagonal grain structure [66] and for the three-dimensional (3D) polycrystals composed of tetrakaidecahedron-shaped grains [67]. They assumed that the longitudinal grain boundaries to the stress axis

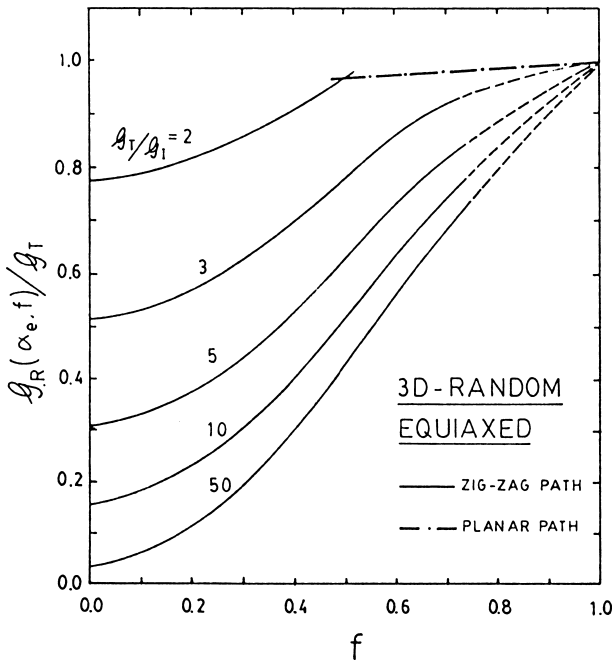


**Fig. 4.10** Effect of the overall fraction of low-energy boundaries,  $f$ , and  $G_T/G_I$  on the toughness of a 3D polycrystal having a random GBCD [67].

would not experience a large normal stress and hence less liable to intergranular fracture irrespective of their character. Two common types of fracture paths are considered as already schematically shown in Fig. 4.5, the “zigzag path” formed by interlinkage of intergranular fracture and the “planar path” formed mainly by transgranular fracture producing relatively smooth fracture surface over the grain size.

Figure 4.10 shows one of the results from the modelling of the fracture toughness as a function of the overall fraction of strong special boundaries ( $f$ ) for the 3D polycrystals having a random GBCD and different  $G_T/G_I$ , where  $G_T$  and  $G_I$  are the toughness of a typical transgranular fracture path and an intergranular fracture path, respectively. It is evident that the fracture toughness of 3D polycrystals increases monotonically with increasing the fraction,  $f$ , of strong special boundaries. Of particular interest is that the fracture toughness can be more effectively enhanced by increasing the fraction ( $f$ ) of strong low-energy boundaries in “brittle materials with a higher value of  $G_T/G_I$ ”. It was also found that a brittle-ductile transition could occur in connection with a change in fracture mode from intergranular fracture with low-toughness to transgranular fracture with high toughness when the overall fraction of strong low-energy boundaries reaches a critical value dependent on the value of  $G_T/G_I$ , being a measure of the brittleness of a material. The brittle to ductile transition occurs at a higher level of the overall fraction of strong boundaries,  $f$ , when  $G_T/G_I$  becomes greater, namely, a polycrystal becomes

more intergranularly brittle. This suggests that an increase of the overall fraction  $f$  works more effectively to toughening brittle material in which intergranular fracture occurs predominantly causing more severe brittleness. In the modelling, the effects of the boundary inclination and the grain aspect ratio on the fracture toughness were also be predicted on the basis of GB-CD-controlled fracture in the 2D and 3D polycrystals [66, 67].

## **4.7 The Control of Intergranular Brittleness by Grain Boundary Engineering**

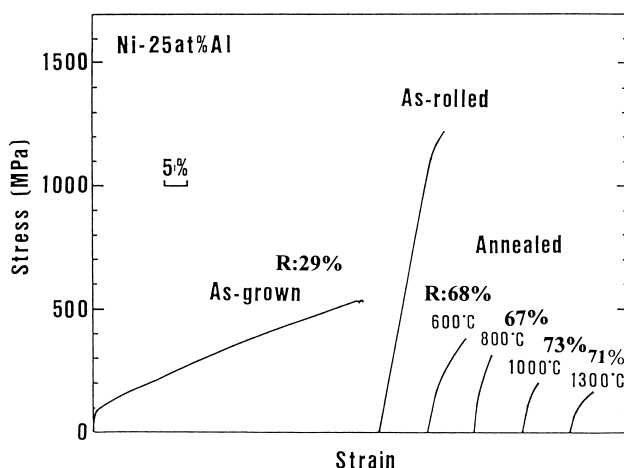
Severe brittleness is the most serious among many problems associated with engineering materials, whether the material may be classified into structural or functional one, because it decisively hinders the material from its fabrication processing, machining and service performance. Until presently, the control of intergranular brittleness of engineering materials has been extensively studied and repeatedly discussed [12, 13, 68, 69] but has not been fully solved yet. Moreover the demand for controlling intergranular fracture and brittleness has been increasing because the size of machine parts has been decreasing, as in the case of microelectronic devices or mechanoelectric machine system (MEMS). The heterogeneity of microstructure may degrade the reliability and stability of materials performance for micromachines. Accordingly the control of severe brittleness of intrinsically and extrinsically brittle polycrystalline materials is urgent. In this chapter we overview recent achievements of the grain boundary engineering for the control of intergranular brittleness and enhancement of ductility in intrinsically and extrinsically brittle materials. We briefly introduce how a breakthrough of the long pending problem has been brought about by the grain boundary engineering.

### ***4.7.1 The Control of Intrinsic Intergranular Brittleness***

Let us begin with the control of intergranular brittleness of intrinsically brittle materials such as refractory metals as molybdenum, intermetallics and ceramics. From the prediction of GB-CD-controlled fracture characteristics mentioned above, we can expect that as increase of the fraction of strong special boundaries such as low- $\Sigma$  boundaries, conversely a decrease of the fraction of weak random boundaries will control intergranular fracture, resulting in an enhancement of ductility of brittle materials. We need to prove the prediction by experimental evidence. So our first evidence for the control of intergranular brittleness by the grain boundary engineering is taken from the early work on “intrinsically brittle” B-free  $\text{Ni}_3\text{Al}$  polycrystalline intermetallics. It is well known that polycrystalline B-free

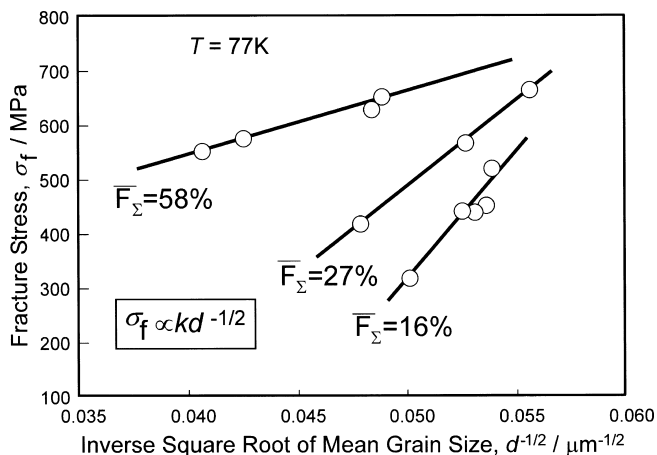
$\text{Ni}_3\text{Al}$  is very brittle, and the addition of a very minute amount (10 ppm) of boron (B) can drastically improve the ductility. However, unfortunately B-addition was found to cause severe brittleness again when the materials is heated at high temperature because of abnormal grain growth due to grain boundary segregation of B. This is a fatal problem to polycrystalline  $\text{Ni}_3\text{Al}$  which is expected its service as high temperature material. Fortunately the control of severe intergranular brittleness of B-free polycrystalline  $\text{Ni}_3\text{Al}$  was successfully achieved by the grain boundary engineering through unidirectional solidification by zone-melting [70–72].

Figure 4.11 shows the stress-strain curves observed for B-free  $\text{Ni}_3\text{Al}$  polycrystalline specimens with different fractions of weak random (R) boundaries, tested at room temperature. It is evident that as-grown (zone-melted) specimen, which had a sharp texture and a lower fraction of random boundaries of 29% or a high fraction ( $\sim 70\%$ ) of low- $\Sigma$  (1, 3, 9) coincidence boundaries, showed excellent elongation greater than 50% at room temperature. However once rolled (25%) and subsequently annealed at temperatures ranging from 600°C to 1300°C, the fraction of random boundaries (R) drastically increased (more than twice of that of as-grown specimen) and excellent ductility of the as-grown specimen disappeared and would never come back, even if the specimens were annealed at very high temperatures of 1300°C ( $= 0.95 T_m$ ). Thus it was revealed that the introduction of a high fraction of strong special boundaries, or the reduction of the frequency of random boundaries can definitely improve the ductility of the material. Surprisingly “thermomechanical processing” ordinarily and extensively applied to metallic materials does not work for ductility improvement in B-free  $\text{Ni}_3\text{Al}$ . This finding gives some warning to the approach to thermomechanical processing in the case of polycrystalline intermetallics.



**Fig. 4.11** Stress-strain curves observed on B-free polycrystalline  $\text{Ni}_3\text{Al}$  specimens with different fractions of random boundaries (R), produced by unidirectional solidification through zone-melting [71].

Next, let us look at the second case of controlling intrinsic brittleness in molybdenum polycrystals produced by thermomechanical processing from single crystal or sintered compact. We could change the grain boundary microstructure in the specimens having a wide range of GBCD and the grain size. The details of this work are known elsewhere [21, 73, 74]. Figure 4.12 shows the fracture stress plotted as a function of the grain size for those three groups of specimens which had different levels of the frequency of low- $\Sigma$  coincidence boundaries ( $F_{\Sigma}=58\%$ ,  $27\%$ ,  $16\%$ ). It is clear that the fracture stress vs grain size plot well obeys the Hall-Petch type relationship for the three groups of specimens, but the slope was found to depend on the level of the frequency of low- $\Sigma$  coincidence boundaries, showing a smaller value for a higher  $F_{\Sigma}$ . This finding has been tentatively explained by suggesting the situation whether crack nucleation or propagation can control the overall percolation and collective behavior of GBCD-controlled fracture processes and characteristics [74], the smaller Hall-Petch slope which was observed on the specimens with higher  $F_{\Sigma}$  and higher level of fracture stress, may reflect the fracture mechanism of a polycrystal controlled by crack initiation, while the greater slope observed on the specimens with lower  $F_{\Sigma}$  may reflect a fracture mechanism controlled by crack propagation. This situation can be imagined by considering brittle-ductile transition of fracture mode depending on  $F_{\Sigma}$ , as previously shown in Fig. 4.5 and predicted by Fig. 4.10. We have demonstrated several experimental evidence for GBCD-controlled intergranular fracture and the applicability of GBE to controlling severe brittleness in intrinsically brittle materials. Next we discuss the case of GBE for extrinsically brittle materials.



**Fig. 4.12** The Hall-Petch type plot of the fracture stress vs the mean grain size, for three groups of polycrystalline molybdenum specimens with different levels of the fraction of low- $\Sigma$  coincidence boundaries  $F_{\Sigma}$  [74].

### 4.7.2 *The Control of Oxidation-Induced Intergranular Brittleness*

Polycrystalline materials become brittle due to the origins extrinsically induced by environmental effects during their fabrication or service. One of examples of such cases is oxidation-induced brittleness occurring in normally ductile materials like copper, nickel and iron. In this section we discuss recent findings on structure-dependent intergranular oxidation obtained from a systematic study and recent achievement of the grain boundary engineering for the control of “extrinsic brittleness” due to oxidation-induced intergranular fracture in Ni-30 at.%Fe alloy. Yamaura et al. are probably the first who have made a systematic investigation into structure-dependent intergranular oxidation [75] and applied the concept of GBE to the control of oxidation-induced brittleness of polycrystalline materials, by using Ni-30 at.%Fe alloy specimens with grain boundary microstructures systematically controlled [76, 77]. On the basis of observed results on structure-dependent intergranular oxidation, they attempted the control of oxidation-induced brittleness, by introduction of optimum grain boundary microstructures produced by unidirectional solidification and subsequent annealing and characterized by the SEM-EBSD/OIM technique.

In order to reveal structure-dependent intergranular oxidation, a careful study of structure-dependent intergranular oxidation were made by measuring the extent of intergranular oxidation from the width of oxidized region at individual grain boundaries with different characters [75]. It was found that high-energy random (R) boundaries could be preferential sites for oxidation, while special low- $\Sigma$  coincidence boundaries were little or only slightly oxidized (see Fig. 4.13). Thus it is evident that high-energy random boundaries can be preferential sites for

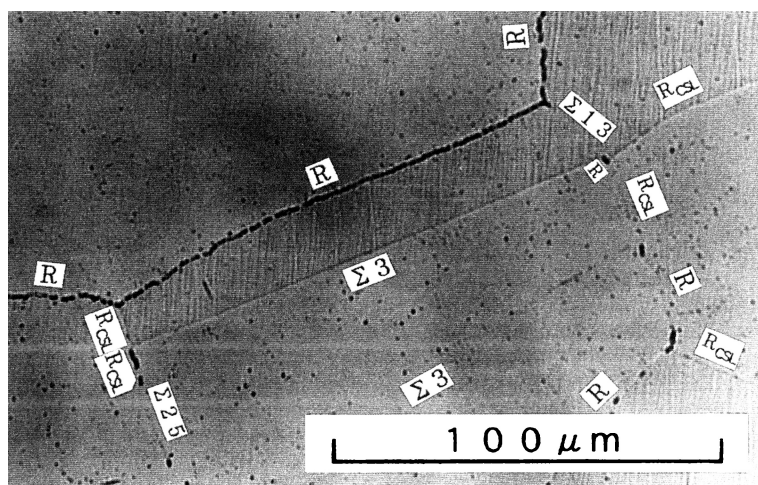


**Fig. 4.13** An example of structure-dependent intergranular oxidation observed in Ni-40 at.%Fe alloy in dilute  $O_2$  atmosphere [75]. Note that random boundaries are preferential sites for oxidation.

oxidation. Another important finding is that the grain boundary structure differently affects intergranular oxidation, depending on the partial pressure of oxygen. In the argon and oxygen mixed gas atmosphere with low oxygen partial pressure, the more significant structure-dependent intergranular oxidation was observed. On the other hand, in pure oxygen gas atmosphere, weaker or less sensitive structure-dependent intergranular oxidation was observed. Thus strong structure-dependent intergranular oxidation and the effect of oxygen partial pressure were revealed in Ni-30 at.%Fe alloy [75, 76]. In order to prove the applicability of the grain boundary engineering to the control of oxidation-induced brittleness, creep-oxidation tests were carried out by using Ni-30%Fe alloy ribbon specimens with the grain boundary microstructures initially controlled by rapid solidification and subsequent annealing, before creep testing [77]. As seen from Fig. 4.14 (a), (b), when the grain size of specimen was small and the fraction of random boundaries is high, thicker oxidized region extended inside more deeply from the surface. On the other hand, when the specimens had a low fraction of random boundaries (a high fraction of low- $\Sigma$  coincidence) showed excellent oxidation resistance, as seen from Fig. 4.14 (c), (d). However it should be kept in mind that when the grain size is large and only a few random boundaries exist, those random boundaries act as preferential sites for oxidation and easy path of crack nucleation and propagation, resulting in the formation of a long intergranu-

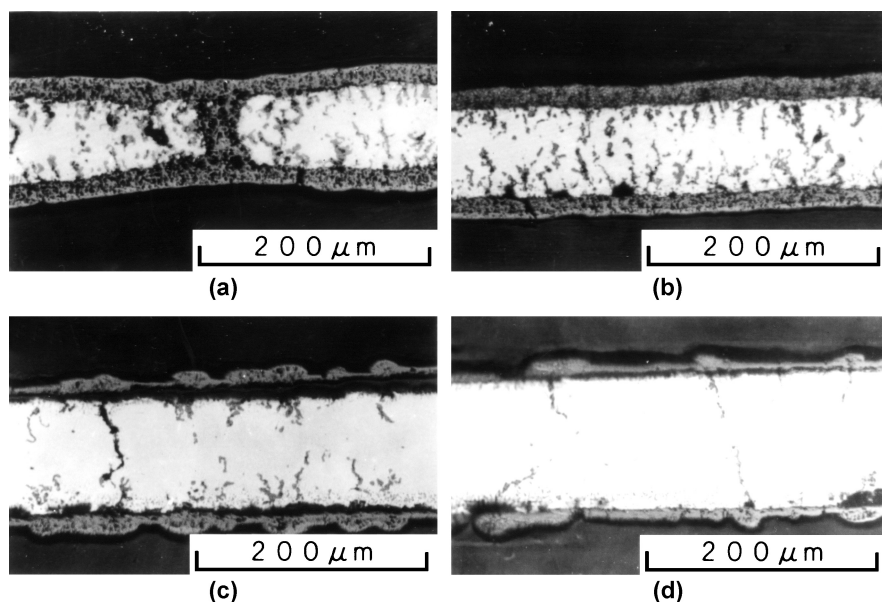


**Fig. 4.14** Optical micrographs showing different oxidation behavior observed on the sectioned planes for Ni-40mass%Fe alloy ribbon specimens differently processed for different grain boundary microstructures [76]. (a) as-solidified at 28.3 m/s,  $d=2\mu\text{m}$ , (b) as-solidified at 14.1 m/s,  $d=3.7\text{ mm}$ , (c) solidified-annealed at 1073 K, 1 h,  $d=3.5\text{ mm}$  (d) solidified-annealed at 1473 K, 1 h,  $d=50\mu\text{m}$ .

lar crack running from the surface. These findings suggest a new approach to the grain boundary engineering, particularly for future development of high performance nickel-base alloys for turbine blades and other parts of aircraft engine, which should be immune from oxidation-induced brittleness at high temperatures in low atmospheric or low oxygen pressure. One more beneficial effect found in this work [77] is that an increase of the fraction of special low- $\Sigma$  coincidence boundaries enhanced high temperature creep strength of polycrystalline ribbon specimens of the alloy, as observed in creep deformation of zinc bicrystals [78], polycrystalline pure nickel [79] and nickel base-alloy [35, 40].

Now let us summarize our findings and discussions regarding structure-dependent intergranular oxidation, oxidation-induced intergranular brittleness during creep deformation at high temperature and the application of GBE for the control of oxidation-induced intergranular brittleness and for enhancement of creep strength in the Ni-30 at.%Fe alloy. Figure 4.15 shows a schematic presentation of the approach to GBE for the control of oxidation-induced intergranular brittleness by manipulation of the grain boundary microstructure, focusing the grain size, GBCD and grain boundary connectivity, based on GBCD-controlled fracture in polycrystalline materials. The control of oxidation-induced intergranular brittleness is possible by introducing “optimum grain boundary microstructure”, i.e. by decreasing the grain size and the fraction of high-energy random boundaries or by increasing the fraction of low- $\Sigma$  boundaries, as indicated by the grain boundary microstructure given on the bottom-left of the figure. We suggest that the direction of GBE summarized above will be generally applicable to both

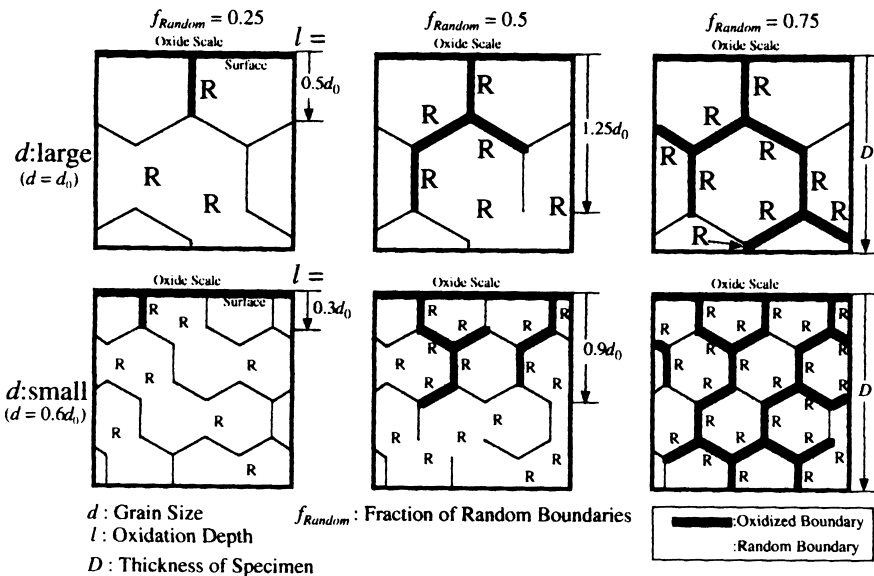


**Fig. 4.15** A schematic illustration of oxidation-induced intergranular fracture controlled by the grain boundary microstructure, i.e., grain size, GBCD and the grain boundary connectivity [76].



“intrinsic” and “extrinsic” intergranular brittleness, irrespective of the origin of intergranular brittleness, as long as intergranular fracture occurs predominantly in polycrystalline materials. The application of GBE to the control of oxidation-induced brittleness to non-oxide ceramics SiC has also been successfully achieved recently [80, 81].

## **4.8 Grain Boundary Engineering by Magnetic Field Application**

The application of external fields has been discussed as a powerful tool to incorporate desirable microstructures into polycrystalline materials during fabrication processing [45, 46]. It is reasonable to imagine that the evolution of microstructure can be affected by the interaction of any external field with lattice defects (including grain and interphase boundaries) which are important components of microstructure [45]. Although there are not many early works on this subject [82–86], more recently the application of a high magnetic field has been drawing an increasing interest of many researchers, in connection with the control of microstructure and texture during annealing, sintering, solidification, phase transformation in iron-base alloys, steels [87–93] and non-ferrous materials [94–97]. This is because a high magnetic field has become applicable at laboratory level without much difficulties, by using a helium-free superconducting magnet. We can produce a high magnetic field up to about 10T. In the last decade we have been deeply involved in basic studies on the related subjects and, quite recently, several review papers on the grain boundary engineering by magnetic field application have been written by the present authors [46, 98, 99]. Hence we briefly introduce some interesting findings obtained from recent our studies.

### ***4.8.1 The Control of Segregation-Induced Brittleness***

It is well known that the segregation of detrimental elements to grain boundaries make normally ductile metals brittle, as in the case of copper by bismuth, iron and steels by tin, sulfur, phosphorus, nickel by sulfur. Those elements which have lower solid solubility in base metal and alloy, tend to segregate to grain boundaries, as predicted by the Seah-Hondros diagram [100]. Moreover it has been found that the amount of grain boundary segregation again depends on the grain boundary structure and that high-energy random boundaries can preferentially accommodate segregants, while segregation is difficult at low-energy special boundaries, as can be understood from the grain boundary segregation diagram [101, 102]. We know that segregation-induced brittleness is often serious problems of ordinary structural materials like steels. Particularly the effect of grain boundary segregation can be increased by accumulation of detrimental impurity

elements by recycling used materials, as is the case of copper taken in steels. How can we solve this problem?

Here we present a very important finding that the amount of segregants can be controlled by application of a high magnetic field [103]. We studied the effect of a magnetic field on grain boundary segregation at high-energy random boundaries and low-energy special boundaries using polycrystalline specimens of iron-0.8 at.%tin alloy which were prepared from the sheet produced by hot-forged, hot-rolled and finally magnetically annealed at 973 K for 6 h in a magnetic field of 3T and 6T in vacuum. As seen in Fig. 4.16 (a), when annealed ordinarily without a magnetic field, a marked segregation of tin to random boundary occurred which was almost 1.5 times higher than the concentration of tin in the grain interior. On the other hand, Fig. 4.16 (b) shows that in the magnetically annealed specimen, the segregation of tin did not occur even at random boundary which is known as preferential site for segregation. The application of a magnetic field restricted the segregation of tin to iron grain boundaries. This finding is very important and has provided us with a new clue to the control of detrimental effects of segregation and segregation-induced intergranular brittleness. In order to confirm the possibility of the control of segregation-induced brittleness by magnetic field application, we have studied the fracture toughness of polycrystalline specimens of iron-0.8 at.%tin alloy, which received magnetic annealing. As shown in Fig. 4.17, it was found that the fracture toughness increases with increasing magnetic field up to 6T, depending on the grain size. It is evident that the application of a high magnetic field is a powerful tool to control segregation-induced brittleness in iron-tin

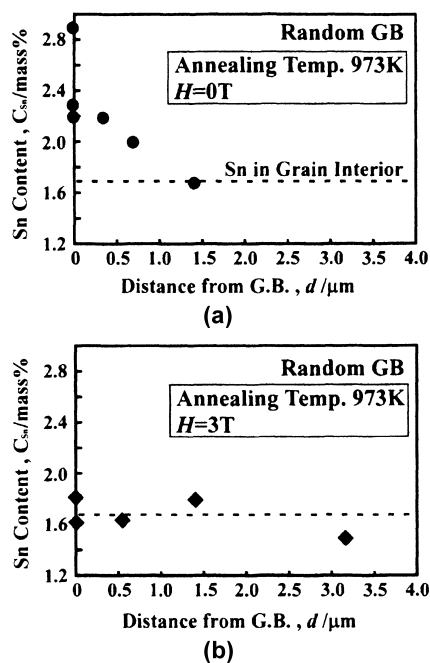
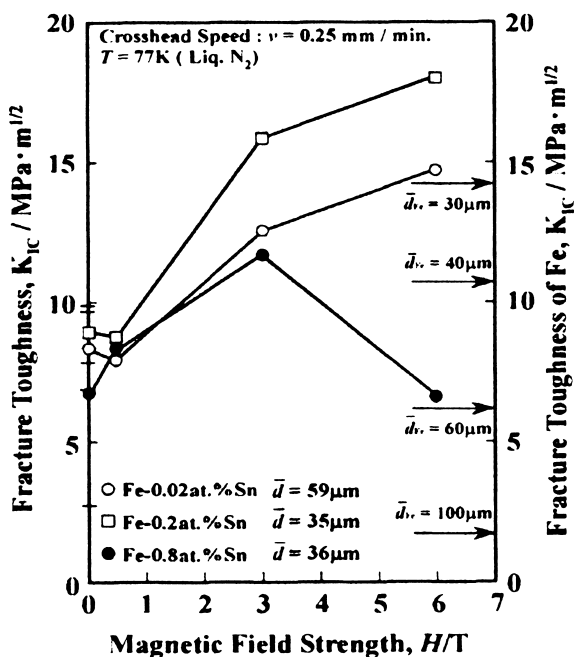


**Fig. 4.16** Effect of magnetic annealing on the segregation of tin (Sn) to random boundaries in Fe-0.8 at.%Sn alloy annealed at 973 K: (a) ordinary annealing without a magnetic field, (b) magnetic annealing in DC magnetic field of 3T [103].

**Fig. 4.17** Fracture toughness as a function of the field strength for magnetic annealing for Fe-0.8 at.%Sn alloy specimens. For comparison, the fracture toughness values for pure iron with different grain sizes are indicated by the arrows along the ordinate on the right hand [103].

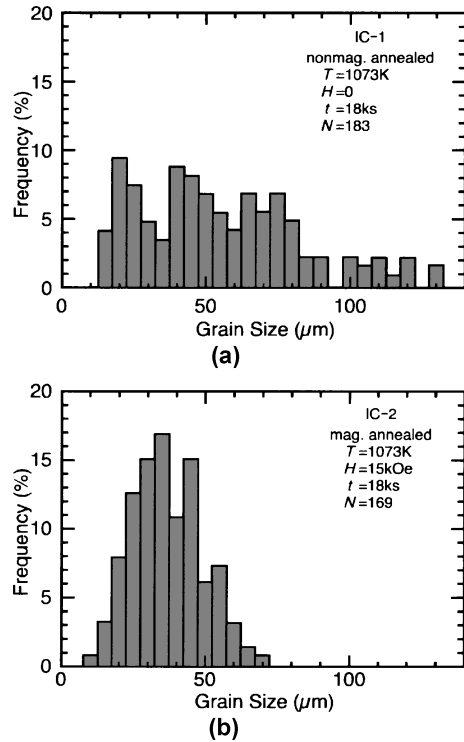


alloy in which tin segregation is known to exert detrimental effects on mechanical and corrosion properties in iron-base alloy and steels. It is very promising that the control of segregation by magnetic field application can be applied to solve a unsolved problem of the accumulation of detrimental impurity or solute elements by multi-recycling of used materials. The most recent findings on the effects of a magnetic field on carbon diffusion [104] and on surface diffusion in iron [105] may be very useful for understanding of the microstructure evolution by magnetic field application in iron-base alloys and steels. Furthermore, the beneficial effect of a magnetic field was found on rejuvenation of damaged iron-base alloy deformed at high temperature [106]. This has a great engineering importance to the application to the materials for turbine blades and nuclear reactors through rejuvenation of damages accumulated during their service.

#### 4.8.2 The Control of Abnormal Grain Growth and Heterogeneous Microstructure

In a polycrystalline material, grain growth inevitably and generally occurs due to the migration of grain boundaries or interphase boundaries, during annealing of deformed state, crystallization from amorphous state, solidification from the melt, sintering of powder compact and vapour deposition. We can easily imagine the situation that grain boundaries play important roles in grain growth phenomenon

**Fig. 4.18** The grain size distribution for Fe-50%Co rapidly solidified ribbons annealed at 1073 K (a) without a magnetic field, (b) with a DC magnetic field of 1.5T [46].



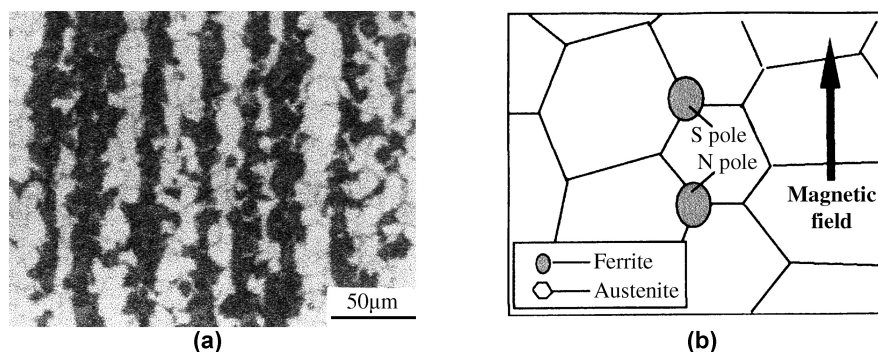
and the evolution of grain structure in a polycrystal. Again we should keep in mind that the migration of grain boundary strongly depends on the grain boundary character and structure, material purity and composition, and other factors, as clearly shown by Gottstein and Shvindlerman in their recent book [63]. The application of a magnetic field was attempted very early to control the microstructure for improvement in magnetic properties of softmagnetic silicon-steel [82]. However, until recently, only a little basic studies were performed to reveal the effect of a magnetic field on grain boundary migration and grain growth phenomena [84, 96].

Figure 4.18 shows one of results observed on the distribution of grain sizes in iron-50 at.%cobalt iron ribbons produced by rapidly solidification and subsequent annealing without or with a magnetic field [46]. Without a magnetic field, the distribution of grain size spread very widely, indicating occurrence of heterogeneous grain structure due to abnormal grain growth, resulting in the occurrence of abnormally grown large grains. On the other hand, the distribution of grain sizes was much narrower in magnetic annealing than that of the former. More uniform grain structure was formed by the application of a magnetic field. In fact, recent basic studies of the effect of a magnetic field on grain growth have revealed that grain growth was enhanced by magnetic field application at very early stage of annealing and grain growth in nanocrystalline nickel and its alloys [107]. It is very

likely that once uniform grain structure is formed and stabilized, normal grain growth may proceed at later stage of annealing, resulting in the formation of homogeneous grain structure. However, at present, the effect of a magnetic field on grain growth, particularly the origin of enhancement of grain growth at early stage by magnetic field application has not been fully understood yet. It is very likely that the interaction of grain boundary with a magnetic field may affect structure-dependent migration of grain boundaries. Unfortunately we know little about the relationship between electromagnetic structure and atomistic structure of grain boundaries in a magnetic field. There is much need for further work on this subject in order to establish the grain boundary engineering based on the control of grain boundary microstructure by magnetic field application.

### ***4.8.3 Microstructure Control by Magnetic Phase Transformation***

The phase transformation is always an important source of the microstructure evolution in polycrystalline materials, because the formation and migration of grain boundaries and interphase boundaries are elementary processes of phase transformation under chemical driving force. However, when another type of the driving forces plays a role, the nucleation and growth of the product phase may be affected during phase transformation, as discussed on magnetic aging associated with spinodal decomposition, discussed by J.W. Cahn early in 1960s [85]. There are several possible origins of the driving force. The following possibilities associated with magnetic fields have been suggested [98]: (a) the difference in magnetic moment between the parent and the product, (b) crystalline magnetic anisotropy, (c) shape-dependent magnetic anisotropy, (d) field-induced magnetization energy, (e) orientation-dependent magnetostriction, (f) the difference in electromagnetic state between the grain boundary and the grain interior, (g) Lorentz force under superposition of electrical and magnetic field. Since the phase transformation is always interface-related phenomenon, we can expect some useful influence of a magnetic field on different kinds of phase transformation to incorporate optimum microstructure into a material. Here we take an example of the microstructure control by magnetic field application based on the effect of a magnetic field on  $\gamma/\alpha$ , or  $\alpha/\gamma$  phase transformation in iron alloys and steels, having a large variety of research interests and engineering importance from the view point of the grain boundary engineering for iron alloys and steels. As well known, in these materials, the phase transformation associated with  $\alpha$ ,  $\gamma$ ,  $\delta$  phases together with the magnetic transformation can produce a much large variety of microstructures. This may endow a high performance to polycrystalline ferrous materials through rich combinations of heat treatments or thermomechanical processings dependent on temperature and magnetism. Quite recently, the application of a magnetic field has been drawing a increasing interest of researchers after Choi et al. renewed our interest in the effect of a magnetic field on  $\gamma/\alpha$  phase transformation that the transformation temperature can be decreased by



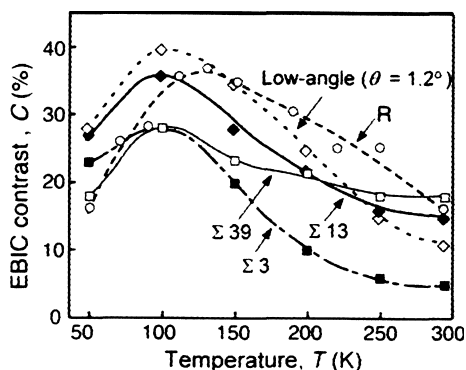
**Fig. 4.19** (a) Microstructure observed after magnetic heating at 1153 K for 33 min and cooled at 10°/min with a magnetic field of 14T, (b) schematic illustration of nucleation of ferrite phase at austenite grain boundary triple junctions along the magnetic field direction [92].

application of a magnetic field and the ferrite phase is formed being aligned in the direction of a magnetic field [91]. More recently several groups have investigated the effect of a magnetic field on microstructure evolution during  $\gamma/\alpha$ , or  $\alpha/\gamma$  phase transformation in steels of similar or different composition, as introduced by recent review by Enomoto [108]. Zhang et al. have studied the effect of a magnetic field on the formation of two-phase lamellar structure composed of aligned ferrite and pearlite phases in plain-carbon steel [92], shown in Fig. 4.19 (a), and they proposed a model for the mechanism of magnetic phase transformation to explain the ferrite phase aligned in the field direction, as schematically shown in Fig. 4.19 (b). Triple junctions are assumed to be preferential sites for nucleation of product ferrite phase and the formation of magnetic dipoles between separating ferrite phases at triple junctions directs the growth of ferrite phase resulting aligned lamellar structure of ferrite and pearlite. From the view point of the grain boundary engineering, the possibility of the formation of elongated lamellar two-phase structure by magnetic field application is of great engineering importance, in connection with the control of interface inclination and the formation of anisotropic multi-phase microstructure which may bring about some anisotropic bulk property.

## 4.9 Grain Boundary Engineering for Photovoltaic Polysilicon

Up to now, we have discussed focusing on structural materials more than functional materials. However we have already studied the grain boundary engineering for functional materials [31], such as ferromagnetic metallic materials, semiconductor and electroceramics. So in this chapter, we introduce the most recent work on the grain boundary engineering by unidirectional and rotational solidification for photovoltaic polysilicon for solar cell. The detail of this work [109] and related basic studies of structure-dependent electric properties of grain boundaries in

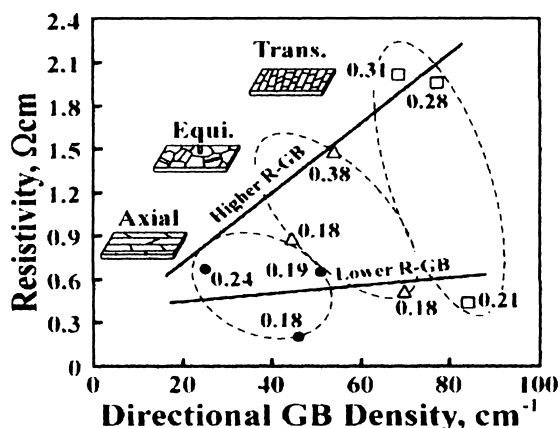
**Fig. 4.20** Changes in EBIC contrast as a function of temperature for silicon grain boundaries with different characters [110].



polysilicon have been reported elsewhere [110, 111]. It has been found that electrical activities observed by EBIC technique strongly depends on the grain boundary character and structure, similarly as observed for mechanical, chemical and thermal properties of grain boundaries in metallic materials. In particular, electrons and positive holes produced by solar beam irradiation tend to cause the recombination, resulting in discharging of electric current. This recombination phenomenon determines the efficiency of solar cell composed of thin film polysilicon. We have revealed that the tendency to recombination is closely related to the character and structure of grain boundary and also temperature [110].

Figure 4.20 shows the measurements of EBIC contrast observed for different types of silicon grain boundaries, plotted as a function of temperature. It is evident that random boundaries showed strong EBIC contrast associated with higher activity than other low- $\Sigma$  coincidence boundaries like  $\Sigma 3$ . Moreover it was found that the EBIC contrast can be affected by the boundary inclination, depending on whether the boundary position is a coherent or incoherent portion of  $\Sigma 3$  twin boundary. Electric activity of coherent  $\Sigma 3$  is extremely low and almost unmeasurable. This means the presence of this kind of special boundaries does not affect the efficiency of energy conversion of polysilicon solar cell. On the other hand EBIC contrast of low-angle boundaries, which are composed of lattice dislocations with large Burgers vector, is so strong as random boundary because lattice dislocations composing a low-angle boundary can effectively scatter electron or positive holes moving in polysilicon. In fact, the overall efficiency of polysilicon solar cell comes from collective and percolation movement of electrons and positive holes generated by sun beam irradiation. Modelling of collective motion of charge carrying particles in solar cells composed of polysilicon with different grain boundary microstructures has been performed in order to compare with the observed electrical properties of polysilicon specimens. Figure 4.21 shows the effect of grain boundary microstructure on the resistivity studied on polysilicon specimens produced by unidirectional and rotational solidification [109]. As clearly seen in this figure, the level of the resistivity is much higher for the group of samples with

**Fig. 4.21** Relationship between electric resistivity and the directional grain boundary density (DGBD) for studied polysilicon specimens. The attached numbers indicate the fraction of random boundaries for respective data points [109].

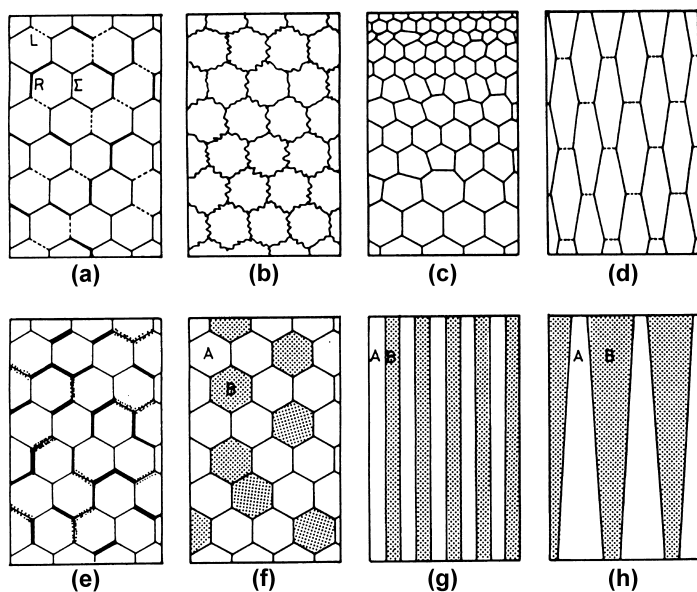


higher fraction of random boundaries ( $>30\%$ ) than the group with lower fraction of random boundaries ( $<20\%$ ). The directional GB density means the density of specific types of boundaries (in this case random (R) boundaries) existing along the defined direction (the direction of electrodes). This kind of information shown by this figure can be used for designing a high performance polysilicon solar cell with a higher efficiency than presently existing one.

## 4.10 Summary and Prospect

We have overviewed a recent progress in the grain boundary engineering (GBE) which was proposed on the basis of structure-dependent grain boundary properties in the early 1980s. We have mainly focused on structural materials which should have a higher resistance to intergranular brittleness caused by intergranular fracture in polycrystalline materials. It has been shown that the grain boundary engineering is a powerful tool to develop high performance and fracture-resistant materials with desirable bulk properties through the introduction of optimum grain boundary microstructure. Until recently, the GBE has dealt mainly with simple materials composed of single phase materials. Now at the beginning of the 21st century, we are facing to the GBE for multiphase materials containing grain and interphase boundaries often together with other type of interfaces like electric and magnetic domain interfaces. Figure 4.22 shows possible grain boundary microstructures that may be realized by future GBE. The most important driving force for GBE is a strong desire and perseverance of researchers who will be involved in this challenging and promising goal.





- |                               |                            |
|-------------------------------|----------------------------|
| (a) single phase polycrystal, | (b) boundary serrated,     |
| (c) grain size grading,       | (d) grain elongated,       |
| (e) boundary decorated,       | (f) two-phase polycrystal, |
| (g) bilayered,                | (h) volume grading.        |

**Fig. 4.22** Schematic representation of possible grain boundary microstructures by the grain boundary engineering for single phase materials (a–d) and bi-phase polycrystalline materials (e–h) [19].

**Acknowledgements** The authors are grateful to their coworkers who have been deeply involved in the long term project on the grain boundary engineering for over two decades, and produced works cited in this paper. One (T.W.) of the authors would like to thank the organizers for the invitation to an invited talk at The International Conference on Microstructure and Textures of Steels (MATS-2008) held on the occasion of the 70th anniversary of the foundation of Tata Steel R&D Ltd. He also thanks Prof. A. Chokshi and Prof. S. Suwas who kindly invited him and arranged for his stay at Indian Institute of Science, Bangalore, which enabled him to attend this conference.

## References

- [1] Honeycombe, R.W.K.: *Steels: Microstructure and Properties*, Edward Arnold, (1981), London.
- [2] Hondros E.D. and McLean M. (ed.): *Structural Materials: Engineering Application through Scientific Insight*, The Institute of Materials, (1996), The University Press, Cambridge.
- [3] Cahn, R.W.: *The Coming of Materials Science*, Pergamon Press, (2001), London.
- [4] Martin, J.W., Doherty, R.D.: *Stability of Microstructure in Metallic Systems*, Cambridge University Press, (1976), Cambridge.
- [5] Baker, T.N. (ed.): *Yield, Flow and Fracture of Polycrystals*, Applied Science Pub., (1983), London.
- [6] Gleiter, H., Chalmers, B.: High-Angle Grain Boundaries, *Prog. in Mater. Sci.*, 16 (1972)
- [7] Chadwick, G.A., Smith, D.A.: *Grain Boundary Structure and Properties*, Academic Press (1976), London
- [8] Balluffi, R. (ed.): *Grain Boundary Structure and Kinetics*, ASM., (1980).
- [9] Wolf D., Yip, S.: *Materials Interfaces; Atomic-level structure and properties*, Chapman & Hall, (1992).
- [10] Ranganathan, S., Pande, C.S., Rath, B., Smith, D.A (eds.): *Interfaces; Structure and Properties*, Trans. Tech Pub., (1993), Switzerland.
- [11] Sutton, A.P., Balluffi, R.: *Interfaces in Crystalline Materials*, Oxford Sci. Pub.(1995), Oxford.
- [12] Low, J.R.: *Trans. Met. Soc. AIME* 245 (1969), pp. 2481–2494, “Impurities, Interfaces and Brittle Fracture”.
- [13] Hahn, G.T.: *Met. Trans.*, 15A (1984), pp. 947–959, “The Influence of Microstructure on Brittle Fracture Toughness”.
- [14] Flewitt, P.E.J., Wild, R.K. “Grain Boundaries; Their Microstructure and Chemistry”, John Wiley&Sons, (2001).
- [15] Watanabe, T. Fujii, H, Oikawa, H., Arai,K.I.: *Acta Metall.*, 37 (1989), pp. 941–952.
- [16] Watanabe,T.: *Textures and Microstructures*, 20 (1993), pp. 195–216.
- [17] Watanabe, T.: *Res Mechanica*, 11 (1984), pp. 47–84, “An Approach to Grain Boundary Design for Strong and Ductile Polycrystals”.
- [18] Aust, K.T., Palumbo, G.: *Advanced Structural Materials*, ed. by D.S. Wilkinson, Pergamon Press, (1989), pp. 215–225.
- [19] Watanabe, T.: *Proc.K.T .Aust Intern. Symp. on Grain Boundary Engineering*, ed. by U. Erb and G. Palumbo, CIMMP, (1993), pp. 57–87.
- [20] Aust, K.T.: *Proc.K.T. Aust Intern. Symp. on Grain Boundary Engineering*, ed.by U. Erb and G. Palumbo, CIMMP., (1993), pp. 197–228.
- [21] Watanabe, T., Tsurekawa, S.: *Acta Mater.*, 47 (1999), pp. 4171–4185.
- [22] Watanabe, T., Tsurekawa, S. Zhao X. Zuo, L.: *Scripta Mater.*, 54 (2006), pp. 969–975.
- [23] Watanabe, T., Takazawa, M., Oikawa,H.: *Strength of Metals and Alloys*, (ICSMSA-8), Pergamon Press, (1988), pp. 1357–1362.
- [24] Watanabe, T.: *Mater. Sci. Eng.*, A176 (1994), pp. 39–49.
- [25] Lawn, B.R, Wilshaw, T.R.: *Fracture of Brittle Solids*, Cambridge Univ. Press, 1975, p. 114.
- [26] Murr, L.E.: *Interfacial Phenomena in Metals and Alloys*, Addison-Wesley Pub.(1975).
- [27] McMahon, C.J., Vitek, V: *Acta Met.*, 27 (1979), pp. 507–513.
- [28] Yoshinaga, H.: *Mater. Trans., JIM.*, 31 (1990), pp. 233–248.
- [29] Watanabe, T.: *Mater. Sci. Eng.*, A166 (1993), 11–23.
- [30] Watanabe, T.: *Met.Trans.*, 14A (1983), pp. 531–545.
- [31] Watanabe, T. Tsurekawa,S.Petit J. Dimitrov, O.Igata,N (eds.): *Annales de Chimie Science des Materiaux*, Vol.27, Suppl. *Interfaces and Related Phenomena* , Elseviewr (2002).
- [32] Watanabe, T.Tsurekawa, S.(eds.): *Sepecial Issue on Grain Boundary Engineering*, *J. Mater. Sci.*, 40 (2005), pp. 817–932.

- [33] Kumar, M. Schuh, C.A. (eds.): Viewpoint set on Grain Boundary Engineering, *Scripta Mater.*, 54 (2006), pp. 961–1070.
- [34] Watanabe, T.: Grain Boundary Structure and Related Phenomena, *JIM*, 27 (1985), pp. 73–82.
- [35] Palumbo, G., Lehecky, E.M. Lin, P.: *J. of Metals (JOM)*, 50 (1998), No.2, pp. 40–43.
- [36] Palumbo, G., Erb, U.: *MRS Bulletin*, Nov.(1999), pp. 27–32.
- [37] Watanabe, T., Tsurekawa, S. Zhao, X, Zuo, L, Esling, C: *J. Mater.Sci.*, 41 (2006), pp. 7747–7759.
- [38] Randle, V.: *Acta Mater.*, 52 (2004), pp. 4067–4081.
- [39] Shimada, M, Kokawa, H. Wang, Z, J Sato, Y.S. Karibe, I: *Acta Mater.*, 50 (2002), pp. 2331–2341.
- [40] Alexandreanu,B., Was,G.S.: *Scripta Mater.*, 54 (2006), pp. 1047–1052.
- [41] Nichols, C.S, Cook, R.F. Clarke, D.R., Smith, D.A.: *Acta Metall. Mater.*, 39(1991), pp. 1657–1665.
- [42] Wang, G, Zuo, L, Esling, C.: *Phil. Mag.*, A82 (2002), 2499–2510.
- [43] Schuh, C.A. Minich, R.W., Kumar, M: *Phil. Mag.* 83 (2003), pp. 711–726.
- [44] Frary, M. Schuh, C.A.: *Phil. Mag.*, 85(2005), pp. 1123–1143.
- [44] Tsurekawa,S. Nakamichi,S. Watanabe,T.: *Acta Mater.*, 54 (2006), pp. 3617–3626.
- [45] McLean, M.: *Metal Science*, 16 (1982), pp. 31–36, "Microstructural Changes in presence of Externally Applied Potential Gradients".
- [46] Watanabe, T.: *Recrystallization and Grain Growth*, ed. by G. Gottstein and D.A. Molodov, Springer (2001), pp.11–20, "External Field Applied Grain Boundary Engineering for High Performance Materials".
- [47] Watanabe,T., Yoshikawa,N, Karashima, S: *Proc. 6th Intern. Conf. on Textures of Materials, (ICOTOM-6), ISIJ.*, (1982), pp. 609–618.
- [48] Adams, B. L., Wright, S.I, Kunze, K.: *Metall.Trans.*, 24A (1993), pp. 819–831.
- [49] Watanabe, T.: *Proc. 4th Intern. Conf. on Recrystallization and Related Phenomena*, ed. by T. Sakai and H.G. Suzuki, *JIM*. (1999), pp. 99–108.
- [50] Sakuma,T., Ikuhara, Y., Yamamoto, T., Yoshida, H.: *Interfaces and Related Phenomena*, Elsevier, (2002), pp. S345–356, "Toward Grain Boundary Engineering in Advanced Ceramics".
- [51] Kobayashi, S., Tsurekawa, S., Watanabe,T.: *Phil. Mag.*, 86 (2006), Nos. 33–35, pp. 5419–5429.
- [52] Baker, T. N. (ed.): *Yield, Flow and Fracture of Polycrystals*, Applied Science Pub., (1983)
- [53] Zhilyaev, A.P. Kim, B.K. Nurislamova, G.V. Baro ,M.D. Spunar, J.A, Langdon, T.G., *Scripta Mater.*, 46 (2002), pp. 575–580.
- [54] Harada,K. Tsurekawa, S. Watanabe, T. Palumbo, G: *Scripta Mater.*, 49(2003), pp. 367–372.
- [55] Watanabe, T. Arai. K.I: Yshimi, K. Oikawa, H.: *Phil. Mag. Letters*, 62 (1990), pp. 9–17.
- [56] Mykura, H.: *Grain Boundary Structure and Kinetics*, ASM, (1980), pp. 445–456.
- [57] Rollet, A.D.: private communication (2003).
- [58] Garbacz A., Grabski M.W.: *Scripta Metall. Mater.*, 23 (1989), pp. 1369–1374.
- [59] Gertsman, V. Yu., Zhilyaev, A.P. Pshenichnyuk, A.I. Variev, R.Z.: *Acta Metall.Mater.*, 40 (1992), pp. 1433–1441.
- [60] Zuo L. Watanabe T., Esling C.: *Z. Metallkd.*, 85 (1994), pp. 554–558.
- [61] Garbacz A. Ralph B. Kurzydowski, K.J.: *Acta Metall.Mater.*, 43 (1995), pp. 12541–1547.
- [62] Alexandrov, I.V. Zhiyaev, A.P. Gertsman V.Yu. Pshnicxhyuk A.I.: *Modelling Simul. Mater. Sci. Eng.*, 3 (1995), pp.149–159.
- [63] Gottstein,G., Shvindlerman, L.S: *Grain Boundary Migration in Metals: Thermodynamics, Kinetics, Applications*, CRC Press, London, (1999).
- [64] Belluz, R.V. Aust, K.T.: *Met.Trans.*, 6A (1975), pp. 219–220.
- [65] Watanabe, T.: *Materials Forum*, 11 (1988), pp. 284–303.
- [66] Lim, L.C, Watanabe, T.: *Scripta Met.*, 23 (1989), pp. 489–495.
- [67] Lim, L.C. Watanabe, T.: *Acta Metall. Mater.*, 38 (1990), pp. 2507–2516.
- [68] Fu,Y., Evans,A.G.: *Acta Metall.*, 33 (1985), pp.1515–1523, pp. 1525–1531.

- [69] Argon, A.S., Qiao, Y.: Mechanisms and Mechanics of Fracture, Proc. the J.F. Knott Symp. TMS, (2002), pp. 3–10.
- [70] Hirano, T.: Acta Metall. Mater., 38 (1990), pp. 2667–2671.
- [71] Watanabe, T., Hirano, T., Ochiai, T., Oikawa, H.: Mater. Sci. Forum, 157–162 (1994), pp. 1103–1108.
- [72] Su, J-Q, Denuma, M., Hirano, T.: Phil. Mag., A82 (2002), pp. 1541–1557.
- [73] Tsurekawa, S., Kokubun, S., Watanabe, T.: Mater. Sci. Forum, 304–305 (1999), pp. 687–692.
- [74] Tsurekaw, S., Watanabe, T.: Mat. Res. Soc. Symp. Proc. 586 (2000), pp. 237–242.
- [75] Yamaura, S., Igarashi, Y., Tsurekawa, S., Watanabe, T.: Acta Mater., 47 (1999), pp. 1163–1174.
- [76] Yamaura, S., Igarashi, Y., Tsurekawa, S., Watanabe, T.: Properties of Complex Inorganic Solids 2, ed. by A. Meike et al., Kluwer Academic/Plenum Pub., (2000), pp. 27–37.
- [77] Yamaura, S., Tsurekawa, S., Watanabe, T.: Mater. Trans., 44 (2003), pp. 1494–1502.
- [78] Watanabe, T., Yamada, M., Karashima, S.: Phil. Mag. A63 (1991), pp. 1013–1022.
- [79] Lehockey, E.M., Palumbo, G.: Mater. Sci. Eng., A237 (1996), p. 168.
- [80] Tsurekawa, S., Watanabe, T., Watanabe, H., Tamari, N.: Key Engineering Materials, 247 (2003), pp. 327–330.
- [81] Tsurekawa, S., Naito, Y., Murthy, V.S.R., Watanabe, T., Tamari, N.: Key Engineering Materials, 247 (2003), pp. 331–334.
- [82] Pender, H., Jones, R.: Phys. Rev., 1 (1913), No. 4, pp. 259–273.
- [83] Smoluchowski, R., Turner, R.W.: J. App. Phys., 20 (1949), pp. 745–749.
- [84] Mullins, W.W.: Acta Metall., 4 (1956), pp. 421–432.
- [85] Cahn J.W.: J. Appl. Phys., 34 (1963), 3581–3586.
- [86] Satyanarayan, K.R., Miodownik, A.P.: The Mechanism of Phase Transformations in Crystalline Solids”, The Inst. Metals, (1969), pp. 162–167.
- [87] Martikainen, H.O., Lindroos, V.K.: Scand. J. Metallurgy, 10 (1981), pp. 3–8.
- [88] Sauthoff, G., Pitsch, W.: Phil. Ma., B56 (1987), pp. 471–483.
- [89] Kakeshita, T., Shirai, H., Shimizu, K., Sugiyama, K., Hazumi, K., Date, M.: Trans. JIM., 28 (1987), pp. 891–897.
- [90] Watanabe, T., Suzuki, Y., Tani, S., Oikawa, H.: Phil. Mag. Letters, 62 (1990), pp. 9–17.
- [91] Choi, J-K, Ohtsuka, H., Xu, Y., Choo, W-Y.: Scripta Mater., 43 (2000), pp. 221–226.
- [92] Zhang, Y.D., He, C., Zhao, X., Zuo, L., Esling, C., He, J.: J. Mag. Magn. Mater., 284 (2004), pp. 287–293.
- [93] Fujii, H., Tsurekawa, S., Matsuzaki, T., Watanabe, T.: Phil. Mag. Letters, 86 (2006), pp. 113–122.
- [94] Uhlman, D.R., Seward, T.P., Chalmers, B.: Trans. Met. Soc. AIME., 236 (1966), pp. 527–531.
- [95] Holloway, A., McCallum, R.W., Arras Smith, S.R.: J. Mater. Res., 8 (1993), pp. 727–733.
- [96] Molodov, D. A., Gottstein, G., Heringhaus, F., Shvindlerman, L.S.: Scripta Mater., 37 (1997), 1207–1213.
- [97] Li, X., Ren, Z., Fautrelle, Y.: Acta Mater., 54 (2006), pp. 5349–5360.
- [98] Watanabe, T., Tsurekawa, S., Zhao, X., Zuo, L.: Scripta Mater., 54 (2006), pp. 969–975.
- [99] Watanabe, T., Tsurekawa, S., Zhao, X., Zuo, L., Esling, C.: J. Mater. Sci., 42 (2006), pp. 7747–7759.
- [100] Seah, M.P., Hondos, E.D.: Proc. Toy. Soc., A335 (1973), pp. 191–212.
- [101] Watanabe, T., Kiatamura, S., Karashima, S.: Acta Metall., 28 (1980), pp. 455–463.
- [102] Lejcek, P., Hofmann, S.: Interf. Sci., 1 (1993), pp. 163–174.
- [103] Tsurekawa, S., Okamoto, K., Kawahara, K., Watanabe, T.: J. Mater. Sci., 40 (2005), 895–901.
- [104] Nakamichi, S., Tsurekawa, S., Morizono, Y., Watanabe, T., Nishida, M., Chiba, A.: J. Mater. Sci., 40 (2005), pp. 3191–3198.

- [105] Rabkin, E., Gabelev, A., Matsuzaki, T., Watanabe, T.: Defect and Diffusion Forum, 237–240 (2005), pp. 560–565.
- [107] Watanabe, T., Tsurekawa, S., Palumbo, G.: Solid State Phenomena, 101–102 (2005), pp. 171–180.
- [106] Watanabe, T., Nishizawa, S., Tsurekawa, S.: Complex Inorganic Solids: Structural Stability and Magnetic Properties of Alloys, ed. by P.E.A. Turch, et. al., Springer, (2005), pp. 327–336.
- [108] Enomoto, M.: Mater. Trans., 46 (2005), pp. 1088–1092.
- [109] Watanabe, T., Kido, K., Tsurekawa, S., Kawahara, K.: Mater. Sci. Forum, 558–559 (2007), pp. 843–850.
- [110] Tsurekawa, S., Kido, K., Harada, S., Watanabe, T., Sekiguchi, T.: Z. Metallkunde, 96 (2005), pp. 197–206.
- [111] Tsurekawa, S., Kido, K., Watanabe, T.: Phil. Mag. Letters, 85 (2005), pp. 41–49.



Tadao Watanabe  
Formerly (1993–2003), Professor  
of Laboratory of Materials Design  
and Interface Engineering,  
Department of Nanomechanics, Graduate  
School of Engineering, Tohoku University,  
Sendai, Japan.

Currently, Invited Professor, Anisotropy  
and Texture of Materials,  
Northeastern University, Shenyang, 110004,  
China.

**Part II**  
**Control of Texture**  
**and Microstructure in Steels**



## Chapter 5

# Texture Development in Low Carbon Sheet Steels for Automotive Application

Jun-Yun Kang, Dong-Ik Kim, and Hu-Chul Lee

**Abstract.** The development of recrystallization texture in three low carbon sheet steels, conventional IF steel, fine grained IF steel, and DP steel, for automotive application was investigated using EBSD technique. The recrystallization texture at the early stage of recrystallization was very similar to that at the final stage in all three steels. A strong  $\alpha$ -fiber texture with  $\{112\}\langle 110\rangle$  peak and weaker  $\gamma$ -fiber texture with  $\{111\}\langle 110\rangle$  peak were developed during the deformation of all three low carbon steels. After recrystallization, they changed to a strong  $\gamma$ -fiber texture with strong  $\{111\}\langle 112\rangle$  component. However, the intensity of the texture components varied in the different steels. The grains of  $\gamma$ -fiber orientations developed from deformed grains of similar orientations and grew rapidly, consuming the neighboring grains to form a strong  $\gamma$ -fiber texture. In conventional IF steels, some recrystallized grains formed at grain boundaries showed weak correlation with  $\{111\}$  orientation, however, the growth rates of these random grains were too slow to affect the final recrystallization texture. In the fine grained IF steel, the intensity of the  $\{001\}\langle 110\rangle$  component after recrystallization was higher than that in the conventional IF steel. Strain induced boundary migration (SIBM) was observed in the fine grained IF steel. The intensity of the  $\gamma$ -fiber texture was much weaker in the DP steel than in the IF steels. Nucleation of the  $\{110\}\langle 001\rangle$  and  $\{001\}\langle 100\rangle$  recrystallized grains from the shear

---

J.-Y. Kang

Department of Materials Science and Engineering, Seoul National University, Seoul,  
151-744 Korea

D.-I. Kim

Materials Science and Technology Division, Korea Institute of Science and Technology, Seoul,  
136-791 Korea

H.-C. Lee

Department of Materials Science and Engineering, Seoul National University, Seoul,  
151-744 Korea



bands in  $\{111\}\langle 112 \rangle$  or  $\{110\}\langle 110 \rangle$  grains was expected. The austenite transformation during the intercritical annealing of the DP steel was found to have little effect on the formation of its final recrystallization texture.

**Keywords:** Recrystallization, Texture, IF steel, DP steel, EBSD

## 5.1 Introduction

Because of its excellent formability and non-aging characteristics, interstitial free (IF) steel has become an indispensable material for automotive outer panel applications. However, because of the recent surge of fuel cost and stringent requirements for safety and emission control, the demand for higher strength sheet steels is on the increase. Steel manufacturers are investigating various types of advanced sheet steels for automotive applications. Figure 5.1 shows the combination of tensile strength and elongation for some examples of modern advanced sheet steels. More advanced high strength sheet steels are now under development. Some of these sheet steels show a good combination of strength and ductility, however, the deep drawability of many of these high strength advanced sheet steels is not yet satisfactory for automotive applications. Improvement in the sheet formability is needed for more general acceptance of these sheet steels for automotive application.

The formability of low carbon sheet steels is strongly dependent on the texture of the sheets. Accordingly, a vast amount of data from experiments and theoretical analyses has been accumulated on the development of texture in low carbon sheet steels. In this paper, we tried to summarize our investigations on the texture development in IF, fine grained IF and DP steels. A comparison was made to understand the differences in the development of texture in these low carbon steels.

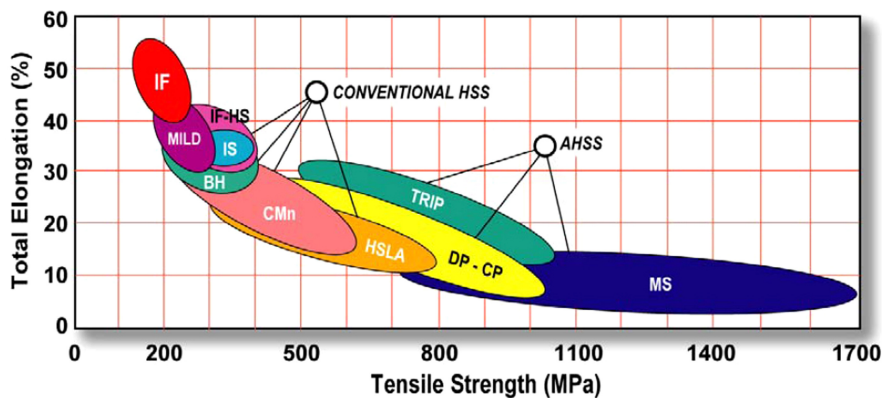
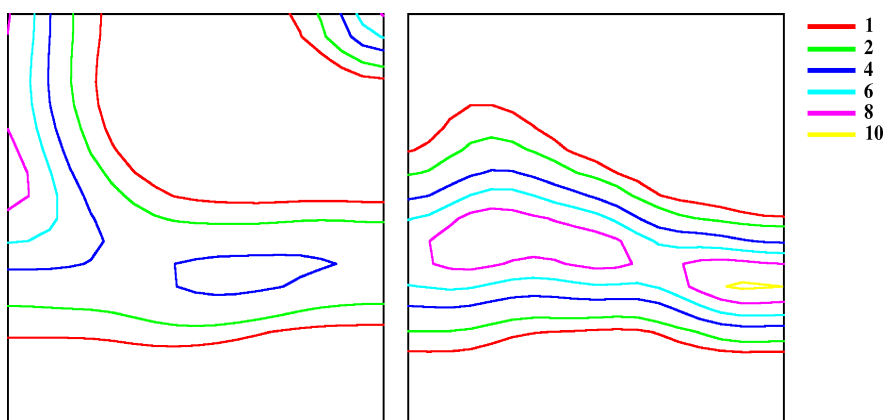


Fig. 5.1 Tensile properties of advanced sheet steels [1].

## 5.2 Texture Development in Low Carbon Sheet Steels

In low carbon steels, it is well accepted that they have a weak or near random texture in the hot band state, strong RD//<110>  $\alpha$ -fiber texture and weaker ND//<111>  $\gamma$ -fiber texture in the cold rolled state, and strong ND//<111>  $\gamma$ -fiber texture in the recrystallized state. Figures 5.2–5.4 show the orientation distribution of the three low carbon steel sheets in their cold rolled and fully annealed states. In the cold rolled state, they show a strong RD//<110> fiber texture with a {112}<110> maximum peak position and ND//<111> fiber texture with a {111}<110> peak position. A strong ND//<111> fiber texture with a {111}<112> maximum peak was developed in the fully recrystallized



**Fig. 5.2** ODF calculated from EBSD data of conventional IF steel (a) cold rolled and (b) fully annealed state.

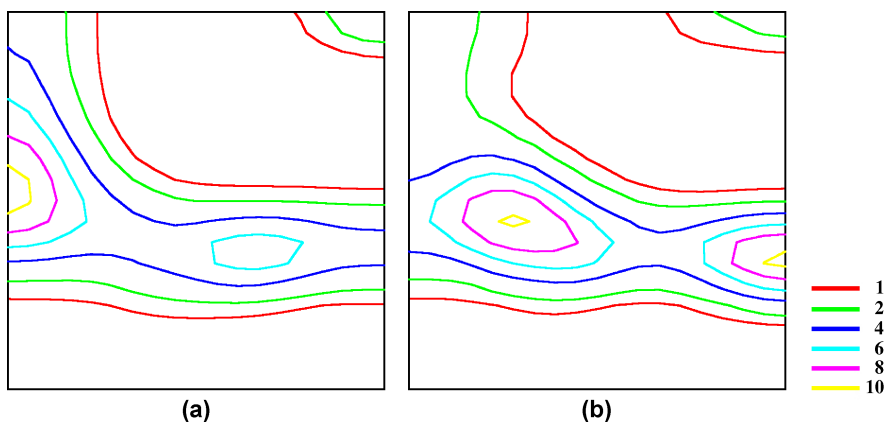


**Fig. 5.3** ODF calculated from EBSD data of fine grained IF steel. (a) cold rolled and (b) fully annealed state.

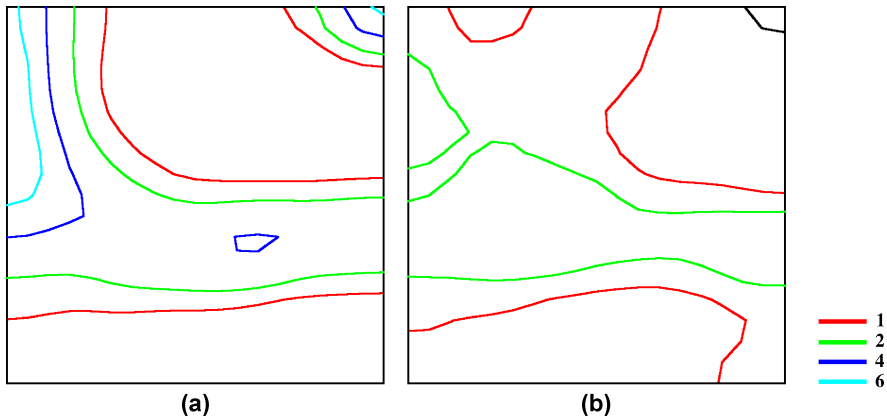


**Fig. 5.4** ODF calculated from EBSD data of DP steel. (a) cold rolled and (b) fully annealed state.

specimen of the two IF steels. This corresponds well with previous observations that the  $\{112\}\langle 110 \rangle$  and  $\{111\}\langle 110 \rangle$  texture components become strong in the greater than 70% cold rolled sheets, and that the  $\{111\}\langle 112 \rangle$  texture component becomes strong in the fully recrystallized sheets [2–7]. In the DP steel, the prevalence of the ND// $\langle 111 \rangle$  texture centered around  $\{111\}\langle 112 \rangle$  was also observed even though the overall intensity of the texture was considerably weakened.

### 5.2.1 Development of Cold Rolled Microstructure and Texture

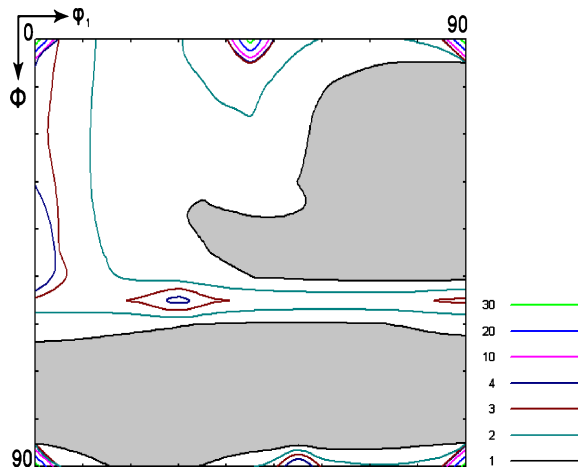
The textures developed after the cold rolling of low carbon steels were very similar to each other as shown in the Figs. 5.2–5.4, even though their relative intensities may vary with microstructural or processing parameters [8–11]. The intensities near the  $\{112\}\langle 110 \rangle$  component and also the intensities of ND// $\langle 111 \rangle$  components were stronger in the IF steels than the DP steel. They were stronger in the fine grained IF steel than the conventional one. It was considered that more homogeneous deformation of the fine grained microstructure led to the stronger rolling texture. The grain size was larger in the DP steel than in the IF steels and the presence of pearlite may cause non-uniform deformation in the DP steel resulting in the development of weaker deformation texture in the DP steel.

During rolling, the more or less random grains in the hot bands rotate toward a more stable orientation. For instance, Inagaki [11–14] reported such paths of crystal rotation as,

(A)  $\{001\}\langle 100 \rangle \rightarrow \{001\}\langle 110 \rangle \rightarrow \{112\}\langle 110 \rangle \rightarrow (223)\langle 110 \rangle$

(B)  $\{110\}\langle 001 \rangle \rightarrow \{554\}\langle 225 \rangle \rightarrow \{111\}\langle 112 \rangle \rightarrow \{111\}\langle 110 \rangle \rightarrow \{223\}\langle 110 \rangle$

**Fig. 5.5** Map of orientation stability during cold rolling of ferrite.



The  $\{223\}\langle 110 \rangle$  orientation was identified as the stable end orientation of the cold rolling texture in the polycrystals. The path (A) goes through the  $\alpha$ -fiber orientations while the path (B) goes through the  $\gamma$ -fiber orientations. Both of them approach the same end orientation,  $\{223\}\langle 110 \rangle$ . Figure 5.5 shows the map of the stability factor from which the rolling texture can be estimated for a given initial

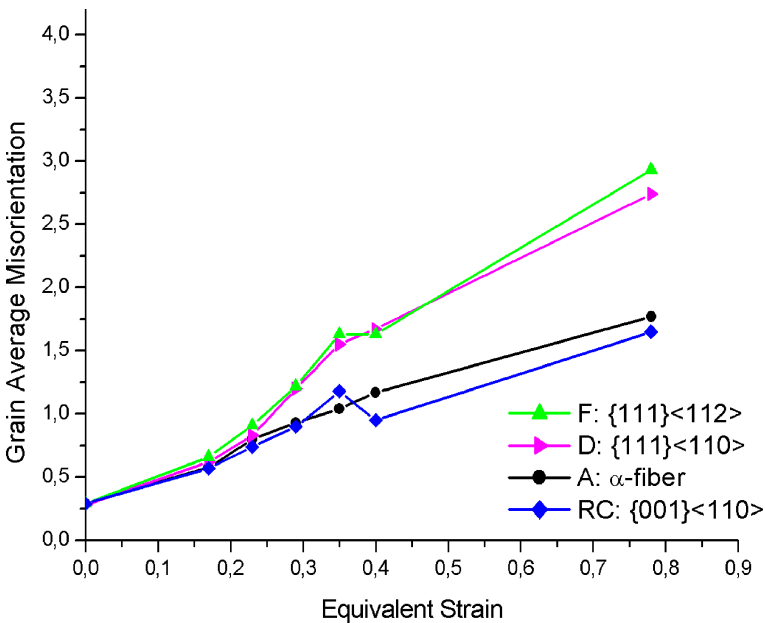


**Fig. 5.6** Development of grain average misorientation (GAM) during cold rolling of IF steel (Each orientation group has a tolerance angle of  $12.5^\circ$  from the ideal orientation. Group A is the partial  $\alpha$ -fiber excluding the D and RC orientation.)

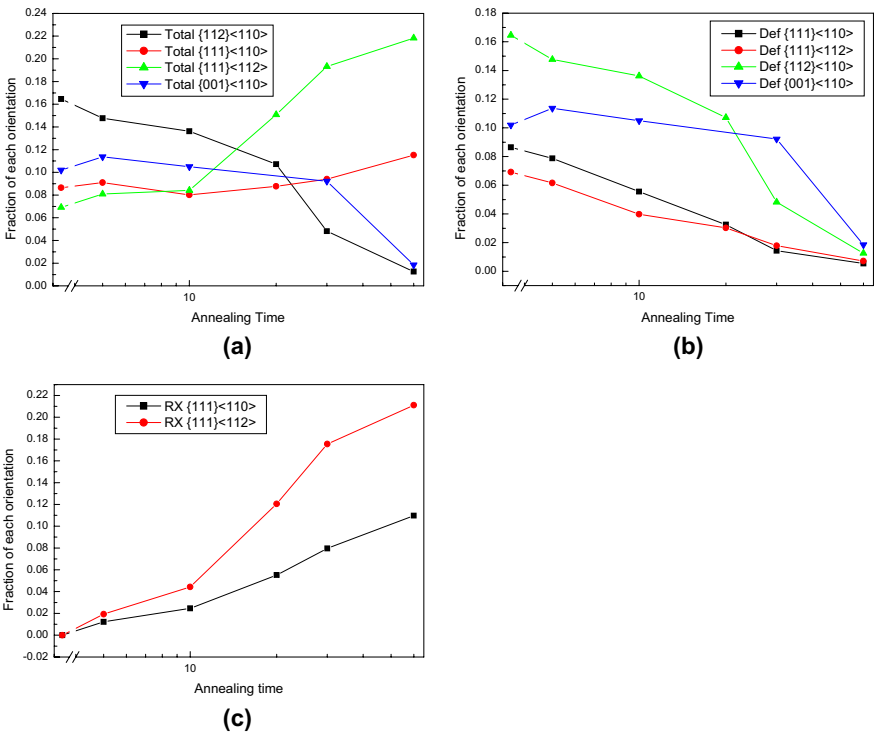
texture (or hot band texture). It clearly shows that the  $\alpha$  grains are more stable against rotation during rolling than the  $\gamma$  grains. Kang et al. [16] postulated that the stability of the grains can be related to the accumulation of the stored energy during rolling. In their work, the instability, or the tendency of reorientation around the main components of the deformation texture is proportional to the accumulation of the intra-granular misorientation. Figure 5.6 shows the grain average misorientation (GAM) for the selected orientation groups as a function of the deformation. The GAM increases with increasing equivalent strain in all of the selected groups. However, it is clear that the F and D groups which belong to  $\gamma$ -fiber showed larger misorientation values than the other two groups belong to  $\alpha$ -fiber.

### 5.2.2 *Development of Recrystallization Texture*

Several theories have been proposed to explain the development of recrystallization texture during the annealing process [17–21]. In the oriented nucleation theory first proposed by Burgers [17], it is assumed that the final recrystallization texture is determined by the preferred nucleation of recrystallized grains of specific orientations. Transmission electron microscope (TEM) was frequently used to identify the nucleated grains and the  $\langle 111 \rangle$ /ND recrystallized grains formed at the highly deformed regions such as the transition bands, shear bands, and kink band were suggested as the nuclei grains [22]. In 1940, Barrett suggested the oriented growth theory [18]. In this theory, it is assumed that the recrystallized grains nucleate in a random orientation, however, the mobility of grain boundaries between some the recrystallized grains and deformed grains with a specific orientation relationship is higher than that of the other boundaries and determines the final recrystallization texture. For example, the growth rate of the  $\{111\}\langle 112 \rangle$  recrystallized grains which have the  $\langle 110 \rangle 27^\circ$  orientation relationship with the  $\{112\}\langle 110 \rangle$  deformed grains is the highest and governs the final recrystallization texture in steels [23]. Compromises between these two theories have also been proposed. The selective growth theory assumes that the recrystallization is initiated by oriented nucleation, and then some recrystallized grains of the specific orientation relationship with the deformed neighboring grains grow faster than the other recrystallized grains and determine the final recrystallization texture [24]. The energy release maximization theory [19] assumes that the recrystallized grains nucleate and grow in such a way as to maximize the release of the stored energy produced by the dislocations during the deformation. These theories are supported by many experimental results obtained over the past several decades, however, none of them attained perfect superiority over the others. Even though the cold rolling textures vary with the microstructural and/or processing parameters of the materials, the range of the variety is not so wide. By contrast, the recrystallization textures are very sensitive to them as shown in Figs. 5.2–5.4. The intensities of the recrystallization texture are much weaker in the DP steel than in the two IF steels.

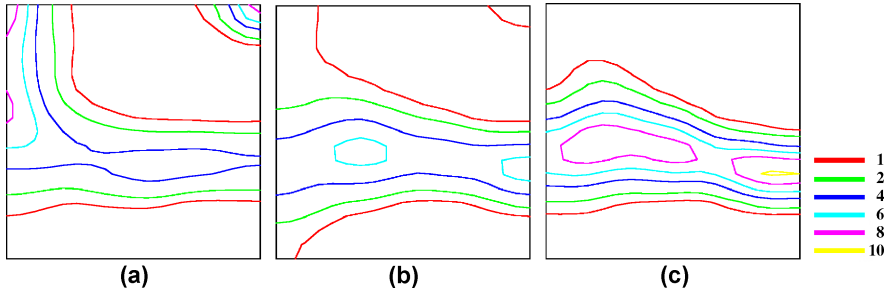
The development of the  $\{001\}\langle 100 \rangle$  and  $\{110\}\langle 001 \rangle$  components are noteworthy in DP steel, which were reported to originate from solute carbon in ferrite [25, 26]. Among the two IF steels, fine grained one has stronger intensities along the  $\alpha$ -fiber, especially at  $\{001\}\langle 110 \rangle$ , which could originate from the fine grained microstructure.

Figure 5.7 (a) shows the variation of the volume fraction of the texture components with the annealing time in the conventional IF steel. As shown in Fig. 5.2, representative  $\alpha$ -fiber and  $\gamma$ -fiber texture components are strongly developed in the fully deformed state. The volume fraction of these texture components does not change up to the mid stage of recrystallization, and, thereafter the  $\{112\}\langle 110 \rangle$  component starts to decrease and the  $\{111\}\langle 112 \rangle$  component starts to increase. The strength of the  $\{111\}\langle 110 \rangle$  component is maintained and slightly increases at the end of recrystallization process. The  $\{001\}\langle 110 \rangle$  component remains for quite a long time and decreases rapidly at the late stage of recrystallization. This is why many previous researchers focused on the transformation of the  $\{112\}\langle 110 \rangle$  texture to the  $\{111\}\langle 112 \rangle$  texture and explained that this phenomena determines the final recrystallization texture. However, if we differentiate the recrystallized grains from the deformed grains in partially recrystallized specimens, all



**Fig. 5.7** Variations of the volume fraction of important texture components with annealing time at 650°C.

the texture components of the deformed grains decrease continuously from the first stage and the  $\{111\}\langle 110 \rangle$  and  $\{111\}\langle 112 \rangle$  recrystallized components develop from the first stage of recrystallization, as shown in Figure 5.7(b) and 5.7(c). The  $\{111\}\langle 110 \rangle$  and  $\{111\}\langle 112 \rangle$  texture components develop from the first stage of recrystallization and determine the final recrystallization texture.



**Fig. 5.8** Orientation distributions at the early stage of recrystallization in conventional IF steel: (a) whole measured area, (b) recrystallized area (10.9% in volume fraction) and (c) full recrystallization texture.

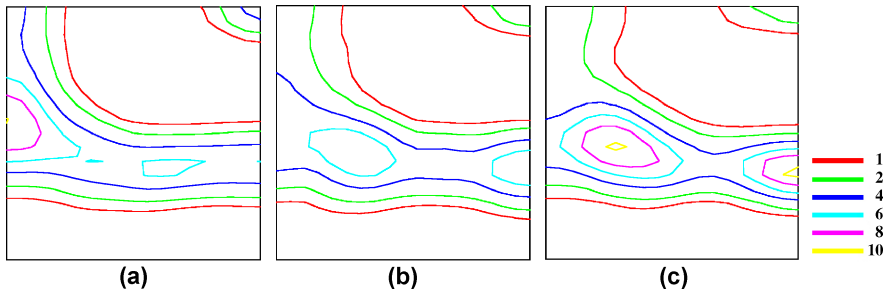


**Fig. 5.9** Orientation distributions at the early stage of recrystallization in fine grained IF steel: (a) whole measured area, (b) recrystallized area (11.9% in volume fraction) and (c) full recrystallization texture.

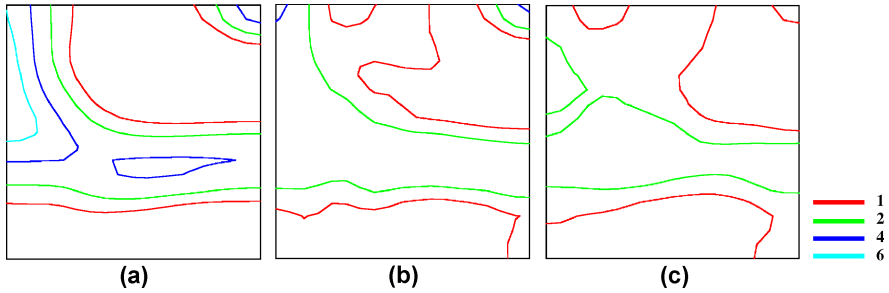


**Fig. 5.10** Orientation distributions at the early stage of recrystallization in DP steel: (a) whole measured area, (b) recrystallized area (14.7% in volume fraction) and (c) full recrystallization texture.

The exchange of the  $\{112\}\langle 110 \rangle$  component with the  $\{111\}\langle 112 \rangle$  component could not properly explain this texture variation of this IF steel.

In Figs. 5.8–5.10, the textures of the recrystallized grains at the early stage of annealing are compared to the final textures of the recrystallized low carbon steels. The textures of recrystallized grains are quite similar to the final textures of the recrystallized sheets. It could mean that the final recrystallization texture in these low carbon steels was determined at the stage of nucleation. However, it can be observed that as the recrystallization proceeds, there are some modifications in the recrystallization texture. The intensity of the  $\{111\}\langle 112 \rangle$  component in the IF steels becomes much stronger after the final recrystallization as shown in Fig. 5.8 and 5.9. The growth of the  $\{111\}\langle 112 \rangle$  grains, previously reported by Lucke, was expected [27]. In the DP steel, no further increase of the ND// $\langle 111 \rangle$  components was observed during growth, as was the case in IF steels, which can be found in Fig. 5.10.

### 5.2.3 Mechanism of the Recrystallization Texture Formation

To reveal the recrystallization behavior of low carbon steels, specimens at the initial stage of recrystallization were investigated by EBSD. As shown in Fig. 5.11, the nucleation of the  $\langle 111 \rangle$ //ND grains from the  $\langle 111 \rangle$ //ND deformed grains was the main governing mechanism throughout the whole recrystallization process of conventional IF steel. The nucleation of the  $\langle 111 \rangle$ //ND grains was concentrated in the region where the  $\{111\}\langle 112 \rangle$  and  $\{111\}\langle 110 \rangle$  grains were mixed. This conforms to the oriented nucleation theory in which recrystallization nuclei forms at the highly deformed area of the similar orientations. The stored energy of deformed grains of the major texture components was estimated by EBSD [16] and TEM [28]. The  $\{111\}\langle 112 \rangle$  grains have the largest stored energy followed by the grains of the  $\{111\}\langle 110 \rangle$ ,  $\{112\}\langle 110 \rangle$  and  $\{001\}\langle 110 \rangle$  orientations [28]. Based on the stored energy estimation, areas of the  $\{111\}\langle 112 \rangle$  orientation are the highest potential area for the nucleation followed by the  $\{111\}\langle 110 \rangle$  grains. As shown in the Fig. 5.7(c), the recrystallized grains of  $\{111\}\langle 112 \rangle$  orientation showed the largest intensity followed by the  $\{111\}\langle 110 \rangle$  grains from the early stage of recrystallization to the final stage of recrystallization. In the area of high stored energy, fine polygonized subgrain structures were developed at the early stage of recovery. The subgrains coalesce during annealing, and they become the nuclei of the similar orientations to the deformed grains [29]. Figure 5.12 shows the formation of recrystallized grains at the grain boundary area of the conventional IF steel. The orientation of recrystallized grains formed at the grain boundary showed a more or less random orientation, which lowered the strength of recrystallized grains at the initial stage of recrystallization. However, their contribution to the final annealing texture was limited during the following grain growth regime.



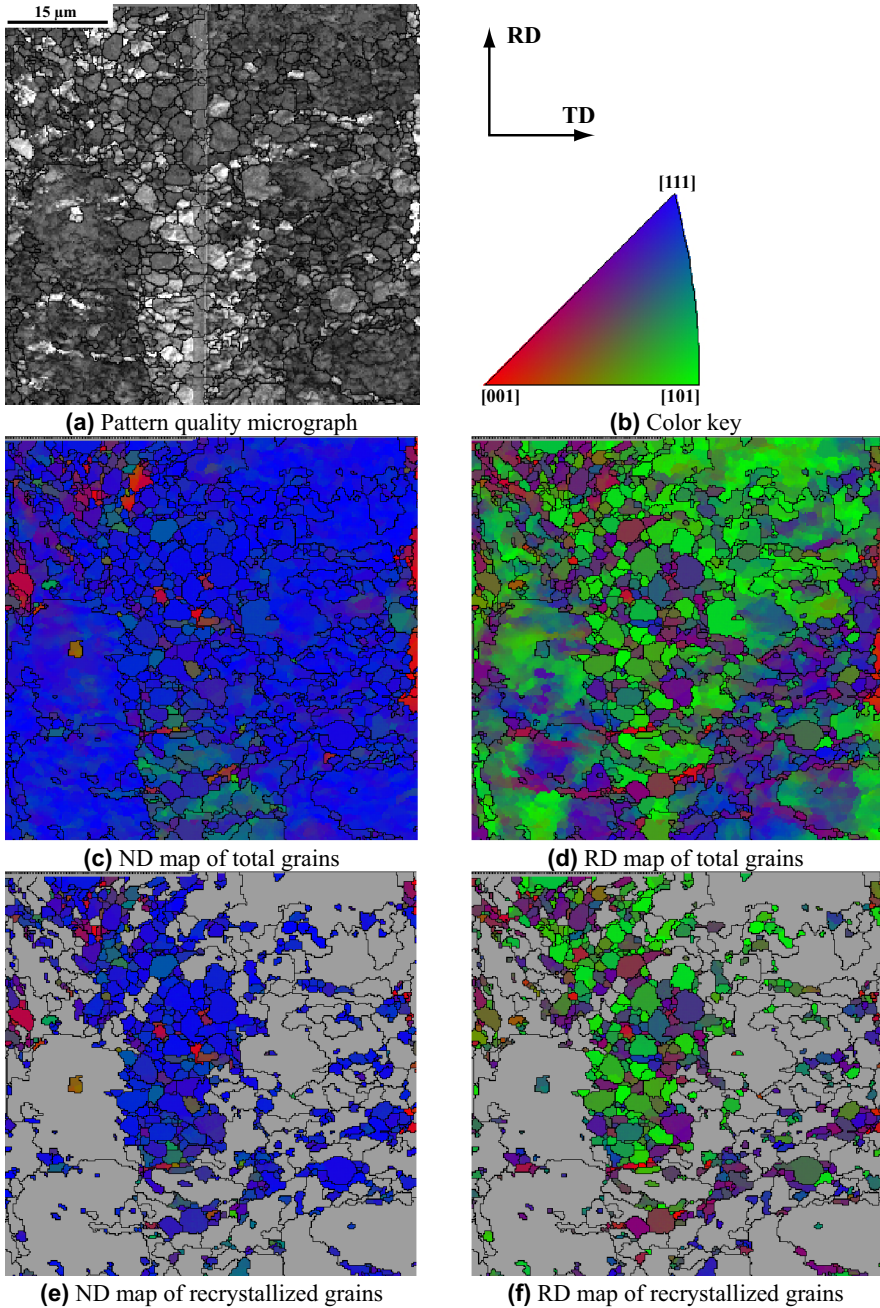


**Fig. 5.11** EBSD analysis of  $\{111\}$ //ND area in conventional IF steel annealed at 650°C for 5 minute: (a) Pattern quality micrograph; (b) Color key; (c) ND map of total grains; (d) RD map of total grains; (e) ND map of recrystallized grains; (f) RD map of recrystallized grains.

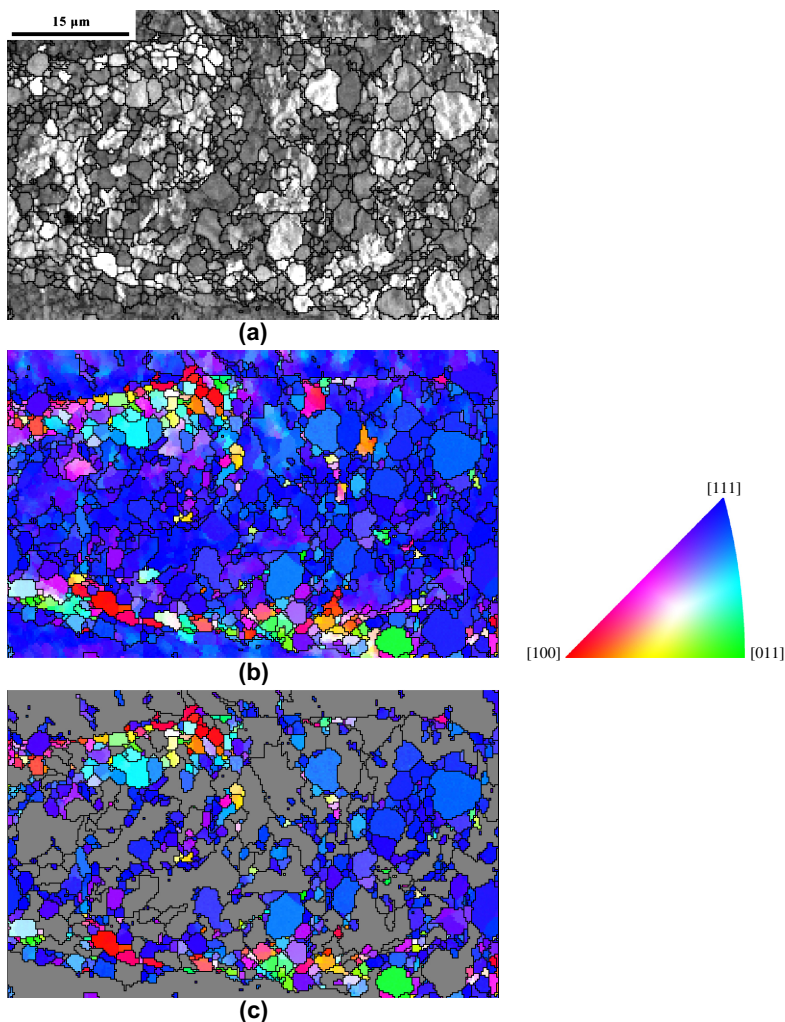


**Fig. 5.12** EBSD analysis of grain boundary area in conventional IF steel annealed at 650°C for 5 minutes: (a) pattern quality micrograph, (b) ND map of the total grains and (c) ND map of the recrystallized grains.

Figure 5.13 shows the subgrain distribution in the deformed  $\alpha$ - and  $\gamma$ -grains in the fine grained IF steel. Fine subgrains are well developed in the  $\gamma$ -fiber grains but not in the  $\alpha$ -fiber grains. Thus, the  $\gamma$ -fiber grains possess higher stored energy than the  $\alpha$ -fiber grains and these subgrains are the potential nuclei for recrystallization. When one of these subgrains grows into a recrystallized grain, the orientation of the grain will be close to  $\gamma$ -fiber orientations. The dislocation density in the  $\alpha$ -grains might be too small to form subgrains or the misfit angles between the subgrains might be too small to be detected by EBSD. Nucleation can not occur

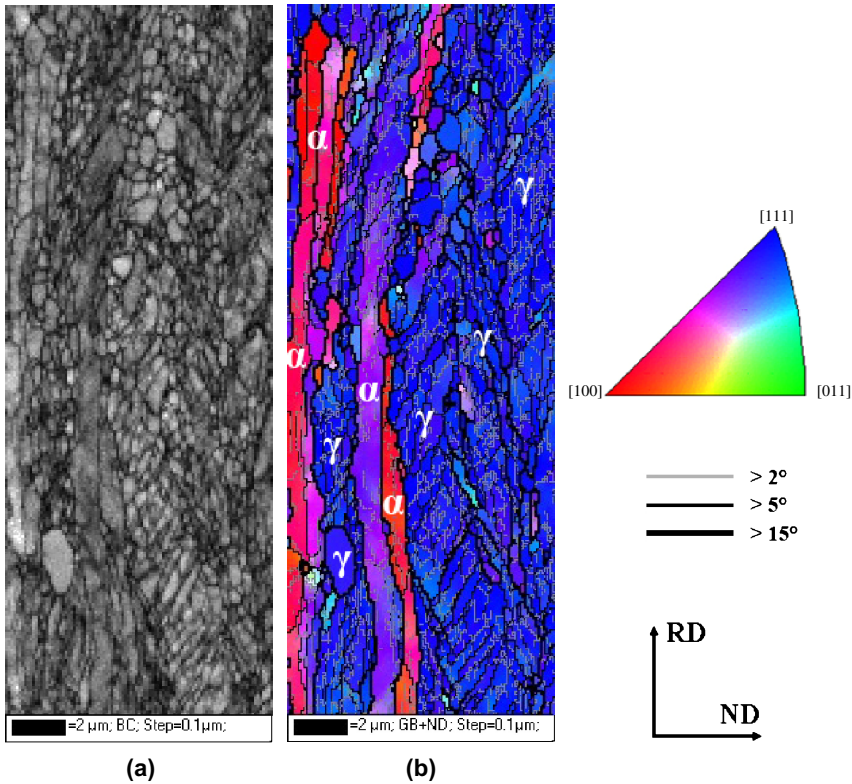


**Fig. 5.13** Subgrain development according to the grain orientation in fine grained IF steel: (a) band contrast micrograph and (b) ND orientation map.

from  $\alpha$ -grains which can be consumed by the growing ND $\langle 111 \rangle$  recrystallized grains. From these results, it could be concluded that the strong  $\gamma$ -fiber components in the two IF steels was inherited from the prevailing strain accumulation in the  $\gamma$ -grains during the deformation. Active subgrain formation and growth in the deformed  $\gamma$ -grains are the main origin of the development of the  $\gamma$ -fiber prevalent recrystallization texture in the IF steels.

Grains of low stored energy can also contribute to the formation of recrystallization texture by another mechanism of nucleation, viz the strain induced boundary migration (SIBM) [30–32]. When the grains having low stored energy are in contact with grains having high stored energy, the grain boundary can migrate into the neighboring high stored energy grains. In this case, low stored energy RD $\langle 110 \rangle$  grains can grow by the consumption of high stored energy ND $\langle 111 \rangle$  grains. This mechanism may not be the major mechanism of the formation of recrystallization texture, however, the probability of SIBM will be greater in steels of larger grain boundary area. This could be the main reason of the higher intensity of the near  $\{001\}\langle 110 \rangle$  components observed in the fine grained IF steel.

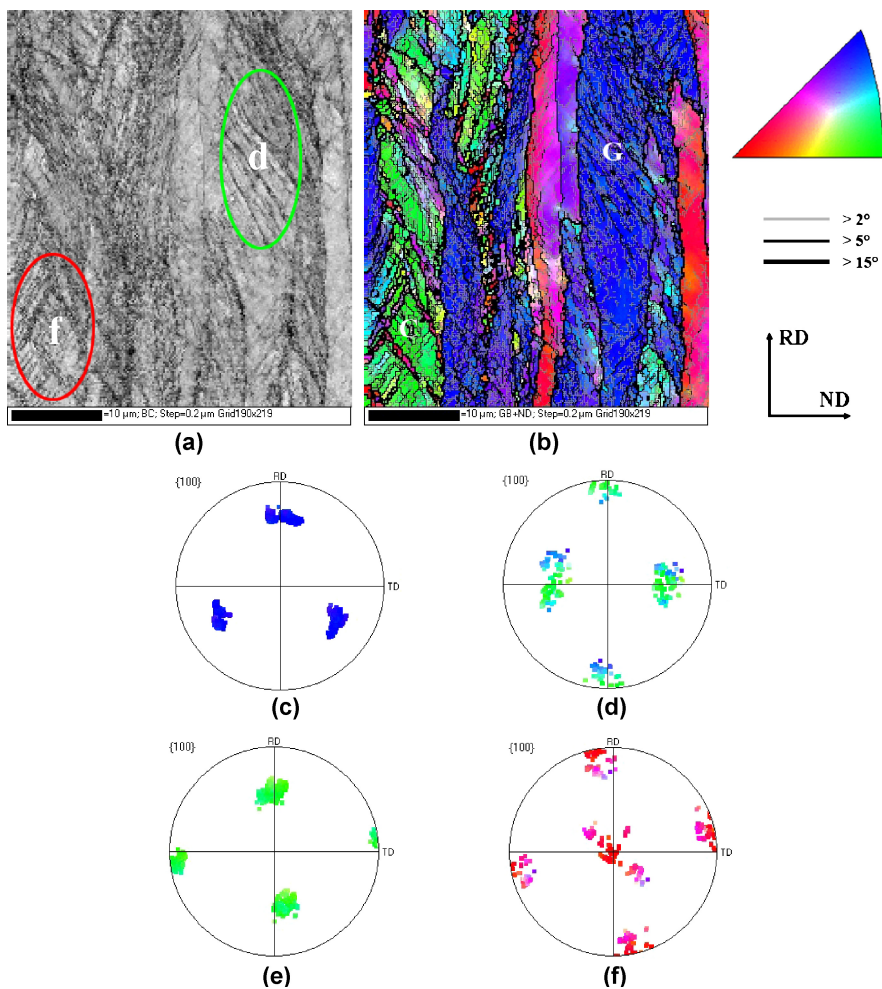


**Fig. 5.14** Orientation of shear bands in relation to the grain orientation: (a) band contrast map, (b) ND orientation map, {100} pole figures of the  $\{111\}<112>$  grain (c) and  $\{110\}<110>$  (e). {100} pole figures of the shear bands (d and f) in the marked region.

Another active nucleation site for recrystallization is the shear band in deformed grains. The shear bands are the areas in which concentrated deformation occurred. In Fig. 5.14, the pole figure of shear bands observed in the DP steel is compared with that of the surrounding deformed grains. The grain orientation of Fig. 5.14 (c) is near  $\{111\}<112>$ , which is known to frequently develop shear bands [26, 33]. The texture of shear bands developed in this grain was close to  $\{110\}<001>$ , viz. the Goss orientation. The Goss components observed in the DP steel are believed to come from grains nucleated from these shear bands. Figure 5.14 (e) and (f) show another case of shear band formation. The grain orientation is close to  $\{110\}<110>$  (rotated Goss) and the orientation of the shear band



formed in this grain was close to the  $\{001\}<100>$  (cube) component. It could be reasoned that the weakening of the  $\gamma$ -recrystallization texture and the strengthening of the Goss and cube components in the DP steel originated from the frequent formation of shear bands in the  $\gamma$ -grains. In the IF steels, shear bands were less frequently observed except in the  $\{111\}<112>$  grains and the orientation of the shear bands was not very different from that of the  $\{111\}<112>$  grains.

Present observation suggests that recrystallization is not a simple phenomenon but a complex one which several mechanisms competing with each other. The development of recrystallization texture may not be explained by a single mechanism. The nucleation of the grains having the similar orientation from the  $\{111\}<112>$  and  $\{111\}<110>$  deformed grains was observed to be the governing mechanism. They grow into the neighboring deformed grains having different orientations and determine the final texture of the fully recrystallized sheets. In the fine grained IF steel, because of the larger grain boundary areas than in the other steels, some of the  $\{001\}<110>$  grains survived by the SIBM mechanism. In the DP steels, the overall texture strength was weakened and the  $\{001\}<100>$  and  $\{110\}<001>$  textures were evolved owing to the active nucleation at the shear bands.

### 5.3 Effect of Austenite Transformation on the Recrystallization Texture of DP Steel

During DP treatment of the low carbon steel, the sheets were heated to the ferrite + austenite temperature and during holding, part of the recrystallized ferrite transformed into austenite and part of this austenite transformed into ferrite again during cooling. Ferrite to austenite and also austenite to ferrite transformation are known to occur satisfying the Kurdjumov-Sacks (K-S) orientation relationship. If we assume the random selection of 24 K-S variants during the transformation, we would expect a significant weakening of the recrystallization texture to be caused by the austenite transformation. Figure 5.15 (b) shows the calculated ferrite texture assuming the random selection of the K-S variants during the ferrite-austenite-ferrite transformation of an IF steel which has the strong ND// $\langle 111 \rangle$  texture of Fig. 5.15 (a). The random selection of the K-S variants practically randomized the initial strong ND// $\langle 111 \rangle$  texture.

Figure 5.16 shows the variation of the texture in the DP steel heated to the full austenite region after recrystallization. Figure 5.16 (a) shows the texture of the DP steel quenched after heating to 780°C and Fig. 5.16 (b) shows the texture of the same steel continuously heated to 950°C and then cooled to room temperature. The steel is completely recrystallized at 780°C and the austenite transformation was finished at 910°C. The transformation texture of Fig. 5.16 (b) is almost identical to the recrystallization texture of Fig. 5.16 (a). Inagaki also reported a similar result [34]. We can conclude that in textured materials, random selection is not a proper assumption for variant selection and the austenite transformation during DP annealing does not significantly affect the final texture of DP steel.

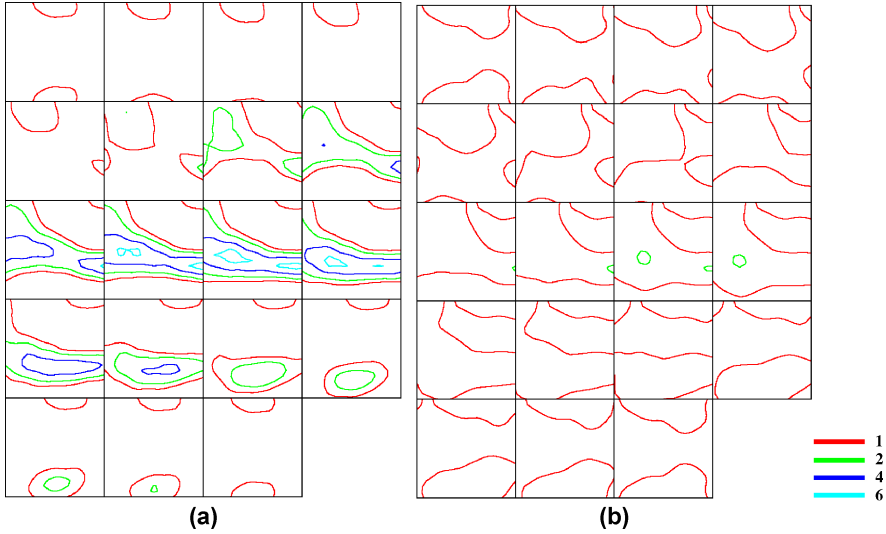


**Fig. 5.15** Weakening of texture due to austenitization (computed assuming random selection of K-S variants): ODF (a) before and (b) after austenitization.

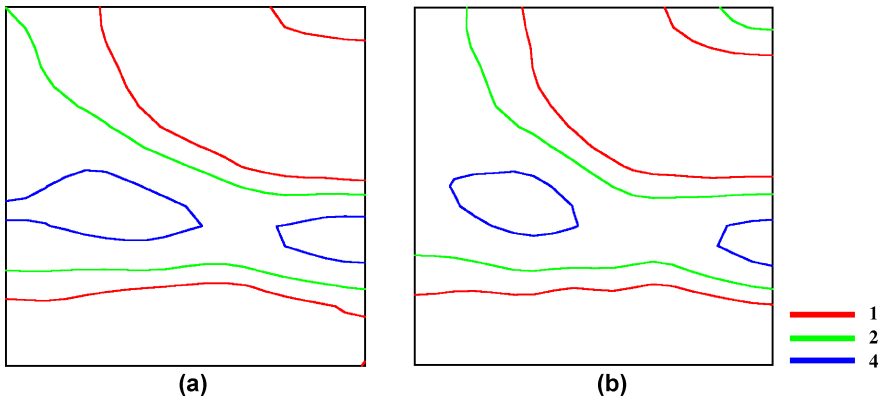


**Fig. 5.16** Texture variation after austenitization of recrystallized DP steel: ODF (a) before and (b) after austenitization.

## 5.4 Summary

The development of the recrystallization texture in conventional IF, fine grained IF, and DP steels was investigated using EBSD technique. During the deformation, a strong  $\alpha$ -fiber texture with  $\{112\}<110>$  peak and weaker  $\gamma$ -fiber texture with  $\{111\}<110>$  peak were developed in all three steels. After recrystallization, they were changed to a strong  $\gamma$ -fiber texture with strong  $\{111\}<112>$

component. However, the intensity of the texture components varied in the different steels. Strain induced boundary migration (SIBM) was observed in the fine grained IF steel and that may result in the higher intensity of the  $\{001\}<110>$  component after recrystallization. Nucleation of the  $\{110\}<001>$  and  $\{001\}<100>$  recrystallized grains from the shear bands in  $\{111\}<112>$  or  $\{110\}<110>$  grains was expected. The austenite transformation during the intercritical annealing of the DP steel was found to have only a limited effect on the formation of its final recrystallization texture.

## References

- [1] Ultra Light Steel Auto Body – Advanced Vehicle Concepts (ULSAB-AVC): Overview report, International Iron and Steel Institute (2002).
- [2] Ray, R.K., Jonas, J.J. and Hook, R.E., *Int. Mater. Rev.*, 1994, 39, 129.
- [3] Park, Y.B., Lee, D.N., and Gottstein, G., *ICOTOM 11*, 1986, 1, 324.
- [4] Emren, F., von Schluppenbach, U. and Lücke, K., *Acta Met.*, 1986, 34, 2105.
- [5] Park, Y.B., Lee, D.N., and Gottstein, G., *Acta Met.*, 1998, 46, 3371.
- [6] Samajdar, I., Verlinden, B., and Van Houtte, P., *Acta Met.*, 1998, 46, 2751.
- [7] Samajdar, I., Verlinden, B., Kestens, L., and Van Houtte, P., *Acta Met.*, 1999, 47, 55.
- [8] U. von Schluppenbach, F. Emren and K. Lucke, *Acta Metall.*, 34 (1986), 1289.
- [9] W. B. Hutchinson, K.-I. Nilsson and J. Hirsch, *Proc. Metallurgy of vacuum-degassed steel products*, ed. R. Pradhan, Warrendale, PA, Metallurgical Society of AIME, 1990, 109.
- [10] A.J. Heckler and W. G. Granzow, *Metall. Trans.*, 1 (1970), 2089
- [11] D. Rabbe, *Mater. Sci. Eng. A*, A197 (1995), 31.
- [12] H. Inagaki, *ISIJ Inter.*, 34 (1994), 313.
- [13] H. Inagaki and T. Suda, *Texture*, 1 (1972), 129.
- [14] H. Inagaki, *Trans. Iron Steel Inst. Jpn.*, 24 (1984), 266.
- [15] H. Inagaki, *Z. Metallkde.*, 78 (1987), 431.
- [16] J.-K. Kang, B. Bacroix, H. Regle, K.-H. Oh and H.-C. Lee, *Acta Mater.*, 53 (2007), 4935.
- [17] Burgers, W.G. and Louwerse, P.C., *Z.physik*, 1931, 67, 605.
- [18] Barrett, C.S., *Trans. A.I.M.E.*, 1940, 137, 128.
- [19] Ibe, G. and Lücke, K., *Recrystallization, grain growth and textures*, ed. h. Margolin, ASM, 1996, p.434.
- [20] Lee, D.N., *Scripta Metall. Mater.*, 1995, 32, 1689.
- [21] Doherty, R.D., Gottstein, G., Hirsch, J., Hutchinson, W.B., Lücke, K., Nes, E. and Wilbrandt, P.J., *Proc. ICOTOM8*, ed. J.S. Kallend and G. Gottstein, Warrendale, 1988, p.563.
- [22] Ridha, A.A. and Hutchinson, W.B., *Acta Metall.*, 1982, 30, 1929.
- [23] Hirsch, J.R., and Lücke, Annealing processes, 7th Riso Inter. Sympo. on Metallurgy and Materials Science, 1986, 107.
- [24] P. Pannière, *proc. ICOTOM 6*, ISIJ, 1981, 181.
- [25] H. Takechi, H. Kato, and S. Nagashima, *Trans. AIME*, 242 (1968), 56.
- [26] M.D. Nave and M.R. Barnett, *Mater. Sci. Forum*, 408–412 (2002), 907.
- [27] G. Ibe and K. Lucke, *Proc. Recrystallization, Grain Growth and Textures*, ed. By Margolin, ASM, Metals Park (1966), 434.
- [28] Samajdar, I., Verlinden, B., Van Houtte, P., and Vanderschueren, D., *Mat. Sci. and Eng. A*, 1997, A238, 343.
- [29] Li, J.C.M., *J. Appl. Physics.*, 1962, 33, 2958.
- [30] P.A. Beck and P.R. Sperry, *J. Appl. Phys.*, 21 (1950), 150.

- [31] S.P. Bellier and R. D. Doherty, *Acta Metall.*, 25 (1977), 521.
- [32] D. Vandershueren, N. Yoshinaga and K. Koyama, *ISIJ Inter.*, 36 (1996), 1046.
- [33] J. Hjelen, R. Ostrund and E. Nes, *Acta Metall.*, 39 (1991), 1377.
- [34] H. Inagaki, *Proc. ICOTOM 6*, ed by S. Nagashima, *ISIJ* (1981), 149.



Hu-Chu Lee  
Professor  
Department of Materials Science  
and Engineering  
Seoul National University  
Seoul, 151-744  
South Korea





## Chapter 6

# Texture and Microstructure Evolution at the Metal-Vapour Interface During Transformation Annealing in a Mn and Al Alloyed Ultra Low Carbon Steel

Leo A.I. Kestens, Jai Gautam, and Roumen Petrov

**Abstract.** This paper investigates the evolution of texture and microstructure at the metal-vapour interface during transformation annealing in vacuum. Interrupted annealing experiments were carried out on cold rolled Mn, Al and Si alloyed ultra low carbon steels. The textures were characterized by X-ray diffraction and SEM-EBSD techniques. The results show the variation in the surface texture components obtained after BCC recrystallisation and double  $\alpha$ - $\gamma$ - $\alpha$  transformation annealing. The recrystallisation texture consists mainly of a  $\langle 111 \rangle$ //ND fibre, while the transformation texture at the surface exhibits a  $\langle 100 \rangle$ //ND fibre in combination with components of the  $\langle 110 \rangle$ //ND fibre. It was revealed that the latter specific surface texture was present in a monolayer of outer surface grains which were in direct contact with the vapour atmosphere. This observed phenomenon could be explained by considering the role of surface energy anisotropy occurring during phase transformation annealing.

**Keywords:**  $\alpha$ - $\gamma$ - $\alpha$  transformation, metal-vapour interface energy, surface texture,  $\langle 100 \rangle$ //ND and  $\langle 110 \rangle$ //ND texture

## 6.1 Introduction

It is well known that anisotropy of surface energy is the driving force for the orientation selection at the metal-vapour interface during solidification. This affects

---

L.A.I. Kestens and J. Gautam

Materials Science and Engineering Department, Delft University of Technology, Mekelweg 2, 2628 CD Delft, The Netherlands

J. Gautam and R. Petrov

Dept. of Metallurgy and Material science, Ghent University, Technologiepark 903, Ghent, B-9052, Belgium

the microstructure and texture evolution of solidifying metals. Although the exact value of the interfacial energy between the atmosphere and the steel surface is largely unknown, it is widely accepted that the bcc  $\{100\}$  and  $\{110\}$  planes have a relatively low surface energy [1, 4, 5, 6, 7].

The austenite-to-ferrite phase transformation, which is an inherent feature of low-alloyed low-carbon steels, has scarcely been investigated to control surface texture evolution. Hashimoto et al. [2, 3] investigated the  $\alpha$ - $\gamma$ - $\alpha$  phase transformation texture at the surface of an ultra low carbon cold rolled steel sheet and reported that a  $\langle 100 \rangle // \text{ND}$  texture was formed rather than the usual  $\langle 111 \rangle // \text{ND}$  texture. They interpreted this experimental result by assuming that the elastic work in the ND direction associated with the transformation could be larger than that in any other direction. Aspeden et al. [4] reported that an annealing treatment in the austenite phase followed by slow cooling in ultra low carbon steel resulted in a stronger  $\langle 100 \rangle // \text{ND}$  texture. They explained their observations by the texture dependence of the surface energy. The  $\langle 100 \rangle // \text{ND}$  surface grains nucleate more rapidly because they have the lowest interfacial energy with the surrounding atmosphere. Tomida and Tanaka [5] revealed that an extremely sharp  $\langle 100 \rangle // \text{ND}$  texture can be formed at the surface of a Mn alloyed low carbon steel by means of an inter-critical annealing or a heat treatment in the  $\gamma$  region.

The surface textures reported in the literature do not include a systematic description of their evolution neither does the literature provide a detailed description of the grain morphology and grain structure at the surface. In the present study an attempt has been made to represent a clear view on the surface texture evolution in ultra low carbon steel alloyed with Mn and Al. The interrupted annealing experiments have been conducted in the dilatometer to ensure a precise temperature and phase fraction control during each step of the annealing treatment. The surface texture has been measured by XRD in a conventional texture goniometer whereas grain structure and morphology was characterised by orientation contrast microscopy (EBSD-OIM of EDAX-TSL<sup>®</sup> type).

## 6.2 Experimental Procedure

Two alloys, denominated as L2 and L3, with the chemical composition listed in Table 6.1, were hot rolled above the  $A_{r3}$  temperature, air cooled and annealed at 700°C in order to simulate the slow cooling trajectory of the industrial hot band coiling process. After pickling the hot rolled sheets were cold rolled to a 70% reduc-

**Table 6.1** Chemical compositions

(wt %)	C	Mn	Si	Al
L2	0.002	1.28	0.22	0.29
L3	0.003	0.75	0.23	0.12

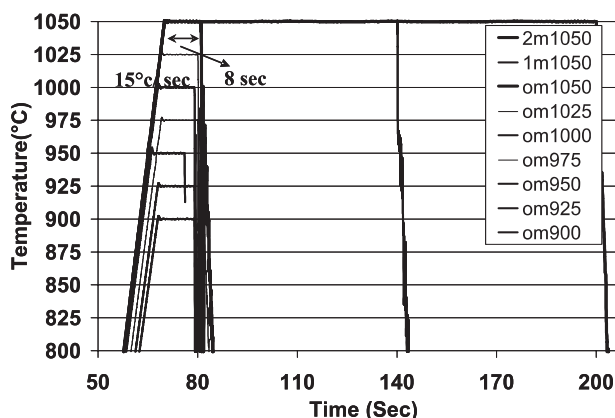


Fig. 6.1 Interrupted annealing treatment.

tion. The cold rolled material was annealed according to the schematic illustration of Fig. 6.1. The dilatometer was employed for this annealing treatment. During annealing the furnace atmosphere was kept vacuum and quenched with helium gas.

The microstructure of the cold rolled sheets was characterized by means of light optical microscopy after mechanical polishing. Orientation contrast imaging was also carried out on selected samples by the EBSD technique. The EBSD system was attached to a FEI<sup>®</sup> Environmental Scanning Microscope (ESEM-XL30) with a LaB6 filament. Four incomplete pole figures ( $\{110\}$ ,  $\{200\}$ ,  $\{211\}$ , and  $\{310\}$ ) were measured on a SIEMENS<sup>®</sup> D5000 X-ray texture goniometer with a molybdenum tube. The bulk of the diffraction data was received from the depth of approximately 8 microns underneath the sheet surface. The orientation distribution functions (ODFs) were calculated from these incomplete pole figures employing the software developed by Van Houtte [8].

## 6.3 Results

### 6.3.1 Surface Texture and Through Thickness Microstructure Before Annealing

The cold rolled sheets of both the alloys L2 and L3 were observed in the optical microscope and the through-thickness microstructures are shown in Fig. 6.2. The cold rolled microstructure is very homogeneous across the thickness. The cold rolled surface textures were examined in the X-ray texture goniometer and the  $\phi_2 = 45^\circ$  sections are shown in Fig. 6.3. The cold rolled surface textures exhibit the typical L-shape morphology of the cold rolling texture as they are composed of the alpha and gamma fibre ( $\langle 110 \rangle // RD$  and  $\langle 111 \rangle // ND$ , respectively).

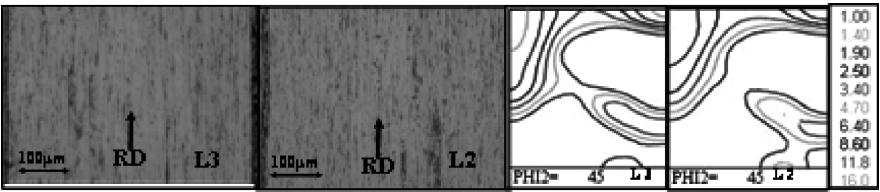


Fig. 6.2 Through thickness microstructures (left) of the cold rolled sheet and X-ray texture (right) observed on the RD-TD surface of materials L2 and L3.

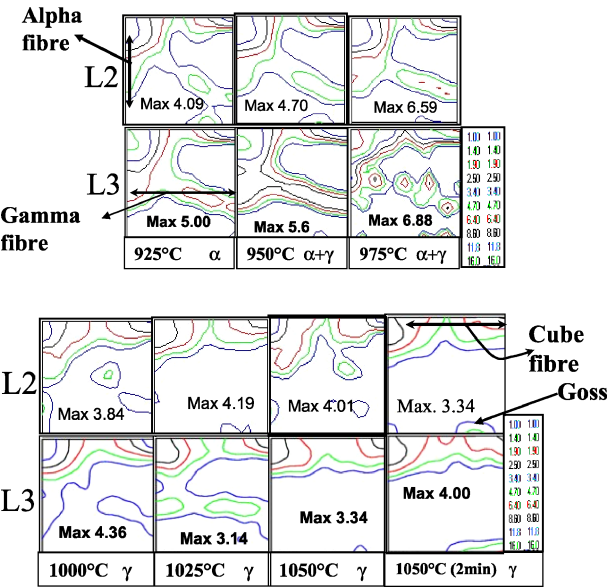


Fig. 6.3  $\Phi_i2=45^\circ$  sections of ODFs measured after interrupted annealing at different temperatures.

### 6.3.2 Surface Texture at Different Temperatures During Interrupted Annealing

After interrupted annealing under vacuum conditions the sample surfaces were examined with the X-ray texture goniometer. ODFs have been analysed and  $\phi_i2=45^\circ$  sections for both alloy compositions at different temperatures are shown in Fig. 6.3. At 925°C the ferrite recrystallisation takes place and as a result of that the texture has evolved towards the rotated cube component and the gamma fibre. The ODFs observed after annealing at 950°C and 975°C represent textures developed during annealing in the mixed phase of ferrite and austenite. The overall intensity of the texture has increased and consists of the rotated cube component, the alpha and the gamma fibre. The  $\phi_i2=45^\circ$  sections observed after annealing at

1000°C, 1025°C and 1050°C represent the textures after complete austenitization and subsequent transformation to ferrite. The surface texture after complete transformation displays a strong cube fibre in combination with a Goss component which is significantly different from the textures observed at lower temperatures.

### 6.3.3 Through Thickness Grain Morphology

Orientation contrast microscopy (EBSD) was carried out on a number of selected samples of the alloy L3 annealed at 925°C (no transformation), at 975°C (partially transformed) and at 1050°C (complete transformation) with a holding time of two minutes. The intention was to reveal a microstructural and textural correlation across the thickness of the sheet at these three different temperatures. Figure 6.4 shows the inverse pole figure maps (in grey scale) obtained at three successive stages during interrupted annealing. The first microstructure (Fig. 6.4 (a)) at 925°C displays a recrystallised grain morphology which consists of equi-axed grains with an average size of approximately 11.6  $\mu\text{m}$ . The second microstructure (Fig. 6.4 (b)) observed after annealing at 975°C shows a partially transformed microstructure which is characterized both by smaller equi-axed grains and larger irregular grains. It is assumed that the former are recrystallized ferrite grains whereas the latter are transformed ferrite grains. The third microstructure (Fig. 6.4 (c)), recorded on a sample annealed in the fully austenite phase at 1050°C for 2 minutes, shows a very irregular grain structure with an average size of approximately 10  $\mu\text{m}$ . It can also be observed that this microstructure exhibits a monolayer of elongated grains at the very edge which contacts the outer atmosphere. This single layer of surface grains represents a specific texture which is dominated by  $\langle 100 \rangle$  and  $\langle 110 \rangle$  fibre grains.

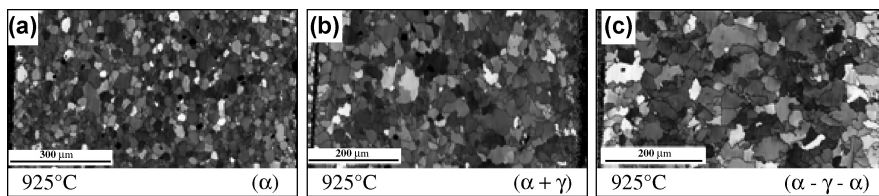


**Fig. 6.4** (a, b and c) Inverse pole figure maps in grey scale observed after recrystallisation, intercritical annealing and after  $\alpha$ - $\gamma$ - $\alpha$  transformation in the RD-ND plane for L3.

## 6.4 Discussion

The  $\alpha$ - $\gamma$ - $\alpha$  transformation textures of the two alloys L2 and L3 have revealed a typical surface texture with  $\{100\}$  and  $\{110\}$  planes parallel to the solid/vapour

interface. It appears that a specific orientation selection mechanism has occurred during  $\alpha$ - $\gamma$ - $\alpha$  transformation at the cold rolled surface. Such a surface texture component has already been reported by several authors (3–7). There are different explanations reported in the literature for the  $\langle 100 \rangle$ //ND texture formation at the surface but the following two mechanisms are found to be more relevant in the present study: (i) an orientation selection mechanism controlled by surface energy or (ii) a variant selection mechanism resulting from the release of transformation stresses towards the normal direction.

In an earlier investigation (10) both mechanisms have been discussed and it has been found that the first possibility of an orientation selection mechanism controlled by surface energy anisotropy is probably the more convincing one. The detailed analysis (11) of the surface microstructure indicates that the surface texture is controlled to a large extent by the interface energy. This is not only true for the solid/vapour interface but also for the grain/grain interfaces in the surface monolayer. This monolayer shows a 40% area fraction of low-energy  $\Sigma 3$  boundaries which significantly exceeds the fraction of 8% which is observed in the bulk of the metal.

The present results indicate that by appropriate control of annealing conditions specific texture components can be introduced at the surface of the sheet. By fine-tuning the annealing conditions it can be attempted to grow the surface grains towards the bulk of the sheet and hence to control the bulk texture as well (6 and 12). Hence, the surface can be used as an additional degree of freedom for the control of textures in steel sheet manufacturing. In order to fully benefit from the potential of this degree of freedom a number of obstacles still needs to be overcome. E.g. it is not yet known in detail how surface chemistry and annealing environment will affect the surface energy anisotropy and the resulting surface texture during  $\alpha$ - $\gamma$ - $\alpha$  phase transformation.

## 6.5 Conclusions

The selected alloy compositions L2 and L3 exhibit a specific surface texture after  $\alpha$ - $\gamma$ - $\alpha$  transformation annealing of a cold rolled sheet. The annealed sheet surfaces of the two alloys exhibit a monolayer of grains in direct contact with the metal/vapour interface and with predominant  $\langle 100 \rangle$ //ND and  $\langle 110 \rangle$ //ND fibre texture. Orientation selection on the basis of minimisation of the metal/vapour interface energy seems to be the most appropriate hypothesis to explain the present results.

## References

- [1] L. Kestens, J.J. Jonas, P. Van Houtte and E.Aernoudt: Textures & microstructures Vol. 26–27 (1996), p. 321.
- [2] C.G. Dunn and Walter: Trans. Met. Soc. AIME Vol. 224 (1962), p. 518.
- [3] O. Hashimoto, S. Satoh, T. Tanaka: Tetsu-to-hagane Vol. 66 (1980), p. 102.
- [4] O. Hashimoto, S. Satoh, T. Tanaka: Tetsu-to-hagane Vol. 66 (1980), p. 112.
- [5] R.G. Aspeden, J. Berger and H.E. Trout: Acta Metallurgica, Vol. 16 (1968), p. 1027.
- [6] T. Tomida and Tanaka: ISIJ International Vol. 35 (1995), p. 548.
- [7] N. Yoshinaga, L. Kestens and B.C. De Cooman: Mater. Sci. Forum Vol. 495–497 (2005), p. 1267.
- [8] P. Van Houtte: The MTM-FHM Software system Version 2 Users Manual (1995).
- [9] D.A. Porter and K.E. Easterling: Phase transformation in metals and alloys (Stanley Thorntons Publishers Ltd, U.K. 1992).
- [10] J. Gautam R. Petrov and L. Kestens, Materials Science Forum, Vol. 550, 503, (2007).
- [11] J. Gautam R. Petrov and L. Kestens and Elke Leunis, Journal of Material Science, 2007 (in press).
- [12] M. Takashima, M. Komatsubara and N. Morito, ISIJ International, Vol. 37 (1997), No. 12, pp. 1263.



Leo Kestens  
Professor  
Microstructural Control in Metals  
Delft University of Technology  
Materials Science and Engineering  
Netherlands





## Chapter 7

# Precipitation Behavior and Textural Evolution in Interstitial Free High Strength (IFHS) Steels

R.K. Ray and P. Ghosh

**Abstract.** Cold rolled and annealed interstitial free high strength (IFHS) steels show various kinds of precipitates. Out of these, FeTiP is the most deleterious, since its formation leads to a loss of strength as well as degradation of the formability of the steel. This effect is much more pronounced in batch annealed IFHS steels than in their continuous annealed counterparts. The harmful effects of FeTiP precipitation in batch annealed steels can be largely avoided by the use of appropriate coiling and annealing temperature, depending on the composition of the steel.

### 7.1 Introduction

Interstitial free high strength steels, commonly known as IFHS steels, have been developed to meet the requirement of higher strength coupled with adequate deep drawability. To achieve this, solid solution strengthening elements, like P and Mn are added to normal interstitial free (IF) steels to produce solid solution strengthening, without any loss of formability. This particular grade of steels has found wide acceptability by the automobile manufacturers for use in different critical shaped parts of car body where strength is also a major issue. As a whole, use of IFHS steels in car body applications should allow the down-gauging of steel sheets with an attendant reduction in weight. This in turn, will result in lowering of fuel consumption and less emission of harmful CO<sub>2</sub>. Unfortunately, very often, deterioration of formability has been noticed in this grade as compared to the normal IF steels. This has very often been attributed to the formation of FeTiP type of precipitates which are suspected to degrade the deep drawability of these steels.

---

R.K. Ray and P. Ghosh  
R & D Division, TATA Steel, Jamshedpur, INDIA 831 007

Not only that, loss of strength has also been reported due to FeTiP formation. FeTiP has been reported to form in the temperature range of 600–900°C [1]. Below 600°C, the kinetics of FeTiP formation is very sluggish and above 900°C, it appears to dissolve. The formation of FeTiP is more harmful in case of batch annealing as the process itself allows sufficient time for the reaction to take place. On the contrary, in case of continuous annealing, many a time FeTiP formation does not take place due to less time for precipitation. Literature reveals that the solubility product plots for FeTiP and TiC are very close and formation of FeTiP may result in less Ti being available to tie up with the carbon, in case FeTiP forms prior to the formation of TiC. The larger amount of carbon left behind in the matrix will be very harmful to {111} texture formation and the formability. Along with this, FeTiP particles have often been observed to be present on the grain boundaries, which may very well restrict the growth of beneficial {111} oriented grains. This also results in poor average  $r$  value. The precipitation and stability of FeTiP particles are very much dependent on the composition as well as processing history of the steels. In this context, a detailed understanding of FeTiP precipitation is very much needed to get the maximum benefit of P addition without losing much of the formability. The present review deals with the effect of composition and processing parameters on precipitation behavior in IFHS steels, in general, with special emphasis on FeTiP formation. It will also take into account the impact of precipitation on texture formation and deep drawability, with a view to suggesting possible ways and means to avoid the deleterious effects of precipitates such as FeTiP.

## 7.2 Precipitation in Batch Annealed (BA) IFHS Steels

IFHS steels are normally processed by the hot rolling, cold rolling and annealing route. Annealing can be done by either the batch or the continuous process. In case of batch annealed IFHS steels, a variety of precipitates with definite shapes can be observed. The most common among them are TiN particles which are mainly square or rectangular in cross-section. The average size of these particles is 1–2  $\mu\text{m}$ . Very often these are observed to be present along with other particles, like Al-oxide or MnS. Al-oxide particles are seen to be surrounded by TiN precipitates, which suggests heterogeneous precipitation of TiN over Al-oxide particles. Some complex precipitates containing Ti, N, Mn and S are often observed in these steels. This may be due to a combination of two separate precipitates, such as TiN and MnS. Sometime these complex precipitates contain Al also. All these features are shown in Fig. 7.1. The size and frequency of TiN particles are perceptibly higher in Ti+Nb IFHS steels as compared to only Ti-added IFHS steels. This could be due to the presence of Nb which is known to increase the effective Ti solute concentration in the matrix and may thus trigger the formation of TiN in the earlier stages of steelmaking [2, 3]. This feature is shown in Fig. 7.2.

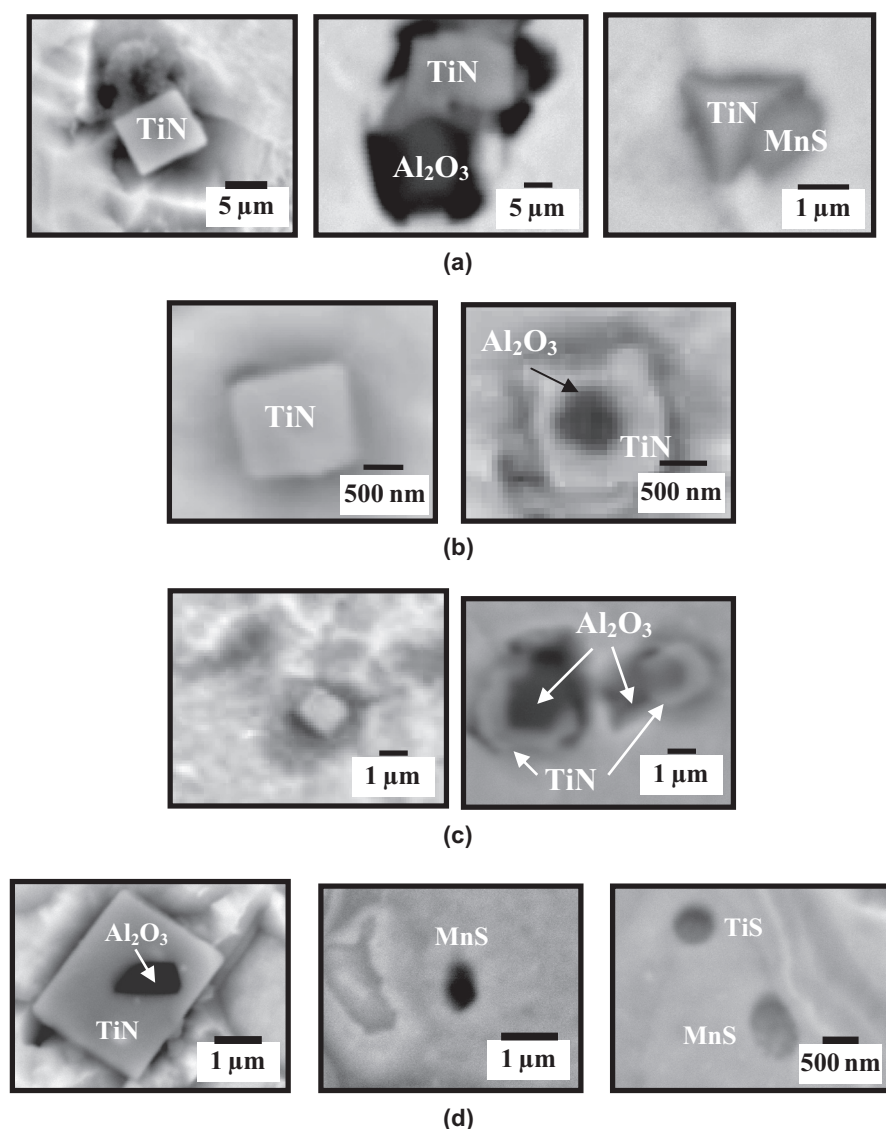


**Fig. 7.1** SEM micrographs of batch annealed IFHS steels showing presence of different precipitates.

Apart from these bigger sized precipitates, numerous fine precipitates are also observed ( $<1\ \mu\text{m}$ ) in these steels. The sizes of these precipitates range between 10 nm and 500 nm. The volume fractions of these precipitates vary with the steel composition. Most of these fine precipitates have been identified as FeTiP/Fe(Ti+Nb)P type with Fe:Ti:P ratio more or less close to 1:1:1. This precipitation occurs during batch annealing at 700°C. Higher amounts of P and Ti in

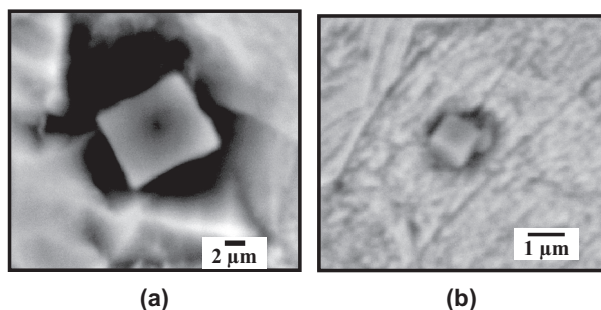


**Fig. 7.2** SEM micrographs showing presence of TiN precipitates in (a) Ti+Nb-IFHS and (b) Ti-IFHS steels processed through batch annealing route.

the steels results in the formation of more FeTiP type of precipitates, whereas lower amounts of these two elements results in a markedly reduced volume fraction of FeTiP. In fact, depending on the amount of P present, steels may or may not show the presence of any carbide precipitates. The solubility product values of TiC and FeTiP are very close as shown in Fig. 7.3 [4, 5]. Thus, there is every possibility that FeTiP may form before TiC precipitation in such steels. As a result of this, most of the Ti will get exhausted and very little Ti may be left out to tie up with the C in the matrix. This may lead to the formation of rather unstable TiC precipitates with low volume fraction. The process will leave behind a substantial amount of C in solid solution in the matrix.

In case of batch annealing of IFHS steels, the precipitation sequence can be as follows:

TiN: forms during steel solidification

TiS: forms during continuous casting and reheating

MnS: forms during hot rolling

Ti<sub>4</sub>C<sub>2</sub>S<sub>2</sub>: forms during coiling after hot rolling (?) [will be discussed in Sect. 4]

Fe(Ti+Nb)P/FeTiP: forms during annealing

TiC: forms during annealing

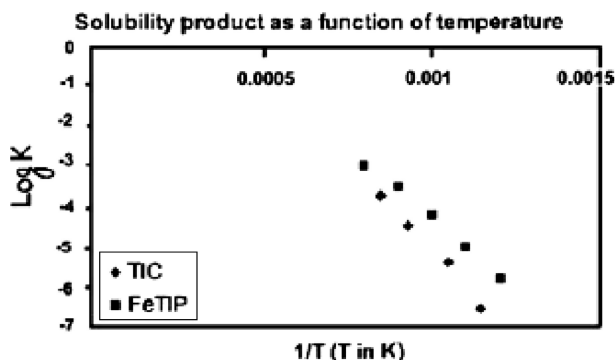


**Fig. 7.3** Solubility product curve as a function of temperature for TiC and FeTiP.

The formation of the last two precipitates is much more sensitive to steel composition and processing.

### 7.3 Precipitation in Continuous Annealed (CA) IFHS Steels

Continuous annealing after cold rolling is very popular with steel makers as the process takes less time and therefore increases the productivity. In this process, after cold rolling the steel sheets are continuously passed through the annealing furnace which is generally kept at a temperature higher than that of normal batch annealing furnaces. However, the holding time is very short, less than 2 min, as compared to batch annealing which involves a holding time of 20–25 hrs. Due to the higher annealing temperature and very short annealing time, the precipitation behavior of continuously annealed IFHS steels is quite different from their batch annealed counterparts.

As in case of BA-IFHS steels, in CA-IFHS steels also the most common precipitates are TiN. These are cubic in shape with square or rectangular cross-section and having a size range from 1–2  $\mu\text{m}$ . However, the frequency of observation as well as the size of the TiN particles is very much dependent on the composition of the steels. For example, if the steel does not contain any Nb but Ti only, the frequency of observation of TiN is very rare and also the size is very small. On the contrary, presence of Nb not only increases the size but the number of such particles as well. This feature is illustrated in Fig. 7.4. This effect is more pronounced in continuously annealed IFHS steels as compared to the batch annealed steels. As mentioned in the previous section, the presence of Nb increases the effective solute concentration of Ti and as a result of this TiN formation is more easy in Ti+Nb-IFHS steels. In case of batch annealing, smaller TiN precipitates may get the chance to grow during annealing, whereas in case of continuous annealing it does not happen. After the formation of TiN particles, precipitation of TiS takes place. The volume fraction of TiS precipitates is much higher in case of continuous annealing as compared to batch annealing. TiS, which forms during continuous casting, is not stable during annealing and gets transformed to other types of precipitates. In case of batch annealing, due to higher annealing time, the transformation is mostly complete whereas, it is not so in case of continuous annealing.

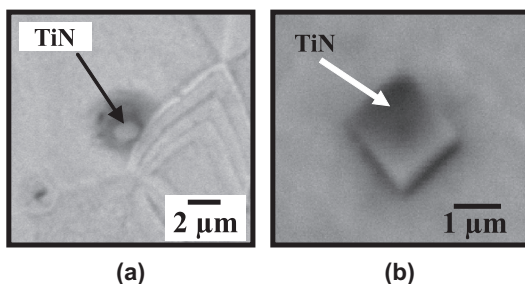
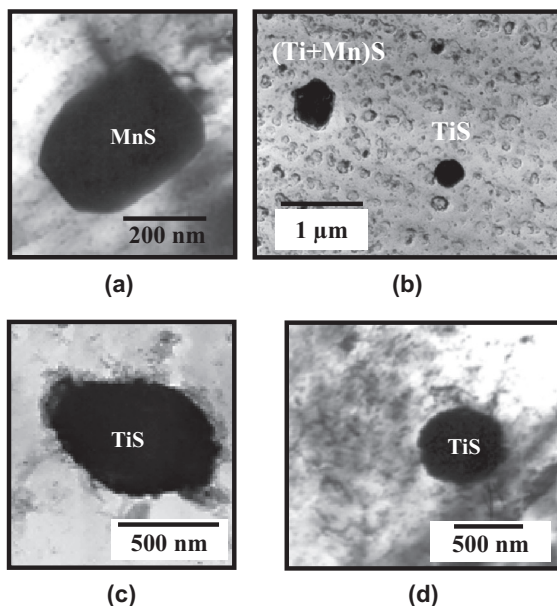


**Fig. 7.4** Presence of TiN precipitates in (a) a Ti-IFHS and (b) a Ti+Nb-IFHS steel.

**Fig. 7.5** Sulphide precipitates in (a–b) Ti and (c–d) Ti+Nb continuously annealed IFHS steels.



As a result, TiS is more frequently observed in continuous annealed IFHS steels. In case of Ti-only IFHS steels, MnS ( $\sim 500$  nm) and (Ti+Mn)S precipitates are mainly noticed. However, Ti+Nb-IFHS steels do not show any such precipitation. These features are shown in Fig. 7.5.

Next comes the carbide precipitation. Fine TiC precipitates are observed throughout the matrix of IFHS steels after annealing. These precipitates generally do not contain any Nb in them, irrespective of the Nb content of the steels, when they are present inside the grains. However, at or near the grain boundaries, the carbide precipitates are often found to contain a little bit of Nb in case of Ti+Nb IFHS steels. The reason is not hard to understand as Nb is expected to segregate at the grain boundary. These features are illustrated in Fig. 7.6. FeTiP or

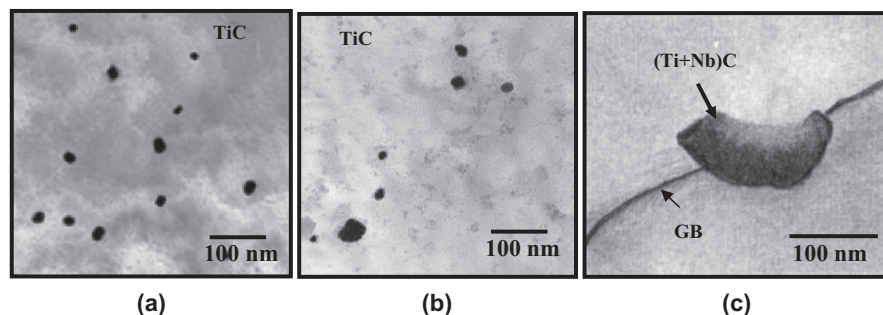
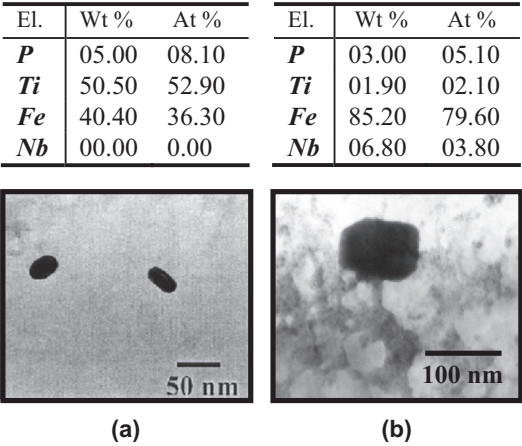


**Fig. 7.6** TEM micrographs of carbide precipitates in continuously added (a) Ti and (b–c) Ti+NB IFHS steels.

**Fig. 7.7** TEM micrographs showing (a) FeTiP type of precipitates in Ti-IFHS (extraction replica) and (b) Fe(Ti+Nb)P type of precipitates in Ti+Nb-IFHS steels (Thin foil).



Fe(Ti+Nb)P type of precipitates are very rarely observed in continuous annealed IFHS steels. Moreover, even if it forms, the amount of P in the precipitates is much lesser than the required stoichiometric amount. During continuous annealing, Fe and Ti instantaneously form some clusters [6] and P starts diffusing in slowly. However, there is not enough time for the P atoms to diffuse completely, resulting in Fe–Ti compounds with very little P in them [6]. These features have been depicted in Fig. 7.7.

In a nutshell, the sequence of precipitation in continuous annealed IFHS steels can be as follows:

- TiN: forms during steel solidification
- TiS: forms during continuous casting and reheating
- MnS: forms during hot rolling
- TiC: forms during annealing.

### 7.4 Precipitation of FeTiP

The main difference in chemical composition between the IF and the IFHS steels lies in the higher P content in the latter, due to which the precipitation behavior becomes much more complicated. It is now quite clear that presence of FeTiP type precipitates in IFHS steels plays a major role in deciding the deep drawability and mechanical properties of these steels. Formation of FeTiP not only degrades the deep drawability, but also results in loss of strength. Researchers have now established a one to one correlation between FeTiP formation and the development of {111} texture in IFHS steels. It is observed that higher volume fraction of FeTiP type precipitates results in less intense {111} annealing texture and consequently poorer  $\bar{r}$  value in IFHS steels.



7.4.1 Structure and Constitution of FeTiP

FeTiP does not appear to be a strictly stoichiometric compound and has a wide range of solid solubility for others elements. In Ti+Nb-IFHS steels, presence of Nb is almost invariably observed in the FeTiP precipitates formed. Very often the ratio of Fe:Ti:P in FeTiP precipitate particles is close to 1:1:1, but not exactly, and this ratio is found to vary from one particle to another. These features have been depicted in Fig. 7.8. The FeTiP precipitates do not appear to have any particular morphology, and can be lenticular, globular or rectangular in shape. These features are illustrated in Fig. 7.9. Ghosh et al. [7] have determined the crystal structure of FeTiP and Fe(Ti+Nb)P type precipitates present in a few IFHS steels. They found that FeTiP has an orthorhombic crystal structure and this structure is quite similar to that of the mineral florenskyite found in meteorites [8]. Simple FeTiP has unit cell dimensions

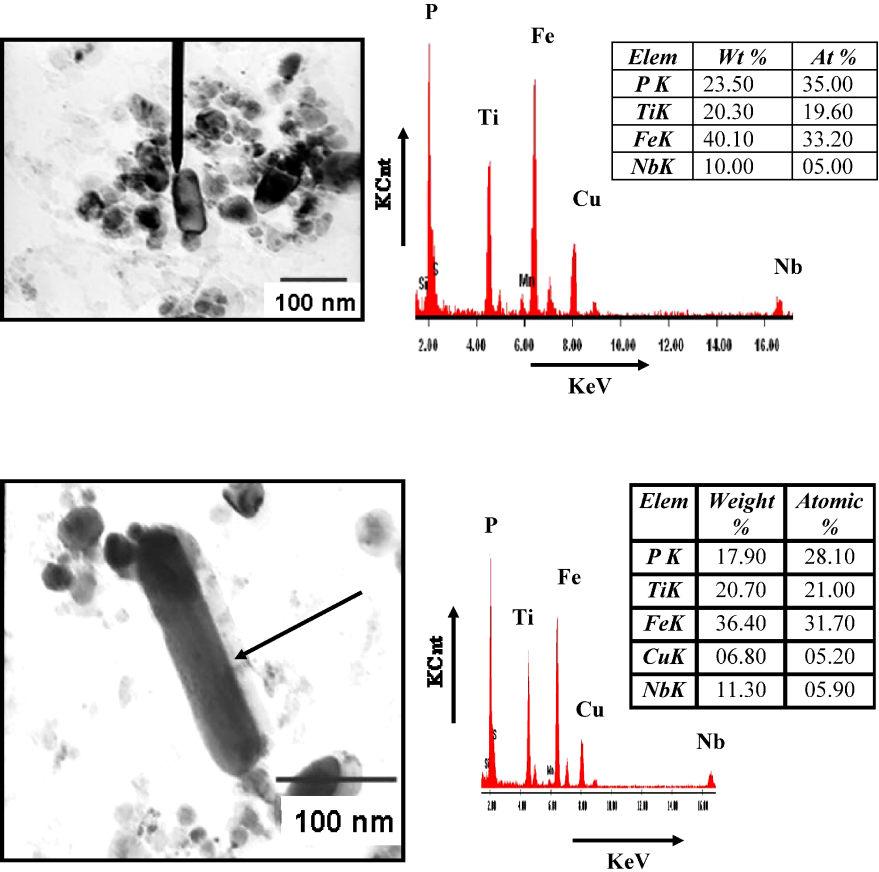
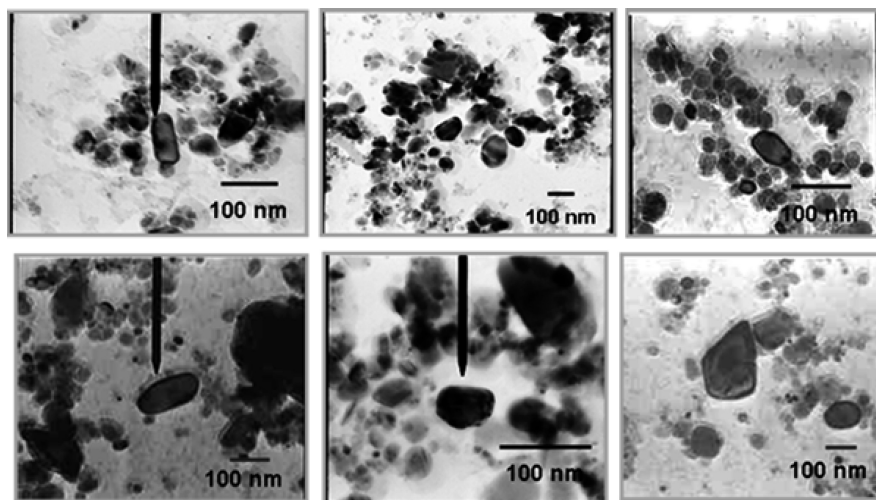


Fig. 7.8 TEM micrographs of FeTiP type of precipitates showing their elemental analyses along with EDS spectrum.



**Fig. 7.9** TEM micrographs of different shaped FeTiP type of precipitates.

$a = 5.816\text{--}5.821 \text{ \AA}$ ,  $b = 3.731\text{--}3.745 \text{ \AA}$  and  $c = 6.554\text{--}6.569 \text{ \AA}$ . The presence of Nb in FeTiP type precipitates does not alter the crystal structure but does increase the unit cell dimensions, especially the length of the c-axis. The unit cell dimensions of Fe(Ti+Nb)P precipitates have been determined as  $a = 5.939\text{--}6.105 \text{ \AA}$ ,  $b = 3.800\text{--}3.817 \text{ \AA}$  and  $c = 7.151\text{--}7.171 \text{ \AA}$ .

#### **7.4.2 FeTiP Formation in Cold Rolled and Annealed Steels**

The volume fraction of FeTiP precipitates in the annealed steels is dependent on the P and Ti content of the steels. Higher the amount of P, higher is the amount of FeTiP formed [see Fig. 7.10], and poorer the properties. This is reflected in the higher intensity of the  $\gamma$  fiber and higher average  $r$  value in BA steels with lower amounts of P. As mentioned earlier, FeTiP type precipitates are very rarely found in continuous annealed steels. As a result, the P containing CA steels show a much higher intensity of the  $\{111\}$  texture and larger average  $r$  value, as compared to corresponding batch annealed steels [Fig. 7.11]. Significantly enough, the FeTiP type precipitates, even if formed in CA steels contain much less P than similar precipitates in the corresponding BA steels. As already discussed in section 2, the solubility products of TiC and FeTiP are very close. As a result, there is always a competition between these precipitates to form. Obviously, the solubility product plot is dependent on the composition of steels as well. If, by any chance, FeTiP forms before TiC formation, there will be less Ti in the matrix to tie up with C. As a result of that, C will be in solution which is considered most deleterious from the point of view of  $\{111\}$  texture formation [9, 10]. In case of

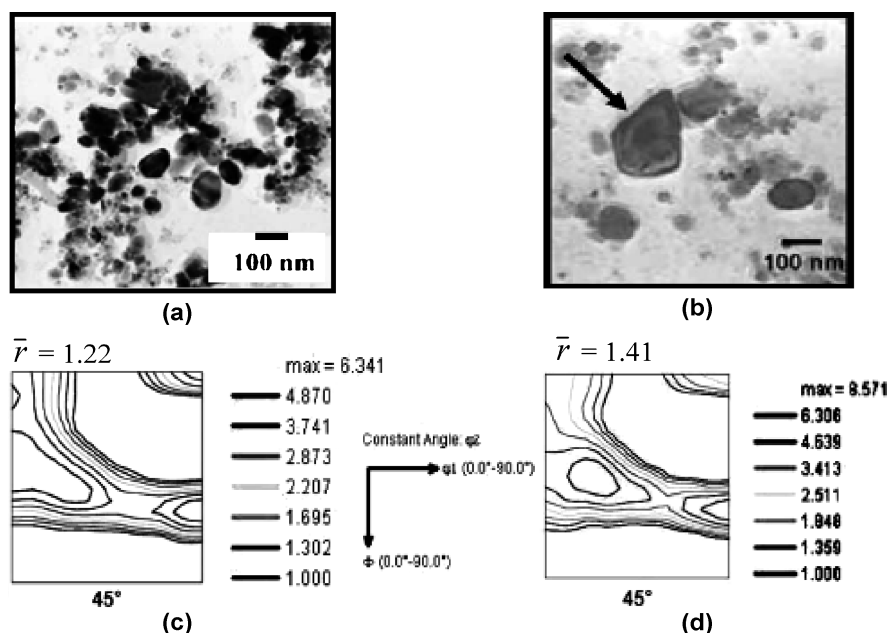


**Fig. 7.10** TEM micrographs of FeTiP type of precipitates (a) in high P and (b) low P batch annealed IFHS steels and corresponding  $\phi_2 = 45^\circ$  sections shown in (c) and (d), respectively.

continuous annealing, TiC will form preferentially before FeTiP formation (if FeTiP forms at all) either because of higher annealing temperature where TiC is more stable than FeTiP or because of much less annealing time involved in the continuous annealing process.

The deleterious effect of FeTiP formation during batch annealing can be reduced to a great extent by coiling the hot band at a higher temperature. It has been found that a batch annealed IFHS steel, which was coiled at the higher temperature of  $620^\circ\text{C}$ , showed a much more intense  $\gamma$  fiber and higher average  $r$  value than when the same steel was coiled at the lower temperature of  $556^\circ\text{C}$  [Fig. 7.12]. Whereas, in the annealed condition, the former showed substantial  $\text{Ti}_4\text{C}_2\text{S}_2$  precipitates plus FeTiP, the latter practically did not show any  $\text{Ti}_4\text{C}_2\text{S}_2$  or TiC, but copious FeTiP precipitates [Fig. 7.13]. These results suggest that  $\text{Ti}_4\text{C}_2\text{S}_2$  in the former precipitated most likely during the coiling process itself, thus taking away quite a bit of C from the matrix. As a result, formation of FeTiP during the annealing stage became less harmful than in the case of the material which was coiled at the lower temperature. Smaller sized FeTiP type precipitates may also affect the growth of  $\{111\}$  recrystallized grains, as very often these are observed to be present on the grain boundaries [Fig. 7.14].

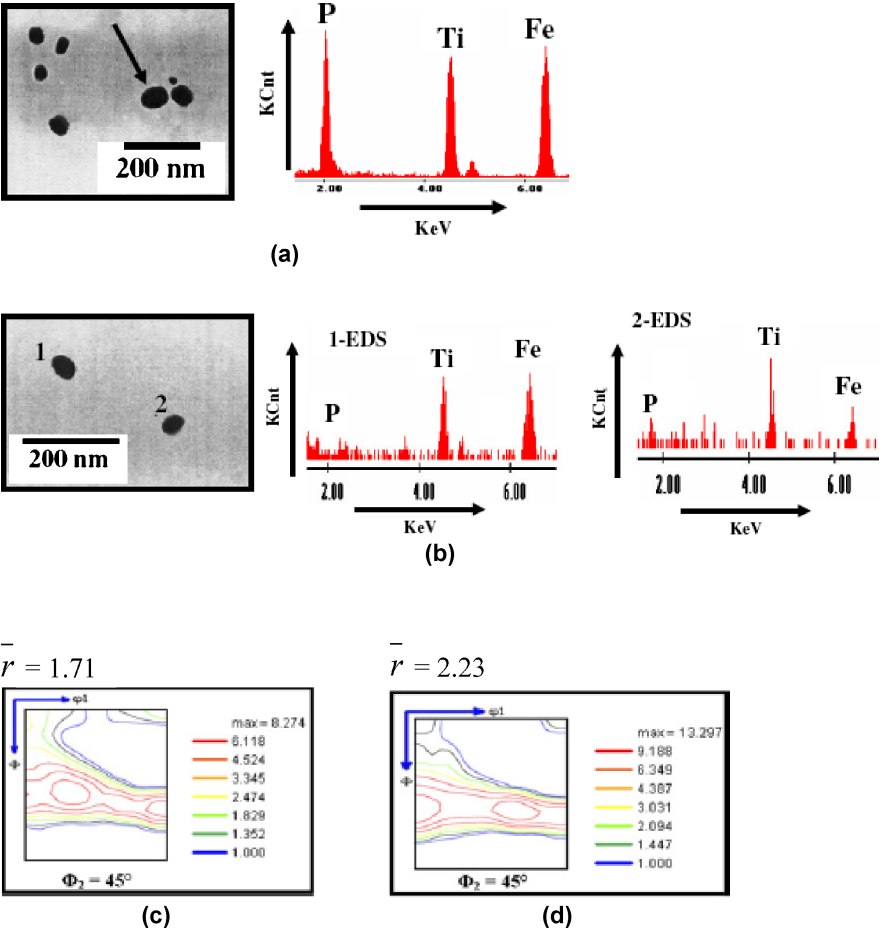


**Fig. 7.11** TEM micrographs of IFHS steels showing FeTi(P) type of precipitates in (a) batch annealed and (b) continuously annealed IFHS steels and corresponding  $\varphi_2=45^\circ$  sections shown in (c) and (d), respectively.

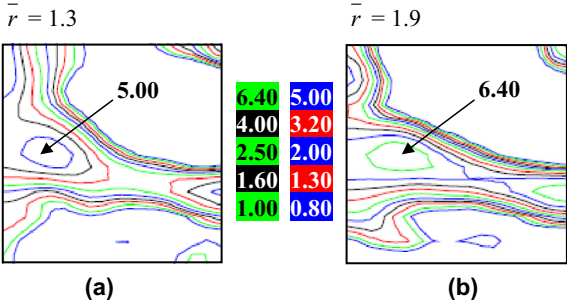


**Fig. 7.12**  $\Phi_2=45^\circ$  sections of the batch annealed IFHS steels coiled at (a) lower temperature of 556°C and (b) higher temperature of 620°C.

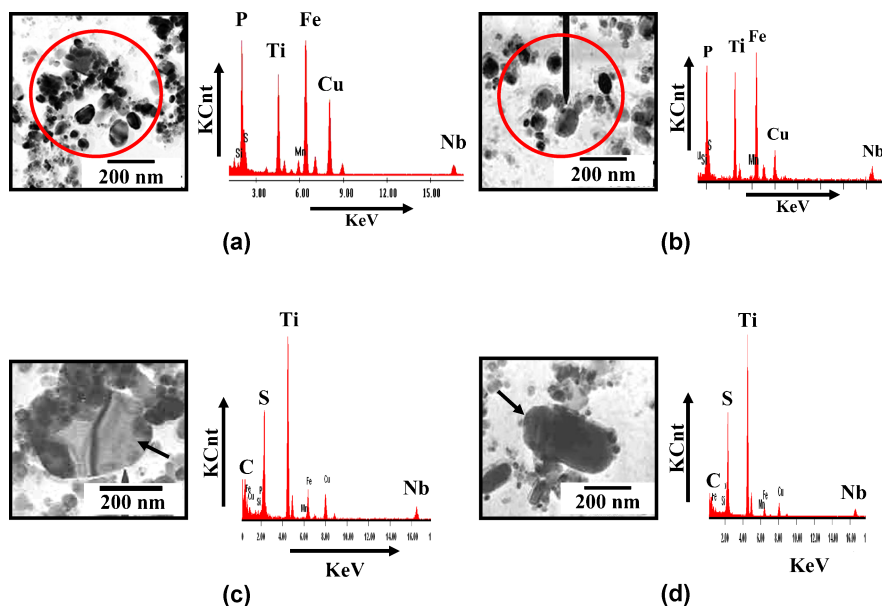


**Fig. 7.13** TEM micrographs showing presence of FeTiP type of precipitates in batch annealed IFHS steels coiled at (a) 556°C and (b) 620°C and (c–d)  $Ti_4C_2S_2$  precipitates only in the steels coiled at 620°C.

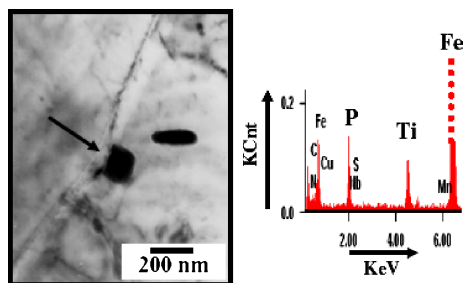


**Fig. 7.14** Thin foil TEM micrograph of FeTiP precipitate sitting on a grain boundary in a batch annealed IFHS steel along with its EDS spectrum.

### 7.4.3 Prevention of FeTiP Formation in BA-IFHS Steels

It is now well understood that the beneficial effect of P will be lost by the formation of FeTiP, which not only degrades the {111} texture, but also results in loss of strength as well. However, P is indispensable as a solid solution strengthening element in IFHS steels. So the major objective of technologists working in this field is how to increase strength by P addition without losing much of the formability. This can only be achieved by suppressing the FeTiP precipitation so that

more P will remain in solid solution. In this context it would be interesting to choose a suitable process window during annealing such that the unwanted FeTiP formation can be avoided. It has been found [11] that a 0.04wt% Ti, 0.04%P and 0.4wt% Mn IFHS steel, when batch annealed at 800°C for an hour, does not give rise to any FeTiP precipitation, whereas annealing at 700°C leads to copious FeTiP formation. In fact, instead of FeTiP formation, annealing at 800°C gives rise to precipitation of  $\text{Ti}_4\text{C}_2\text{S}_2$  particles, which is highly beneficial. On the contrary, in case of the 700°C annealed material, apart from FeTiP, few TiC and  $\text{Ti}_4\text{C}_2\text{S}_2$  particles are also observed. As expected, the steel annealed at 800°C shows much sharper  $\{111\}$  texture and better  $\bar{r}$  value than the steel annealed at 700°C. It appears that by controlling the coiling temperature and the temperature of annealing, the deleterious effect of FeTiP precipitation in batch annealed IFHS steels can be largely avoided. Of course, the exact temperatures, to achieve the most beneficial effects of these operations, will depend on the composition of the steels.

## 7.5 Conclusions

- (i) Various kinds of precipitates such as TiN, TiS, MnS,  $\text{Ti}_4\text{C}_2\text{S}_2$ , FeTiP/Fe(Ti+Nb)P and TiC form in cold rolled and annealed IFHS steels.
- (ii) Precipitation of FeTiP in IFHS steels leads to a loss of strength as well as deterioration of favorable  $\{111\}$  texture, leading to degradation of deep drawability.
- (iii) The batch annealed IFHS steels suffer from this problem to a great extent, whereas the magnitude of this problem is much less in case of continuous annealed IFHS steels.
- (iv) During batch annealing the deleterious effect of FeTiP formation can be largely reduced by using appropriate coiling and annealing temperatures, which will primarily depend on the steel composition.

## References

- [1] Z. Zhao, M. Mao and Y. Yu; Journal of university of Science and Technology Beijing: Mineral Metallurgy Materials, 2000, 7 (3), 197–203.
- [2] J. Moon, S. Kim, H. Jeong, J. Lee and C. Lee; Material Science and Engineering A 454–455 (2007) 648–653.
- [3] A.I. Fernandez, P. Uranga, B. Lopez and J.M. Rodriguez-Ibabe, Materials Science and Engineering A361 (2003) 367–376.
- [4] O. Hamart, T. Lung and S. Lanteri: in: 40th MWSP Conf. Proc., 1998, 189.
- [5] T. Gladman: in Physical Metallurgy of Microalloyed Steels, Springer, Berlin, 1977.
- [6] P. Ghosh, B. Bhattacharya R. K. Ray: Scripta Materialia, 2007, 56, 657–660.
- [7] P. Ghosh, R.K. Ray and D. Bhattacharjee: Scripta Materialia, 2007, 57, 241–244.

- [8] A.V. Ivanov, M.E. Zolensky, A. Saito, K. Ohsumi, S.V. Yang, N.N. Kononkova and T. Mikouchi: *American Mineralogist*, 2000, **85** (7–8), 1082–1086.
- [9] W.B. Hutchinson, K.-I. Nilson and J. Hirsch: in *Metallurgy of Vacuum Degassed Steel Products*, TMS, 1990, 109–126.
- [10] F.J. Held: *Mechanical Working and Steel Processing Conference ISS*, 1965, 3–38.
- [11] P. Ghosh, C. Ghosh, R.K. Ray and D. Bhattacharjee; Communicated to *Scripta Materialia*.



Ranjit Kumar Ray  
Visiting Scientist  
R&D Division, Tata Steel  
Jamshepdur-831007  
India  
Formerly:  
Professor  
IIT, Kanpur  
India

## Chapter 8

# Texture, Microstructure and Properties of Coatings on a few Industrially Produced Galvanized and Galvannealed Interstitial Free Steels

D. Bhattacharjee, A. Chakraborty, R. Pais, and R.K. Ray

**Abstract.** The substrate steel texture appears to control the texture of galvanized and galvannealed coatings on interstitial free steels. Again, the powdering resistance of coatings depends on the type of textures produced in them. An attempt has been made to correlate the textures of the substrate and the coating with the forming behavior of the latter. In the galvannealing operation, using lower galvannealing power (lower strip temperature) improves the coating formability. The formation of an almost continuous  $\{01.3\}$  fiber and lower amount of iron present in the coating layer could be the possible reasons for this behavior.

**Keywords:** Galvanized and galvannealed coating, Eta and delta phase, Substrate and coating texture, Powdering resistance

## 8.1 Introduction

Among all the coated steels used in automotive bodies, zinc and zinc alloy coated steel sheets are the most widely used. In the galvanizing process, preheated steel sheet is immersed in a liquid Zn-0.18wt.%Al bath which causes the formation of a Zn layer eta ( $\eta$ ) on the steel substrate. A schematic view of the galvanized coating is shown in Fig. 8.1. In galvannealing process, the preheated steel sheet is first immersed in a liquid Zn-0.14wt.% Al bath and then given a post coating heat treatment. The heat treatment causes the zinc in the coating to inter-diffuse with the substrate iron to form several iron-zinc intermetallic

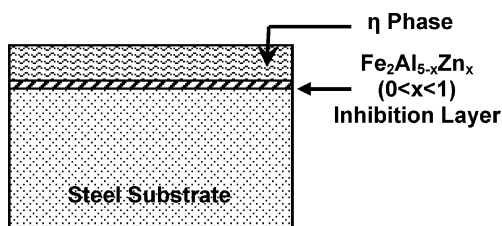
---

D. Bhattacharjee, A. Chakraborty, and R.K. Ray  
Research and Development Division, TATA STEEL, Jamshedpur, India

R. Pais  
Cold Rolling Mill, TATA STEEL, Jamshedpur, India



**Fig. 8.1** Schematic View of Galvanized Coating.



phases, namely gamma ( $\Gamma$ ), gamma<sub>1</sub> ( $\Gamma_1$ ), delta ( $\delta$ ) and zeta ( $\zeta$ ) which are stacked over the steel substrate. Fig. 8.2 represents a schematic view of the microstructural development during galvannealing [1].

The properties of any material depend not only on the microstructure but also on the preferred crystallographic orientation of the constituent grains or texture. For example, the formability, frictional behavior as well as corrosion resistance of

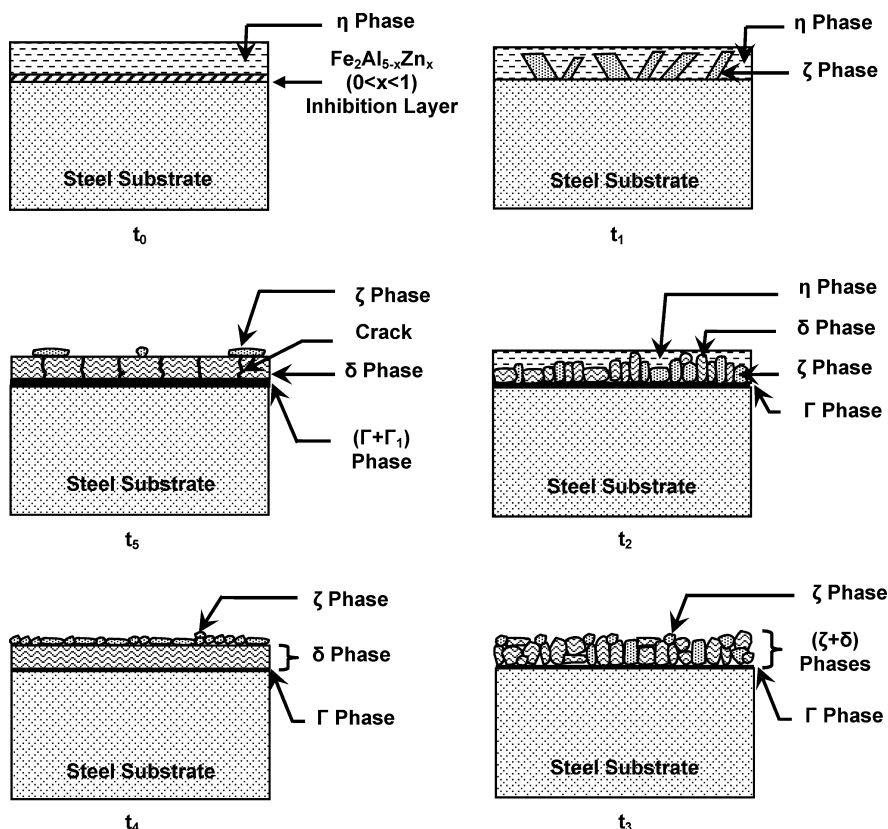


**Fig. 8.2** Schematic view of the Phenomenological Model of Galvannealed Morphology Development,  $t_0$  Corresponds to Zero Time of the as-Galvanized Structure, and Development occurs according to time such that  $t_1 < t_2 < t_3 < t_4 < t_5$  [2].

Again, in galvanized coating, the formation and growth of the different Fe-Zn intermetallic phases appear to be governed by the substrate steel texture [8]. It therefore appears that texture, whether from the steel substrate or from the coating, has a major role to play in determining the optimum properties of the coated steels.

## 8.2 Experimental Procedure

**Table 8.1** Composition of Substrate Steel (wt.%).

[illegible]

pur, India. The different processing parameters during galvanizing and galvannealing are given in Table 8.2. Galvanizing was carried out on steel IFGI and galvannealing on steel IFGA. In another set of experiments galvannealing was carried out on steel IFGA (600), IFGA (900), IFGA (1200) using three different powers of the induction furnace namely, 600, 900 and 1200 kW as shown in Table 8.2. The corresponding strip temperatures were 450, 485 and 525°C respectively. The three galvannealing powers were tried on the same coil in order to maintain uniformity of chemistry and previous history. The Galvannealing (GA) Power refers to the input power of the induction furnace in which the galvannealing operation was carried out. Increasing the GA power leads to an increase in the strip temperature during galvannealing. Cross-sectional Scanning Electron Microscopy (SEM) along with Energy Dispersive Spectroscopy (EDS) study was carried out in a FEI Quanta-200 SEM operated at 20 kV. X-Ray Diffraction (XRD) studies of the samples were carried out in the usual manner in a PaNalytical X'pert PRO X-ray diffractometer, using CuK $\alpha$  radiation. The X-ray generator voltage was 45 kV and the tube current was 40 mA. Crystallographic texture of the coating surface was determined using a PaNalytical X'pert PRO XRD machine coupled with a texture goniometer. The goniometer resolution of the equipment was 0.001°. For this purpose (00.2), (10.0), (10.1) and (10.2) pole figures for the galvanized coating and (23.3), (05.4), (33.0), (24.1) and (24.9) pole figures for the galvannealed coating were measured experimentally. The Orientation Distribution Functions (ODFs) were calculated from the pole figures after correction (for defocusing and absorption) and symmetrization using the series expansion method with a limit of  $l_{\max}=22$  by the method of Bunge [13] using Labotex software. The chemical compositions of the coatings were determined by ASTM standard Gravimetric method [14]. The overall percentages of Fe, Zn and Al were measured using an Inductive Coupled Plasma Spectroscopy (ICPS), Spectro Analytical Instrument, GmbH version 2.0e/8/88, Germany. The powdering resistance of the coatings was measured by the Double Olsen Test method.

The textures of the steel substrates were measured by Electron Back Scattered Diffraction (EBSD) technique using an Orientation Imaging Microscope (OIM) camera attached to a FEI Quanta 200 SEM. Before measuring the substrate texture the coatings were removed by dipping the samples in 50% dilute HCl solution followed by electro-polishing.

**Table 8.2** Galvanizing and Galvannealing Processing Parameters.

Sample No.	Bath Al (wt.%)	Steel Sheet Thickness (mm)	Line Speed (meter/min.)	Galvannealing Power (kW)
IFGI	0.185	0.9	75	—
IFGA	0.134	0.7	92	826
IFGA (600)	0.134	0.8	87	600
IFGA (900)	0.134	0.8	87	900
IFGA (1200)	0.134	0.8	87	1200

### 8.3 Experimental Results

The SEM micrographs in Fig. 8.3 (a), (b) compare the top surfaces of the galvanized coating on sample IFGI and the galvanized coating on sample IFGA. The galvanized coating is essentially made up of grains of Zn ( $\eta$  phase), while the top surface of the galvanized coating has been formed to be made up of grains of mostly the  $\delta$  phase (as found out by XRD). The cross-sectional scanning electron micrographs of the above coatings are shown in part (a) of the Figures 8.4 and 8.5. The corresponding X-ray maps for Fe and Zn are represented in parts (b) and (c) of the same figures, respectively. During sample preparation for SEM study there was a distinct possibility of the edges of the coating falling off the substrate or getting damaged. To prevent this, a 200  $\mu\text{m}$  thin copper strip was used as the supporting material. The EDS profiles of the galvanized and galvanized coatings are shown in Fig. 8.6 (a), (b). Obviously, the galvanized coating is made up of almost 100% Zn, while the galvanized coating shows substantial amount of Fe also. The percentage thicknesses of the different Fe-Zn intermetallic phases were determined by superimposing the compositional ranges for the different phases on the above profiles. The results are given in a tabular form in Table 8.3. This table clearly indicates that the percentage of  $\eta$  phase (almost pure Zn) is very high in sample IFGI whereas for the sample IFGA there is no  $\eta$  phase, the main phase being  $\delta$ . Table 8.4 shows the important crystallographic data of the  $\eta$  and  $\delta$  phases. The XRD patterns of the galvanized and galvanized coatings are shown in Fig. 8.7 (a), (b). It is apparent from these figures that the most intense diffraction takes place from the (00.2) planes of the  $\eta$  phase and from the (33.0) planes of the  $\delta$  phase. Fig. 8.8 (a, b) represent the experimental (00.2) pole figure of the galvanized coating texture and the (33.0) pole figure of the galvanized coating texture. Figure 8.9 (a), (b) represent the  $\Phi_2$  ODF sections of the galvanized and the galvanized coatings respectively. While the  $\eta$  of the galvanized coating shows

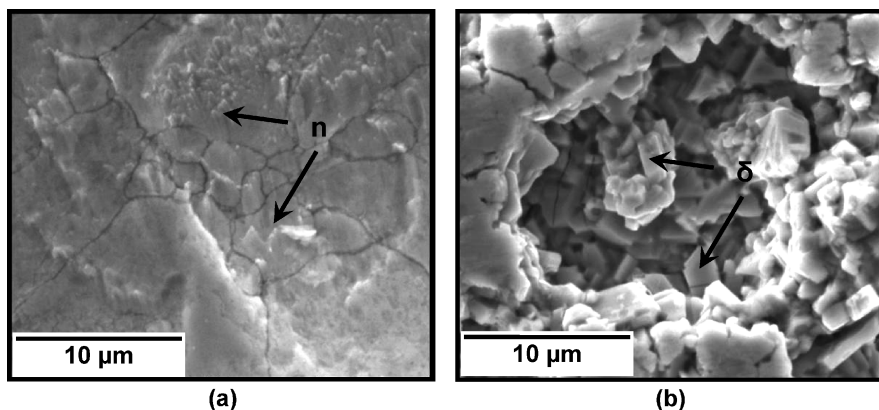


**Fig. 8.3** SEM Micrographs of Top Surface of (a) Galvanized Coating on Sample IFGI and (b) Galvanized Coating on Sample IFGA.

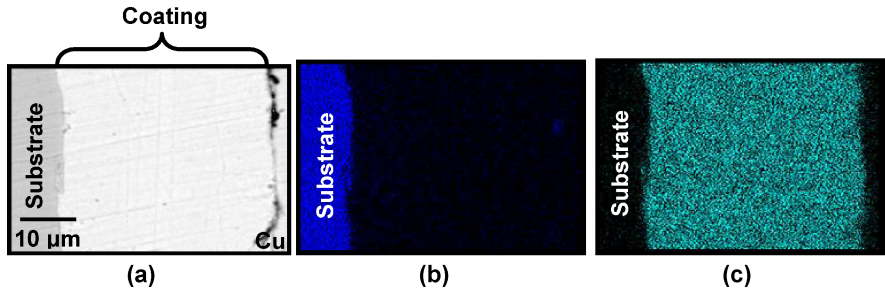


**Fig. 8.4** Cross-sectional (a) SEM Micrograph, (b) X-Ray Map of Fe and (c) X-Ray Map of Zn of Galvanized Coating over Sample IFGI.

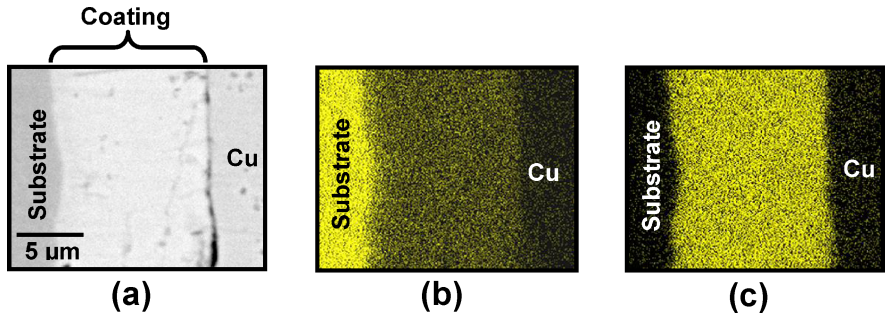


**Fig. 8.5** Cross-sectional (a) SEM Micrograph, (b) X-Ray Map of Fe and (c) X-Ray Map of Zn of Galvannealed Coating over Sample IFGA.

a very strong  $\{00.2\} \langle uv.w \rangle$  type of fiber texture, a weak fiber of the type  $\{01.3\} \langle uv.w \rangle$  can be found in the texture of the outermost  $\delta$  phase in the galvannealed coating. Figures 8.10 (a) and 8.10 (b) show the  $\Phi_2=45^\circ$  sections of the ODFs of the substrates in the IFGI and IFGA steel samples, respectively. Using EBSD technique, color coded crystal orientation maps were obtained from these substrates, as shown in Fig. 8.11. In these maps grains having orientations  $\{113\} \langle 110 \rangle$  and  $\{111\} \langle 110 \rangle$  have been highlighted. The volume fractions of these two components have also been calculated along with those maps.

**Table 8.3** Percentage Thicknesses of different Fe-Zn Intermetallic Phases Present in Galvanized and Galvannealed Coatings.

Sample No.	$\Gamma$	$\Gamma+\Gamma_1$	$\Gamma_1$	$\Gamma_1+\delta$	$\delta$	$\zeta+\delta$	$\zeta$	$\eta+\zeta$	$\eta$
IFGI	0.51	0.63	0.57	1.10	1.18	0.21	0.29	0.37	95.14
IFGA	3.23	2.69	2.15	18.28	73.66	—	—	—	—
IFGA (600)	1.08	0.60	5.42	15.53	77.36	—	—	—	—
IFGA (900)	1.29	0.57	1.00	22.17	74.97	—	—	—	—
IFGA (1200)	1.64	2.73	6.54	18.17	70.93	—	—	—	—

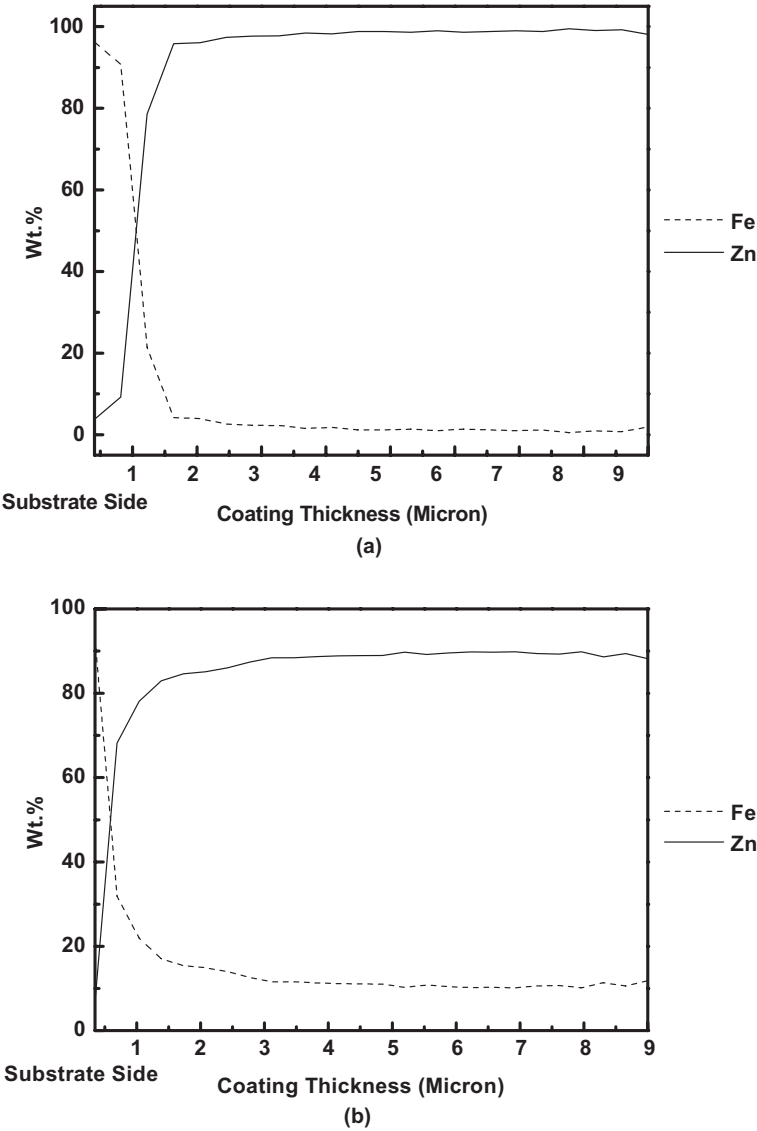


**Fig. 8.6** EDS Profiles of (a) Galvanized Coating on Steel Sample IFGI and (b) Galvannealed Coating on Steel Sample IFGA.

**Table 8.4** Crystallographic Data of  $\eta$  and  $\delta$  Phases [15].

Phase	Crystal Structure	Lattice Parameters ( $\text{\AA}$ )	c/a	Atoms/Unit Cell
Eta ( $\eta$ )	hcp	a=2.665, c=4.947	1.86	6
Delta ( $\delta$ )	hcp	a=12.799, c=57.59	4.50	555

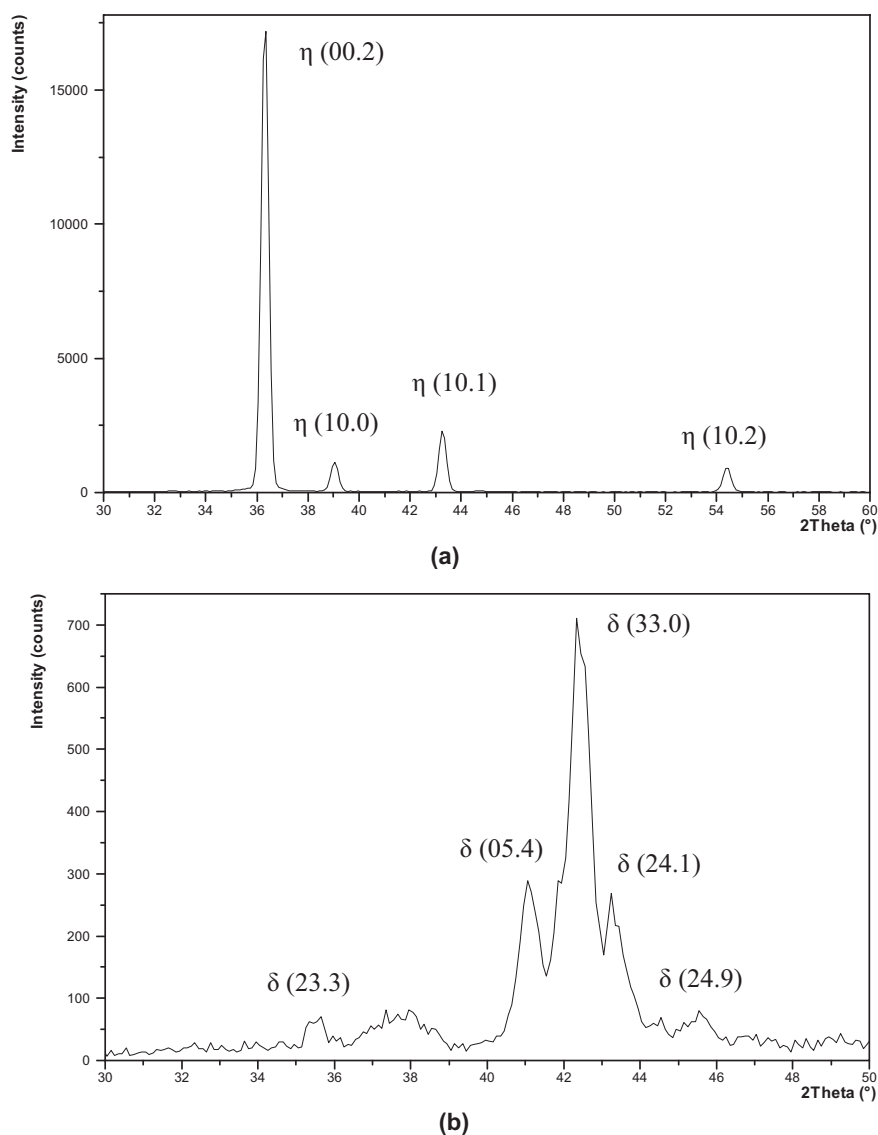


**Fig. 8.7** XRD patterns of (a) Galvanized Coating on Sample IFGI and (b) Galvannealed Coating on Sample IFGA.

The GA power was varied during the galvannealing process on steels IFGA (600), IFGA (900) and IFGA (1200). In the three samples IFGA (600), IFGA (900) and IFGA (1200) the GA power used was 600, 900 and 1200 kW respectively. Table 8.5 represents the percentages of Fe, Zn and Al present in the galvannealed coatings produced by the different GA powers. The EDS profiles of the galvannealed coatings in the three cases are shown in Fig. 8.12 (a–c). In this case also the percentage thick-

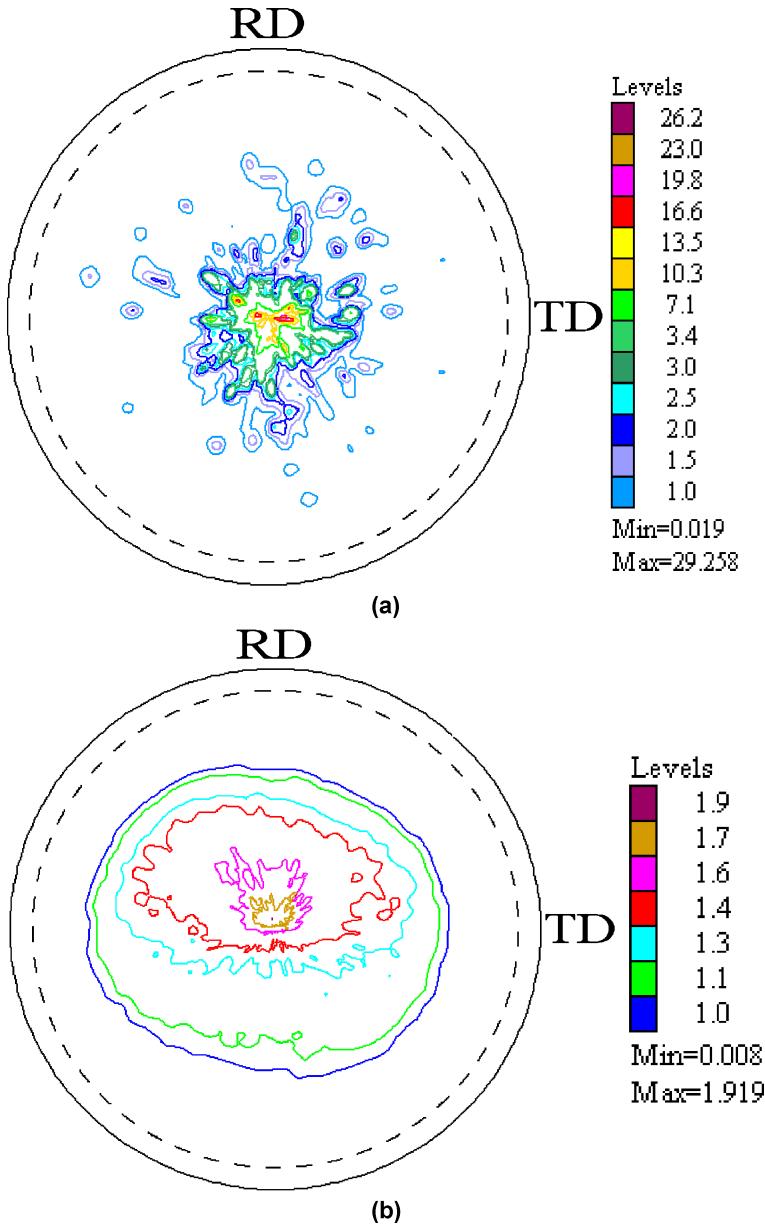


**Fig. 8.8** Experimental (a) (00.2) pole figure of Galvanized Coating on Sample IFGI and (b) (33.0) pole figure of Galvannealed Coating on Sample IFGA.

nesses of the different Fe-Zn intermetallic phases were determined and reported in a tabular form in Table 8.3. The relevant portions of the XRD patterns of the samples IFGA (600), IFGA (900) and IFGA (1200) are shown in Fig. 8.13 (a–c). These pat-



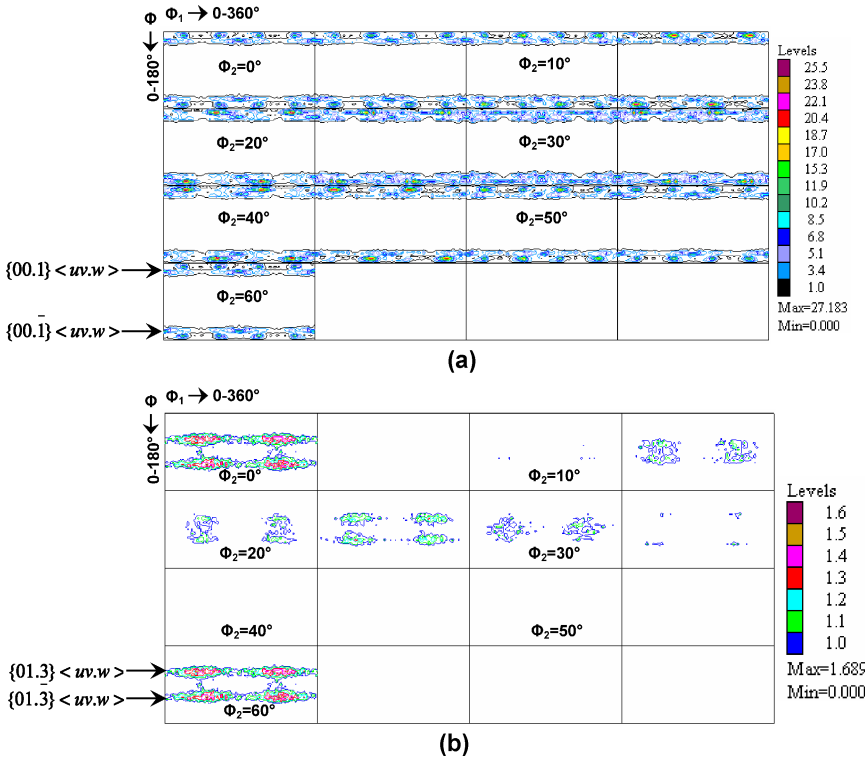


Fig. 8.9  $\Phi_2$  ODF sections of (a) Galvanized Coating on Sample IFGI and (b) Galvannealed Coating on Sample IFGA.

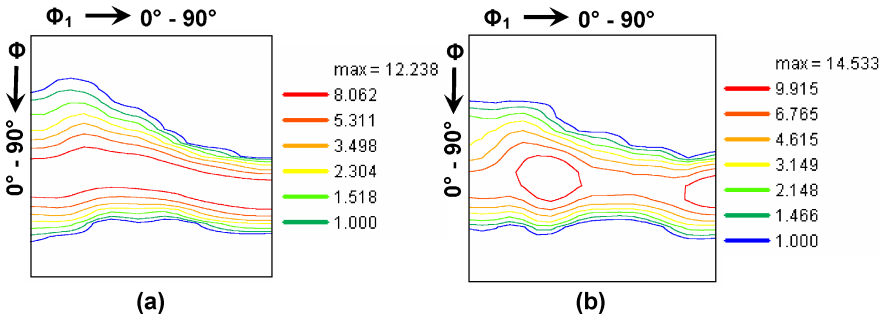
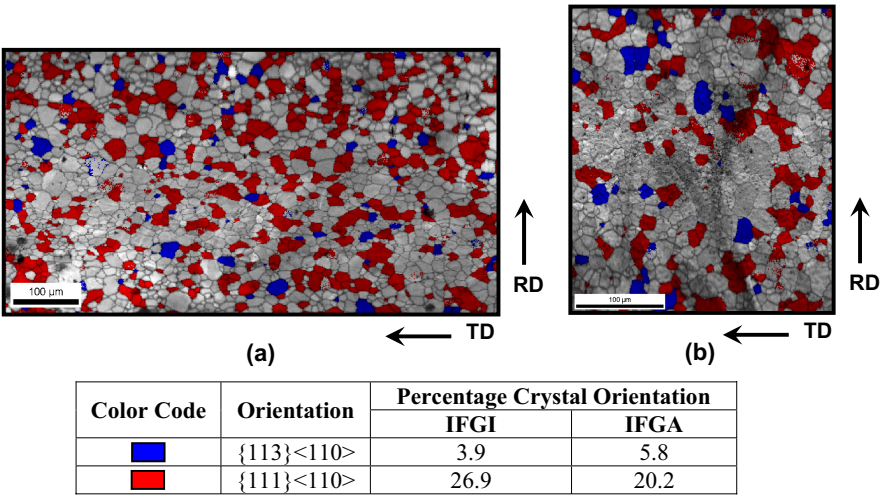


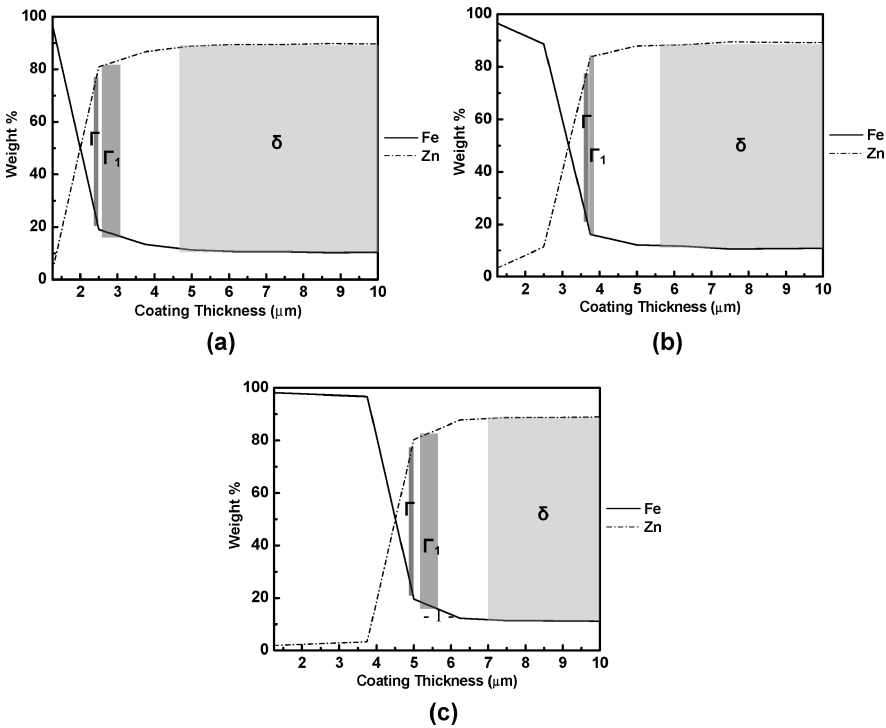
Fig. 8.10  $\Phi_2 = 45^\circ$  ODF sections of substrate steel of sample (a) IFGI and (b) IFGA.

Table 8.5 Chemical Compositions of the Coatings (wt.%).

Sample No.	Al	Fe	Zn
IFGA (600)	0.1952	9.2248	90.5800
IFGA (900)	0.2268	13.7724	86.0008
IFGA (1200)	0.2254	14.2463	85.5283



**Fig. 8.11** Color coded maps of crystal orientation of substrate steel sample (a) IFGI and (b) IFGA.



**Fig. 8.12** EDS profiles of galvanized coating of (a) Sample IFGA (600) produced by 600 kW (b) Sample IFGA (900) produced by 900 kW and (c) Sample IFGA (1200) produced by 1200 kW Galvannealing Power.

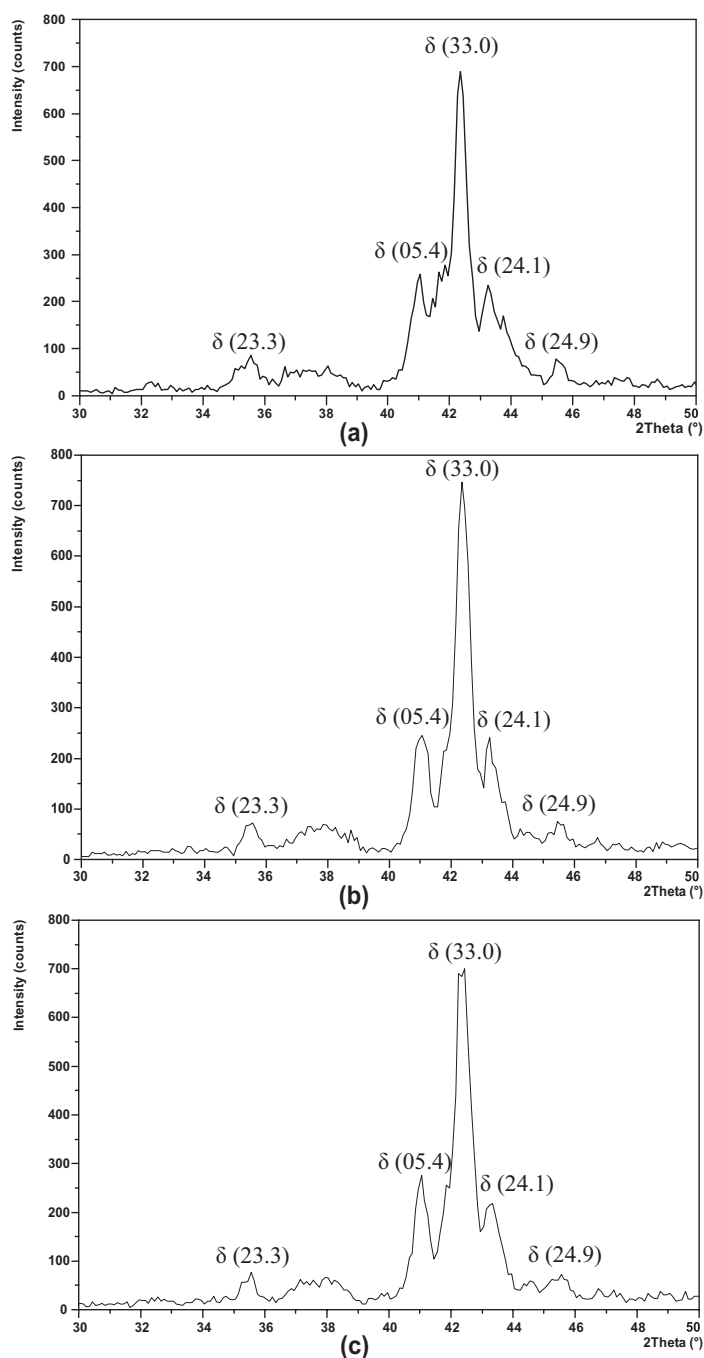


**Fig. 8.13** XRD patterns of Galvannealed Coating on (a) Sample IFGA (600) produced by 600 kW (b) Sample IFGA (900) produced by 900 kW and (c) Sample IFGA (1200) produced by 1200 kW Galvannealing Power.

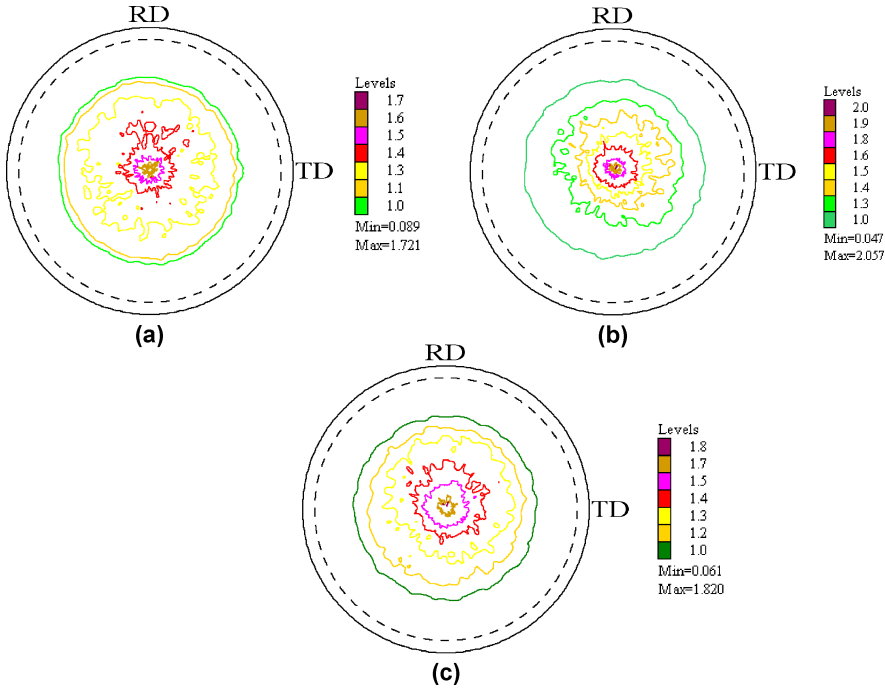


**Fig. 8.14** Experimental (33.0) pole figures of Galvannealed Coating on (a) Sample IFGA (600) produced by 600 kW (b) Sample IFGA (900) produced by 900 kW and (c) Sample IFGA (1200) produced by 1200 kW Galvannealing Power.

terms clearly indicate the presence of mainly the  $\delta$  phase in the outer surfaces of the coatings. The experimental (33.0) pole figures of galvannealed coatings on IFGA (600), IFGA (900) and IFGA (1200) samples are shown in Fig. 8.14 (a)–(c). The  $\Phi_2$  sections of the complete ODF of the galvannealed coatings on IFGA (600), IFGA (900) and IFGA (1200) are presented in Figs. 8.15, 8.17 and 8.19 respectively. All the above figures appear rather similar, although there are some subtle differences. This has been brought out clearly in Figs. 8.16, 8.18 and 8.20, where the  $\Phi_2 = 0^\circ$  sections of the ODFs of the three samples have been shown on a magnified scale. The weight losses measured during the powdering resistance test of the coatings of the samples are depicted in Table 8.6.

**Table 8.6** Powdering Test Results.

Sample No.	Weight Loss (mg)
IFGI	15.30
IFGA	11.50
IFGA (600)	10.40
IFGA (900)	11.70
IFGA (1200)	14.60

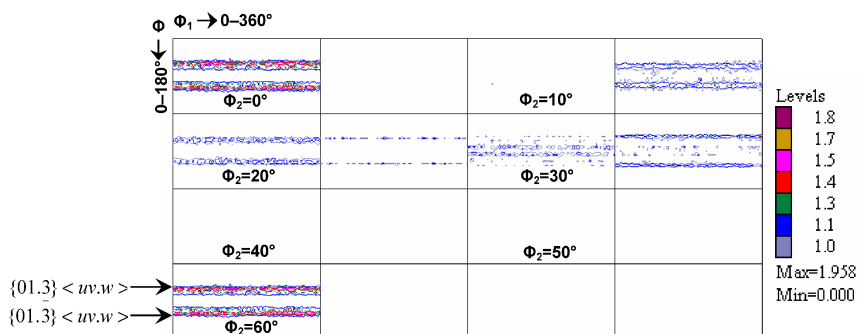


**Fig. 8.15**  $\Phi_2$  Sections of the ODF of the Galvannealed Coating on Sample IFGA (600) produced by 600 kW Galvannealing Power.

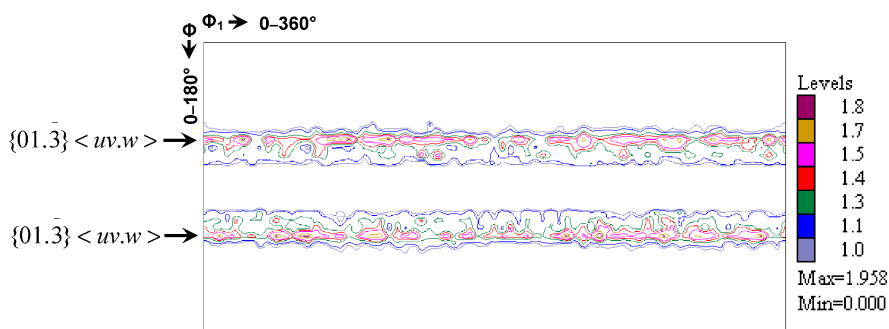


**Fig. 8.16** Magnified View of  $\Phi_2 = 0^\circ$  Section of Fig. 8.15 of Galvannealed Coating on Sample IFGA (600) produced by 600 kW Galvannealing Power.

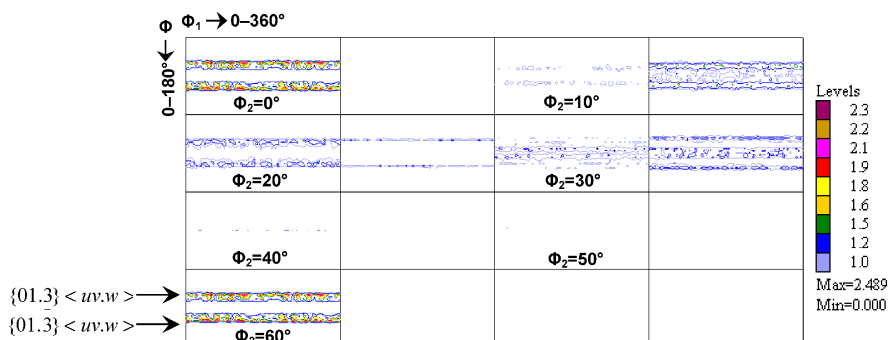


**Fig. 8.17**  $\Phi_2$  Sections of the ODF of the Galvannealed Coating on Sample IFGA (900) produced by 900 kW Galvannealing Power.

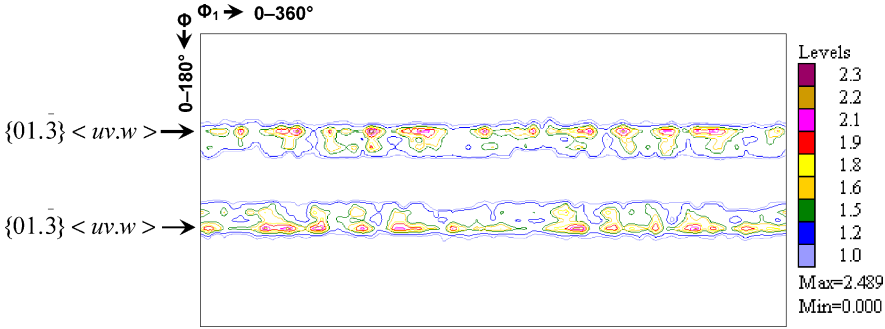


**Fig. 8.18** Magnified View of  $\Phi_2=0^\circ$  Section of Fig. 8.17 of Galvannealed Coating on Sample IFGA (900) produced by 900 kW Galvannealing Power.

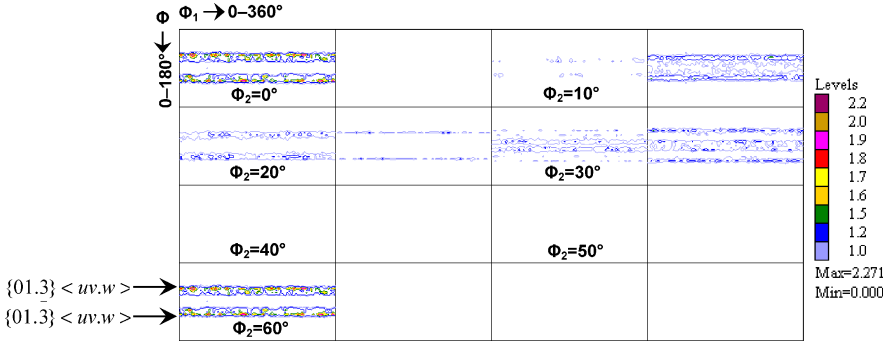


**Fig. 8.19**  $\Phi_2$  Sections of the ODF of the Galvannealed Coating on Sample IFGA (1200) produced by 1200 kW Galvannealing Power.

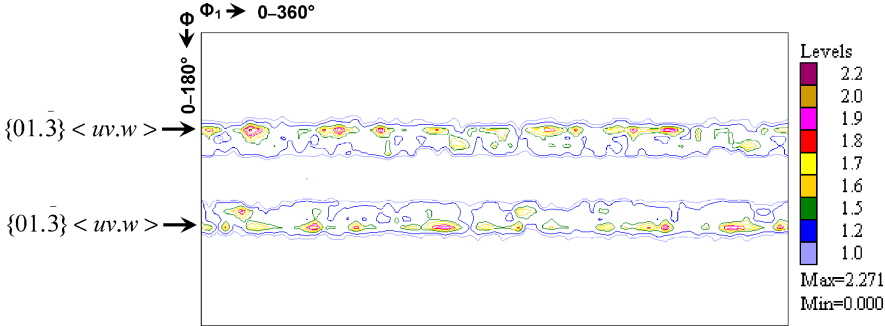


**Fig. 8.20** Magnified View of  $\Phi_2=0^\circ$  Section of Fig. 8.19 of Galvannealed Coating on Sample IFGA (1200) produced by 1200 kW Galvannealing Power.

## 8.4 Discussion

During galvanizing a highly Zn rich eta ( $\eta$ ) phase forms on top of the steel substrate. In galvannealing, however, diffusion of Fe and Zn is allowed to take place, resulting in the formation of various Fe-Zn intermetallic compounds, such as zeta ( $\zeta$ ), delta ( $\delta$ ), gamma ( $\Gamma$ ) and gamma<sub>1</sub> ( $\Gamma_1$ ), as one progresses from the surface of the coating to the substrate. Grains of  $\eta$  crystals and columnar shaped  $\delta$  crystals are clearly observed in Fig. 8.3 (a, b). The cross-sectional scanning electron micrographs [Figs. 8.4 and 8.5] along with the corresponding X-ray maps for Fe and Zn clearly show that there is no Fe present in the galvanized coating whereas a decrease in Fe content from the substrate to the Cu side is observed for the galvannealed coating. In the latter case the gradation in Zn content is not that clear, possibly because of the overall high amount of Zn. The XRD results from the top surfaces of the coatings in steel IFGI [Fig. 8.7 (a)] clearly indicate that in the galvanized material, the coating is almost completely made up of the  $\eta$  phase. On the other hand, the predominant phase in the coating of the galvannealed steel IFGA is  $\delta$  [Fig. 8.7 (b)]. These results also corroborate the findings of the SEM-EDS results. The above phases in the coatings of the two steels extend to a substantial thickness from the top to the interior, as a result of which the XRD data could be collected from essentially these phases only without much interference from the other phases or from the substrate steel.

Crystallographic texture of the coating of the galvanized steel, from both pole figure and ODF data [Figs. 8.8 (a) and 8.9 (a)] clearly indicates the presence of a strong basal texture,  $\{00.2\}\langle uv.w \rangle$ . In contrast, the texture of the coating of the galvannealed steel, from both pole figure and ODF [Figs. 8.8 (b) and 8.9 (b)] appear to be quite different from the basal. In fact, here the orientation peaks are obtained at  $\sim 60^\circ$  away from the exact basal locations. These orientation maxima have been identified as  $\{01.3\}\langle uv.w \rangle$ . In addition, there are a number of low intensity minor texture components also.

It has been shown [16] that hot dipped Zn coatings in galvanized steels very often develop a basal texture in which the  $\{00.2\}$  planes of Zn remain parallel to the surface of the steel substrate. On the other hand, a non basal texture  $\{01.3\}\langle uv.w \rangle$  predominantly forms in the galvannealed coated surface of the IFGA steel, presumably from the outermost rather thick  $\delta$  layer. An effort was made to find out the correlation, if any, between the substrate steel texture and the coating texture. Wegria et al. [16] suggested that if  $\{113\}\langle 110 \rangle$  texture component forms at the expense of the  $\{111\}\langle 110 \rangle$  in the substrate steel an alloy layer is formed on the substrate which finally leads to a reduction in intensity of the basal texture in the Zn coating. This has been found to be true for both galvanized and galfan coatings. Although in this work we are basically dealing with two different types of coating based on Zn, the materials in both the coatings have the hexagonal close packed (hcp) structure (Table 8.4). The similarity in the crystal structure of the two coatings and the dissimilarity in the manner of texture formation prompted us to look into the substrate steel texture in both the steels more

closely. The  $\Phi_2=45^\circ$  sections of the ODFs of the two substrate steels [Fig. 8.10 (a), (b)] show some differences although basically both exhibit a reasonably strong gamma ( $\gamma$ ) fiber. Out of the two, the IFGI sample shows a more uniform but somewhat lower intensity  $\gamma$  fiber, whereas the IFGA sample exhibits a somewhat stronger intensity but less uniform  $\gamma$  fiber. In fact, in the latter, the  $\{110\}<112>$  component appears to be the strongest.

Using EBSD technique, color coded maps of  $\{113\}<110>$  and  $\{111\}<110>$  crystal orientation were obtained from the steel substrate of both the galvanized and galvanized samples [Fig. 8.11 (a), (b)]. The ratios of the volume fractions of  $\{113\}$  and  $\{111\}$  orientations in the galvanized and the galvanized steel substrates has been found to be 0.14 and 0.29 respectively. According to the criteria of Wegria et al. [16], a higher value of this ratio should favor an off-basal texture. In fact this has been found to be true in case of the galvanized coating which shows  $\{01.3\}<uv.w>$  type, i.e. a predominantly off-basal texture. On the other hand, the galvanized coating, with a lower value of the above ratio for the substrate steel, shows a strong basal texture. Thus there appears to be some correlation at least between the substrate texture and the coating texture in these two steels.

Shaffer et al. [17] found that in electrogalvanized materials no cracking takes place when the basal plane makes an angle between  $40\text{--}70^\circ$  with respect to the substrate surface. In that case, under applied stress a significant amount of resolved shear stress exists on the basal planes and slip will be promoted. In the present investigation, perfect basal texture was obtained for the galvanized coating, whereas for the galvanized coating the basal plane was observed to make  $\sim 60^\circ$  angle (angle between  $\{01.3\}<uv.w>$  and  $\{00.1\}<uv.w>$ ) with the substrate. Therefore, based on the observation of Shaffer et al. [17], the galvanized coating should show better powdering resistance as compared to the galvanized coating, under similar test conditions. To measure the formability (powdering resistance) of the galvanized and galvanized coatings, Double Olsen Test was carried out on both materials. Although, in industrial practice, the above test is not common for galvanized coatings, still it was used to get a comparative idea about the powdering behavior of the two types of coatings. Table 8.6 compares the weight losses of the coatings after the test. It clearly indicates that the powdering resistance is better in case of the galvanized coating under similar test conditions. Thus the coating texture appears to have a significant effect on the powdering resistance.

In samples IFGA (600), IFGA (900) and IFGA (1200), GA power was varied in order to find out its effect on the formability behavior of the coating. A study of the three EDS profiles [Fig. 8.12 (a–c)] clearly indicates that the cross-over point (50wt.% Fe and 50wt.% Zn) for the zinc and iron lines shows a significant shift towards the right as the GA power increases. This precisely means an increase in the Fe content of the coatings (and the corresponding decrease in the Zn content) with increasing GA power. This is clearly reflected in Table 8.5 also. These results indicate that the amount of  $\delta$  phase is expected to be highest in sample IFGA (600). And this is what has been found out by precise thickness measurements of the different phase layers (Table 8.3). The increase in the relative thicknesses of



the  $\Gamma$  and  $\Gamma_1$  layers and the corresponding decrease in the thickness of the  $\delta$  layer with increasing GA power can be linked to the higher amount of iron diffusion from the substrate steel towards the coating. The powdering test results corroborate the above findings pretty well. As expected, the sample IFGA (600) (with the least GA power) shows the minimum weight loss, while the sample IFGA (1200) (with the highest GA power) shows the maximum weight loss.

Since all other processing parameters (excepting GA power) were kept constant, the variations in weight loss must be related to GA power (or, the strip temperature). As the continuous annealing temperature of the substrate steel in all the three cases was kept constant (at 840°C), variation in the microstructure and texture of the substrate can be ruled out and therefore variation in weight loss can not be related to these factors also. On the other hand, there are perceptible differences in the crystallographic texture of the coatings in the three samples. (33.0) pole figures in all the three cases are quite similar in nature [Fig. 8.14 (a)–(c)]. From the  $\Phi_2$  ODF sections it is clearly observed that there are no perceptible differences present in the crystallographic textures of the coatings in the three samples. Although the major texture components of the coatings in all the three cases are of the type  $\{01.3\}\langle uv.w \rangle$  [Figs. 8.15, 8.17 and 8.19], a careful examination of the  $\Phi_2=0^\circ$  ODF sections [Figs. 8.16, 8.18 and 8.20] clearly indicates that for the sample IFGA (600) there exists almost a complete fiber of the type  $\{01.3\}\langle uv.w \rangle$ , the fiber character changes into a set of discrete orientations with increasing GA power.

According to the criteria of Shaffer et al. [17], the coatings of the above three galvanized samples should possess satisfactory powdering resistance. However, the presence of an almost continuous fiber of the type  $\{01.3\}\langle uv.w \rangle$  as found in case of IFGA (600) sample, seems to be most beneficial in this respect. Break-down of this fiber into discrete orientations appears to cause a deterioration in the powdering resistance behavior, as exemplified by the samples IFGA (900) and IFGA (1200). Of course, the best powdering resistance observed in case of IFGA (600) must also be related to the least amount of Fe content in the coated layer, as compared to the IFGA (900) and IFGA (1200) samples.

## 8.5 Conclusions

A qualitative difference in the substrate steel texture may get reflected in a perceptible manner in the coating texture of industrially produced galvanized and galvanized interstitial free steels. This will result in significant differences in the powdering resistance of the coatings. In case of galvanized coating the best powdering resistance behavior is obtained with the least GA power (least strip temperature) during the galvannealing operation. This can be ascribed to the formation of an almost continuous  $\{01.3\}\langle uv.w \rangle$  fiber and the least amount of Fe present in the coated layer.

## References

- [1] A.R. Marder, Progress in Materials Science v 45 (2000) 191.
- [2] C.E. Jordan and A.R. Marder, Editor: A.R. Marder, The Physical Metallurgy of Zinc Coated Steel, Warrendale, PA: TMS, 1994, p 197.
- [3] V. Rangarajan, C.C. Cheng and L.L. Franks, Surface and Coating Technology, v 56, 1993, p 209.
- [4] P.R. Sere, J.D. Culcasi, C.I. Elsner and A.R.D. Sarli, Surface and Coating Technology, v 122, 1999 p 143.
- [5] H. Park and Z.A. Szpunar, Corrosion Science, v 40, n 4, 1998, p 525.
- [6] A.W. Silimperi, D.K. Matlock and J.G. Speer, in Proceedings of the International Symposium, Texas, USA, 1998, p 195.
- [7] J.L. Millan, Journal of Materials Engineering and Performance, v 1, 1992, p 275.
- [8] A. Chakraborty and R.K. Ray, Scripta Materialia, v 56, n 8, 2007, p 653.
- [9] S. Gaignard and C. Esling, ICOTOM-12, Proceedings of the 12th International Conference on Texture of Materials, v 2, 2001, p 997.
- [10] G. Vincent, C. Counhaye and C. Esling, Solid State Phenomena, v 105, 2005, p 371.
- [11] A. Semoroz, L. Strezov and M. Rappaz, Metallurgical and Materials Transactions A, v 33A, 2002, p 2695.
- [12] M.B. Moon, J.H. Seo and Y.B. Park, Materials Science Forum, v 408–412, 2002, p 1209.
- [13] H.J. Bunge, Texture Analysis in Materials Science, Cuvillier Verlag, Gottingen, 1993.
- [14] Standard Test Method for Weight [Mass] of Coating on Iron and Steel Articles with Zinc or Zinc Alloy Coatings, ASTM Designation: A 90/A 90M – 01.
- [15] J.H. Hong, S.J. Oh and S.J. Kwon, Intermetallics, v 11, 2003, p 207.
- [16] J. Wegria, M. Dubois, M.J. Philippe and C. Esling, in Proceeding of International Symposium, San Antonio, Texas, USA, 1998, p 261.
- [17] S.J. Shaffer, J.W. Moris and H.R. Wenk, in Proceedings of the International Symposium, Detroit, Michigan, USA, 1990, p 129.



Debashish Bhattacharjee  
Chief of R&D and SS  
Tata Steel, Jamshedpur 831007  
India



# Chapter 9

## Effects of Microalloying in Multi Phase Steels for Car Body Manufacture

Wolfgang Bleck and Kriangyut Phiu-on

**Abstract.** Microalloying elements like Al, B, Nb, Ti, V can be used to optimise the microstructure evolution and the mechanical properties of advanced high strength steels (AHSS). Microalloying elements are characterised by small additions  $<0.1$  mass% and their ability to form carbides or nitrides. They can increase strength by grain refinement and precipitation hardening, retard or accelerate transformations and affect the diffusion kinetics. Thus, by their addition the AHSS with their high requirements to process control can be adopted to existing processing lines. Different combinations of microstructural phases and different chemical compositions have been investigated for AHSS in order to combine high strength with excellent formability.

### 9.1 Introduction

Car manufacturers focus the main design criteria of a modern car on reduced weight and high safety in order to fulfil the customer's expectations and the legal requirements and standards. In this context, new steel grades have been developed not only for weight saving but also to improve crash safety of vehicles. These steels combine an increased formability with a high strength level at a wide temperature and strain rate spectrum. Advanced high strength steels, among them especially dual phase and TRIP steels, feature promising results in this field, while their extraordinary mechanical properties can be tailored and adjusted by alloying and processing. Microalloying is an effective tool in controlling the processing of advanced high strength steels by their effects on recrystallisation

---

W. Bleck and K. Phiu-on

Department of Ferrous Metallurgy, RWTH Aachen University, Intzestr. 1, D-52072 Aachen, Germany

and transformation and in controlling the properties by microstructural refinement and precipitation hardening.

9.2 Definition

The terminus high strength steel (HSS) is used for cold formable steels if the minimum yield strength of the respective steel grade is between 210 and 550 MPa. If the minimum yield strength is higher than 550 MPa these grades are called ultra-high strength steels (UHSS) [1]:

Min. YS                                      HSS 210–550 MPa                                      UHSS > 550 MPa

Numerous high strength steels have been developed in the last 25 years. The conventional mechanisms to increase the strength in steel such as solid solution hardening or precipitation hardening are accompanied by a noticeably inferior formability.

The introduction of a new group of steels with a microstructure consisting of at least two different components has led to an enlargement of the strength level without a deterioration of ductility. These multi phase steels therefore offer very attractive combinations of strength and ductility which are due to the coexistence of the different microstructure components, their different mechanical behaviour and their mutual interactions. The components of interest are regarded on the scale of light microscopy, i.e. with typical dimensions of a few micrometers.

Multi phase steels can for example contain a relatively soft matrix phase being responsible for a low yield strength and a good formability along with a high tensile strength as a result of the presence of a hard second phase as in the case of dual phase steels (Fig. 9.1). It is possible to vary the mechanical properties, and to tailor them for the respective application foreseen by adjusting type, morphology

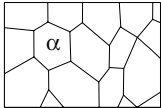
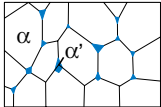
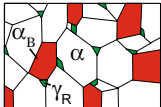
Steel type		Parameters	Phases
Single phase (Mild steel)		- Grain size - Grain shape	$\alpha$ = ferrite
Two phase (Dual phase steel)		- Grain sizes - Volume fractions - Local chemical composition	$\alpha$ = ferrite $\alpha'$ = martensite
Multi phase (TRIP steel)		- Grain sizes - Volume fractions - Local chemical composition - Phase stability	$\alpha$ = ferrite $\alpha_B$ = bainite $\gamma_R$ = retained austenite

Fig. 9.1 Microstructural characteristics of multi phase steels.

**Table 9.1** Conventional high strength steels, advanced high strength steels and high manganese steels.

HSS	AHSS	HMS
BH = Bake hardening	DP = Dual phase	HMS-TRIP = High Mn-transformation induced plasticity
IF-HS = High-strength IF	TRIP = Transformation induced plasticity	
P = Rephosphorised	CP = Complex phase	HMS-TWIP = High Mn-twinning induced plasticity
IS = Isotropic	PM = Partly martensitic	
CMn = Carbon-manganese		
HSLA = High-strength low alloy		

and orientation and above all volume fraction, size and distribution of the different phases. Furthermore the microstructure or some phases within the microstructure might be mechanically instable which results in stress-assisted or strain-induced transformations. These transformations improve the formability by significant strain hardening and prolonging the uniform straining behaviour.

Conventional high strength steels (HSS) in order of increasing strength are listed in Table 9.1 together with advanced high strength steels (AHSS) and high manganese steels (HMS). AHSS are multi phase steels which contain phases like martensite, bainite and retained austenite in quantities sufficient to produce unique mechanical properties. Compared to conventional high strength steels, AHSS exhibit higher strength values or a superior combination of high strength with good formability.

Recently, a new group of austenitic steels with high manganese contents have been developed for automotive use. These high manganese steels (HMS) combine excellent mechanical properties with an alloying concept which is less costly than conventional or new high-strength austenitic stainless steels. This group is divided into transformation induced steels (HMS-TRIP) and twinning induced plasticity steels (HMS-TWIP) due to the characteristic phenomena occurring during plastic deformation. The different steel grades for car body use can be characterised by their microstructure or their alloying concept as shown in Table 9.2. The microstructures can be single phase ferrite  $\alpha$  or single phase austenite  $\gamma$ ; beside these, in multi phase steels tetragonal or cubic martensite  $\alpha'$ , bainite  $\alpha_B$  or retained austenite  $\gamma_R$  might occur. The used abbreviations for the steel grades are mentioned in the Table 9.2.

Typical mechanical property ranges of these different steels are indicated in Fig. 9.2. It is obvious that AHSS offer higher strength values than HSS. Furthermore the strength-ductility relationship of AHSS is improved compared to HSS. The recently developed HMS show extraordinary strength-ductility relationships which are even improved compared to austenitic stainless steels [2,3]. The reasonable upper strength limit for cold formable steels is a matter of discussion; depending of the type of forming and the sheet thickness even grades with a strength level above 1200 MPa might be suitable for cold forming.

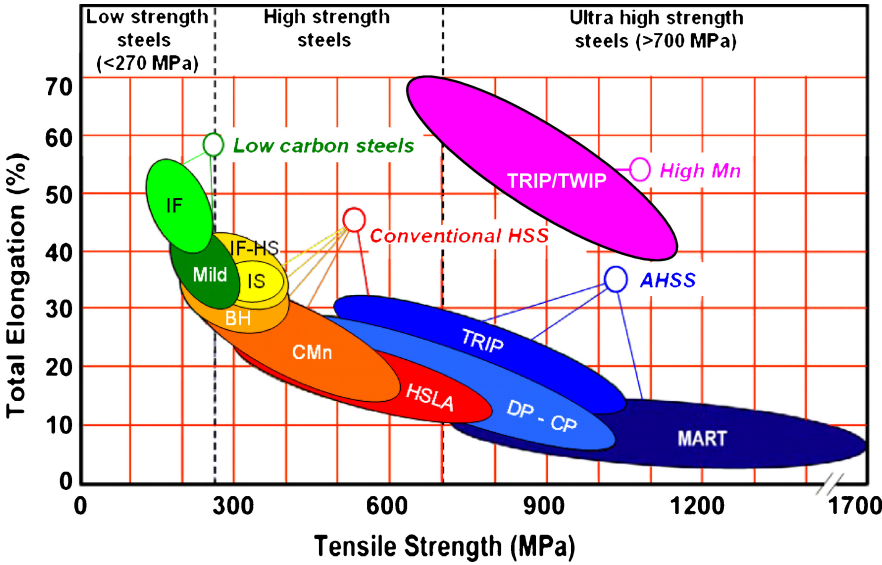


Fig. 9.2 Typical mechanical properties of mild and high strength steels.

Table 9.2 Microstructure and characteristics of steel grades for car body use.

Steels	Micro-structure	Characteristics
Mild steels	$\alpha$	– LC: unalloyed Al-killed low carbon steel; extra deep-drawing grade
		– IF: interstitial free steel; microalloyed extra deep-drawing grade
HSS	$\alpha$	– BH: bake hardening steel grades, which show additional strengthening during paint bake treatment by controlled C aging
		– IF-HS: high-strength interstitial free steel, strengthened by Mn and P addition
		– P: P alloyed high strength steels
		– IS: steels with medium yield strength and isotropic flow behaviour, microalloyed with Ti or Nb
		– CMn: high strength steels with increased C, Mn and Si contents for solid solution strengthening
		– HSLA: high strength low alloy steel, strengthened by microalloying with Nb or Ti
AHSS	$\alpha + \alpha'$	– DP: dual phase steels with a microstructure of ferrite and 5–30 volume% martensite islands
	$\alpha + \alpha_B + \gamma_R$	– TRIP: transformation induced plasticity steels with a microstructure of ferrite, bainite and retained austenite
	$\alpha' + \alpha$	– PM: partly or fully martensitic steels
	$\alpha + \alpha_B + \alpha'$	– CP: complex phase steels with a mixture of strengthened ferrite, bainite and martensite
HMS	$\gamma$ or high fractions of $\gamma$	– HMS-TRIP: steels with an alloying concept that strain-induced? $\gamma \rightarrow \epsilon \rightarrow \alpha'$ transformation occurs
		– HMS-TWIP: steels with an alloying concept that mechanical twinning occurs during straining

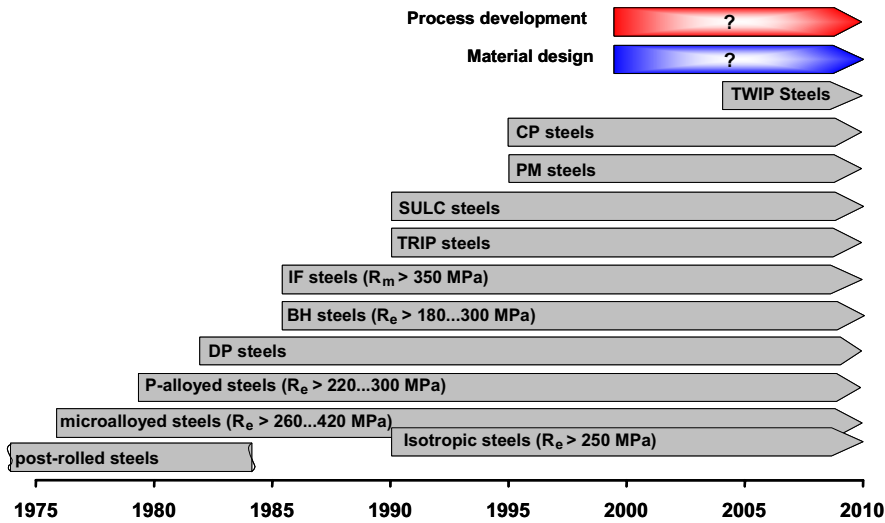


Fig. 9.3 Chronological development of high strength steels.

The history of high strength steels for car body applications is given in Fig. 9.3 which indicates the approximate first appearance of a new steel grade industrially processed on the European market. The development of HSS started prior to 1980. Dual phase steels development was the first among AHSS but the usage was limited up to the 1995 when the ULSAB consortium investigated the chances of their application in modern car body design. HMS are still under development.

### 9.3 Alloy Concepts

Numerous alloying concepts have been developed for high strength steels in order to adjust the desired microstructure and properties. The alloying elements change the thermodynamic stability of the phases and the kinetics of the transformations whereby the transformation temperatures are shifted, the transformations are either promoted or hindered and the phase distribution is altered. Additionally, the elements might act as solid solution or precipitation hardeners and affect the grain size. Some of the most common alloying concepts for dual phase and TRIP steels are summarised in Table 9.3 [4, 5, 6, 7, 8].

**Alloying elements in DP steels.** The main alloying element is carbon by which all transformations are noticeably affected and by which the final microstructure and the mechanical properties are controlled. Carbon stabilises the austenite which leads to the formation of martensite in the case of dual phase steels and to the retention of austenite in the case of TRIP steels. However, other requirements such as weldability limit the use of carbon to round about 0.2 mass%.



**Table 9.3** Chemical compositions of some high strength steels, contents in mass%.

Steel	Grade	C	Mn	Si	Al	P	Cr	Nb	Ti	V
BH	H180BD	0.04	0.70	0.50	0.04	0.01	–	–	–	–
	"	0.01 <sup>1)</sup>	0.70	0.50	0.04	0.01	–	–	–	–
IF-HS	H260YD	0.003	0.40	0.10	0.03	0.05	–	0.04	0.02	–
P	H220PD	0.06	0.70	0.50	0.04	0.07	–	–	–	–
HSLA	H320LA	0.07	0.35	0.01	0.04	0.01	–	0.04	–	–
DP	H300X	0.10	1.00	0.50	0.04	0.01	–	–	–	–
	"	0.10	1.00	0.10	0.04	0.05	–	–	–	–
	H340X	0.10	1.20	0.10	0.04	0.01	0.80	0.04	–	–
	"	0.07	1.40	0.10	0.04	0.04	–	0.04	–	–
	H300X	0.08	1.50	0.10	0.04	0.07	0.40	–	0.03	–
PM	MS1000-W	0.17	2.20	2.00	0.04	0.01	1.00	–	–	–
TRIP	RA700K	0.20	1.50	1.50	0.04	0.01	–	–	–	–
	"	0.20	1.50	0.10	1.80	0.01	–	–	–	–
	"	0.15	2.00	0.10	0.04	0.04	–	–	–	–
	"	0.20	1.50	1.10	0.04	0.01	–	0.04	–	–
	RA800K	0.20	1.50	1.50	0.04	0.01	–	–	–	0.10
HMS	TRIP	0.02	15	3	3	–	–	–	–	–
	TWIP	0.03	25	3	3	–	–	–	–	–
	TWIP	0.60	22	–	–	–	–	–	–	–

<sup>1)</sup> batch annealed

Other important alloying elements for dual phase steels are silicon and manganese. Silicon in the first place promotes ferrite formation, whereas manganese retards pearlite and bainite formation and allows martensite formation to occur during cooling from intercritical temperature. Phosphorus or aluminum (sometimes in combination with chromium) can be used to reduce or replace silicon, which may cause problems during hot rolling and coating.

Niobium in the state of solid solution retards static and dynamic recrystallisation during hot deformation as well as the austenite to ferrite transformation. Small carbonitrides which form when niobium combines with carbon and nitrogen also delay recrystallisation, constitute an massive obstacle to grain growth and result in effective strengthening.

**Alloying elements in TRIP steels.** Higher carbon levels are applied for TRIP steels which is due to the necessity to produce a highly enriched austenite with a carbon content above 0.8 mass%. Apart from carbon, manganese and silicon play an important role so as to control the transformation behaviour and to stabilise the retained austenite. Silicon does prevent or at least retard carbide precipitation during bainite formation and allows the carbon to diffuse into the retained austenite. Manganese as an austenite stabilising element lowers the transformation temperature of the austenite, and in this way helps to avoid martensite formation during cooling to room temperature. Moreover, manganese as well as silicon increase the strength of the material by solid solution hardening.

**Table 9.4** Effect of microalloying elements on microscopic features and macroscopic properties of steels.

Element	Microscopic effect						Macroscopic effect				
	Coarse precipitates	Fine precipitates	Grain boundary segregation	Grain refinement	Cementite formation	C enrichment in $\gamma_R$	Kinetics of recrystallisation	Kinetics of $\gamma/\alpha$ -transformation	Kinetics of $\gamma/\alpha_B$ -transformation	$M_s$ -temperature	Matrix strengthening
Al		+		+	–	+		+		+	
B		+	+					–			
Nb		+		++		+	–	–, +	–	–	++
Ti	+	+		+			–	+			
V		+		+			–	+			+

+ = promote/increase

– = hinder/retard/reduce

As a higher silicon content can be responsible for a poor surface quality of hot rolled steel and a poor coatability of cold rolled steel, a partial or complete substitution of silicon by other alloying elements has been considered. Another element, which is not soluble in cementite, and therefore has to diffuse from the interface of the carbide particle, before the particle can continue to grow, is aluminium, which also promotes the generation of ferrite. But as the effect of aluminium is weaker and as the solid solution hardening potential is lower, it is often used in combination with higher carbon contents or in combination with phosphorus, that reduces the kinetics of cementite precipitation on the one hand and is a very effective solid solution hardening element on the other hand. If the addition of phosphorus exceeds a certain amount, phosphorus might segregate to the grain boundaries and deteriorate the ductility. Aluminium addition significantly increases carbon concentration in retained austenite, due to the rise of  $T_0$  temperature where austenite and ferrite have identical free energies [9].

Microalloying elements can be used for different purposes in AHSS. Their microscopic features and their effect on macroscopic properties are discussed in Table 9.4. Microalloying elements are defined by small alloying additions of <0.1 mass% and by the fact that they can form precipitates which significantly affect directly or indirectly the mechanical properties.

The well known effects of microalloying elements such as niobium on grain boundary motion and element migration also influence the TRIP effect. The different phase transformations during hot rolling, intercritical annealing, cooling, isothermal holding in the temperature range of bainite formation, and straining are modified thus resulting in superior mechanical behaviour. Direct effects of niobium on the preservation of austenite at room temperature and indirect effects

arising from the improved carbon enrichment of the austenite must probably be distinguished. Vanadium might also be used to control the transformation behaviour of TRIP steels. Vanadium reduces the bainite packet size and tends to develop carbide free bainite phase, furthermore it has strong precipitation strengthening potential of 60–100 MPa if 0.1 mass% vanadium is added [8].

Additions of molybdenum to niobium bearing steels are reported to bring about a further improvement of the combination of strength and ductility and to constitute another possibility of lowering the silicon level required [10]. Molybdenum exerts an important solute drag effect and delays the transformation of austenite to ferrite and to pearlite strongly. Although molybdenum lowers the activity of carbon in austenite and promotes carbide formation from the thermodynamic point of view, the contrary effect is observed in practice. Due to the strong solute drag effect the carbide precipitation is even retarded in the presence of molybdenum. Moreover, molybdenum raises strength due to solid solution hardening.

**Alloying elements in HMS.** High manganese steels composed of single austenite phase or multi phase with high fractions of austenite phase can be alloyed a large amount of alloying elements. Effect of alloying element on properties of high manganese steels is shown in Table 9.5 [11, 12, 13, 14].

Carbon improves the stability of austenite and strengthens the steels. It inhibits the formation of  $\epsilon$  martensite by increasing the stacking fault energy.

For HMS alloyed with aluminium and carbon, aging of the steels at temperatures from 500 to 750°C generally causes the precipitation of the  $\kappa$  phase,  $(\text{Fe,Mn})_3\text{AlC}_x$ , which is considered to be a possible hardening mechanism. However, the presence of  $\kappa$  phase can cause brittle fracture and severe loss in impact energy. To avoid the precipitation of  $\kappa$  phase, carbon should be limited to within about 0.67% [15].

Manganese stabilises austenite. However if its content is less than 15%,  $\alpha'$  martensite is formed which aggravates the formability. The  $\gamma \rightarrow \epsilon$  transformation temperatures decrease with increasing Mn content.

The high aluminium addition in HMS increases the SFE of austenite. The formation of  $\epsilon$  martensite is suppressed by aluminium addition. In addition, an aluminium addition is very effective for improving low temperature toughness. Aluminium can reduce  $\text{SiO}_2$  and  $\text{MnO}$  from slag to silicon and manganese. The

**Table 9.5** Effect of alloying elements on properties of high manganese steels.

Element	$\gamma$ stabiliser	Solid solution strengthening in $\gamma$ austenite	$\epsilon$ -martensite refinement	Hot Ductility
C	+	+		
Mn	+			
Si		+	+	
B				+
Ti				+
N	+	+		

increase in  $\text{Al}_2\text{O}_3$  and the decrease in  $\text{SiO}_2$  and  $\text{MnO}$  will increase the viscosity of the slag, which leads to difficulties in casting. This results in quality lacking in the inside and the surface of the slab. Therefore requirements of casting techniques e.g. development of casting powder are investigated [16].

Aluminium can segregate on the grain boundaries during solidification, and produce a low melting point intermetallic compound such as  $\text{Fe}_2\text{Al}_5$  having a melting point about  $1170^\circ\text{C}$  on the grain boundaries, which cause a weakness in the casting structure. Adding small amounts of boron, titanium or zirconium into the HMS alloyed with aluminium can improve the hot ductility of the steels [13].

Silicon improves strengths by solid solution strengthening. Silicon addition is effective for refining  $\epsilon$  martensite plates and increasing fracture strength, although it does not improve ductility [12].

Nitrogen is an effective strengthening element in austenite. Adding nitrogen to the Fe-16.5Mn alloy decreases the martensite start temperature and also reduces the volume fraction of  $\epsilon$  martensite [14].

Microalloying elements such as titanium and aluminium form nitrides that perform a core role in producing twins during forming of steel sheets, thereby improving the formability and strength [11].

### 9.4 Processing

Various process routes for dual phase steels and TRIP steels are either already in use or are subject to discussion depending on the final product. Figure 9.4 summarizes the different routes and demonstrates that hot rolled, cold rolled and galvanised products can be produced. Some steels are available in all product forms, some are only processable as hot or cold strip, Table 9.6 [17, 18, 19, 20]. It should be mentioned that the optimum process routes for HMS are still a matter of research.

**Table 9.6** Product forms of different steels in commercial product or customer trials.

HSS	Hot rolled strip	Electro-galvanised (hot) strip	Hot dip galvanised (hot) strip	Cold rolled strip	Electro-galvanised (cold) strip	Hot dip galvanised (cold) strip
BH				✓	✓	✓
IF-HS				✓	✓	✓
P				✓	✓	✓
IS				✓	✓	✓
HSLA	✓	✓	✓	✓	✓	✓
DP	✓	✓		✓	✓	✓
TRIP	✓	✓		✓	✓	✓
CP/PM	✓	✓	✓	✓	✓	

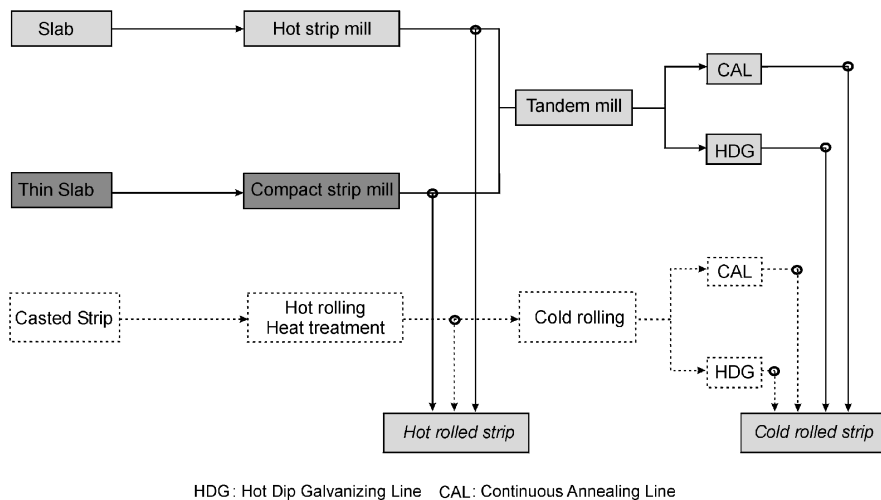


**Fig. 9.4** Process routes for hot and cold rolled multi phase steels.

**Effect of microalloying on hot strip processing.** Special attention has to be paid to the cooling strategy after finishing rolling when producing hot rolled multi phase steels. After austenitisation and the different steps of rolling in roughing and finishing mill, the microstructure and the mechanical properties are finally adjusted in the cooling section consisting of run out table and coiler. A variation of the cooling intensity and the coiling temperature allows to change the transformation behaviour and to vary the strength level in a wide range.

The temperature-time-schedule for the production of hot rolled dual phase and TRIP steels is presented schematically in Fig. 9.5. The development of the desired microstructure might prove to be difficult as some transformations are necessary whereas others would be detrimental, which restricts the possible cooling path. For dual phase steels the cooling rate must be low enough to enable the transformation of about 85% austenite to ferrite to take place, associated with an carbon enrichment of the austenite, and at the same time high enough to avoid the formation of pearlite and bainite, and to ensure the formation of martensite at low coiling temperatures of about 200°C. Hence, a holding step has to be inserted in the temperature range of the maximum ferrite formation kinetics or the alloying concept has to be adapted in order to accelerate the ferrite formation.

For TRIP steels a lower cooling rate is applied, as ferrite formation is delayed due to the different alloying concept in general and the higher carbon content in particular and as the subsequent bainite is striven for. Coiling is therefore carried out in the temperature range of bainite formation at round about 500°C and the final microstructure comprises 50 to 60% ferrite, 25 to 40% bainite, and 5 to 15% metastable retained austenite that does not-transform to martensite, since the carbon enrichment during ferrite and bainite transformation shifts the martensite start temperature below room temperature.

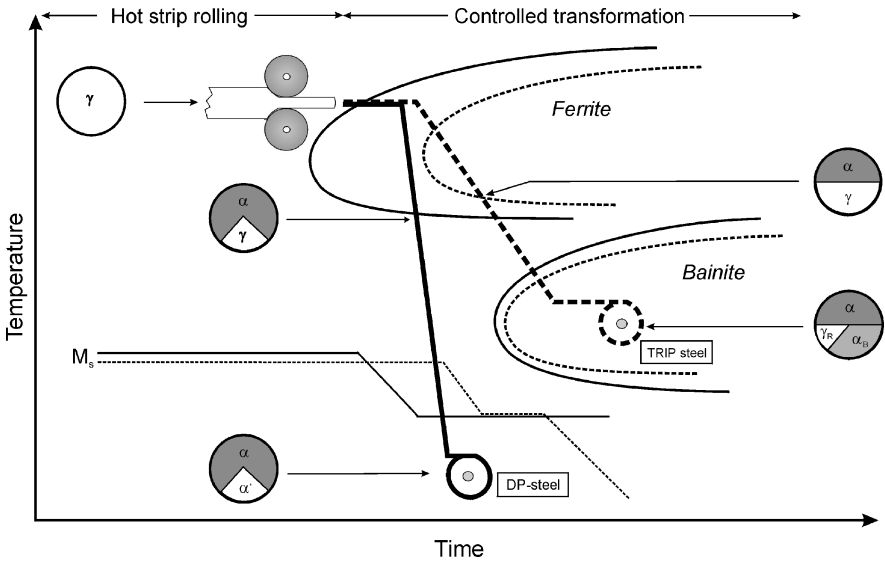


Fig. 9.5 Temperature-time-schedule for hot rolled multi phase steels.

The addition of niobium to dual phase steels not only provides noticeable grain refinement and thus improved ductility but also renders an additional holding step in the temperature range of maximum ferrite formation unnecessary and enables continuous cooling to be applied after finish rolling (Fig. 9.6). Ferrite formation involves carbon enrichment of the austenite thus retarding pearlite and bainite formation and facilitating martensite formation.

**Optimum coiling temperature.** For cold rolled multi phase steels two different hot rolling schedules prior to cold rolling are conceivable. The first of them

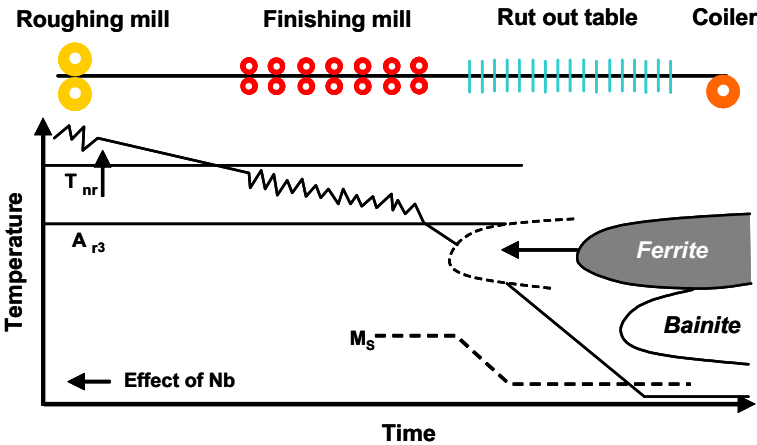


Fig. 9.6 Effect of niobium on hot strip processing of DP steel.

leads to a soft material with a microstructure of ferrite and pearlite. This microstructure stems from the application of a high coiling temperature of around 700°C. The material is well suited to subsequent cold rolling. Alternatively, a hot rolling cycle making use of a lower coiling temperature in the range of bainite formation can be applied. Bainite forms at about 500°C and represents a relatively hard microstructural component.

Rolling forces must be applied when cold rolling the material. However, it is expected that process route leads to a more homogeneous and fine grained microstructure, therefore superior properties of the as annealed product. The effect of hot strip coiling temperature and niobium on the martensite start temperature after intercritical annealing is shown in Fig. 9.7. It reveals the strong inhibition of martensite formation that can be achieved by niobium. This is particularly true, if a low coiling temperature of about 500°C is applied after hot rolling. The low coiling temperature leads to a decrease of the  $M_S$ -temperature of the niobium free TRIP steel as well, which has been suggested to be explained by the homogeneous and very fine structure of the bainite and the homogeneous distribution of carbon. The microstructure of ferrite and pearlite resulting from the use of a coiling temperature of approximately 700°C, however, contains coarse cementite that possibly does not dissolve completely or at least entails an inhomogeneous carbon distribution during intercritical annealing.

A similar positive effect is ascribed to the addition of niobium, which accounts for the generation of a fine grained ferrite due to the retardation of recrystallisation and grain growth, and due to a ferrite formation that takes place at low temperatures, but possesses a distinctly higher driving force and a higher nucleation rate.

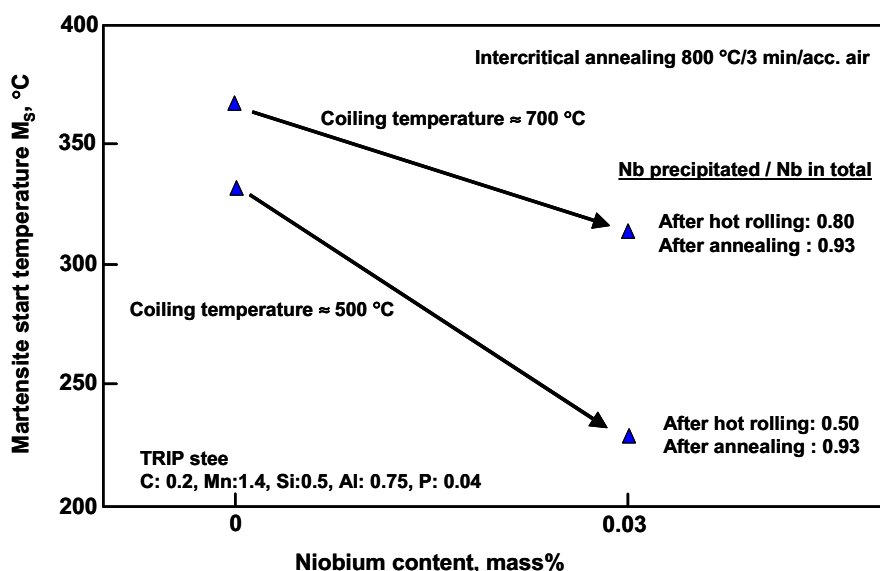
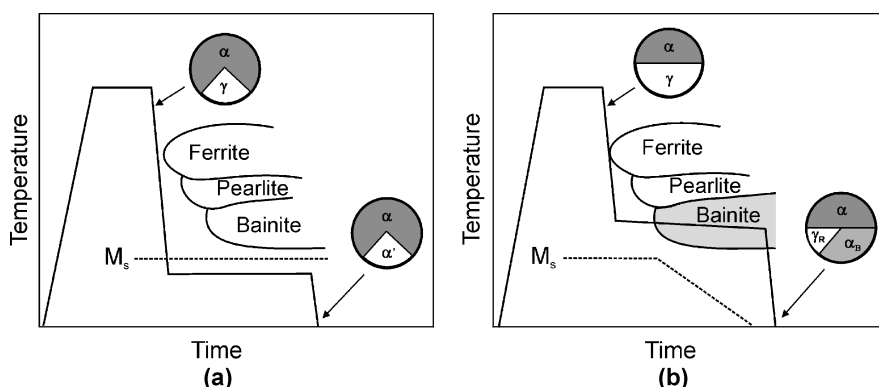


Fig. 9.7 Effect of niobium content and hot strip coiling temperature on the  $M_S$ -temperature of cold-rolled TRIP steels.

However, the effect of niobium is restricted, when coiling is performed at 700°C, as precipitates become coarser and thus less effective concerning the suppression of grain growth during the slow cooling. If coiling is carried out at about 500°C, only 50% of niobium is precipitated after hot rolling, whereas 50% is determined to be chemically soluble which is the result of chemical isolation analysis and includes niobium in solid solution as well as very small precipitates with a diameter of less than 20 nm. As the measurements indicate that the precipitated fraction of niobium after intercritical annealing is irrespective of hot rolling conditions and amounts to more than 90%, extensive precipitation must take place during intercritical annealing in the case of the low coiling temperature. The favourable nucleation conditions surely result in the precipitation of very small particles. These precipitates not only control the grain size, encourage carbon diffusion and ensure a highly homogenized microstructure, but apparently also impair martensite nucleation considerably. The result is another decrease of the  $M_s$ -temperature by almost 100°C.

**Effect of microalloying on cold strip processing.** After cold rolling the sheet material has to undergo a heat treatment that can be realized in continuous annealing lines and in hot dip galvanising lines, Fig. 9.8 (a). No full austenitisation is performed during the heat treatment of dual phase steels. An annealing temperature slightly above  $A_{C1}$  is applied and only a small part of 10 to 15% of the microstructure composed of ferrite and pearlite or ferrite and bainite is transformed to austenite during this intercritical annealing. Afterwards the material is quenched and the austenite transforms to martensite during cooling to room temperature, so that the final microstructure consists of a dispersion of martensitic islands in a ferritic matrix.

TRIP steels are subjected to a two step heat treatment with intercritical annealing in the temperature range between 780°C and 880°C, cooling and another isothermal annealing between 350°C and 450°C, which is then followed by cooling to room temperature as shown in Fig. 9.8 (b). The microstructure of TRIP steels after intercritical annealing contains almost identical percentages of ferrite and



**Fig. 9.8** Temperature-time-schedule for cold rolled dual phase (a) and TRIP (b) steels.



austenite, but in contrast to the microstructure of hot rolled TRIP steels, the ferrite has been part of the microstructure prior to annealing and does not form during cooling from the intercritical temperature. Cooling is interrupted in the temperature range of bainite formation for several minutes, before cooling to room temperature. During the second isothermal holding the austenite is mostly transformed to bainite thus leading to a final microstructure of approximately 50% to 60% ferrite, 25 to 40% bainite, and 5 to 15% retained austenite.

The austenite of dual phase and TRIP steels is enriched in carbon due to the phase transformations and the martensite start temperature is lowered. The high carbon content of the austenite in dual phase steels retards ferrite, pearlite and bainite formation and reduces the critical cooling rate to ensure complete transformation of austenite to martensite, whereas the carbon enrichment in TRIP steels is even sufficient to suppress martensite formation during cooling to room temperature.

**Isothermal bainite transformation.** The  $\gamma_B$  stability can be attributed to the higher carbon content of TRIP steels and the favourable conditions during the second annealing step. Bainite formation enables a further carbon enrichment in austenite to occur, whilst carbide formation that withdraws carbon from the austenite can be suppressed, which is indispensable in preserving a considerable amount of metastable retained austenite even at room temperature. If the second annealing is too short and if therefore too little bainite is formed, carbon enrichment of the austenite is not sufficient and the unstable austenite is transformed to martensite during cooling down to room temperature. Nevertheless, efforts are made to minimise or even to omit the isothermal bainite transformation step. Figure 9.9 depicts how the alloying elements affect transformation behaviour during continuous annealing [20, 21].

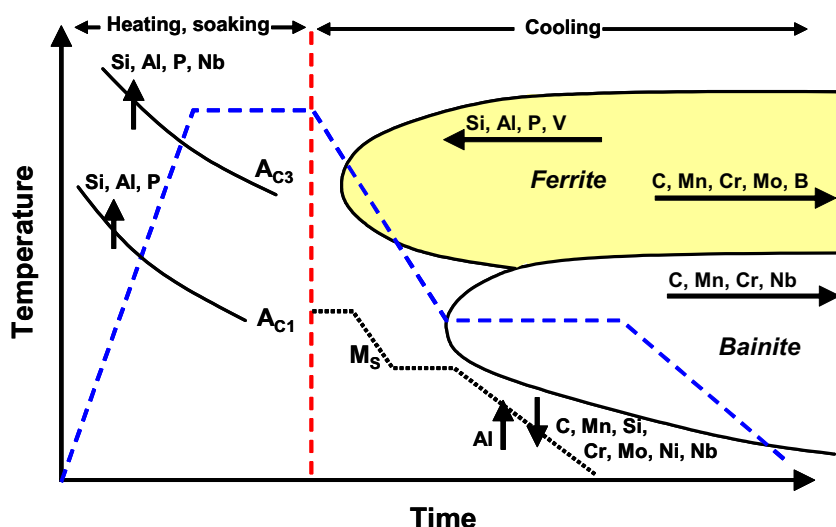
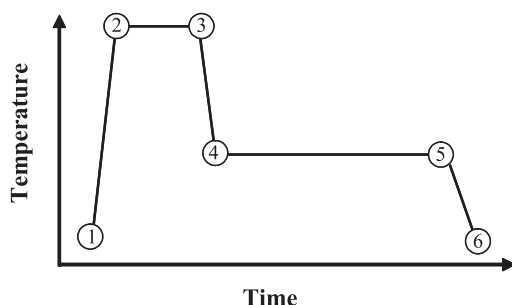


Fig. 9.9 Effect of alloying elements on transformation behaviour during continuous annealing of TRIP steels.

The processes taking place during the various steps of the heat treatment of TRIP steels are listed in Fig. 9.10. The essential requirement is to transform part of the initial microstructure to austenite, to bring all carbon atoms in solid solution and to prevent any precipitation in the austenite, so that a sufficient amount of retained austenite with a sufficient carbon content is obtained. The significant role of niobium is hinted at and will be discussed in detail.

Figure 9.11 demonstrates that bainite formation is also delayed by niobium, which might also be attributed to the blocking of the nucleation sites by the very fine dispersed carbonitrides. This hypothesis is supported by the fact that the retarding effect is much more pronounced at a lower transformation temperature of 350°C, at which the displacive character of the bainite formation should prevail.

Another possible mechanism according for reduced bainite formation is ferrite formation during cooling due to the fine grained microstructure and the enhanced nucleation and growth conditions. A similar effect might be accomplished by using a lower cooling rate. Dilatometric experiments confirm that a transformation actually takes place during cooling. A ferrite formation would enable further carbon enrichment of the austenite and lower the bainite start temperature. This assumption conforms to the fact that aside from the velocity of bainite formation, the total amount is reduced [22].



Steps	Metallurgical features	Niobium effect
1→2	Recrystallization Dissolution of cementite	Delay Acceleration
2→3	Alloying element and carbon segregation Grain growth Precipitation carbonitrides	Acceleration Delay, Fine grain Formation of NbC
3→4	Transformation of pearlite & ferrite to austenite Transformation of austenite to ferrite Carbon segregation	Acceleration/delay Acceleration/delay Acceleration/delay
4→5	Transformation of austenite to bainite Carbon segregation Possible precipitation	Delay Acceleration Acceleration
5→6	Possible transformation of austenite to martensite	Control of $M_s$ -temp.

**Fig. 9.10** Metallurgical features during the processing of cold rolled TRIP steels.

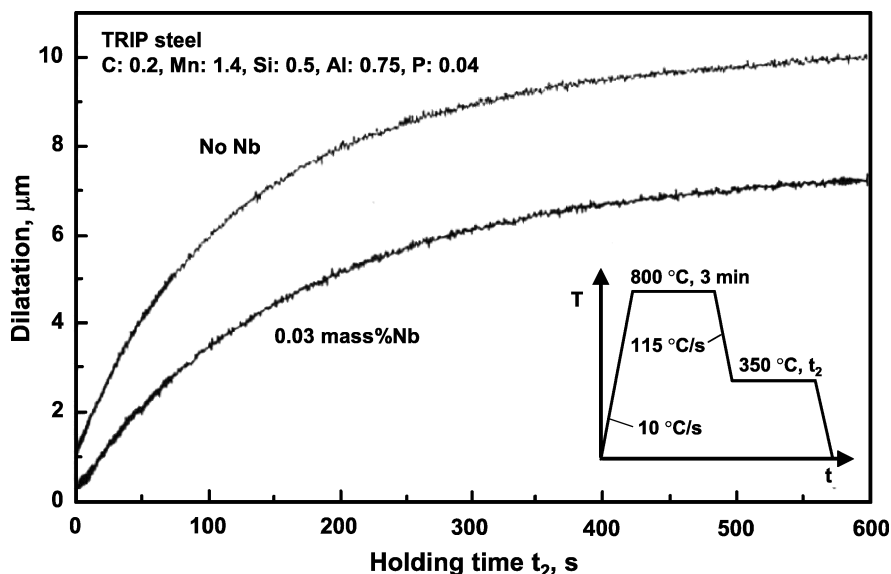


Fig. 9.11 Effect of niobium on isothermal bainite formation of TRIP steels at  $350^\circ\text{C}$ .

## 9.5 Properties

A small mean martensite island diameter improves the total elongation significantly, it shows nearly no effect on the yield strength, Fig. 9.12 [23]. The tensile strength is affected when the martensite islands become quite small, typically smaller than  $4\mu\text{m}$ . However, results of metallographic examinations like these are sometimes prone to easy misinterpretation, as the major effect on the mechanical properties in dual phase steels is the volume fraction of the hard phase and second to this the hardness itself. Thus, minor changes in the quantitative determination of

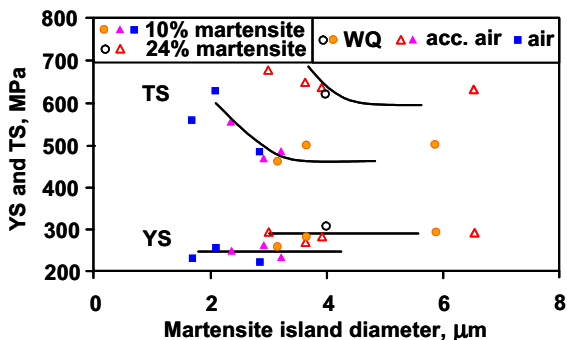
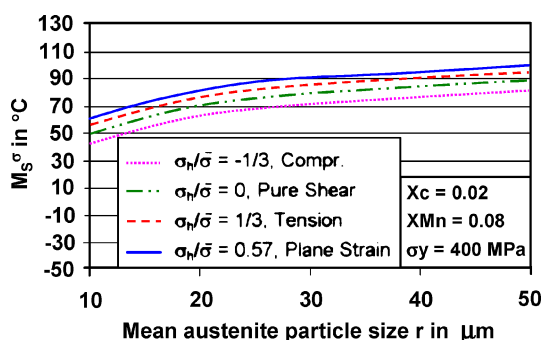


Fig. 9.12 Mechanical properties as a function of the martensite island size.

**Fig. 9.13** Effect of austenite grain size on the  $M_s$  temperature for different stress states.



martensite or in the visibility of martensite islands might change the mechanical properties significantly. Furthermore, when the martensite volume has been measured quite accurately there seems to be an island diameter effect which is most likely to be superimposed by different carbon contents due to the easier enrichment during intercritical annealing in fine grained structures.

In dual phase steels beside the martensite retained austenite might be detected. For steels oil-quenched from various temperatures it was found that the content of retained austenite increased with temperature in the intercritical range. This behaviour was understood on the basis of increasing amount of austenite with the temperature and the carbon content. An additional effect was a decrease in the size of the austenite grains which effectively stabilises the austenite against martensite transformation. It was furthermore found that the retained austenite was extremely stable on further cooling to lower temperatures, whereas during plastic deformation it quite readily transformed to martensite, Fig. 9.13 [24].

In TRIP microstructures crack initiation was found to start at hard phases, such as retained austenite and/or martensite. The crack initiation and development in the multi phase microstructure depends on the amount of crack initiation point, the stress-strain state and the neighbourhood conditions. The morphology, size and strength of the bainite islands and the banded structure are important for the crack development, because they can be the background for crack connections in several points in the microstructure. The sizes of cleavage areas and bainite islands were estimated by selecting these exemplarily from SEM fractography and LOM micrograph. It can be seen that most of the cleavage areas between 20 and 140  $\mu\text{m}^2$  have a comparable size distribution with the bainitic islands, Fig. 9.14. The presence of much larger cleavage areas, 140 to 220  $\mu\text{m}^2$ , proves in fact the possibility of crack connections inside of the bainitic islands leading to larger cleavage areas.

Thus, it can be concluded that a decrease of austenite size during intercritical annealing, a small martensite island diameter and a small bainite packet diameter are beneficial for the mechanical properties of multi phase steels. This microstructural refinement can be made possible by proper microalloying. On top of that, small precipitates can further strengthen the ferrite matrix or other phases and by this increase the strength level of AHSS.

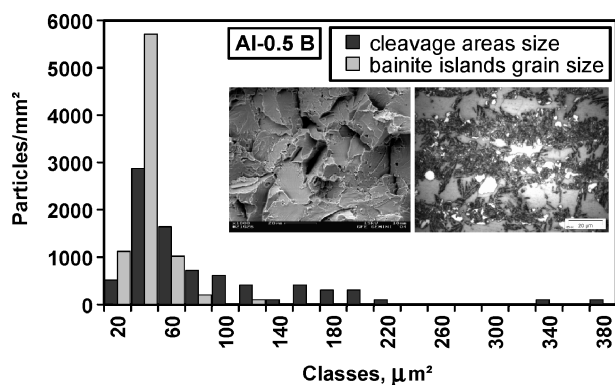


Fig. 9.14 Diagram of cleavage areas size distribution and bainite packet size.

## 9.6 Conclusion

Microalloying in multi phase steel can be used

- to control the thermomechanical rolling by a change of  $T_{nr}$  temperature,
- to control the evolution of the microstructure in the hot strip run out table by their effect on transformation,
- to increase strength by grain refinement and precipitation hardening,
- to control the annealing process after cold rolling by altering recrystallisation and grain size control,
- to improve ductility by small martensite island in DP steel and small bainite areas in TRIP steels,
- to improve hot ductility in high manganese-high aluminium steels.

## References

- [1] ULSAB-AVC Consortium: Technical Transfer Dispatch #6, May 2001
- [2] Hofmann, H., Göklü, S., Gerlach, J. and Bruex, U.: Proceedings IDDRG International Deep Drawing Research Group 2004 Conference, Sindelfingen, Germany, pp. 270–279
- [3] Viscorova, R., Wendelstorf, J., Spitzer, K.-H., Kroos, J. and Flaxa, V.: Proceedings IDDRG International Deep Drawing Research Group 2004 Conference, Sindelfingen, Germany, pp. 261–269
- [4] Bleck, W.: International Conference on TRIP-Aided High Strength Ferrous Alloys, Ghent, Belgium 2002, pp. 13–23
- [5] Bleck, W., Frehn, A. and Ohlert, J.: Proc. Inter. Symposium Niobium 2001, USA, pp. 727–752
- [6] Frommeyer, G., Brüx, U. and Neumann, P.: ISIJ International, Vol. 43 (2003), No. 3, pp. 438–446

- [7] Allain, S., Chateau, J.-P., Dahmoun, D. and Bouaziz, O.: Materials Science and Engineering A 387–389 (2004), pp. 272–276
- [8] Scott, C., Maugis, P., Barges, P. and Goune, M.: International Conference on Advanced High Strength Sheet Steels for Automotive Applications, Colorado, USA, June 6–9, 2004, pp. 181–193
- [9] Sugimoto, K., Hashimoto, S. and Ikeda, S.: International Conference on Advanced High Strength Sheet Steels for Automotive Applications, Colorado, USA, June 6–9, 2004, pp. 63–70
- [10] Hashimoto, S., Ikeda, S., Sugimoto, K. and Miyake, S.: International Conference on Advanced High Strength Sheet Steels for Automotive Applications, Colorado, USA, June 6–9, 2004, pp. 195–203
- [11] Kim, T.W., Han, J.K., Chang, R.W. and Kim, Y.G.: US Patent 5431753, 1995
- [12] Takaki, S., Furuya, T. and Tokunaga, Y.: ISIJ International, Vol. 30 (1990), No. 8, pp. 636–637
- [13] Kim, T.W., Kim, Y.G. and Park, S.H.: US Patent 5647922, 1997
- [14] Bliznuk, V.V., Glavatska, N.I., Söderberg, O. and Lindroos, V.K.: Material Science and Engineering, A338 (2002), pp. 213–218
- [15] Huang, H., Gan, D. and Kao, P.W.: Scripta Metallurgica et Materialia, Vol. 30 (1994), pp. 409–504
- [16] Gigacher, G., Bernhard, C. and Kriegner, W.: BHM, 149. Jg. (2004), Heft 3, S. 112–117
- [17] ThyssenKrupp Steel, Auto Division – Product Overview, Updated: August 2007
- [18] [www.mittalsteel.com/Products/Automotive+Applications/Sheet+Steels.htm](http://www.mittalsteel.com/Products/Automotive+Applications/Sheet+Steels.htm), accessed on October 3, 2007
- [19] [www.poscoauto.co.kr/docs/eng/rnd/rnd\\_material3\\_01.jsp](http://www.poscoauto.co.kr/docs/eng/rnd/rnd_material3_01.jsp), accessed on October 3, 2007
- [20] Ehrhardt, B., Gerber, T. and Schaumann, T.W.: International Conference on Advanced High Strength Sheet Steels for Automotive Applications, Colorado, USA, June 6–9, 2004, pp. 39–50
- [21] Bouet, M. et al.: Proc. of the International Conference on Microalloying in Steels, San Sebastian, Sept. 7–9, 1998, pp. 319–326
- [22] Hulka, K., Bleck, W. and Papamantellos, K.: Proc. of the 41st Mechanical Working and Steel Processing Conference, Baltimore, Oct. 24–27, 1999, pp. 67–77
- [23] Maid, O.: Einfluss der Gefügeparameter auf die mechanischen Eigenschaften von warm- und kaltgewalztem Flachzeug aus Dualphasen-Stahl (Dr.-Ing. Thesis, Aachen, Germany, 1986)
- [24] Haidemenopoulos, G.N.: Modelling of dispersed austenite stability in low-alloy TRIP steels (final report of ECSC contract 7210-EC702-95-D3.03e: New cold rolled deep-drawing qualities, University of Thessaly, Volos, Greece)



Wolfgang Bleck  
Professor  
Department of Ferrous Metallurgy  
RWTH Aachen University  
Intzestr. 1.  
D-52072 Aachen  
Germany



# Chapter 10

## State-of-the-Science of High Manganese TWIP Steels for Automotive Applications

**B.C. De Cooman, L. Chen, Han S. Kim, Y. Estrin, S.K. Kim,  
and H. Voswinckel**

**Abstract.** Recent trends in automotive industry towards improved passenger safety and reduced weight have led to a great interest in AHSS (Advanced High Strength Steel), and DP, TRIP, CP, MA and high-Mn TWIP (TWinning Induced Plasticity) steels are particularly promising due to their superior toughness and ductility. The properties of low SFE (Stacking Fault Energy) austenitic high Mn FeMnC steel exhibiting twinning-induced plasticity have recently been analyzed in detail. It is argued that although the mechanical properties of TRIP and TWIP steels are often assumed to be solely due to effects related to strain-induced transformation and deformation twinning, respectively, other mechanisms may also play an essential role such as point-defect cluster formation, planar glide, pseudo-twinning, short range ordering, and dynamic strain ageing, e.g. in the case of TWIP steel. At low strain rates, the plastic deformation of TWIP steels is often controlled by the movement of very few well-defined localized deformation bands. The formation and propagation of these Portevin-LeChatelier (PLC) bands lead to serrated stress-strain curves, exhibiting a small negative strain rate sensitivity.

---

B.C. De Cooman, L. Chen, and Han S. Kim

Materials Design Laboratory, Graduate Institute of Ferrous Technology, Pohang University of Science and Technology, Pohang, South Korea, San 31, Hyoja-Dong, Nam-Gu, Pohang, 790-784, South Korea  
e-mail: decooman@postech.ac.kr

Y. Estrin

Department of Materials Engineering, Monash University, and CSIRO Division of Materials Science and Engineering, Clayton, Victoria, Australia

S.K. Kim

POSCO Technical Research Laboratories, Gwangyang Works, Gwangyang, South Korea

H. Voswinckel

Department of Ferrous Metallurgy (IEHK), RWTH Aachen University, Aachen, Germany



The present contribution offers a critical analysis of the mechanical properties of high-Mn TWIP steels and focuses on their potential as automotive materials. In addition, the challenges related to the production and applications of high-Mn TWIP steels are discussed. The new insights in the properties of TWIP steels result from the use of new experimental techniques combining high sensitivity infrared thermo-graphic imaging and optical in situ strain analysis. Finally the importance of the use of TEM (Transmission Electron Microscopy) in understanding the development of deformation microstructures in TWIP steel is also illustrated.

## 10.1 Introduction

Steel is still the material of choice for car bodies, with 99% of the passenger cars having a steel body, and 60–70% of the car weight consisting of steel or steel-based parts. There has been only a slight increase in the use of Al, Mg and plastics, but the automotive industry is expected to continue making excursion in the area of light materials applications. At present, most car makers are routinely testing multi-materials concepts, which are not limited to the obvious use of light materials for closures, e.g. the use of Al for the front lid or thermosetting resins for trunk lids. There is a continuous challenge to the central role of steel in auto body manufacturing, and the steel industry has been making sure that current automotive steel grades are not perceived as commodity products but as advanced materials. With this new perception, steel may even be able to gain back some of the ground it lost to alternative materials.

Improved safety standards, reduced automotive body-in-white weight, and manufacturing processes requiring a superior formability, have led to a strong interest in AHSS and high toughness, high Mn steel characterized by TWinning-Induced Plasticity (TWIP). The TWIP effect is believed to lead to high flow stresses (600–1100 MPa) and exceptional elongations (60–95%). Extensive research has already been reported on high Mn TWIP steels with slightly different compositions, but very similar properties: Fe25Mn3Al3Si [1], Fe22Mn0.6C [2, 3], Fe27Mn0.02C [4], Fe30Mn3Al3Si [5], Fe12Mn1.1C [6], Fe12Mn1.2C [7], Fe13Mn1.2C [8], Fe32Mn12Cr0.4C [9] and Fe23Mn2Si2Al [10]. A review of their mechanical properties is given in Fig. 10.1.

The mechanical properties of TWIP steel are mainly due to a combination of deformation twinning and dislocation motion in conditions of pronounced planar glide. In low SFE austenitic steels, the increased partial dislocation separation of favorably oriented screw dislocation segments [11] results in the ease of twin nucleation once a critical shear stress, the twinning stress, is reached. During deformation, the grains are progressively subdivided by the twinning process, and the internal twin boundaries increase the strain hardening. Although the actual twinning strain is limited and the twin formation itself may actually cause softening, the twin boundaries reduce the dislocation slip distances progressively, and promote dislocation accumulation and storage [2–4].

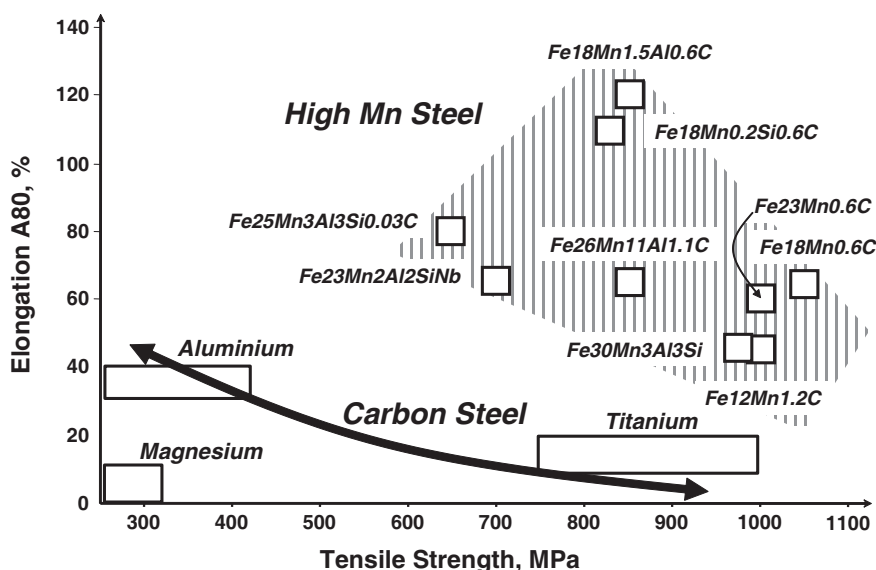


**Fig. 10.1** Overview of the materials currently used in the construction of car bodies. TWIP steels have a high manganese concentration in the range of 15~30 mass%, which results in a fully austenitic microstructure. The twinning-induced plasticity is due to their SFE of  $\sim 20 \text{ mJ/m}^2$ . Industrial research has focused mainly on Fe18Mn0.6C and Fe22Mn0.6C TWIP steels, which may be alloyed with Al and/or Si.

The mechanism leading to a high strain hardening in TWIP steel is however still a matter of debate. The pronounced strain hardening may not necessarily be caused by twinning only, as alloying additions and high temperatures, both of which suppress deformation-induced twinning, have been reported to have not much influence the strain hardening [6]. Alternative explanations stress the fact that a pronounced planar glide can also lead to a high strain hardening [12, 13]. In high Mn TWIP steel, the strong attractive interaction between C and Mn leads to a non-random distribution of interstitial C atoms in which there is a very high probability that a C atom occupies an octahedral interstitial position and forms an octahedral cluster for which the number of Mn atoms on the six nearest-neighbor positions is higher than the site occupancy expected on basis of the atomic Mn concentration [12]. This clustering leads to a higher lattice resistance to dislocation glide, as the passage of a partial dislocation will in general change the local position of both substitutional and interstitial atoms. This disordering process results in a gradual reduction of the stress required to move each of the following dislocations on the same glide plane, tending to confine slip to a single slip plane. The more pronounced planar glide will results in a higher strain hardening [13]. In addition, the process of twinning in TWIP steel interacts with the ordering, as the homogeneous twinning shear also alters the degree of short range order as it results in a different pair correlation and interstitials in different positions (pseudo-twinning) [14, 15].

The flow curve of high Mn TWIP steels containing interstitial carbon is often characterized by serrations, the Portevin-LeChatelier (PLC) phenomenon, and a negative strain rate sensitivity. Both result from a microscopic Dynamic Strain Aging (DSA) process. DSA results in an increase in flow stress and strain hardening, but a decrease in post-uniform elongation and a reduction of area at fracture.

Serrated flow curves were observed by Allain [3] who reported on the properties of low SFE Fe22Mn0.6C TWIP steel with an ultimate tensile stress of 1400 MPa and a true uniform elongation of  $\sim 0.5$ . Allain et al. [2] have published flow curves for Fe22Mn0.6C steel (SFE 12–35 mJ/m<sup>2</sup>) clearly showing the serrated flow of DSA, but they did not discuss the implications of this feature in their paper. Similar observations were made by Karaman et al. [7] for Fe12Mn1.2C steels (SFE 23 mJ/m<sup>2</sup>) for which twinning produces a higher strain-hardening than the one observed in austenitic steels not experiencing twinning. Fe12Mn1.2C single crystals, oriented along [001] and [111] for multiple slip, had serrated flow curves when deformed in compression. Hong et al. [18] reported on the Fe32Mn12Cr0.4C TWIP steel in the  $-150^{\circ}\text{C}$  to  $+150^{\circ}\text{C}$  temperature range. No DSA and no negative SRS were observed in this case. The observations of Grassel et al. for Fe25Mn3Si3Al TWIP steel [1] were similar. Vercammen [5], who studied Fe30Mn3Al3Si TWIP steel, did not discuss the serrations present on the measured flow curves. He reported that no local necking occurred prior to fracture, a strong indication for low or negative strain rate sensitivity.

The present contribution will mainly focus on the tensile properties of type of TWIP steel which are currently getting most of the attention for the industrialization of TWIP steels: X60Mn22 and X60Mn18. Note that these TWIP steels may also be Al- and/or Si-alloyed. These additions are made in order to control the stacking fault energy. The typical microstructure of this type of TWIP steels is shown in Fig. 10.2.

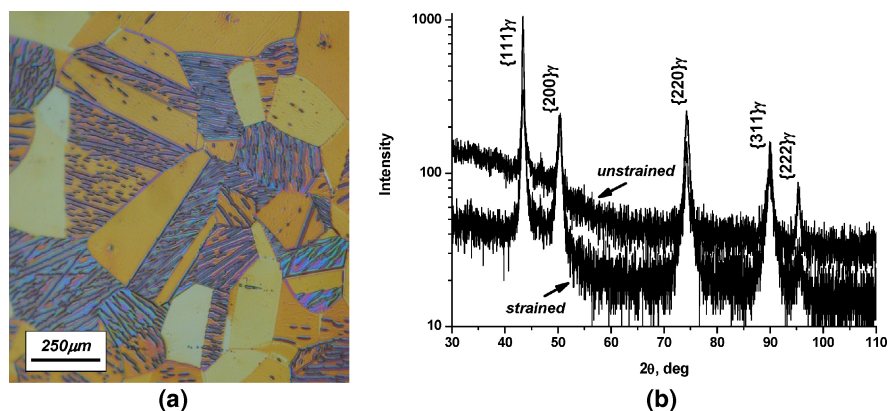


**Fig. 10.2** Typical microstructure of a high Mn FeMnC TWIP steel (a). During uniaxial straining the microstructure is stable against strain-induced transformation to  $\epsilon$  or  $\alpha'$ , as shown by the XRD data (b). Note that the use of a logarithmic scale for the intensity is to allow for a better observation of small amounts of transformation products.

## 10.2 Experimental

The experimental results reported in the present contribution focus on capturing the dynamic nature of the deformation process of high Mn FeMnC TWIP steel. Most tensile tests were carried using a screw driven ZWICK Z100 machine equipped with an automated high resolution mechanical strain gauge. A CEDIP Silver 420M camera was used to monitor specimen temperature by high resolution infrared thermo-graphy. The temperature space resolution of the camera was  $3\sim5\text{ }\mu\text{m}$  and the temperature sensitivity was 20 mK. A VIALUX Autogrid automated optical grid analysis system was used to measure the strain distribution in situ during deformation. The data acquisition system allowed for the simultaneous capture of flow curve, localized strain and thermographs. In addition, the microstructures before and after tensile testing were studied by conventional transmission electron microscopy (CTEM) using a PHILIPS Tecnai operated at 200 keV.

## 10.3 Results

At low strain rates ( $\sim 10^{-3}\text{ s}^{-1}$ ) and a true strains less than 0.45, the room temperature stress-strain curve of Fe-18-Mn-0.6C TWIP steel often displays step-like discontinuities in stress, separated by plateau regions in which the deformation proceeded with a small increase of the stress. These “type A” serrations, are caused by the repetitive continuous propagation of localized deformation bands, PLC bands, moving smoothly from one end of the specimen to the other along the specimen length. At a true strain of 0.45, the stress-strain curve shows random serrations. These multiple un-correlated discontinuities in the stress-strain curve are usually referred to as “type B” serrations. For typical type A serrations, the stress-strain curve is flat during band propagation as all the deformation is concentrated in the band only. In the present case “modified Type A” bands were observed, the stress-strain curve was not flat during band propagation and it showed a small continuous increase in the plateau region. This suggests that there was some strain hardening in the region outside the PLC band. PLC bands are usually observed for materials with negative strain rate sensitivity. This was also observed for TWIP steels. Figure 10.3 shows that the strain rate sensitivity assumed a very small value and at low strains, negative values. In comparison, the strain rate sensitivity values for low C Al-killed steels are typically  $\sim 0.015$ , and the strain rate sensitivity of HSLA steels is in the 0.005–0.010 range.

Figure 10.4 illustrates the time-dependence of stress, strain and temperature at the center of the specimen. The stress showed a discontinuity, each time a single deformation band was initiated at one end of the specimen. During the plastic deformation, the temperature at the specimen center increased each time the PLC band passed the measuring point. In Fig. 10.4, it can be seen that the temperature increase was  $\sim 5^{\circ}\text{C}$  for the first deformation band and increased to  $\sim 20^{\circ}\text{C}$  for the last PLC band. In the

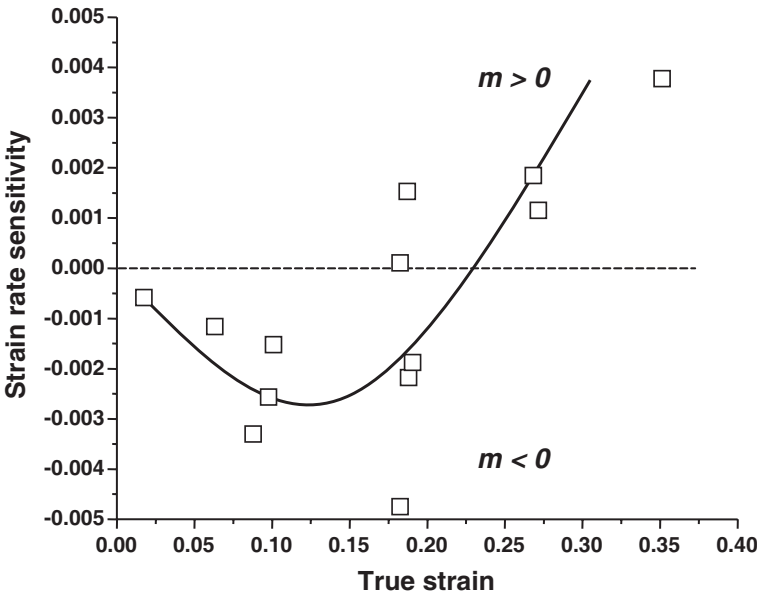


Fig. 10.3 Strain rate sensitivity of Fe18Mn0.6C TWIP steel.

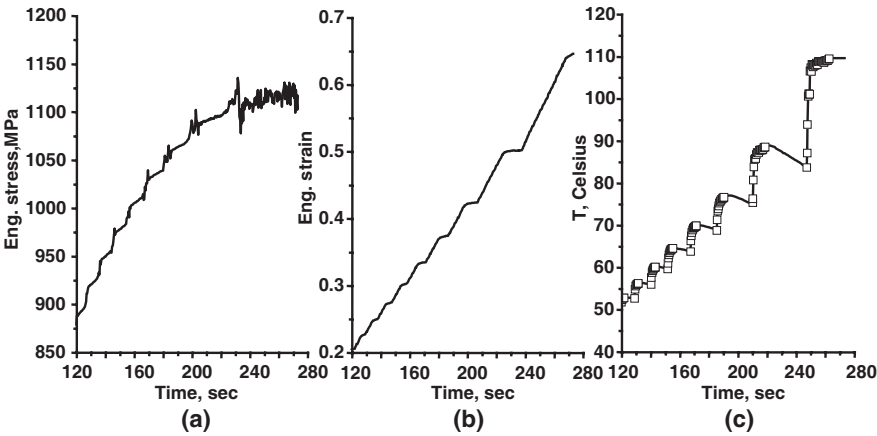
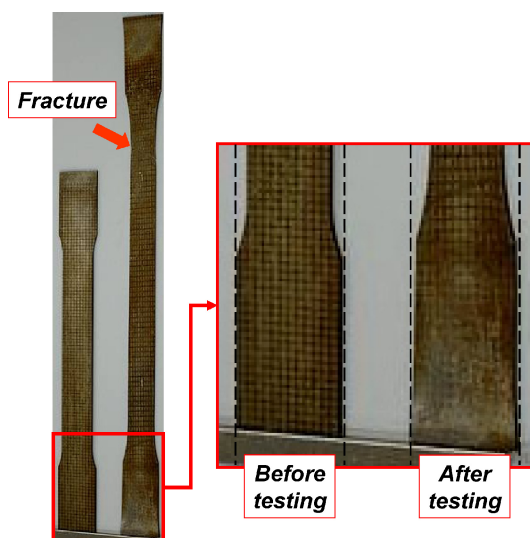


Fig. 10.4 Time dependence of the engineering stress (a), engineering strain (b) and mid-sample position temperature (c) during the tensile deformation of a TWIP steel. Type A serrations are characterized by sudden steep rises in stress and plateau-like features in the strain. The steep rise in stress corresponds to the initiation of a PLC band outside the strain gauge measuring range. The plateau segment in strain corresponds to the passage of the PLC band outside the strain gauge measuring range. The passage of a PLC band in the measuring gauge range increases the strain, and is associated with a small increase in stress. A pronounced increase in temperature occurs each time a PLC band passes through the center of the sample.

**Fig. 10.5** TWIP steel tensile specimens before and after testing (left). The extensive deformation of the ends of the sample reveals the importance of these sample neck as a nucleation place of the successive PLC bands.



time between the passages of two successive PLC bands, the temperature decreased only very slightly. The final temperature prior to fracture was typically  $\sim 100^{\circ}\text{C}$ .

The successive deformation bands tended to be nucleated at the end of the specimen as illustrated in Fig. 10.5. The bands tended to be initiated at one end of the specimen, and moved to the opposite end of specimen, producing a strain increment in their wake. A possible explanation may be provided by the fact that the specimen shoulders acted as stress concentrators.

The highly concentrated deformation caused by the PLC bands resulted in a pronounced local heating. This made it possible to record thermographs and the temperature profile from each of the individual narrow bands moving through the sample as shown in Figs. 10.6 and 10.7. The overall picture that emerges from the observations is that, as a result of the very low heat conductivity of the material, adiabatic conditions prevail. Each PLC band leaves behind a nearly uniform temperature increment. In other words, after the passage of a band, the specimen is heated uniformly. When a next band starts propagating, it sees this increase background temperature and leaves behind a further temperature increment, which is larger, as the strain in the band is higher. Due to a relatively sharp decay of the excess temperature in front of a moving band, a more or less abrupt step in the temperature increment is seen in front of the band. With the progress of straining, this step becomes more diffuse as the band velocity is decreased.

As a PLC band moved through the specimen, the rest of the specimen underwent little or no deformation, except for an elastic deformation. Due to the finite width of the band and the finite width of the slip distance of the dislocations in the band, the plastic flow spilled over to the adjacent undeformed region, and the band propagated through the sample. The PLC bands were typically about 4 mm wide and were inclined at  $53.1^{\circ}$  to the tensile axis. This angle is close to  $54.74^{\circ}$ , the characteristic angle for localize necking of an isotropic material prior to fracture.

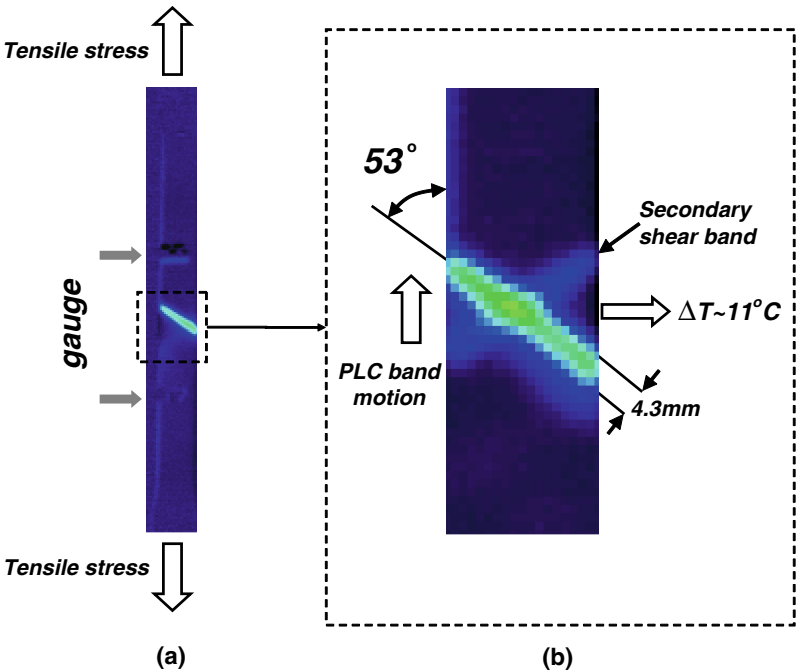


**Fig. 10.6** IR Thermograph of a propagating PLC band (a). The band is initiated at the bottom of the specimen, and moves to the opposite end of specimen, straining the whole specimen. Enlargement of the thermograph of a deformation band (b) at a true strain of 0.38,  $\Delta T = 11.4^\circ\text{C}$ .

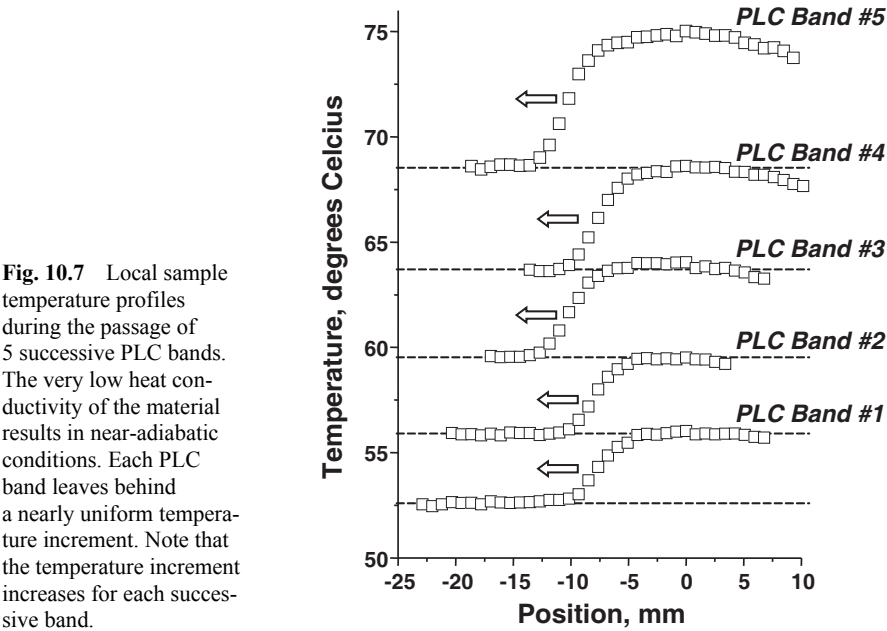


**Fig. 10.7** Local sample temperature profiles during the passage of 5 successive PLC bands. The very low heat conductivity of the material results in near-adiabatic conditions. Each PLC band leaves behind a nearly uniform temperature increment. Note that the temperature increment increases for each successive band.

The small deviation observed in the present case may be due to the normal anisotropy of the tested TWIP steel. The angle is a clear indication of the fact that the strain along the band is prevented by the undeformed regions adjoining the band.

The PLC band velocity decreased linearly with strain. This implies that the material was strengthened when a band passed through the specimen and a large amount of barriers to plastic flow were generated, suppressing the movement of successive bands. The specimen fractured when the motion of the bands was fully suppressed, i.e. when the band velocity became zero. Assuming that the band velocity was equal to the dislocation velocity, the measured fraction of mobile dislocations ( $10^{10}$ – $10^{11}\text{m}^{-2}$ ) was found to be low, consistent with the fact that serrated flow is caused by an effective pinning of the dislocations. The effective strain rate in the deformation band was very high due to the localized nature of the deformation, a considerable local strain rate increase by a factor of 100 was measured.

The strain associated with an isolated PLC band was obtained by local strain analysis before and after the passage of a PLC band. Typical results are shown in Fig. 10.8. As the strains were registered continuously, the passage of individual bands and their associated strains could be observed readily by the discontinuous jumps of the local value of the major strains. Note that, as the thickness and width strains were found to have very similar values, the normal anisotropy (*r*-value) of TWIP steel is close to unity.

A direct consequence of the previous observations is that they allow for a better understanding of the behaviour of TWIP steel during the hole expansion test. In contrast to standard deep drawing steels, most advanced high strength steel (AHSS) grades have a low hole expansion performance. The hole expansion ratio (HER) is a measure of stretch flangability, reflecting the risk of a cut edge cracking during

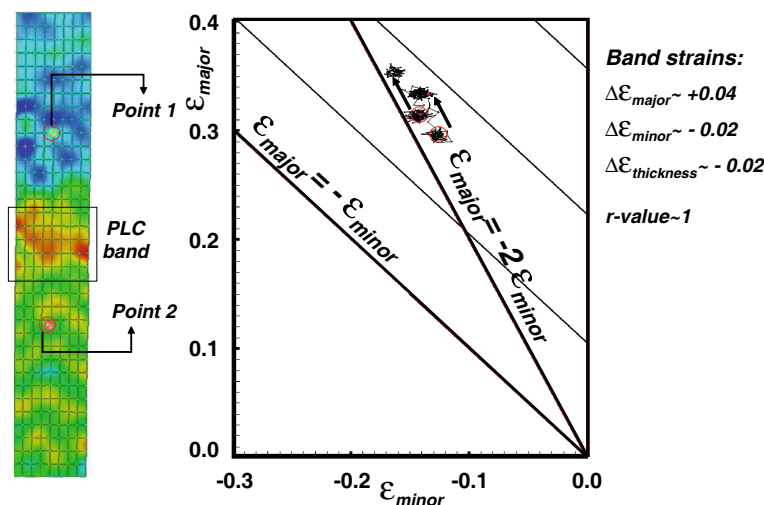


**Fig. 10.8** In situ PLC band strain measurement. Note that the width and thickness strains are equal. The observed strain path is a clear indication that the normal anisotropy is very close to 1. Note that since the PLC band is only a few millimeters, the strain parallel to the band must be zero.



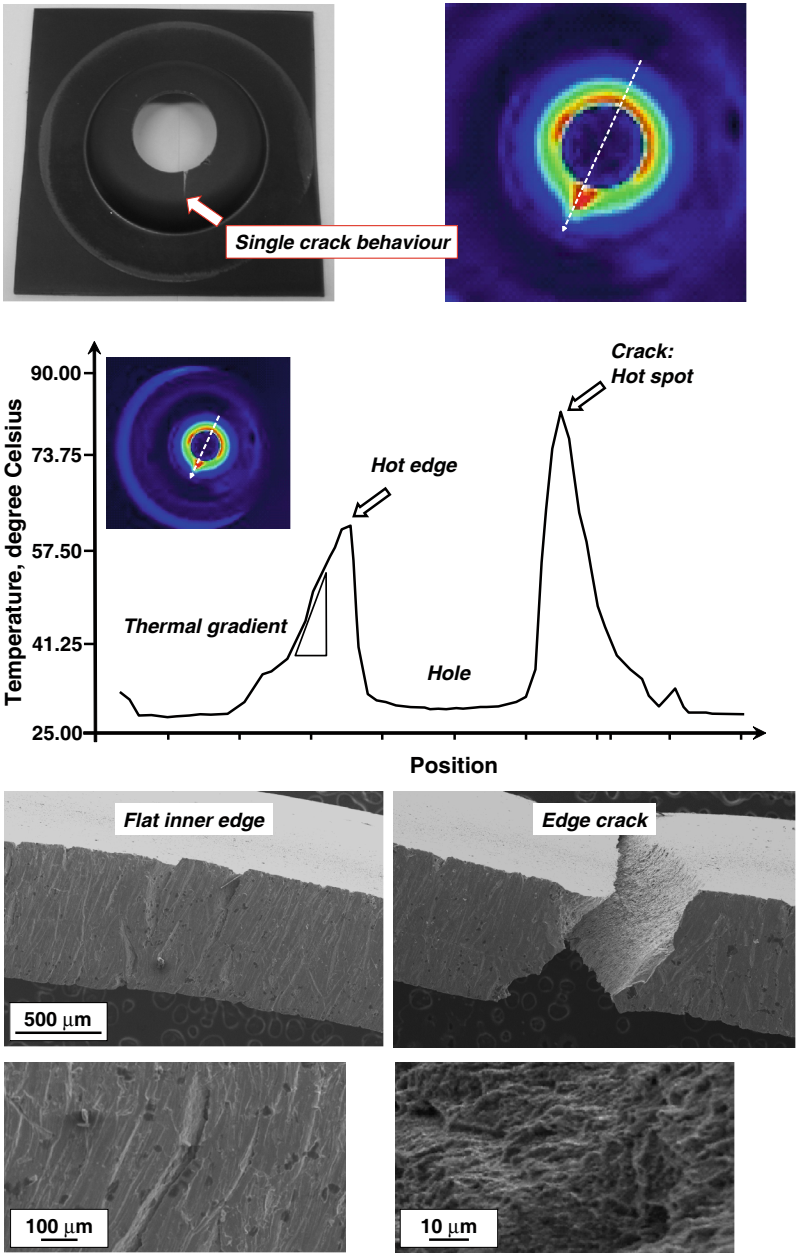


**Fig. 10.9** Hole expansion behaviour of TWIP steel. TWIP sample exhibiting the characteristic single crack failure (top, left). Thermograph of the same sample during the crack propagation stage. Temperature profile of the sample during the hole expansion test, revealing the extensive local heating at the crack tip (middle). SEM micrographs of the inner edge of the hole expansion sample (below), showing the presence of a large amount of micro-cracks (below, left) and the very finely dimpled fracture surface of the single large crack (below, right).

forming operations. It is one of the critical properties of sheet steel. Figure 10.9 shows the main characteristics of the hole expansion behaviour of TWIP steel. Thermo-graphic analysis of the sample during hole expansion revealed a pronounced local heating of the edge. In the present case, the local temperature in the crack reached almost 90°C during the crack initiation and propagation stage. These observations are in agreement with the quasi-adiabatic conditions observed during the tensile deformation. They are due to the low thermal conductivity of TWIP steels. SEM micrographs of the inner edge of the hole expansion sample showed the presence of a large amount of micro-cracks. Despite the fact that the flat appearance of the macroscopic crack surface suggests that failure is by brittle crack propagation, fractographic analysis of the fracture surface at high magnification revealed the presence of very small dimples. The sudden failure is very likely the result of the very small value of the strain rate sensitivity.

## 10.4 Microstructural Analysis

The microstructures of undeformed and deformed high Mn FeMnC TWIP steel were studied by TEM. Byun [11] has shown that the dissociation of a dislocation segment in the screw orientation can become comparable to the grain size when the shear stress reaches a critical value. This critical shear stress is the twinning stress. For a SFE of 20 mJ/m<sup>2</sup>, this critical stress is 267 MPa (Fig. 10.10). Deformation twinning

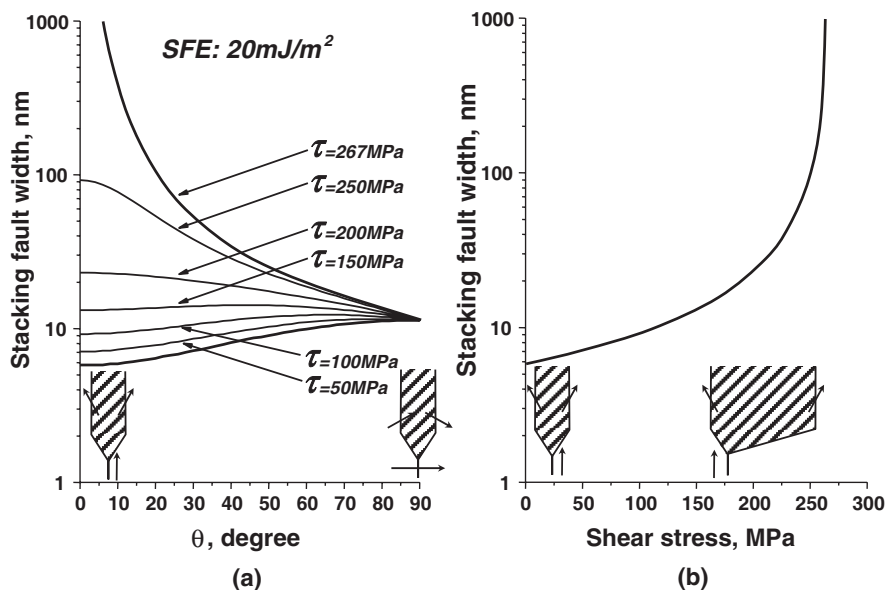


**Fig. 10.10** Schematic showing the change in dissociation width at increasing shear stress on the glide plane for SFE = 20 mJ/m<sup>2</sup>. One of the partial dislocations of a dislocation in the screw orientation ( $\theta = 0$ ) can undergo run-away when the shear stress exceeds 267 MPa (b).

does not initiated from the start of plastic deformation. Dislocation generation and glide are predominant deformation mechanisms at low strains. As the flow stress increases with strain, the size of the stacking faults will increase, and eventually the critical twinning stress will be achieved. The TEM observations support this model of twinning-induced plasticity. In the undeformed samples, large grains ( $\sim 30\ \mu\text{m}$ ) and wide annealed twins ( $\sim 500\ \text{nm}$ ) were observed. The dislocation density before testing was very low. However, widely dissociated partial dislocations and wide stacking fault were observed. This is indicative of the low stacking fault energy of FeMnC. From the available literature data, based mainly on theoretical calculations, the stacking fault energy of the Fe-18-Mn-0.6C TWIP steel used for the present research was

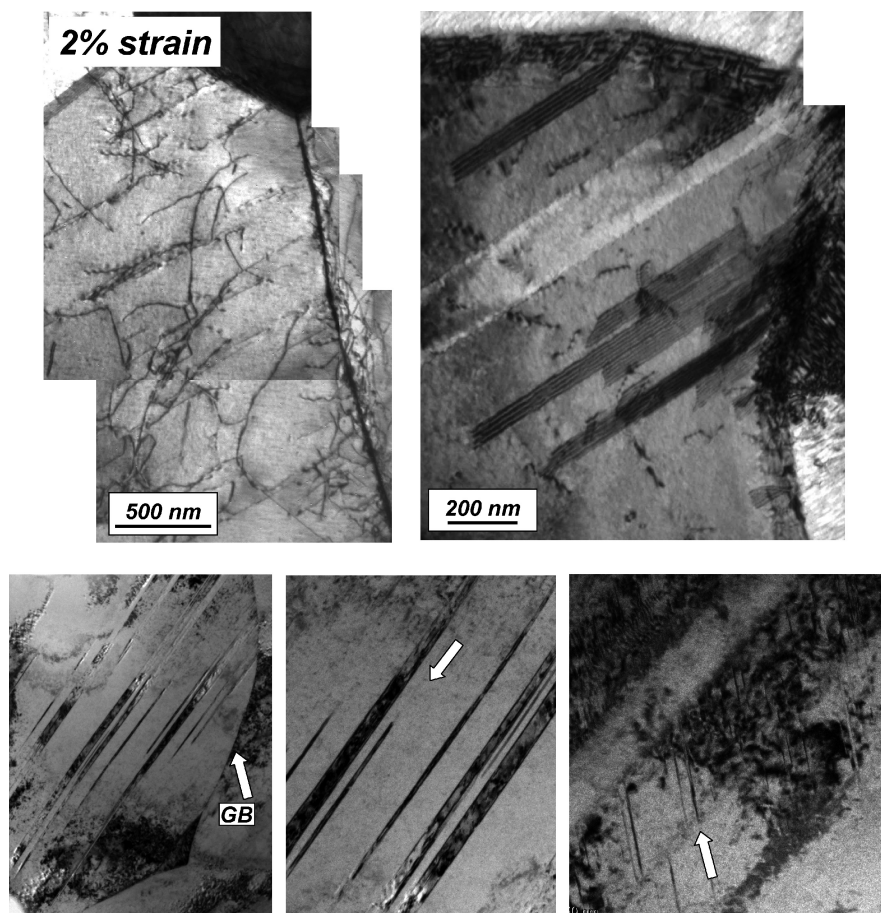


**Fig. 10.11** TEM micrograph of deformed TWIP steel. At low strains, isolated dislocations and some stacking faults are observed (2% strain, top). Large amounts of twins are observed in the microstructure at larger strains (10% strain, below). The larger twins are often parallel to one of the  $\langle 110 \rangle$  directions within individual grains. These twins terminate at grain boundaries. They are also internally faulted by micro-twin formation (below, right).

about  $20 \sim 30 \text{ mJ/m}^2$ . At low strains (2% strain, Fig. 10.11), isolated dislocations and some stacking faults were observed. Large amounts of twins were observed in the microstructure at larger strains (10% strain, Fig. 10.11). The larger twins were often parallel along a single  $\langle 110 \rangle$  direction within individual grains. These twins terminated at grain boundaries. They were also internally faulted by micro-twin formation. At fracture, the mean width of larger deformation twins was about 60 nm. A high density of micro-twins was formed within the major twins. No evidence for the formation of h.c.p.  $\epsilon$ -martensite or b.c.c./b.c.t.  $\alpha'$  martensite was found.

## 10.5 Discussion

The plastic deformation of TWIP steel exhibits a complex combination of different phenomena. Their characteristic, high rate of strain hardening ( $n > 0.4$ ) is caused by deformation twinning and/or a pronounced planar glide. The pronounced DSA and the negative strain rate sensitivity are related to solute-dislocation interactions. In the following paragraph it will be argued that, in the case of Fe18Mn0.6C TWIP steel, these phenomena are very likely interacting strongly with each other.

The origin of the high rate of strain hardening of TWIP steel at room temperatures is yet not known and different theories have been proposed. They are reviewed schematically in Fig. 10.12. In the low SFE theory, it is assumed that the width of the stacking faults will reduce the frequency of cross slip to such an extent that planar slip will prevail and cause the high strain hardening rate (Fig. 10.12 (a)).

Since a low SFE facilitates deformation-induced twinning during plastic straining, Bouaziz and Guelton [4] suggested that deformation twinning had a strong influence on the work-hardening rate of TWIP steel. They argue that the density of fine twins increases during deformation and gradually reduces the effective grain size. The mean free glide distance of dislocations will steadily be reduced as the twin boundaries act as effective barriers to their motion. This “dynamical Hall-Petch effect” causes the high strain hardening (Fig. 10.12 (b)). The stacking fault energy may not be the only parameter influencing the strain hardening and Gerold and Karnthaler [13] argue that short range order (SRO) or short range clustering (SRC) in solid solution are the main cause of planar slip in f.c.c. materials. Planar slip can actually occur in high stacking fault energy alloys. During planar slip, dislocations cannot easily avoid obstacles to their glide, and this results in an increased strain hardening (Fig. 10.12 (c)). The origin of planar glide in concentrated solid solutions exhibiting SRO or SRC is due to the fact that dislocation glide removes the order or the clustering (Fig. 10.12 (d)). The glide of a first dislocation on a glide plane requires a higher stress than the following dislocations on the same glide plane. The higher stress is provided by trailing dislocations, generated by a dislocation source, on the leading dislocation. The high stress on the leading dislocation increases its velocity and plastic deformation, as the trailing dislocations face a reduced lattice resistance after the passage of the first dislocation. The phenomenon, a fast deformation localized on a single glide plane, is known as “glide softening”.

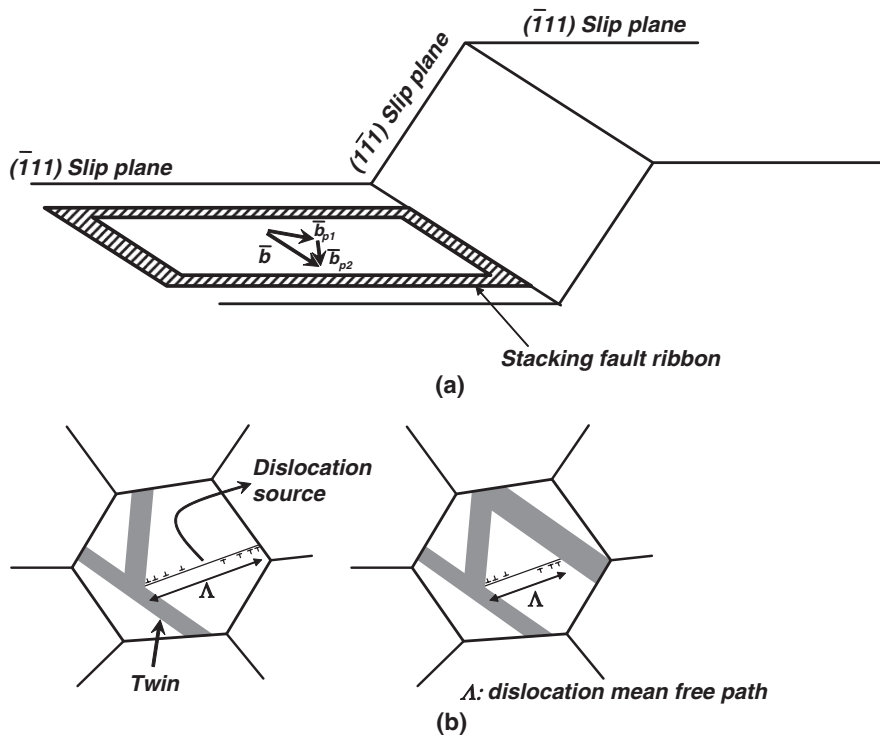


**Fig. 10.12 (a), (b)** (a) Low SFE model: a low SFE leads to widely dissociated partial dislocations, which cannot cross slip. This leads to a pronounced planar slip and results in a high strain hardening rate. (b) Dynamic Hall-Petch model of Bouaziz-Guelton: at low SFE, twinning is promoted. The intersection of twins forms a cell structure. The twin boundaries act as obstacle for dislocation glide.

In FeMnC alloys the SRO or SRC is very likely of a statistical nature, and related to the formation of octahedral clusters by substitutional Mn and interstitial C atoms (Fig. 10.12 (d)). Owen and Grujicic [12] have proposed a local-order model, in which the ordering is measured by the likelihood that a C atom will occupy the interstitial position in an octahedral cluster of metal atoms with  $n$ , an integer between 0 and 6, Mn nearest neighbors. They were able to calculate the stress opposing dislocation motion for a single isolated dislocation and for a sequence of dislocations moving on the same slip plane, and provided an adequate description of DSA in high Mn alloys.

Dastur and Leslie [6] have proposed an extension of the Cottrell theory of DSA in low carbon steels to explain the phenomenon of rapid strain hardening in Mn steels. According to them, the high rate of strain hardening is associated with serrated stress-strain curves characteristic of DSA, and negative strain rate sensitivities. In this model, the attractive interaction between C and Mn atoms leads to the formation of Mn-C pairs. These atomic pairs can interact with dislocations by their fast reorientation at the core of moving dislocations (Fig. 10.12 (e)).

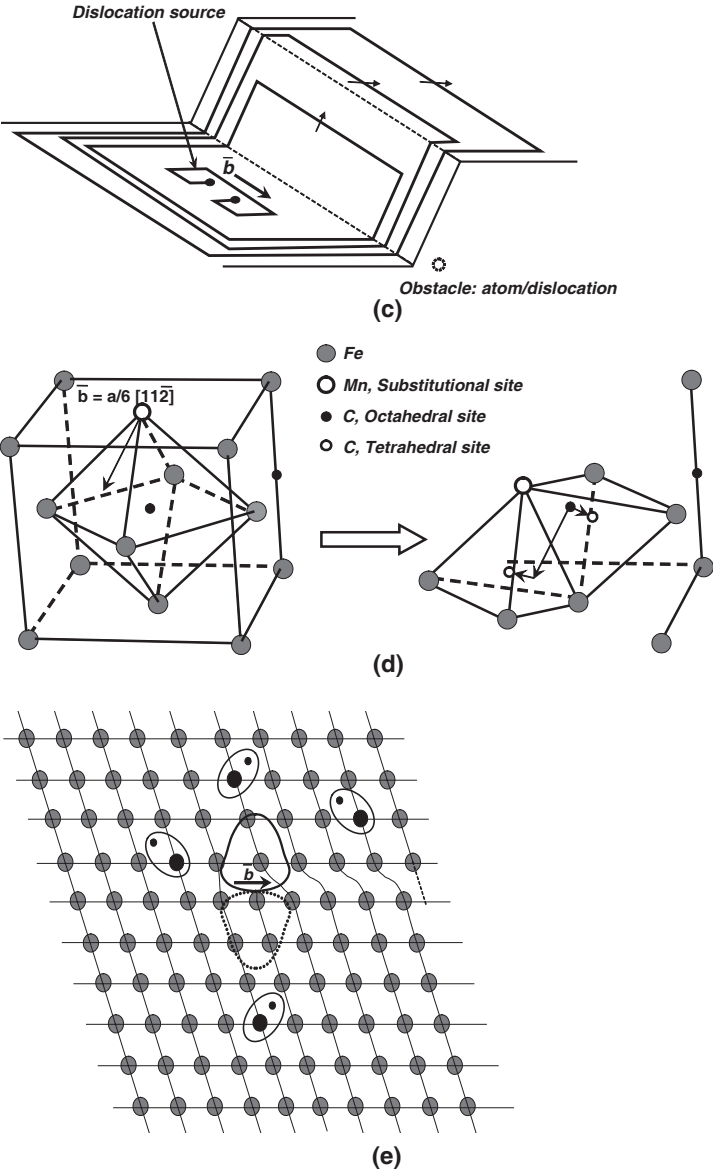


**Fig. 10.12 (c), (d), (e)** (c) Planar slip model: in concentrated solid solution alloys, short range order (SRO) is possible and dislocations will destroy the SRO on their slip plane. Whereas the leading dislocation experiences a high resistance to its motion, subsequent dislocations can glide more easily in the same slip plane. This favors planar slip and result in a high rate of strain hardening. (d) Illustration of the reduction of the SRO during the passage of partial dislocation on their glide plane: the octahedral clusters are sheared and the C atoms are transferred to tetrahedral interstitial sites. Left: before slip. Right: after slip. (e) Dastur-Leslie model: dynamic strain aging in FeMnC alloy is caused by the re-orientation of Mn-C clusters in the dislocation stress field during dislocation motion.

In low SFE interstitial f.c.c. alloys, a  $1/6\langle 112 \rangle$  type shear disturbs the original f.c.c., ABCABC stacking sequence and traps the interstitial C atoms in transient interstitial position as illustrated in Fig. 10.12 (d). In the case of a single partial dislocation, a C atom will be transferred from an octahedral position to a tetrahedral position, and back to an octahedral position when the f.c.c. lattice is restored by the trailing partial dislocation. For a twinning dislocation the situation is different for two reasons: (a) there is no trailing partial dislocation restoring the f.c.c. lattice, and (b) there is a partial on every successive slip plane. In both cases the C atoms are transferred to higher energy tetrahedral positions, from which they can jump to reposition themselves in an octahedral position, considering the relatively small activation required for this. In the case of dislocation motion, if the C atoms can reposition themselves in an octahedral site before the passage of the trailing partial, this will require a higher stress.

## 10.6 Conclusion

The development of high Mn TWIP steel faces a number of important technical challenges related to steelmaking and processing, before TWIP sheet steel can be made widely available to the automotive industry. In addition, the TWIP steels must be developed as a different class of steels and a number of grades with specific strength-elongation characteristics will have to be developed to meet specific needs of the automotive industry. One particular challenge is the fact that TWIP steels have relatively low yield strengths. This implies that the high tensile strengths are only available after the considerable straining of the material. This is illustrated in Fig. 10.13. As true strains of 1.0 and more are only rarely achieved during the press forming of car body parts, some steelmakers are evaluating the option of cold rolling TWIP to certain strength levels as a means to develop strength-elongation classes on the basis of a single composition.

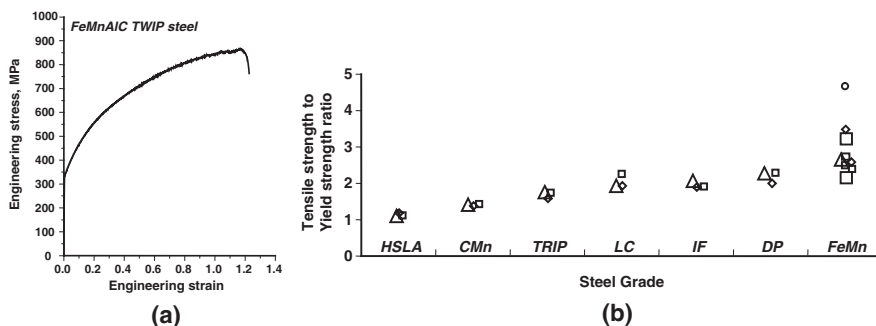


**Fig. 10.13** Stress strain curve illustrating the considerable strain hardening of high Mn TWIP steels (a). Comparison of the ratio of tensile strength to yield strength for different steel grades (b).

From a technological point of view, the PLC phenomenon, and hence DSA, must be avoided. This ensures stable material behavior during sheet forming processes as DSA gives rise to non-homogeneous plastic flow and may lead to surface defects on formed parts. The impact of the pronounced DSA during the press forming of TWIP steels has not yet been studied. As a rule, DSA and negative strain rate sensitivity lead to lower uniform elongations and smaller post-uniform elongations. In other words, DSA has a negative influence on formability. It must also be taken into account that DSA is usually observed within a specific critical strain and strain rate interval. In general, the critical strain for DSA increases when the strain rate increases. This is illustrated schematically for TWIP steel in Fig. 10.14. This would tend to suggest that no detrimental effects are to be expected from DSA if the strain rates during press forming are high enough. Press forming is however usually carried out at strain rates in the DSA-free region, and therefore it should not be a cause of much concern. In addition, TWIP grades with higher SFE are being developed to address this problem. Having said this, the relatively low strain rate sensitivity of TWIP steels is also detrimental in press forming, as there can only be a very limited useful stretching after the onset of diffuse necking.

High Mn steels have a lower thermal conduction compared to ferritic steel. In addition, they are characterized by a higher thermal expansion. Both properties must be taken into account when combining TWIP steel and low carbon ferritic steels in car bodies.

Finally, it is well known that unstable austenitic stainless steel grades are subject to a catastrophic type of damage often referred to as “delayed fracture”, resulting from the combination of high residual stresses and the presence of martensitic phases in the microstructure of pressed parts. This phenomenon, which can also be observed in certain TWIP steels (Fig. 10.15), has been related to H-cracking, and should also be carefully examined in the case of the high Mn steels.

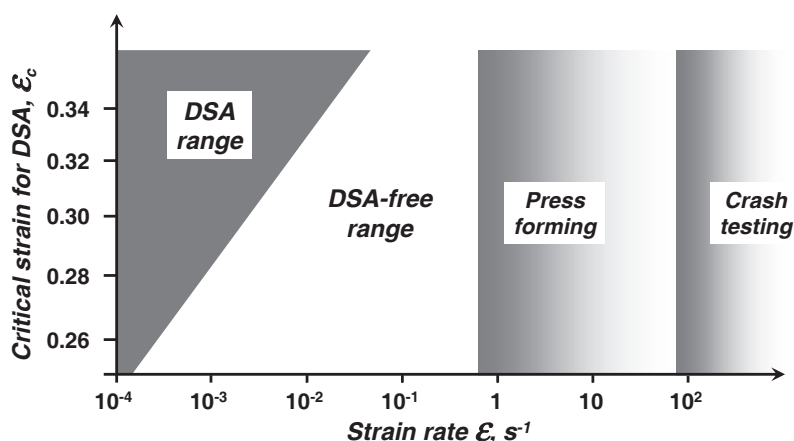


Fig. 10.14 Schematic showing the strain rate range in which DSA occurs for FeMnC TWIP steel.





**Fig. 10.15** Example of delayed fracture in deep drawn FeMnC TWIP steel.

**Acknowledgement** The authors gratefully acknowledge financial support of POSCO. The FeMnC austenitic TWIP steel was provided by the POSCO Technical Laboratories, South Korea.

## References

1. O. Grässel, L. Krüger, G. Frommeyer, L.W. Meyer, *Int. J. Plast.*, 16 (2000), 1391
2. S. Allain, J.-P. Chateau, O. Bouaziz, *Mater. Sci. Eng.* A387–389 (2004) 143
3. S. Allain, Doctoral Thesis, Institut National Polytechnique de Lorraine, 2002
4. O. Bouaziz, N. Guelton, *Mater. Sci. Eng.*, A319–321 (2001), 246
5. S. Vercammen, Doctoral Thesis, Katholieke Universiteit Leuven, 2004
6. Y. N. Dastur, W.C. Leslie, *Metall. Trans.*, 1981, 12A, 749
7. I. Karaman, H. Sehitoglu, K. Gall, Y.I. Chumlyakov, H.J. Maier, *Acta Mater.*, 48, 2000, 1345
8. S. Kibey, J.B. Liu, M.J. Curtis, D.D. Johnson, H. Sehitoglu, *Acta Mater.*, Vol. 54, 2006, 2991
9. E. Bayraktar, F.A. Khalid, C. Levaillant, *J. of Material Processing Tech.*, Vol. 147, 2004, 145
10. B.X. Huang, X.D. Wang, Y.H. Rong, L. Wang, L. Jin, *Mater. Sci. Eng.*, Vol. A438–440, 2006, 306
11. T.S. Byun, *Acta Materialia*, 51 (2003), 3063
12. W.S. Owen, M. Grugicic, *Acta Mater.*, Vol. 47, No. 1, 1999, 111
13. V. Gerold, H.P. Karnthaler, *Acta Metall.*, Vol. 37, 1989, 2177
14. F. Laves, *Acta Metall.*, Vol. 14, 58, 1966
15. J.W. Cahn, *Acta Metall.*, 25, 1621, 1977



Han Soo Kim  
Assistant Professor  
Materials Design Laboratory  
GIFT, Pohang  
South Korea



## Chapter 11

# Third Generation of AHSS: Microstructure Design Concepts

David K. Matlock and John G. Speer

**Abstract.** In recent years there has been an increased emphasis on the development of new advanced high strength sheet steels (AHSS), particularly for automotive applications. Descriptive terminology has evolved to describe the “First Generation” of AHSS, i.e. steels that possess primarily ferrite-based microstructures, and the “Second Generation” of AHSS, i.e. austenitic steels with high manganese contents which include steels that are closely related to austenitic stainless steels. First generation AHSS have been referred to by a variety of names including dual phase (DP), transformation induced plasticity (TRIP), complex-phase (CP), and martensitic (MART). Second generation austenitic AHSS include twinning-induced plasticity (TWIP) steels, Al-added lightweight steels with induced plasticity (L-IP<sup>®</sup>), and shear band strengthened steels (SIP steels). Recently there has been increased interest in the development of the “Third Generation” of AHSS, i.e. steels with strength-ductility combinations significantly better than exhibited by the first generation AHSS but at a cost significantly less than required for second generation AHSS. Approaches to the development of third generation AHSS will require unique alloy/microstructure combinations to achieve the desired properties. Results from a recent composite modeling analysis have shown that the third generation of AHSS will include materials with complex microstructures consisting of a high strength phase (e.g. ultra-fine grained ferrite, martensite, or bainite) and significant amounts of a constituent with substantial ductility and work hardening (e.g. austenite). In this paper, design methodologies based on considerations of fundamental strengthening mechanisms are presented and evaluated to assess the potential for developing new materials. Several processing routes will be assessed, including the recently identified Quenching & Partitioning (Q&P) process developed in the authors’ own laboratory.

---

D.K. Matlock and J.G. Speer

Advanced Steel Processing and Products Research Center, Colorado School of Mines, Golden, Colorado 80401, USA

## 11.1 Introduction

Current automotive designs that utilize sheet steels and emphasize optimization of both vehicle weight and performance, e.g. fuel economy along with crash worthiness for safety and stiffness for drivability, require higher strength materials with good combinations of strength, formability, fatigue resistance, and toughness. As a consequence of the increased demands on steels, new products referred to as “advanced high strength sheet steels” (AHSS) have been designed and are now being utilized. To optimize material designs, automotive manufactures are incorporating a variety of different higher-strength materials into assemblies. For example, it was recently reported [1] that the number of different materials used in the construction of a body-in-white (BIW) for a recent (2006) models increased from approximately 5 materials seven years ago to over 10 materials for the vehicle produced today. The material types and portions by weight for the current vehicle are seven steel grades (91%), two aluminum grades (3%), and thermoplastics and other materials (6%) [1]. During this same time period the average yield strength for the BIW materials also increased by 50%, from approximately 200 MPa to 300 MPa.

New AHSS steels are sometimes referred to by “generation” and those steels in the “first generation” include dual phase (DP), transformation induced plasticity (TRIP), complex-phase (CP) and martensitic (MART) steels [2]. A desire to produce materials with significantly higher strengths has led to the development of a “second generation” of AHSS which are austenitic steels with high manganese contents and are closely related to conventional austenitic stainless steels. First and second generation AHSS exhibit a wide variety of deformation behaviors as

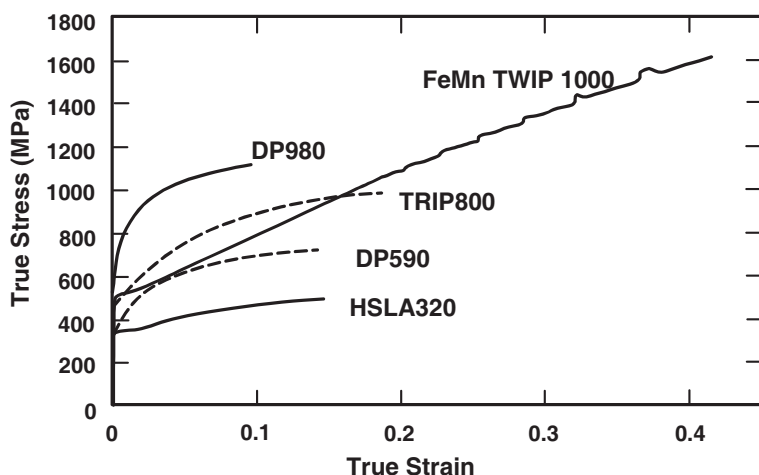


**Fig. 11.1** Stress strain curves for typical first and second generation AHSS. Data are plotted approximately up to the point of necking and thus maximum strains represent the true uniform strain at instability. Adapted from [3].

illustrated in the family of true stress versus true strain curves presented in Fig. 11.1 [3]. Figure 11.1 includes data for HSLA320, a steel primarily consisting of ferrite and cementite with a minimum yield strength of 320 MPa, and selected AHSS grades: two DP steels consisting primarily of ferrite with dispersed martensite and with minimum ultimate tensile strengths (UTS) of 590 or 980 MPa; TRIP800 with an 800 MPa minimum UTS consisting of ferrite and a combination of other constituents including retained austenite; and TWIP1000, a Fe-Mn austenitic steel with a minimum UTS of 1000 MPa. In comparison to HSLA320, the DP steels exhibit high strain hardening rates at low strains owing to the effects of martensite, along with good ductilities relative to the tensile strengths achieved. The TRIP1000 exhibits initial strain hardening rates between the HSLA and DP steels, but higher strain hardening rates at high strains due to deformation induced transformation of austenite to martensite, leading to the observed higher uniform strain. The TWIP1000 also exhibits an inflection on yielding followed by an essentially constant work hardening behavior (ignoring localized variations associated with serrations due to dynamic strain aging), a consequence of deformation twinning that is maintained up to high strains leading to the high ductility. As illustrated in Fig. 11.1, AHSS steels can be designed with significantly different deformation behaviors and understanding the differences in behavior is critical in order to make the correct choice for a specific vehicle component design.

Figure 11.2 maps typical AHSS yield strength/ductility combinations and compares these to “conventional” low strength (interstitial free, IF; bake hardenable, BH; or mild steels) or high strength (carbon manganese – CMn or high strength low alloy – HSLA) sheet steels [2]. This figure has evolved from numerous publications and is widely employed as a frame of reference for assessing new AHSS developments. The property band that includes DP, TRIP, CP, and MART steels (referred to as “first generation” AHSS [2]) incorporates other steels that also possess primarily ferritic-based microstructures. Within the band the advantageous properties of TRIP steels, i.e. higher elongations for a specific strength range, are evident. Developments continue to enhance the properties of first generation AHSS as evidenced by recent work on a new class of steels with retained austenite and controlled amounts of martensite produced by the quenching and partitioning process (Q&P) and having properties superior to the MART steels [4]. The first

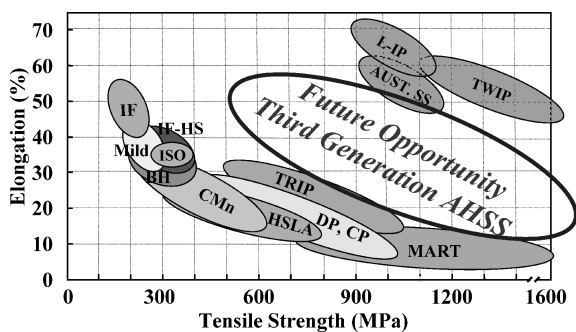


**Fig. 11.2** Summary of tensile strength and tensile elongation data for various classes of conventional and advanced high strength sheet steels (AHSS) [2].

generation of AHSS is well established and properties and applications have been summarized in a recent IISI guidelines publication [5]. Figure 11.2 also shows property combinations for these steels referred to as twinning-induced plasticity (TWIP) steels or lightweight steels with induced plasticity (L-IP<sup>®</sup>), along with the material property band for typical austenitic stainless steels. Similar materials that use shear band formation for strengthening (SIP steels) are also currently being developed [2]. For high-production automotive applications these second generation AHSS steels are attractive due to their excellent formability. However, the steels offer processing challenges relative to low carbon sheet steels and are expensive due to the high alloy additions required to produce an austenitic microstructure. Currently there is increasing interest to develop a new class of steels, referred to as the “third generation” advanced high strength steels, with anticipated properties in the intermediate band identified in Fig. 11.1 [2]. If high strength steels could be produced with enhanced properties, e.g. tensile strength of 1000 MPa combined with a total elongation of 30%, but without the level of expensive alloy additions required in the second generation AHSS, then significant use of these steels might be economically incorporated into advanced automotive designs.

The fundamental basis for the strength-elongation response of the various steel classes summarized in Fig. 11.2 is well-founded in the historical steel literature. The basics for development of the first generation AHSS were the subject of several conferences in the 1970s and early 1980s on HSLA and DP steels [6–9], and the results of those conferences remain important resources today. More recently a systematic analysis which provides a basis for development of the “third generation” AHSS steels was presented [10]. The analysis considered strengthening mechanisms in AHSS and developed predictions of new material properties based on a simplified composite model. The results of the previous paper [10] are summarized here and are extended to provide a more complete assessment of new product development approaches. Data from selected examples of novel steel processing methodologies that are currently being evaluated to develop new “third generation” AHSS are also presented.

## 11.2 Analysis of Strengthening in AHSS Steels

Assessments of strength/ductility relationships for new third generation AHSS require an understanding of the effects of microstructure on tensile stress-strain behavior and an assessment of the effects of microstructure on operating deformation mechanisms. In this section, the important aspects of stress-strain behavior in tension are reviewed along with a consideration of models that can be incorporated to assess the behavior of potential steels with unique new microstructural combinations.

The interrelationships between microstructural constituents, strength, strain hardening, and ductility in tension are often considered in terms of equations that

relate operable strengthening mechanisms to strain-dependent expressions of strength, and then are evaluated by applying the instability condition (Eq. 11.1) to determine the true uniform strain, one important component of the total elongation or formability. This discussion concentrates on factors that control uniform strain and recognizes that the total elongation in tension is the sum of the uniform and post uniform strains. While not considered here, fracture mechanisms that may limit formability (e.g. hole expansion, etc.) remain important in these new steels, and the effects of microstructure on fracture during sheet metal forming should be incorporated into future studies of new AHSS grades.

$$\frac{d\sigma}{d\varepsilon} = \sigma_{\text{instability}} \quad (11.1)$$

The true stress at instability,  $\sigma_{\text{instability}}$ , can be viewed as the sum of two terms, the yield stress,  $\sigma_y$ , and the change in stress due to strain hardening,  $\Delta\sigma$ , and Eq. 11.1 can be rewritten as [11]:

$$\frac{d\sigma}{d\varepsilon} = \sigma_y + \Delta\sigma \quad (11.2)$$

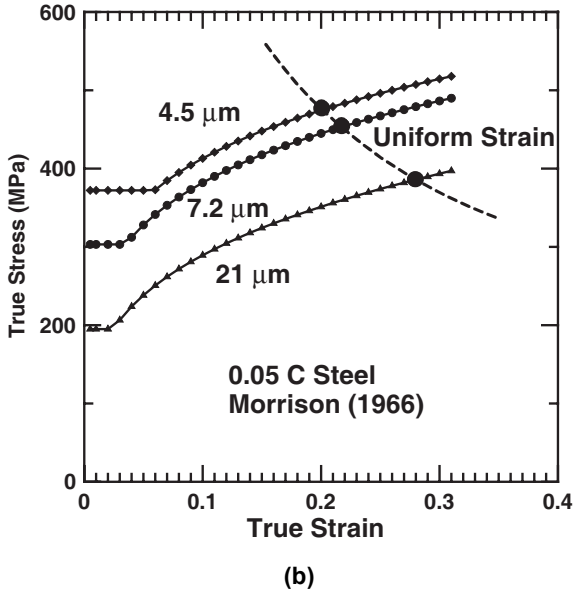
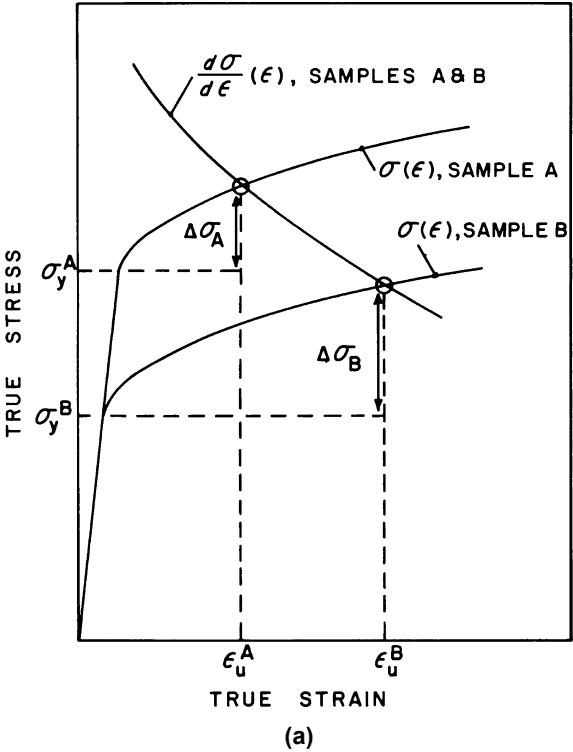
In Eq. 11.2,  $\Delta\sigma$  represents the accumulated strength increase beyond yielding and the magnitude of  $\Delta\sigma$  depends on the stress-strain curve shape [11].

The terms in Eq. 11.2 are illustrated by Fig. 11.3, which presents a series of true stress versus true strain curves, both schematic (Fig. 11.3 (a)) [11] and actual data as a function of ferrite grain size for a low carbon steel (Fig. 11.3 (b)) [12]. Figure 11.3 (a) shows two steels, A and B, with different yield strengths but equivalent strain-dependent strain hardening functions. The increase in yield strength results in a decrease in uniform strain due to the decrease in the magnitude of  $\Delta\sigma$  required to satisfy instability. The behavior in Fig. 11.3 (a) mirrors the effects of ferrite grain size shown in Fig. 11.3 (b). It is interesting to note that the data in Fig. 11.3 (b), which were taken from a 1966 publication [12], are almost identical to recent results in a study on ultra fine grain IF steels with grain sizes in the range of 0.2 to 13  $\mu\text{m}$  [13]. For the most general case, each term in Eq. 11.2 will depend on microstructure, and  $(d\sigma/d\varepsilon)$  and  $\Delta\sigma$  will be independent functions of strain. Thus, in AHSS, consideration of specific mechanisms to independently control each term in Eq. 11.2 is critical to defining final strength/elongation combinations.

The analysis shown in Eq. 11.2 and Fig. 11.3 (a) has been extended [10, 11] to evaluate the effects of systematic variations to strain hardening behavior, as evidenced by shapes of stress strain curves, to show that the total ductility depends *both* on the initial yield strength and the overall strain hardening behavior, which may differ at low and high strains. To illustrate this latter point, Fig. 11.4 shows true stress versus true strain curves for a set of constant composition dual phase steels processed with different cooling rates (and thus different martensite volume fractions indicated in the figure) [11]. The uniform strain and thus ductility are shown to decrease with an increase in martensite volume fraction (MVF). The strain hardening rate at low strains increases significantly with MVF while the strain hardening behaviors at



**Fig. 11.3** True stress versus true strain curves illustrating contributions to uniform strain controlled by yielding and strain hardening behavior as described in Eqs. 11.1 and 11.2: (a) Schematic stress-strain curves showing two curves with different yield strengths and equivalent strain hardening behavior [11]; (b) Effects of ferrite grain size on the yielding and strain hardening behavior of a low carbon steel [12].



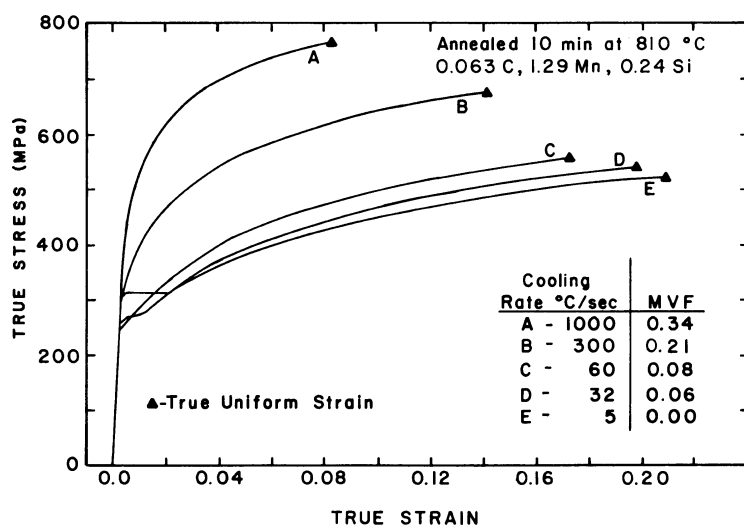


Fig. 11.4 True stress-true strains curves for Fe-0.063C-1.29Mn-0.24Si steel intercritically annealed at 810°C and cooled at different rates [11]. Each stress-strain curve is plotted up to the point of instability.

strains near instability are essentially independent of MVF. Thus, the decrease in uniform strain with increase in MVF is due primarily to a rapid increase in strength at low strains and not a fundamental change in strain hardening behavior at high strains, consistent with Fig. 11.3 (a).

The instability criterion (Eqs. 11.1 and 11.2) was applied to predict potential strength/ductility behaviors for new advanced high strength steels by utilizing a model that incorporates contributions of the individual microstructural constituents [10], and the results of that analysis are reviewed here. In general, all AHSS have complex multi-phase microstructures and consist of various combinations and distributions of ferrite, bainite, martensite, austenite, and carbide/nitride precipitates. If multiple ductile phases are load-bearing, then composite models based on the rule of mixtures (such as for an iso-strain composite) may be employed. This approach has been successfully used to describe strength-ductility combinations in dual phase steels [14] and metastable austenitic stainless steels [15]. If the load-bearing capacity of the second phase can be ignored, as is the case for a closely-spaced distribution of fine carbides in ferrite, then contributions to strength can be modeled based on conventional precipitation hardening models or with models that consider the effects of strain gradients between phases on dislocation accumulation [16–18].

For each model considered here, an expression for the stress-strain behavior of each individual constituent is required along with an expression that describes interactions between phases. For steels with a primarily ferritic matrix, strengthening is derived by grain refinement, solute additions, cold work, crystallographic

texture control and the presence of precipitates. The strength of ferrite can be described by a general equation of the form [19, 20]:

$$\sigma_y = \sigma_i + \sigma_{SS} + \sigma_D + \sigma_{PPTN} + k_y d^{-1/2} \quad (11.3)$$

where  $\sigma_y$  is the flow stress, usually taken at a strain of 0.002 for yielding,  $\sigma_i$  is the friction stress of pure iron,  $\sigma_{SS}$  is the strengthening increment from solid solution strengthening (usually written as the linear sum of the contributions of the individual elements, i.e.  $\sigma_{SS} = \sum k_i [c_i]$  where  $c_i$  is the concentration of the  $i$ th solute and  $k_i$  is the strength coefficient for the  $i$ th solute),  $\sigma_D$  is the strain-dependent strengthening from dislocation substructure,  $\sigma_{PPTN}$  is the contribution from precipitation hardening,  $k_y$  is the Hall-Petch slope (referred to as the grain boundary strength coefficient), and  $d$  is the grain diameter. In Eq. 11.3, contributions from different strengthening mechanisms are taken to be additive. Equation 11.3 may be applied to both yield stress and strain-dependent flow stress data.

Ashby [16] evaluated the deformation behavior of plastically non-homogeneous alloys in a different fashion. In this analysis the microstructure was assumed to consist of a ductile primary constituent with a dispersion of hard non-deforming particles, and the methodology provided an approach to predict the strength and strain hardening behavior as a function of the volume fractions of individual constituents. Application of the model was illustrated to describe the deformation behavior of a variety of multi-component materials and thus may be applicable to new AHSS steels with multiple constituents [16]. Ashby assumed that the strength of a multiphase material can be described by a “one-parameter” theory where strain-dependent strength depends only on the strain dependence of the average dislocation density,  $\rho_{AVG}$ . The average dislocation density equals the sum of the geometrically necessary,  $\rho_G$ , and statistically stored,  $\rho_S$ , dislocation densities, each which depends on “characteristic lengths”,  $\lambda_G$  and  $\lambda_S$ , respectively. For a specific microstructure,  $\lambda_G$  is strain independent and characteristic of the morphology, volume fraction and distribution of the second phase in the initial microstructure. For example, for dual phase steels with finely dispersed equiaxed martensite particles in a ferritic matrix,  $\lambda_G$  is given by the ratio of the average particle radius,  $r$ , to the martensite volume fraction,  $f$ . In contrast,  $\lambda_S$  is strain dependent and characterizes the dislocation mean free path or cold-work induced dislocation substructure. Ashby’s analysis predicts that  $\rho_G$  controls the properties at low strains and  $\rho_S$  controls at high strains [16]. The resulting strength and dislocation density expressions are:

$$\sigma = \sigma_o + \alpha \mu b \sqrt{\rho_{AVG}} \quad (11.4)$$

and

$$\rho_{AVG} = 4\gamma \left[ \frac{1}{\lambda_G} + \frac{1}{\lambda_S} \right] \quad (11.5)$$

where  $\sigma$  is the applied true stress,  $\sigma_0$  is the intragranular friction stress which includes all contributions to matrix strength other than due to the second phase,  $\mu$  is the shear modulus,  $b$  is the Burgers vector,  $\rho_{AVG}$  is the average dislocation density,  $\alpha$  is a constant, and  $\gamma$  is the shear strain.

To assess the applicability of Ashby's analysis [16] to AHSS steels, the deformation behavior of the series of dual phase steels shown in Fig. 11.4 is considered here. If it is assumed that  $\rho_G \gg \rho_S$  (i.e. a condition applicable at low strains), and that the martensite in dual phase steels exists as discrete fine particles, then following Ashby's analysis [16], the strain hardening rate is proportional to MVF,  $f$ , and martensite island radius,  $r$ , as shown in Eq. 11.6:

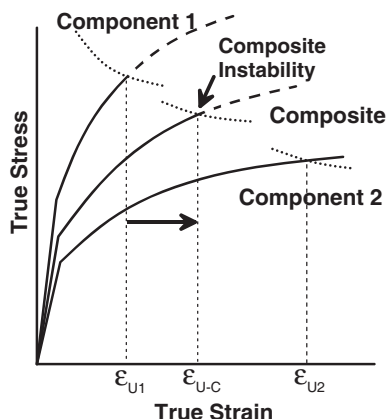
$$\frac{d\sigma}{d\epsilon} \propto \sqrt{\frac{f}{r}} \quad (11.6)$$

Application of Eqs. 11.4 to 11.6 to the DP samples processed with MVF values of 0.34 and 0.08 (Fig. 11.4), which correspondingly exhibited average martensite island radii of approximately 10 and 2  $\mu\text{m}$  respectively, would predict  $f/r$  values and correspondingly strain hardening rates that are nearly independent of MVF. Clearly the observed stress-strain behaviors are not consistent with such a model. Ashby's approach [16] is believed more applicable for low martensite volume fractions, and fine dispersed martensite islands, where the strain hardening rate at low strains significantly increases with martensite volume fraction, consistent with an increase in  $\rho_G$ , and is essentially independent of martensite volume fraction at high strains where the strengths would be primarily controlled by  $\rho_S$ .

From the discussion associated with Ashby's model, it is concluded that descriptions of multiphase materials which consist of a primary ductile phase with properties modified by the effects of other higher strength constituents is applicable to primarily ferritic materials such as dual phase steels with discrete martensite particles in a ductile matrix [17, 18], but may not be applicable to microstructures with significant volume fractions of multiple phases (e.g. as is the case for the dual phase steel in Fig. 11.4 with MVF=0.34). Thus, alternate approaches as discussed below based on deformation of multi-constituent composites are required to describe strengths and ductilities of materials with higher volume fractions of high strength constituents, as might be anticipated for new AHSS grades.

With two or more ductile load bearing constituents (e.g. ferrite plus martensite, or ferrite plus martensite plus bainite) the procedure outlined by Mileiko [21], and later adopted by Garmon and Thompson [22], applies the rule of mixtures to describe the composite yield stress, the plastic instability condition (i.e. true uniform strain), and the ultimate tensile strength. In this analysis it is assumed that there is sufficient interfacial bonding that the composite reaches the plastic instability condition described by Eq. 11.1. For this condition, plastic instability of individual components is prevented prior to necking of the composite as a whole, and the composite deforms with the resulting properties shown

**Fig. 11.5** Schematic stress strain curves showing the composite prediction based on the rule of mixtures of two ductile phases according to the model of Mileiko [21].



schematically in Fig. 11.5. To apply the model, the relationship between true stress,  $\sigma$ , and true strain,  $\epsilon$ , for each component was assumed to follow a power law expression:

$$\sigma = K\epsilon^n \quad (11.7)$$

where  $K$  and  $n$  are characteristic parameters for the constituent of interest. While the simple power law function in Eq. 11.7 is cited here, the methodology can be extended easily to include other stress-strain functions [22]. The assumption of sufficient interfacial bonding is believed satisfactory for predicting uniform tensile ductility, but interfacial strength is critical in understanding fracture mechanisms at higher strains which control behavior in some other forming modes [17, 23, 24].

In TRIP steels with unstable microstructures in which the constituent volume fractions change with strain, the approach of Olson [15], which considers stress assisted and strain assisted transformation of austenite to martensite, can be applied. In this case, the phase fractions are strain dependent. With characteristic stress-strain equations (i.e. Eq. 11.7) for individual phases, along with knowledge of the strain dependent formation of martensite from austenite, direct predictions can be made of the stress-strain behavior, and thus strength/ductility relationships in TRIP steels. A simple model based on this approach is presented in Sect. 3 below.

### 11.3 Predictions of AHSS Microstructures and Properties

Opportunities exist to apply the multi-phase and composite models described above to guide development of third generation AHSS. As summarized previously [10], there are several significant observations from the literature that assist in focusing potential development approaches. Steels in the first generation

AHSS strength/ductility band primarily derive their properties from the strength and hardening response of ferrite, the dominant phase, even in DP and “conventional” TRIP steels. The properties of ferrite can be modified by solid solution alloying, grain size control, cold work, and precipitation. However, for ferritic steels with stable microstructures, there is significant evidence in the literature to suggest that the strain hardening behavior *at high strains* is essentially independent of the microstructure/composition modifications associated with the various steel classes, and opportunities are limited to significantly increase the strain hardening behavior of these steels at high strains. The independence of high strain hardening rates to microstructural modifications has been demonstrated with systematic variations in grain size as shown in Fig. 11.3 (b) [12], cold work, substitutional alloy additions [25], and martensite volume fractions (as controlled by cooling rate) in DP steels [11]. TRIP steels, through strain-dependent control of the austenite to martensite transformation, offer greater opportunity to modify the high-strain work hardening behavior of ferritic-based steels. This benefit is illustrated in Fig. 11.2 where as a consequence of enhanced strain hardening at high strains, TRIP steel properties occupy the top of the first generation AHSS property band.

Alternate processing approaches to modify the dislocation structure of ferrite (and thus strain hardening behavior) are limited. It has been suggested that deformation of ferrite in the dynamic strain aging (DSA) range, which leads to a higher dislocation density than obtained by equivalent cold work at room temperature [26], may be beneficial. However, Li and Leslie [27] have shown that this is not the case in their study of a 0.22 wt pct carbon steel where prestrains of 3% or 5% at DSA temperatures (e.g. 200 to 400°C) led to a significant decrease in room temperature ductility due to a corresponding increase in room temperature lower yield stress.

Materials with strength/ductility combinations significantly greater than observed for the first generation AHSS require incorporation of complex microstructures that contain constituents added to increase strength (e.g. martensite) and enhance strain hardening (e.g. austenite). One approach to the development of new AHSS steels is to utilize steels with significant amounts of metastable austenite, along with critical control of the mechanical properties of each of the other constituents. There is also potential for the use of controlled strain hardening as might be obtainable by heavy temper rolling (or other mechanisms) to produce the required yield strength increase.

As will be shown below, the austenite stability can also be an important factor. Austenite stability against transformation increases with a decrease in austenite particle size [28], an increase in test temperature [15], and an increase in the addition of austenite-stabilizing elements (e.g. C, Ni, Mn, etc) [15, 20, 29, 30]. However, control of austenite transformation to maximize uniform strain may also lead to a significant decrease in post uniform strain [29, 30]. The strength of the martensite is also a critical factor, as well as the strain hardening behavior of the austenite [17]. The austenite properties are especially important in the case where austenite is stable and TRIP is suppressed.

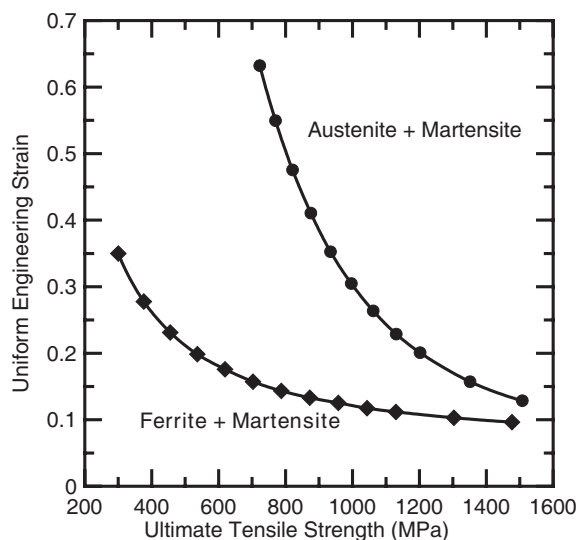
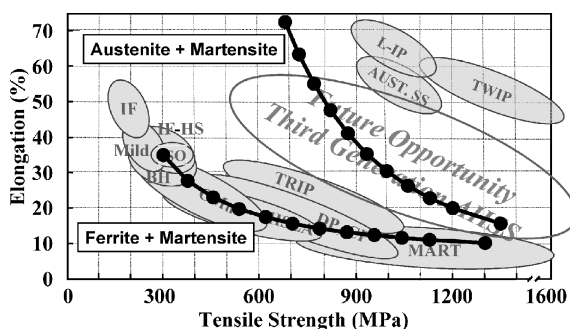


**Fig. 11.6** Predicted strength/ductility relationships for two hypothetical steel microstructures: ferrite + martensite (i.e. DP steel) and stable austenite + martensite. The plotted data were calculated by applying Mileiko's model and varying the martensite volume fraction [21]. The following ultimate tensile strength and true uniform,  $\epsilon_u$ , data were used for each material: Ferrite, UTS = 300 MPa,  $\epsilon_u = 0.3$  [14, 31]; stable austenite, UTS = 640 MPa,  $\epsilon_u = 0.6$  [29]; and martensite, UTS = 2000 MPa,  $\epsilon_u = 0.08$  [14, 31].

The models outlined in Sect. 2 present a methodology to assess effects of microstructural variables in new AHSS grades. The approach based on the composite model of Mileiko [21] will provide the necessary predictions and is discussed further below. First, specific microstructure and mechanical property combinations are identified, and the sensitivity of the predictions to properties of individual components is assessed. Then, recent novel alloying and processing methodologies which suggest possible new AHSS grades are reviewed.

Interesting implications from the application of Mileiko's composite model are illustrated by predicting the effects of volume fraction martensite on the ductility-versus-strength behavior of steels comprised of ferrite plus martensite and austenite plus martensite. Initially composites based on *stable* austenite are considered. For this analysis, the stress strain behavior of each component is assumed to follow Eq. 11.7, and the required inputs to obtain  $K$  and  $n$  are ultimate tensile strength (an engineering stress) and the true strain at instability, taken also to equal " $n$ " in Eq. 11.7. For these calculations, data for the stable austenite are for a 25 wt pct Mn austenitic steel [29], and data for the martensite and ferrite are based on the results of Davies [14, 31]. Figure 11.6 shows the resulting predictions plotted as engineering uniform strain versus ultimate tensile strength, where the increase in strength corresponds to an increase in martensite volume fraction. The specific properties for each material are also summarized in the figure caption. For both hypothetical steel

**Fig. 11.7** Superposition of the strength/ductility predictions from Fig. 11.5 on the strength/ductility map shown in Fig. 11.1. For this figure the austenite was assumed stable against transformation to martensite with deformation [10].



families, the ductility increased with a decrease in strength, but the sensitivity to volume fraction martensite was much greater for the austenite plus martensite steel.

Figure 11.7 compares the predictions from Fig. 11.6 with the AHSS property bands in Fig. 11.2. It is noted that this comparison ignores the contributions of post uniform strain to the total elongation, but since the uniform strain constitutes the majority of the useful strain in uniaxial tension, for discussion purposes the comparison is valid. Interestingly, the predictions for the ferrite plus martensite microstructure (with volume fraction martensite ranging from 0 to 70 pct) directly match the behavior of the first generation of AHSS. Data for the TRIP steels plot at higher strain values than predicted by the composite model, consistent with the fact that enhanced strain hardening due to the austenite to deformation induced martensite transformation was ignored in this calculation. Predicted properties for the hypothetical austenite plus martensite steel considered here fall directly within the property band identified for the third generation AHSS. However, as illustrated by the data in Fig. 11.3 (b) and the analysis associated with Eqs. 11.3–11.6, the analyses that consider design of new materials based on stable ferritic microstructures will not provide the necessary strength-ductility combinations required for the third generation of AHSS.

The sensitivity to variations in the mechanical properties of the microstructure components was assessed. Figure 11.8 presents one example which shows the significance of increasing the strength of the stable austenite from 640 MPa, used in Fig. 11.6, to 850 MPa with a corresponding decrease in uniform strain from 0.6 to 0.4. These property changes are consistent with a mechanism such as temper rolling or refinement of the austenite grain size, and the implications are consistent with property changes discussed in conjunction with Fig. 11.3 (b). For Fig. 11.8, the volume fraction of martensite was varied from 0 to 0.7, and the martensite properties were assumed constant. An increase in austenite strength with a corresponding *decrease* in the true uniform strain, is shown to lead to an *increase* in ductility of the composite at a given strength level. The observation that increasing the strength of one phase leads to a ductility increase is interesting, counterintuitive, and illustrates the importance of phase interactions on the overall properties of multi-phase steels.



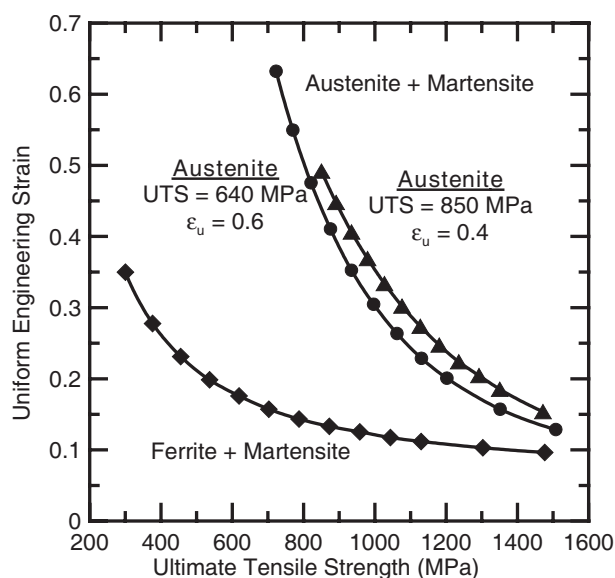
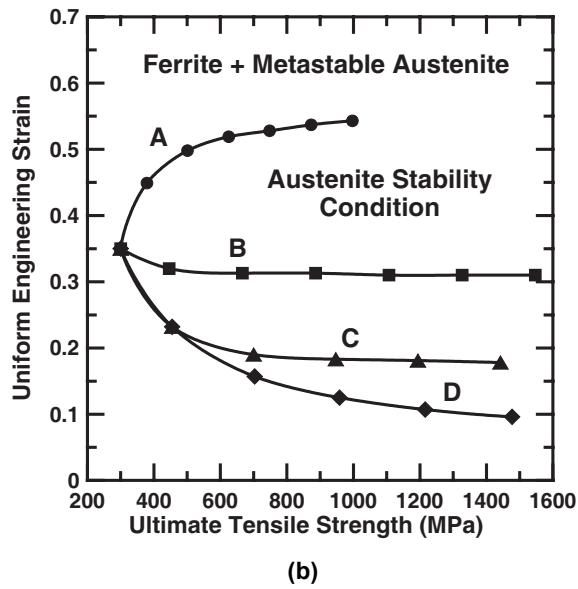
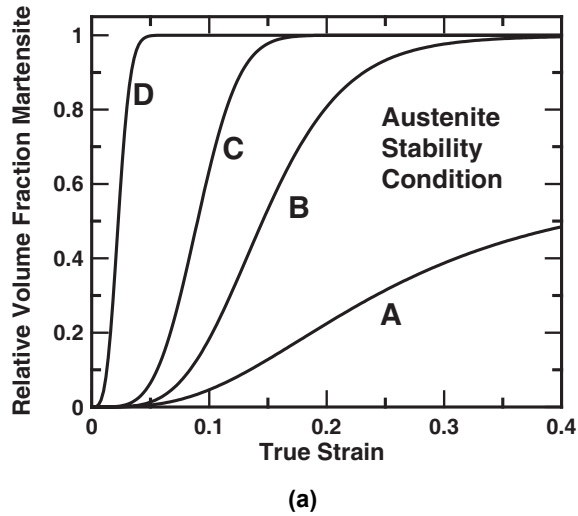


**Fig. 11.8** Influence of austenite properties on the predicted strength/ductility combinations shown in Fig. 11.6. The effect of increasing the austenite UTS to 850 MPa with a corresponding decrease in ductility are shown. The ferrite + martensite data from Fig. 11.6 are included here for reference.

The importance of austenite transformation to martensite with strain and austenite stability is illustrated for a series of ferrite plus *metastable* austenite composites in which the initial austenite content was varied between 0 and 85%. Four hypothetical austenite stabilities based on the austenite stability function of Olson [15] were considered, as shown in Fig. 11.9 (a). Following the composite modeling approach used to generate Figs. 11.6 and 11.8, Fig. 11.9 presents predictions that illustrate the dramatic effect of austenite stability on strength-ductility combinations. These predictions illustrate that the best combinations of strength and ductility are only obtained for materials with high volume fractions of relatively stable austenite. This behavior is perhaps not surprising, as ferrite/austenite mixtures with very unstable austenite would be expected to decay with strain into the regime of behavior exhibited by DP steels (e.g. condition “D” in Fig. 11.9). Even though the predictions in Figs. 11.6 to 11.9 were based on a composite model with simplified assumptions [2, 10], the significance of the results is apparent, and the methodology provides a clear understanding of the importance of the mechanical properties of the individual constituents in AHSS with complex microstructures. The analyses leading to Figs. 11.6 to 11.9 unmistakably suggest that the next generation of AHSS may consist of complex microstructural combinations with significant contents of high strength phases, which could be martensite as considered here, or ultra fine grained or cold worked ferrite, and highly-ductile phases with significant capacity for strain hardening phases (e.g. austenite). Once a desirable combination of properties and microstructure is identified, then novel techniques must be identified to produce the desired microstructure constituents with the necessary deformation response.

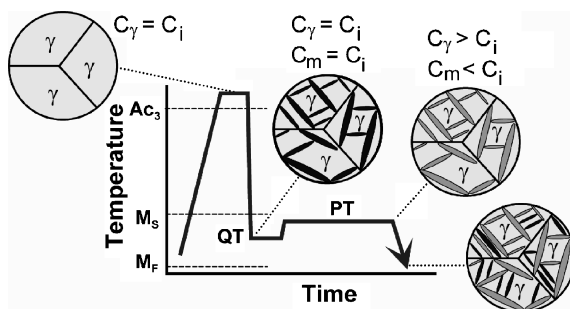
**Fig. 11.9** Assessment of the effects of austenite stability against transformation to martensite with strain. (a) Effect of strain on austenite stability for four hypothetical materials indicated by letters A to D; (b) Predicted relationship for ferrite + metastable austenite composites based on the four austenite stabilities shown in (a).



### 11.4 Evaluation of Methodologies to Produce Third Generation AHSS

In this section, results of three recent studies, designed to produce materials with high volume fractions of austenite and thus represent potential paths to produce third generation AHSS, are reviewed. A new process, referred to as “quenching

**Fig. 11.10** Schematic representation of the 2-stage quenching and partitioning (Q&P) process for a sample with an initial fully austenitic microstructure, where the partitioning temperature (PT) is greater than the quench temperature (QT).



and partitioning” (Q&P), has recently been shown to be a unique processing route for the production of high strength steels with significant amounts of retained austenite [4,32–36], and has been assessed for potential to provide strength/ductility combinations in high strength sheet steels. The Q&P process is shown schematically in Fig. 11.10. Depending on initial annealing temperature, the starting microstructure is either fully austenitic (as shown in Fig. 11.10) for samples cooled from above the  $A_{c3}$ , or contains controlled volume fractions of ferrite and austenite for samples intercritically annealed. The materials are rapidly cooled to a specific quench temperature (QT) between  $M_s$  and  $M_f$  to create controlled fractions of martensite and austenite, the amounts of which can be predicted [33]. This is followed by a thermal treatment at the partitioning temperature (PT) which can either be equal to QT (a “one-step” process) or greater than QT (a “two-step” process). At PT, carbon migrates from martensite to austenite to increase the austenite stability resulting in higher austenite fractions at room temperature after cooling from PT. In the Q&P process, formation of iron carbides is intentionally suppressed, and the austenite is intentionally stabilized rather than decomposed.

Several recent publication have considered the sensitivity to the Q&P process to alloy content and processing temperatures, and have shown that the Q&P process works in a variety of alloy systems [32–36]. Of particular interest here are the recent mechanical property results of Streicher et al. who evaluated the heat treating response of a 0.19C, 1.59Mn, 1.63Si (wt pct) alloy processed with Q&P temperature-time histories as well as thermal histories designed to simulate more conventionally heat treated Q&T and austempered TRIP steels [4,36]. Figure 11.11 correlates ultimate tensile strengths with total elongations for one-step and two-step Q&P materials annealed from both above and below the  $A_{c3}$ , with similar data on dual phase, TRIP, and martensitic steels. In addition to steels processed by Streicher et al., Fig. 11.11 also includes data from the literature [4,36]. The Q&P materials included samples with austenite volume fractions up to 16 pct. The dual phase steels included here were of relatively high strength, owing the effects of relatively high martensite fractions. The data in Fig. 11.11 show that strength-ductility combinations characteristic of the third generation of AHSS were obtained indicating that Q&P processing may be a viable route to produce new steel grades. Clearly the data obtained to date are promising, but significantly

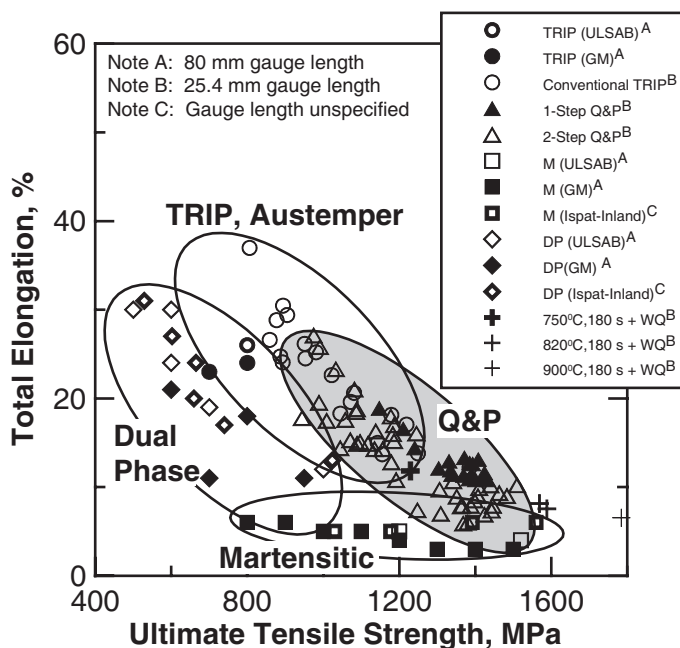


**Fig. 11.11** Total elongation vs. ultimate tensile strength for sheet steels processed with microstructures characteristic of TRIP, dual phase (DP), martensitic, Q&P materials. References for the individual data are summarized elsewhere [4, 36].

more work is required to optimize Q&P processing and design alloys, and process histories compatible with current and future production constraints.

Recently, two studies designed to extend current production technologies have also been shown to produce materials with properties in the third generation AHSS property band in Fig. 11.2. Wakita et al. [37], in their study on thermomechanical controlled processing (TMCP), evaluated ultrafine TRIP-aided multi-phase microstructures in a 0.19C, 1.96Si, 2.01Mn (wt pct) low carbon steel. They found that heavy deformation at low austenite rolling temperatures led to the formation of 2  $\mu$ m ferrite, a high volume fraction of retained austenite (on the order of 25 pct) and a modification of the retained austenite morphology from film-like to granular. The resulting ultra-fine TRIP microstructure exhibited a tensile strength of 1080 MPa and total elongation of 26.9 pct. The high ductilities were attributed to austenite which was partially stabilized by the ultrafine microstructure and only transformed at higher strains, leading to high work hardening rates which suppressed necking. The results of this study provide another production path to control austenite stability consistent with the model predictions of Fig. 11.9.

In comparison to the work of Wakita et al. [37], Merwin [38, 39] evaluated the effects of processing on the TRIP behavior of a series of 0.1 wt pct C steels with Mn contents in the range of 5.2 to 7.1 wt pct. Data were obtained for material in the as-hot-rolled and in the cold-rolled and annealed conditions. In the as-hot-

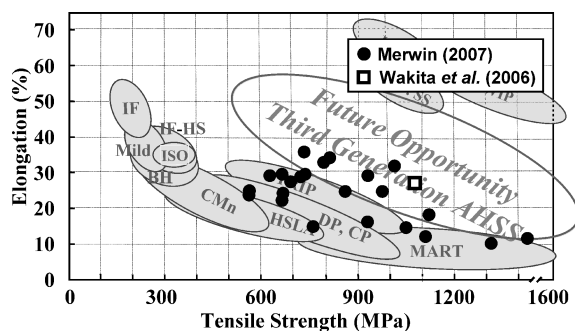


**Fig. 11.12** A comparison of tensile strength and tensile elongation data for thermomechanically controlled processed Mn-modified low carbon steels with fine microstructures, some with significant amounts of retained austenite compared to the opportunity band for third generation AHSS. Data shown from Wakita et al. [37] and Merwin [38, 39].

rolled condition all microstructures were martensite, i.e. the alloys were fully hardenable even at the coil cooling rates applicable to conventional hot strip mill processing. Cold rolling and annealing of the initially martensitic structure resulted in very fine ferrite-austenite microstructures, with the amount of austenite dependent on the annealing temperatures and times that were chosen to simulate hot and cold spots in batch annealing. In the cold rolled and annealed samples, retained austenite contents up to approximately 38 pct were observed, the amount of retained austenite increasing with Mn content and decreasing with hold time at the annealing temperature. Tensile data were obtained and Fig. 11.12 correlates UTS and total elongation values for cold rolled and annealed materials with the desired property band for third generation AHSS steels. Also shown is the result from the thermomechanical processing study of Wakita et al. [37]. Selected samples from Merwin [38, 39] and the data of Wakita et al. [37] fall directly within the desired property band and indicate that development of the next generation of steels may be possible with controlled Mn additions along with controlled thermomechanical processing to produce ultrafine grained ferrite for strength and high volume fractions of retained austenite for ductility.

## 11.5 Summary

This paper review approaches to develop new steels with microstructures that produce mechanical properties characteristic of the third generation of AHSS. The importance of combining an understanding of fundamental deformation mechanisms with predictions based on appropriate composite models, to describe the deformation behavior of multiphase materials is illustrated. From these analyses, it is predicted that the third generation of AHSS will require significant amounts of high strength constituent, e.g. martensite or ultra fine grained ferrite, along with significant amounts of austenite. Furthermore, the austenite must be designed with

controlled deformation induced transformation behavior. While the required microstructures are complex through alloying and processing approaches, particularly involving Q&P processing or Mn-addition might be used to produce the desired microstructures. It is also clear that significant research is still required to design alloying and processing methodologies to optimize third generation AHSS material properties.

The composite methodology based on iso-strain deformation, while simplistic, can be used to predict the effects of microstructural, property, and testing variables including grain size, second phase volume fraction, size, and distribution, imposed strain rate, strain hardening behavior of the martensite, etc.

**Acknowledgements** The authors gratefully acknowledge the support of the sponsors of the Advanced Steel Processing and Products Research Center, an industry/university cooperative research center at the Colorado School of Mines, and the National Science Foundation through award number CMMI-0729114.

## References

- [1] M. Pfestorf, D. Copeland, Great Designs in Steel Seminar 2007, American Iron and Steel Institute, [www.autosteel.org](http://www.autosteel.org), 2007.
- [2] "Third Generation Advanced High Strength Steel (AHSS)", Research and Development Solicitation, American Iron and Steel Institute, Washington, DC, 2006.
- [3] D. Cornette, P. Cugy, A. Hildenbrand, M. Bouzekri, and G. Lovata, SAE Technical Paper # 2005-01-1327, SAE, Warrendale, PA, 2005.
- [4] A.M. Streicher, J.G. Speer, D.K. Matlock, and B.C. De Cooman, International Conference on Advanced High Strength Sheet Steels for Automotive Applications Proceedings, ed. by J.G. Speer, AIST, Warrendale, PA, 2004, pp. 51–62.
- [5] "Advanced High Strength Steel (AHSS) Application Guidelines", Committee on Automotive Applications, International Iron & Steel Institute, Brussels, Belgium, 2005.
- [6] Microalloying '75, Proceedings of an International Symposium on High-Strength Low-Alloy Steels, Union Carbide Corp., New York, 1977.
- [7] Formable HSLA and Dual-Phase Steels, ed. By A.T. Davenport, TMS-AIME, Warrendale, PA, 1977.
- [8] Structure and Properties of Dual-Phase Steels, ed. By R.A. Kot and J.W. Morris, TMS-AIME, Warrendale, PA, 1979.
- [9] Fundamentals of Dual-Phase Steels, ed. By R.A. Kot and B.L. Bramfitt, TMS-AIME, Warrendale, PA, 1981.
- [10] David K. Matlock and John G. Speer, Proceedings of the The 3rd International Conference on Structural Steels, ed. by H.C. Lee, The Korean Institute of Metals and Materials, Seoul, Korea, 2006, pp. 774–781.
- [11] D.K. Matlock, G. Krauss, and F. Zia-Ebrahimi, in Deformation, Processing, and Structure, ed. by G. Krauss, ASM, Metals Park, OH, 1984, pp. 47–87.
- [12] W.B. Morrison, Trans. ASM, vol. 59, 1966, pp. 824–846.
- [13] N. Tsuji, Proceedings of the The 3rd International Conference on Structural Steels, ed. by H.C. Lee, The Korean Institute of Metals and Materials, Seoul, Korea, 2006, pp. 49–59.
- [14] R.G. Davies, Metall. Trans. A, vol. 9A, 1978, pp. 451–455.
- [15] G.B. Olson, in Deformation, Processing, and Structure, ed. by G. Krauss, ASM, Metals Park, OH, 1984, pp. 391–425.

- [16] M.F. Ashby, in *Strengthening Methods in Crystals*, ed by A. Kelly and R.B. Nicholson, Elsevier Pub., Amsterdam, 1971, pp. 137–192.
- [17] D.A. Korzekwa, R.D. Lawson, D.K. Matlock, and G. Krauss, *Scripta Metall.*, vol. 14, 1980, pp. 1023–1028.
- [18] D.A. Korzekwa, D.K. Matlock, and G. Krauss, *Metall. Trans. A*, vol. 15A, 1984, pp. 1221–1228.
- [19] T. Gladman, *The Physical Metallurgy of Microalloyed Steels*, The Institute of Metals, Cambridge, England, 1997, p. 49.
- [20] F.B. Pickering, in *Toward Improved Toughness and Ductility*, Climax Molybdenum Development Company, Japan, 1971, pp. 9–32.
- [21] S.T. Mileiko, *J. of Mat. Sci.*, vol 4, 1969, pp. 974–977.
- [22] G. Garmon and R.B. Thompson, *Metall. Trans.* vol. 4, 1973, pp. 863–873.
- [23] S.B. Lee, *Microstructural Influences on the Fracture Behavior of Multi-Phase Sheet Steels*, PhD. Thesis, Colorado School of Mines, Golden, CO, 2005.
- [24] S.B. Lee, D.K. Matlock, and J.G. Speer, *Proceedings of the Nineteenth Conference on Mechanical Behavior of Materials – September 1–2, 2005*, The Korean Institute of Metals and Materials, Seoul, Korea, 2005, pp. 183–197, 2005.
- [25] G. Langford, P.K. Nagata, R.J. Sober, and W.C. Leslie, *Metall. Trans.*, vol. 3, 1972, pp. 1843–1849.
- [26] W.C. Leslie and A.S. Keh, in *Mechanical Working of Steel 2*, AIME, New York, 1965, p. 337.
- [27] C.C. Li and W.C. Leslie, *Metall. Trans. A*, vol. 9A, 1978, p 1765.
- [28] W.C. Jeong, D.K. Matlock, and G. Krauss, *Materials Science and Engineering*, 1993, *Mat. Sci. and Eng.*, vol. A165, 1993, pp. 1–8.
- [29] G. Frommeyer, U. Brück, and P. Neumann, *ISIJ Int.*, vol. 43, no. 3, 2003, pp. 438–446.
- [30] P.J. Jacques, J. Ladrière, and F. Delannay, *Metall. Trans. A*, vol. 32A, 2001, pp. 2759–2768.
- [31] R.G. Davies, *Metall. Trans. A*, vol. 9A, 1978, pp. 41–52.
- [32] J.G. Speer, D.K. Matlock, B.C. DeCooman, and J.G. Schroth, *Acta Materialia*, vol. 51, 2003, pp. 2611–2622.
- [33] J.G. Speer, A.M. Streicher, D.K. Matlock, F. Rizzo, and G. Krauss, *Austenite Formation and Decomposition*, ed. by E.B. Damm and M.J. Merwin, TMS, Warrendale, PA, 2003, pp. 505–522.
- [34] A.J. Shutts, J.G. Speer, D.K. Matlock, D.V. Edmonds, F. Rizzo, and E.B. Damm, in *Proceedings of International Conference on New Developments in Long and Forged Products: Metallurgy and Applications*, ed. by J.G. Speer, E.B. Damm and C.V. Darragh, AIST, Warrendale, PA, USA, 2006, pp. 191–202.
- [35] E. De Moor, S. Lacroix, L. Samek, J. Penning, and J.G. Speer, *Proceedings of the The 3rd International Conference on Structural Steels*, ed. by H.C. Lee, The Korean Institute of Metals and Materials, Seoul, Korea, 2006, pp. 873–878.
- [36] A. Clarke, PhD Thesis, *Carbon Partitioning Into Austenite From Martensite In A Silicon-Containing High Strength Sheet Steel*, Colorado School of Mines, Golden, CO, 2006.
- [37] M. Wakita, Y. Adachi, and Y. Tomota, *Materials Science Forum*, vols. 539–543, 2007, pp. 4351–4536.
- [38] M.J. Merwin, SAE Technical Paper #2007-01-0336, SAE, Warrendale, PA, 2007.
- [39] M.J. Merwin, *Proceedings of Steel Properties and Applications Conference*, edited by L.C. Oldham, AIST, Warrendale, PA, 2007, pp. 1017–1038.



David K. Matlock  
Advanced Steel Processing and Products  
Research Center  
Department of Metallurgical and Materials  
Engineering  
Colorado School of Mines  
Golden, CO 80401  
USA





## **Part III**

# **Modeling**



# Chapter 12

## Crystal Plasticity Based Modelling of Deformation Textures

P. Van Houtte

**Abstract.** Focus is on the multi-level character of existing or currently developed models for polycrystal deformation. A short overview is presented of two-level models ranging from the full-constraints Taylor model to the crystal-plasticity finite element models, including the description of a few recent and efficient models (GIA and ALAMEL). Validation efforts based on experimental cold rolling textures obtained for an aluminium and a steel alloys are discussed.

### 12.1 Introduction

Crystallographic textures are responsible for anisotropy of the mechanical behaviour of the material. This includes the strength of the metal which varies with the direction in which it is measured; the  $r$ -value (ratio between plastic strain to thickness plastic strain in a tensile test), which also varies with the test direction; other measures of formability, such as the limiting drawing ratio in a cup test and the earing behaviour. During the forming of a car body sheet, thickness distribution and failure will also be influenced by the texture; so finite element (FE) simulations of such processes should take texture-induced anisotropy into account. In principle they should also take the *evolution* of the texture during the forming operation into account, because the mechanical anisotropy also changes when the texture changes. Since the latter (effect of texture on yield stress etc.) is a quantitative effect, it is clear that any model used by the FE code to simulate the evolution of the texture must also be quantitatively correct. This implies that validations –

---

P. Van Houtte

Departement MTM, Katholieke Universiteit Leuven, Kasteelpark Arenberg 44 Bus 02450  
BE-3001 Leuven, Belgium. Fax: +32 16 32 19 90; Phone: +32 16 32 13 04  
e-mail: Paul.VanHoutte@mtm.kuleuven.be

i.e. comparison of predicted deformation textures with measured ones – must be done in a quantitative way. In the present paper, these comparisons will be based on ODFs using the Bunge [1] convention. Validations were done for one aluminium alloys (AA1200) and for IF steel. These are single-phase materials.

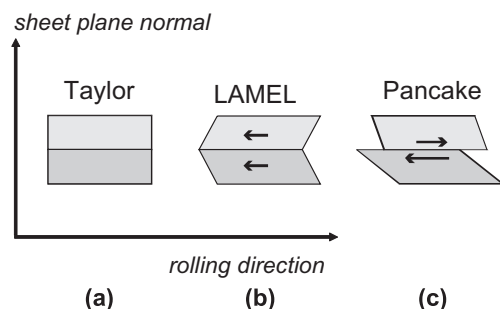
The texture of metal sheets which have been hot rolled has been measured using X-ray diffraction. The sheets have then been cold rolled (various thickness reductions). The texture has been measured again after the last cold rolling pass (prior to annealing), and in some cases also after some intermediate rolling passes. The ODF (Bunge [1]) has been calculated for all these textures. The ODFs of transfer slab textures have been transformed into sets of discrete orientations and then used as starting textures of the simulations of the rolling textures. Various methods have been used for these simulations, ranging from the full-constraints Taylor method (FC Taylor) to the crystal plasticity finite element method (CPFEM). Some of these methods focus on the interaction between neighbouring grains, and these methods were found to give the best results.

## 12.2 Crystal Plasticity Based Models

### 12.2.1 General

It is assumed that plastic deformation is achieved by means of crystallographic slip on  $\{111\} \langle 110 \rangle$  slip systems (fcc metals) or on  $\{110\} \langle 111 \rangle$  combined with  $\{112\} \langle 111 \rangle$  slip systems (bcc metals, such as low carbon steel). So in fcc metals, there are 12 slip systems which can (but do not need) be simultaneously active. In bcc metals, there are 24 of them (at least as assumed in the present paper). In principle all models to be discussed take the generalised Schmid law for the plastic deformation of crystals into account. This law states that a slip system is active when the resolved shear stress reaches a critical level, the “critical resolved shear stress”  $\tau^c$ . The resolved shear stress is the “effect” of the applied stress on a particular slip system. Some models that will be discussed use the visco-plastic approximation of the generalised Schmid law. In most models, the same value is

**Fig. 12.1** Shape of a stack of two grains after plane strain (as approximation for the deformation in the mid-plane of a rolling process), according to several statistical models. (a) Taylor full constraints model. (b) LAMEL model. (c) Pancake Relaxed Constraints model.



assigned to the “critical resolved shear stress”  $\tau^c$  for all slip systems. However, its value should be increased as deformation goes on (work hardening), at least when not only the deformation texture, but also the mechanical properties are to be calculated. Figure 12.1 illustrates three models: the full constraints Taylor model (FC Taylor), the Lamel model and the Pancake Relaxed Constraints model (RC Pancake). They are statistical models. A hypothetical set of two grains taken from the mid-plane section of a rolled sheet is shown. The crystal orientations of the two grains are chosen at random from a discrete set which describes the current texture. The initial set is derived from the ODF (Orientation Distribution Function) (Bunge [1]) which describes the texture of the material prior to the plastic deformation. This ODF can be obtained from an OIM measurement or from pole figures measured by X-ray or neutron diffraction. The interface between the grains is supposed to be parallel to the rolling plane, and the grains are supposed to have had a cubic shape before rolling. After rolling, this shape will change. According to the Taylor full constraints model [2–4] it becomes brick-like, with the two grains having the same shape. This is a result of the basic assumption of the FC Taylor theory, namely that the plastic strain of all individual grains is equal to the average plastic strain of the polycrystal (Fig. 12.1 (a)). According to the LAMEL model [5–6], the average shape change of a set of two stacked grains is still equal to the average shape change of the polycrystal, but in each of the two grains, shears have been allowed to take place (Fig. 12.1 (b)), which are referred to as “relaxations”. A relaxation shear in one grain is the opposite of the corresponding one in the other grain. Figure 12.2 shows the types of relaxations which are considered. The Pancake Relaxed Constraints model [4, 7–9] is similar (Fig. 12.1 (c)), but it does not require that the relaxations in the grains are each others’ opposite. The reason to develop models which allows for such relaxation shears is, that due the plastic anisotropy of the individual grains, the plastic work needed to achieve a given thickness reduction (in rolling) is smaller than when no relaxation are allowed (i.e. in the FC Taylor theory). The drawback of allowing for these relaxation strains is, that the deformations of adjacent grains are not necessarily compatible to each other, as they are according to the FC Taylor theory. Note that the deformations of the two grains (one placed on top of the other) considered in the LAMEL model (Fig. 12.1 (b)) are compatible. However, there is no guarantee for compatibility

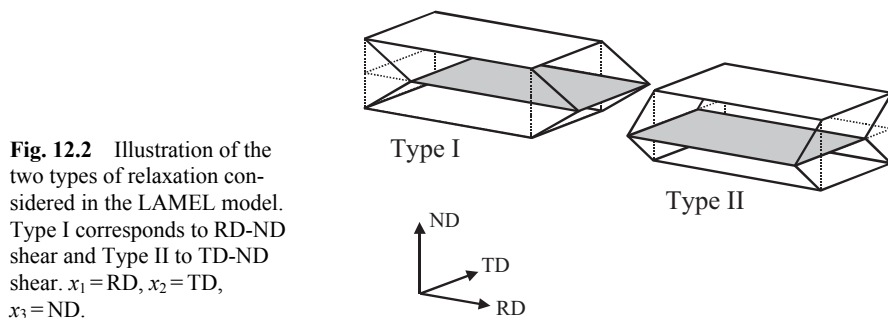


**Fig. 12.2** Illustration of the two types of relaxation considered in the LAMEL model. Type I corresponds to RD-ND shear and Type II to TD-ND shear.  $x_1 = \text{RD}$ ,  $x_2 = \text{TD}$ ,  $x_3 = \text{ND}$ .

with other neighbouring grains. It is implicitly assumed, that in reality, some complicated plastic deformation pattern is superimposed on the deformation field assumed by the model in order to accommodate the misfits between neighbouring grains. This superimposed accommodation field is NOT calculated explicitly by the LAMEL model. Note also that it is indeed a strong assumption of the LAMEL model that the interface between the two grains is parallel with the rolling plane. It is only acceptable for a materials with elongated grains which have aligned themselves with the rolling plane. The Pancake Relaxed Constraints model also assumes that the plane used for the definition of the relaxation shear (Fig. 12.1 (c)) is parallel to the rolling plane. In the FC Taylor theory, grain boundaries which would be parallel with the rolling plane do not play a special role.

### 12.2.2 Full Constraint (FC) Taylor Theory

Crystal plasticity based models are used to identify the active slip systems for a given increment of macroscopic strain, find the slips and also (in case of the LAMEL model and the Pancake Relaxed Constraints model) the relaxations. For this, kinematical equations are used relating the slip rates  $\dot{\gamma}_s$  and the relaxations to a given macroscopic strain rate tensor  $\mathbf{D}$ . The components of  $\mathbf{D}$  are  $d_{ij}$ . For the FC Taylor model, this can be done for each grain separately, leading to the following equation (elastic strains are neglected):

$$\mathbf{D} = \sum_{s=1}^N \mathbf{M}^s \dot{\gamma}_s \quad (12.1)$$

in which the tensors  $\mathbf{M}^s$  are geometrical constants which describe the unit shear on a slip system  $s$ . Their components are given by [3–6]:

$$M_{ij}^s = \frac{1}{2} (b_i^s m_j^s + m_i^s b_j^s) \quad (12.2)$$

$N$  is the total number of available slip systems (12 for fcc metals, 24 for bcc metals, such as the ferrite phase in steel.).  $\mathbf{b}^s$  is the unit vector in slip direction of slip system  $s$  (proportional to the Burgers vector), and  $\mathbf{m}^s$  is the unit vector normal to the slip plane of slip system. Note that it is assumed that the volume does not change (i.e.  $d_{11} + d_{22} + d_{33} = 0$ ). But the sum of the right-hand sides of Eq. 12.1 for  $ij=11, 22, 33$  is also zero because of the orthogonality between the vectors  $\mathbf{b}^s$  and  $\mathbf{m}^s$ . As a result, only 5 of the 6 eqs. (1) are independent. It thus appears that Eq. 12.1 stands for a system of 5 independent linear equations with 12 or 24 unknowns slip rates  $\dot{\gamma}_s$ . So there are not enough equations to find an unique solution for the slip rates. Taylor [2] proposed an additional condition to be fulfilled: the plastic work  $P^*$  dissipated in the grains should be minimised. It

has been shown that this is equivalent to applying the generalised Schmid law [10–11]. Again for the FC Taylor model, and for each grain separately:

$$P^* = \sum_{s=1}^N \tau_s^c |\dot{\gamma}_s| = \text{Min} \quad (12.3)$$

$\tau_s^c$  is the value of  $\tau^c$  for the slip system  $s$ . For the method of solving Eqs. 12.1–12.3) we refer to the literature [3–6]. Once the slips are known, the local deviatoric stress ( $\sigma'$ ) and the lattice rotations can be obtained [3–6]. The lattice rotations are then used to simulate the change in deformation texture caused by the increment of macroscopic strain.

### 12.2.3 LAMEL Model

In the case of the LAMEL model, the two grains shown in Fig. 12.1 (b) cannot be treated separately. The kinematical equations look as follows:

$$\mathbf{D} = \sum_{s=1}^N \mathbf{M}^{1s} \dot{\gamma}_s^1 + \sum_{r=1}^R \tilde{\mathbf{M}}^r \dot{\gamma}_r^{RLX} \quad (12.4)$$

for grain 1, and

$$\mathbf{D} = \sum_{s=1}^N \mathbf{M}^{2s} \dot{\gamma}_s^2 - \sum_{r=1}^R \tilde{\mathbf{M}}^r \dot{\gamma}_r^{RLX} \quad (12.5)$$

for grain 2. Equation 12.2 defines  $\mathbf{M}^{1s}$  and  $\mathbf{M}^{2s}$  separately for each of the two grains, which have different crystal orientations and hence vectors  $\mathbf{b}^s$  and  $\mathbf{m}^s$  with different orientations. In a similar way,  $\dot{\gamma}_s^1$  and  $\dot{\gamma}_s^2$  indicate the slip rates in grain 1 and grain 2. On the other hand, the index  $r$  in  $\mathbf{D}^r$  and  $\dot{\gamma}_r^{RLX}$  does not indicate a grain, but rather refer to the Type I and Type II relaxation modes shown in Fig. 12.2.  $\tilde{\mathbf{M}}^r$  represents a strain tensor of a unit shear according to the chosen relaxation.  $\dot{\gamma}_r^{RLX}$  then is the magnitude of the shear rate representing the rate of relaxation.

Equation 12.3 is now replaced by:

$$P^* = \sum_{l=1}^2 \sum_{s=1}^N \tau_s^{cl} |\dot{\gamma}_s^l| = \text{Min} \quad (12.6)$$

So  $P^*$  is the rate of plastic work for the two grains of the stack together. Equations 12.4–12.6 have to be solved simultaneously. The solution consists of the values of the slip rates in both grains (many of them zero) and the values of the relaxations ( $\dot{\gamma}_r^{RLX}$ ). More mathematical details can be found in other papers [5–6].



It is interesting to note that the solution found for the deviatoric stress respects the stress equilibrium along the boundary separating the two grains of the stack, at least as far as the shear stresses are concerned [5, 6]:

$$\sigma_{13}^{i1} = \sigma_{13}^{i2} \quad \text{and} \quad \sigma_{23}^{i1} = \sigma_{23}^{i2} \quad (12.7)$$

in which  $x_1$  is the rolling direction,  $x_2$  the transverse direction and  $x_3$  the normal to the sheet (RD, TD and ND in Fig. 12.2, respectively).

The LAMEL model is called an “interaction” model because it focuses on the interaction between two adjacent grains, each with a lattice orientation taken at random from the texture. The original LAMEL models only allows for the Type I and Type II relaxations shown in Fig. 12.2. The occurrence of deviations of this type from the homogeneous strain assumption of the FC Taylor model can be physically justified once the rolling strain has flattened the grains and brought them parallel with the rolling plane. Indeed, the reaction stresses caused by such strain misfits at the grain boundaries would only affect a minor volume fraction of the grains. Finally it should be noted that Eq. 12.4 (without Eq. 12.5) combined with Eq. 12.3 can be used for the RC Pancake model [9]. Each grain is treated separately.

#### 12.2.4 Grain Interaction (GIA) Model

The *Grain Interaction Model* (GIA) [12] is another new model which works with a cluster of 8 grains, arranged  $2 \times 2 \times 2$  in a “brick”-shaped volume in which there

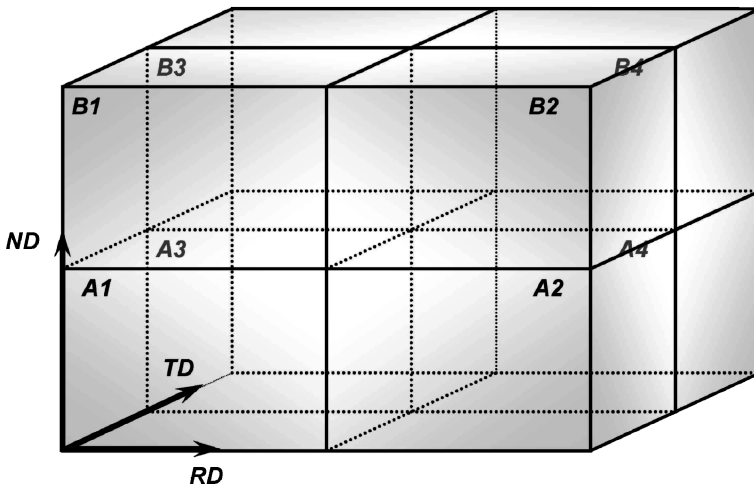
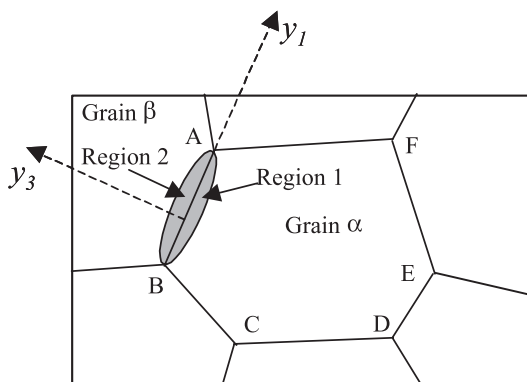


Fig. 12.3 Cluster of 8 grains used in the GIA-model.

are 3 internal interfaces (Fig. 12.3). Each of these is subdivided in 4 parts which each are the boundaries between 2 adjacent grains within the cluster of 8. Similar equations as in the LAMEL model are used for each of these pairs of adjacent grains. The cluster as a whole must satisfy the Taylor condition: the average strain of the cluster must be equal to the macroscopic strain. As long as this condition is satisfied, the grains within the cluster are allowed to relax; however, these relaxations may cause plastic strain misfits inside the cluster as well as at the outer cluster boundaries. These misfits are “penalised” by an energy term. The final solution is obtained by minimising the total work: work dissipated by the slip systems augmented by the penalty term [12]. It should be pointed out that as opposed to the LAMEL model, the GIA model can also be used for other deformation processes than rolling.

### 12.2.5 Advanced Lamel Model (ALAMEL)

More recent still is the Advanced Lamel Model (ALAMEL). Figure 12.4 shows its principle. The slip rates are not estimated in the centre of a grain, as the FC Taylor model implicitly does, but rather at grain boundaries [5]. A set of grain boundary segments is randomly chosen from the microstructure (measured or assumed). The slip rates are then calculated in the regions at both sides of the grain boundary, and very close to it (Regions 1 and 2, Fig. 12.4). In this, the stress equilibrium across the grain boundary segment is to be taken into account. This can be achieved by using the same constitutive equations as in the LAMEL model. A difference with the latter model is that the interfaces between two regions need not be parallel with the rolling plane. As strain goes on, the grain boundary segments tend to rotate towards the rolling plane. As a result, the predictions of the LAMEL and ALAMEL models are expected to converge at large thickness reductions in rolling. However, the ALAMEL model is not limited to rolling; it can also be used to simulate other deformation processes.



**Fig. 12.4** Schematic representation of a microstructure as assumed by the ALAMEL model.

### 12.2.6 Crystal Plasticity Finite Element Models (CPFEM)

Crystal plasticity finite element models (CPFEM) are of course also grain interaction models [13–14]. They have also been used in this study. A simulation of a 70% thickness reduction of a polycrystal consisting of 1000 grains has been carried out (Fig. 12.5). Each grain was represented by one element.

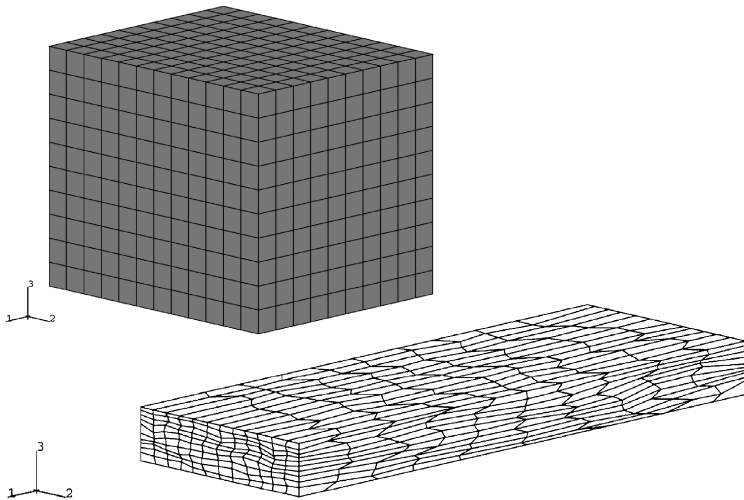


**Fig. 12.5** FE mesh used in the CPFEM simulation: (a) initially, (b) after cold-rolling simulation (70% reduction).

## 12.3 Model Validation

The texture of technically pure aluminium (AA1200) produced during the VIRFORM project [15] has been measured. Figure 12.6 shows the resulting ODF. The main component is the cube component. This material has then been rolled at room temperature until a thickness reduction of 98% was reached. Results are reported here for the thickness reductions of 40% and 95%. As an example, Fig. 12.7 shows the measured ODFs for AA1200. Simulations have been done as well, using the ODF shown in Fig. 12.6 as initial texture, after conversion into 3000 discrete grains, using the “statistical method” [16].

The results of deformation texture simulations are obtained as sets of weighted discrete orientations. They are converted into continuous ODFs by putting a Gaussian distribution of the type  $\exp(\psi/\psi_0)^2$  with a spread of  $\psi_0 = 7^\circ$  upon each of the orientations (Bunge [1]). These ODFs have been compared to those of experimentally observed deformation textures. For a quantitative comparison of the texture indices  $I(\Delta f)$  of the difference ODFs can be used. The texture index is the integral of

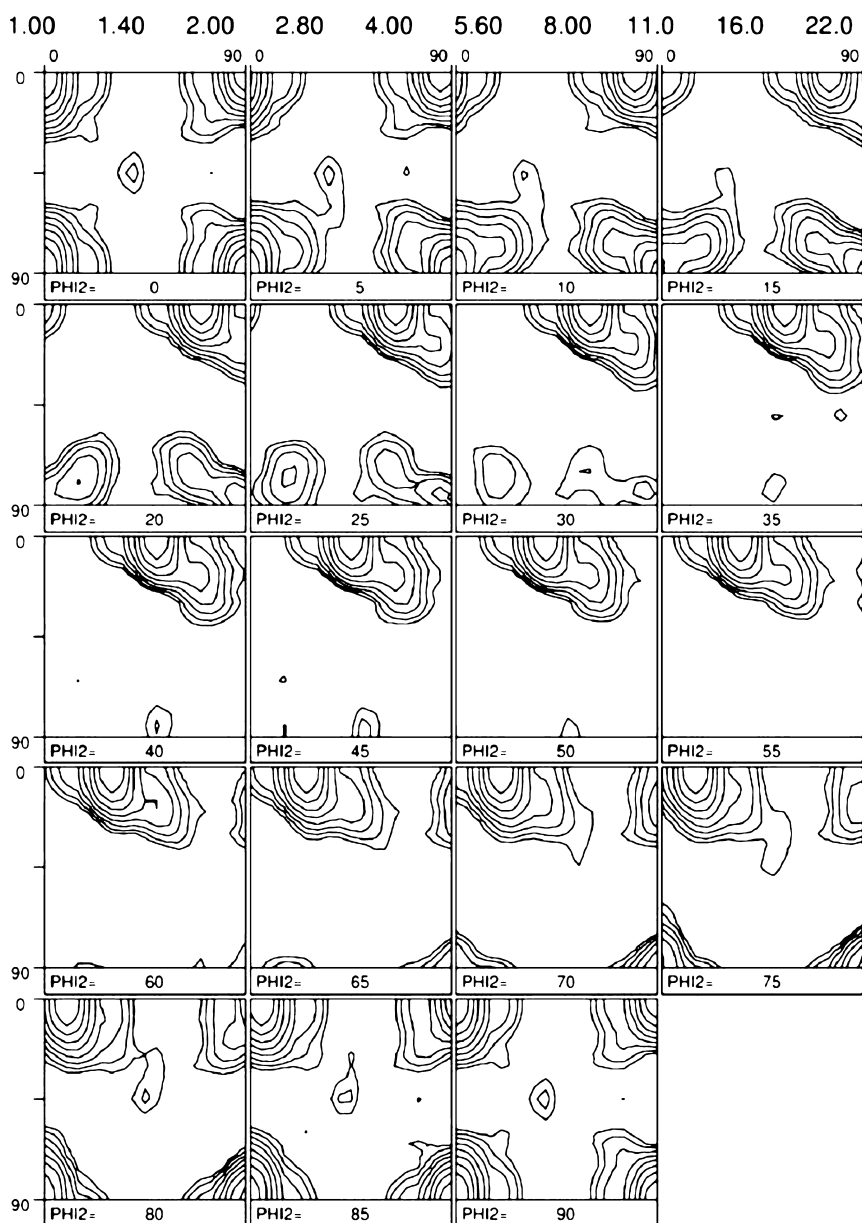


**Fig. 12.6** ODF of the initial texture of the commercially pure aluminium alloy (AA1200).

the square of the difference between the ODF of the experimental rolling texture and the one simulated by a model:

$$I(\Delta f) = \int \left[ f_{\text{model}}(g) - f_{\text{exper}}(g) \right]^2 dg \quad (12.8)$$

**Table 12.1** Texture indices  $I(\Delta f)$  of the difference ODFs (Eq. 12.8) of predicted and measured deformation textures. Only the results of the original version of the GIA model are given. The last row shows  $I_{\text{exper}}$ , the texture index of the ODFs of the experimental rolling textures. The ratio  $I(\Delta f)/I_{\text{exper}}$  can be regarded as a normalised texture difference index.

Material	AA1200	
<i>Reduction</i>	40%	95%
FC Taylor	0.54	1.87
RC Pancake	4.20	5.92
CPFEM	0.42	1.48
GIA	0.57	1.35
Lamel	0.89	1.26
ALamel	0.49	1.07
$I_{\text{exper}}$	2.59	6.87

(g: crystal orientation). The integrals are taken over entire orientation space. Table 12.1 shows results obtained for 40% and 95% thickness reduction in rolling.

It is equally instructive to present the results as intensity plots along the  $\beta$ -fibre of the ODF, starting at the Cu-orientation  $\{112\} \langle 111 \rangle$  at  $\varphi_2 = 45^\circ$ , along the S-orientation  $\{123\} \langle 634 \rangle$  at  $\varphi_2 = 65^\circ$  and ending at the Brass orientation  $\{110\} \langle 112 \rangle$  at  $\varphi_2 = 90^\circ$  (see also Fig. 12.7 (b)). Figure 12.8 gives such representations of the experimental rolling textures and the predictions by the CPFEM, GIA and ALAMEL models for the AA1200 alloy.

Figures 12.9–11 show results for IF steel obtained by the Taylor, CPFEM, GIA and ALAMEL models. First, Fig. 12.9 shows the location of the main components of steel textures in a  $\varphi_2 = 45^\circ$  section of the ODF. Table 12.2 gives the explanation of the letter codes used in the drawing for the ideal orientations. Note that there are several variants of the ideal orientations E and F which are crystallographically equivalent (at least in a rolling texture), and which are distinguished from each other by a subscript. Figure 12.10 then gives such sections for the hot rolling texture (used as input texture) and of cold rolling textures obtained after 70% thickness reduction: the experimentally observed texture as well as the simulated textures. It is seen that the three latter are quite close to each other, all of them still slightly deviating from the experimental texture, whereas the Taylor model actually made the texture worse than it was before the simulation. It should be noted that the finish temperature during the last hot rolling step was already in the ferritic range. As a result, the hot rolling texture has the typical aspect of a cold rolling texture. Figure 12.11 then gives the evolution of the intensity of the ODF along the  $\gamma$ -fibre (from  $E_2$  to  $F_2$  in Fig. 12.9). This figure illustrates spectacularly how much better the results of the interaction models (CPFEM, GIA and LAMEL) are as the results of the Taylor model. The figure was made before the development of the ALAMEL model; however, for this example, the latter gives almost the same results as the LAMEL model, as is illustrated by Fig. 12.10.

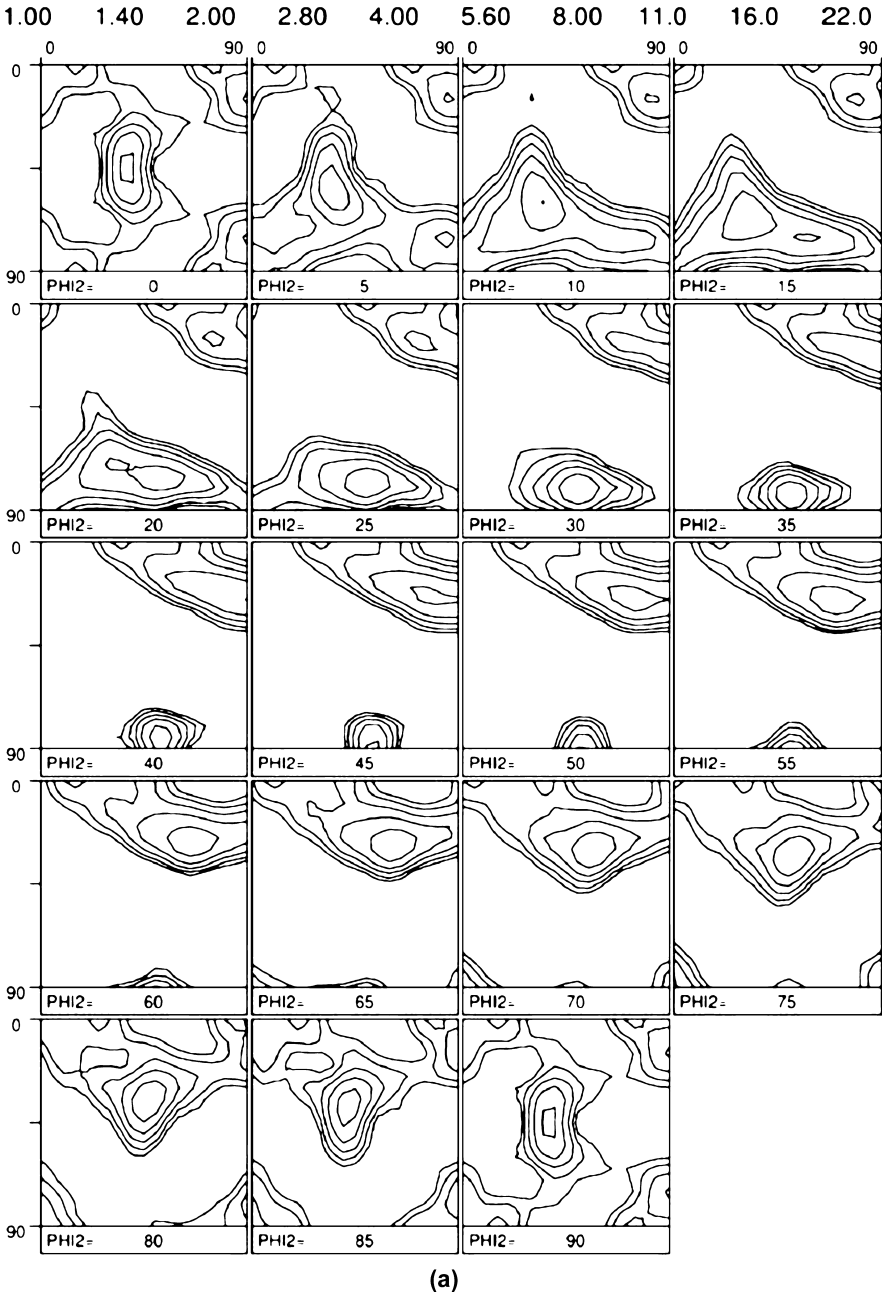


Fig. 12.7 (a) Cold rolling texture of AA1200. 40% thickness reduction.

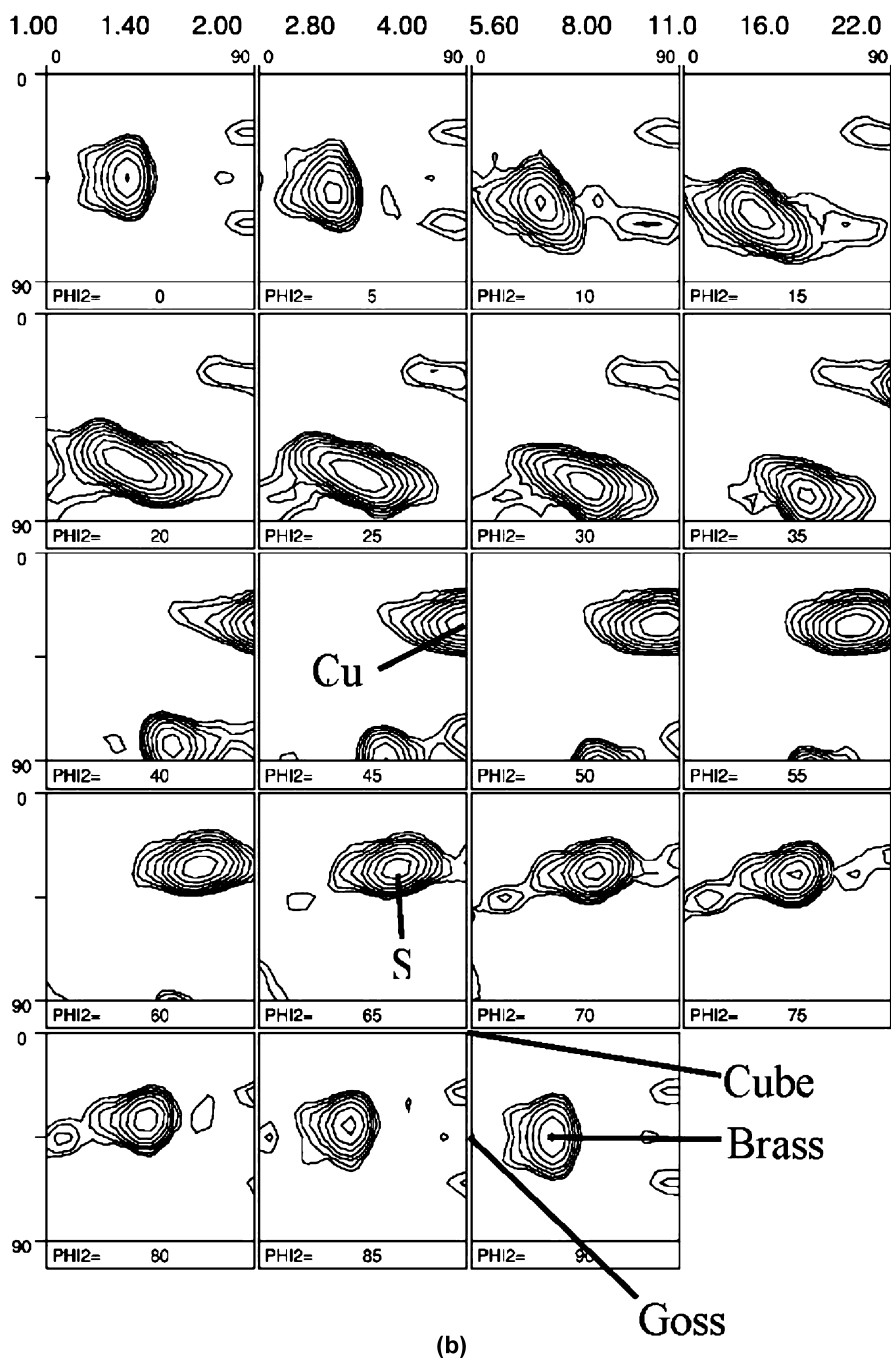
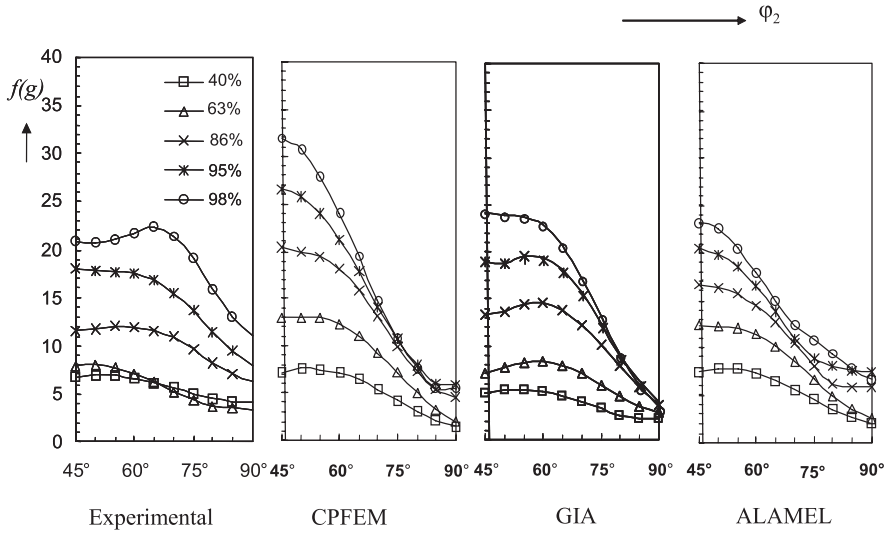
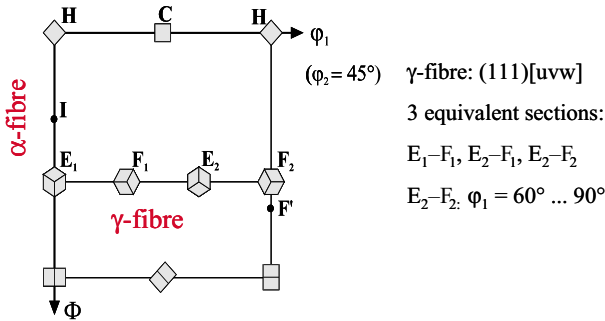


Fig. 12.7 (b) Cold rolling texture of AA1200. 95% thickness reduction.



**Fig. 12.8** Intensity distribution of ODFs of measured cold rolling texture of AA1200 alloy and those simulated by the CPFEM, GIA and ALAMEL models. The maximum intensity in each  $\varphi_2$ =constant section through the  $\beta$ -fibre is shown.



**Fig. 12.9** Location of the main components of steel textures in a  $\varphi_2=45^\circ$  section of the ODF. Table 12.2 gives the explanation of the letter codes used for the ideal orientations.

**Table 12.2** Labels used for texture components in Fig. 12.9.

Label	Miller indices
H	$\{001\}\langle 110 \rangle$
I	$\{112\}\langle 110 \rangle$
E	$\{111\}\langle 110 \rangle$
F	$\{111\}\langle 112 \rangle$
C	$\{100\}\langle 001 \rangle$



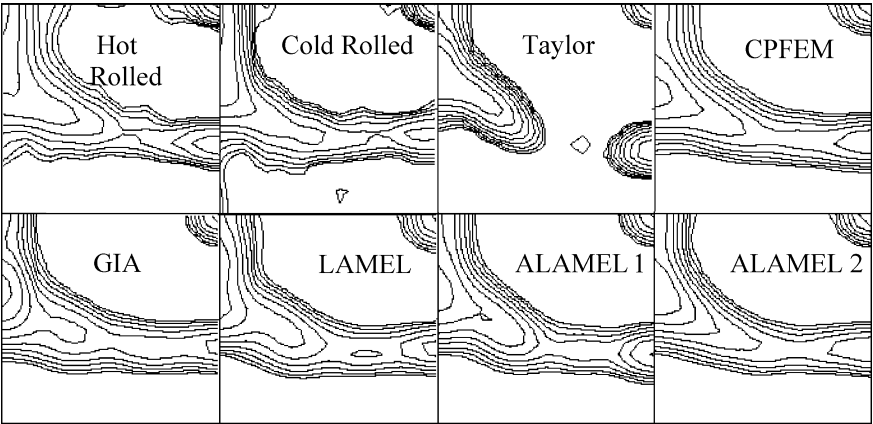
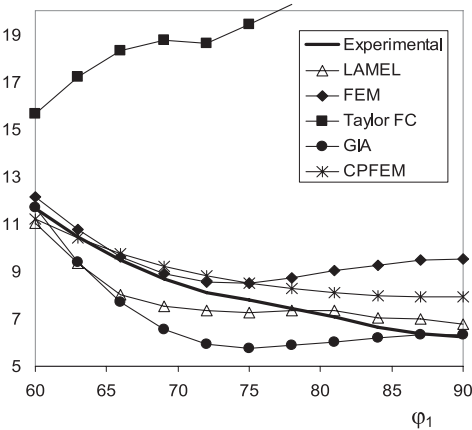


**Fig. 12.10**  $\varphi_2=45^\circ$  sections of the ODF (Bunge [1]) of 8 textures of IF steel: Initial texture (i.e. a hot band texture, with last rolling passes in ferritic range); after 70% cold rolling reduction; simulated textures according to 6 models. CPFEM by Bate [13]. ALAMEL 1 started from equiaxed grains and used  $\{110\} \langle 111 \rangle$  and  $\{112\} \langle 111 \rangle$  slip systems; ALAMEL 2 started from elongated grains (as if the grains of the hot rolled microstructure already had 40% rolling reduction) and used additional  $\{123\} \langle 111 \rangle$  slip systems. Levels: 1; 1.4; 2; 2.8; 4; 5.6; 8; 11; 16; 22

**Fig. 12.11** Skeleton line intensity along  $\gamma$ -fibre, IF steel, 70% rolled. Simulation results feature two results of crystal plasticity finite element codes, called FEM and CPFEM, and obtained using software by Bate [13] and Kalidindi [14], respectively.



Skeleton line intensity along  $\gamma$ -fibre,  
IF steel, 70% thickness red., rolling.

12.4 Discussion and Conclusions

Table 12.1 and Figs. 12.8, 12.10 and 12.11 show that the predictive quality of some of the interaction models (CPFEM, GIA, LAMEL and ALAMEL) is sys-

tematically better than that of the other models. The predictions of the relaxed constraints pancake model are particularly bad. Figure 12.8 reveals that the predictions of GIA and ALAMEL are quite satisfactory for AA1200. However, this is not true for all aluminium alloys, for some of which no known generic models can make satisfactory predictions.

A comment must be devoted to the performance of the CPFEM model. Table 12.1 and Figs. 12.7, 12.8 and 12.11 show, that they do not give the best predictions, although the present authors had in fact expected that they would. The results shown have all been obtained for simulations with several thousands of grains, with calculation times several orders of magnitude larger than those of GIA or ALAMEL. However, each grain was represented by only one element. It is expected that at least for AA1200 the quality of these simulations would substantially increase when 8 or 27 elements would be taken per grain, because the intragranular heterogeneity of plastic strain would then be better captured. However, this would further increase the required calculation time, which would be prohibitive for the use of this model in FE simulations of forming processes.

In spite of what is said above, it remains puzzling that at 70% thickness reduction of IF steel, LAMEL and ALAMEL unexpectedly perform better than the two CFEM models. A remark must be given here. It has not yet been checked whether this ranking would also be valid when the initial texture (hot rolling texture) would differ much more from the final textures as in the case studied here.

The work described here is only an initial study. Validations of the CPFEM, ALAMEL and GIA models must also be done for other deformation modes than rolling, and for other materials than AA1200 and IF steel. Besides, it would be worthwhile checking whether these models could not be used advantageously for predictions of plastic anisotropy ( $r$ -values, yield surfaces).

A strong limitation of the work presented here is that only single phase materials have studied so far. It can not be excluded that texture evolution during plastic deformation would also be of interest in two-phase or multiphase materials. This is also a possible direction of future work.

**Acknowledgement** The author gratefully acknowledge financial support by the European Union through the VIRFORM-project (Contract No G5RD-CT-1999-00155) as well as by the Interuniversity Attraction Poles Programme from the Belgian State through the Belgian Science Policy agency, contract IAP6/24. They thank all partners of the VIRFORM consortium for their collaboration and support, as well as P. Bate, M. Crumbach, G. Gottstein, O. Engler, L. Delannay, M. Seefeldt and I. Samajdar for help with the simulations and for many valuable discussions.

## References

- [1] Bunge, H.G., Texture Analysis in Materials Science. Butterworth, London. (1982).
- [2] Taylor, G.I., J. Inst. Metals 62 (1938) 307–324.

- [3] Kocks, U.F., Tomé, C.N., Wenk, H.-R., *Texture and Anisotropy. Preferred Orientations in Polycrystals and their Effect on Material Properties*. Cambridge University Press, Cambridge, U.K. (1998).
- [4] Aernoudt, E., Van Houtte, P. and Leffers, T., *Plastic Deformation and Fracture of Materials*, (Vol. 6 of *Materials Science and Technology: A Comprehensive Treatment*, edited by R.W. Cahn, P. Haasen and E.J. Kramer), edited by H. Mughrabi. Weinheim, Federal Republic of Germany: VCH (1993) 89–136.
- [5] Van Houtte P., Li S., Seefeldt, M., Delannay L., *Int. J. Plasticity* 21 (2005) 589–624.
- [6] Van Houtte, P., Kanjarla, A.K., Van Bael, A., Seefeldt, M., Delannay, L., 2006. *European Journal of Mechanics A/Solids* 25, 634–648.
- [7] Honeff, H., Mecking, H., In: (Ed.), *Proc. ICOTOM 6*, vol.1 (edited by S. Nagashima), The Iron and Steel Institute of Japan, Tokyo (1981) 347–355.
- [8] Kocks, U.F., Chandra, H., *Acta Metall.*, 30 (1982) 695–709.
- [9] Van Houtte, P., On the equivalence of the relaxed Taylor theory and the Bishop-Hill theory for partially constrained plastic deformation of crystals.. *Mater. Sci. Eng.* 55 (1982) 69–77.
- [10] Bishop, J.F.W., Hill, R., A theory of the plastic distortion of a polycrystalline aggregate under combined stress. *Phil. Mag.* 42 (1951) 414–427.
- [11] Bishop, J.F.W., Hill, R., A theoretical derivation of the plastic properties of a polycrystalline face-centred metal. *Phil. Mag.* 42 (1951) 1298–1307.
- [12] Crumbach, M., Pomana, G., Wagner, P., Gottstein, G., *Recrystallisation and Grain Growth*, *Proc. First Joint Conference*, edited by G. Gottstein, and D.A. Molodov, Springer, Berlin (2001) 1053–1060.
- [13] Bate, P., Modelling deformation microstructure with the crystal plasticity finite-element method. *Philos. T. Roy. Soc. A* 357:1756 (1999) 1589.
- [14] Kalidindi, S.R., Bronkhorst, C.A., Anand, L., *J. Mech. Phys. Solids*, 40 (1992) 537–569.
- [15] P. Van Houtte, S. Li, and O. Engler: “Modelling deformation texture of aluminium alloys using grain interaction models”, *Aluminium* 80/6 (2004) 702–706.
- [16] Toth, L.S., Van Houtte, P., *Textures and Microstructures*, 19 (1992) 229–244.



Paul Van Houtte  
 Professor  
 Department of MTM  
 Katholieke Universiteit Leuven  
 Belgium

# Chapter 13

## Simulation of Persistence Characteristics of Textures During Plastic Deformation

László S. Tóth

*László S. Tóth dedicates this paper to Ranjit Kumar Ray, for his friendship and his lifetime achievements.*

**Abstract.** The ideal orientations of textures that develop at large strains can be identified with the help of crystal plasticity simulations. In this short review, an overview is presented on these types of simulations that helped in the identification of the deformation texture components of fcc, bcc and hcp materials in pure shear (rolling) as well as in simple shear (torsion) during the last 20 years. The technique is based on the so-called persistence parameter that was introduced by Tóth, Gilormini and Jonas in 1988 [*Acta Metall.*, 36, 3077–3091]. The formation of textures and several texture effects can be understood with the help of the persistence parameter together with the rotation field of orientations in Euler space and the divergence quantity. The stability of ideal orientations is especially investigated and it is shown that simple shear distinguishes from pure shear in a very particular way; all ideal orientations of simple shear are positioned at orientations where the divergence is zero while in rolling they are situated within a negative divergence field.

### 13.1 Introduction

Large plastic monotonic deformation leads to the formation of ideal orientations in a polycrystalline material that is characteristic to both the applied strain mode as well as to the crystal structure. Around the ideal texture components, the lattice

---

L.S. Tóth  
Laboratoire de Physique et Mécanique des Matériaux, Université Paul Verlaine Metz, France

rotation is locally minimum. Polycrystal models are able to predict the lattice spin which can be directly used to identify the ideal orientations. Such analysis has been carried out for simple shear of f.c.c. [1, 2], b.c.c. [3], rolling of f.c.c. [4], simple shear of h.c.p. crystals [5] as well as for rolling of b.c.c. [6]. In order to understand the texture development, one has to look also into the velocity field of the lattice rotation in Euler space and the divergence quantity. The latter is particularly different when simple shear and rolling are compared. For simple shear, all ideal orientations are situated at the boundary lines between convergent and divergent regions of orientation space while in rolling they are all within a convergent region. These differences explain several texture effects that can be observed especially in simple shear and in ECAE. These effects will be reviewed in this presentation.

## 13.2 Principles of Orientation Stability

### 13.2.1 Stability Condition

A coherent crystal domain (grain, or subgrain, or dislocation cell) can be identified in orientation space with three Euler angles,  $\phi_1, \varphi, \phi_2$ , that define the location of the grain by the vector  $\vec{g}$ , see Fig. 13.1:

$$\vec{g} = (\phi_1, \varphi, \phi_2). \quad (13.1)$$

The orientation changes due to plastic deformation, which is characterized by the orientation velocity vector  $\vec{\dot{g}}$ :

$$\vec{\dot{g}} = (\dot{\phi}_1, \dot{\varphi}, \dot{\phi}_2). \quad (13.2)$$

$\vec{\dot{g}}$  can be calculated from a crystal plasticity model. In the present work, the viscoplastic Taylor model is employed for this purpose.

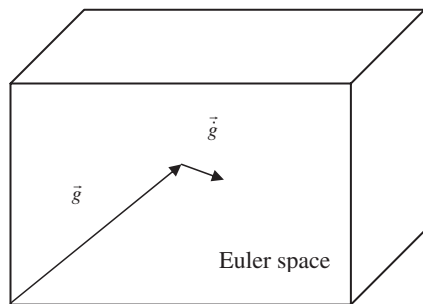
An orientation is stable if the following four conditions are satisfied:

$$\vec{\dot{g}} = (\dot{\phi}_1, \dot{\varphi}, \dot{\phi}_2) = 0, \quad (13.3)$$

$$\frac{\partial \dot{\phi}_1}{\partial \phi_1} < 0, \quad \frac{\partial \dot{\varphi}}{\partial \varphi} < 0, \quad \frac{\partial \dot{\phi}_2}{\partial \phi_2} < 0. \quad (13.4)$$

The latter three conditions assure that if the orientation is near to the stable point, it will rotate into it. The four conditions together assure that a grain oriented in the vicinity of the stable point will not leave from there. These are the single-crystal stability conditions. When a polycrystal is considered, individual orientations are not discerned and the texture is described by a continuous orientation

**Fig. 13.1** Orientation space showing the grain orientation vector and the orientation velocity vector.



distribution function, called ODF. For that case, stability means that the intensity of the ODF increases and remains high at the stable point. This can be expected when condition (3) is satisfied together with:

$$\text{div } \vec{\dot{g}} = \frac{\partial \dot{\phi}_1}{\partial \phi_1} + \frac{\partial \dot{\phi}}{\partial \phi} + \frac{\partial \dot{\phi}_2}{\partial \phi_2} < 0 . \quad (13.5)$$

Here  $\text{div } \vec{\dot{g}}$  is the divergence quantity. When it is negative, it means that more grain orientations flow into the  $\vec{g}$  orientation than leave.

### 13.2.2 Evolution of Orientation Density

Equation 13.5 has to be valid in the vicinity of the ideal position. For polycrystals, we have to examine the variation of the ODF as a function of time. This can be done in two ways [7, 8]. The first is the so-called Lagrangien continuity equation:

$$\dot{f}/f + \dot{\phi} \cdot \cot \phi + \text{div } \dot{\mathbf{g}} = 0 . \quad (13.6)$$

The second is the Eulerien formalism:

$$\left( \dot{f}/f \right)_g + \dot{\phi} \cdot \cot \phi + \text{div } \dot{\mathbf{g}} + \dot{\mathbf{g}} \cdot \text{grad}(\ln f) = 0 . \quad (13.7)$$

In these two equations, the  $\dot{\phi} \cdot \cot \phi$  quantity accounts for the distortion of the Euler space.  $\dot{f}/f$  describes the evolution of the ODF. For weak textures, the  $\dot{\mathbf{g}} \cdot \text{grad}(\ln f)$  can be neglected near the ideal positions which are expected to be at positions where  $\dot{\mathbf{g}}$  is zero. In conclusion, in both equations, the  $\dot{\mathbf{g}}$  and the  $\text{div } \dot{\mathbf{g}}$  quantities that are decisive in the development of the ODF intensities near the ideal orientations. Therefore, it is sufficient to examine these quantities in the whole Euler space in order to identify the persistence characteristics of ideal orientations of textures. First we will examine the velocity field, then the divergence.

### 13.2.3 Role of Rigid Body Rotation

In the following, it will be shown that the rigid body rotation plays an important role in the slip system activity of stable orientations. For this purpose, it is more practical to use the lattice spin  $\underline{\underline{\dot{\Omega}}}$  than the orientation velocity vector  $\dot{\mathbf{g}}$ . They, of course, express the same thing; the rate of orientation change of an orientation. The main difference is that the lattice spin,  $\underline{\underline{\dot{\Omega}}}$ , is a tensorial quantity, and usually expressed in the sample reference system, while  $\dot{\mathbf{g}}$  is a vector quantity and is expressed in orientation space. They are, of course, related to each other through the transformation formula:

$$\underline{\underline{\dot{T}}} = \underline{\underline{\dot{\Omega}}} \underline{\underline{T}}, \quad (13.8)$$

where  $T$  is the transformation going from the sample to the crystal system and is defined by the Euler angles. The transformation formulas between  $\underline{\underline{\dot{\Omega}}}$  and  $\dot{\mathbf{g}}$  are given by:

$$\begin{aligned} \dot{\phi}_1 &= -\dot{\Omega}_{12} - \dot{\phi}_2 \cos \phi \\ \dot{\phi} &= -\dot{\Omega}_{23} \cos \phi_1 - \dot{\Omega}_{31} \sin \phi_1 \\ \dot{\phi}_2 &= -\dot{\Omega}_{23} \frac{\sin \phi_1}{\sin \phi} + \dot{\Omega}_{31} \frac{\cos \phi_1}{\sin \phi}. \end{aligned} \quad (13.9)$$

The lattice spin is the difference between the rigid body spin  $\underline{\underline{\dot{\beta}}}$  and the plastic spin  $\underline{\underline{\dot{\omega}^s}}$  [1]:

$$\underline{\underline{\dot{\Omega}}} = \underline{\underline{\dot{\beta}}} - \underline{\underline{\dot{\omega}^s}}. \quad (13.10)$$

The rigid body spin is simply the rigid rotation part of the imposed deformation, while the plastic spin is defined by the crystallographic glide rate  $\dot{\gamma}^s$  in a slip system that is given by the slip plane normal  $\vec{n}$  and slip direction  $\vec{b}$  as follows:

$$\underline{\underline{\dot{\omega}^s}} = \dot{\gamma}^s (\vec{b} \otimes \vec{n}). \quad (13.11)$$

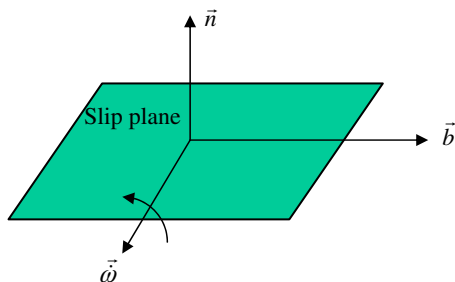


Fig. 13.2 Representation of plastic spin.

The meaning of the plastic spin is a rotation around a direction that is perpendicular to both  $\bar{n}$  and  $\bar{b}$ , see Fig. 13.2.

Using Eq. 13.10, two main cases can be distinguished:

- a/ Tests where there is imposed rigid body rotation (example: simple shear)
- b/ Tests where there is no imposed rigid body rotation ( $\underline{\dot{\beta}} = 0$ ; rolling, tension, compression).

### 13.2.3.1 Rolling Test

It is important to note that in case b, the expression of the lattice spin is simply:  $\underline{\dot{\Omega}} = -\underline{\dot{\omega}}^s$ . Let us examine the consequences of this result in order to obtain more precise information about the slip system characteristics of an ideal orientation in such a case (rolling). As the main condition of stability of an orientation is zero lattice spin, it is the plastic spin which has to be zero:

$$\underline{\dot{\omega}}^s = 0. \quad (13.12)$$

It can, however, be zero only if there are at least four slip systems active simultaneously [9]. Actually, it is evident from Fig. 13.2, that the plastic spin cannot be zero for one slip system; also, it cannot be zero for any combination of two systems because of their different orientations. The condition of minimum four slip systems means that all ideal orientations of rolling textures are such that crystals in such orientations are deforming simultaneously by at least four slip systems. This is important information about the micromechanics of the crystal, which is decisive, for example, in the hardening behavior of the crystal during rolling.

### 13.2.3.2 Simple Shear Test

The other extreme case, when the deformation is simple shear, will now be investigated. It is obvious from Eq. 13.10 that for zero lattice spin; the following condition has to be satisfied:

$$\underline{\dot{\omega}}^s = \underline{\dot{\beta}}. \quad (13.13)$$

Now the situation is opposite with respect to rolling; the plastic spin has to be high. This is only possible if the number of operating slip systems is very low, otherwise the differently oriented slip systems cancel each others' contribution to the resultant plastic spin. It has been shown in [1, 2] that the number of operating slip systems for all ideal orientations of simple shear (torsion) textures is actually limited to two. This is an information that is again of capital importance in the behavior of a crystal oriented ideally in torsion. Namely, as deformation proceeds, characteristic shear texture develops at large strains where the majority of grains



approach the ideal orientations, thus their slip system activity will be limited to one or two slip systems being active. Comparing to rolling or other deformation modes where there is no rigid body rotation, the smaller number of active slip systems I shear should involve a different strain hardening because of the reduced interaction of the different slip systems. Such differences are well known in the hardening behavior of materials when tension and torsion is compared and can be interpreted with the help of the differences in the slip system activity [10].

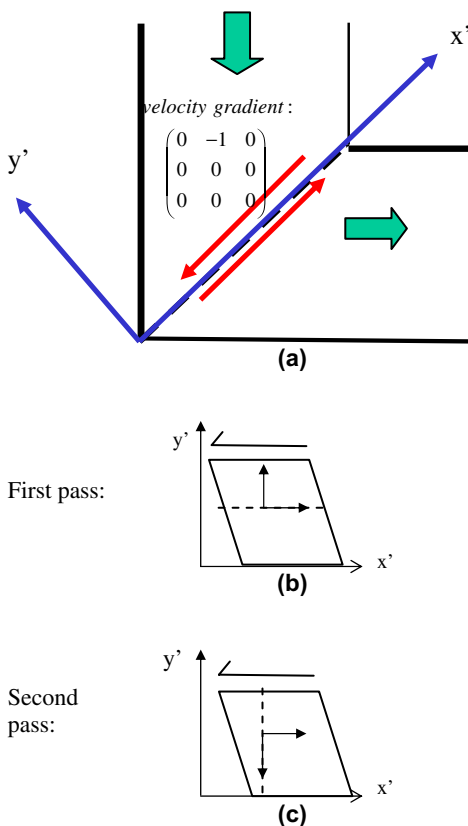
### 13.2.3.3 Equal Channel Angular Extrusion (ECAE) Test

The role of the rigid body rotation in a more recent testing, the ECAE test, is also very important. In ECAE, the billet is deformed in two equal section channels that are connected at an angle, usually, at  $90^\circ$ , see Fig. 13.3 (a). The deformation is nearly simple shear in the intersection plane of the two channels, as it is indicated in the figure. In the local reference system, which is rotated by  $45^\circ$  with respect to the pressing, the velocity gradient is simple shear:

$$\underline{\underline{L}} = \dot{\gamma}_{shear} \begin{pmatrix} 0 & -1 & 0 \\ 0 & 0 & 0 \\ 0 & 0 & 0 \end{pmatrix}, \quad (13.14)$$

where  $\dot{\gamma}_{shear}$  is the shear rate. If we examine the behavior of a stable texture component, it must have zero lattice spin;  $\underline{\underline{\dot{\Omega}}} = 0$ . Considering, as an example, one of the main ideal orientations where the number of active slip systems is only one (the 'A' orientation, see Fig. 13.3 (b)), one can easily see that the slip rate in the slip system  $\dot{\gamma}_{slip}$  is equal to the imposed ECAE shear rate:  $\dot{\gamma}_{slip} = \dot{\gamma}_{shear}$ . The particularity of the ECAE test that the sample can be re-passed several times in the die. In a subsequent pass, in Route A, where there is no rotation around the sample longitudinal axis, the billet will be deformed by shear perpendicularly to the previous shear, see Fig. 13.3 (c). However, the operating slip system still remains the same, just rotated by  $90^\circ$  with respect to the shear. (One can readily obtain this by considering that the applied shear stress is acting always on two perpendicular planes, because of the equilibrium condition.) Having the same slip system perpendicular to the imposed shear direction will lead to an opposite slip in that slip system:  $\dot{\gamma}_{slip} = -\dot{\gamma}_{shear}$ . This means that the plastic spin changes into opposite sign while the rigid body spin remains the same. The result is that this orientation now cannot be stable; its lattice rotation becomes very high; one obtains:  $\underline{\underline{\dot{\Omega}}} = 2\underline{\underline{\dot{\beta}}}$ . In general, while a shear texture is formed during one pass in ECAE, it will be completely unstable during the next ECAE pass and large lattice rotations are forced onto the material. This effect must be important in the result-

**Fig. 13.3** Kinematics of the ECAE process. (a): The imposed strain mode, (b): Shear of a crystal in orientation stable with one slip system active during the first pass. (c): Same in a subsequent pass (Route A).



ing microstructure of the material, especially in the grain refinement process which is very efficient in ECAE deformation.

The above described effect can be clearly seen in some experiments as well. As an example, we show the textures that were measured and simulated in ECAE of polycrystalline magnesium at 250°C [11]. The initial texture was a basal fiber with its axis initially coinciding with the extrusion direction, see Fig. 13.4. After one-pass ECAE in a 90° die, the texture was basically rotated in the direction of the applied ECAE-shear by about 100°. This value, however, is much larger than the possible rigid body rotation imposed by the shear; for a 90° die, where the shear is  $\gamma = 2$ , the rigid body rotation is only 57.3°. The observed 110° is about twice as large! This rotation was possible to explain in [11] by an analytical crystal plasticity calculation by considering that only basal slip was activated. During the second pass, the situation is nearly repeated, only the angle of lattice rotation was slightly reduced, see Fig. 13.4. Self consistent polycrystal simulations were also carried out in [11] which reproduced faithfully the experimental textures.

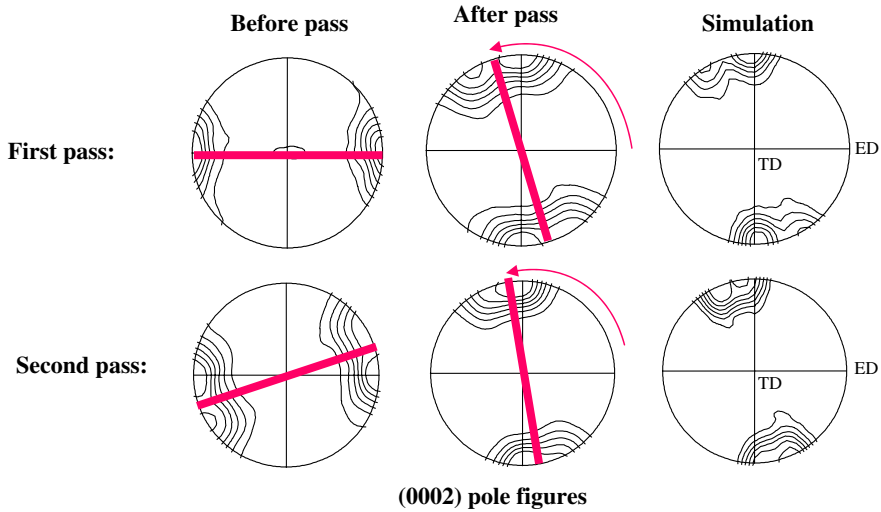


**Fig. 13.4** Measured and simulated ECAE-shear textures in polycrystalline Mg deformed in a 90° die at 250°C [11].

### 13.3 How to Identify Ideal Orientations?

#### 13.3.1 The Persistence Parameter

Crystal plasticity simulations can be used to identify the ideal orientations of deformation textures. The first such work was presented in 1988 [1]. In that work, the so-called persistence parameter  $S$  was introduced for that purpose. It is defined from the lattice spin as follows:

$$S(\phi_1, \phi, \phi_2) = \ln \frac{1}{\left| \dot{\underline{\Omega}}(\phi_1, \phi, \phi_2, \dot{\underline{\varepsilon}}) \right| / \bar{\dot{\varepsilon}}}, \quad (13.15)$$

$$\left| \dot{\underline{\Omega}}(\phi_1, \phi, \phi_2, \dot{\underline{\varepsilon}}) \right| = \left( \dot{\underline{\Omega}}_{32}^2 + \dot{\underline{\Omega}}_{31}^2 + \dot{\underline{\Omega}}_{12}^2 \right)^{1/2}$$

where  $\bar{\dot{\varepsilon}}$  is the von Mises equivalent strain rate corresponding to the imposed Eulerian strain rate tensor  $\dot{\underline{\varepsilon}}$ .  $S$  is high when  $\dot{\underline{\Omega}}$  is small and inversely. Thus, high values of  $S$  correspond to orientations that move very slowly in orientation space. There appears a numerical problem when  $\dot{\underline{\Omega}}$  is zero, which is expected to be the case for the exact ideal orientation positions, however, when maps of  $S$  are made, these orientations can be left out and still made visible by the other high intensity lines that necessarily pass near to them. Thus making maps of the

$S$  parameter, the locations where  $S$  is very high can be identified. They are the suspected locations of ideal texture components.

### 13.3.2 Examples for Persistence Maps

#### 13.3.2.1 Simple Shear of FCC Polycrystals

The first example was developed for the case of torsion of fcc polycrystals [1]. Part of the obtained map is shown in Fig. 13.5. The names of the main ideal orientation are also shown in these maps. As can be seen, they are all at maximum values of the persistence parameter. 'Tubes' appear in orientation space with their center points coinciding exactly with the known fiber positions of simple shear textures. For all locations where  $S$  is locally maximum, there is a known ideal texture component of experimental textures. No new orientations were found in that analysis.

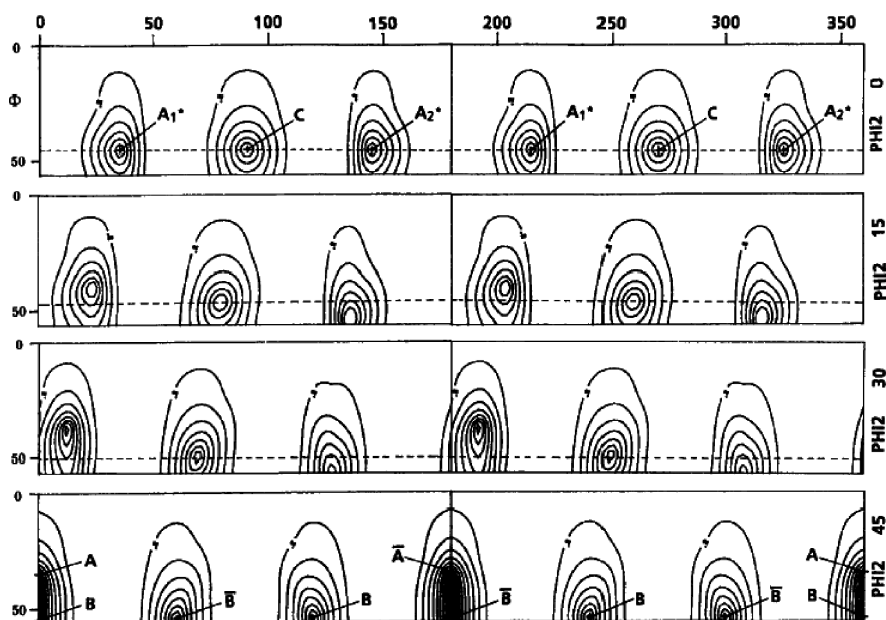
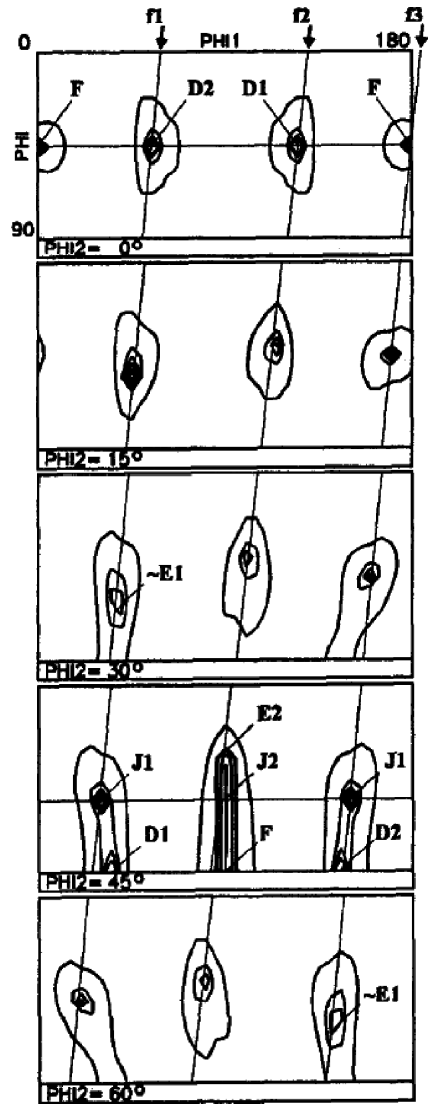


Fig. 13.5 Orientation persistence map for simple shear of fcc polycrystals (from [1]).

#### 13.3.2.2 Simple Shear of BCC Polycrystals

The same analysis was repeated for bcc torsion in [3]. The obtained map is presented in Fig. 13.6. Again, all identified ideal positions correspond to experimen-

**Fig. 13.6** Orientation persistence map for simple shear of bcc polycrystals (from [3]).



tally known components; the main ones are indicated in the figure. Three fibers were identified, which were named  $f_1$ ,  $f_2$  and  $f_3$ . They are indicated by connecting the maximum  $S$  positions with straight lines in Fig. 13.6.

**13.3.2.3 Comparison of FCC and BCC Simple Shear**

There is a striking similarity between the ideal orientations of fcc and bcc simple shear ideal texture positions. This is illustrated in two sections of Euler space; in the

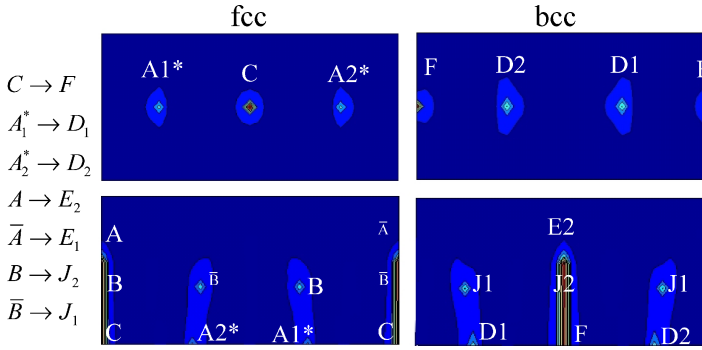


**Fig. 13.7** Comparison of fcc and bcc ideal orientations in simple shear. The correspondence between ideal orientations is indicated on the left side of the figure.

$\phi_2 = 0^\circ$  and  $\phi_2 = 45^\circ$  sections in Fig. 13.7. Actually, the persistence map of bcc materials coincides with the fcc case for the following transformation of the Euler angles:

$$\begin{aligned}\phi_1^{bcc} &= \phi_1^{fcc} + 90^\circ \\ \phi^{bcc} &= \phi^{fcc} \\ \phi_2^{bcc} &= \phi_2^{fcc}.\end{aligned}\quad (13.16)$$

As can be seen, the main ideal orientations can be transformed according to the following rule:

$$C \rightarrow F, \quad A_1^* \rightarrow D_1, \quad A_2^* \rightarrow D_2, \quad A \rightarrow E_2, \quad \bar{A} \rightarrow E_1, \quad B \rightarrow J_2, \quad \bar{B} \rightarrow J_1. \quad (13.17)$$

This equivalence between the ideal orientations of fcc and bcc shear textures can be explained as follows. In the fcc case, the operating slip systems are the type  $\{111\} \langle 110 \rangle$ . In bcc, this is the opposite:  $\{110\} \langle 111 \rangle$ . (Let us neglect for a moment the possible contribution of the  $\{112\} \langle 111 \rangle$  and  $\{123\} \langle 111 \rangle$  slip systems as well as pencil glide.) Under these conditions, a given fcc slip system transforms into a bcc type using the following transformation:

$$\underline{b}^{(fcc)} \rightarrow \underline{n}^{(bcc)}, \quad \underline{n}^{(fcc)} \rightarrow -\underline{b}^{(bcc)}. \quad (13.18)$$

This is also illustrated in Fig. 13.8. The  $\underline{n}$  and  $\underline{b}$  vectors are the slip plane normal and the slip direction, respectively. Now, the resolved shear stress is calculated from the stress state using the usual formula:

$$\tau_r = (\underline{\underline{\sigma}} \underline{n}) \underline{b}. \quad (13.19)$$

It can be shown that in general the  $\underline{n}$  and  $\underline{b}$  vectors can be interchanged when the resolved shear stress is calculated:

$$\tau_r = (\underline{\underline{\sigma}} \underline{n}) \underline{b} = \sigma_{ij} m_{ij} = \sigma_{ji} m_{ji} = \sigma_{ij} m_{ji} = (\underline{\underline{\sigma}} \underline{b}) \underline{n}. \quad (13.20)$$

Using in Eq. 13.20 the transformation formulas of Eq. 13.18, it follows:

$$\tau_r^{fcc} = -\tau_r^{bcc}, \text{ that is; } \dot{\gamma}_s^{fcc} = -\dot{\gamma}_s^{bcc}. \quad (13.21)$$

Now we calculate the plastic spin using its definition:

$$\dot{\omega}_{ij} = \sum_{s=1}^n \frac{1}{2} (m_{ij}^s - m_{ji}^s) \dot{\gamma}_s = \sum_{s=1}^n \frac{1}{2} (b_i^s n_j^s - n_i^s b_j^s) \dot{\gamma}_s. \quad (13.22)$$

Now using relations (Eq. 13.18) and the second in Eq. 13.21, the following result is obtained:

$$\dot{\omega}_{ij}^{fcc} = -\dot{\omega}_{ij}^{bcc}. \quad (13.23)$$

That is, the plastic spin simply changes sign. Obviously, if the plastic spin becomes opposite, the same orientated fcc or bcc crystal cannot be both in stable position. This is why the ideal orientations are not at the same Euler angle positions. However, by rotating the orientation of the crystal by  $90^\circ$  along the  $\phi_1$  axis, the lattice spin becomes opposite. (This can be readily shown by exchanging  $\mathbf{n}$  with  $\mathbf{b}$  in Eq. 13.22.) Thus, the same lattice spin is obtained as in fcc but now we are in the bcc crystal structure. The transformation formulas of 13.16 are then confirmed.

Nevertheless, the above calculation was done for the simplified case when the  $\{110\} \langle 111 \rangle$  slip system is considered in bcc simple shear. Interestingly, when the second family, the  $\{112\} \langle 111 \rangle$  is also considered – which was the case in the calculation of the persistence maps in Fig. 13.6 – the transformation formulas in (16) still remain valid. This is rather surprising, but interestingly, the addition of this second family does not change the plastic spin if it was already zero without adding it. This is a numerical finding. It was also found in numerical calculations, that the second slip system family, namely the  $\{112\} \langle 111 \rangle$  is active only in selected ideal orientations but not for all orientations along the ideal fibre. (This result was obtained for rate insensitive slip by taking the rate sensitive solution to its limiting case.) This must be due to the complex shape of the yield surface of the single crystal.

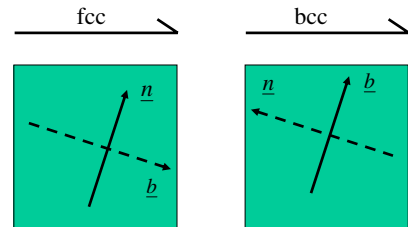


**Fig. 13.8** Illustration of the relation between fcc and bcc slip systems for the same grain orientation.

### 13.3.2.4 Simple Shear of HCP Polycrystals

The persistence maps for the case of simple shear of hcp crystals was published very recently [5]. As the ideal orientations were not known before for the hcp case, this work is very useful in this respect. For hexagonal materials several slip modes are possible. They are: basal slip, prismatic slip, pyramidal  $\langle a \rangle$  type slip and pyramidal  $\langle c + a \rangle$  slip. As the obtained result depends on the relative strengths of these different families, it was decided to derive the ideal orientations first for the limiting cases, meaning, when one of the families has a very low resistance with respect to all others. The results obtained in this way are shown in Fig. 13.9. The calculation was done for high strain rate sensitivity of the crystallographic slip (a value of  $m = 0.2$  was used) for the reason that hexagonals usually are deformed at higher temperatures.

Using the  $S$  parameter-maps in Fig. 13.9, five ideal fibres were identified in simple shear of hcp crystals. They were named as B, P, Y, C1 and C2 fibres. B corresponds to basal slip, P is to prismatic, Y is pyramidal  $\langle a \rangle$  while C1 and C2 are pyramidal  $\langle c + a \rangle$  fibres. When another set of relative strength is used among the slip system families, the relative strength of the fibres changes, however, their position in orientation space remains unchanged. For example, in Mg, the B fibre is the strongest, while in Ti, the P fibre is also strong. See more details in Ref. [5].

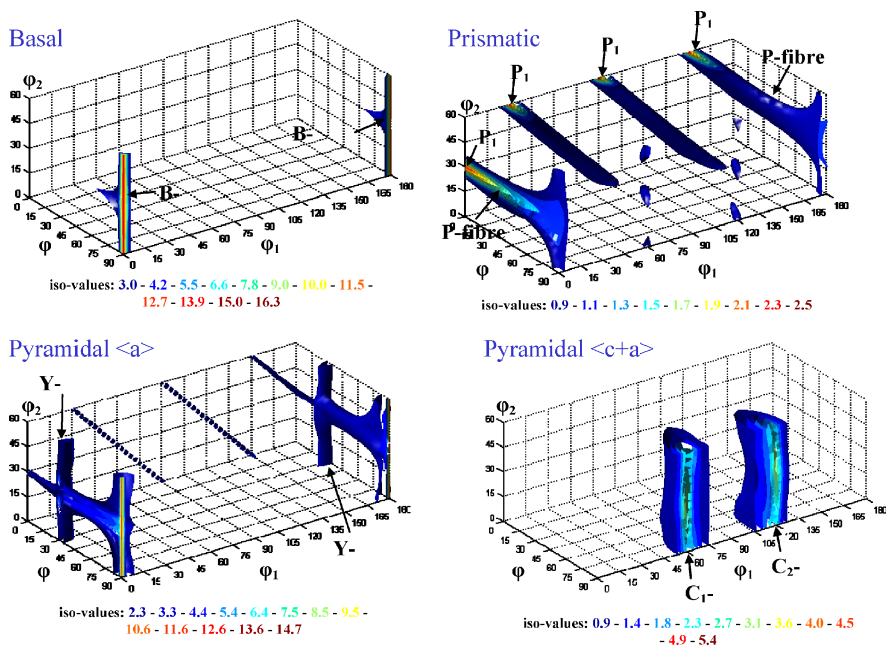


**Fig. 13.9** Maps of the persistence parameter  $S$  for simple shear of hexagonal crystals in Euler space. Each map corresponds to the indicated slip system family when all other families have a very high resistance with respect to the selected one.



### 13.3.2.5 Rolling of BCC Polycrystals

The case of rolling is very important in the steel industry as most of the steel products are produced in form of sheet. The persistence map was also calculated for rolling of bcc materials using both the  $\{110\} \langle 111 \rangle$  and  $\{112\} \langle 111 \rangle$  slip system families with a resistance ratio of 0.95 between the resistances of  $\{112\}$  and  $\{110\}$  slip [6]. That is, the  $\{112\}$  slip was favoured. The result obtained is shown in Fig. 13.10. As can be seen, the stability parameter is high along the  $\phi_1$  and  $\phi_2$  fibres. It is especially high along the  $\phi_1$  fibre, in the vicinity of the  $(112)[1\bar{1}0]$  and  $(445)[1\bar{1}0]$  orientations. The high intensity of  $S$  means only that orientations rotate very slowly at those positions. In general,  $S$  is not expected to be in monotonic relation with the possible ODF intensities. In order to have ideas about the possible relative intensities of texture components, the divergence quantity has to be also examined together with the rotation field, see below.

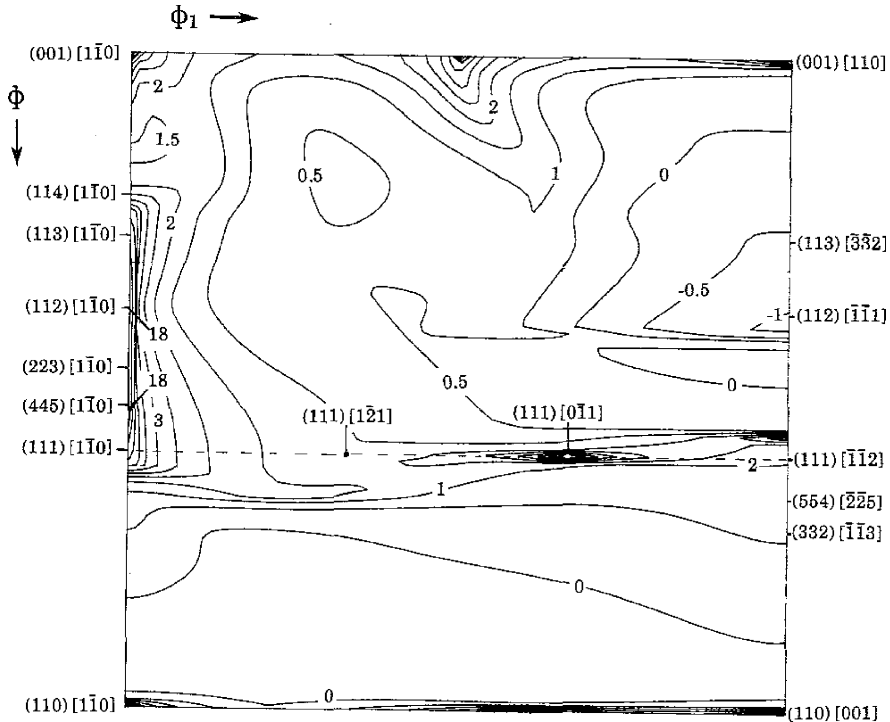


**Fig. 13.10** Map of the persistence parameter  $S$  for rolling of bcc crystals in the  $\phi_2 = 45^\circ$  section of Euler space (from [6]).

### 13.3.3 *The Role of Strain Rate Sensitivity in the Persistence of Shear Textures*

The introduction of viscosity into crystal plasticity was an important step to solve the well known ambiguity problems that arise in rate independent theories. The most common strain rate sensitive constitutive law used in the scientific community is the one proposed by Hutchinson [12]:

$$\tau_s = \tau_0 \operatorname{sgn}(\dot{\gamma}_s) \left| \frac{\dot{\gamma}_s}{\dot{\gamma}_0} \right|^m = \tau_0 \frac{\dot{\gamma}_s}{\dot{\gamma}_0} \left| \frac{\dot{\gamma}_s}{\dot{\gamma}_0} \right|^{m-1}. \quad (13.24)$$

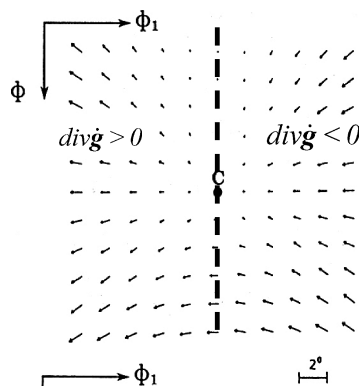
Here  $\tau_s$  is the resolved shear stress in the slip system indexed by 's',  $\dot{\gamma}_s$  is the slip rate, the  $\tau_0$  value is the reference stress level (at which the slip rate is  $\dot{\gamma}_0$ ), and  $m$  is the strain rate sensitivity index.

Using the above constitutive law for slip in Taylor type crystal plasticity modeling, an important result was developed in [1] and [2], namely, that the lattice spin is **not** zero at the ideal positions of shear textures. Thus, one of the most important conditions (Eq. 13.3) of orientation stability is not satisfied. In this way, the division of  $S$  by a zero value of lattice spin does not arise in the definition of  $S$  in Eq. 13.15. It also means that orientations can cross the ideal positions. This might take a long time, depending on the value of the strain rate sensitivity index  $m$ . The time needed increases by a decrease in  $m$ .

A particular behavior is obtained in the Newtonian viscous case, that is, when  $m=1$ . Although this case is not realistic in experiments,  $m$  increases as a function of temperature and it is always important to know the limiting behaviors. It has been shown in [1] that the plastic spin disappears for  $m=1$ , thus the lattice spin is equal to the rigid body spin, independently of orientations and the imposed strain mode. This means that in simple shear testing, the texture merely rotates in the direction of the imposed shear, in a rigid manner. However, for the case when there is no imposed shear in the experiment, like rolling, tension or compression, the lattice rotation would be zero for all crystals and the texture would not change at all. Of course, this is only valid when the deformation mechanism is only crystallographic slip. When  $m$  is increased, usually other mechanisms, like diffusion and grain boundary sliding are also operational, which might change the texture as well. Nevertheless, the effect of texture changes due these latter mechanisms is probably small and the trend of the texture evolution as it is predicted above is still visible experimentally.

Another important feature of the rotation field in simple shear is that the major trend in the direction of the lattice rotation is the direction of the rigid body rotation. This is illustrated in Fig. 13.11 for the case of the C orientation in simple shear of fcc crystals. This effect is of primary importance in the formation of the texture and will be discussed below.

**Fig. 13.11** Rotation field around the ideal C orientation of fcc simple shear textures. The direction of the rigid body spin is to the left.



### 13.4 The Role of the Divergence Quantity in the Formation of Textures

As discussed in Sect. 2 above, the divergence quantity is also of capital importance in the formation of crystallographic texture. This is why it was also examined in all the works presented above for the *S*-maps. Here we consider all above cases to explore the role of the divergence in the formation of texture for simple shear as well as for rolling.

The divergence quantity, as defined by Eq. 13.5 and calculated numerically, has been plotted in orientation space for simple shear of fcc crystals in Fig. 13.12. As can be seen, negative and positive regions are present periodically. The most striking feature, however, is that the ideal orientations that were identified in the map of Fig. 13.5 lie exactly on the boundary lines between these opposite divergence zones. More close inspection reveals that the divergence quantity is exactly zero at the location of the ideal orientation. The zero line of the divergence is also indicated in Fig. 13.11 for the case of the C ideal orientation. This feature of the rotation field in shear is in complete disagreement with the stability conditions that were pronounced in Eqs. 13.3–13.5; none of these conditions are satisfied. Similar features were obtained in the bcc and hcp cases of simple shear, see in [3] and [5], respectively.

The consequence of these particular features of the rotation field in simple shear are multiple. Let us examine the case of simple shear of fcc crystals. Fig. 13.13 shows the textures measured in large strain torsion of copper at shears of 2, 5.5 and 11 (from [13]). Three ideal texture components are visible in the selected ODF section ( $\phi_2 = 0$ ); the A1\*, C and the A2\*. The direction of the main drift of orientations is to the left, indicated by the arrow in Fig. 13.13, which is the direction of the imposed rigid body rotation in Euler space. As can be seen, all three texture components are formed at the shear of 2.0. One can see, however, that the C and A2\* components are formed in shifted positions; opposite to the applied shear. Such tilts are characteristic to torsion textures; they vary with strain

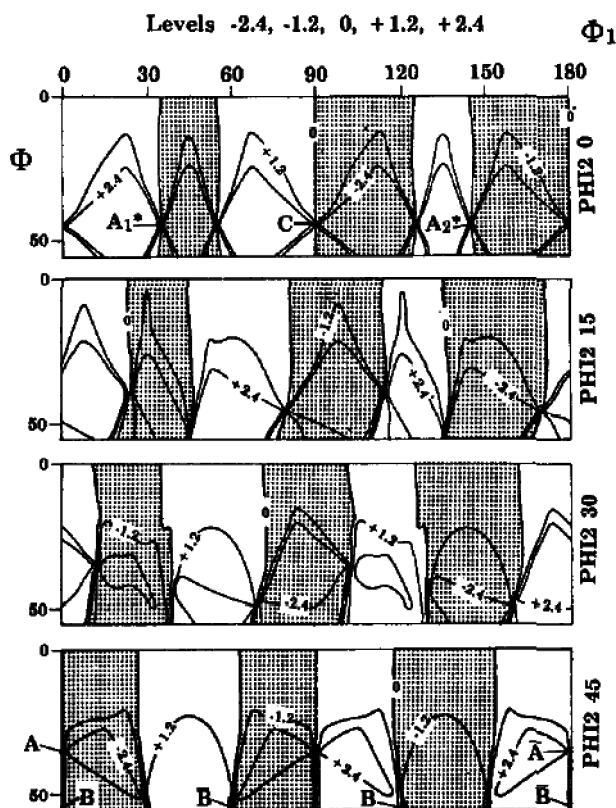
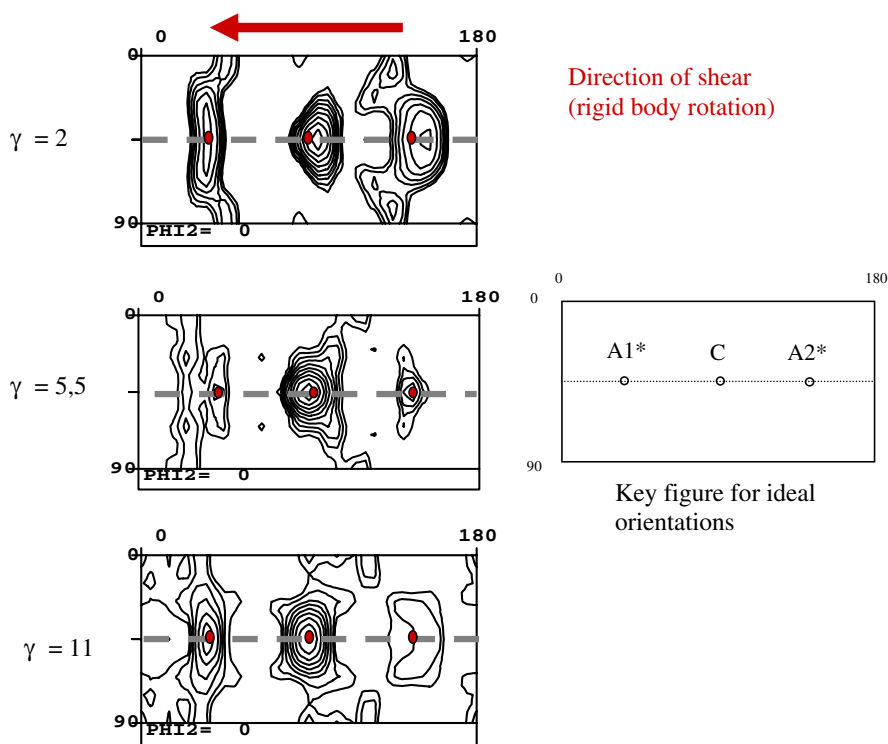


Fig. 13.12 Map of the divergence quantity in orientation space for simple shear of fcc crystals. In the shaded areas, the divergence is negative (from [2]).

and depend also on the texture components [13]. They are due to the asymmetric nature of the rotation field around the ideal components. Grains that are to the right from the ideal position slow down and accumulate at the right side of the ideal position (because they are in a negative divergence area), while grains that are on the left, they are in positive divergence area, thus, they accelerate and disappear rapidly from the ideal component. This process leads to the 'tilts' of the components. The tilts are not the same for each texture component because the rotation field is not exactly the same around them, only their main features are similar.

At larger strains, see at  $\gamma = 5.5$  in Fig. 13.13, the texture is quite different from the lower strain case. Now the C component is much stronger and the  $A_1^*$ ,  $A_2^*$  components are very weak. The tilts are nearly zero. This effect is due to a texture transition,  $A_2^* \rightarrow C$ , which can take place due to the possibility that grain orientations are able to cross the ideal positions in viscoplastic slip as it was discussed above in simple shear. This is why the tilt decreases and this makes possible the observed texture transition. The procedure continues at larger strains; now the  $A_1^*$



**Fig. 13.13** Texture development in torsion of Cu at large strains (from [5]).

increases in intensity due to grains that it receives from the C component. The tilts might even be on the opposite side at these large strains.

The same effects exist in shear of bcc crystals [3]. One can also understand the relative strengths of the texture components using the rotation field characteristics. An example is shown in Fig. 13.14, which is taken from [3]. It shows the rotation field around the D1 and D2 components of bcc shear textures, which are the major components. As can be seen, the rotation fields are similar, however, they are asymmetric with respect to the shear direction which is from the left to the right in this case. The divergence quantity is negative on the left, where there is a convergent rotation field. There is, nevertheless, a large difference in the nature of the convergence. Before D2, there is a kind of one-dimensional convergence while before the D1 ideal orientation; there is a three dimensional convergent rotation field. It is then expected that more orientations arrive to the vicinity of D1 than into D2. Consequently, larger intensity of D1 expected than D2. This is exactly the same as the experimental observation; see the ODF section in Fig. 13.14. This figure shows the  $\phi_2 = 0$  section of the ODF measured in torsion of an IF steel at an equivalent strain of 0.95 [3]. Obviously, when the shear is reversed, the rotation vectors are inverted around the ideal orientations and an opposite relative density develops: the D2 would be strong and D1 would be weak.

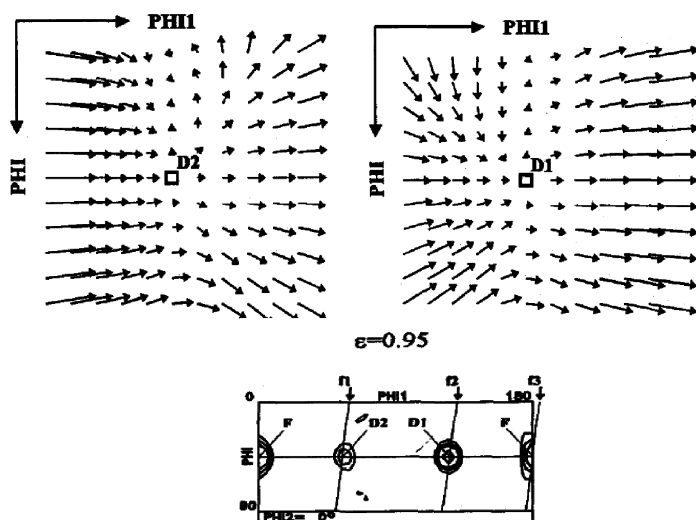
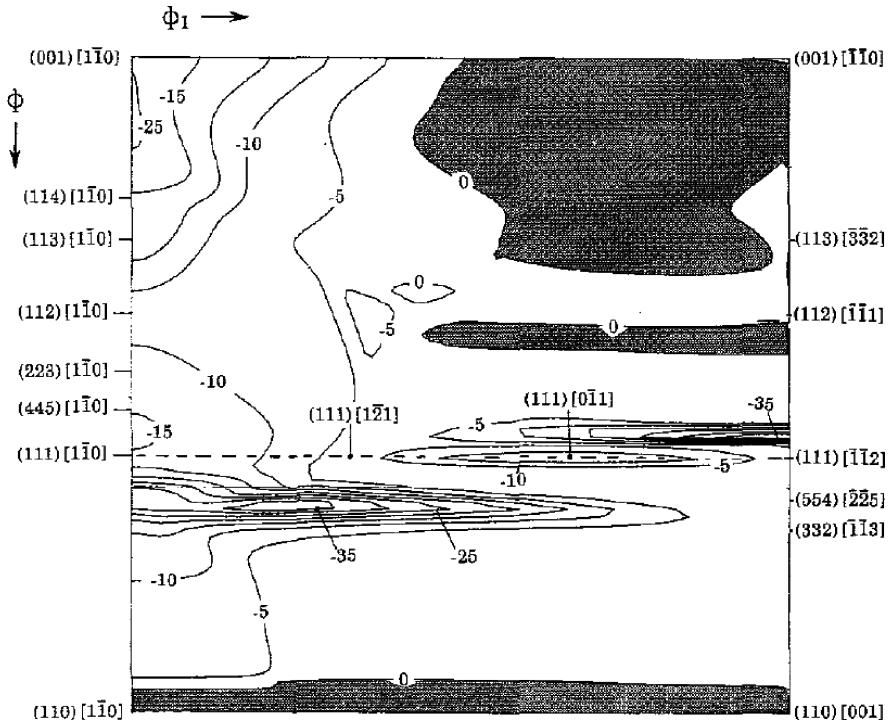


Fig. 13.14 Rotation field around the D1 and D2 ideal orientations of bcc shear texture and one ODF section ( $\phi_2 = 0$ ) of the texture measured in torsion of IF steel (from [3]).

Now the case of rolling will be examined. A map of the divergence quantity (normalized by the equivalent strain rate) is plotted in Fig. 13.15 for rolling of bcc crystals. The main feature in this map is that all ideal orientations of this section – which are the  $\alpha$  and  $\gamma$  fibres – are situated within a negative divergent region. At the same time, the lattice rotations are zero along the ideal fibres when the Taylor model is used. These features are in good accordance with the criteria that are defined in Eqs. 13.3–13.5 concerning the stability conditions of the ideal texture components. This means also that the formation of the ideal texture components in rolling takes place in a three dimensional manner; orientations approach the ideal positions from all possible directions around them. For shear, however, this is not the case. As it was shown above, they can approach the ideal positions only from one side, because of the special asymmetric feature of the divergence quantity. One important conclusion from this is that shear textures are supposed to be less strong as rolling textures. The other difference between shear and rolling is that in shear, grain orientations can cross the ideal positions, while in rolling, they cannot (as long as the deformation conditions remain Taylor). This effect can give rise to specific texture component transitions in shear, see the above discussed examples. The directional nature of the rotation field – namely the preferred rotation direction in the sense of the rigid body spin in shear – induces still another specific feature in the development of shear textures. Namely, because of this drift of the orientations, many grain orientations remain outside of the ideal fibre tubes or at least stay outside of the tubes for a long time. From simulations, it can be estimated that about 50% of the grains are always outside of the tubes at any deformation stage. This is also an important difference between rolling and shear and leads to a smaller general intensity of the deformation textures observed in shear.



**Fig. 13.15** Map of the divergence quantity in the  $\phi_2 = 45^\circ$  section of orientation space for rolling of bcc steel (from [6]). In the white areas the divergence is negative while shaded areas correspond to positive divergence.

### 13.5 Summary and Conclusions

In this work, a short overview was presented about the persistence characteristics of textures that develop due to large plastic deformation in crystalline materials. First the principles of orientation stability were examined, and then orientations stability maps were presented for simple shear and rolling. The role of the lattice rotation and the divergence quantity was discussed in detail in the formation of the ideal texture components for both rolling and shear. From the present overview, the following general conclusions can be drawn:

- a. The persistence parameter introduced in [1] appears to be a very useful parameter in the identification of the ideal orientations of deformation textures with the help of crystal plasticity simulations. It helps to identify the ideal orientations in shear and rolling for both fcc and bcc materials. In shear, it was also employed to the hcp case.

- b. The role of the rigid body rotation is decisive in the number of active slip systems in shear and rolling. For the ideal components, the active slip systems are limited to two in shear while they are at least four in rolling.
- c. Shear textures are very different from rolling textures because of the differences in the nature of the rotations field. All ideal orientations lie on a zero divergence line in orientations space in shear while all of them are situated within a negative divergent region in rolling. This implies large differences in the intensities of the textures and explains why shear textures are weaker than rolling textures.
- d. The asymmetrical nature of the rotation field in shear is responsible for the 'tilts' of the ideal texture components from their symmetry positions. The non-zero lattice spin in the ideal positions of shear textures allows some texture components to weaken and others to strengthen.

**Acknowledgement** The Author acknowledges the help received from Dr. Benoît Beausir (University of Metz, France) in the construction of Fig. 13.7. He is also grateful to Tata Steel Jamshedpur, India, for their kind invitation to the MATS2008 conference where this lecture was delivered.

## References

- [1] Tóth LS, Gilormini P, Jonas JJ. Effect of rate sensitivity on the stability of torsion textures, *Acta Metall.* 1988;36:3077–3091.
- [2] Tóth LS, Neale KW, Jonas JJ. Stress response and persistence characteristics of the ideal orientations of shear textures. *Acta Metall.* 1989;37, 2197–2210.
- [3] Baczynski J, Jonas JJ. *Acta Mater* 1996;4273:4288.
- [4] Zhou Y, Tóth LS, Neale KW. On the stability of the ideal orientations of rolling textures for fcc polycrystals. *Acta Metall. et Mat.* 1992;40:3179–3193.
- [5] Beausir B, Tóth, LS, Neale KW. Ideal orientations and persistence characteristics of h.c.p. crystals in simple shear. *Acta Materialia* 2007;55: 2695–2705.
- [6] Tóth LS, Jonas JJ, Daniel D, Ray RK. Development of ferrite rolling textures in low and extra low carbon steels. *Metallurgical Transactions* 1990;21A:2985–3000.
- [7] Clement A, Coulomb P. Eulerian simulations of deformation textures. *Scripta Metall.* 1979;13:899–901.
- [8] Clement A, Coulomb P. Representation of distribution function of texture by a series of stereographic projections and by a series of coefficients, *Memoires Scientifiques de la Revue de Metallurgie*, 1976;73:63–69.
- [9] Tóth LS, Jonas JJ, Neale KW. Comparison of the minimum plastic spin and rate sensitive slip theories for loading of symmetrical crystal orientations, *Proc. Roy. Soc. Lond.* 1990;A427: 201–219.
- [10] Ungar T, Tóth LS, Illy J, Kovacs I. Dislocation structure and work hardening in polycrystalline OFHC copper rods deformed by torsion and extension, *Acta Metall.*, 1986;34:1257–1267.



- [11] Beausir B, Suwas S, Tóth LS, Neale KW, Fundenberger J-J. Analysis of texture evolution in magnesium during equal channel angular extrusion, *Acta Mater.* 2008;56:200–214.
- [12] Hutchinson, J.W., Bounds and self-consistent estimates for creep of polycrystalline materials. *Proceedings of the Royal Society of London* 1976 ;A348 :101–127.
- [13] Tóth LS, Jonas JJ, Daniel D, Bailey JA, Texture development and length changes in copper bars subjected to free end torsion, *Textures and Microstructures.* 1992;19:245–262.



Laszlo Toth  
Professor  
Laboratoire de Physique et Mecanique  
des Materiaux  
Universite Pail Verlaine Metz  
France

# Chapter 14

## DXRD and Its Applications Leading to New Modelling

D. Juul Jensen

**Abstract.** In the present paper the specifications and potentials of the 3 dimensional x-ray diffraction (3DXRD) method is shortly described and examples of applications are reviewed. The main focus is however on 3DXRD results leading to advancements in recrystallization modelling. 3DXRD measurements have shown that all investigated individual grains have different recrystallization kinetics – not two grains are alike. This is found for samples deformed both to high and very high strains. Based on the experimental results, a JMAK model has been advanced to incorporate distributions of growth rates or anisotropic growth directionality. Effects of the new modelling are analysed and compared to standard JMAK modelling. Also effects of experimentally observed distributions of nucleation sites are analysed using JMAK simulations. Finally it is discussed in more general terms how modelling may be advanced through experimental verifications.

### 14.1 Introduction

Most materials microstructures are three dimensional (3D) and complete characterization thus requires 3D measurements. Most experimental characterization techniques commonly available today, however, operates in 2D – prominent among them are electron microscopy techniques, which allow detailed microstructural characterization even to the subnanometer scale. It has often been stated that cautions should be taken when using 2D methods to characterize 3D microstructures [1], and 3D techniques are becoming more and more popular. Mechanical serial sectioning have long been used to get the 3D information [2]. Many laboratories now operate dual beam

---

D. Juul Jensen

Center for Fundamental Research: Metal Structures in Four Dimensions,  
Materials Research Department, Risø DTU, DK-4000 Roskilde, Denmark

focused ion beam microscopes, which allow automatic serial sectioning. Results of this new technique are starting to appear in literature [3].

The sectioning methods are, however, (as the name says) destructive; the samples do no longer exist after the characterization, which rules studies of dynamics. So if the dynamics are of importance for a given investigation other methods have to be used. 3D x-ray diffraction method (3DXRD) [4] or 3D x-ray crystal microscopy [5] allows non-destructive 3D characterizations and can thus be used for dynamic studies of the microstructural evolution.

Many papers have already dealt with for example the 3DXRD method and its applications. Therefore the purpose of the present paper is to go one step further and discuss how the 3DXRD and other 3D results may assist in advancement of present days models. The chosen example is recrystallization. So after a short description the 3DXRD method, 3D results for nucleation and growth during recrystallization are summarized and it is shown how these results may affect recrystallization modeling. The JMAK [6–10] modeling scheme is used for the latter as this scheme easily allows investigations of effects of variations in just one modeling parameter. In this paper, effects of growth rate *distributions*, anisotropic growth and clustered nucleation shall be discussed.

## 14.2 3DXRD

The 3DXRD concept is based on measuring local crystallographic orientations and thereby generating a map of the microstructure. To ensure high penetration depth e.g. 5 mm in steel and 4 cm in Al, high energy (50–100 kV) X-rays are

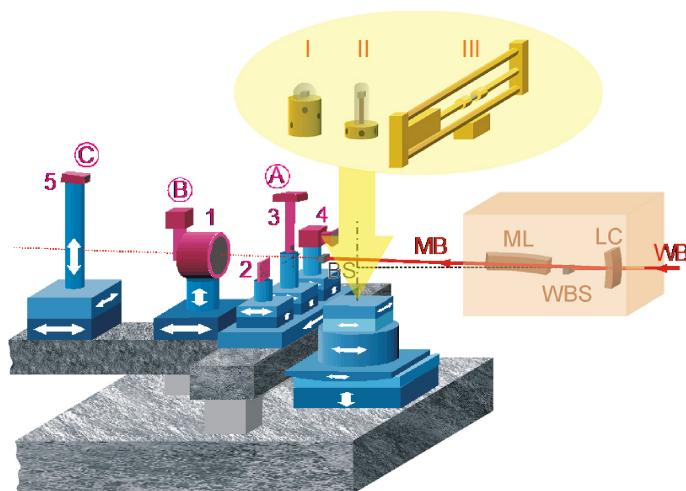


**Fig. 14.1** Sketch of the 3DXRD microscope operating at the European Synchrotron Radiation Facility in France.

used. A sketch of the set-up is shown in Fig. 14.1. To probe the complete sample structure within the gauge volume, the sample is rotated around an axis perpendicular to the incoming beam. At present the mapping precision is about  $5\text{ }\mu\text{m} \times 5\text{ }\mu\text{m} \times 1\text{ }\mu\text{m}$ , while microstructural elements down to 70 nm can be detected provided that they have a sufficient crystallographic orientation difference to avoid overlap of diffraction spots on the detector. The angular resolution is 0.05 degrees.

The 3DXRD methodology can be tailored to provide dynamic data on a hierarchy of levels. The simplest approach is to measure the diffracted intensity from selected, structural elements as function of time; this provides the volume kinetics of individual elements with a time resolution of seconds or even subseconds. On the highest level, full shape change information can be acquired by repeating the acquisition of microstructure maps.

Sample auxiliaries include a series of furnaces, which operates up to 1500°C, and a 25 kN Instron tensile machine. Typically, the measurements of orientation or elastic strain are so fast that the development in orientation or strain can be followed in situ, for example, during deformation or during annealing. For further information on the 3DXRD method the best reference is [4].

## 14.3 Growth During Recrystallization

### 14.3.1 Growth Rate Distributions

By 3DXRD it is possible to detect single individual nuclei in the bulk of large samples and follow their growth in situ while annealing the deformed sample. For experimental information see [11]. The noise limit for detecting a nucleus is approximately  $2\text{ }\mu\text{m}$  (diameter). Its development and growth can be followed with a time resolution of the order of seconds. For each observed nucleus, a full curve of volume versus annealing time is obtained. An example of such growth curves are shown in Fig. 14.2.

It can be seen that each nucleus/grain has its own nucleation and growth behavior. Such data are unique as they for the first time allow us to see the behavior of single grains of known orientations in the bulk during annealing. The data have also shown that even grains within one group of orientations have very different growth behavior.

Most kinetics models of recrystallization have their genesis in the phase transformation models of Kolmogorov, Johnson and Mehl and Avrami (JMAK) [6–10]. The JMAK models were developed assuming a constant nucleation rate and constant growth rate, assumed to be the same for each grain. The new data obtained by 3DXRD e.g. Fig. 14.2 shows that the basic assumptions of constant and identical growth rate of all grain are violated. A much better description would be to consider a distribution of growth rates.

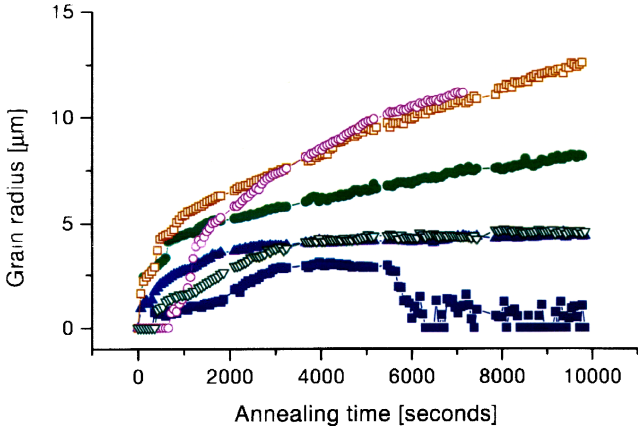


**Fig. 14.2** Growth kinetics of 6 individual grains in 90% cold-rolled aluminum (AA1050) annealed at 270°C [11].

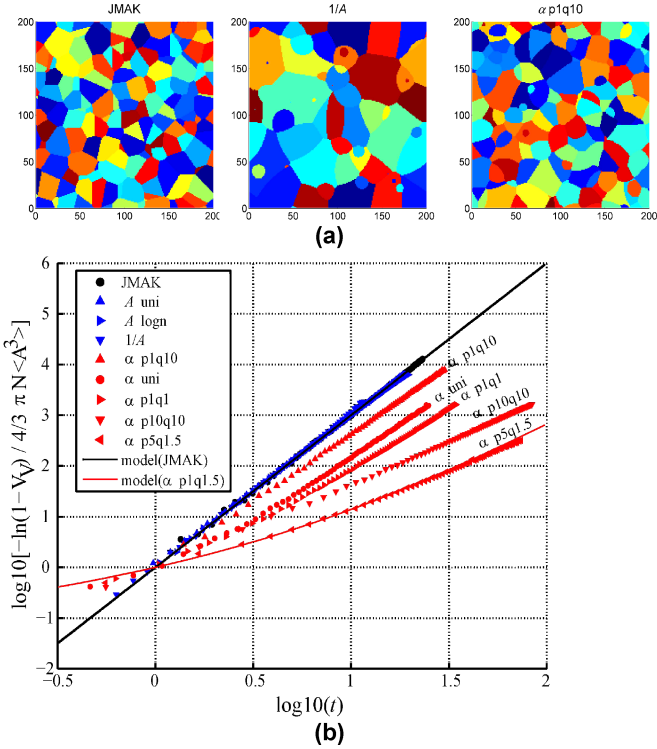


**Fig. 14.3** Results from geometric simulations of the effects of growth rate simulation microstructure. (a) Microstructures simulated by three simulations: MJAK conditions (left, distribution in A (middle) distribution is where the radius  $r = At^{-\alpha}$ . Different colors mark different grains. (b) Kinetics curves blue points/curve is MJAK and A distributions whereas red points/curves are for a distribution [12].

The effects on recrystallization kinetics and microstructure of growth rate distributions rather than one identical growth rate for recrystallizing grains have been investigated by geometric simulations [12]. The grains were set to grow as spheres with radii  $r = At^{1-\alpha}$ . The results show that distributions in  $A$  and  $\alpha$  may produce significant changes in the microstructure and texture as shown in Fig. 14.3 (a). It is clear from this figure that growth rate distributions may affect the recrystallized grain size distribution and as it is discussed in [12] the presence of growth rate distributions may explain why experimental grain size distribution often are broader than what classic simulations predict.

Also the kinetics is affected if a distribution of growth rates instead of only one is assumed. Here, however, only distributions in  $\alpha$  (not in  $A$ ) lead to changes in the shape of the curve. This is seen in Fig. 14.3 (b) where all the red points/curves are for various  $\alpha$ -distributions [12]. Results of this type are considered to be very important as they show that significant errors may be obtained if kinetics curves are interpreted based on the classical constant identical growth rate assumption and the grains in reality each growth with a rate different from the others.

### 14.3.2 Anisotropic Growth

Films of grains growing during recrystallization has been recorded by 3DXRD [14]. It was observed that generally the grains grow significantly faster along one direction than along the other 2 directions. Not many films have yet been recorded and analyzed by 3DXRD and it is not possible to state a general observation on growth anisotropy based on these few results. However, also simple microscopy of fully recrystallized microstructures reveals elongated grains suggesting that the growth has not just been spherical growth (isotropic in all 3 directions).

Effects of anisotropic growth have been investigated by geometric simulations of randomly oriented shape preserved ellipsoids in three dimensions [13]. Earlier simulations in 2 dimensions [15–17] have suggested very significant effects of anisotropical growth. In the new 3D simulations [13] grains will grow until they impinge upon an other grain, then this intersected section of the grain boundary(ies) will no longer move, but all other sections of the grain boundary(ies) are still free to move. This means that a grain with a fast growing boundary may grow around an other grain which happens to have a slower boundary migration in that particular direction. The results show that this “growing around mechanism” strongly reduces the effects of anisotropic growth on the overall recrystallization kinetics [13]. An example is shown in Fig. 14.4. Only for very extreme anisotropy e.g. aspect ratios of 4 or above the recrystallization kinetics is significantly affected. For recrystallization such large aspect ratios are not common, and anisotropy does not need to be included in JMAK modeling if the preferred growth directions of the grains are randomly oriented.

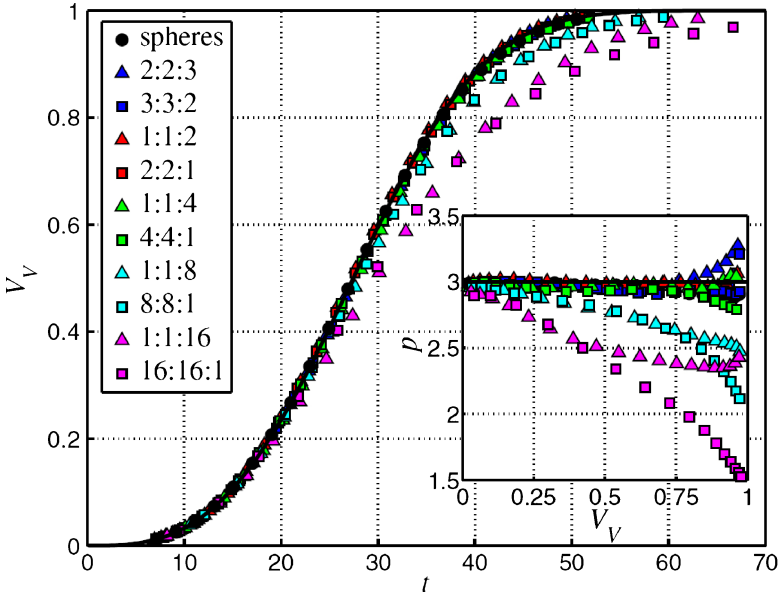


**Fig. 14.4** Volume fractions of recrystallized material  $V_V(t)$  are plotted as a function of time. The full line is the JMAK model and the points are for simulations with various aspect ratios as given in the list. The inset shows the Avrami parameter  $p$  for the simulations [13].

### 14.4 Distribution of Nucleation Sites

3DXRD allows mapping of large sample areas [18] and as it is discussed in the introduction it is a very powerful method to use when studying dynamics. If, however, only statics, like determination of the spatial distribution of nucleation sites, are needed, other methods like serial sectioning may be easier to use.

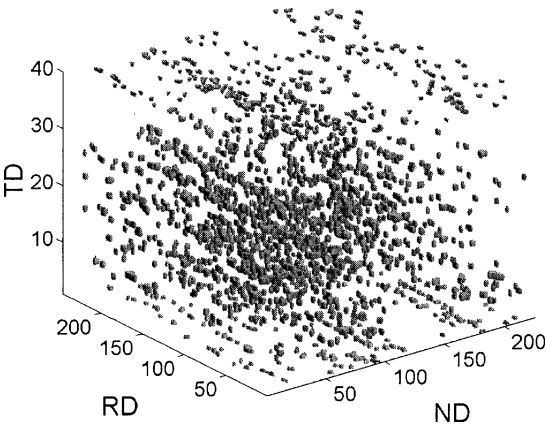


**Fig. 14.5** Visualization of the experimentally observed 3D distribution of nucleation sites in 90% cold-rolled aluminum (AA1050) annealed for 1h at 280°C [19].

For 90% cold-rolled aluminium (AA1050) the position of nuclei very determined by serial sectioning in 8 sections  $5\text{ }\mu\text{m}$  apart each covering a sample area of  $245\text{ }\mu\text{m}\times 225\text{ }\mu\text{m}$ . The result is visualized in Fig. 14.5. It appears that the distributions are non-random but clustered on planes. To understand the effects of this clustering alone (not including effects of other parameters like growth rate distributions etc.) geometric simulations were carried out using the experimentally determined sites of the nuclei ( $x$ ,  $y$ ,  $z$ ) as input but otherwise applying standard JMAK assumptions. The simulation results reveal that the clustering of the nuclei strongly affects the evolution of the kinetics curve, which starts deviating from JMAK already when the sample is less than 50% recrystallized. Also the recrystallized grain size distribution is significantly broadened.

## 14.5 Discussion and Conclusion

Reasons for developing and using models are manifold. An obvious reason is to be able to predict some overall parameters as the average grain size or the crystallographic texture as a function of process parameters like the deformation strain and annealing temperature. Another obvious reason is to use the model to get a better understanding of some underlying physical mechanism(s).

Validation of a model may be quite different in the two cases. In the first case care must be taken to examine the processing interval well enough and not to extend the application of the model too far beyond the examined parameter and material range. But otherwise the model requirements may not be too critical and simplifying assumptions are often acceptable and useful. In the second case the validation is more complex as the result of the modeling i.e. the physical understanding typically depends so intimately on every modeling step and often it is not enough to measure experimentally simple parameters like grain size and texture to be sure the modeling result is correct. As an example of this, it can be mentioned that in a simulation of recrystallization where only the nucleation rate (instantaneous or continuous), the distribution of nucleation sites (random or clustered) and the relative growth rate of two orientations of grains were varied, 15 out of 59 conditions i.e. 25% of the simulations gave identical texture and average grain size results [20]. If also the nucleation density was allowed to vary the percentage of very different nucleation and growth conditions giving the exact same texture and grain size result would have been even larger.

Advancing in particular the second type of modeling depends on the experimental possibilities. Here 3D and 4D (3D plus time) methods may be of importance. In the present paper 3 and 4D recrystallization results are presented and recrystallization modeling is discussed. It is shown that the recrystallized microstructures depend on growth rate distributions, anisotropic growth and on the distributions of nucleation sites. Although not discussed above, it is clear that these 3 parameters may also strongly affect the evolution of the recrystallization texture – for example if grains of certain orientations have growth rates in the high end of the growth rate distribution, have more anisotropic growth or are less clustered



than other grains. Also the recrystallization kinetics is affected but here the growth anisotropy is of less importance for the kinetics if the preferred growth directions of the individual grains are randomly oriented in space.

**Acknowledgements** The author gratefully acknowledges the Danish National Research Foundation for supporting the Center for Fundamental Research: Metal Structures in Four Dimensions within which the work was performed.

## References

- [1] G. Spanos, 3D Materials Characterization, VP set, Scripta Mater. 2006.
- [2] M.V. Kral and G. Spanos, Acta Mater. 1999, 47, 711.
- [3] C.A. Volkert et al., in Proceedings: 25th Risø Int. Symp. on Mat. Science. C.Gundlach et al. (Eds.), Risø National Laboratory, Roskilde, Denmark, 2004, 171.
- [4] H.F. Poulsen, Three-Dimensional X-Ray Diffraction microscopy. Mapping polycrystals and their dynamics., Springer, Berlin, 2004.
- [5] B.C. Larson et al., Nature 2002, 415, 887.
- [6] W.A. Johnson and R.F. Mehl, Trans. Metall. Soc. AIME 1939, 135, 416.
- [7] M. Avrami, J. Chem. Phys. 1939, 7, 1103.
- [8] M. Avrami, J. Chem. Phys. 1940, 8, 212.
- [9] M. Avrami, J. Chem. Phys. 1941, 9, 177.
- [10] A.E. Kolmogorov, B. Acad. Sci. 1937, 1, 355.
- [11] E.M. Lauridsen et al., Acta Mater. 2003, 51, 4423.
- [12] R.B. Godiksen et al., Scripta Mater. 2007, 57, 345.
- [13] R.B. Godiksen et al., Scripta Mater. 2008, 58, 279.
- [14] S. Schmidt et al., Science 2004, 305, 229.
- [15] D.P. Birnie and M.C. Weinberg, J. Chem. Phys. 1995, 103, 3742.
- [16] T. Pusztai and L. Granasy, Physical Review B 1998, 57, 14110.
- [17] B.J. Kooi et al., Journal of Applied Physics 2004, 95, 924.
- [18] K. Hannesson, D. Juul Jensen, in Proceedings: Recrystallization and grain growth III. Vol. Jeju Island, Korea, S.-J.L.Kang et al. (Eds.), Trans Tech Publications Ltd., 2007, 751.
- [19] Z. Sükösd et al., in Proceedings: Recrystallization and grain growth III. Vol. Jeju Island, Korea, S.-J.L.Kang et al. (Eds.), Trans Tech Publications Ltd., 2007, 345.
- [20] D. Juul Jensen, Metallurgical and Materials Transactions A-Physical Metallurgy and Materials Science 1997, 28, 15.



Dorte Juul Jensen  
Head  
Risø National Laboratory  
Materials Research Department  
Building 228, P.O. Box 49  
DK-4000 Roskilde  
Denmark

# Chapter 15

## 3D Image-Based Viscoplastic Response with Crystal Plasticity

Anthony D. Rollett, Sukbin Lee, and Ricardo A. Lebensohn

**Abstract.** An efficient digital FFT-based viscoplastic method was applied to calculating the viscoplastic stress-strain response on a 3D image of a serial sectioned nickel alloy. A single strain step under uniaxial tensile loading was calculated using crystal plasticity. Analysis of the results indicated higher stresses near grain boundaries than in the bulk of grains. All types of grain boundary gave similar results and no special cases, such as the twin boundaries, were identified. A new analysis for clusters of high stress points was introduced; the distribution of sizes of high stress clusters was found to be close to log-normal.

### 15.1 Introduction

As 3D images of polycrystalline materials become available from sources such as serial sectioning, there is a self-evident need to investigate the dependence of properties on microstructure and understand that which was not accessible from conventional methods. Such 3D datasets are inevitably large with millions of points in current images and the prospect of billion-voxel sets in the near future. Methods are being developed to generate finite element (FE) meshes from such images and perform FE calculations. This approach is limited, however, by both the challenges of generating uniformly high quality meshes and the computation time required for problems with a large number of degrees of freedom. Accord-

---

A.D. Rollett and S. Lee  
Materials Science & Engineering Dept., Carnegie Mellon University,  
Pittsburgh, PA 15213, USA

R.A. Lebensohn  
Materials Science and Technology Division, Los Alamos National Laboratory,  
Los Alamos, NM 87544, USA

ingly we present an alternative approach well suited to materials problems in which the viscoplastic response is calculated directly on the image. Use of digital Fast Fourier Transforms means that the solution procedure is highly efficient. This numerical method was proposed (1) for approximating linear and nonlinear mechanical properties of materials based on voxelized microstructural data. The method provides an exact solution of the equilibrium equation, has better numerical performance than small-scale FEM, and has been successfully modified to approximate the elastic or viscoplastic response of either polycrystalline or composite materials. It is limited, however, to cases where the representative volume element (RVE) is subject to periodic boundary conditions and the dimension of each direction must be a power of 2. The requirement for periodic boundary conditions can be relaxed, however, by inclusion of a buffer layer that does not participate in the deformation (2). Here, we examine the local stress and strain-rate field, based on the rate-sensitivity approach, under uniaxial tension loading.

Clearly there is an extensive literature on simulation of stress-strain behavior of polycrystalline solids using crystal plasticity constitutive: see (3) for a recent review. Certain groups have focused on grain-scale effects, see for example (4) although this has largely been conducted in two dimensions. The recent availability of 3D images has made it possible to perform calculations on actual microstructures although the destructive serial sectioning technique means that one only obtains the initial structure; see (5, 6) for recent examples.

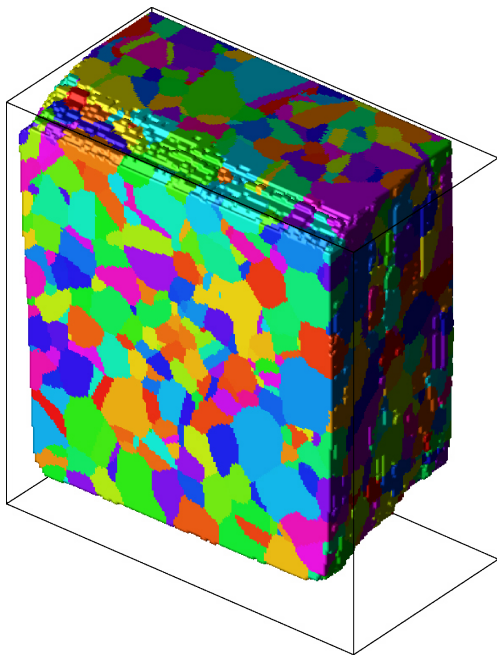
## 15.2 FFT Method

Since the complete derivation of the local solution of a heterogeneous viscoplastic medium undergoing an applied strain has been described in detail elsewhere (7, 8, 1) we present, in brief, some essential features of the algorithm. Given a heterogeneous representative volume element (RVE) with periodic boundary conditions as shown in Fig. 15.1, the local constitutive equations for stress and strain-rate for each Fourier point are solved. The key point of the approach is to introduce the local heterogeneity parameters in a homogeneous reference medium of stiffness when solving the differential equations. Applying the Green's function method, one can find the solutions for the velocity gradient and the strain rate fields as convolutions in the real space. Since any convolution in the real space can be, however, expressed as a tensor product in the Fourier space, we can calculate the strain rate field using the Fast Fourier Transform (FFT) algorithm. The stress and strain rate at each Fourier point is obtained in an iterative manner using the standard power law relationship (9):

$$\dot{\epsilon}(x) = \dot{\gamma}_o \sum_s m^s(x) ([m^s(x) : \sigma'(x)] / \tau_o^s(x))^n, \quad (15.1)$$

where  $m^s(x)$  is the Schmid tensor for a specific slip system  $s$ ,  $|\tau_o^s(x)$  is the critical resolved stress, and  $\dot{\gamma}_o$  is a normalization factor.  $n$  is known as the viscoplastic, or

**Fig. 15.1** Visualization of the  $191 \times 203 \times 98$  image of a serial-sectioned sample of IN100 Ni-based alloy. Pairs of layers were aligned by minimizing the misorientation between adjacent pixels.



rate-sensitivity exponent and, in general, the value of  $n$  for viscoplastic behavior is set equal to or greater than 10 so that texture development is in the rate-insensitive regime. The updated deviatoric stress tensor  $\sigma'_{ij}$  is used for calculation of the stress field.

### 15.3 3D Image of Nickel Alloy

Figure 15.1 shows the set of aligned EBSD maps from a series of cross-sections of a Ni-based alloy obtained through serial sectioning in a dual-beam FEI system. The data was collected and provided by Air Force Research Laboratory (AFRL) (10). The number of serial sections was 98 and the area of each scanned section was about  $50^2 \mu\text{m}^2$ , with a point spacing of  $0.25 \mu\text{m}$ . The registration was based on the assumption that all layers were sufficiently parallel to each other that the only adjustment required was a translation confined to integer valued shifts along  $x$  and  $y$  directions in each plane (i.e. the layers could be assumed to be parallel to one another, with no rotations between layers). We used the orientation information inherent in the EBSD maps to align the successive layers, which exhibited significant displacements relative to one another (11). The average disorientation ( $D$ ) was calculated as shown in Eq. 15.2 as the average of the product of disorientation,  $\Delta g$ , between each well-indexed pixel in the upper layer and its one or more neighboring pixels in the layer below and a weighting factor,  $w$ , that decreases the contribution

to  $D$  from points in the layer below having a low confidence index and low image quality. The expectation is that good alignment will generate a small average disorientation between pixels in adjacent layers.

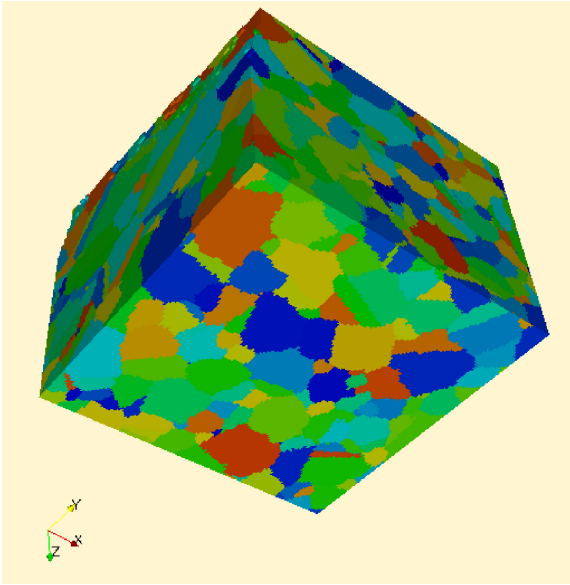
$$D = \frac{1}{N} \sum_i w_i \Delta g_i, \quad \begin{cases} w_i = 1, & \text{if } CI_{neigh} \geq 0.1 \text{ and } IQ_{neigh} \geq 100 \\ w_i = (2.0 - 10.0 \times CI_{neigh}), & \text{otherwise} \end{cases} \quad (15.2)$$

A  $128 \times 128 \times 128$  subset of the image was extracted for use in the FFT model described in the next section. This was chosen so as to include the entire thickness (98 voxels deep) in the x-direction and padded with a single orientation of a different material whose strength was set to be very low compared with the material of interest. The resulting structure is periodic in both the y and z directions. This introduces some mismatch between grains on the x-z and x-y surfaces. The perturbation in the behavior is expected to be minor, however, based on previous experience with calculating misorientation development in work that compares calculated with measure evolution in a copper sample (2). A single strain step in uniaxial tension parallel to the y-direction was applied to the image. The calculation required of the order thirty minutes on a multiprocessor Macintosh computer with eight cores and used the FFTW ([www.fftw.org](http://www.fftw.org)) parallel FFT package for computing discrete Fourier transforms. Each grain was assigned the average orientation determined during the registration and alignment procedure described above. The standard description of crystal plasticity in fcc metals was used with twelve  $\{111\} \langle 110 \rangle$  slip systems and a strain rate exponent of ten.

## 15.4 Results and Discussion

Figure 15.4 shows a view of the simulated structure colored by von Mises stress level. Since the critical resolved shear stress is set at one, the stress shows the Taylor factor in effect. Variations in the stress at the grain scale are evident, with significant variations within individual grains. The number of grains in the image used was 1,156; the stress in each grain was uncorrelated with size, as expected in a model that does not incorporate any length scale in the constitutive relations. As mentioned above, the main objective was to determine the characteristics of highly stressed regions and their association, if any, with grain boundaries. Accordingly the structure was analyzed and each voxel was assigned a boundary type according to whether it was adjacent to a particular boundary type or in the bulk of a grain. Boundaries were classified as low angle if the disorientation was less than  $15^\circ$ , or general high angle, or a coincident site lattice (CSL) if the disorientation satisfied Brandon's criterion for nearness to, e.g., the  $\Sigma 3$  type; see Fig. 15.3 for area fractions. Note that about two-thirds of the boundaries are general high angle boundaries, one-third are twin boundaries (mostly coherent annealing twins) and a small fraction belong to some other CSL type. Omitting the low angle bounda-

**Fig. 15.2** Visualization of the  $128^3$  volume element used for FFT-viscoplastic calculations. The grid is colored by grain number to reveal the polycrystalline nature of the material. Note that there is a high density of annealing twins present, which are apparent as thin plates in the microstructure.



ries makes little difference to the fractions because of the low fraction of such boundaries. Figure 15.5 shows the stress (von Mises equivalent) at points adjacent to  $\Sigma 3$  grain boundaries only, in a magnified view. Note how the stress varies from high to low across individual twin boundaries.

**Fig. 15.3** Histogram of the relative frequency of different types of grain boundary according to CSL sigma value. Note that about two-thirds of the boundaries are general high angle boundaries, one-third are twin boundaries (mostly coherent annealing twins) and a small fraction belong to some other CSL type. Omitting the low angle boundaries (light color bars makes little difference to the fractions).

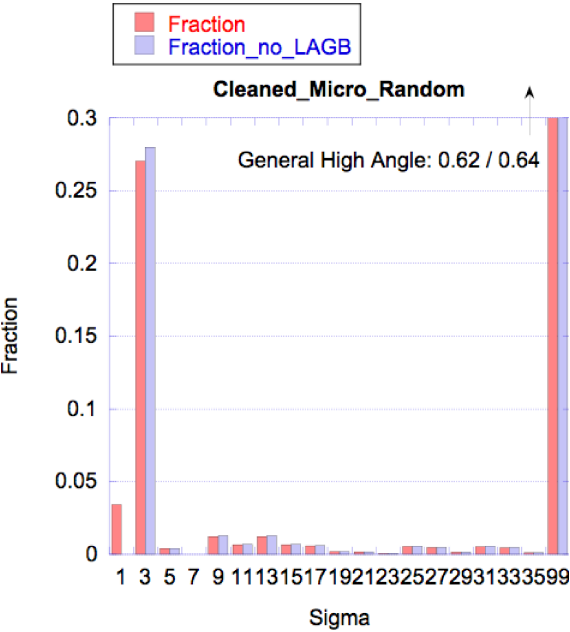
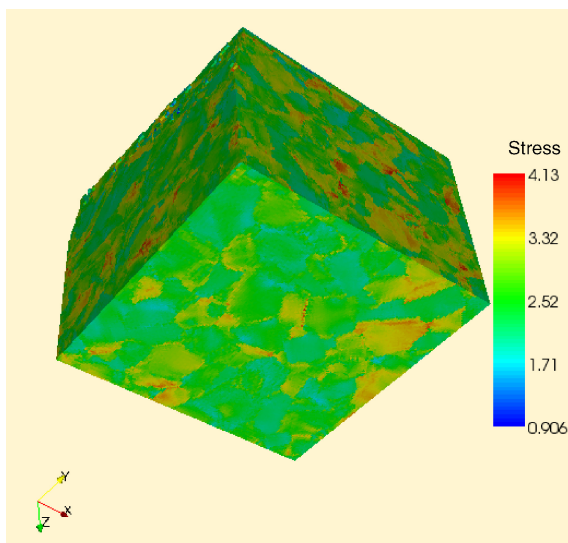


**Fig. 15.4** View of the simulated volume showing the local von Mises equivalent stress. Since the critical resolved shear stress is set at one, the stress shows the Taylor factor in effect. Variations in the stress at the grain scale are evident, with significant variations within individual grains.



This typing of voxels according to grain boundary adjacency thus permitted a simple analysis of relative stress (and strain rate) levels near to boundaries versus the bulk of grains by simply calculating averages and variances in stress and strain rate in the various types of voxels. Table 15.1 displays the results from this analysis.

Analysis of the results indicated higher stresses near  $\Sigma 3$  grain boundaries than in the bulk of grains. The same averages calculated including all types of high angle grain boundary, however, gave essentially identical results. The conclusion is that any high grain boundary tends to be more highly stressed than the interiors of grains. It appears that twin boundaries were not any more likely to generate high stresses than any other boundary type. This result is very similar to that ob-

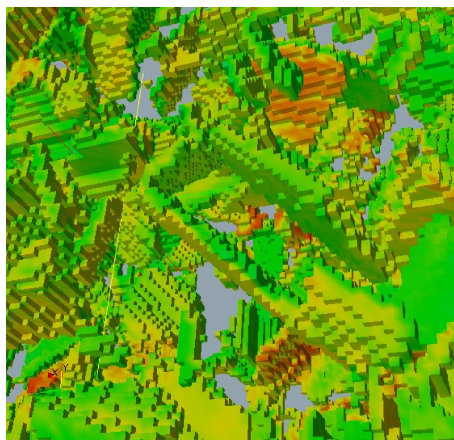


**Fig. 15.5** Stress (von Mises equivalent) at points adjacent to S3 grain boundaries, in a magnified view. Note how the stress varies from high to low across individual twin boundaries.

**Table 15.1** Stresses and Strain Rates.

	Average stress	Standard deviation in stress	Average strain rate	Standard deviation in strain rate
Bulk of grains	1.94	1.34	1.13	0.52
Adjacent to $\Sigma 3$ boundaries	2.79	0.45	1.14	0.47

tained by the NRL group (12). One caution however, is that no account was taken in this analysis concerning grain boundary plane; this is likely to be important because the (deviatoric) loading on any given grain boundary region will vary depending on the inclination of the boundary with respect to the loading axis.

Another view of the mechanical response is obtained by thresholding the image for high stress regions. Figure 15.6 shows the clusters of high stress points for a threshold of 3.5, the total volume of which is 2.6% of the simulated volume. The sizes of the clusters are obviously widely distributed. However, when the logarithm of the sphere equivalent radii of the grains, normalized by the mean value, is binned and the cumulative distribution plotted on a probability scale, Fig. 15.7, the distribution is log-normal. Lastly, Fig. 15.8 shows the fraction of voxels in each cluster that are adjacent to either a grain boundary (without distinguishing the type) or adjacent to a  $\Sigma 3$  grain boundary. The results suggest that high stress clusters occur close to grain boundaries, regardless of size, as expected from the analysis

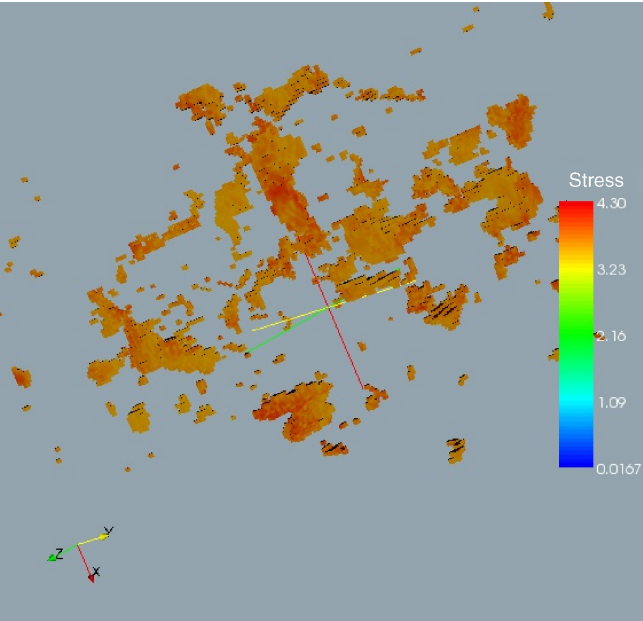


**Fig. 15.6** Visualization of high stress locations (von Mises equivalent stress above 3.5). Clusters of high stress points are evident and there is a wide range of sizes present.



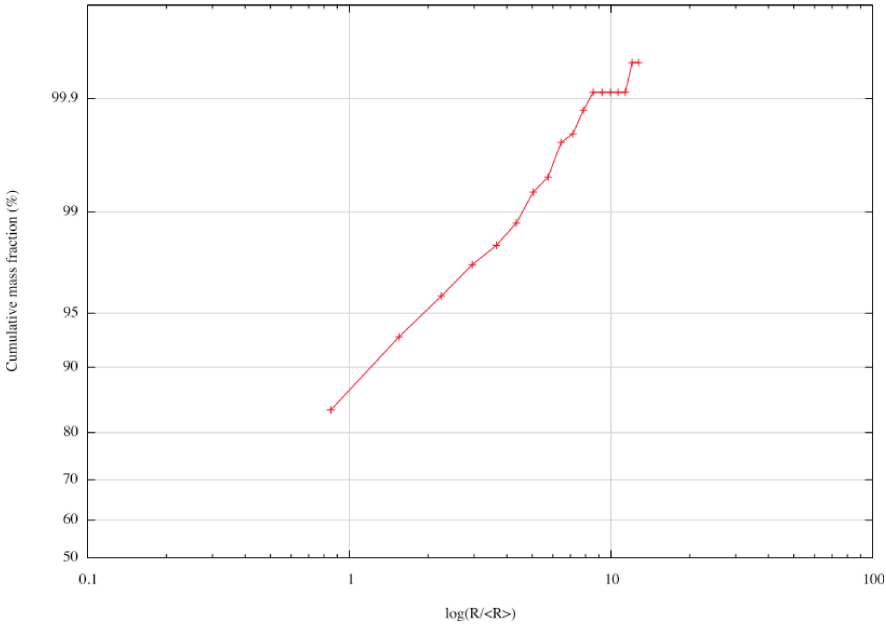


**Fig. 15.7** Probability plot of the cumulative distribution (CDF) for the log of the normalized size (sphere equivalent radius) of clusters of points with stress  $> 3.5$ . The CDF is close to a straight line, indicating that the distribution is close to log-normal. Note that the average radius is only 2.03 voxels.

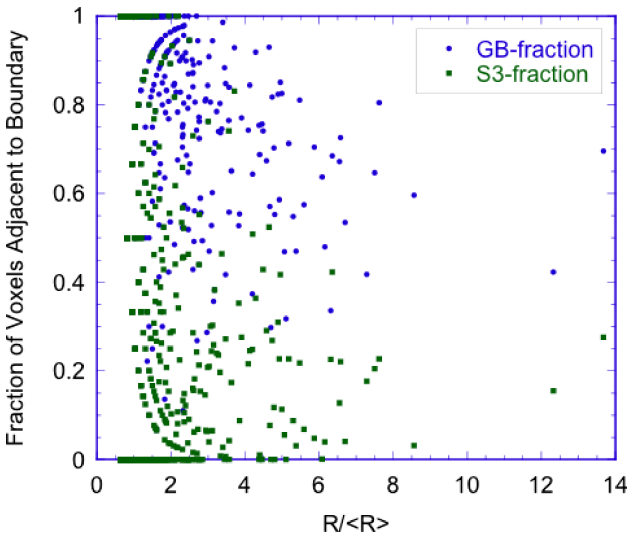


**Fig. 15.8** Plot of the fraction of voxels in each cluster that are adjacent to either a general grain boundary (round symbols) or to twin boundaries (square symbols). The average values roughly match the overall fractions (Fig. 15.3) although the smaller clusters show high fractions.

performed above. The fractions of voxels corresponding to twin boundaries is lower simply because twin boundaries comprise only about one third of all boundaries. Again, no strong variation in the fraction with size is apparent.

## 15.5 Summary

An efficient FFT-based method for analyzing the viscoplastic response of polycrystalline materials was applied to a microstructure with a high fraction of annealing twins. The microstructure was derived from a serial section dataset. The results showed that high stresses tend to occur next to grain boundaries but no specificity in terms of boundary type when analyzed according to the coincident site lattice (CSL) theory. A new analysis for clusters of high stress points was introduced; the distribution of sizes of high stress clusters was found to be close to log-normal.

**Acknowledgement** The authors are grateful to R.A. Lebensohn for use of his viscoplastic FFT code, and to C.W. Roberts for parallelizing the FFT calls. M. Uchic and M. Groeber of the AFRL are thanked for supplying the image. Use of facilities provided by the MRSEC at CMU under NSF grant number is DMR-0520425 is gratefully acknowledged.

## References

1. Moulinec H, Suquet P. 1998. A numerical method for computing the overall response of nonlinear composites with complex microstructure. *Computer Methods in Applied Mechanics and Engineering* 157:69–94.
2. Lebensohn RA, Brenner R, Castelnau O, Rollett AD. 2008. Orientation image-based micromechanical modelling of subgrain texture evolution in polycrystalline copper. *Acta mater.* in press.
3. Mishnaevsky Jr L, Schmauder S. 2001. Continuum mesomechanical finite element modeling in materials development: A state-of-the-art review. *Applied Mechanics Reviews* 54: 49–74.
4. Ma A, Roters F, Raabe D. 2006. Studying the effect of grain boundaries in dislocation density based crystal-plasticity finite element simulations. *International Journal Of Solids And Structures* 43:7287–303.
5. Lewis AC, Geltmacher AB. 2006. Image-based modeling of the response of experimental 3D microstructures to mechanical loading. *Scripta mater.* 55:81–5.
6. Lewis AC, Suh C, Stukowski M, Geltmacher AB, Rajan K, Spanos G. 2008. Tracking correlations between mechanical response and microstructure in three-dimensional reconstructions of a commercial stainless steel. *Scripta mater.* 58:575–8.
7. Lebensohn RA. 2001. N-site modeling of a 3D viscoplastic polycrystal using Fast Fourier Transform. *Acta mater.* 49:2723–37.
8. Michel JC, Moulinec H, Suquet P. 1999. Effective properties of composite materials with periodic microstructure: a computational approach. *Computer Methods in Applied Mechanics and Engineering* 172:109–43.
9. Kocks UF, Tomé C, Wenk H-R, eds. 1998. *Texture and Anisotropy*: Cambridge University Press, Cambridge, UK. 675 pp.

10. Uchic MD, Groeber MA, Dimiduk DM, Simmons JP. 2006. 3D microstructural characterization of nickel superalloys via serial-sectioning using a dual beam FIB-SEM. *Scripta mater.* 55:23–8.
11. Rollett AD, Lee SB, Campman R, Rohrer GS. 2007. Three-dimensional characterization of microstructure by electron back-scatter diffraction. *Annual Review of Materials Research* 37:627–58.
12. Lewis AC, Geltmacher AB, Spanos G. 2008. Determination of Critical Microstructural Features in an Austenitic Stainless Steel Using Image-Based Finite Element Modeling *Metall. Mater. Trans.* in press.



A.D. Rollett  
Professor  
Department of Materials Science &  
Engineering  
Carnegie Mellon University  
Pittsburgh, PA 15213-3890  
USA

**Part IV**  
**Specialized Characterization Techniques**



## Chapter 16

# Diffraction Techniques in Steel Research: An Overview

Stefan Melzer and Jaap Moerman

**Abstract.** Acquiring knowledge about microstructures and textures is crucial for the improvement and development steel products, because these two characteristics are controlling factors for the properties of steel. Diffraction techniques using X-rays, electrons or neutrons are suitable to study microstructures (e.g. phase relationships) and textures (crystallographic orientations). X-ray diffraction (XRD) and electron backscatter diffraction (EBSD) are generally available techniques within an industrial research environment.

Different examples from daily research within Corus RD&T are shown, where these diffraction techniques have been used. For the development of new high-tech multi-phase steels we study phase composition and microstructure to optimise product properties. Retained austenite may easily be detected and quantified by XRD, using the right approach. Moreover, using an area-sensitive 2D-detector, such as e.g. the GADDS system, the textures of ferrite and austenite components may be identified simultaneously during a single measurement. Micro XRD (beam diameter down to 100  $\mu\text{m}$ ) allows us to study small-scale welding joints within TRIP steels and how these welds evolve with time. Even more interesting is the possibility to study recrystallisation and phase transformations in situ at high temperature in real time, e.g. to make phase transformations visible during inter-critical annealing.

Another fascinating and beneficial attribute of XRD and EBSD is to study coatings/platings such as Ni in relation to the underlying steel substrate. Not only it is possible to identify the thickness of a plating or the phases in a coating, but textural and microstructural relations between the substrate and the surface layer can also be visualised. The understanding of microstructure opens the way to grain boundary engineering in coated products to help improve the corrosion properties.

---

S. Melzer and J. Moerman  
Corus RD&T, IJmuiden, The Netherlands

## 16.1 Introduction

Properties of steel or other metals are generally visible on a macroscopic scale (e.g. surface roughening, tensile strength, corrosion). These material properties are, however, controlled by microstructure and texture. The control of microstructure and texture evolution during the fabrication processes of steel is therefore essential to meet specified product properties. In turn, for the improvement and development of steel products it is a prerequisite to acquire knowledge about the evolution of textures and microstructures during various rolling and annealing steps. Diffraction techniques using X-rays, electrons or neutrons are widely used to characterise microstructure and texture of steel, because most process steps result in phase transformations or significant changes in crystal orientations that can be detected by diffraction techniques.

X-ray diffraction (XRD) and electron backscatter diffraction (EBSD) are the most commonly used diffraction techniques in industrial environments. Therefore, we will concentrate on XRD and EBSD and demonstrate how suitable and valuable these techniques have been and are for steel research, and how new developments (e.g. high temperature XRD; new detectors) can take us one (or more) step(s) further. We will present various examples from the daily research within Corus RD&T where these diffraction techniques have been used.

## 16.2 Experimental Details

### 16.2.1 *Equipment*

X-ray diffraction measurements have been performed using fully automated Bruker D8 (texture analyses, micro-XRD, HT-XRD) and Panalytical X'pert Pro (retained austenite) diffractometers equipped with an area-sensitive detector (GADDS) and position-sensitive detector (Xcelerator), respectively. EBSD analyses have been done using either a conventional Jeol 5900 SEM equipped with a HKL channel 5 EBSD system (steel substrates Ni-platings) or a Zeiss Ultra 55 FEG-SEM equipped with a TSL OIM EBSD system (TRIP steels, Ni-platings).

### 16.2.2 *Techniques*

Both diffraction techniques, XRD and EBSD, can detect phases and crystallographic orientations, but the area from which the information is obtained is generally totally different (Fig. 16.1). It is easy to analyse a few mm<sup>2</sup> or even cm<sup>2</sup> using XRD, but it is very time consuming to scan one mm<sup>2</sup> using EBSD. Moreover, data obtained by EBSD are from the upper few nm of steel surface, whereas the pene-

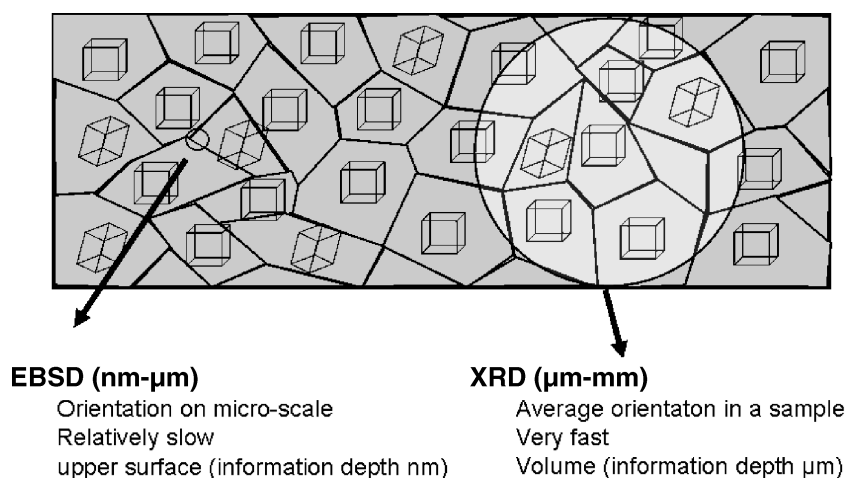


**Fig. 16.1** Schematic sketch illustrating the differences between EBSD and XRD.

tration depth of XRD reaches at least a few  $\mu\text{m}$ . On the other hand, an EBSD system mounted on a FEG-SEM allows the analysis of microstructure on a nm scale, while the spatial resolution of XRD is limited to  $100\ \mu\text{m}$ . Therefore, the two different techniques are complementary rather than competitive. Frequently, results from both methods are required to understand and solve problems related to the microstructure and texture of steel alloys.

## 16.3 Characterisation of Advanced High-Strength Steels

Transition induced plasticity (TRIP) steels belong to a group of advanced high-strength steels that show a good formability along with high strength. This steel type is definitely of significant importance for the automotive industry to produce lighter cars.

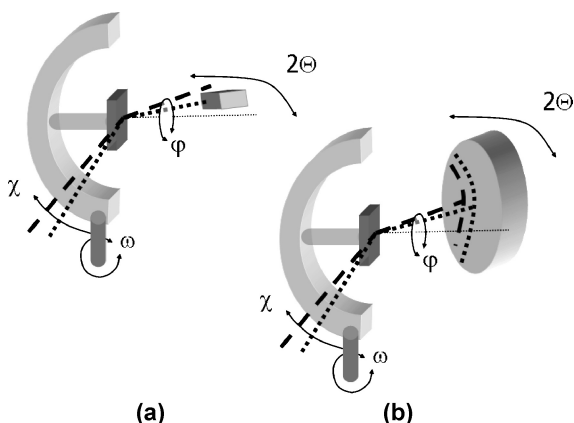
In the course of the development of new high-tech multi-phase steels, the knowledge about texture, phase composition and microstructure is essential to optimise product properties. Fast and accurate methods are required within a steel company to deliver reliable data on time for further development steps.

### 16.3.1 Texture Measurement of Ferrite and Austenite Phase

Because TRIP steels are composed of austenite and ferrite, texture measurements are necessary for both the phases to understand mechanical properties. Using a classical texture goniometer equipped with a point detector (Fig. 16.2) individual measurements have to be performed for ferrite and austenite phases. Moreover, in



**Fig. 16.2** Schematic sketch of texture goniometer equipped with a conventional detector (a) and an area-sensitive detector (b).



circular scanning mode (see e.g. Bunge and Puch, 1984) a large number of pole-figure points are needed to achieve an acceptable angular resolution.

A texture goniometer equipped with an area detector (Fig. 16.2) allows certain pole figures of ferrite and austenite to be obtained simultaneously with a single measurement. A modern multi-wire detector such as the GADDS has a high sensitivity and a very fast read-out such that short data acquisition times are possible. The two dimensions of the detector are used in  $2\Theta$ -direction (Bragg angle) and  $\chi$ -direction (angle along a Debye-Scherrer ring) such that for these two dimensions higher angular resolutions may be achieved (Fig. 16.3).

The second dimension of the pole figure  $\phi$  still has to be derived by step-scanning. Therefore a complete (110) pole figure of ferrite is determined from 236

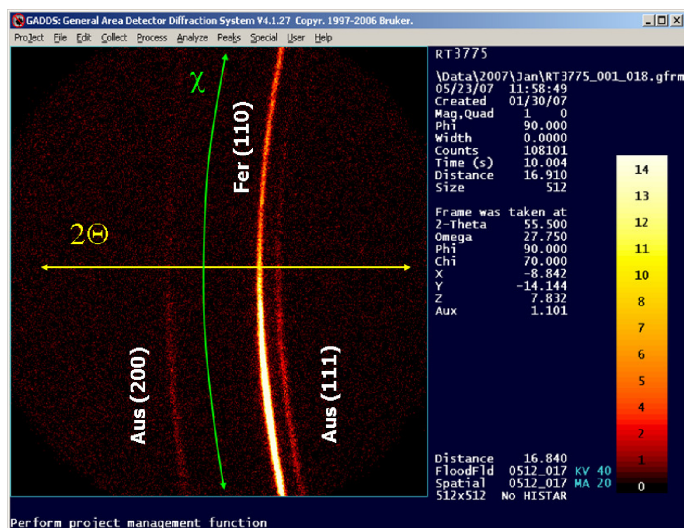


**Fig. 16.3** Single frame recorded with an area-sensitive detector.

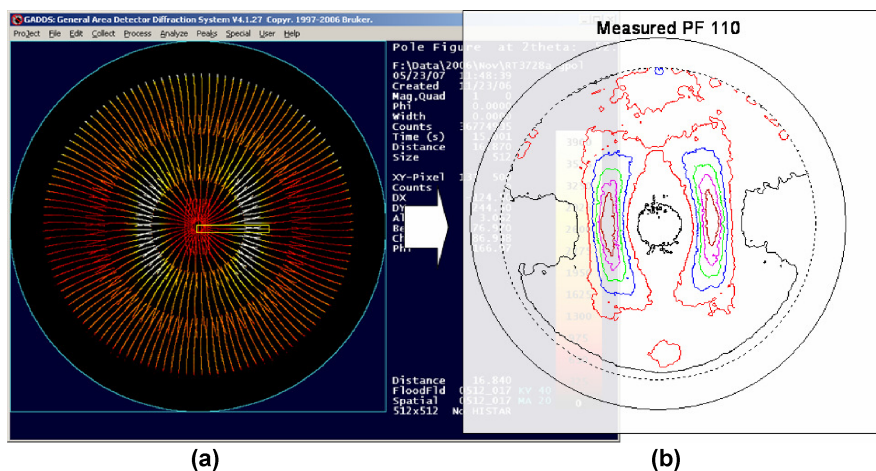


**Fig. 16.4** Complete pole figure (ferrite) derived from 236 single frames (a) and corresponding calculated intensities (b).

individual frames (Fig. 16.4). Besides step-scanning, sample movement during the measurement is another time-consuming step, but is absolutely necessary to obtain good statistics. Therefore the measurement of a complete pole figure takes about 50 minutes.

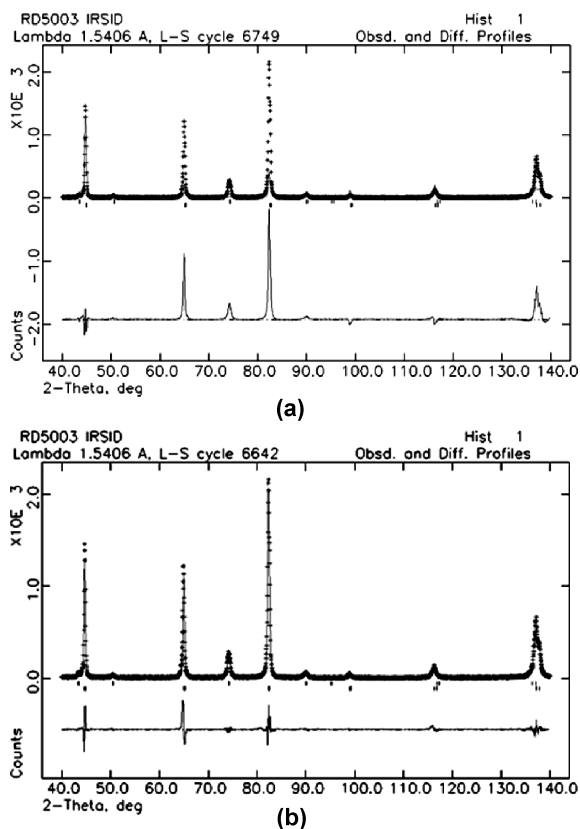
However, at least for multiple-phase steels containing austenite and ferrite, the total data acquisition time is reduced to about 3 hours, in comparison to 6 hours measuring the textures of both the ferrite and austenite phases, using a conventional point detector. Figure 16.4 shows a typical intensity plot of the (110) pole figure obtained for the ferrite phase in TRIP steels.

### 16.3.2 Retained Austenite

An important quality parameter of TRIP steel is the volume fraction of retained austenite, because austenite is responsible for the TRIP effect. X-ray diffraction is commonly used to quantify the amount of austenite in TRIP steels. In the past, a more or less empirical method, using simple peak-fitting along with calculated theoretical line intensities, was used to derive the proportion of austenite (Jatczak et al. 1980). Rietveld analysis is increasingly coming to replace this analytical approach. The Rietveld method provides numerous advantages over the conventional quantitative analysis methods. Since the method uses a full pattern-fitting algorithm, all lines of each phase are explicitly taken into account. Preferred orientation of crystallites, i.e. the crystallographic texture, is not a major problem with full-pattern methods, at least for powder samples.

Nevertheless, the X-ray patterns of strongly textured metals have to be refined carefully, and a suitable correction procedure for preferred orientations has to be

**Fig. 16.5** Measured X-ray pattern (crosses) along with refined pattern (light grey line) (a) without any texture correction and (b) applying the spherical harmonic correction procedure.

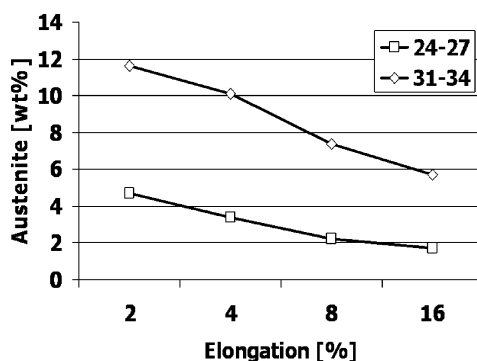


performed. Figure 16.5 (a) shows the refined X-ray pattern of conventional TRIP steel using the GSAS software package (Larson and Van Dreele, 1985) without any texture correction. An enormous misfit between the measured and the refined pattern is observed. The steel would contain 14.4 wt% austenite according to this poor refinement.

Crystallographic textures can be described using a spherical harmonics model that is available in GSAS. Moreover, it is possible to refine the coefficients within the model using orthorhombic sample symmetry as a constraint. This is also used for texture analysis of rolled metals at half thickness. Such a high symmetry lowers the number of coefficients, and consequently the degrees of freedom in the refining algorithm. Highly symmetric phases, such as austenite and ferrite, show few reflections. Having too many refinable parameters may potentially result in over-parameterisation and incorrect phase fraction estimates.

Using the spherical harmonics model (for correcting preferred orientation and forcing it to orthorhombic sample symmetry) even extremely textured TRIP steels may be refined (Fig. 16.5 (b)). Using this procedure an amount of 11.5 wt% of retained austenite is detected, which is as expected for this type of TRIP steel. This

**Fig. 16.6** Amount of austenite in two different TRIP steels as a function of elongation for tensile specimens.



volume fraction is in good agreement with the austenite content derived by other techniques.

Even using advanced correction methods, the  $2\Theta$ -range of data acquisition is very critical. For Cu-K $\alpha$  radiation, upper  $2\Theta$ -limits to  $100^\circ$  and  $130^\circ$  will yield austenite fractions of 13.5 wt% and 12.5 wt%, respectively. These values are significantly high. By cutting off ferrite reflections at higher  $2\Theta$ -angles (which are relatively strong as a result of the strong texture) the deviation is clear.

However, an adequate refinement will give reliable and consistent volume fractions of austenite and ferrite. Figure 16.6 shows the tensile test results of two different TRIP steels. As expected, in both TRIP steels the amount of austenite decreases with increasing elongation.

### 16.3.3 Detection of Complex Microstructures

Electron back-scatter diffraction is used to characterise the microstructure of complex multi-phase steels. It is relatively easy to distinguish austenite and ferrite due to their different crystal structures (Fig. 16.7 (a)). However, it should be mentioned that the amounts of austenite derived by EBSD sometimes differ significantly from those obtained by XRD or using magnetic methods. A possible explanation is the different penetration depth of the techniques, see Sect. 2.2. The magnetisation saturation measurement (e.g. Zhao et al. 2001) is clearly a bulk method and specimens of several  $\text{cm}^3$  may be studied. X-rays still reach a few  $\mu\text{m}$  beneath the surface. Electrons only penetrate the upper few nm of steel specimen. Another artefact to keep in mind is that polishing of the sample during preparation may result in a spontaneous transformation of austenite located at the surface. It is clear, that surface sensitive techniques as EBSD are affected by this phenomenon.

Bainite plays an important role in the stabilisation of austenite, and hence the detection of bainitic regions is essential. Bainite is composed of ferrite and carbides. Bainitic ferrite shows significant internal stresses (caused by the combined diffusive-displacive transformation) that result in reduced pattern qualities (band-contrast) compared to normal ferrite (big blue grains in Fig. 16.7 (a)). To identify

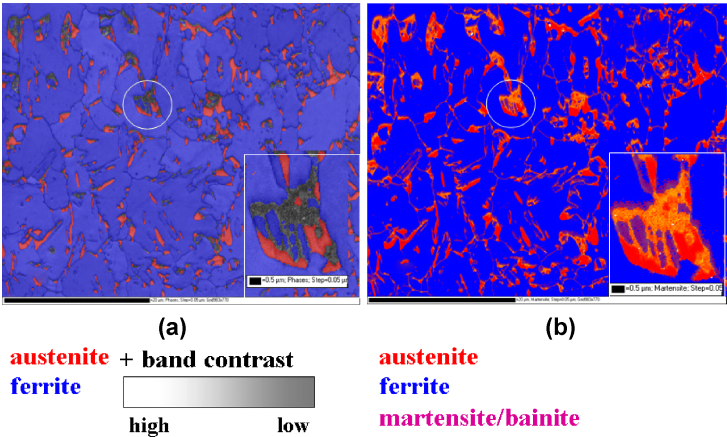


**Fig. 16.7** Microstructure of a TRIP steel showing (a) the two crystallographically different phases austenite and ferrite. (b) The band contrast was used to identify bainitic or martensitic regions.

bainitic regions a band contrast map can be used. Figure 16.7 (a) shows the band contrast with a phase map as an overlay. Some ferritic regions show a significantly lower band contrast (dark blue regions in Fig. 16.7 (a)) than other regions. One

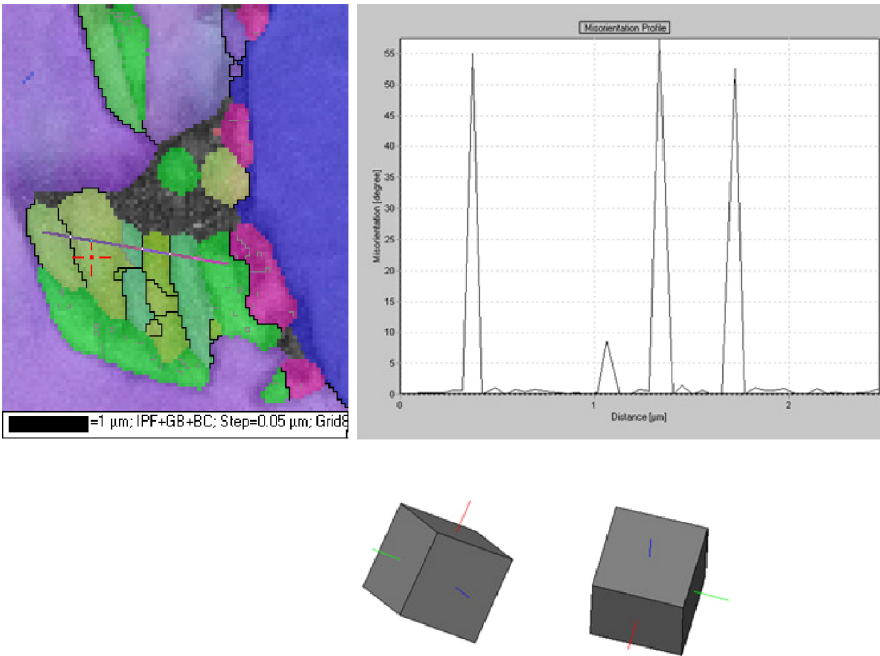


**Fig. 16.8** Misorientation of grain boundaries along a traverse within a bainitic/martensitic region (green grains).

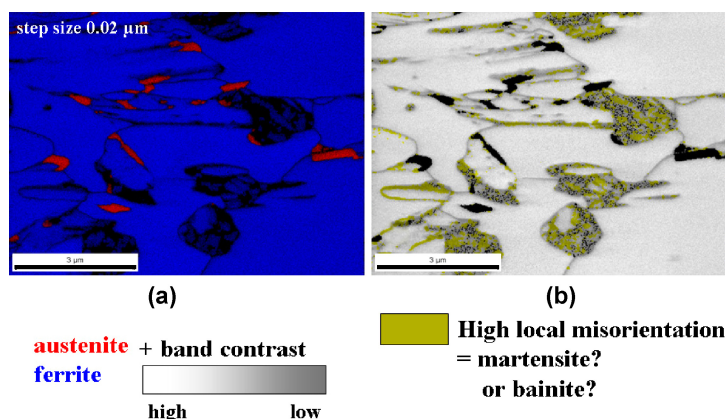


**Fig. 16.9** Microstructure of a TRIP steel showing (a) austenite and ferrite phases. (b) Local misorientation was used to identify bainitic or martensitic regions.

possibility is to assume that all these low band contrast locations consist of bainite. (indicated in violet in Fig. 16.7 (b)).

One problem is that the violet regions could also be martensite, because the structure of martensite is also highly strained, and consequently martensite also appears as ferrite with a lower band contrast in an EBSD map. To solve this problem often the misorientation of grain boundaries is taken into account.

The austenite-ferrite phase transformation is characterised by special crystallographic orientation relationships, namely the Kurdjumov-Sachs correspondence and the Nishiyama-Wasserman correspondence. Both relationships are used to describe the orientation correlation between parent-austenite and daughter-ferrite. Misorientation angles typically are close to  $0^\circ$  or around  $60^\circ$ . These characteristic values are visible for ferritic grains present in a highly strained region (Fig. 16.8). However, the orientation relationships hold for martensite and bainite

Another possible approach to identify bainitic or martensitic locations is to use Kernel local misorientation plots. Average misorientations are calculated between one point and all its direct neighbours. Strained locations such as bainite or martensite show high average misorientations (Fig. 16.9).

### 16.3.4 Welds

Producing acceptable welds in TRIP steels is often difficult, and sometimes impossible. For automotive applications the welding behaviour of the steel and the mechanical properties of the weld are very important. In order to understand welding problems, we analysed the microstructure around welds using XRD and EBSD.

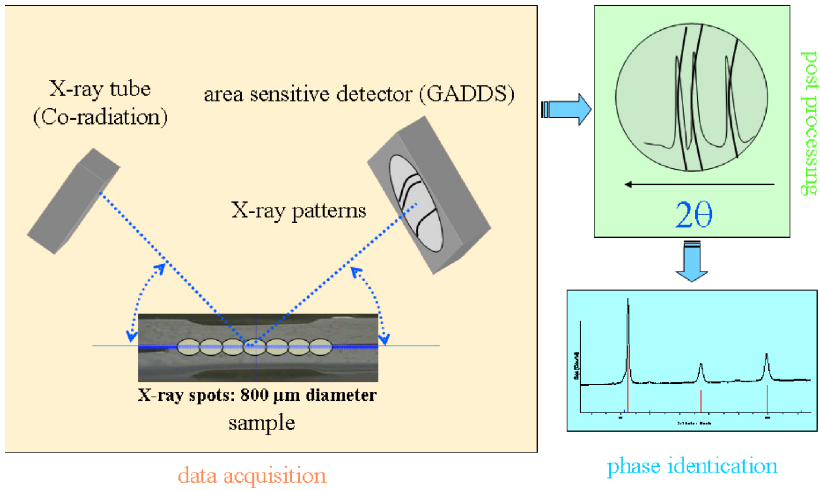


**Fig. 16.10** Data collection and processing procedure using an area sensitive detector during micro XRD-analysis (beam diameter 800  $\mu\text{m}$ ) of a welded TRIP steel.

Failing of welds may be related to phase transformations occurring during the welding process. To investigate this, the variation of phase fractions has been studied across a weld using micro XRD (Fig. 16.10).

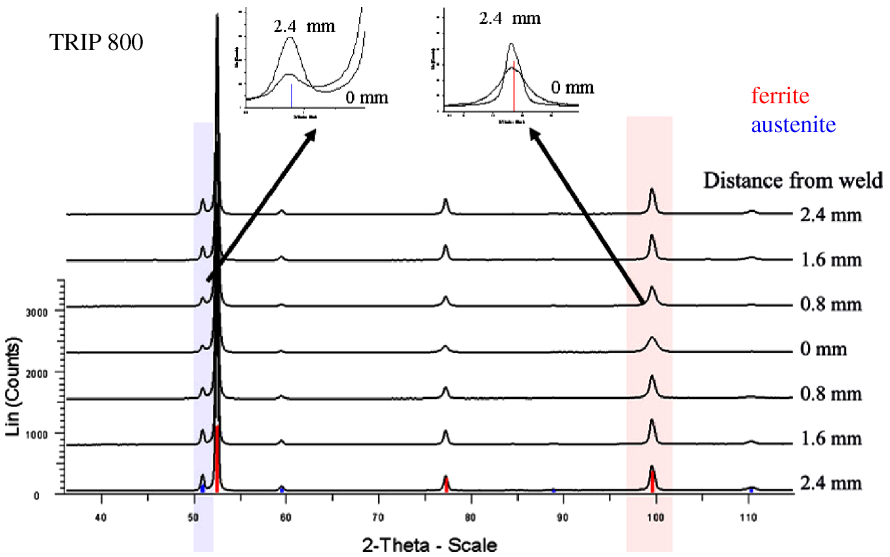


**Fig. 16.11** X-ray patterns recorded across the centre of a weld (0 mm) in TRIP steels along with identified phases. Enlarged inserts show the differences between the centre and the edge of the weld.

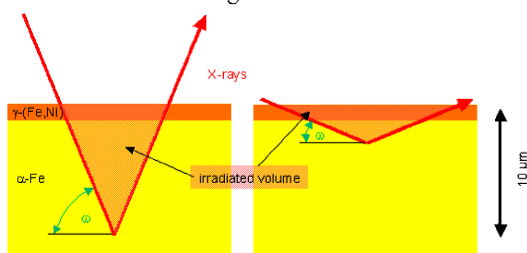
Using a beam diameter of  $800\text{ }\mu\text{m}$  (Fig. 16.10), it is possible to measure variations in phase fractions between the centre of the weld, the heat-affected zone and the original TRIP steel. Figure 16.11 shows that the centre of weld contains less austenite compared to the unaffected TRIP material. Moreover, ferrite reflections close to the centre (0 mm in Fig. 16.10) are relatively broad compared to the reflections of ferrite located far away from the weld (2.4 mm in Fig. 16.10). The stressed lattice of martensite results in broader reflections. This indicates the presence of a higher fraction of martensite in the weld than in the TRIP steel.

## 16.4 Characterisation of Nickel Plated Battery Steels

Most of the sheet steel is coated or plated by various materials, e.g. Zinc or Nickel. Galvanised steels are used for the automotive industry. Nickel plating is used for battery cans to prevent corrosion. Characterisation of the Ni-plating and the corresponding steel matrix is done for a better understanding of the corrosion behaviour of batteries.

Phases in thin layers can be identified using the grazing incidence technique (Fig. 16.12). Using the conventional Bragg-Brentano geometry, the detection of phases in the coating is obscured by their relatively low concentration in the penetrated volume. It is possible to significantly increase the contribution of the top layer to the total diffracted intensity by keeping the incident beam angle  $\omega$  small (Fig. 16.12 top right). To study platings or coatings the incident beam angle  $\omega$  is fixed whereas the diffracted beam angle varies (Fig. 16.12 bottom).

Irradiated volume vs. incident beam angle



Grazing incidence approach

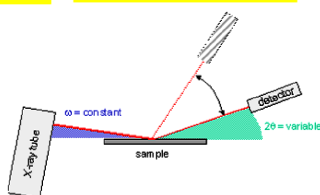


**Fig. 16.12** Schematic sketch illustrating the relation between incident X-ray beam angle  $\omega$  and irradiated volume (penetration volume). The contribution of the surface layer to the total diffracted X-rays is clearly higher for lower incident beam angles.



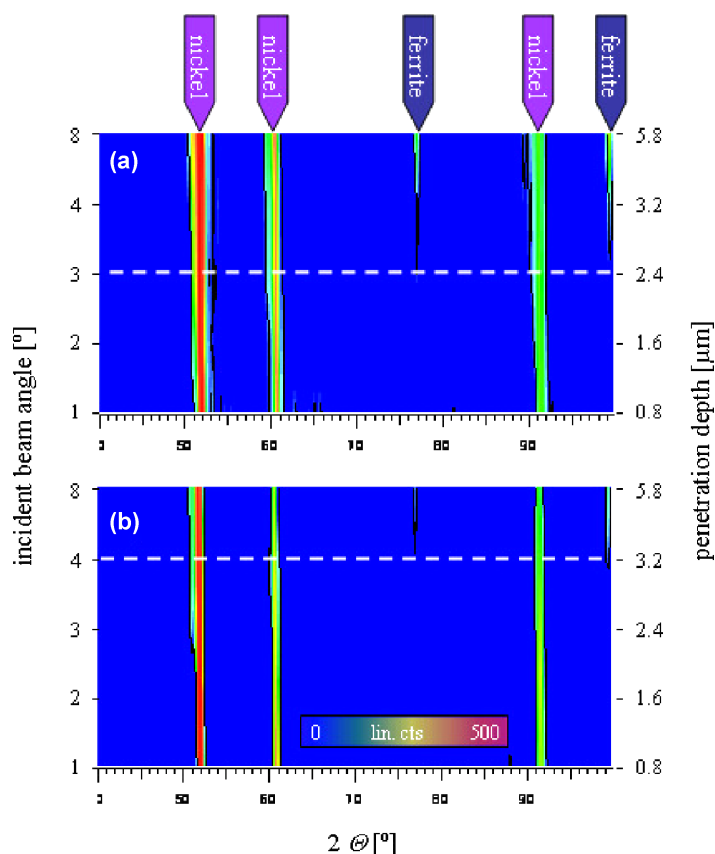


**Fig. 16.13** X-ray intensities as a function of  $2\theta$  and incident beam angle. The first appearance of ferrite reflections corresponds to the thickness of the Ni-layer, (a) outside and (b) inside of the battery can.

To measure the thickness of the Ni-layer, the penetration depth of the X-ray beam has been varied by using different incident beam angles (Fig. 16.13). For an incident beam angle of  $1^\circ$ , the penetration depth of  $\text{CoK}\alpha$ -radiation is  $0.8\ \mu\text{m}$ , whereas for an incident beam angle of  $8^\circ$  the beam penetrates about  $5.8\ \mu\text{m}$  into the Ni-layer. The penetration depth, for which the first ferrite reflection appears, corresponds to the thickness of the Ni-layer (Fig. 16.13). Using this technique, thicknesses of  $3.2\ \mu\text{m}$  and  $2.4\ \mu\text{m}$  have been derived for the inside and the outside of the battery can, respectively.

Using EBSD it is also possible to characterise the microstructure and texture of the Nickel plating. Possibly, the properties of the Ni-plating are related to the texture and grain characteristics of the steel substrate.

Adequate sample preparation is a prerequisite to obtain sharp and high-contrast EBSD patterns, because of the very thin Ni-layer ( $1\text{--}3\ \mu\text{m}$ ). Generally, mechanical polishing and subsequent electro-polishing give suitable sample surfaces. There-

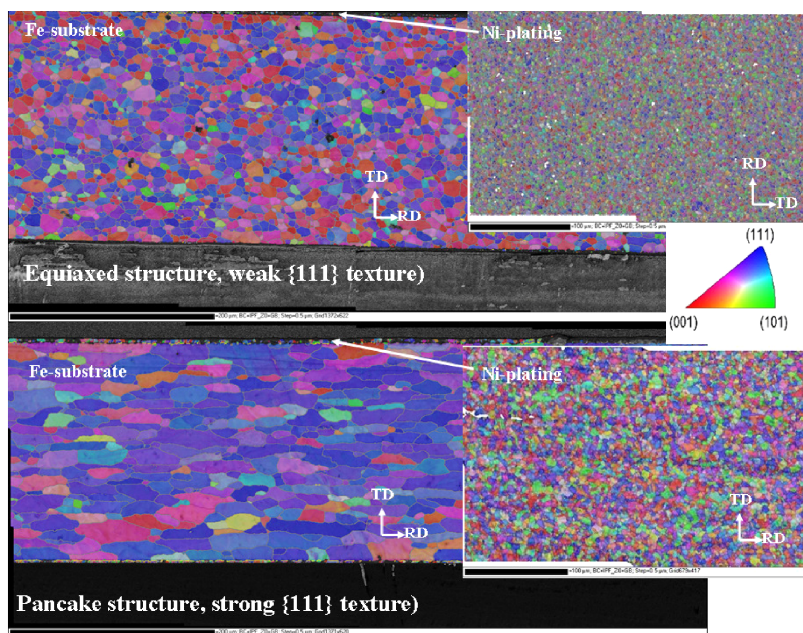


**Fig. 16.14** Inverse pole figure maps of steel with different microstructures (full thickness transverse plane view) used for battery cans along with orientation maps of the corresponding Ni-plating (normal plane view).

fore, surface specimens have been prepared by only soft electro polishing. Following this approach only a few  $\mu\text{m}$  of material has been removed and only the Ni-structure has been detected in the surface layer.

The inverse pole figure maps demonstrate that the steel substrates of all samples have a  $\{111\}$ -fibre texture (Fig. 16.14 left). The equiaxed grains visible in the first sample are a result of severe cold rolling and subsequent recrystallisation. The second specimen shows an elongated grain structure; pancake formation due to interaction of AlN precipitation during recrystallisation. The corresponding Ni-layers are composed of much smaller grains with a weak cube texture (Fig. 16.14 right).

Grain size distributions have been calculated for the steel substrate and the corresponding Ni-layers to determine possible relations between their microstructures (Fig. 16.15 top). The inverse pole figure maps (Fig. 16.14) give the impression that larger ferrite grains possibly trigger the formation of larger Ni-grains. This impression does not hold, when grain size distributions of all different samples are considered. There is at least one other sample (dark green curves in Fig. 16.15), where the steel substrate consists of significantly larger crystals, but where the Ni-grains are rather small. Orientation distribution functions show strong maxima along the  $\gamma$ -fibre for the steel substrate typical for recrystallised material. In the Ni-layers a weak cube texture has been developed that is characteristic for recrystallised FCC metals. There is no indication of a relation between the texture of the Fe-substrate and that of the Ni-plating.

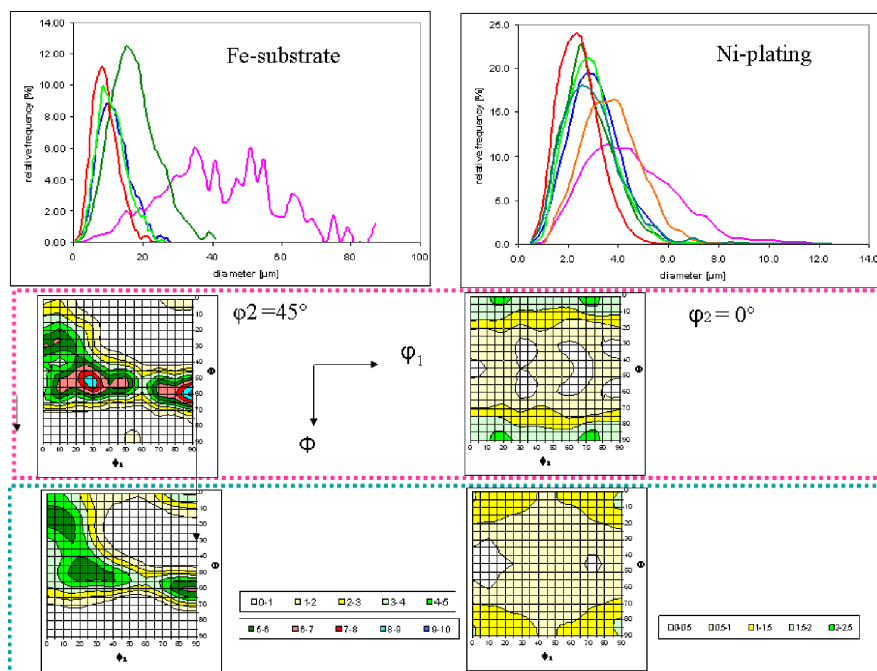


**Fig. 16.15** Grain size distributions for various steels and corresponding Ni-platings used for battery cans. For two samples (border colours correspond to curve colours at the top) the ODF plots of steel base and Ni-plating are shown.

Grain boundary engineering become increasingly popular in recent years to improve the corrosion properties of metals. For Nickel it is known that the amount of  $\Sigma 3$ -boundaries shows a direct correlation with the corrosion resistance. Grain boundaries can be detected well using EBSD, and the amount of  $\Sigma 3$ -boundaries can be easily derived (Fig. 16.16). Interestingly the proportion of  $\Sigma 3$ -boundaries varies strongly between different materials. In the next step, the corrosion behaviour of the different Ni-platings will be studied to see whether large amounts of  $\Sigma 3$ -boundaries improve the corrosion resistance of thin Ni-plating as well.

## 16.5 In situ Real-Time Measurement Techniques

Process related research is normally based on characterisation of samples taken before and after certain process steps. Generally, this approach is successful and often the only way to obtain reliable and suitable results. But occasionally, it is not possible to detect mechanisms responsible for textural and microstructural phenomena, because they occur at high temperatures and are simply not quenchable. This lack of information may result in insufficient information about process pa-

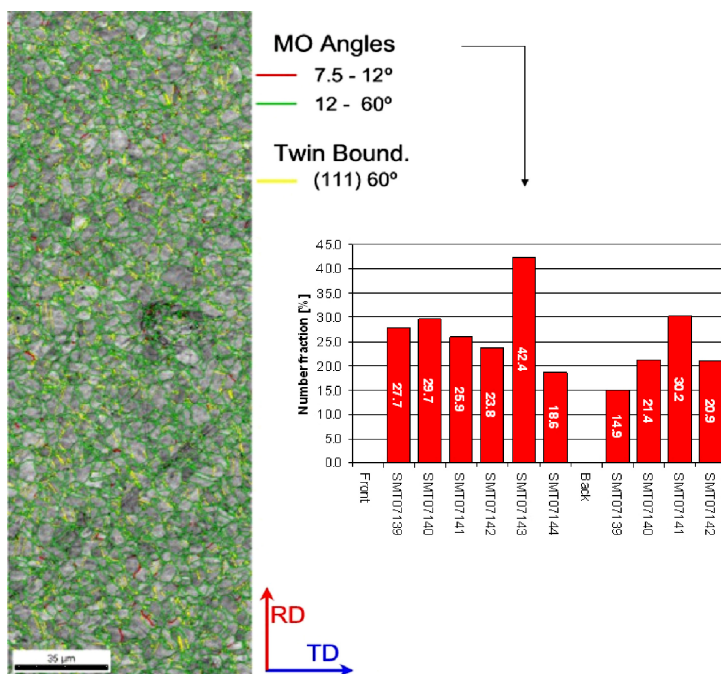
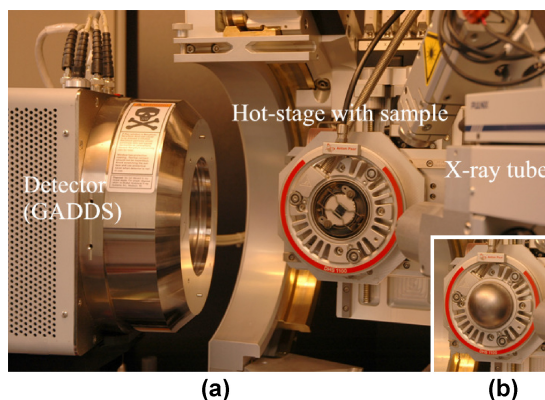


**Fig. 16.16** Grain boundary map for a typical Ni-plating (left) showing  $\Sigma 3$ -boundaries. The amount of  $\Sigma 3$ -boundaries significantly differs from sample to sample (right).

rameters or model constraints. Moreover, this experimental approach is often extremely time-consuming and very expensive, because large numbers of samples are required.

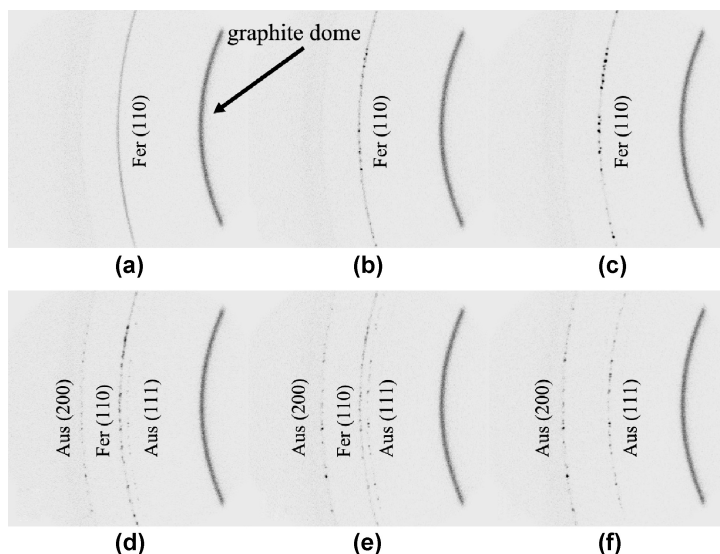
Recently experimental techniques have been developed to analyse microstructures and textures in situ at high temperatures in real time. Recrystallisation of metals after rolling changes the texture completely. By high-temperature X-ray diffraction (HT-XRD) the texture change can be used to study the recrystallisation kinetics. The recrystallisation kinetics of hot-rolled aluminium have been derived using this technique (Melzer et al. 2004). Heating rates in this method are limited to 20°C/minute. Modern area-sensitive detectors and different types of heating stages (Fig. 16.17), allow heating rates of up to 200°C/minute, close to those obtained in continuous annealing lines. So the recrystallisation of steel can be monitored. The ferrite-austenite transformation also can be detected. Figure 16.18 shows individual frames of diffraction patterns recorded during heating of a DP steel grade. The X-ray patterns demonstrate the change of the microstructure with increasing temperatures. At 500°C the recorded part of the Debye-Scherrer ring for ferrite (Fer (110) in Fig. 16.18 (a)) is a continuous line without any spottiness. At 590°C the material starts to recrystallise and spots appear (Fig. 16.18 (b) and (c)) due to the growth of larger individual crystallites. Finally, the ferrite transforms into austenite (Fig. 16.13 (d) to (f)).

**Fig. 16.17** Anton Paar Heating stage DHS1100 mounted on a Bruker D8 diffractometer equipped with an area-sensitive detector and an open Euler cradle, (a) open to mount sample and (b) closed with a graphite dome to use an inert gas atmosphere.

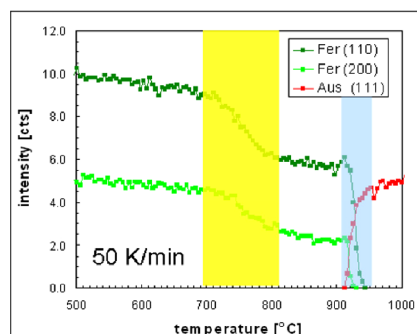
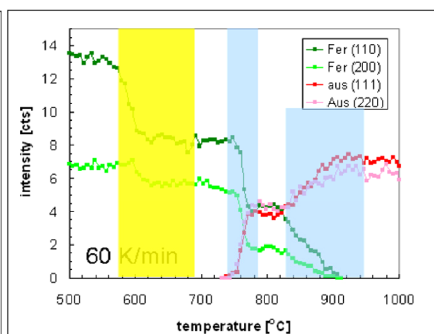


In order to quantify the results, the integral intensities for a specific reflection (e.g. Fer 110) have been calculated for the entire part of the Debye-Scherrer ring. Figure 16.19 shows the variation of these intensities as a result of increasing temperatures. For ultra-low carbon steel the recrystallisation starts at 700°C (see intensity drops for both the (110) and the (200) reflection of ferrite). Between 910°C and 920°C the ferrite transforms into austenite. This observation indicates that the temperature control at the hot stage is quite accurate.

Dual phase steel recrystallises at lower temperatures. The intensity of the (110) reflection of ferrite decreases sharply. The (200)-reflection does not change, in contrast to ULC-steel. The transformation behaviour differs from that observed for



**Fig. 16.18** Frames recorded for DP steel. (a) 500°C; 0 min, (b) 590°C; 5 min, (c) 720°C; 11.5 min, (d) 790°C; 15 min, (e) 870°C; 19 min and (f) 930°C; 22 min.

**ULC-steel****DP-steel**

**Fig. 16.19** Integral intensities for ferrite and austenite reflections as function of temperature during heating.

ULC-steel. Firstly at 750°C, within a short range of about 10°C, ferrite located in perlitic areas transforms into austenite. Up to 820°C the relative fractions of ferrite and austenite remain constant. Above 820°C the rest of the ferrite continuously converts into austenite.

From this data, it is possible not only to derive recrystallisation kinetics of different materials, but also to identify different mechanisms of microstructure development in steel.

## 16.6 Summary

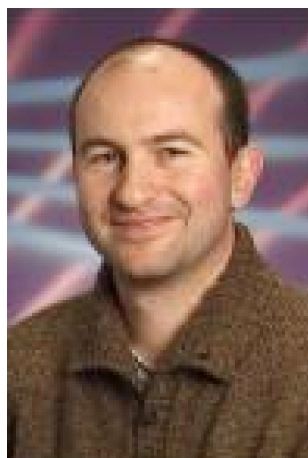
Within a modern steel research laboratory, diffraction techniques are quite unique and crucial to study microstructures and textures of steel products. Besides routine analyses, such as identification and quantification of phases, in situ methods to simulate processes such as continuous annealing are becoming ever more important. We have demonstrated here, with several examples of work done at Corus RD&T, that EBSD and XRD deliver data that are required for process control and for the development of new steel qualities. Ongoing development is necessary to match the demands and challenges of future research.

## References

- [1] Jatzcak F, Larson JA, Shin SW (1980): Retained austenite and its measurement by X-ray diffraction' sp-453C. (SAE) Society of Automotive Engineers 0-89883-224-1.
- [2] Larson AC, Van Dreele RB (1985): Generalized structure analysis system. Los Alamos National Laboratory Report No. LA-UR.86-748



- [3] Melzer S, Liu S, van der Winden M. (2004): High-temperature X-ray diffraction: A new technique to study recrystallisation kinetics of aluminium. *Aluminium* 80: 660–666.
- [4] Zhao L, van Dijk NH, Brück E, Sietsma J, van der Zwaag S (2001): Magnetic and X-ray diffraction measurements for the determination of retained austenite in TRIP steels. *Mat Sci Engineering A*: 145–152.



Stefan Melzer  
Principal Scientist  
Ceramics Research Centre  
Corus RD&T  
IJmuiden  
Netherlands

## Chapter 17

# Non-Contact Non-Destructive Measurement of Texture Using an Electro-Magnetic Acoustic Transducer (EMAT) Sensor

C.L. Davis

**Abstract.** The formability of sheet metals is strongly influenced by, and can be predicted from, crystallographic texture, and is generally assessed in terms of an r-value and/or n-value off-line from tensile test samples. There is interest in the development of a non-destructive, cheap and simple to operate system for texture assessment. Ultrasonic velocity is directly related to a material's elastic modulus and metal single crystals can have significantly different elastic properties along their principal crystal axes. Hence, if a polycrystalline sample has preferred texture then variations in ultrasonic velocity with angle to the rolling direction are expected. In this work the ultrasonic velocity anisotropy, measured using a non-contact electro-magnetic acoustic transducer (EMAT) system, with respect to sheet rolling direction was determined and compared to calculated elastic modulus anisotropy, using quantified texture components (from X-ray diffraction or EBSD and their known individual anisotropies), and mechanically measured modulus values, at 0°, 45° and 90° to the rolling direction, for aluminium and steel sheets. Predictions of elastic anisotropy based on surface texture determination, as characterised by X-ray diffraction or surface EBSD, gave poor correlations with EMAT velocity anisotropy for aluminium sheets that contained significant through thickness texture variations, however, accounting for this using multiple EBSD scans through thickness gave good correlations. For steel it was found that the EMAT velocity anisotropy matched the measured modulus variation with angle, with differences between samples with different textures (as-rolled and heat treated conditions) being observed. However the predicted modulus variation did not show much difference between samples, resulting in some discrepancies with the EMAT velocity and measured modulus values. Results from this work, and data from the literature, suggest that monitoring the recrystallisation process in alumin-

---

C.L. Davis

Department of Metallurgy and Materials, University of Birmingham, Edgbaston, Birmingham, B15 2TT, UK



ium using an EMAT sensor is much more straight forward than for steel due to aluminium showing greater differences in elastic modulus, and hence ultrasonic velocity, anisotropy between the as-rolled and recrystallised textures.

## 17.1 Introduction

Metal single crystals can have significantly different elastic properties along their principal crystal axes, Table 17.1. Bunge [2] developed expressions for the anisotropy in the modulus of elasticity of a crystal (described by direction cosines  $l$ ,  $m$  and  $n$ ), which are well described by Nye [2], and reported in detail by numerous other researchers [3, 4]. The variation in elastic modulus with angle for the major texture components seen in aluminium alloys and steels can then be calculated and are given in Figs. 17.1 and 17.2 respectively.

From Figs. 17.1 and 17.2 it can be seen that the different texture components have significantly different elastic anisotropies. It can also be seen that measurements of the elastic modulus at a limited number of angles with respect to the rolling direction, for example  $0^\circ$ ,  $45^\circ$  and  $90^\circ$ , are likely to give a reasonable indication of the anisotropy in behaviour, however not all the textures would be distinguished, for example the  $\{110\} \langle 001 \rangle$  and  $\{110\} \langle 1-1\ 2 \rangle$  textures would not be fully described. For polycrystalline metals complex textures are seen, for aluminium the rolling textures are typically mixtures of Copper, S and Brass,

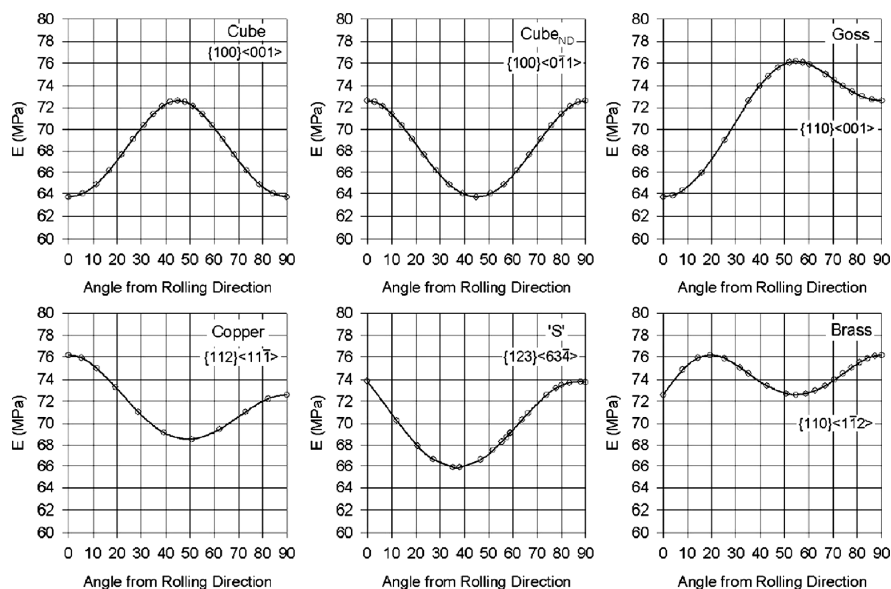


**Fig. 17.1** Variation in elastic modulus with angle (in degrees) for the major texture components seen in aluminium alloys.

**Table 17.1** Elastic modulus values (GPa) for single crystals along different directions [1].

	$\langle 100 \rangle$	$\langle 110 \rangle$	$\langle 111 \rangle$
Steel	125.0	210.5	272.7
Aluminium	63.7	72.6	76.1
Copper	66.7	130.3	191.1

whereas the annealing textures are typically mixtures of Cube, Cube<sub>ND</sub> and Goss. In practice commercially produced aluminium sheet contains varying amounts of all six texture components. Analysis of steel sheets is more complex due to the larger number of texture components seen and the fact that strip often contains mixed rolling, recrystallisation and transformation textures. In addition Fig. 17.2 indicates that the {111} texture components, which are highly desirable in deep drawing and interstitial free (IF) grades as they give high r-values, do not show any significant elastic anisotropy. However, it can be seen from the ODF presented in Fig. 17.3 that the associated rolling/transformation textures of {554}  $\langle -2-2\ 5 \rangle$  and {332}  $\langle -1-1\ 3 \rangle$ , which have similar elastic anisotropy to each other, and {112}  $\langle 1-1\ 0 \rangle$ , {223}  $\langle 1-1\ 0 \rangle$  and {113}  $\langle 1-1\ 0 \rangle$ , which also have similar anisotropies (see Fig. 17.2), are very close in position to {111}  $\langle -1-1\ 2 \rangle$  and {111}  $\langle 1-1\ 0 \rangle$  respectively. Therefore steel strip with high r-values, and therefore high gamma fibre texture, would be expected to show significant elastic anisotropy. The {554}  $\langle -2-2\ 5 \rangle$  texture is also purposefully introduced in thin sheet (particularly can-stock material) to reduce earring.

It is well known that the ultrasonic velocity in a material is directly related to the material's elastic modulus. Therefore ultrasonic velocity will vary with propagation direction through a single crystal and, if a polycrystalline metal sample has preferred texture (i.e. a preference of crystallographic orientations along, for example, the rolling direction of a sheet) then variations in ultrasonic velocity with

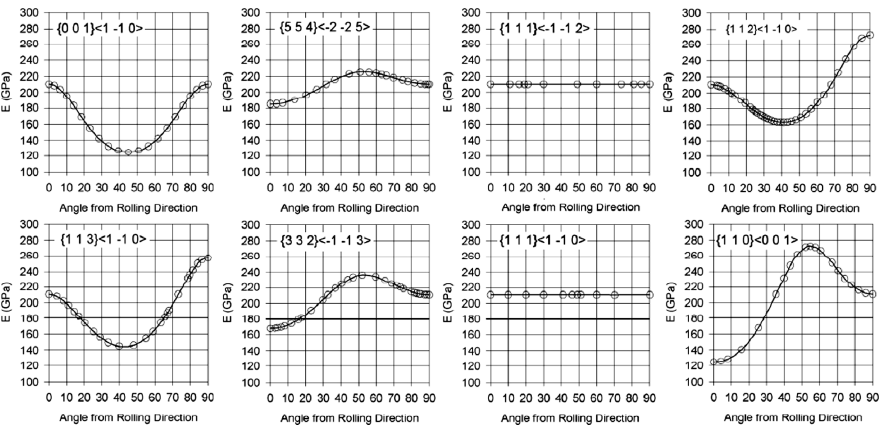


**Fig. 17.2** Variation in elastic modulus, with angle (in degrees) to the rolling direction, for the major texture components seen in steels.



## 17.2 Materials and Experimental Method

An EMAT-EMAT non-contact sensor system was used to measure the angular variation in ultrasonic velocity ( $S_0$  wave) for the metal sheets tested. The EMAT system consists of a single broadband transmit EMAT optimised to generate zero-order symmetric Lamb waves, and one or two broadband receive EMATs optimised to detect the same. Each EMAT consists of a single cylindrical neodymium iron boron magnet with pole orientation orthogonal to the plane of the sheet under test, as shown in Fig. 17.4. A number of turns of insulated wire are wrapped around each magnet (varying in wire diameter and coil width between the transmit and receive EMAT(s)). A broad band (temporally sharp) current pulse is passed through the wire coil of the transmit EMAT. The transient magnetic field set up by this pulse generates a reciprocal current in the metal sheet over which the EMAT is placed. This current exists in a superposition of both the transient magnetic field from the coil, and the permanent magnetic field from the magnet. Each of these fields exerts a force on the moving electrons, which is transmitted to the metal of the sheet as a whole as shown in Fig. 17.4. By configuring the coil and magnet directions to generate a dominantly in-plane force in the sheet, the transmit EMAT can be optimised to produce a symmetric Lamb wave which, for a current pulse centre frequency of approx. 200 kHz, is effectively entirely zero-order for the thicknesses of sheet considered (0.25–4 mm). Detection of the Lamb wave by the receive EMATs happens by a similar process in which the motion of the sheet (due to the ultrasonic wave) in the presence of the magnetic field causes eddy currents in the sheet which in turn induce current in the coil of the EMAT. The fact that the EMATs couple electromagnetically with the sheet under test means that they can be held at a standoff (typically 0.5 mm) above the sheet surface and rotated on an arm, as shown in Fig. 17.5. This allows a comprehensive measure-

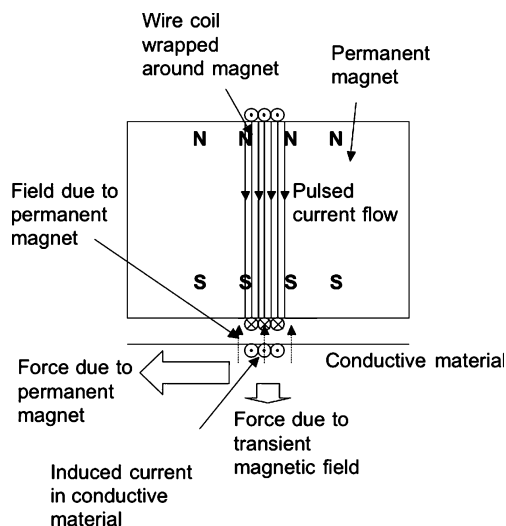


Fig. 17.4 Operation of a simple transmit EMAT.

ment of the variation of Lamb wave velocity (and thus effective elastic modulus in the sheet) at all angles in the plane of the sheet.

The average elastic modulus at a particular angle (from the rolling direction) was also estimated from the volume fraction of the texture components present ( $V_{nTex}$ ) and their elastic moduli ( $E_n$ )

$$E_{avg\_ \theta} = \frac{\sum V_{nTex} E_n}{\sum V_{nTex}} \quad (17.1)$$

The materials examined in this study were commercially pure aluminium supplied at varying thicknesses and temper conditions (annealed, half hard) and a 0.8 mm thick deep-drawing grade (DC04) steel in the cold rolled as-received (sample designated SG4) and heat-treated conditions (to provide varying texture components). The heat treatments were: 690°C for 4 hours and air-cooled (sample designated SG1 having a predominantly recrystallised texture), 950°C for 1 hour and air-cooled (sample designated SG2 having a transformation texture), and 1140°C for 30 minutes and air-cooled (sample designated SG3 having a stronger transformation texture and larger grain size). The samples were prepared for optical metallography by sectioning, mounting in bakelite, grinding, polishing and etching. The texture pole figures were measured by an X-ray texture goniometer and the orientation distribution functions were calculated using Labotex software by the Bunge series expansion method. The texture of the aluminium sheets was also determined using through thickness or surface (for comparison) samples using a JEOL 7000 SEM system fitted with an Oxford Instruments INCA Crystal EBSD system. Texture quantification was carried out using an angular spread of 15° around the ideal texture angular position since the crystallographic orientations of grains in practice are rarely perfectly aligned to the ideal position. Any ‘remainder’

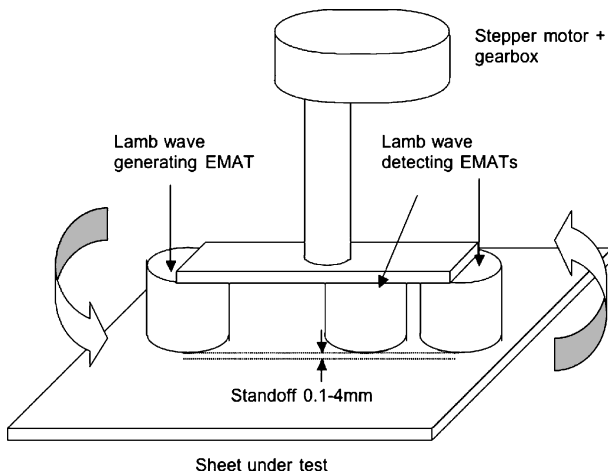


**Fig. 17.5** Rotating assembly for measuring Lamb wave velocity as a function of angle in the plane of a sheet.

texture reflects the random crystallographic alignment of other grains (i.e. not close to the defined angles for the main texture components). A  $15^\circ$  angular spread was selected since it was found that a  $5^\circ$  spread was not particularly sensitive to texture variations and the  $10^\circ$  and  $15^\circ$  results did not show any significant differences in the ratios of texture components present for the steel samples [14] and gave better matching to the mechanically measured modulus values for the aluminium samples. Using an angular spread larger than  $15^\circ$  would result in significant overlap between the texture peaks during quantification. Mechanically measured elastic modulus values were determined at the National Physical Laboratory (NPL) using tensile samples conforming to standard ASTM E8 [ASTM E8 2003] with strain gauges bonded to both sides of the specimen to take bending into account and ensure a reliable modulus value. With the exception of the aluminium 2 mm thick sheet (fully annealed condition), which had a very low proportional limit and yielded almost immediately upon loading, a series of repeat loading-unloading tests were carried out and an average value of modulus calculated for each material and orientation. In most cases the test was repeated on a second sample. With the NPL setup, typical uncertainties of  $\sim 0.5\%$  in the measured modulus could be expected for a homogeneous material, but the scatter was significantly larger than this, probably due to a combination of practical difficulties associated with the testing of thin sheet and variation within the materials themselves.

### 17.3 Results and Discussion

The predicted elastic modulus anisotropy (for quantified texture measurements), measured elastic modulus anisotropy and ultrasonic velocity anisotropy were compared for several aluminium sheet samples. Whilst the ultrasonic wave velocity can be predicted from the texture components (using the orientation distribution coefficient, ODC, values), or the elastic modulus predicted from the ultrasonic velocity using well established relationships, e.g. [13, 15], in this work only a comparison of wave shape is carried out because the EMAT sensor was not calibrated for absolute velocity, which varied because of lift-off and residual stress differences between the sheets being tested. There are also some uncertainties about the exact Lamé constants to use for aluminium samples [16]. Therefore values of elastic modulus were not calculated from the velocities, but the trends in data with respect to angle from the rolling direction should still hold and these were assessed in this work.

Initially elastic modulus values were predicted using the standard surface X-ray diffraction texture data, however it was found that some of the aluminium sheets analysed contained significant through thickness texture variations, which can form during hot rolling due to the shear-influenced deformation near surface changing to plane strain compression at the centre during the rolling process [17]. Subsequent cold rolling and annealing will not completely remove texture variations established during hot rolling. Additionally, cold rolling of aluminium alloys using different roll gap geometries has been shown to generate different texture gradients through thick-

ness [18, 19]. Through thickness texture quantification can be carried out using neutron diffraction or by using multiple X-ray or EBSD measurements on slices removed at varying thickness positions, or from through thickness samples. In this work through thickness EBSD scans were used to assess the through thickness texture. Results for a 3 mm thick aluminium sheet (supplied in the half-hard condition) are shown in Fig. 17.6, it can be seen that there are significant variations in the amount of Cube (recrystallisation) and S (rolling) type textures in particular through thickness,

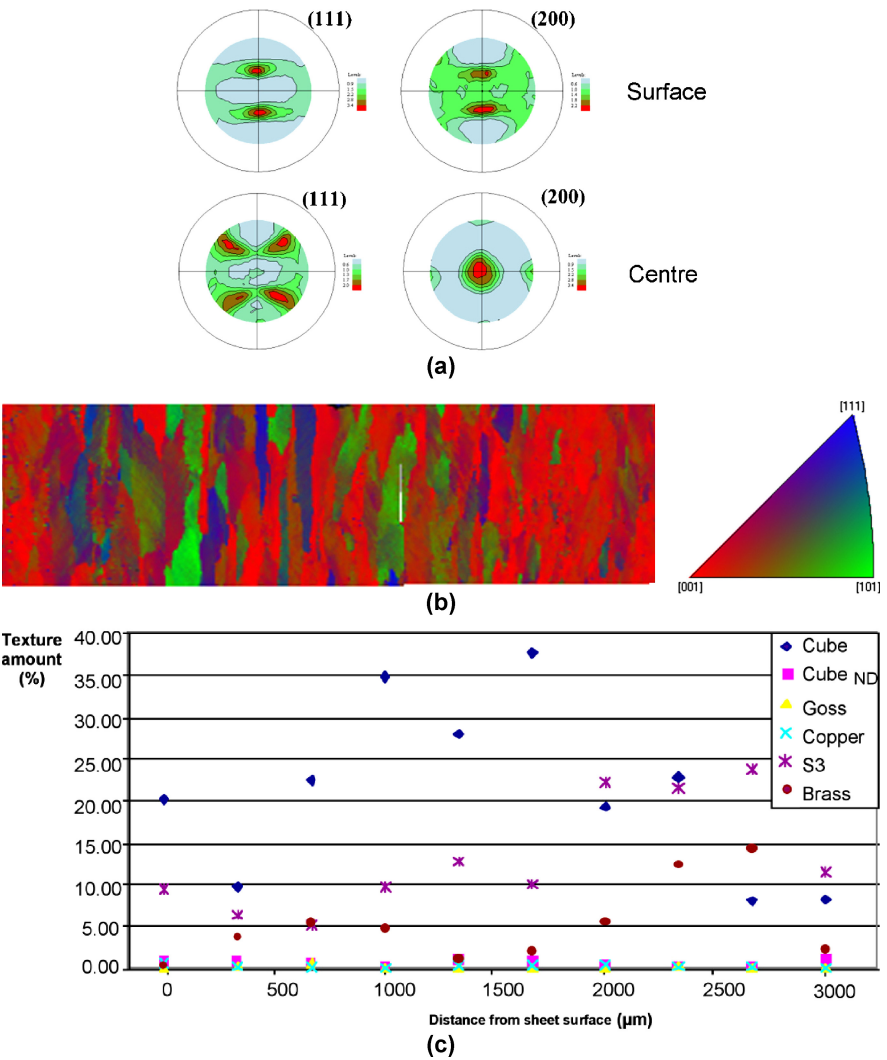


**Fig. 17.6** (a) (111) and (200) X-ray pole figures for the surface (3 mm position in (c)) and centre of the sheets (b) EBSD scan from surface (left hand side) to centre showing variation in texture components, and (c) quantified through thickness texture components from EBSD measurements for the 3 mm thick aluminium sheet.

which have very different elastic anisotropies, see Fig. 17.1. The average texture in the sheet was calculated and used for subsequent prediction of elastic modulus; this was found to give good agreement with the EMAT velocity anisotropy (the  $S_0$  wave travels through the bulk of the sample for thin sheets hence it is influenced by the average through thickness texture), Fig. 17.7. It can be seen from Fig. 17.7 that the surface EBSD prediction and Labotex X-ray surface prediction are very similar, as would be expected as they are both quantifying the surface texture levels, and show a profile strongly influenced by the S texture anisotropy (see Fig. 17.1), whereas the average through thickness profile shows a much stronger influence of the Cube texture anisotropy.

Further aluminium sheets were assessed using EBSD and EMATs and compared to mechanically measured elastic modulus values, determined from tensile tests. The results for a second 3 mm (called sheet 2, also in the half hard condition) and a 2 mm (annealed) sheet are given in Fig. 17.8. In each case the results are plotted as a deviation from average as comparison is being made between three values on different axes (the mechanically determined and EBSD predicted modulus values are not equivalent as the EBSD modulus value depends on the angular spread used [14, 20]). Figure 17.8 clearly shows that the trend in variation in modulus with angle can be predicted well compared to the measured values, however the amount of variation is less than the mechanical measurements suggest. This may be explained for the EBSD predicted values in that the amount of texture quantified depends on the angular spread taken. An increase in angular spread increases the amount of texture quantified, and will therefore increase the amount of predicted modulus variation, however if too large an angular spread is taken then overlap between neighbouring textures is

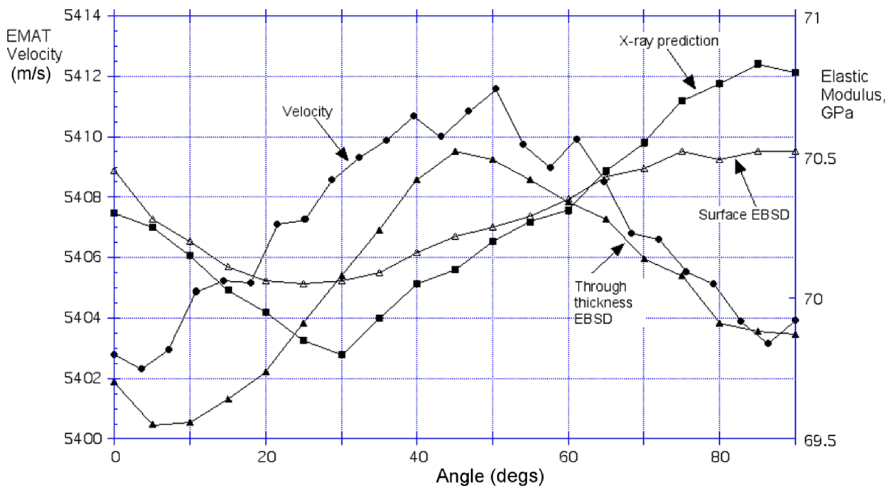


**Fig. 17.7** Plot for the 3 mm half hard aluminium sheet showing similarity between the predicted modulus values from surface X-ray and surface EBSD texture quantification but poor agreement with the EMAT velocity profile. Good agreement between the through thickness EBSD modulus prediction and EMAT velocity with angle to the rolling direction on the sheet can be seen.



seen with a corresponding loss in accuracy. Results for velocity and predicted modulus anisotropy variation for a 1 mm sheet (in the as-rolled condition) are given in Fig. 17.9, which shows that there is little through thickness texture variation resulting in excellent agreement between the surface and through thickness predicted elastic anisotropy, and good agreement to the velocity anisotropy. It can also be seen that the strong rolling texture present (high quantified values of S and brass texture components) results in a large elastic modulus variation (approx 4 GPa compared to approx 1 GPa for the 3 mm half hard sheet). The shape of the anisotropy curves between 0° and 90° to the rolling direction ('hill' rather than 'trough') also indicates that the recrystallisation process, i.e. the reduction in rolling (S and brass) textures and increase in recrystallisation (Cube) texture, can be readily followed for aluminium

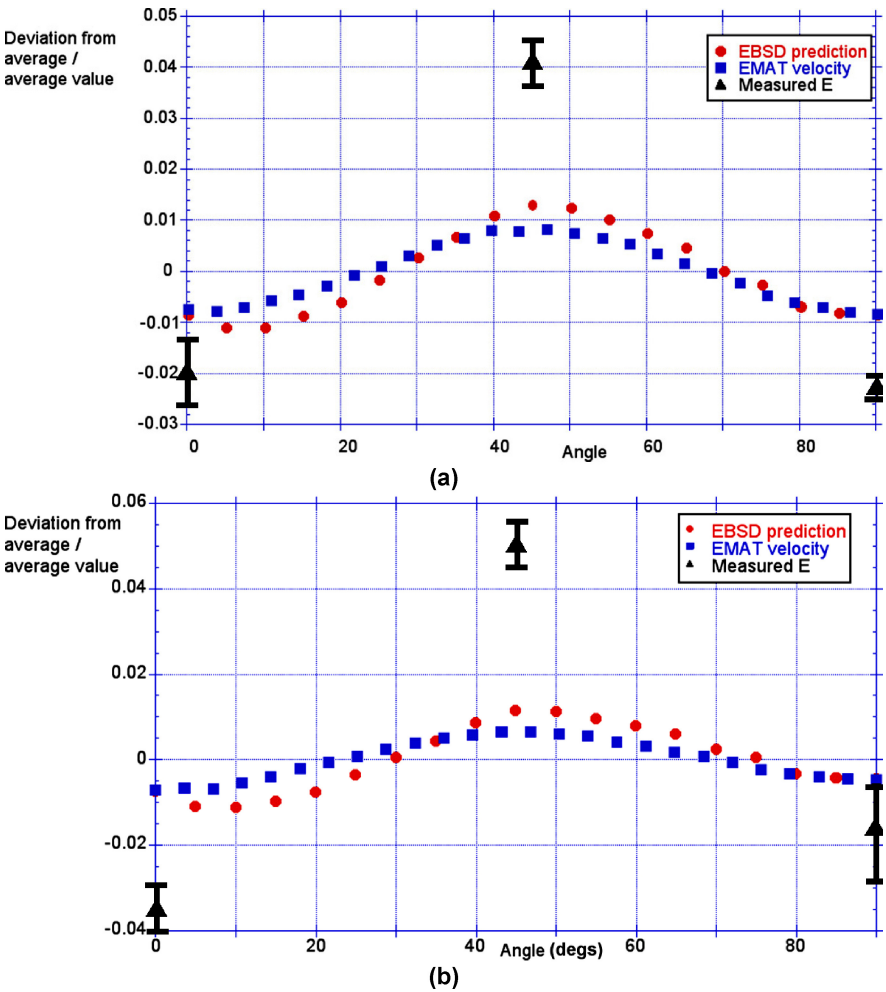


**Fig. 17.8** Comparison between EMAT velocity, EBSD predicted modulus and measured (from tensile samples) modulus values for (a) 3 mm (sheet 2) and (b) 2 mm aluminium sheets.

alloys because of the distinct curves produced. The differences in the elastic (and by inference the velocity anisotropy) curves for rolling and recrystallisation textures has also been observed in the literature, for example by Zeng et al. [21] and shown in Fig. 17.10. Thompson et al. has also observed a ‘trough’ shaped curve for the  $S_0$  ultrasonic wave using an as rolled nominally pure aluminium sheet [22].

Analysis of the steel sheets used in this study was more complex due to the larger number of texture components present and the close proximity of some of the ‘ideal’ texture angular positions, especially  $\{111\} \langle -1-1\ 2 \rangle$ ,  $\{554\} \langle -2-2\ 5 \rangle$  and  $\{332\} \langle -1-1\ 3 \rangle$  components, Fig. 17.3. Since steel sheets contain significantly more texture components than the eight given in Fig. 17.2, full analysis of the sheets was carried out, identifying 19 separate texture components. However, it was found that there was no significant difference in the predicted elastic modulus anisotropy when using the eight or nineteen texture components [14], despite the greater overlap in texture seen when using nineteen components. This is probably due to the fact that

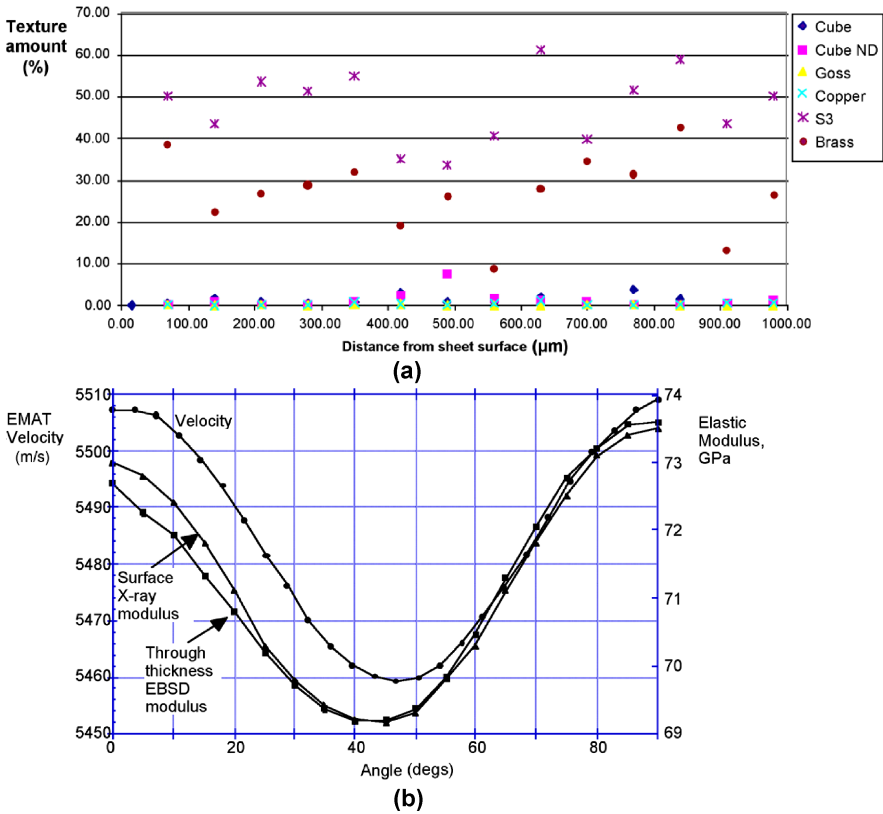


**Fig. 17.9** (a) Through thickness EBSD texture quantification and (b) plot for the 1 mm as-rolled sheet showing agreement between the predicted modulus values (based on surface X-ray texture quantification and through thickness EBSD texture quantification) and EMAT velocity profile with angle to the rolling direction on the sheet.

many of the additional texture components showed very similar anisotropy, as might be expected from the similarity in texture type, e.g. five additional  $\{hkl\} \langle 1\bar{1}0 \rangle$  textures were identified in the sheets, with four of them showing very similar anisotropy (the exception was  $\{hk0\} \langle 1\bar{1}0 \rangle$  where in-plane  $\langle 001 \rangle$  is sampled) [14]. Since full quantification to nineteen texture components did not produce different elastic anisotropies only the 8 major textures are considered in the analysis below.

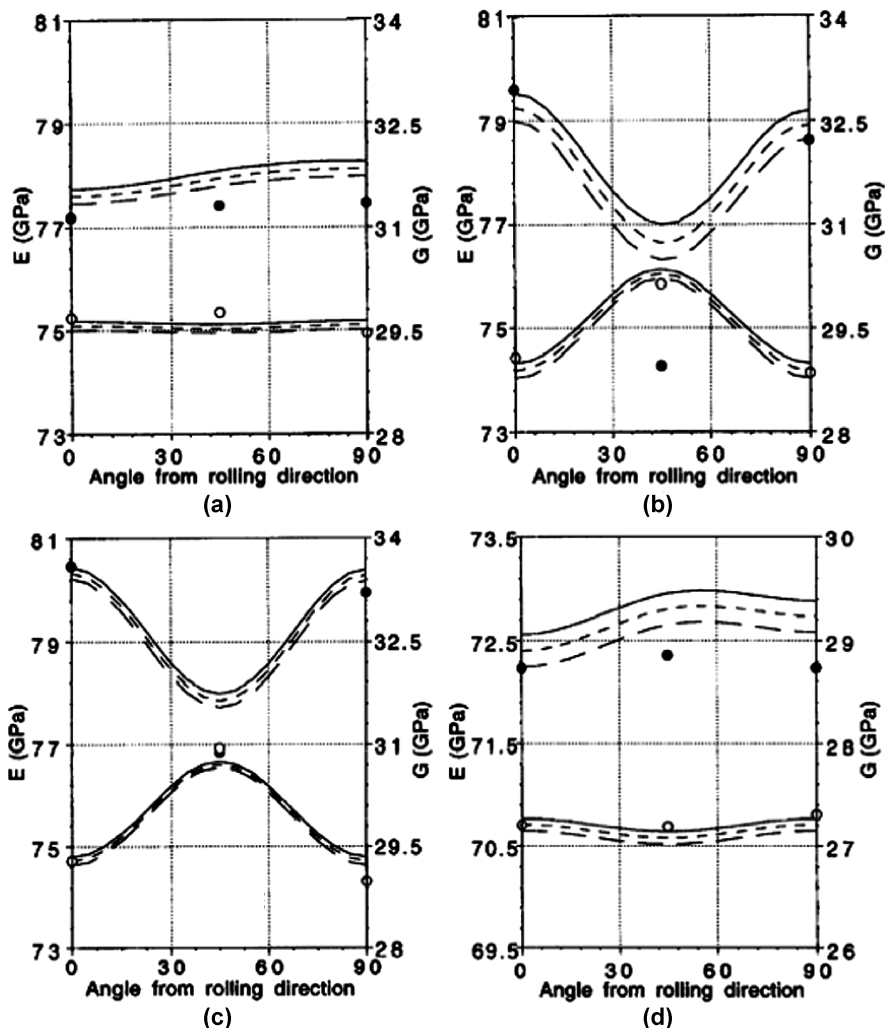
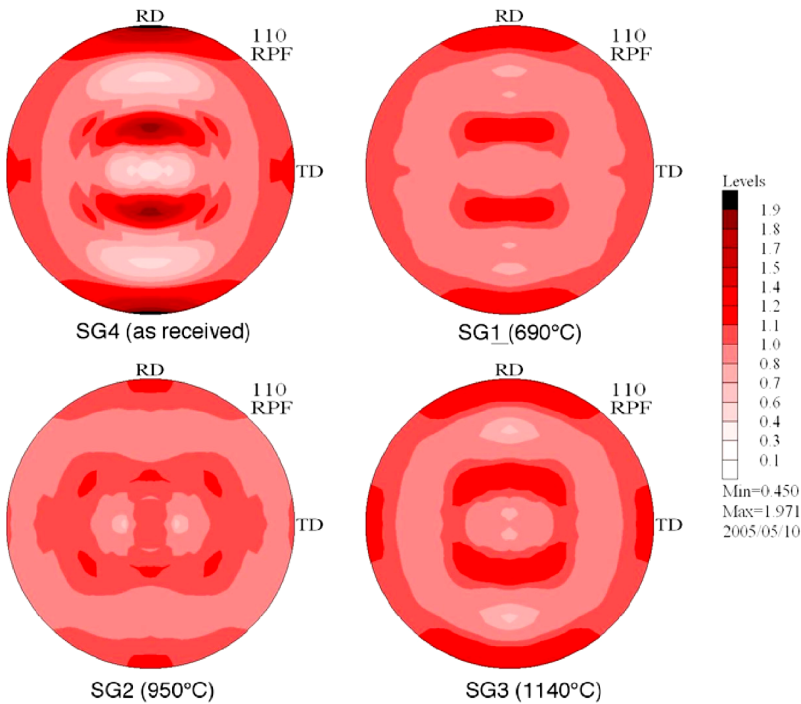


Fig. 17.10 Elastic and shear modulus predicted from bulk average texture data determined by neutron diffraction (using the Voigt, Reuss and Hill methods represented by ----; -- --; - - - - respectively) and measured values (solid circles for elastic and open circles for shear modulus, determined by a resonance technique) for (a) recrystallised 8090 sample A, (b) unrecrystallised 8090 C, (c) unrecrystallised 2090 sample E, d) recrystallised sample F. Graphs from Zeng et al. [21].

The different heat treatments, used to create a range of texture types (as-rolled, recrystallised, transformation), resulted in visually similar X-ray pole figures (except for sheet SG2), with all showing relatively weak texture (maximum texture level 1.9 seen for the as-rolled (SG4) sample compared to a maximum intensity of 2.6 for the 3 mm aluminium sheet and 4.2. for the 1 mm aluminium sheet discussed earlier), Fig. 17.11. The LaboTex X-ray quantification of texture components, given in Table 17.2, using a 15° angular spread about the ideal texture position, suggests that the majority of grains show a preferred orientation despite the weakly textured pole figures; this is due to the overlap of texture components. Comparing the different textures present (as a percentage of the total defined texture, i.e. excluding the ‘remainder’ texture), Table 17.3, indicates that the four steel sheets do not show that much difference in the texture components present, with the exception of the (001)[1–1 0] texture, which is significantly increased in the SG3 sheet. Therefore it is not surprising that the predicted elastic modulus anisotropies for the four sheets are very similar. The results for the predicted modulus anisotropy, the measured modulus and the velocity anisotropy are plotted in Fig. 17.12. It can be seen in Fig. 17.12 that the measured elastic modulus anisotropy is small (<4% i.e. <8 GPa) due to the comparatively weak texture of the samples (it should be noted that the anisotropy of single crystal iron is significantly greater than that of single crystal aluminium, where the measured elastic modulus anisotropy has been found to be less than 5% (<4 GPa)



**Fig. 17.11** (110) X-ray pole figures for the deep drawing (DC04) as received steel sheet and the three heat-treated conditions.

with a stronger texture (X-ray maximum texture strength of 4.2 compared to this steel of 1.9) observed in the samples. However, even allowing for the above comments, the trends in measured elastic modulus anisotropy are well represented by the EMAT velocity data, with correlation between the angles at which maxima and minima appear in both data sets. The variation in predicted modulus value based on X-ray data shows similar trends to the measured modulus values, except for sheet SG1, however the deviations are greater than seen with the EMAT data. This is partially due to the

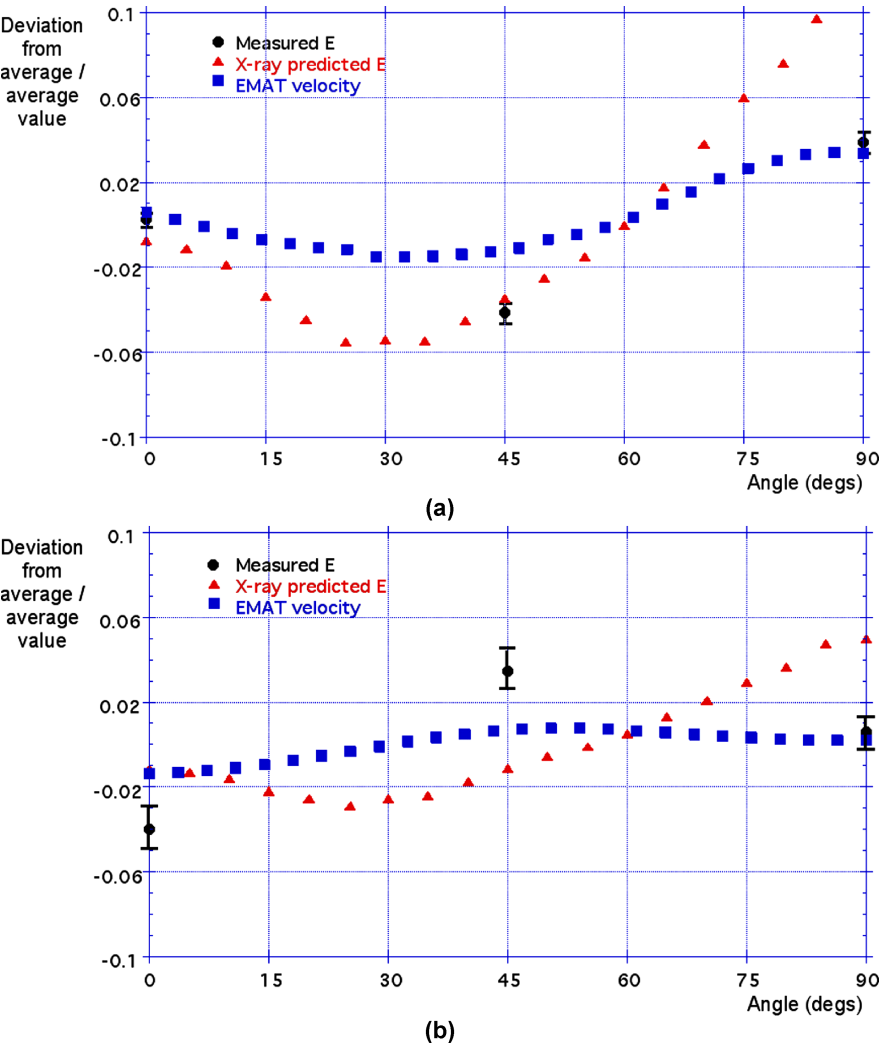


**Fig. 17.12 (a), (b)** Comparison between EMAT velocity, X-ray predicted modulus and measured (from tensile samples) modulus values for the deep drawing (DC04) as received steel sheet SG4 (a) and the three heat-treated conditions (b) SG1 (690°C), (c) SG2 (750°C) and (d) SG3 (1140°C).

angular spread being used to determine the predicted modulus resulting in significant overlap and hence large quantified texture percentages, but also the X-ray data were taken from much smaller samples than either of the other measurements (the EMAT technique determines the velocity between a send and receive EMAT spaced by 150 mm, comparable with the gauge length in the tensile test). The discrepancy observed for sheet SG1 cannot presently be explained. It is possible that there is some texture variation through thickness in sheet SG1, which could occur if full recrystallisation during the heat treatment was not achieved; this remains to be confirmed. It can

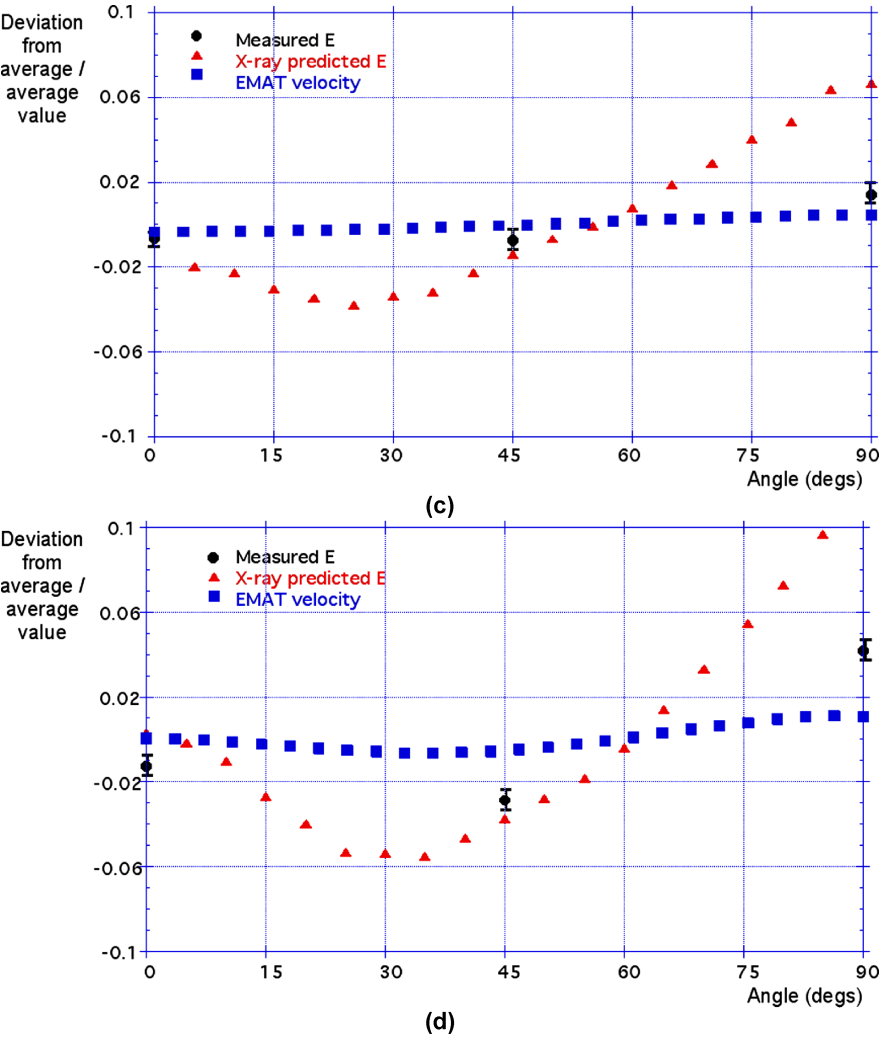


**Fig. 17.12** (c), (d) Comparison between EMAT velocity, X-ray predicted modulus and measured (from tensile samples) modulus values for the deep drawing (DC04) as received steel sheet SG4 (a) and the three heat-treated conditions (b) SG1 (690°C), (c) SG2 (750°C) and (d) SG3 (1140°C).

**Table 17.2** Quantified amounts (%) of the eight main texture components in the as received deep drawing (DC04) steel sheet and the three heat-treated samples.

Texture	Source of texture	SG4	SG1	SG2	SG3
(111)[1-2 1]	Cold rolling, annealing	11.2	7.0	8.9	9.6
(554)[-2-2 5]	Cold rolling, annealing	10.9	7.2	9.1	9.7
(332)[-1-1 3]	Transformation	10.5	7.2	8.9	9.5
(111)[1-1 0]	Cold rolling, annealing	11.0	6.9	9.3	8.9
(112)[1-1 0]	Cold rolling	11.7	5.7	8.4	9.1
(113)[1-1 0]	Transformation	12.0	4.9	7.3	10.0
(001)[1-1 0]	Transformation	9.5	5.2	4.6	15.3
(110)[001]	Transformation	3.6	2.2	3.1	4.1
Remainder		19.7	53.7	40.4	26.8

be noted that as the strength of texture increased (e.g. SG4 compared to SG1-3) the discrepancy was reduced.

The data presented for the DC04 as-rolled and heat treated sheets are similar to the results found by Artymowicz et al. for four cold rolled packaging steel samples [13]. X-ray ODF maps of the four sheet samples in Fig. 17.13 show that for the two differ-

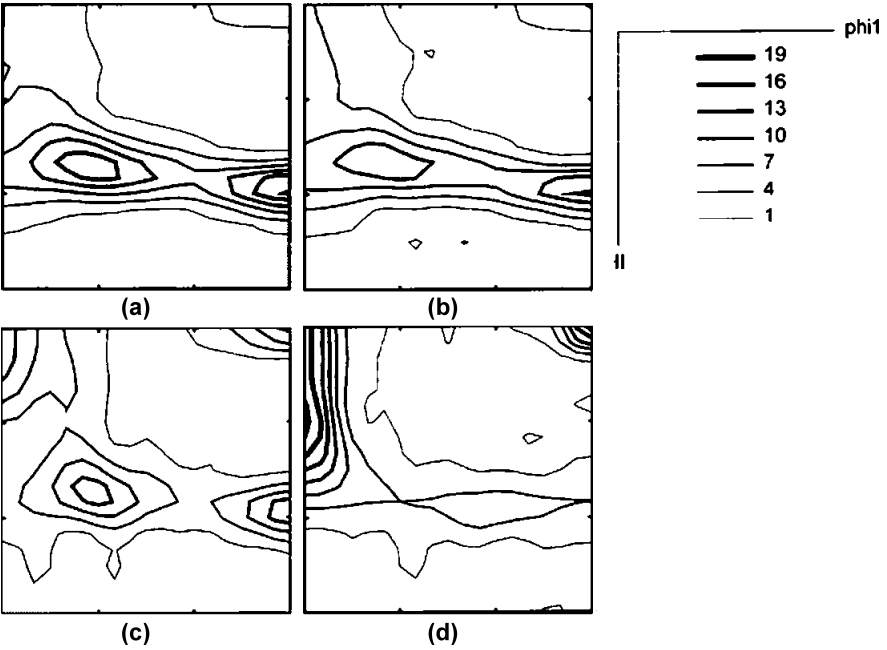


**Fig. 17.13** Sections through Euler space with  $\phi_2=45^\circ$  for sheet materials ( $\Pi\sim45^\circ$ ) (a) steel A fully recrystallised 0.14 mm thick sheet, (b) steel A 70% recrystallised 0.17 mm thick sheet, (c) steel B cold-rolled 0.22 mm thick sheet and (d) steel B fully recrystallised 0.24 mm thick sheet: calculations were performed with Voigt, Hill, and Reuss approximations. Graphs from Artymowicz et al. [13].

**Table 17.3** Texture component as a percentage of total defined texture (i.e. excluding ‘remainder’ texture) in the as received deep drawing (DC04) steel sheet and the three heat-treated samples.

Texture	SG4	SG1	SG2	SG3
(111)[1-2 1]	13.9	15.1	14.9	15.2
(554)[-2-2 5]	13.6	15.6	15.3	15.3
(332)[-1-1 3]	13.1	15.6	14.9	15.0
(111)[1-1 0]	13.7	14.9	15.6	14.1
(112)[1-1 0]	14.6	12.3	14.1	14.4
(113)[1-1 0]	14.9	10.6	12.2	15.8
(001)[1-1 0]	11.8	11.2	7.7	24.2
(110)[001]	4.5	4.8	5.2	6.5

ent steel compositions examined (A and B, no details given) the fully recrystallised, partially recrystallised and cold rolled textures are very similar. This is reflected in the predicted (using the X-ray texture quantification and Christoffel’s equation) and measured (using an EMAT sensor) ultrasonic velocity anisotropy as shown in Fig. 17.14 [13]. It can be seen that the shape of the predicted and measured velocity

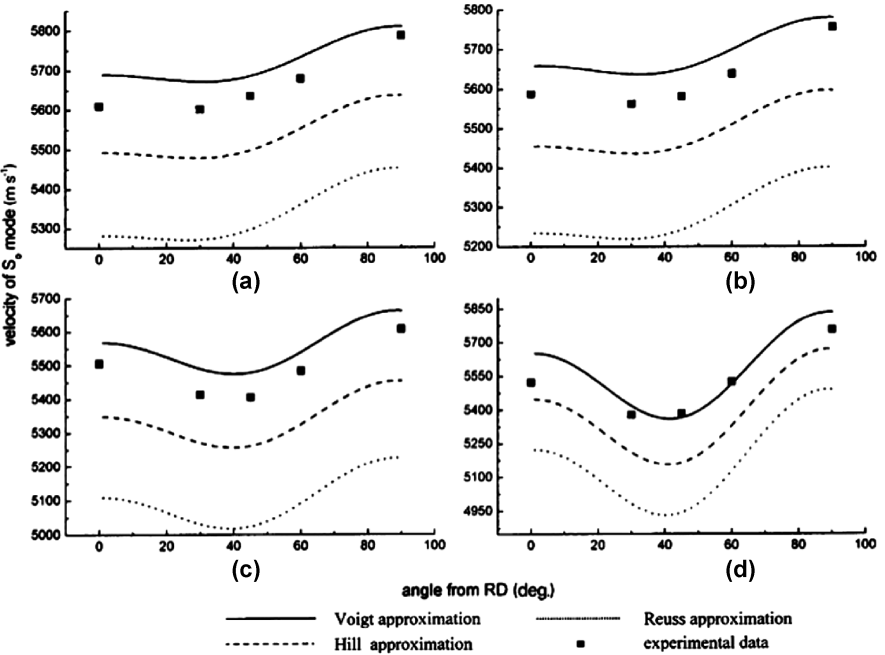


**Fig. 17.14** Calculated and experimental propagation velocities for  $S_0$  modes in specimens (a) steel A fully recrystallised 0.14 mm thick sheet, (b) steel A 70% recrystallised 0.17 mm thick sheet, (c) steel B cold-rolled 0.22 mm thick sheet and (d) steel B fully recrystallised 0.24 mm thick sheet: calculations were performed with Voigt, Hill, and Reuss approximations. Graphs from Artymowicz et al. [13].



anisotropy is extremely similar to the elastic modulus anisotropy predicted from the X-ray texture of the DC04 sheets, and the EMAT measurements (except sheet SG1). It is interesting to note that there is no obvious change in shape of the curves following partial or full recrystallisation for the two steel chemistries examined. Artymowicz et al. suggest that annealing of the thin sheet steels could be monitored using the change in absolute velocity at the  $90^\circ$  to the rolling direction position (compare Fig. 17.14 (c) and (d)). However, extreme care would be required in any industrial application since changes in steel chemistry could affect the results obtained, as would any changes in lift off during testing.

It is also worth noting that the ultrasonic velocities reflect the elastic modulus variation that exists in the material but, in theory, this elastic modulus variation can be generated by different texture component combinations in the material. For example in aluminium the Cube<sub>ND</sub> single crystal elastic modulus profile is very similar to the 'S' single crystal elastic modulus profile, see Fig. 17.1, although the former is a recrystallisation texture and the latter a rolling texture, and they have very different pole figures, Fig. 17.15. Other combinations of texture components in aluminium can give the same elastic modulus variation, although a difference in absolute value (which may not be detected if the sensor is not calibrated to absolute values, or experiences measurement error due to lift off variation). For example Fig. 17.16 shows how combined Cube and Cube<sub>ND</sub> (recrystallisation textures) can give similar elastic modulus variation as combined 'S' and Brass (rolling textures) in aluminium. A similar situation can occur in steel; Fig. 17.17 shows how combined  $\{110\} \langle 001 \rangle$  with  $\{112\} \langle 1-10 \rangle$  gives a similar profile to  $\{332\} \langle -1-13 \rangle$ , although these textures would have unique (200) pole figures, Fig. 17.15. Obviously the exact texture combinations described are unlikely and any industrially produced metal sheet will have a complex set of texture components, but this analysis does indicate that whilst EMAT (and other ultrasonic techniques) can show elastic modulus anisotropy, deconvolution of these signals to texture components is not possible unless the

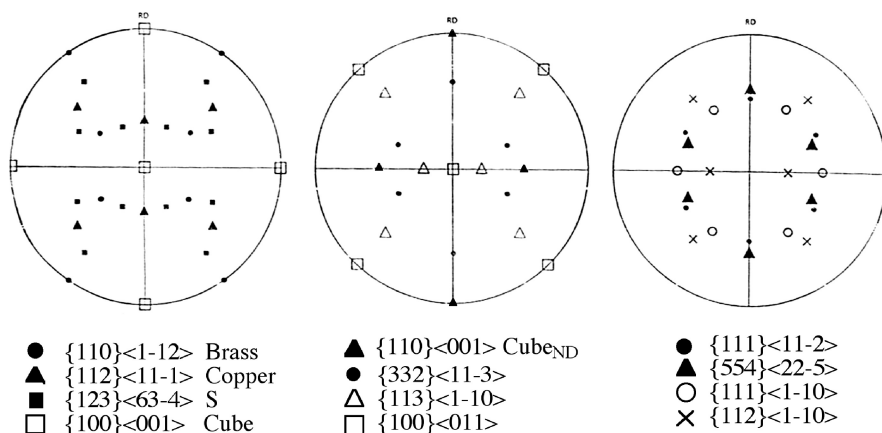


**Fig. 17.15** (200) pole figures for the single textures seen in cubic metals [ref. 23, with Cube<sub>ND</sub> added in this analysis].

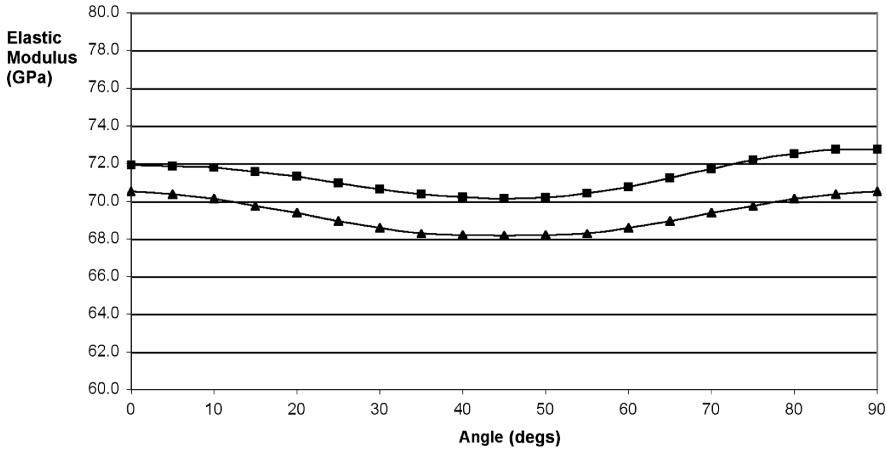


**Fig. 17.16** Combined aluminium textures Cube (12%)  $\{100\} \langle 001 \rangle$  and Cube<sub>ND</sub> (38%)  $\{100\} \langle 0-11 \rangle$  with remaining background to produce a similar profile to S (25%)  $\{123\} \langle 63-4 \rangle$  and Brass (25%)  $\{110\} \langle 1-12 \rangle$  with background.

approximate texture levels/types are already known. For example Hoddinott and Davies, working with iron and niobium cold rolled to 95%, related elastic modulus values, determined using the transverse resonant-vibration method, to varying fractions of texture components assuming that only a combination of four deformation textures ( $\{100\} \langle 011 \rangle$ ,  $\{112\} \langle 110 \rangle$ ,  $\{111\} \langle 110 \rangle$  and  $\{111\} \langle 112 \rangle$ ) were present [24]. This problem in determining texture components may also cause potential errors in extending any ultrasonic analysis to considering r-value determination.

In summary it can be seen that recrystallisation of rolled aluminium sheet, with the associated change in texture from predominantly S and Brass types, to pre-

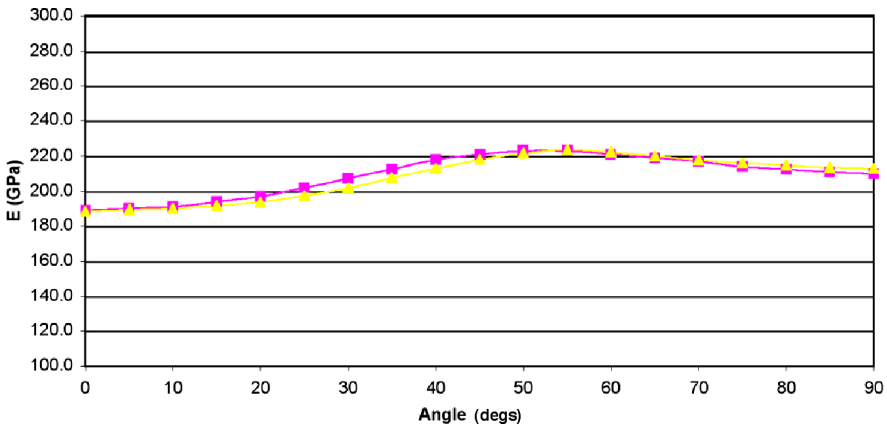


**Fig. 17.17** Combined steel textures  $\{110\} \langle 001 \rangle$  (25%) with  $\{112\} \langle 1-10 \rangle$  (5%) and background (70%) gives a similar profile as  $\{332\} \langle -1-13 \rangle$  (50%) with remaining background.

dominantly Cube, can be monitored using EMAT sensors due to the significant change in elastic modulus anisotropy, and hence velocity anisotropy, with angle to the rolling direction. Changes in texture due to recrystallisation and transformation in steel are more complex and do not necessarily result in significant differences in elastic modulus or ultrasonic velocity anisotropy curves.

## 17.4 Conclusions

X-ray diffraction, with associated texture quantification software (Labotex), and/or EBSD (INCA) quantification was used to determine the texture levels in nominally pure aluminium in the half hard or annealed conditions, and as-rolled and heat treated steel sheets. The quantified texture levels were used to predict the elastic modulus anisotropy with angle to the rolling direction. This predicted elastic modulus anisotropy was compared to measured elastic modulus values at 0°, 45° and 90° to the rolling direction and to the ultrasonic velocity anisotropy, measured using an EMAT sensor. The main conclusions of the work are as follows:

- For aluminium sheets containing through thickness texture variations surface X-ray diffraction determined texture, and hence elastic modulus anisotropy, did not agree well with through thickness EBSD elastic modulus anisotropy or EMAT velocity anisotropy. Through thickness EBSD texture determination gave good agreement with the EMAT results.
- The recrystallisation process can be easily followed using an EMAT sensor for aluminium sheets due to the distinct differences in the velocity anisotropy curve shapes for rolled and recrystallised textures.
- Velocity anisotropy showed reasonable good agreement with the variation in mechanically measured modulus values for the steel sheets. Agreement was less good with the predicted (from X-ray diffraction texture quantification) modulus anisotropy.
- Recrystallisation is more difficult to monitor in steel sheets, compared to aluminium sheets, due to the smaller differences in the velocity anisotropy curves.
- Similar elastic modulus anisotropy has been shown to be possible from different texture combinations. Whilst these different textures can be distinguished using X-ray diffraction or EBSD quantification they would not be identifiable from ultrasonic measurements.

**Acknowledgements** The authors would like to thank the UK Engineering and Physical Sciences Research Council and Corus plc. for their support of this research. The experimental work carried out by Dr Ahmad Sulaiman, Dr Prantik Mukhopadhyay, Dr Mark Potter, Tracey Holmes and Jim Morrison is gratefully acknowledged. Thanks are also given to Drs Steve Dixon, Martin Strangwood and Peter Morris for extremely useful discussions. The assistance of Dr Jerry Lord, at the National Physical Laboratory, in measuring the mechanically determined elastic modulus values is very gratefully acknowledged.

## References

1. R.W. Herzberg, *Deformation and Fracture Mechanics of Engineering Material*, 4th edition, John Wiley & Sons, New York, 1996.
2. H. J. Bunge, *Texture Analysis in Materials Science*, Butterworths, London, 1982, p. 321.
3. J. F. Nye, *Physical Properties of Crystals*, Oxford University Press, London 1957.
4. J. Lewandowski, *NDT&E International*, 1999, vol. 32, pp.383–396.
5. R. B. Thompson, S. S. Lee and J. F. Smith, *Ultrasonics*, 1987, vol. 25, p. 133.
6. A. Moreau, D. Leevesque, M. Lord, M. Dubois, J.-P. Monchalain, C. Padioleau, J.F. Bus-sieere, *Ultrasonics*, 2002, vol. 40, pp. 1047–1056.
7. R.B. Thompson, S.S. Lee, J.F. Smith, *J. Acoust. Soc. Am.*, 1986, vol. 80, pp. 921–931.
8. K. Kawashima, *J. Acoust. Soc. Am.*, 1990, vol. 87, pp. 681–690.
9. K. Kawashima, T. Hyoguchi, T. Akagi, *J. Nondestruct. Eval.* 1993, vol. 12, no. 1, pp. 71–77.
10. M. Hirao and H. Ogi, *Ultrasonics*, 1997, vol. 35, pp. 413–421.
11. S.R. Agnew, J.R. Weertman, *Mats. Sci. and Eng.*, 1998, vol. A242, pp. 174–180.
12. C. M. Sayers and G. G. Proudfoot, *Mech. Phys. Solids*, 1986, vol. 34, no. 6, pp. 579–592.
13. D. Artymowicz, B. Hutchinson, and M. Nogues, *Mats. Sci. and Tech.*, 2002, vol. 18, pp. 1142–1146.
14. C.L. Davis, P. Mukhopadhyay, M. Strangwood, M. Potter, S. Dixon and P.F. Morris, *Comparison between elastic modulus and ultrasonic velocity anisotropy with respect to rolling direction in steels*. Accepted by Ironmaking and Steelmaking
15. R. J. Dewhurst, C. Edwards, A. D. W. McKie, and S. B. Palmer, *Appl. Phys. Lett.*, 1987, vol. 51, pp. 1066–1068.
16. M.D.G. Potter, S. Dixon, J.P. Morrison, A.S. Sulaiman, *Ultrasonics*, 2006, vol. 44, pp. e813–e817.
17. M. P. Miller and T. J. Turner, *Int. J. of Plasticity*, 2001, vol. 17, pp. 783–805.
18. O.V. Mishin, B. Bay, G. Winther and D. Juul Jensen, *Acta Materialia*, 2004, vol. 52, pp. 5761–5770.
19. S. E. Schoenfeld and R. J. Asaro, *Int. J. of Mech. Sci.*, 1996, vol. 38, pp. 661–683.
20. C.L. Davis, M. Strangwood, M. Potter, S. Dixon and P.F. Morris, *Prediction of elastic modulus anisotropy using X-ray and EBSD texture quantification and ultrasonic (EMAT) measurements in aluminium sheets*. Accepted by Mat. Trans.
21. X.-H. Zeng and T. Ericsson, *Acta Mater.* Vol. 44, No. 5, 1996, pp. 1801–1812
22. R.B. Thompson, J.F. Smith, S.S. Lee and G.C. Johnson, *Met. Trans. A* 20, 1989, pp. 2431–2447.
23. R.K. Ray and J. Jonas, *Int. Mats. Review*, 1990, vol. 35, pp. 1–35.
24. D.S. Hoddinott and G.J. Davies, *J. Inst. Metals*, 1969, vol. 97, pp. 155–159.



Claire L. Davis  
Reader in Ferrous Metallurgy  
School of Engineering  
University of Birmingham  
UK



## Chapter 18

# Texture Transition in Steel ST37K, in situ Measurement at High Temperatures Using High-Energy X-rays

H.-G. Brokmeier, S.B. Yi, and J. Homeyer

**Abstract.** High energy X-rays are well known due to their high penetration power particular in materials testing devices. For diffraction experiments high energy X-rays with more than 50 keV can be obtained at storage rings or using a tungsten X-ray tube. According to the high penetration power, these beamlines offer a very high photon flux and an excellent brilliance. That means measurements can be carried out fast. As an example, the complete texture measurement at one position of a steel shaft with 34 mm in diameter has taken 45 minutes non-destructively. On the other hand the high photon flux allows to measure foils or thin wires down to 50–100  $\mu\text{m}$ . These new and fast options make it possible to measure in situ textures under tension, compression and at high temperatures. We have used 100 keV X-ray to measure the texture transition as well as the phase transition in a steel sample. The experiments were done at the high energy beamline BW5 (Hasylab at DESY/Hamburg). 100 keV X-rays have a wavelength of 0.1240 Å which means due to the Bragg's law very low scattering angles. Using a MAR345 image plate detector one obtains a set of complete Debye-Scherrer cones in a 2 $\theta$ -range of 7° in about 1 sec. At room temperature we found 100% ferrite. During heating up till the austenite region we were able to investigate the thermal expansion and the texture relation between ferrite and austenite, which follows in our case the Kurdjumov-Sachs model. Furthermore, the program pack-

---

H.-G. Brokmeier

Institute of Materials Science and Engineering TU Clausthal, Agricolastr. 6,  
D-38678 Clausthal-Zellerfeld, and  
GKSS Forschungszentrum, Max-Planck-Str. 1, D-21502 Geesthacht, Germany

S.B. Yi

Institute of Materials Science and Engineering TU Clausthal, Agricolastr. 6,  
D-38678 Clausthal-Zellerfeld

J. Homeyer

Hasylab at DESY, Notkestraße 85, 22607 Hamburg, Germany

age MAUD offers the possibility to follow the phase transition, so that the composition at all temperatures can be documented during heating. It has to be pointed out that the texture influence on the quantitative phase analysis can be included by MAUD, so that even for strong crystallographic textures the relation ferrite/austenite can be given very well.

## 18.1 Synchrotron Radiation

In materials science high energy X-rays are long-time restricted to material testing. Standard material testing devices operate from 120 keV to 450 keV due to their application field for non-destructive testing (NDT), such as failure analysis in pipelines, quality control in wheel rims and many other technical products. Typical diffraction experiments for phase, texture and strain analysis were carried out by conventional X-ray equipments using Cu-, Co or Cr-tubes with much lower X-ray energies. Firstly, the development of synchrotron storage rings opens the field of diffraction for high energy X-rays, which ranges from about 50 keV up to 450 keV [1, 2, 3].

One main advantage of high energy X-rays is the penetration power. Figure 18.1 shows the penetration length into some metals (Mg, Al, Ti and Fe) in the range up to 250 keV. The penetration length is given in cm for a loss of 50% of the primary beam intensity. The two marked lines present on one hand Cu K $\alpha$  X-rays with 9 keV as X-ray tube voltage (1.5418 Å) and on the other hand our mainly used synchrotron wavelength of 0.124 Å wavelength with 100 keV. In the case of 200 keV X-rays the penetration length is in the same order as for thermal neutrons, which are well known in materials science applications (texture and strain analyses) as high penetrating radiation. [4, 5].

In comparison with laboratory scale X-ray devices a storage ring has a much higher photon flux. But to get an optimized flux for the so called hard X-rays one

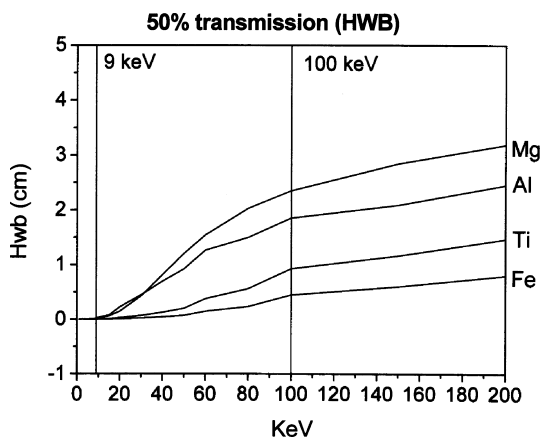


**Fig. 18.1** X-ray transmission of Fe, Ti, Al and Mg as function of the energy.

need special arrangements of the wiggler, which is realized recently at the new hard wiggler beamline HARWI-II of the GKSS Research Center Geesthacht GmbH at the Hasylab storage ring Doris, DESY-Hamburg (Germany). With BW5 and Harwi-II two high energy X-ray beamlines are available at Hasylab/DESY Hamburg.

According to the much higher flux of these synchrotron beamlines one gets a fantastic brilliance. High brilliance means an excellent parallel photon beam, so that only those grains are in reflections condition, which have the ideal orientation to the incoming beam. Even small misorientations of crystallites to the Bragg condition results in the fact that these crystallites cannot be seen, like single crystal orientation determination.

The combination of a high penetration power, a high photon flux and an excellent brilliance offers new options for diffraction experiments in materials science applications. Firstly, a high photon flux results in a good counting statistics and short counting times [3]. Short counting times are the bases of time resolved investigations (recrystallization or phase transitions) and for in situ studies [6, 7, 8]. Secondly, the excellent brilliance combined with the high photon flux allows local measurements in the  $\mu\text{m}$ -scale [8]. Thirdly, the high penetration power on one hand and the high photon flux on the other hand made it possible to measure rather small samples such as wires or foils [9] but also relatively large samples of some cm in diameter such as a steel shaft. In Fig. 18.2 special sample holders including

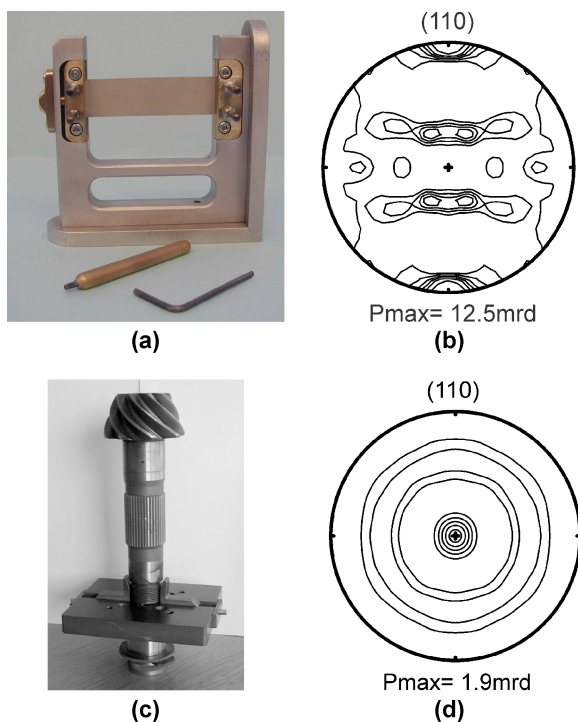


**Fig. 18.2** Two examples of for successful synchrotron texture analysis, (a) Fe-foil of  $10 \mu\text{m}$  thickness and (c) steel shaft of  $34 \text{ mm}$  thickness including two  $(110)$  pole figures (b) and (d).



a thin Fe-foil of 10  $\mu\text{m}$  (Fig. 18.2 (a)) and a comparably heavy steel sample of 34 mm thickness and 100 mm high (Fig. 18.2 (c)) are shown. Both samples were measured at the high energy beamline BW5 and evaluated by the iterative series expansion method for quantitative texture analysis. In both cases a beam cross section of  $1 \times 1 \text{ mm}^2$  was used. The recalculated (110) pole figures are presented in Fig. 18.2 (b) (Fe-foil) and in Fig. 18.2 (d) (steel shaft).

### 18.1.1 Hard X-ray Instrumentation

The beam path of a high energy synchrotron diffractometer is close to a conventional pin whole device, which is long-time used by film techniques [10]. A system of magnets called bending magnet, undulator or wiggler generates a synchrotron beam over a wide range of energies between 1 keV up to 400 keV. Firstly a filter and secondly a monochromator are used to produce a high intense monochromatic beam. Figure 18.3 (a) shows the beam path at BW5 including the monochromator tank (yellow) and the sample stage with an Eulerian cradle. The heavy sample stage is able to carry different equipments such as furnaces, loading cells and so on. Following the pin-whole camera technique the monochromatic beam is guided by different diaphragms (D), which can be driven automatically to get a very precise beam cross section. The pin-whole technique in conventional X-ray diffractometry allows the transmission as well as the reflection method. According to the high penetration power of high-energy X-rays, the transmission method is preferred, as shown in Fig. 18.3 (b).

Due to the high energy of about 100 keV the wavelength with 0.124 Å is short and consequently one can get a set of complete Debye-Scherrer cones on an area detector. In Fig. 18.4 (a) one can see the image plate picture of Fe-powder obtained in 5 sec. using a MAR345 image plate detector. All Debye-Scherrer rings show random orientate grains with nearly identical intensities around the rings.

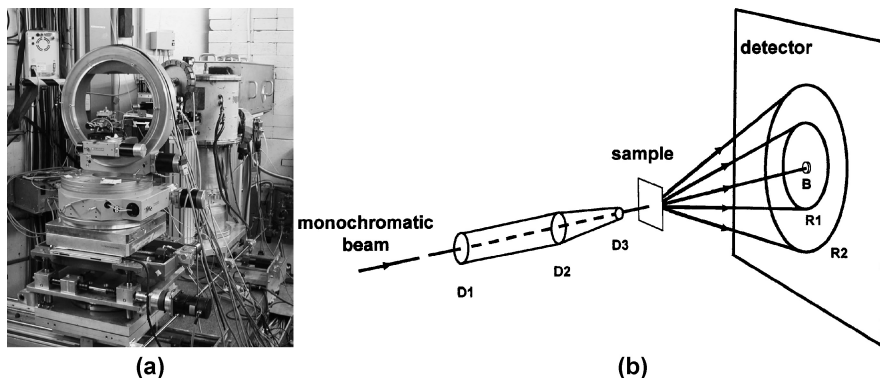


**Fig. 18.3** Beam path of a synchrotron diffractometer (a) BW5-instrument; (b) pin whole technique (D – diaphragms, R – Bragg-reflections on the detector, B – beam stop).

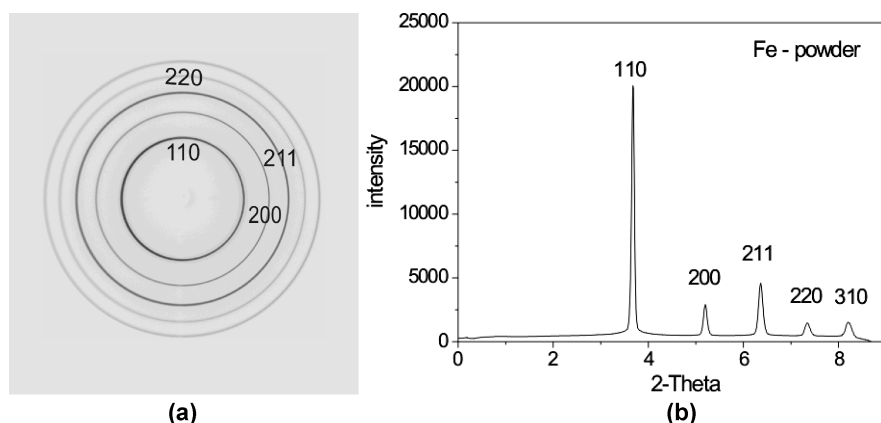


**Fig. 18.4** Diffraction pattern of Fe-powder; (a) complete Debye-Scherrer rings on an area detector, (b) sum pattern after integration over the complete Debye-Scherrer rings.

The sum-diffraction pattern calculated by integration along the rings is given in Fig. 18.4 (b) with (110) as dominating reflection.

### 18.1.2 Texture Measurements by High Energy Synchrotron Radiation

The working horse for texture measurements is still based on laboratory X-rays, which is described in many papers [11]. The principles of the pole figure measurement using synchrotron radiation is very close to that of conventional X-rays with an X-ray tube. That means, the texture analysis using high energy X-rays with a two-dimensional position sensitive detector is firstly a step back to the early methods well known as film techniques [12, 13, 14] and secondly a big step forward to combine a brilliant radiation source with modern detectors such as CCD-cameras and image-plate detectors. Experiments recently carried out at Harwi-II (Hasylab@Desy) using a new MAR555 detector, take only 5–10 min for a complete texture measurement.

Two main differences exist between X-ray energies of 100 keV ( $\lambda = 0.124 \text{ \AA}$ ) and of 9 keV ( $\lambda = 1.5418 \text{ \AA}$ ). In both cases a set of complete Debye-Scherrer rings can be detected simultaneously by an area detector, depending on the sample to detector distance (see Fig. 18.4 (a)). The stereographic projection of one Debye-Scherrer cone in the case of perpendicular transmission is shown in Fig. 18.5 (a). The circle in the stereographic projection is connected with the reflection angle  $2\theta$  and the radius of the projected circle in the 'pole figure' is  $90^\circ - \theta$ .

On one hand one can conclude that for very low  $\theta$ -values only an  $\omega$ -rotation is necessary (Fig. 18.5 (b) and Fig. 18.5 (c)) but that on the other hand a blind area for higher  $\theta$ -values exists (13). Moreover, due to the high penetration power of

synchrotron radiation one obtains complete pole figures in the case of round samples. The second advantage of 100 keV synchrotron radiation is also related to the low scattering angle because a low scattering angle needs only a comparable small opening angle of shielding and so on. In comparison with only one rotation axis this allows the construction of special loading cells and furnaces which are not available for conventional X-rays.

The high brilliance of high energy synchrotron radiation yields to a very special pole figure window [15]. Due to the quantitative texture itself  $\Delta\omega$  has to be cho-

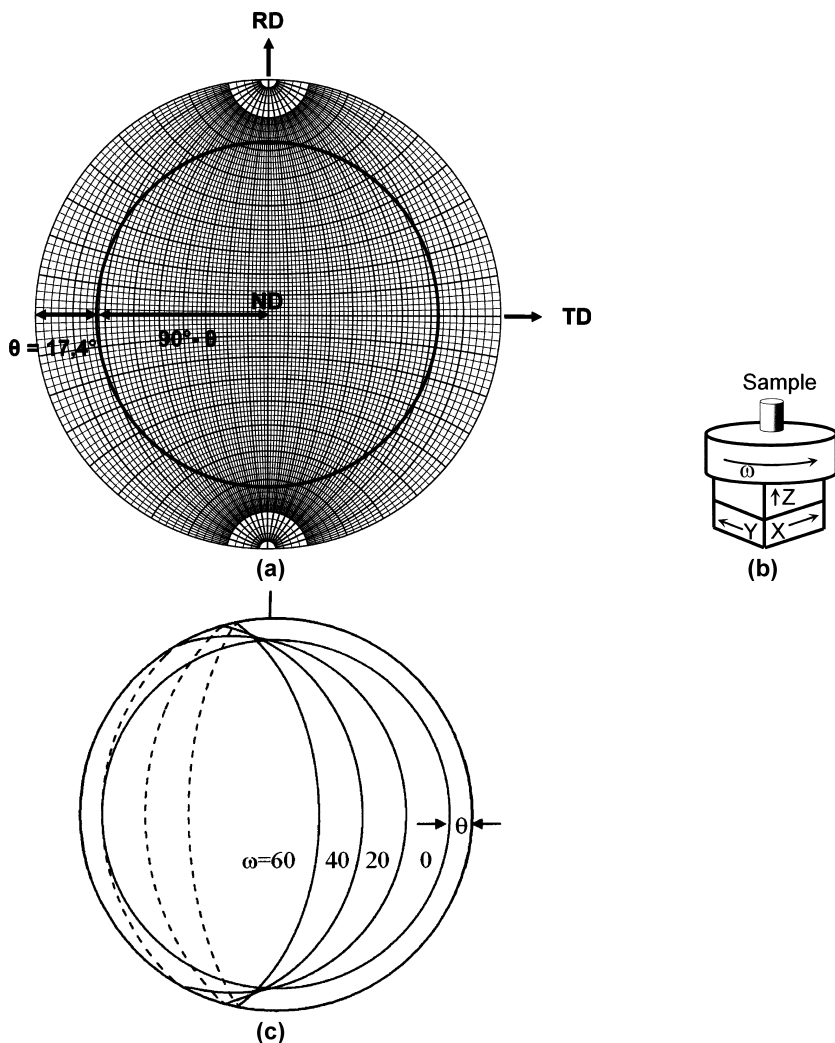


**Fig. 18.5** (a) Pole figure with the projection of one Debye-Scherrer ring with  $\theta = 17.4^\circ$  (b) sample table with only one  $\omega$ -rotation table (c) projection of the Debye-Scherrer ring for different  $\omega$ -rotations.

sen, so that the texture sharpness has to be reproduced correctly. The nearly parallel synchrotron beam allows the investigation of very sharp textures if  $\omega$  is scanned in small steps ( $\Delta\omega = 1^\circ$  or less). Another point of interest is that for low symmetric textures  $\omega$  must be scanned from  $-90^\circ$  till  $+90^\circ$ . A typical beam size is between  $1\text{ mm} \times 1\text{ mm}$  and  $1\text{ mm} \times 4\text{ mm}$ , which is comparably small to neutron diffraction the favoured method for global texture measurements. In the case of round samples, see Fig. 18.2 (c), one need in single phase materials no materials dependent corrections. For other sample shapes (rectangular sheets, semi finished products) corrections for absorption and constant volume has to be carried out.

As already pointed out synchrotron radiation is much more intense than conventional X-rays and therefore the total counting can be much lower. Thus time resolved in situ texture measurements are possible, such as in situ investigations of texture evolutions under tensile load [16], compressive load [17] or high temperatures [18].

## 18.2 High Temperature Measurements by High-Energy Synchrotron Radiation

Due to the high photon intensity of synchrotron radiation fast in situ measurements can be carried restricted mainly by the read-out time of the detector and the heating rate of the furnace. Moreover, the high penetration power allows the transmission of furnace wall and heating shield without any problems.

### 18.2.1 Sample Description and Experimental Conditions

The investigated test sample was a steel ST37 K with a chemical composition of 0.10C, 0.01Si, 0.72Mn, 0.027P, 0.027S balanced Fe. For the synchrotron measurement a stick of  $5 \times 5\text{ mm}^2$  with a high of 10mm was prepared. In addition neutron diffraction was performed to control the results of room temperature measurements. Therefore, a sample cube of  $10 \times 10 \times 10\text{ mm}^3$  was prepared. A dome furnace (Fig. 18.6 ), constructed by Hasylab, was positioned on the omega table, see Fig. 18.5 (b).

The couple of the dome furnace was  $\text{SiO}_2$ -glas, so that for all sample rotations in omega and a wide range of sample tilt identical conditions exist. Heating was realized by a graphite foil heating system (Fig. 18.6 (b)). Graphite as a light element has very high transmission for high-energy X-rays so that the graphite was not seen by the synchrotron radiation. The whole area under the graphite foil has nearly identical temperature. In the centre of the graphite foil the sample sheet was positioned. To control the temperature a thermocouple was fixed at the lower part of the sample, which is not in the beam. In Fig. 18.6 (c) one can see the furnace as central part of the instrumentation with the MAR345 area detector in the back.

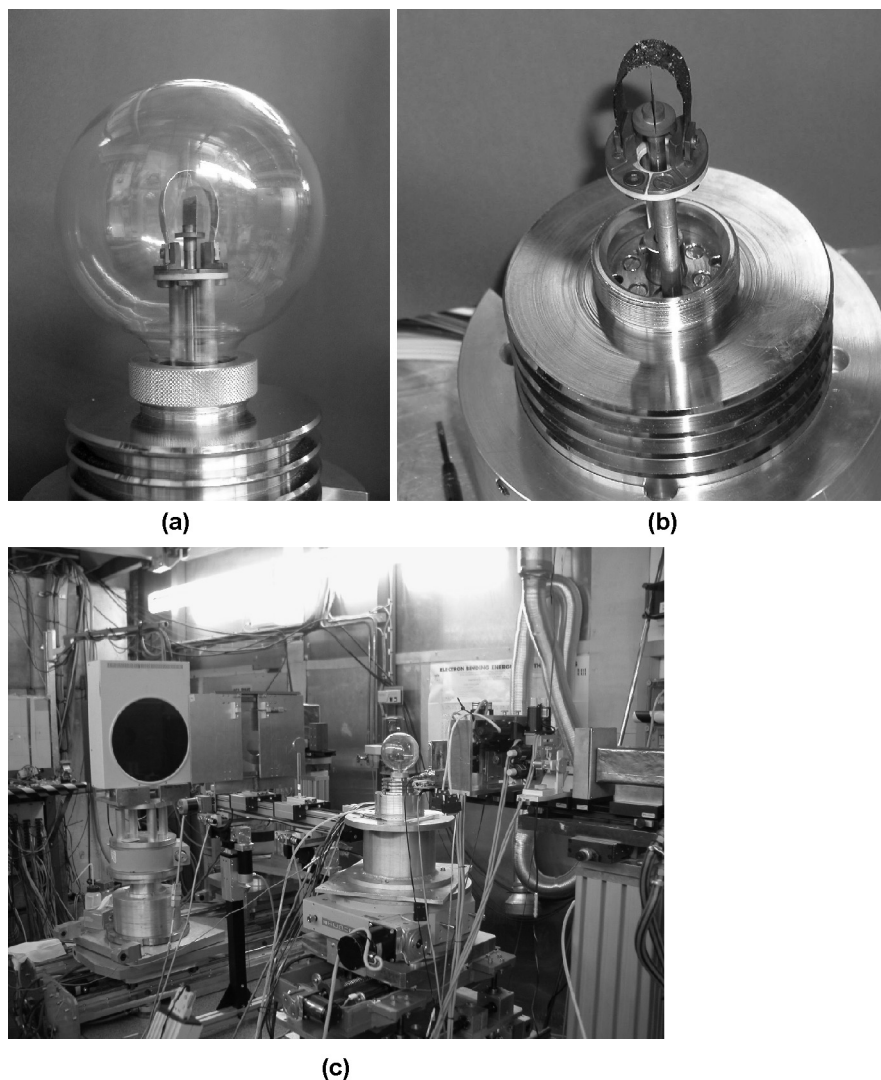
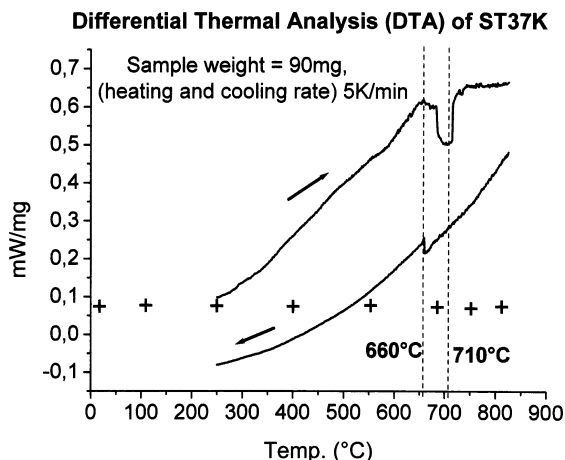


**Fig. 18.6** Dome furnace mounted at the high energy beamline BW5, Hasylab at Desy, Hamburg.

The measurements were carried out with a primary slit system of  $1 \times 1 \text{ mm}^2$  and a wavelength of  $0.124 \text{ \AA}$  ( $100 \text{ keV}$ ).

The list of experiments include a texture measurement at room temperature, a measurement in the two phased region, texture measurements after cooling and phase analysis at different temperatures during heating and cooling. To verify the temperature a DTA analysis was included seeing the phase transition. The crosses show the measurement points of the in situ heating experiment with five points below the phase transition (bcc-phase), one point in the two phased region and two points in the fcc-phase region.

**Fig. 18.7** DTA of ST37K including the measurement points of the in situ heating experiment.



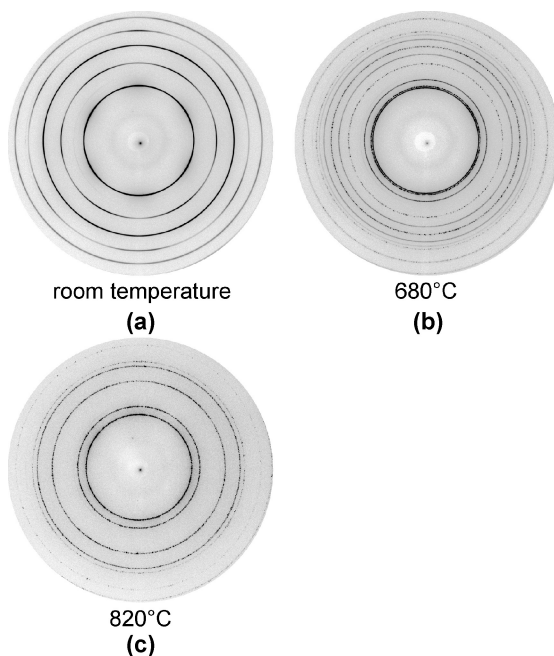
The phase analysis was carried out with single shots for each point with exposure times of 15 and 7 sec. Due to the readout time of about 90 sec., some additional measurements in the two-phased region with constant temperature and the cooling cycle, where we also take data, the whole experiment takes about 50 min. For quantitative texture analysis a set of individual measurements with  $\Delta\omega$  of  $5^\circ$  from  $\omega = -90^\circ$  till  $\omega = +90^\circ$  were done, which take much more time than the phase analysis. Therefore, the texture analysis was carried out at room temperature before and after heating and in the fcc-region.

### 18.2.2 In situ High-Temperature Phase Analysis of ST37K

In Fig. 18.8 one can see three typical image plate pictures for the different regions. Firstly, at room temperature the set of Debye-Scherrer rings (see Fig. 18.8 (a)) shows identical configuration as already explained for the powder spectra in Fig. 18.4 (a), i.e. ferritic bcc. The main difference between the powder measurement and the solid material is that the intensity distribution along the Debye-Scherrer ring varies. This is an indication of preferred orientation in the sample. Secondly, in Fig. 18.8 (c) the measurement at  $820^\circ\text{C}$  is shown. All Debye-Scherrer rings are spotty, which results from an insufficient grain statistics. That means, at  $820^\circ\text{C}$  the material is much coarser. It can also be seen that the positions of the Debye-Scherrer rings have changed. The diffraction pattern in Fig. 18.8 (c) represents now the finger print of the austenite phase with the hkl sequence (111), (200), (220), (311), (222).

In Fig. 18.8 (b) an overlap of both diffraction pattern were obtained. On one hand bcc ferrite is observed which has spotty Debye-Scherrer rings. That means less ferrite grains in the scattered volume. This can be explained by two reactions, one is the decreasing volume fraction by partly phase transition to the fcc-phase and second is a grain growth. A soft grain growth was observed during heating

**Fig. 18.8** Diffraction pattern of ST37 K at room temperature, at 680°C and at 820°C.



from room temperature to 550°C. On the other hand one can see more or less good developed Debye-Scherrer rings of fcc austenite with sufficient grain statistics. Further heating to 750°C and 820°C result in grain growth of austenite grains that the Debye-Scherrer rings became spotty. It has to be noticed that the data analysis of two-phase steel is always influenced by the narrow Bragg-reflections of bcc (110) and fcc (111) as shown in Fig. 18.9. This picture is a zoom of a part of the complete Debye-Scherrer ring of Fig. 18.8 (b). In the case of the individual grains on the Debye-Scherrer ring the error bar of the lattice constant determination is much to high.

The data evaluation for lattice constants, thermal expansion coefficient and volume fraction in the two-phased region was carried out by MAUD [19] a free software package for Rietveld analysis [20] and quantitative texture determination. In a first step detector corrections for precise center of the image plate picture and a misalignment by little tilt and rotation must be done. Due to the sample to detector distance of 100 cm small errors in the detector position can influence the lattice constants determination in the Å-range. Next step is the calculate sum-diffraction

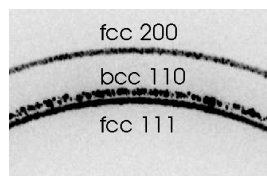
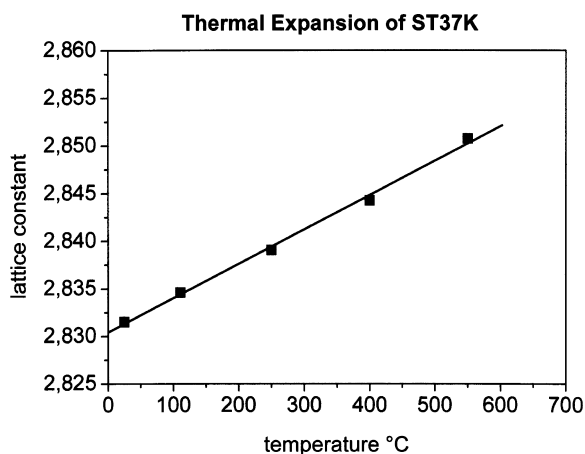


**Fig. 18.9** Partly diffraction pattern of ST37 K at 680°C with narrow reflections of bcc (110) and fcc (111).

**Fig. 18.10** Lattice constant of ferrite between room temperature and 550°C.



pattern to integrate over the whole Debye-Scherrer cone. A better grain statistics results and the influence of preferred orientation is minimized. A Rietveld refinement carried out with MAUD results in the lattice constants and the linear thermal expansion coefficient. The linear thermal expansion coefficient  $\alpha$  was calculated by the following equation to  $0.9 \times 10^{-6} \text{ K}^{-1}$ .

$$\alpha = l(T) - l_0 / l_0 - T = \varepsilon_{\text{therm}} / T$$

Lattice parameters for ferrite vary from 2.83135 Å at RT to 2.85076 Å at 550°C, see Fig. 18.10.

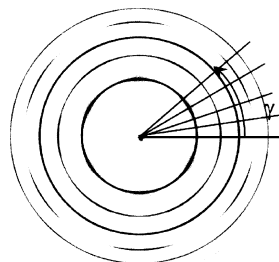
The composition of the sample at 680°C was investigated for phase analysis. A first shot was made directly after reaching the temperature of 680°C and a second measurement was carried out 5 min later. It results a ratio of 64.2% : 35.8% of ferrite : austenite for the first measurement, while after 5 min the austenite concentration increases to a ratio of 57.5% : 42.5% (ferrite : austenite).

### 18.2.3 In situ High-Temperature Texture Analysis of ST37K

As already pointed out, texture analysis is much more time consuming than phase analysis. Nevertheless synchrotron measurements are comparably fast due to the reduced number of single measurement, see Fig. 18.5. In the case of triclinic sample symmetry one needs a scan with 37 measurements having a resolution in  $\omega$  of 5°. Two methods can be used to extract the pole figure data from the area detector data. In both cases one has to define a set of sections as shown in Fig. 18.11.  $\gamma$  is the angle along the Debye-Scherrer ring and with  $\Delta\gamma$  the resolution in  $\gamma$  and the size of the section is defined. For our investigation we worked with  $\Delta\gamma = 5^\circ$  and  $\Delta\gamma = 1^\circ$ . Sectioning can be done for each Debye-Scherrer ring (pole figure) separately as realized by program systems of Sangbong Yi [21] or Ulf Garbe [22]. Each section is given by  $2\theta$ ,  $\omega$  and  $\gamma$  and the averaged reflection intensity of the



**Fig. 18.11** Sectioning of an area detector measurement for quantitative texture analysis ( $\Delta\gamma = 5^\circ$ ).



reflection  $hkl$ . A second possibility is to extract complete diffraction patterns for each section and to use a Rietveld refinement program like MAUD to obtain simultaneously all pole figures, which are included in the area detector data. The main difference is that Rietveld refinement needs the crystallographic data of the investigated material, while other programs work only with indexing the pole figures ( $hkl$ ). In both cases a transformation has to be carried out to calculate the pole figure angles ( $\alpha$ ,  $\beta$ ) from the reflection angle  $2\theta$ , the sample rotation angle  $\omega$  and the section angle  $\gamma$ . A detailed description of the transformation was given by Bunge and Klein [23].

Three texture measurements were carried out, at room temperature, at  $820^\circ\text{C}$  and at room temperature after cooling. A scanning routine with a set of 37 image plate pictures took between 60 min.

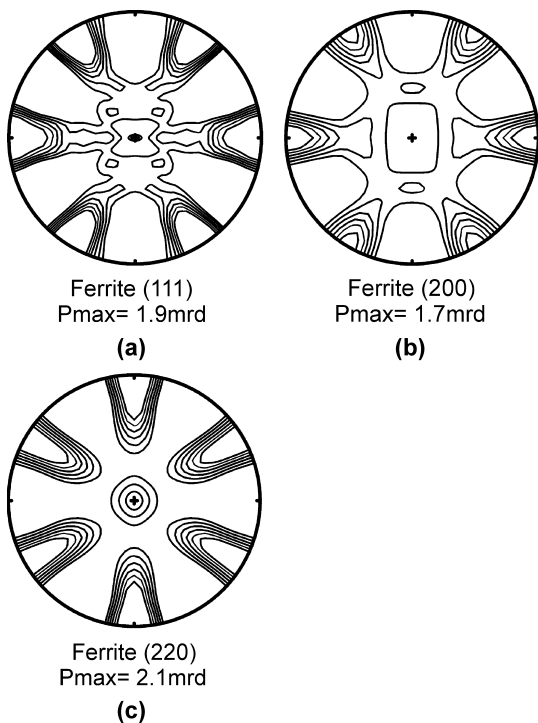
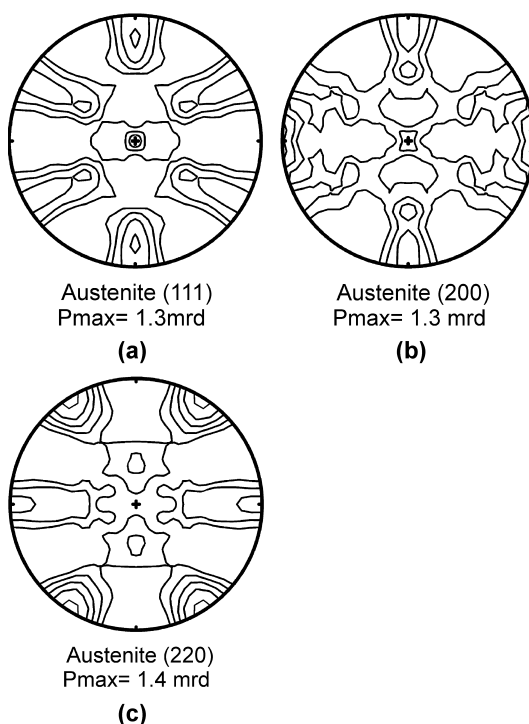


**Fig. 18.12** Ferrite pole figures measured at room temperature (counter levels 1.0, 1.1, 1.2, 1.3 ...).

**Fig. 18.13** Austenite pole figures measured at 820°C (counter levels 1.0, 1.1, 1.2, 1.3 ...).



The data transformation gave an equal angular set of values in  $\alpha$  and  $\beta$ , such as a  $5 \times 5$  matrix or a  $5 \times 1$  matrix. Thereafter, the orientation distribution was calculated using the iterative series expansion method with a  $l_{\max} = 22$  as degree of series expansion. In Fig. 18.12 recalculated pole figure of ferrite measured at room temperature were shown. Mrd stands for multiple random. In the present case a weak texture was determined.

### 18.3 Conclusion

High-energy synchrotron radiation has many advantages over other techniques such as conventional X-rays ( $\text{CuK}\alpha$ ) or neutron diffraction. For crystallographic texture analyses a broad spectrum of applications is available to measure small samples and local textures on one side and comparably large semi-finished products on the other side. One point of interest is the combination of a high photon flux, an excellent brilliance and a low wavelength which is favoured for in situ experiments. Using an ST37K sample in situ phase development, thermal expansion coefficient and texture transition has been demonstrated. The thermal expansion coefficient was calculated to  $\alpha = 0.9 \times 10^{-6} \text{ K}^{-1}$ . Integration over complete Debye-Scherrer ring allows the determination of volume fractions ferrite/austenite ratio in

about 60 sec. counting time with minimized texture influence. With a MAR345 and a dome furnace one needs about 60 min. to obtain quantitative texture data. First test with a new detector system and less readout time have shown that 5 to 10 min is realistic for a complete texture measurement. In future, a more detailed in situ texture analysis is possible than demonstrated in this paper. For the present example we detect an  $\alpha \rightleftharpoons \gamma$  transformation following the Kurdjumov-Sachs model.

**Acknowledgements** This work has been funded by the German Ministry of Education and Research (BMBF) under the contract number 05KS1MCA/2.

## References

- [1] O.V. Mishin, E.M. Lauridsen, N.C. Krieger Lassen, G. Brückner, T. Tschentcher, B. Bay, D. Juul Jensen and H.F. Poulsen, *J. Appl. Cryst.* 33, 2000, 364.
- [2] H.-R. Wenk and S. Grigull, *J. Appl. Cryst.* 36, 2003, 1040.
- [3] H.J. Bunge, *Adv. X-ray Analysis* 47, 2004, 359.
- [4] H.-G. Brokmeier and Sang Bong Yi, In: W. Reimers, A. Pyzalla, A. Schreyer, H. Clemens (eds.), *Neutrons and Synchrotron Radiation in Engineering Materials Science*, Wiley VCH Verlag, Weinheim, 2008 in press.
- [5] H.-G. Brokmeier, *Physica B: Condensed Matter* 385–386, Part 1, 2006, 623.
- [6] H.-G. Brokmeier: In: *Advanced Materials 2005* eds: M. Farooque, S.A. Rizvi, J.A. Mirza KRL Rawalpindi Pakistan, 2007, 292.
- [7] H.-G. Brokmeier, S.B. Yi, B. Schwebke and J. Homeyer, *Z. Kristallographie, Supl.* 26, 2007.
- [8] D. Juul Jensen, E.M. Lauridsen, L. Marulies, H.F. Poulsen, S. Schmidt, H.O. Sørensen and G.B.M. Vaughan, *Materials Today* 9, 2006, 18.
- [9] H.-G. Brokmeier, B. Weiss, S.B. Yi, W. Ye, K.D. Liss and T. Lippmann, *Mater. Sci. Forum* 495–497, 2005, 131.
- [10] B.D. Cullity, *Elements of X-ray diffraction*, Addison Wesley, 1978.
- [11] H.- F. Kocks, C. Tome, H. R. Wenk, *Texture and Anisotropy*, Cambridge University Press 1998.
- [12] J.F.H. Clusters: *Philips Techn. Rundschau* Vol. 7 (1942)
- [13] G. Wassermann and J. Grewen: *Texturen Metallischer Werkstoffe*, Springer Verlag Berlin 1962.
- [14] H. R. Wenk; *Schweiz. Min. Petr. Mitt.* 46, 1966, 518.
- [15] K. Moras, A.H. Fischer, H. Klein and H.J. Bunge, *J. Appl. Cryst.* 33, 2000, 1162.
- [16] S.-B. Yi, C.H.J. Davis, H.-G. Brokmeier, R.E. Bolmaro, K.U. Kainer and J. Homeyer, *Acta Mat.* 54, 549–562, 2006
- [17] C.H.J. Davies, S.B. Yi, J. Bohlen, K.U. Kainer, H.-G. Brokmeier and J. Homeyer, *Materials Science Forum* 495–497, 2005, 1633.
- [18] Sangbong Yi, H.-G. Brokmeier, J. Homeyer, *Materials Science Forum* 561–565, 2007, 183.
- [19] L. Lutteroti, <http://www.ing.unitn.it/~maud/>
- [20] H.M. Rietveld, *J. Appl. Cryst.* 2, 1969, 65.
- [21] Sangbong Yi, *PhD Theses TU Clausthal* 2005
- [22] Ulf Garbe private communication
- [23] H.J. Bunge and H. Klein, *Z. Metallkunde* 87, 1996, 465.
- [24] Z. Nishiyama, *Martensitic Transformation*, Academic Press, New York, 1978



Heinz-Gunter Brokmeier  
Professor  
Institute of Materials Science and Engineering  
Technical University Clausthal  
Clausthal Agricolastr. 6  
38678 Clausthal-Zellerfeld  
Germany



**Part V**  
**Texture and Microstructure Development**  
**During Special Processes and Materials**



# Chapter 19

## Ultra-fine Grain Materials by Severe Plastic Deformation: Application to Steels

Satyam Suwas, Ayan Bhowmik, and Somjeet Biswas

*Dedicated to Prof. Ranjit Kumar Ray for his invaluable  
teaching and guidance to the scientific community working  
on texture of materials*

**Abstract.** Severe plastic deformation techniques are known to produce grain sizes up to submicron level. This leads to conventional Hall-Petch strengthening of the as-processed materials. In addition, the microstructures of severe plastic deformation processed materials are characterized by relatively lower dislocation density compared to the conventionally processed materials subjected to the same amount of strain. These two aspects taken together lead to many important attributes. Some examples are ultra-high yield and fracture strengths, superplastic formability at lower temperatures and higher strain rates, superior wear resistance, improved high cycle fatigue life. Since these processes are associated with large amount of strain, depending on the strain path, characteristic crystallographic textures develop. In the present paper, a detailed account of underlying mechanisms during SPD has been discussed and processing-microstructure-texture-property relationship has been presented with reference to a few varieties of steels that have been investigated till date.

### 19.1 Introduction

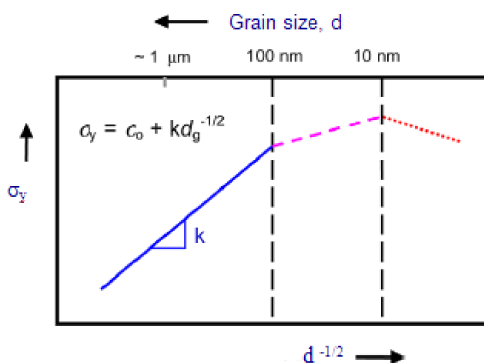
Grain size strengthening is one of the fewer methods where one can expect improvement in strength as well as ductility [1–4]. In view of this, ultra-fine grained

---

S. Suwas, A. Bhowmik, and S. Biswas  
Department of Materials Engineering, Indian Institute of Science, Bangalore-560012, India



**Fig. 19.1** The variation of Hall-Petch relationship with varying range of grain size.



materials have generated a lot of interest. Materials with ultra fine grain size offer ultra high yield and fracture strength, superior formability even at lower temperature and higher strain rates as well as better wear resistance. In this context, it is in place to define the term ‘ultra-fine’ grain size. According to Prangnell et al. [5, 6], a grain size aggregate having an average spacing of high angle grain boundaries (misorientation angle greater than  $15^\circ$ ) less than  $1 \mu\text{m}$  in all orientations are known as ultra-fine grained materials. Typically, the grain size within ultra-fine grain materials varies from 100–1000 nm and the ratio of high angle grain boundaries to the total boundary area in the material greater than 70%. The strength of such materials is derived from the Hall-Petch relationship,

$$\sigma_y = \sigma_0 + k d_g^{-1/2}$$

[7, 8] as shown in Fig. 19.1, however with a reduced value of the hardening coefficient,  $k$ , where  $\sigma_y$  represents the yield stress,  $\sigma_0$ , the friction stress and  $d_g$ , the diameter representative of the grain size.

In the recent past, coupled with the spurt in activities on nanostructured materials, a number of methods have been employed to obtain ultra-fine/nanometer scale grain sizes in bulk materials. These processes include grain refinement by adding various elements during solidification that act as grain refiners, mechanical working involving phase transformation, mechanical milling followed by consolidation, pulse electro-deposition, and recently developed severe plastic deformation techniques [10–13]. However, of all the processes, severe plastic deformation (SPD) possess certain convincing advantage, overcoming a number of difficulties associated with residual porosity in compacted samples, impurities from ball-milling, addition of costly alloying elements during solidification, processing of large-scale billets and complexities of thermo-mechanical treatments. With large deformation during rolling or drawing resulting in highly elongated grains with sub-structure having low angle grain boundaries, the substructures formed from SPD are generally equiaxed, at least after several passes, bounded by high angle boundaries, in majority.

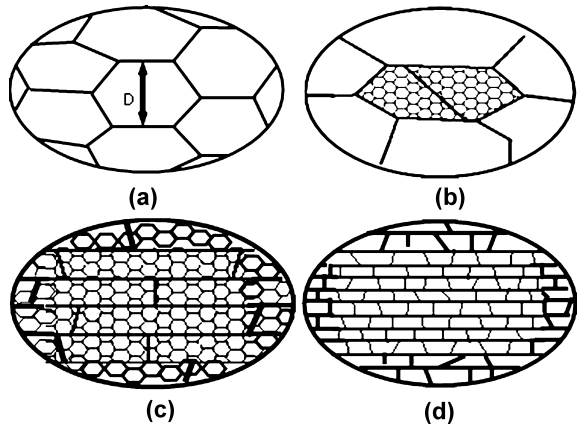
## 19.2 General Characteristics of Severe Plastic Deformation

Severe Plastic Deformation refers to a class of mechanical deformation process that imparts very large plastic strain in materials [14–16, 18]. These processes are generally carried out at low temperatures and under high pressure [17, 19–21] to avoid any restoration processes like recovery to set in the materials; however, in many cases it cannot be completely avoided. Refinement of grains to produce ultra-fine grain microstructure has been found to accumulate strains  $\sim 4$  or more. Thus, the basic requirement of grain refinement by SPD is a very large increase in grain boundary area. This can either occur by extension of pre-existing boundaries which results from boundaries extending in proportion to the strain [22] or by generation of new high angle grain boundaries (HAGB) by grain sub-division, which is a consequence of crystallographic nature of plastic deformation [23]. This stage is followed by mechanisms leading to sub-grain rotation. Hence, the underlying principles of grain refinement involves: i) increase the dislocation density by heavily deforming the materials, ii) formation of ordered arrangement of dislocation walls, and iii) transformation of those dislocation walls into grain boundaries [5, 6, 24–26].

The mechanism of grain refinement during SPD is now universally accepted. The first stage of deformation involves subdivision of grains by arrangement of trapped glide dislocations into cell boundaries [5, 6, 23, 27–29, 31], leading to deformation banding. The misorientation between deformation bands increases as the deformation proceeds leading to a tendency of rotation towards one of the nearest stable orientations. This decides the texture for a given deformation mode. If orientations diverge greatly, new boundaries with high angle misorientations can be formed. The interaction amongst the grains as well as other heterogeneities may lead to strain gradients by local variation. Subdivision of grains occurs first at largest length scale, that is, within primary deformation bands. As the strain increases, it gradually perpetuated to the next available level (cell blocks or microband boundaries). In addition to these well-known mechanisms, a few additional factors may also play an important role in the deformation processes. For example, at high strains, flow softening can lead to concentrated slip occurring in shear bands. This may cause the rotation of material within a shear band leading to the creation of additional HAGBs. In addition, changes in strain path may also contribute to the process of grain refinement, by promoting shear banding and disrupting directions deformation structure. Alloys in which slip is restricted may develop high misorientation boundaries by twinning under the action of imposed deformation.

The mechanisms leading to grain refinement at various intermediate strains of SPD has been elaborated by Humphreys et al. [30, 32] (Fig. 19.2 (a)–(d)). At low von Mises strain ( $\epsilon_{vm} < 2$ ), original grains split into zones of varying misorientations by the classical deformation banding. On increasing the strain ( $\epsilon_{vm} > 3.5$ ), the misorientations between the cell blocks increase and they get aligned along the direction of shear leading to the formation of ‘lamellae’-like structures. At moderate strains ( $\epsilon_{vm} \approx 4.5$ ), the average spacing of lamellar boundaries (grain width) slowly

**Fig. 19.2** Mechanism of formation of submicron grains with different levels of strains, namely, (a) Initial grain structure, (b) Subgrains and grain subdivision, (c) Alignment of high angle grain boundaries (HAGBs), (d) Ribbon grain structure [30].



decreases to the dimension of a subgrain. The resulting deformation structure consists of thin ribbons with high aspect ratio and variable length. This structure has high stability. At very high von Mises strains ( $\epsilon_{vm} \approx 6$ ), these ribbons progres-

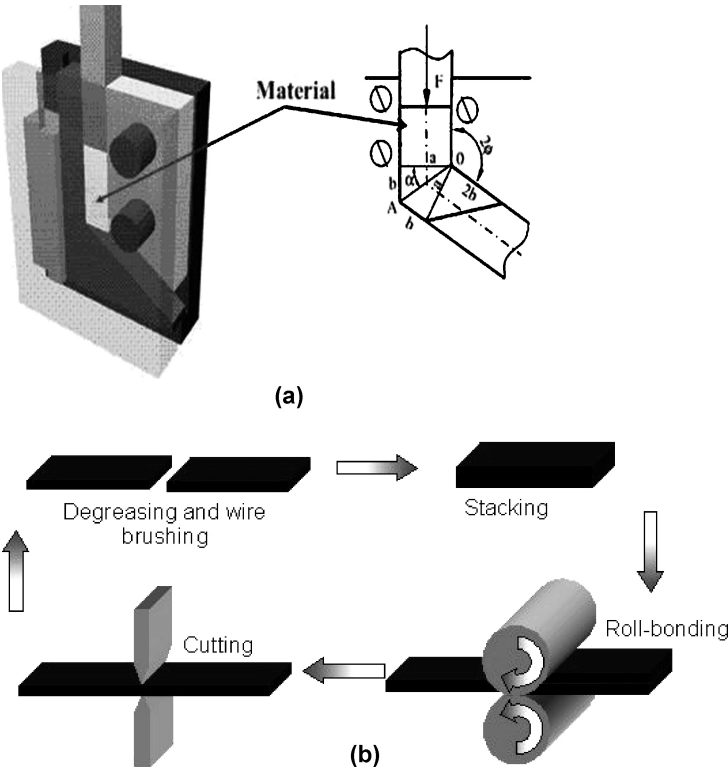


**Fig. 19.3** Schematic representations of three severe plastic deformation processes namely (a) Equal Channel Angular Extrusion, (b) Accumulative Roll Bonding.

sively break up into shorter segments, eventually giving rise to a homogenous sub-micron grain structure.

In spite of the fact that during the process of SPD, dislocations get generated and absorbed at the grain boundaries, ultimately leading to HAGBs, the microstructure are characterized by a high density of non-equilibrium grain boundaries [33–35]. The two main features of such boundaries are: (a) excess grain boundary energy and (b) the presence of long range elastic stresses resulting from discontinuous distortion of an otherwise crystallographically ordered structured grain boundary.

Of all the SPD processes, Equal Channel Angular Extrusion (ECAE) [36–45] and Accumulative Roll Bonding (ARB) [51–58] and are the most experimented ones. The schematic representations of these processes have been given in Fig. 19.3 (a) and (b). In addition to the above processes, a few other methods of SPD process that have been tested include – High Pressure Torsion (HPT) [46–50], Repetitive Corrugation and Straightening (RCS) [59–62], Conshearing Process [63], Continuous Confined Strip Shearing (C2S2) [64], and ECAP-Conform [65]. However, due to complicated design and other constraints they have not been so actively pursued.

### 19.2.1 *Equal Channel Angular Extrusion*

Amongst the SPD processes, ECAE has received maximum attention because it provides an easy means to produce an ultra-fine grain size in bulk material with improved mechanical properties [66–73]. In this process, large strains can be given without changing sample dimension significantly resulting in a refined microstructure and a characteristic texture. As it can be seen in Fig. 19.3 (a), in the ECAE setup the inlet and the outlet channels of the die have the same cross-section and the material gets sheared through as it passes over a shear zone around the plane of intersection of the two channels of the die. The strain imparted along the pass depends on the interchannel die angle as given equation 19.1, and for a 90° die the strain per pass is about 1.16 [44]. Using the geometry of the die (Fig. 19.3), the shear strain introduced per pass of ECAE can be calculated as follows:

$$\begin{aligned}\alpha &= \pi/2 - \phi \\ b/a &= \tan\alpha = \cot\phi \\ \gamma &= 2b/a = 2a \cdot \cot\phi/a = 2\cot\phi,\end{aligned}$$

where  $\phi$  is the interchannel die angle and  $\alpha$  is the angle subtended by the outer arc of the channel. The von Mises strain is given by

$$\epsilon = \gamma/\sqrt{3} = (2\cot\phi)/\sqrt{3} \quad (19.1)$$

The three possible variations, namely routes A, B and C of the ECAE process are depicted in Fig. 19.4. In Route A, the sample from the previous pass is re-inserted into the die without any rotation about its longitudinal axis. In the case of route B, the

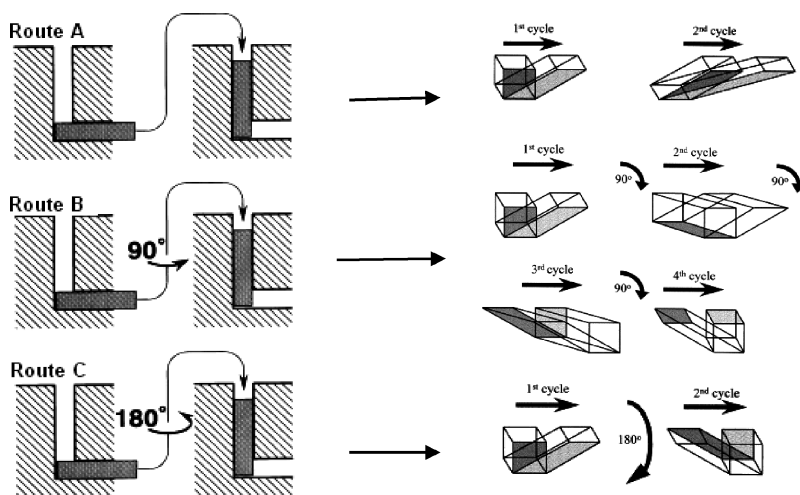


**Fig. 19.4** Various possible routes of ECAE and schematic illustration of shearing after different passes [82].

sample is rotated by  $90^\circ$  about the longitudinal axis after each pass. When the rotation is in the same sense, either clockwise or anticlockwise ( $+$  or  $-90^\circ$ ), it is called route  $B_c$ ; on the other hand, when the sample rotated by alternating  $+$  and  $-90^\circ$ , the route is named as  $B_A$ . If during each subsequent pass, the rotation about the longitudinal axis is  $180^\circ$ , it is termed route C. The shearing characteristic of each route and pass, considering a cubic element in the starting material, is shown in Fig. 19.4 [82].

The evolution of grain shape during ECAE as a function of passes has been reported in addition to the grain size. It reveals that an initial spherical grain of  $0.1\mu\text{m}$  elongates to form an elliptical grain with major axis scaling to  $0.45\mu\text{m}$  after two passes (Fig. 19.5). The gradual change in the grain structure over multiple passes of ECAE through a die with inter-channel die angle of  $90^\circ$  is presented in Table 19.1. An enormous increase in the aspect ratio of the grains accompanied by a decrease in the angle of inclination with respect to the extrusion direction could be easily visualized.

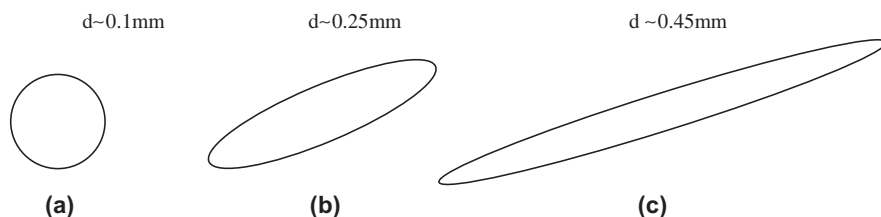


**Fig. 19.5** Schematic representation of the shape and size of a grain (a) initially, (b) after one pass, and (c) after two passes of ECAE following route A. 'd' represents the length of the major axis of the ellipse [73].

**Table 19.1** Table showing comparison of the equivalent strain achieved in conventional rolling, extrusion and ECAE processes. Here  $t_0$  represents the thickness of the initial plate during rolling process,  $D_0$  refers to the diameter of the starting billet for extrusion and  $D$  stands for the diameter of then final product obtained in all the three cases-conventional rolling, extrusion and ECAE.

Equivalent reduction ratio	Original plate thickness, $t_0$	Original billet diameter, $D_0$	Number of passes
3.2	3.2D	1.8D	1
105.0	105.0D	10.2D	4
10100.0	10100.0D	100.0D	8

Like most SPD processes, during ECAE, in general, the grains are refined as a result of subdivision due to activation of the slip systems which is a characteristic of the crystal structure. In the second pass, slip direction is changed in accordance with rotation of the sample between the two passes. It is to be mentioned here that all the routes of ECAE, including Route A, lead to change in strain path. This can be visualized in the schematic diagram given in Fig. 19.6. In this condition it is quite likely that other possible slip systems get activated in order to accommodate further deformation. This leads to the development of misorientation gradients across the grains. Formation of dislocation cells or subgrains is facilitated by this process. By further ECAE passes, cell/subgrain boundaries become high angle boundaries. This could be either by the rotation of subgrain boundaries in order to achieve even shear strain distribution at all the boundaries or by the absorption of lattice dislocations in the pre-existing grain boundaries.

A comparison between multi-pass ECAE and conventional rolling and extrusion, the two most popular metal working processes in Table 19.2, shows that strain induced after four pass of ECAE is equivalent to a reduction ratio of 105 in case of rolling and about 10 for extrusion. It is therefore, quite obvious that the strain level achieved after eight passes of ECAE is virtually beyond the scope of conventional processing techniques.

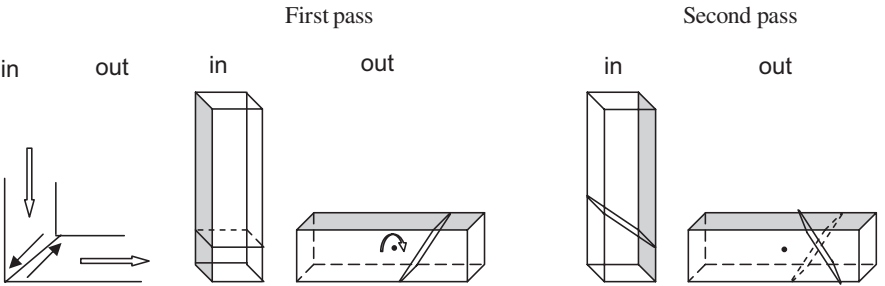


**Fig. 19.6** Schematic representation showing the change in strain path during subsequent passes of ECAE following route A. The dotted plane represents the shearing plane in the preceding pass.

**Table 19.2** The variation of grain morphology with number of ECAE passes.

Number of passes	Von Mises strain	Equivalent ratio of reduction	Equivalent reduction of area (%)	Angle of element inclination (degrees)	Aspect ratio of element	Element surface area ratio
0	0.00	0.0	0.00	0	1	1.0
1	1.15	3.2	69.00	22	5	1.4
2	2.31	10.2	90.00	13	17	2.0
4	4.62	105.0	99.00	7	65	3.4
8	9.24	10100.0	99.99	3	257	6.0

### 19.2.2 Accumulative Roll Bonding

Another very important variant of SPD process is accumulative roll bonding (ARB). Figure 19.3 (b) illustrates the principle of ARB process. It is well known that rolling is the most important process for continuous production of bulk sheets; however, the total reduction in thickness, which corresponds to the total strain achieved, is limited because of decrease in strip thickness with increasing reduction [53, 58]. In ARB, the rolled material is cut, stacked to be equal to the initial thickness and rolled again. Therefore, the achieved strain is unlimited in this process because one can repeat this process theoretically endlessly. In case of ARB, referring to Fig. 19.2 (b), when the reduction is 50% per cycle, thickness of the initial strip after 'n' cycles is given by

$$t = t_0 / 2^n,$$

where  $t_0$  is the initial thickness of the strips. The total reduction  $r$ , after  $n$  passes is given by

$$r = 1 - (t/t_0) = 1 - (1/2^n)$$

Assuming plane strain condition, the von Mises strain after  $n$  passes is calculated as

$$\varepsilon = \{(2/\sqrt{3}) \ln (1/2)\} * n$$

To achieve good bonding, surface of the adjoining sheets is treated by processes like degreasing and wire-brushing. The sheets are then stacked together. Rolling at elevated temperature is advantageous for joining the sheets, though too high temperature would induce restoration processes and reduce the accumulated strain. Therefore, it is crucial to optimize the process parameters. Generally, ARB process is carried out at moderate temperatures.

## 19.3 Severe Plastic Deformation Processes as Applied to Steels

Steels are technologically one of the most important classes of materials that have shown itself worthy of a wide spectrum of engineering applications. Although numerous investigations have been carried out on tailoring the optimal microstructure-property relationship and many of them are quite successful, of late, special interests have generated to improve the mechanical properties by means of grain refinement as ultra-fine grained steels with relatively simpler compositions. Grain refined lean alloyed steels could be a potential alternative for High Strength Low Alloy (HSLA) steel. The drive to improve the properties of steel by means of grain refinement is due to the fact that it offers strengthening of the material along with improved toughness. In addition, lowering of ductile-brittle transition temperature is also an important driver for grain refinement. A comparison of the extent of grain refinement of ferrite possible for various conventional processing techniques like rolling shows that a final grain size of  $1\mu\text{m}$  and  $5\mu\text{m}$  is obtained for conventional hot rolling followed by air cooling plus controlled rolling with water cooling respectively with an increase in the yield strength by about 80 MPa. However, on decreasing the grain size from 5 to  $1\mu\text{m}$ , there is an increase in yield strength by  $\sim 350$  MPa alongside lowering of ductile-to-brittle transition temperature by about  $200^\circ\text{C}$  ( $-20^\circ\text{C}$  to  $-200^\circ\text{C}$ ). On further reduction of grain size to  $0.2\mu\text{m}$ , there is an increase in yield strength by  $\sim 680$  MPa takes place leading to a resultant yield strength 1000 MPa even for steels having lean composition.

The two most widely used methods to produce ultra fine grain (UFG) steels are advanced thermomechanical processing and severe plastic deformation. While the former ones involve continuous treatments involving phase transformations, the latter ones are discontinuous methods more suited for relatively softer materials. Of these two the major benefits derived out of refining grains by SPD means are high yield stress and excellent toughness at minimal alloying. This could lead to cost benefit as well as energy benefit by skipping complicated additional heat treatments like soft annealing, quenching and tempering. Another advantage could be an improved weldability of the resultant steels owing to the reduced required content of carbon and other alloying elements. Of all the SPD processes, ECAE and ARB are the two most common SPD processes that have been applied successfully on steels.

### 19.3.1 Equal Channel Angular Extrusion

*Low Carbon Steels:* Equal Channel Angular Extrusion process has potential application for rods and bars. The microstructure-property relationship has been quite extensively studied [83–88] for low carbon steels processed via. ECAE. Shin et al. [83] obtained sub-micron size equiaxed grains in low carbon ferrite-pearlite steels reaching a von Mises strain,  $\epsilon_{\text{vm}} \sim 4$ . This steel exhibited UTS over 900 MPa



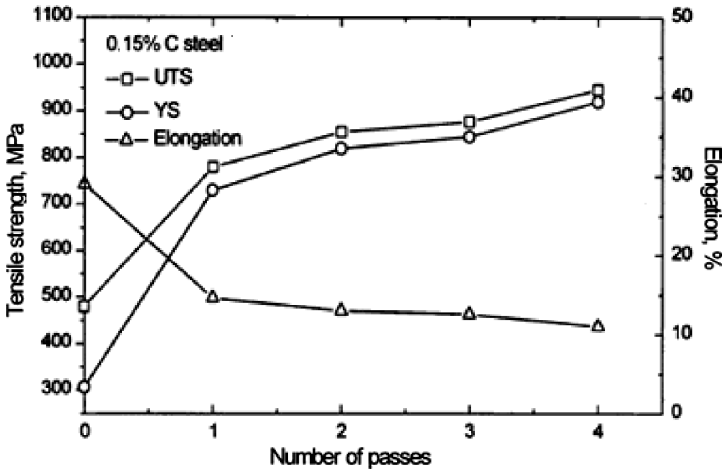


Fig. 19.7 Variation of tensile properties of low carbon steel as a function of ECAE passes [83].

and a reasonable ductility  $\approx 10\%$  at room temperature, Fig. 19.7. The fatigue properties of ultra fine grain low carbon steel processed through ECAE had shown degradation due to less tortuous path that the crack had to propagate through compared to its coarse grained counterpart, leading to a lower fatigue crack growth resistance [87].

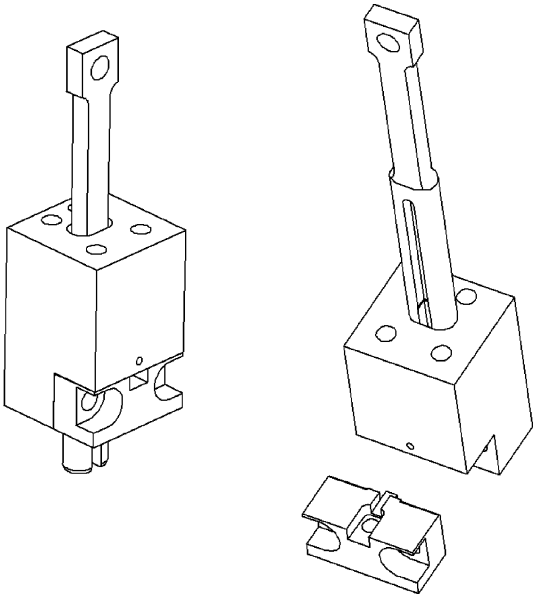


Fig. 19.8 Isotropic view of the die used to carry out the ECAE experiments [74].

**Table 19.3** Table showing microstructural features and mechanical properties of coarse and UFG ferrite-martensite dual phase steel [89] where  $V_m$  is the martensite volume fraction;  $d_m$ , martensite island size;  $d_f$ , ferrite grain size;  $\sigma_{YS}$ , yield strength;  $\sigma_{TS}$ , ultimate tensile strength;  $\epsilon_u$ , true uniform strain and  $\epsilon_f$ , the total engineering elongation.

Microstructure	$V_m$ (%)	$d_m$ ( $\mu\text{m}$ )	$d_f$ ( $\mu\text{m}$ )	$\sigma_{YS}$ (MPa)	$\sigma_{TS}$ (MPa)	$\epsilon_u$ (%)	$\epsilon_f$ (%)
Coarse grain	22	9.8	19.4	510	843	9.8	13.5
UFG	28	0.8	0.8	581	978	9.3	17.6

*Dual-Phase Steels:* ECAE of ferrite-martensite dual phase steel (0.15% C, 0.25% Si, 1.06% Mn, <0.01 % P, <0.008% S, 0.003% N) was reported by Son et al. [89] up to four passes ( $\epsilon \approx 4$ ) with subsequent intercritical annealing at 730°C for 10 min followed by water quenching. The microstructure constituted of martensite islands of  $\sim 1 \mu\text{m}$  uniformly distributed throughout the UFG ferrite matrix without being confined to the former pearlite colonies. This may result from dissolution of carbon atoms from pearlite, cementite and their concurrent diffusion into UFG ferrite during ECAE, making the average carbon content reach the equilibrium content to form austenite during subsequent inter-critical annealing. The details of the microstructural features and the mechanical properties [89] are summarized in Table 19.3. There is a notable reduction in the size of both martensite islands as well as grain of ferrite matrix with the increase in the yield strength and elongation values.

*Interstitial-free steels:* Interstitial-free (IF) steels constitute an important class of steels having carbon percentage as low as below 0.01. These steels are extensively used in automotive industries for making car bodies owing to the high formability that they possess. In recent years, efforts have been made to improve the strength of these classes of steels by means of grain refinement mostly through SPD processes. Studies on the microstructural and texture evolution of IF steel during ECAE following various routes and passes have been reported by various authors [73, 75–81]. However, there is a lack of unanimity amongst these investigators. For example, Kim et al. [73] reported that grain refinement during ECAE of IF steels is more rapid in route A than in route C. Li et al. [77, 79] conducted ECAE of IF steel up to eight passes for all the four routes A, B<sub>C</sub>, B<sub>A</sub> and C. It was found that the rate of grain refinement rate was highest in route C after two passes but in route B<sub>C</sub> after four passes.

The present authors investigated ECAE of IF steel using the die shown in Fig. 19.8. The die has a design similar to that of a modified square die due to Mathieu et al. [74]. The extrusions were carried out at a temperature of about 300°C upto four passes using routes A and B<sub>C</sub>. The microstructure obtained are shown in Fig. 19.9 in the form of inverse pole figure maps superimposed on pattern-quality maps obtained by electron back scatter diffraction (EBSD). It can be seen that grain sizes below 0.5  $\mu\text{m}$  could be achieved. The grain size in both the routes got saturated after second pass and remained almost constant till the fourth pass.

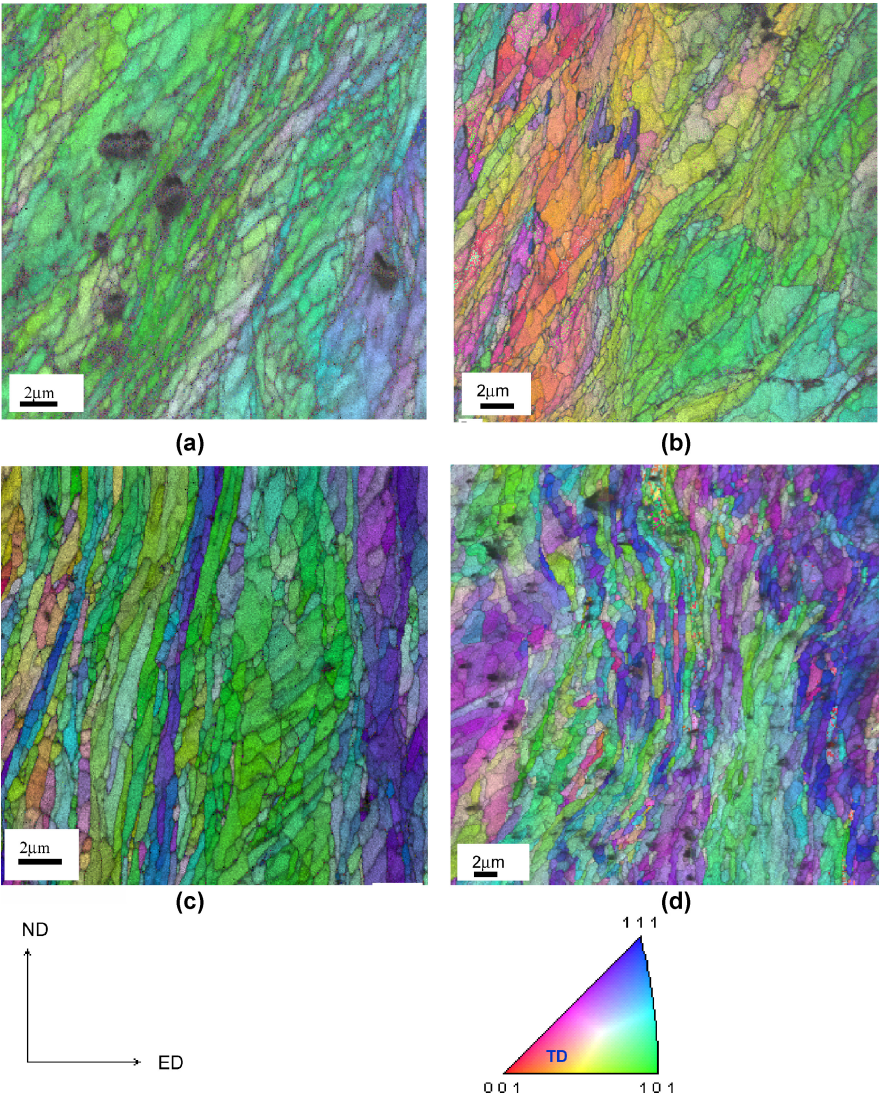


**Fig. 19.9** Inverse Pole Figure map superimposed on pattern quality maps of (a) route A, pass 2, (b) route B, pass 2, (c) route A, pass 4, (d) route B, pass 4.

**19.3.1.1 Texture Development During ECAE of Steel**

It is well-known that texture development is an important attribute of ECAE processing. A few researchers have studied textures of different grades of steels processed by

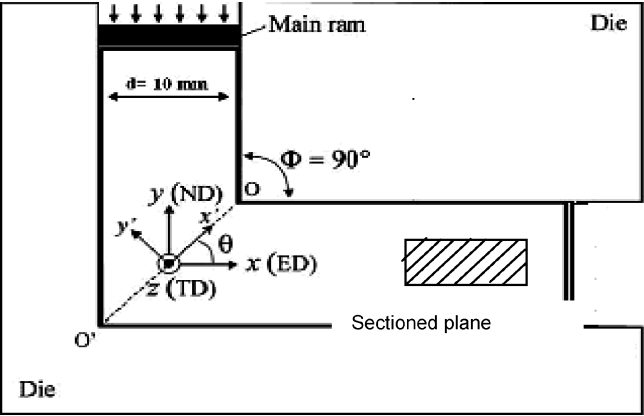


**Fig. 19.10** Schematic representation of the ECAE die. The x-y sample co-ordinate axes are related to the x'-y' axes by rotation through angle,  $\theta$ , about TD-axis.

ECAE. The typical experimental textures that develops during ECAE are characterized by  $\{110\} \langle uvw \rangle_0$  and  $\{hkl\} \langle 111 \rangle_0$ , where  $\theta$  stands for rotation about the TD-axis to transform the x-y (ED-ND) co-ordinate system into new x'-y' co-ordinate system as shown in the Fig. 19.10, where x' and y' corresponds to the macroscopic shear direction and the normal to the shear plane respectively. The ideal (110) pole figure after first pass, shown in the Fig. 19.11, represents that of a negative simple shear rotated by  $\theta$  about the TD-axis [76, 78, 80]. Table 19.4 documents the position of the ideal orientations and fibers in a single pass of ECAE using a die having inter-channel die angle of  $90^\circ$ , for bcc materials.

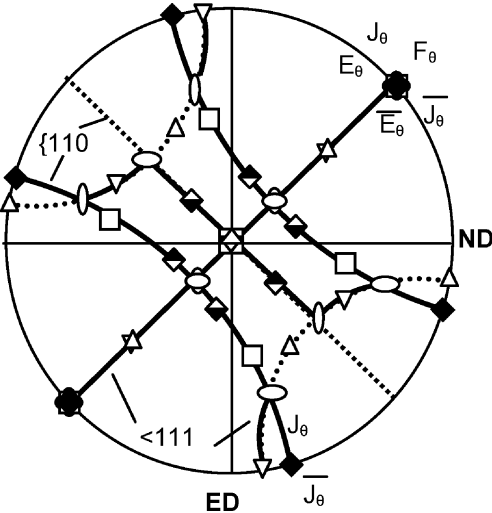


**Fig. 19.11** Ideal (110) pole figure after first pass of ECAE.

**Table 19.4** Locations of ideal components after first ECAE pass [79].

Notation	Euler angles (°)		Miller indices			Equivalent representation with TD-rotation by $\theta$	
	$\varphi_1$	$\varphi_2$	$\phi$	ND	ED		
$D_{10}$	99.74/279.74	0	45.00	[1 1 8]	[4 4 $\bar{1}$ ]	[ $\bar{1}$ $\bar{1}$ 0]	( $\bar{1}$ $\bar{1}$ 2)[111] $_{\theta}$
	9.74/189.74	45	90.00				
$D_{20}$	170.26/350.26	0	45.00	[4 4 $\bar{1}$ ]	[1 1 8]	[ $\bar{1}$ 1 0]	(1 1 $\bar{2}$ )[111] $_{\theta}$
	80.26/260.26	45	90.00				
$E_{\theta}$	135		35.26	[9 1 4]	[ $\bar{1}$ $\bar{1}$ 5]	[ $\bar{1}$ 1 2]	(1 1 0)[1 $\bar{1}$ 1] $_{\theta}$
$\bar{E}_{\theta}$	315		35.26	[ $\bar{9}$ $\bar{1}$ $\bar{4}$ ]	[1 1 $\bar{5}$ ]	[ $\bar{1}$ 1 2]	( $\bar{1}$ $\bar{1}$ 0)[ $\bar{1}$ $\bar{1}$ 1] $_{\theta}$
$J_{\theta}$	15/135/255		54.74	[15 4 11]	[ $\bar{7}$ $\bar{2}$ 6 19]	[ $\bar{1}$ 1 1]	(1 1 0)[1 $\bar{1}$ 2] $_{\theta}$
$\bar{J}_{\theta}$	75/195/315		54.74	[ $\bar{15}$ $\bar{4}$ $\bar{11}$ ]	[7 26 $\bar{19}$ ]	[ $\bar{1}$ 1 1]	( $\bar{1}$ $\bar{1}$ 0)[ $\bar{1}$ $\bar{1}$ 2] $_{\theta}$
$F_{\theta}$	45/225	0	45.00	[3 3 4]	[ $\bar{2}$ 2 3]	[ $\bar{1}$ 1 0]	{1 1 0} <001> $_{\theta}$
	135/315	45	90.00				

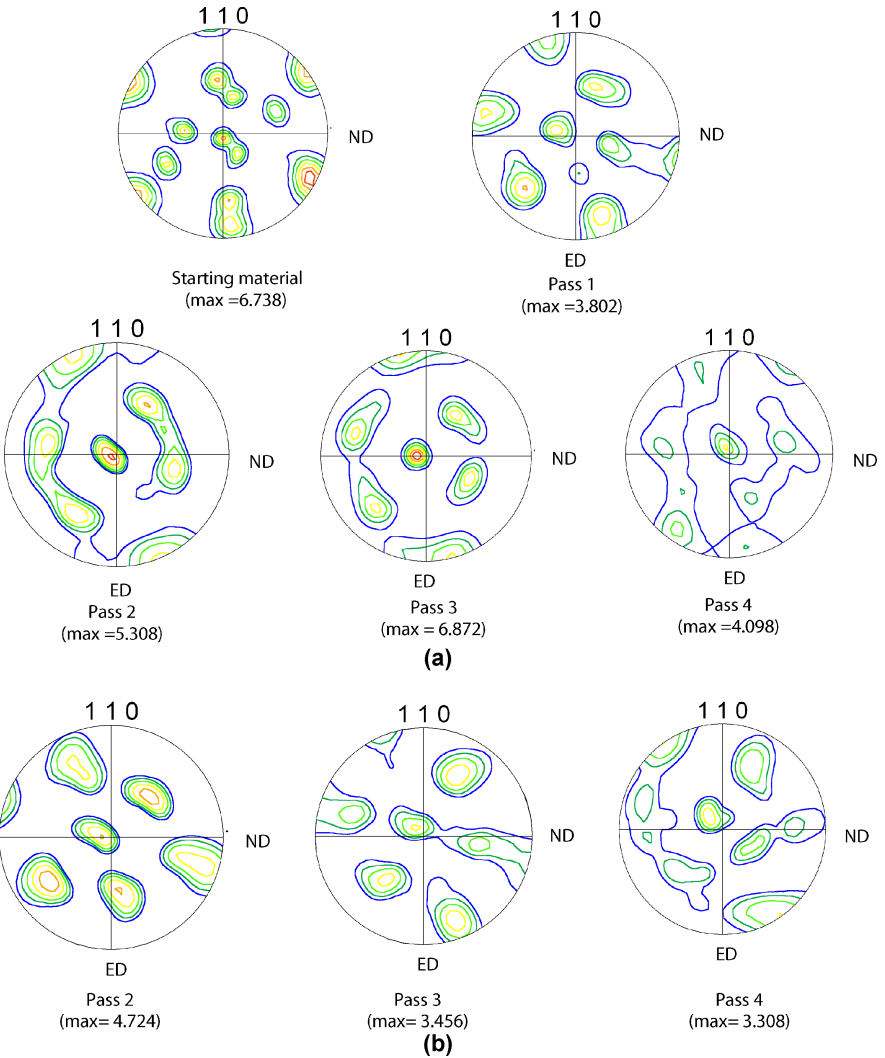


**Fig. 19.12** Experimental pole figures for (a) route A, and (b) route B.

A detailed study on texture evolution in ECAE processed IF steel were carried out by the present authors [92]. The experimental  $(110)$  pole figures are shown in Fig. 19.12. As expected, monoclinic sample symmetry with TD as the dyad axis is seen in the texture components developed in the case of route A. No such symmetry is evident in the pole figure of route B<sub>c</sub> processed material, which is due to the perpendicular rotation of the specimen about the longitudinal axis. The texture component present in the previous pass does not get aligned in symmetric position with respect to the deformation in the next pass. The experimental textures show the presence of  $\{110\}_0$  and  $\langle 111 \rangle_0$  fibers which reflects the tendency of the crys-

tallographic slip planes and direction to rotate along the macroscopic shear plane and shear direction. As seen from the figure, the starting material almost had a typical shear type bcc texture. After the first pass, a decrease in the intensity of texture is observed. In route B<sub>c</sub>, the intensity increased after the next pass and then monotonically decreases till the end of the fourth pass. However, no such trend is exhibited by samples processed through route A.

### **19.3.2 Accumulative Roll Bonding**

As mentioned earlier, Accumulative Roll Bonding (ARB) is an efficient method for development of fabricating ultra-fine grained bulk materials in the form of flat products. Tsuji et al. have carried out ARB on interstitial-free (IF) steels at 500°C till upto 5 [91] and 7 [58] cycles. The von Mises strain per pass in his experiment was  $\sim 0.8$ . Starting from an initial grain size of  $\sim 20\ \mu\text{m}$ . ARB processed materials are characterized by longitudinal ‘pancake’-like shape grains with  $d_{\text{length}} = 700\ \text{nm}$  and  $d_{\text{width}} = 210\ \text{nm}$  in the first case, and  $d_{\text{length}} = 900\ \text{nm}$  and  $d_{\text{width}} = 200\ \text{nm}$  in the latter case. Costa et al. [90] also obtained almost similar grain dimensions along the width,  $d_{\text{width}} = 0.3\ \mu\text{m}$  with IF steel rolled at 500°C upto three cycles. The authors of this paper also carried out some ARB of IF steel [93]. In this study, it was noted that well elongated grains formed at the center of the sheet while the grains are less elongated at the subsurface region where the grains are more refined. It was also noted that an inherent heterogeneity of texture prevailed along the thickness of the roll bonded strip. At the surface, a shear type texture forms which was expected to be due to the shear strain developed on the surface due to high friction generated between the strip surface and the rolls. At the center, however, typical rolling texture formed.

## **19.4 Summary and Perspective**

It was understood that severe plastic deformation is a useful method for grain refinement in bulk metallic materials. The capability of the process is well understood with reference to FCC metals and alloys. However, there is a lot to understand with regards to the extent of grain refinement and the stability of the grain structure as well as the implication of the refined grains on different properties. There has been relatively a fewer studies on severe plastic deformation of steels, therefore a lot of work is needed. Although, ECAE is the most popular and well investigated SPD technique, the potential for scaling up this process is yet to be explained. The other SPD processes, for example, accumulative roll bonding shows a great potential for being an industrially viable process. However, the important attributes like microstructural and texture development and benefits

from this process in terms of mechanical properties of ARB processed materials is not yet established. In nut-shell, there is an ample scope of study the issues pertaining to SPD processes, both in steels as well as other materials.

**Acknowledgement** The authors are thankful to Dr. D. Bhattacharjee, Dr. N. Gope and Prof. R.K. Ray, R&D Division, Tata Steel for their encouragement and support to this work. The financial support from Tata Steel through a collaborative project “Investigations on Ultra fine grain Steel” is duly acknowledged. This work also uses the facility set up under Institute Nanoscience Initiative sponsored by DST-FIST program.

## References

- [1] S. Lee, P.R Berbon, M. Furukawa, Z. Horita, M. Nemoto, N.K. Tsenev, R.Z. Valiev, T.G. Langdon, *Mater. Sci. Eng.* A272, 1999, p.63
- [2] A.J. Barnes. *Mater. Sci. Forum*, 170–172, 1994, p. 701.
- [3] K. Osada and H. Yoshida. *Mater. Sci. Forum*, 170–172, 1994, p.715.
- [4] T.G. Langdon *Acta Mater.* 42,1994 ,p.2437
- [5] P.B. Prangnell , J.R. Bowen, A. Gholinia, *Proceedings of the 22nd Riso International Symposium on Materials Science, Science of Metastable and nanocrystalline Alloys Structure, Properties and Modeling*, Riso National Laboratory, Roskilde, Denmark, 2001, p.105.
- [6] P.B. Prangnell, J.R. Bowen and F.J. Humphreys, *Mat.Sci. and Tech.*, 16, 2000, p.1246
- [7] E.O. Hall *Proc. Roy. Soc. B*, 64,1951, p. 747
- [8] N.J. Petch *J. Iron Steel. Inst.*, 174, 1953, p. 25
- [9] Valiev R.Z., editor. *Ultrafine-grained materials prepared by severe plastic deformation*, vol. 21, *Annales de Chimie. Science des Materiaux*, 1996, p. 369, Special issue.
- [10] H. Gleiter. *Progr. Mat. Sci.*,33,1989, p. 223.
- [11] J.R. Weertman. *Mater. Sci. Eng A*166, 1993, p. 161.
- [12] C.C. Koch and Y.S. Cho. *Nanostructured Mater*, 1, 1992, p. 207.
- [13] D.G. Morris. In: *Mechanical behavior of nanostructured materials* *Trans Tech. Publ, Switzerland*, 1998, p. 85.
- [14] R.Z. Valiev, A.V. Korznikov and R.R. Mulyukov. *Mater. Sci. Eng A*168, 1993, p. 141.
- [15] R.Z. Valiev, O.A. Kaibyshev, R.I. Kuznetsov, R.Sh. Musalimov and N.K. Tsenev. *DAN SSSR* 301 4, 1988, p. 864.
- [16] R.Z. Valiev, I.V. Alexandrov and R.K. Islamgaliev. In: G.M. Chow and N.I. Noskova Editors, *Nanocrystalline materials: science and technology* *Nato ASI Kluwer Academic Publishers, Dordrecht*, 1998, p. 121.
- [17] V. A. Pavlov. *Phys. Met. and Metallogr* 67 ,1989, p. 924.
- [18] R.Z. Valiev, N.A. Krasilnikov and N.K. Tsenev. *Mater. Sci. Eng A*137, 1991, p. 35.
- [19] G. Langford and M. Cohen. *Trans. ASM* 82, 1969, p. 623.
- [20] V.V. Rybin. *Large plastic deformations and destruction of metals* *Metallurgia, Moscow*, 1987.
- [21] F. Li and P.S. Bate, *Acta Metall Mater* 39, 1991, p. 2639.
- [22] J. Gil Sevillano, P. Van Houtte and E. Aernoudt. *Progr. Mat. Sci* 25, 1980, p. 69.
- [23] D.A. Hughes and N. Hansen, *Metall Trans A* 24, 1993, p. 2021.
- [24] N. Hansen and D. Juul Jensen, *Phil Trans R Soc Lond A* 357, 1999, p. 1447.
- [25] P.J. Hurley and F.J. Humphreys, *Acta Mater*, 51, 2003, p. 1087.
- [26] Q. Liu, D. Juul Jensen and N. Hansen, *Acta Mater*, 46, 1998, p. 5819.
- [27] J.R. Bowen, A. Gholinia, S.M. Roberts and P.B. Prangnell, *Mat Sci. Engg. A*287, 2000, p.87.
- [28] J.R. Bowen, P.B Prangnell, and F.J. Humphreys, *Mat Sci. Forum*, 331–337, 2000, p. 545.



- [29] J.R. Bowen, P.B. Prangnell, and F.J. Humphreys, Proceedings of the 20th Riso International Symposium, Deformation-induced Microstructures: Analysis and Relation to Properties, Riso National Laboratory, Roskilde, Denmark, 1999.
- [30] F.J. Humphreys, P.B. Prangnell, J.R. Bowen, A. Gholinia, *Phil. Trans. R. Soc.Lond.* 357A, 2003, p.1663.
- [31] Z. Horita, D.J. Smith, M. Furukawa, M. Nemoto, R.Z. Valiev, T.G. Langdon, *J. Mater. Res.*, 11, 1996, p.1880.
- [32] A. Gholinia, F.J. Humphreys, P.B. Prangnell, *Mat.Sci. and Tech.*,16, p. 1251.
- [33] R.Z. Valiev, Yu. V. Ivanisenko, E.F. Rauch and B. Baudelet. *Acta Mater* 44, 1997, p. 4705.
- [34] R.Z. Valiev, E.V. Kozlov, Yu. F. Ivanov, J. Lian, A.A. Nazarov and B. Baudelet, *Acta metall. mater.* 42, 1994, p. 2467
- [35] .A.D. Rollet and U.F. Kocks, *Solid State Phenomena*, 35–36, 1994, p. 1.
- [36] R.Z. Valiev, K. Islamgaliev and I.P. Semenova , *Mat Sci Engg A* 463, 2007, p. 2.
- [37] R.Z. Valiev and R.K. Islamgaliev. *Fiz. Met. Metalloved* 85, 1998, p. 161.
- [38] V.M. Segal, V.I. Reznikov, A.E. Drobyshevskij and V.I. Kopylov. *Metally* 1, 1981, p. 115.
- [39] Y. Iwahashi, J. Wang, Z. Horita, M. Nemoto and T.G. Langdon. *Scripta Mater* 35 (1996), p. 143.
- [40] V.M. Segal. *Mater. Sci. Eng A*197, 1995, p. 157.
- [41] V.M. Segal, V.I. Reznikov, V.I. Kopylov, D.A. Pavlik and V.F. Malyshev. In: *Processes of plastic transformation of metals Navuka i Teknika*, Minsk, 1984, p. 295.
- [42] Y. Iwahashi, Z. Horita, M. Nemoto and T.G. Langdon. *Acta Mater* 46, 1998, p. 1589.
- [43] S. Ferrase, V.M. Segal, K.T. Hartwig and R.E. Goforth. *Metall. Mater. Trans* 28A, 1997, p. 1047.
- [44] Y. Iwahashi, Z. Horita, M. Nemoto and T.G. Langdon. *Acta Mater* 45, 1997, p. 4733.
- [45] N.H. Ahmadeev, R.Z. Valiev, V.I. Kopylov and R.R. Mulyukov. *Russian Metally* 5, 1992, p. 96.
- [46] N.A. Smirnova, V.I. Levit, V.I. Pilyugin, R.I. Kuznetsov, L.S. Davydova and V. A. Sazonova. *Fiz. Met. Metalloved* 61, 1986, p. 1170.
- [47] N.A. Smirnova, V.I. Levit, V.I. Pilyugin, R.I. Kuznetsov and M.V. Degtyarov. *Fiz. Met. Metalloved*, 62, 1986, p. 566.
- [48] Valiev RZ. Synthesis and processing of nanocrystalline powder. In: David L. Bourell, editors. *The Minerals, Metals and Materials Society*, 1996, p.153.
- [49] I.V. Alexandrov, Y.T. Zhu, T.C. Lowe, R.K. Islamgaliev and R.Z. Valiev. *Nanostructured Mater* 10, 1998, p. 49.
- [50] I.V. Alexandrov, Y. Zhu, T. Lowe, R.K. Islamgaliev and R.Z. Valiev. *Metall. Mater. Trans* 29A, 1998, p. 2253.
- [51] Y. Saito, N. Tsuji, H. Utsunomiya, T. Sakai and R.G. Hong, *Scripta Mater*,39, 1998, p. 1221.
- [52] Y. Saito, H. Utsunomiya, N. Tsuji and T. Sakai, *Acta Mater*, 47, 1999, p. 579.
- [53] S.H. Lee, Y. Saito, N. Tsuji, H. Utsunomiya and T. Sakai, *Scripta Mater*, 46, 2002, p. 281.
- [54] S. H. Lee, Y. Saito, T. Sakai and H. Utsunomiya, *Mater Sci. Engg A*325, 2002, p. 228.
- [55] L. Jiang, M.T. Pérez-Prado, P. A. Gruber, E. Arzt, O.A. Ruano and M.E. Kassner, *Acta Mater* 56, 2008, p. 1228.
- [56] S. Ohsaki, S. Kato, N. Tsuji, T. Ohkubo and K. Hono, *Acta Mater*, 55, 2007, p. 2885.
- [57] J.A. del Valle, M.T. Pérez-Prado and O.A. Ruano, *Mater. Sci. Engg A* 410–411, 2005, p. 353.
- [58] N. Tsuji, Y. Saito, H. Utsunomiya and S. Tanigawa, *Scripta Mater.*, 40,1999, p. 795.
- [59] J.Y. Huang, Y.T. Zhu, H. Jiang and T.C. Lowe, *Acta Mater*, 49, 2001, p. 1497.
- [60] Dong Hyuk Shin, Jong-Jin Park, Yong-Seog Kim and Kyung-Tae Park, *Mater Sci. Engg A* 328, 2002, p. 98.

- [61] Zhu, Y.T, Metall. Mater. Trans. 32A, 2001, p. 1559.
- [62] M.Y. Huh, J.P. Lee, J.C. Lee, J.W. Park, Y.H. Chung, Mater. Sci. Forum. 396, 2002, p. 447.
- [63] Y. Saito, H. Utsunomiya, H. Suzuki and T. Sakai, Scripta Mater., 42, 2000, p.1139–1144.
- [64] J.-C. Lee., H.-K. Seok, J.-H. Han, Y.-H. Chung. Materials Research Bulletin, 36, 5, 2001, p. 997.
- [65] G.J. Raab, R.Z. Valiev, T.C. Lowe, Y.T. Zhu, Mater Sci. Engg A 382, 2004, p.30.
- [66] W. Skrotzki, N. Scheerbaum, C.-G. Oertel, R. Arruffat-Massion, Satyam Suwas, L.S. Tóth, Acta Mater, 2007, 55, p. 2013.
- [67] Beyerlein, L.S. Tóth, C.N. Tomé and Satyam Suwas, Philosophical Magazine, 87, 2007, p. 885.
- [68] W. Skrotzki, B. Klöden, I. Hünsche, R. Chulist, Satyam Suwas, L.S. Tóth, Mat Sci Forum, 558–559, 2007, p. 575.
- [69] Satyam Suwas, R. Arruffat Massion, L.S. Tóth, J.J. Fundenburger A. Eberhardt and W. Skrotzki, Metall. and Mater Trans 37A, 2007, p. 739.
- [70] W. Skrotzki, N. Scheerbaum, C.-G. Oertel, H.-G. Brokmeier, Satyam Suwas, L.S. Tóth, Mat Sci Forum, 503–504, 2006, p.99.
- [71] Satyam Suwas, L.S. Toth, J.-J. Fundenberger, A. Eberhardt, Solid State Phenomena, 105, 2005, p. 357.
- [72] R. Arruffat-Massion, Satyam Suwas, L.S. Tóth, W. Skrotzki, J.-J. Fundenberger, A. Eberhardt, Mat Sci Forum, 495–497, 2005, p. 839.
- [73] László S. Tóth, Roxane Arruffat Massion, Lionel Germain, Seung C. Baik, Satyam Suwas, Acta Mater, 52, 2004, p. 1885.
- [74] J.-P. Mathieu, S. Suwas, A. Ebarhardt, L.S. Toth, P. Moll. Journal of Mat. Proc. Tech. 173, 2006, p. 29–33.
- [75] S. Li, I.J. Beyerlein. Model Simul Mater Sci Engg, 13, 2005, p.509.
- [76] S. Li, I.J. Beyerlein, MAM Bourke. Mater Sci Eng A394, 2005, p.66.
- [77] S. Li, A.A. Gazder, I.J. Beyerlein, E.V. Pereloma, C.H.J. Davies. Acta Mater, 54, 2006, p. 1087.
- [78] F Dalla Torre, R Lapovok, J Sandlin, PF Thomson, CHJ Davies, EV Pereloma. Acta Mater, 52, 2005, p. 4819.
- [79] S. Li, A.A. Gazder, I.J. Beyerlein, E.V. Pereloma, C.H.J. Davies. Acta Mater, 55, 2007, p.1017.
- [80] A.A. Gazder, F. Dalla Torre, C.F. Gu, C.H.J. Davies and E.V. Pereloma, Mater Sci. Engg A415, 2006, p. 126.
- [81] J. De Messemaeker, B. Verlinden and J. Van Humbeeck, Acta Mater, 53, 2005, p. 4245.
- [82] M. Furukawa, Y. Iwahashi, Z. Horita, M. Nemoto and T.G. Langdon, Mater. Sci. Eng.A 257 (1998), p. 328.
- [83] Dong Hyuk Shin and Kyung-Tae Park, Mater. Sci. Eng. A 410–411, 2005, p. 299.
- [84] D. H. Shin, B.C. Kim, Y.S. Kim and K.-T. Park, Acta Mater. 48 (2000), p. 2247.
- [85] Y. Fukuda, K. Oh-ishi, Z. Horita and T.G. Langdon, Acta Mater. 50 (2002), p. 553.
- [86] K.-T. Park, Y.S. Kim, J.G. Lee and D. H. Shin, Mater. Sci. Eng. A293 (2000), p. 165.
- [87] Ho-Kyung Kim, Myung-II Choi, Chin-Sung Chung and Dong Hyuk Shin, Mater. Sci. Eng. A340, 2003, p.243.
- [88] Dong Hyuk Shin, Chang Woo Seo, Jongryoul Kim, Kyung-Tae Park and Wung Young Choo, Scripta Mater., 42,2000,p. 695.
- [89] Young Il Son, Young Kook Lee, Kyung-Tae Park, Chong Soo Lee and Dong Hyuk Shin, Acta Mater.,53,2005,p.3125.
- [90] A.L.M. Costa, A.C.C. Reis, L. Kestens and M.S. Andrade, Mater. Sci. Engg A406, 2005, p.27.
- [91] N. Tsuji, R. Ueki and Y. Minamino, Scripta Mater, 47, 2002, p.69.
- [92] A. Bhowmik, Satyam Suwas, R.K. Ray, D. Bhattacharjee, Acta Mater, to be communicated.
- [93] Bhowmik, Satyam Suwas, R.K. Ray, D. Bhattacharjee, in manuscript.



Dr. Satyam Suwas  
Assistant Professor  
Department of Materials Engineering  
Indian Institute of Science  
Bangalore-560 012  
India

## Chapter 20

# Development of Texture from the HAZ to Weldmetal Across the Fusion Boundary

Martin Strangwood and Claire Davis

**Abstract.** The textures and grain sizes within the heat affected zone (HAZ) and weldmetal regions of single phase bcc (Fe-3 wt% Si; 430 stainless steel) and fcc (AA5182 and 5251) alloys in spot and metal inert gas (MIG) welds have been determined using electron back-scattered diffraction (EBSD); optical and scanning electron microscopy (SEM) techniques. In all the situations studied, the grains that developed into the columnar weldmetal grains from the HAZ had a misorientation of less than  $10^\circ$  between  $\langle 100 \rangle$  and the maximum thermal gradient ( $\nabla T_{\max}$ ). The initial weldmetal columnar grain width can be related to the HAZ grain diameter at the fusion boundary by a simple relationship involving the proportion of grains with the favourable low misorientation texture in weldmetal and HAZ. This relationship does not hold throughout the whole weldmetal region due to competitive growth between columnar grains (steel) and a columnar-to-equiaxed transition (CET; Al-based alloys).

### 20.1 Introduction

A number of models, both academic and commercial, exist for the thermo-mechanical conditions associated with various welding processes [1, 2]. These are supplemented by the models for the development of microstructures and properties through the heat affected zone (HAZ) and weldmetal. The foundations for these models are the mechanisms of recovery, recrystallisation, nucleation and growth of phases and precipitates, and the dependency of these on temperature and stress.

---

M. Strangwood and C. Davis  
Phase Transformations and Microstructural Modelling Group, The University of Birmingham,  
Department of Metallurgy and Materials, Elms Road, Edgbaston, Birmingham, B15 2TT, UK.  
e-mail: m.strangwood@bham.ac.uk

The models use a range of techniques in order to describe the different aspects of HAZ and weldmetal behaviour, and their accuracy tends to be greater when applied to ferrous systems, for which more extensive databases exist.

The solid-state transformations within the HAZ altering aspects such as grain size [3, 4], phase fraction [5] and precipitate distributions [6–8], have been modelled and verified against model and real alloy systems. In addition, the solid-state transformation within the weldmetal have also been addressed [9], although these aspects often require the solidification grain size to be assumed or used as an input. Currently, this reduces the ability of models to predict weldmetal microstructure (and properties) without either the production of a trial weld or for a narrow range of conditions around a well-characterised weld structure.

Weldmetal solidification by the epitaxial growth of solid on the melted-back HAZ grains has been established for many years [10]. It is expected that there will be a dependence of weldmetal grain width on the grain size in the coarse grained (CG) HAZ, but no quantitative relationship has yet been established. The high thermal gradients established through the solidifying weldmetal result in largely columnar grains and, for cubic metallic alloys, the development of columnar grains with small mismatches between  $\langle 100 \rangle$  and  $\nabla T_{\max}$  so that the orientation of the CGHAZ grains will need to be considered as well as their size. Whilst the CGHAZ grain size and weldmetal grain width can be readily measured using appropriate etches and automated image analysis software, the traditional approach to texture determination, i.e. X-ray pole figures, has made the localised determination of texture across the fusion boundary far less easy. The development of faster and more reliable electron back-scattered diffraction (EBSD) techniques in scanning electron microscopes (SEMs) has opened up the possibility to determine local textures and so investigate relationships between HAZ and weldmetal grain sizes and orientations across the fusion boundary.

This paper will report initial studies into these relationships using single-phase ferrous and aluminium-based alloy systems.

## 20.2 Experimental

Single-phase bcc (ferritic stainless and electrical steel) and fcc alloys (two commercial Al-Mg alloys), Table 20.1, have been used in the present work in order to reduce the effects of solid-state transformation on the solidification texture. Specifically 430 (1.2 mm thick), Fe-3 wt% Si (0.25 mm thick), 5251H34 (1.2 and 2.0 mm thickness) and 5182 (1.5 mm thickness) sheets were used as typical non-heat treatable alloys with different tempers.

Initially, overlapping 1.2 mm thick 430 stainless steel and 0.25 mm thick Fe-3.5 wt% Si were spot welded using 5 mm diameter copper electrodes, 7 kA current, clamping force of 3 kN and welding times between 0.2 and 0.5 s. 1.5 mm thick 5182 sheets were spot welded using a 6 kN electrode force for 200 ms, a preheat current of 2 kA for 40 ms prior to welding at 27.5 kA for 80 ms followed by 200 ms

**Table 20.1** Compositions (wt%) of sheet alloys used in this study.

Alloy	Composition
Fe-3 wt % Si	Fe-0.002 C-3.012 Si-0.068 Mn-0.001 S-0.017 Ni-0.019 Cr
430 Stainless Steel	Fe-0.12 C-1.0 Mn-1.0 Si-18.0 Cr-0.04 P-0.03 S
AA5251	Al-1.72 Mg-0.37 Si-0.5 Fe-0.13 Mn-0.15 Cr-0.15 Cu-0.15 Zr
AA5182	Al-4.52 Mg-0.07 Si-0.2 Fe-0.32 Mn-0.006 Cr-0.04 Cu

hold before removal of the electrodes. The use of resistance spot welds with a stationary heat source allowed the grain structure and texture to be related to the variation in  $\nabla T_{\max}$ . Sheets of 2.0 mm thick 5251 measuring 450 mm  $\times$  150 mm, were welded with automated wire feed gas metal arc welding (MIG) perpendicular to the rolling direction of the work piece. Filler wire 5356 of 1.2 mm diameter was used. The welding parameter were 19.4 V, 116 A and a travel speed of 0.9 m/min. to give a heat input of 0.15 kJ/mm; argon gas shielding was used.

After solidification the welds were sectioned through the sheet thickness across the weld nugget diameter/bead width. These sections were mounted in Struers Durofix and polished to a 0.4  $\mu$ m OPA paste finish. Weldment dimensions were determined using Axiovision 4 software and an MRc5 digital camera. The specimens were then examined in a Jeol 7000 operating at 20 kV and the grain orientations from basemetal through HAZ and across the nugget were mapped using INCA EBSD software at a spacing of 600  $\mu$ m and count time of 0.2 s. The grain size variation longitudinally and through thickness in terms of length, breadth and area using KS400 software on a Zeiss Axioskop 2 microscope.

## 20.3 Results and Discussion

### 20.3.1 Fe-3 wt% Si Steel

The Fe-3 wt% Si steel was an electrical grade, which had been rolled and annealed to produce a large grain size (mean value 0.5 mm) with a strong GOSS texture (up to 40  $\times$  random in X-ray pole figures). The combination of large grain size and dominant texture for a single-phase material meant that no HAZ variation was expected.

Processing and heat treatment of the Fe-3 wt% Si steel sheet resulted in grains extending through thickness with dominant  $\langle 100 \rangle$  along and within  $\pm 20^\circ$  of the rolling direction. The large grain size and high annealing temperature used meant that there was no significant change through the HAZ up to the fusion boundary. EBSD of the weldmetal and HAZ, Fig. 20.1, showed that the weldmetal was formed by extension of a suitably oriented grain directly across the weld nugget before any growth from the other side, which corresponded to a misorientation of 15–20° from  $\nabla T_{\max}$ . The growth rate was also fast enough to be complete before surface nucleation occurred.

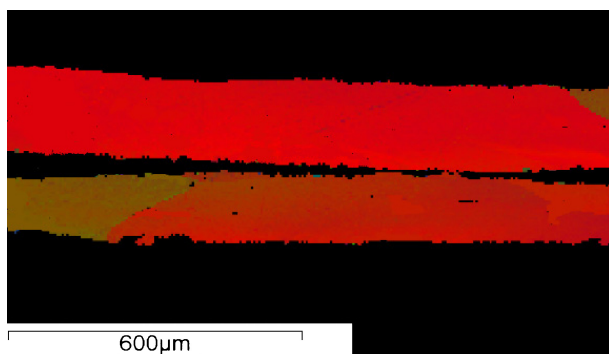


**Fig. 20.1** Texture map of spot weld and adjacent unjoined sheets of Fe-3 wt% Si.

## 20.3.2 430 Stainless Steel

### 20.3.2.1 HAZ and Weldmetal Structure

The Fe-3 wt% Si steel sheet is an extreme case of weldmetal solidification with very limited competition between HAZ grains, but shows that grains with suitably oriented  $\langle 100 \rangle$  in the HAZ can dominate the weldmetal structure. The 430 stainless steel sheet was pinch-rolled and offers a number of grains through thickness, whose orientations vary from pre-dominantly  $\{110\}/\{111\}$  at the surfaces with a greater proportion of  $\{100\}$  towards the centre of the sheet, Fig. 20.2 (a). Overall, Fig. 20.2 (b), X-ray pole figures show a weak texture, quantified (with a  $12^\circ$  spread) at 32%  $\{110\}$ , 10%  $\{100\}$  and 9%  $\{111\}$ .

The finer grain size (average equivalent circle diameter of  $55 \mu\text{m}$ ) of the 430 stainless steel sheet and stored energy from cold rolling resulted in recrystallisation and grain growth in the HAZ. Recovery is unlikely due to the rapid heating rates

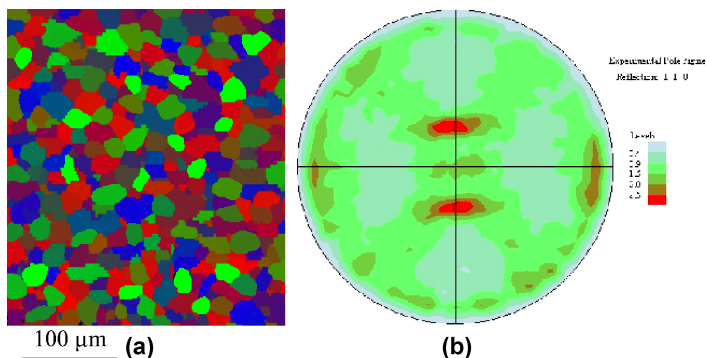


**Fig. 20.2** (a) EBSD images of grains on the ND-RD plane; and (b) (110) X-ray pole figure of 430 sheet.

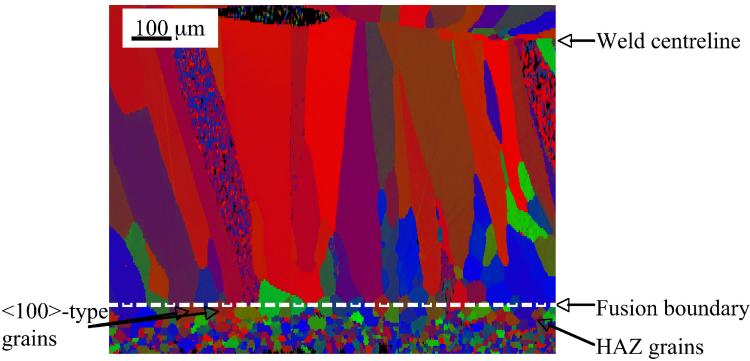


**Fig. 20.3** EBSD map of textures in HAZ and weldmetal grains for spot weld in 430 stainless steel.

experienced in spot welding. Under the electrodes there is increased driving force due to the pinch rolling pass applied, but the electrodes apply a clamping force during welding, which can alter the grain growth behaviour in these regions and is manifested as a sinking in of the sheet surface. The recrystallisation results in an increase in {100} and {111} type grain orientations at the expense of {110}, Fig. 20.3. The recrystallisation and grain growth occurring through the HAZ determine the size and orientations of the grains at the fusion boundary (FB), from which the columnar weldmetal grains develop. As seen in Fig. 20.3, these columnar grains extend throughout the weld nugget from FB to the original sheet interface. The transformations taking place through the HAZ below the electrodes is therefore:

$$\begin{aligned} \{110\}/\{111\}/\{100\} &\rightarrow \text{recrystallisation completed with grain growth} \\ &\rightarrow \{111\}/\{100\} \uparrow / \{110\} \downarrow \rightarrow \text{solidification} \rightarrow \{100\} \end{aligned}$$

The overall fractions of each texture type varies as shown by EBSD quantification using image analysis, whilst detailed examination of the precise orientations of HAZ grains shows that the grains belong to the five specific types listed in Table 20.2. These ideal grain orientations will present <100> fast solidification directions at different angles to the rolling direction and so would be parallel to the maximum thermal gradient,  $\nabla T_{\text{max}}$ , at different positions around the diameter of a spot weld nugget. Sections through the diameter of the weld nugget will represent a 2-D section

**Table 20.2** 430 stainless steel spot weld HAZ grain and angular positions from the rolling direction with minimum misorientations of <100> from  $\nabla T_{\text{max}}$ .

Grain orientation	Angle from rolling direction for minimum <100>: $\nabla T_{\text{max}}$ (°)
{100}<011>	90.0
{111}<01 $\bar{1}$ >	54.7
{111}<01 $\bar{2}$ >	30.0° out of plane at 54.7
{110}<001>	0.0
{112}<1 $\bar{1}$ 0>	15.0° out of plane at 90



where  $\nabla T_{\max}$  lies within the plane of the section. If this section is parallel to the rolling direction then  $\nabla T_{\max}$  will be parallel to the rolling direction at the ends of the weld nugget, occurring at greater angles to the rolling direction until it is normal to the rolling direction between the electrodes. For this section, Table 20.2,  $\{100\}\langle 011 \rangle$  should dominate the weldmetal grains between the electrodes where  $\nabla T_{\max}$  is normal to the rolling direction. Beyond the edges of the electrodes the angle between  $\nabla T_{\max}$  and the rolling direction decreases so that first  $\{111\}\langle 01\bar{1} \rangle$  grains become most favourable before  $\{110\}\langle 001 \rangle$  becomes most favourable at the ends of the nugget. The  $\{111\}\langle 11\bar{2} \rangle$  grains have  $\langle 100 \rangle$  misoriented too far out of the plane of  $\nabla T_{\max}$  to be viable and are not expected to be observed within the weldmetal, although the smaller out-of-plane misorientation of  $\{112\}\langle 1\bar{1}0 \rangle$  means that some grains of this orientation may be observed between the electrodes. This is summarised schematically in Fig. 20.4 (a) along with the EBSD of a 430 stainless steel spot weld in Fig. 20.4 (b). From the images in Fig. 20.4 there is general agreement between the experimentally observed columnar weldmetal grain orientations and those predicted. Whilst qualitatively correct, this mapping does not give the deviations from these ideal orientations that can form the columnar weldmetal grains.

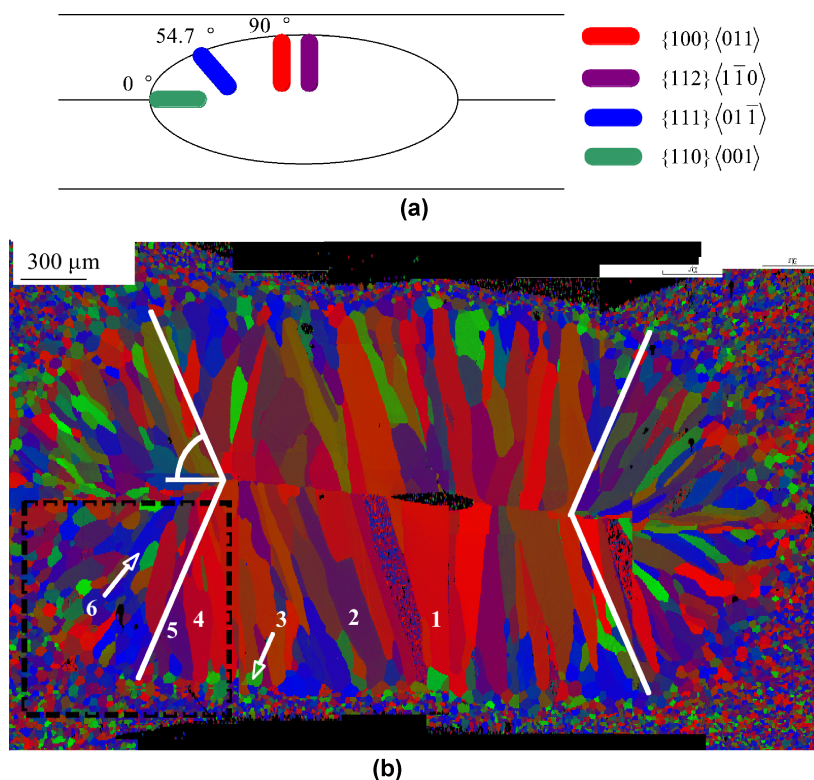


**Fig. 20.4** (a) Schematic diagram of grains expected to develop from HAZ into columnar weldmetal grains; (b) EBSD map of basemetal, HAZ and weld nugget in 430 stainless steel spot weld.

20.3.2.2 Misorientation Criterion

The higher resolution of EBSD compared with X-ray texture techniques allows the orientations of individual grains to be determined. Figure 20.5 shows a magnified image of the central nugget section shown in Fig. 20.4 (b), covering the complete range of  $\nabla T_{\max}$  directions with respect to the rolling direction. This example image has a selection of weldmetal grains numbered (7–12), which represent grains that have continued through the weld nugget (8–11) and those that have been pinched-off (7 and 12). The precise grain orientations have been determined along with the direction of  $\nabla T_{\max}$  with respect to the rolling direction at the fusion boundary, i.e. at the onset of columnar grain growth from the HAZ. From these results the minimum misorientations between  $\langle 100 \rangle$  and  $\nabla T_{\max}$  have been determined and are presented in Table 20.3.

The values in Table 20.3 show that grains with a minimum misorientation of  $< 10^\circ$  between  $\langle 100 \rangle$  and  $\nabla T_{\max}$  are able to grow across the weld nugget, whereas those with higher values get pinched-off by adjacent faster growing grains. Table 20.3 is

**Table 20.3** Orientations of grains 7–12 from Fig. 20.5 along with the minimum misorientation of  $\langle 100 \rangle$  from  $\nabla T_{\max}$ .

Grain number	Grain orientation (with respect to rolling direction)	Minimum misorientation between $\langle 100 \rangle$ and $\nabla T_{\max}$	Pinched-off?
7	$(6\bar{3}2)[56\bar{6}]$	30.0	Yes
8	$(191)[7\bar{1}2]$	8.9	No
9	$(\bar{3}\bar{2}14)[\bar{2}30]$	6.5	No
10	$(\bar{6}51)[106]$	9.0	No
11	$(1415)[13\bar{7}\bar{1}]$	2.5	No
12	$(03\bar{5})[453]$	30.0	Yes

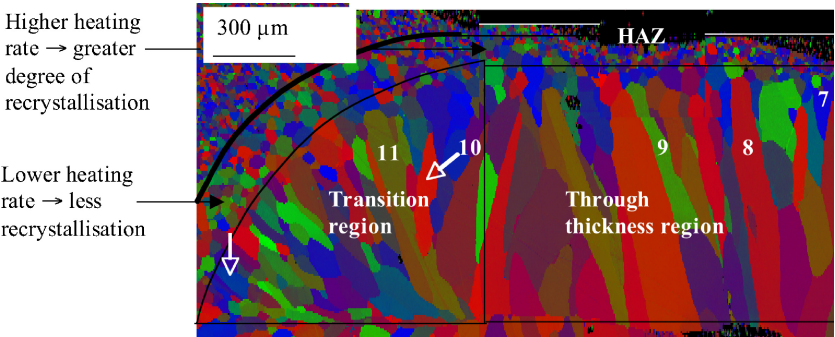


**Fig. 20.5** Upper left hand quadrant of EBSD map of 430 stainless steel spot weld showing individual grains used for grain orientation studies; grain 12 is arrowed at bottom left.

a selection of the grains characterised in this way, but, for all the grains studied, a misorientation of  $< 10^\circ$  was shown for columnar weldmetal grains that continued growing towards the original interface, whilst grains that were pinched-off had a misorientation greater than  $10^\circ$ .

### 20.3.2.3 Grain Width

The misorientation criterion established above indicates that the number of columnar weldmetal grains will be related to the number of HAZ grains with a favourable orientation. With a small range of misorientations ( $0\text{--}10^\circ$ ) that result in columnar grains then there is a dominant texture-type in the different regions (noted above) of the nugget. Between the electrodes, for example  $\{100\}$ -type textures dominate the columnar weldmetal grains. These grains develop from equiaxed HAZ grains, which show a narrow distribution of grain sizes so that it is expected that there is a relationship between the fractions of grains with the dominant texture in HAZ and in the weldmetal and the grain sizes in these regions. This has been assessed using the texture-type volume fraction and grain widths between the electrodes, Fig. 20.6; the weldmetal grain width ( $b$ ) has been predicted based on the HAZ grain size ( $a$ ), and the volume fractions of  $\{100\}$ -oriented grains in the weldmetal ( $y$ ) and HAZ ( $x$ ) by:

$$b = \left( \frac{y - x}{x} \times a \right) + a$$

As shown in Table 20.4, the prediction is initially good (up to  $300\text{ }\mu\text{m}$  from the FB), i.e. within experimental scatter, but under-predicts the width at greater depths ( $600\text{ }\mu\text{m}$  from the FB). From Figs. 20.5 and 20.6, this is due to continued lateral growth of the columnar grains away from the FB, by a mechanism that has not

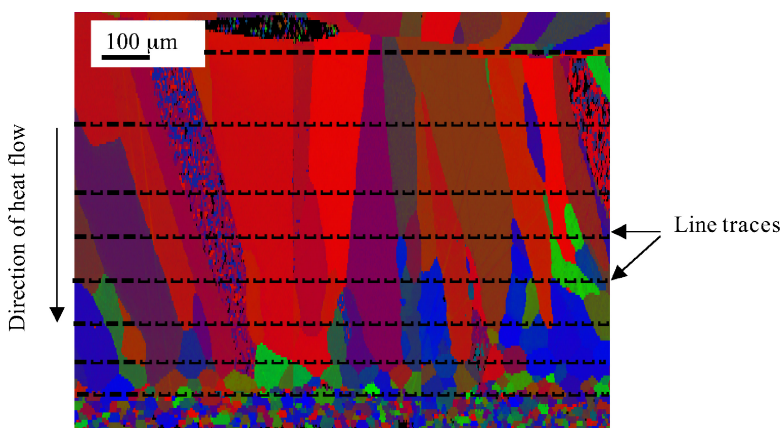


**Fig. 20.6** Region between electrodes used for linear intercept grain width measurements in 430 stainless steel spot weld nugget.

**Table 20.4** Measured texture fraction and predicted and measured grain sizes for the 430 stainless steel spot weld between the electrodes.

Distance from FB ( $\mu\text{m}$ )	% of $\{100\}$	Measured grain width ( $\mu\text{m}$ )	Predicted grain width ( $\mu\text{m}$ )
0	42	$48 \pm 12$	—
300	94	$102 \pm 26$	100
600	100	$134 \pm 41$	114

been identified yet, but when done would need to be incorporated into the simple predictive expression above.

### 20.3.3 AA5182 Spot Weld

As for the 430 stainless steel, recrystallisation and grain growth occurred within the HAZ of the AA5182 spot, which, being single phase fcc, gave grains with orientations of  $\{100\}\langle 011 \rangle$ ;  $\{123\}\langle 41\bar{2} \rangle$ ;  $\{112\}\langle 11\bar{1} \rangle$ ;  $\{110\}\langle 001 \rangle$ ; and  $\{110\}\langle \bar{1}12 \rangle$ . For the central section through the weld nugget where the 2-D nature of heat flow means that  $\nabla T_{\text{max}}$  lies in the plane of the section throughout, the first four textures give  $\langle 100 \rangle$  in the plane or only  $8^\circ$  out of plane and so would satisfy the  $10^\circ$  misorientation criterion at some point around the FB.  $\{110\}\langle \bar{1}12 \rangle$ , however, has  $\langle 100 \rangle$  at least  $35^\circ$  out of plane and so would not be expected to produce columnar weld-metal grains that develop across the nugget. The expected grain orientations around the weld nugget are shown schematically in Fig. 20.7 (a), which is approximately the pattern shown by EBSD analysis of the real spot weld in Fig. 20.7 (b). Analysis of the minimum misorientations between  $\langle 100 \rangle$  and  $\nabla T_{\text{max}}$  for the grains in Fig. 20.7 (b) confirms that the  $10^\circ$  criterion holds for this fcc example as it did for the bcc example in Sect. 3.2, Table 20.5.

**Table 20.5** Orientations of grains 1–8 from Fig. 20.7 (b) along with the minimum misorientation of  $\langle 100 \rangle$  from  $\nabla T_{\text{max}}$ .

Grain number	Grain orientation (with respect to rolling direction)	Minimum misorientation between $\langle 100 \rangle$ and $\nabla T_{\text{max}}$	Pinched-off?
1	$(121)[21\bar{4}]$	3.5	No
2	$(1301)[\bar{1}013]$	4.0	No
3	$(011)[11\bar{1}]$	45.0	Yes
4	$(\bar{1}21)[101]$	45.0	Yes
5	$(\bar{1}\bar{3}1)[127]$	8.0	No
6	$(\bar{3}\bar{4}0)[001]$	25.0	Yes
7	$(5\bar{2}\bar{3})[161318]$	4.7	No
8	$(0\bar{1}5)[051]$	2.0	No

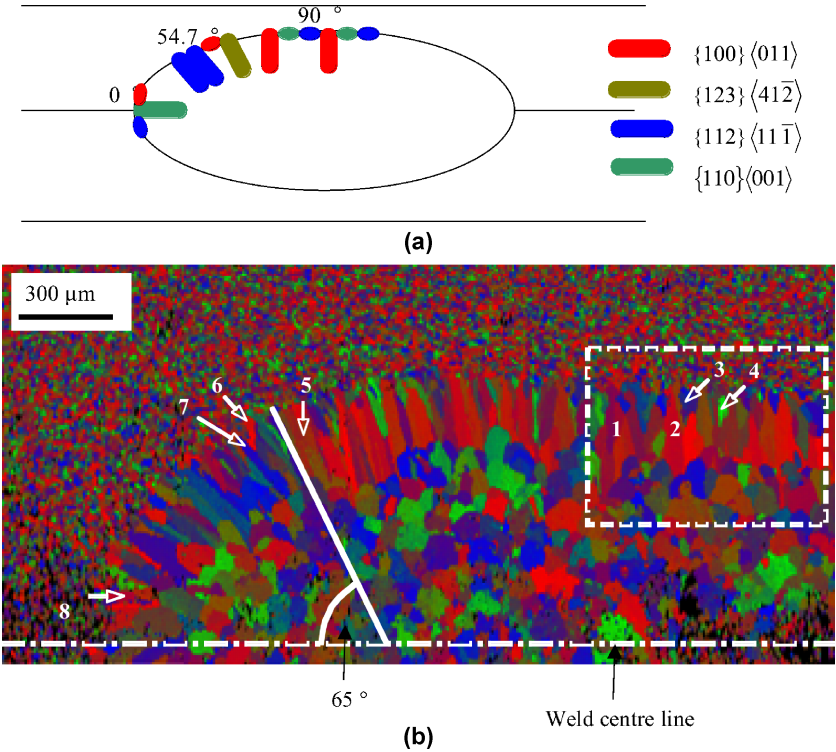


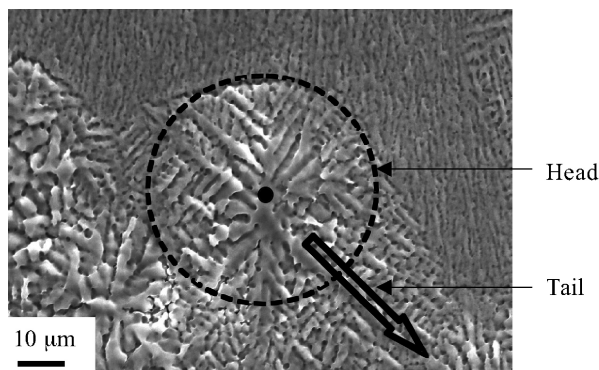
**Fig. 20.7** (a) Schematic diagram of grains expected to develop from HAZ into columnar weld-metal grains; (b) EBSD map of basemetal, HAZ and weld nugget in AA5182 spot weld.

Having confirmed the misorientation criterion, the equation above was applied to the texture proportions and grain widths on the central section between the electrodes, Table 20.6. As for the 430 stainless steel spot weld, the relationship held for columnar grain widths close to the FB (200 μm), but, further from the FB (300 μm), the proportion of {100} texture and grain width decrease. This is due to a columnar-to-equiaxed transition (CET), which is a second nucleation event that randomises texture and gives isotropic growth until impingement so that the grain size is governed by the nucleation rate rather than the HAZ structure. Examples of three nucleation events have been observed in the AA5182 spot weld, Fig. 20.8;

**Table 20.6** Measured texture fraction and predicted and measured grain sizes for the AA5182 spot weld between the electrodes.

Distance from FB (μm)	% of {100}	Measured grain width (μm)	Predicted grain width (μm)
0	28	19 ± 10	–
200	61	37 ± 14	42
300	58	26 ± 18	40

**Fig. 20.8** Example of 'comet' grain with head at CET and tail extending into equiaxed region of AA5182 spot weld.



these are (i) stray grains detached from the HAZ/columnar structure; (ii) nucleation on high stability intermetallic (Fe-rich) particles introduced into the weldpool from the melted back basemetal; and detached dendrite arms from the columnar grains. These nucleation sites only become active once the G/R ratio has decreased to a suitable level, which is why the columnar weldmetal grains in this spot weld maintain a similar length around the nugget. Insufficient examples have yet been identified and characterised to quantify or even rank these three mechanisms in order of importance. A full description of the weldmetal grain size would require the CET mechanism(s) to be identified so that the equiaxed grain size as well as the columnar grain widths can be predicted.

### 20.3.4 AA5251 MIG Weld

#### 20.3.4.1 Columnar Grains

The characterisation of the spot welds has established the solidification behaviour for static heat sources and so the analysis was extended for a moving heat source, still in single phase material, using MIG welds in AA5251 sheet. Overall, Fig. 20.9, these exhibited many features similar to those seen in the AA5182 spot weld, namely recrystallisation and grain growth in the HAZ, columnar weldmetal grains with a preferred texture growing for a certain distance from the HAZ grains; and a CET when the G/R ratio becomes favourable. Although this is a moving source weld, the travel speed was such that  $\nabla T_{\max}$  at the FB is at 80–85° to the welding direction, i.e. only 5–10° out of plane on transverse sections, Fig. 20.9 (b). The transverse section of this weld, Fig. 20.9 (a), shows that the columnar weldmetal grains along the sheet centreline are dominated by  $\{100\}$ -type textures, as expected for the HAZ grain textures at the FB ( $\{100\}\langle 001 \rangle$  and  $\{110\}\langle 001 \rangle$ , which both give  $\langle 100 \rangle$  parallel to  $\nabla T_{\max}$  along the sheet centreline). As for the spot weld nuggets outside the electrodes, the FB curves towards the surfaces of the sheet  $\{123\}\langle 41\bar{2} \rangle$ , then  $\{110\}\langle 1\bar{1}2 \rangle$  and finally  $\{112\}\langle 11\bar{1} \rangle$  become favour-



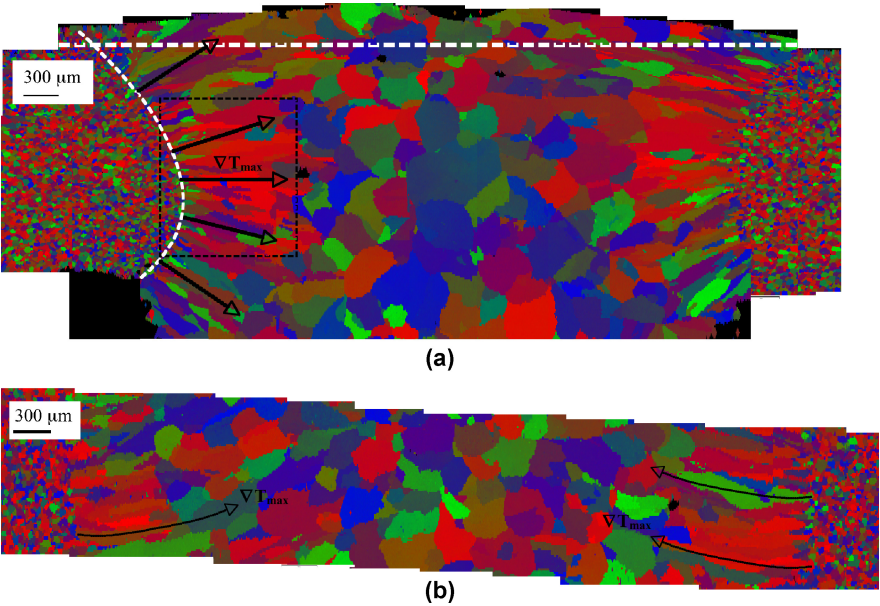


**Fig. 20.9** EBSD maps of HAZ and weldmetal regions of AA5251 MIG weld (a) transverse section and (b) plan view, showing example  $\nabla T_{\max}$ .

able and develop into columnar grains. Individual grain analysis, taking into account the out-of-plane angle of  $\nabla T_{\max}$ , confirms that grains with  $\langle 100 \rangle$  misoriented by  $< 10^\circ$  from  $\nabla T_{\max}$  develop into columnar grains, whilst those at greater misorientations are pinched off at around 300 μm from the FB.

The solidification front between the electrodes in the spot welds is planar and so there is no change interfacial area as the columnar grains grow. In the MIG weld the FB is curved and so a single grain, as it grows, would be expected to expand latterly due solely to geometric factors. The simple expression above relating grain size to  $\{100\}$  texture proportion has therefore to be modified to take the boundary curvature into account. If this is done then, for the columnar weldmetal grains, the agreement between predicted and measured grain widths is good, as illustrated for the weld centreline position in Table 20.7.

**Table 20.7** Measured texture fraction and predicted and measured grain sizes for the AA5251 MIG weld at the weld centreline.

Distance from FB (μm)	% of $\{100\}$	Measured grain width (μm)	Predicted grain width (μm)
0	40	$43 \pm 14$	—
300	47	$58 \pm 18$	61
600	56	$83 \pm 22$	89

### 20.3.4.2 CET

As for the AA5182 spot weld there is a CET in the MIG weld at 900–1000  $\mu\text{m}$  from the FB, which is associated with a randomising of the texture and an increase in grain size. This would suggest that the nucleation rate is lower in the MIG weld compared with the spot weld as the equiaxed grains in the MIG weld can grow to a larger size before impingement. The nucleation events appear to be similar in the spot and MIG welds. Secondary dendrite arm spacings (SDAS) have been measured and used to estimate local solidification rates,  $R$ , through the weld beads/nuggets, whilst SYSWELD has been used to model thermal profiles through the HAZ (verified by thermocouple measurements for the MIG weld). The thermal balance at the FB has been used to estimate the cooling rate,  $G$ , through the weld beads/nuggets. These values were used to construct the variation in  $G/R$  through the weld bead/nugget, e.g. Fig. 20.10. The  $G/R$  value at CET has then been determined for the Al-based alloy welds; 30 for AA5251 MIG weld and 7.1 for AA5182 spot weld. At the corresponding position to the AA5182 CET in the 430 stainless steel weld  $G/R$  was 10.5, which suggests that formation of equiaxed grains is feasible, but that viable nucleation sites are absent. This would support the role of heterogeneous nucleation on inclusions as the 430 stainless steel was very clean, but both Al-based alloys contained significant numbers of large Fe- and Mn-rich intermetallic particles, Table 20.8.

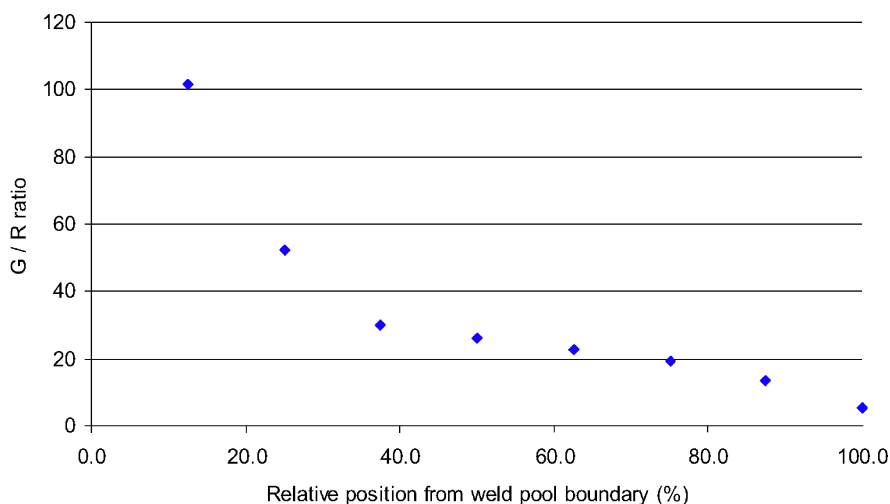


**Fig. 20.10** Variation of  $G/R$  with distance from the FB for the AA5251 MIG weld.



**Table 20.8** Average basemetal particle dimensions, area % and range of values seen.

Alloy		Area ( $\mu\text{m}^2$ )	Breadth ( $\mu\text{m}$ )	Length ( $\mu\text{m}$ )	Aspect ratio	Area %
5182	Average	$2.50 \pm 0.71$	$1.22 \pm 0.19$	$2.56 \pm 0.34$	$0.52 \pm 0.06$	$0.59 \pm 0.22$
	Range	0.51–32.33	0.57–6.32	1.00–13.06	0.21–0.91	0.46–1.94
5251	Average	$2.82 \pm 0.99$	$1.04 \pm 0.08$	$1.98 \pm 0.15$	$0.56 \pm 0.01$	$0.83 \pm 0.17$
	Range	0.54–31.24	0.52–6.20	1.16–14.31	0.20–0.91	0.54–1.01

## 20.4 Conclusions and Further Work

The grain orientation work has identified a criterion for  $\langle 100 \rangle : \nabla T_{\text{max}}$  of  $< 10^\circ$  for HAZ grains at the FB to develop into weldmetal columnar grains. Grains with misorientations greater than this value were pinched off by more favourably oriented grains.

The width of the columnar weldmetal grains has been shown to be related to the HAZ grain size at the FB and the proportion of  $\{100\}$  texture in the HAZ and weldmetal. Hence, weldmetal grain width and texture could be predicted if that in the HAZ could be measured or predicted from basemetal recrystallisation and grain growth behaviour.

These trends have been found for single phase bcc and fcc alloys for static (fcc and bcc) and moving (fcc) heat sources. The precise room temperature as-solidified textures and grain sizes will vary for allotropic alloys, but the solidified grains can be dealt with using this analysis.

Full quantification of weldmetal grain structures will need the mechanism of and parameters for CET to be defined, whilst the mechanism of lateral columnar grain growth also requires determination.

## References

- [1] Ø. Grong, "Metallurgical Modelling of Welding", The Institute of Materials, London, 1994.
- [2] G. Mangialenti, and T. Carter, "New capabilities of the software product SYSWELD for the prediction of welding residual stresses and distortions" (Report, SYSTUS Intl, ESI Group), 2004.
- [3] I. Hrivnak, in "Mathematical Modelling of Weld Phenomena, 2", H. Cerjak (ed), The Institute of Materials, London, 1995, pp 162–171.
- [4] M.F. Ashby and K.E. Easterling, *Acta Metall.*, **30**, 1969, p 1982.
- [5] J.M. Vitek and S.A. David, in "Mathematical Modelling of Weld Phenomena, 4", H. Cerjak (ed), The Institute of Materials, London, 1998, pp 321–331.
- [6] O.R. Myhr, Ø. Grong, H.G. Fjær and C.D. Marioara, *Acta Metall. Mater.*, **52**, 2004, pp 4997–5008.
- [7] O.R. Myhr and Ø. Grong, *Acta Metall. Mater.*, **39**, 1991, pp 2703–2708.
- [8] H.R. Shercliff and M.F. Ashby, *Acta Metall. Mater.*, **38**, 1990, pp 1789–1802.

- [9] H.K.D. H. Bhadeshia and L.-E. Svensson, in “Mathematical Modelling of Weld Phenomena”, H. Cerjak and K.E. Easterling (eds), The Institute of Materials, London, 1993, pp 109–180.
- [10] G.J. Davies and J.G. Garland, *Int. Met. Rev.*, **20**, 1975, pp 83–106.



Martin Strangwood  
Professor  
Phase Transformation and Microstructural  
Modelling Group  
Department of Metallurgy and Materials  
University of Birmingham  
UK



# Chapter 21

## Evolution of Recrystallization Texture in AISI300 Series Austenitic Stainless Steels After Cold Rolling to Large Strain

Sandip Ghosh Chowdhury, P. Sahu, B. Mahato, and P.K. De

**Abstract.** The present paper deals with the evolution of texture in austenitic stainless steels during annealing after 95% cold rolling. After 95% cold rolling, the texture is mainly of the brass type  $\{110\} \langle 112 \rangle$  along with a scatter towards the S orientation  $\{123\} \langle 634 \rangle$  and Goss orientation  $\{011\} \langle 100 \rangle$ . Weak evidence of Cu component is observed at this high deformation level. During annealing, recovery is observed before any detectable recrystallization. After recrystallization, the overall texture intensity was weak; however, there are some discernible texture components. There was no existence of the brass component at this stage. Major components are centered on Goss orientation and Cu component  $\{112\} \langle 111 \rangle$  as well as the BR component  $\{236\} \langle 385 \rangle$ . Also, there are some few orientations which come up after recrystallization i.e.  $\{142\} \langle 2 -1 1 \rangle$  and  $\{012\} \langle 221 \rangle$ . With increase in annealing temperature the textural evolution shows emergence of weak texture with another new component i.e.  $\{197\} \langle 211 \rangle$ . The evolution of texture was correlated with the deformation texture through twin chain reaction.

### 21.1 Introduction

Austenitic stainless steels are important technological material for nuclear power industry, petrochemical and fertilizer industries. This grade of steels is different from other grades of this series due to addition of Mo ( $\sim 2.5\text{wt}\%$ ). This addition of Mo is known to improve both corrosion resistance and hot deformation (creep)

---

S.G. Chowdhury, P. Sahu, B. Mahato, and P.K. De  
Materials Science & Technology Division, National Metallurgical Laboratory, Jamshedpur,  
831007 India  
e-mail: sgc@nmlindia.org

behaviour. Mo in solid solution acts as a favourable element in reducing dislocation mobility. This grade of steel has a high work-hardening and that results in excellent mechanical properties during deformation. High work-hardening is related to stacking fault energy (SFE) of the material and magnitude of SFE controls the ease of cross-slip and thus, different deformation mechanisms can be activated at different stages of deformation [1, 2].

Cold rolling textures of FCC materials are very much dependent on the composition and temperature of deformation. One of the major metallurgical parameters that govern the above two factors is SFE. In case of non-ferrous alloys, there are a lot of work on the effect of SFE on the development of texture and microstructure. However in comparison, not much work has been reported on steels. Most austenitic steels, such as austenitic stainless steels [3], high manganese Hadfield steels [4] and high manganese TWIP steels (Fe-30Mn-3Al-3Si) [5] have low to moderate SFE and therefore, tend to form extended stacking faults, deformation twins and planar dislocation structures. These different lattice defects strongly influence the stress-strain response and the evolution of the texture during cold rolling.

The deformation textures formed by cold rolling in FCC metals can be categorized into two groups: high SFE leads to a copper (or pure metal) type texture whereas lower SFE induces a brass (or alloy) type texture [6]. The texture transition from the copper type to the brass type is a very much controversial subject and various microscopic mechanisms have been put forward to account for the copper type (normal slip induced deformation) as well as for the brass type texture (mechanical twinning, shear banding).

Recrystallization of deformed metallic materials is accomplished by the formation of new undeformed grains in the as-deformed microstructures – which is commonly denoted as ‘nucleation’ and their subsequent growth into the neighbouring deformed matrix. These mechanisms are characterized by the formation and motion of high angle grain boundaries, recrystallization leads to a change in the crystallographic texture. While the rolling texture changes with decreasing stacking fault energy (SFE), the corresponding recrystallization textures usually change more drastically.

In the present paper, an investigation has been made to study the textural evolution during cold rolling and recrystallization for medium-low materials. Two 300 series steel, namely AISI 304L and AISI 316L have chosen for this purpose. The SFE of these materials are  $\sim 18 \text{ mJ/m}^2$  for 304L and  $64 \text{ mJ/m}^2$  for 316L. Therefore, considering the SFE of the materials, it is aimed to investigate the evolution of recrystallization texture in these two materials with similar deformation texture.

## 21.2 Experimental Procedure

The chemical compositions of the materials in the hot rolled condition are given in Table 21.1. Samples were cut from the hot rolled and annealed plate, and cold

**Table 21.1** Chemical composition of austenitic stainless steel (wt.%).

	C	Si	Mn	Cr	Ni	Mo	Fe
AISI 304L	0.06	0.75	1.3	18.1	8.4	–	Bal.
AISI 316L	0.018	1.13	1.75	17.1	8.51	1.82	balance

rolled at room temperature in a two high rolling mill unidirectionally under the lubrication of machine oil upto the final thickness of  $t=0.4$  mm ( $\epsilon=2.5$ ). The heat treatment of the cold rolled samples had been carried out under isothermal annealing condition from 500 to 1000°C at an interval of 100°C. For each case, the samples were quenched in water after annealing. Temperature was maintained with an accuracy of  $\pm 2^\circ\text{C}$  in all cases.

After annealing, texture analysis was performed at the normal direction (ND) (i.e. on the sheet plane) with Co-K $\alpha$  radiation. Texture was measured on an area of  $24 \times 14$  mm<sup>2</sup> with a flat surface that had been prepared by mechanical polishing and grinding. From three incomplete pole figures ( $0^\circ \leq \alpha \leq 80^\circ$ ), i.e.  $\{111\}$ ,  $\{200\}$  and  $\{220\}$  for 316L and  $\{200\}$ ,  $\{220\}$  and  $\{311\}$  for 304L, ODFs were calculated after correction without imposing any restriction on symmetry, that is assuming triclinic sample symmetry by ADC method [7]. All the ODFs shown here are corrected for the elimination of ghost error.

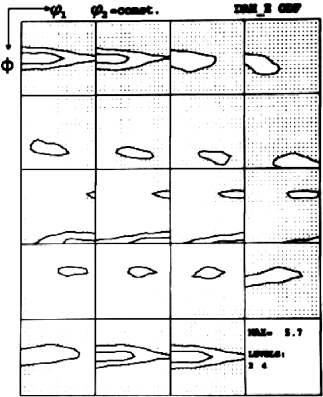
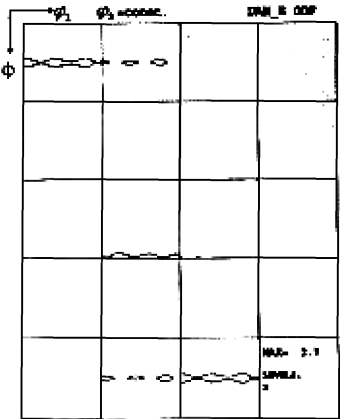
## 21.3 Results

### 21.3.1 Deformation Texture

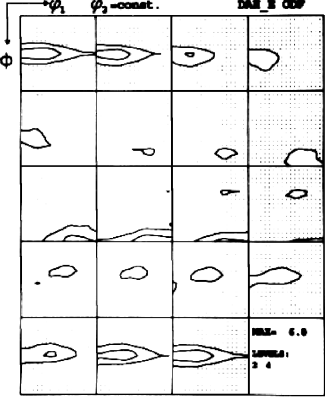
#### 21.3.1.1 316L

The ODF of the hot rolled and annealed sample is shown in Fig. 21.1. There is a weak orientation scatter along the  $\alpha$ -fiber. ODFs upto 40% cold reduction showed the presence of Cu orientation  $\{112\} \langle 111 \rangle$  and S orientation  $\{123\} \langle 634 \rangle$  along with the brass component  $\{110\} \langle 112 \rangle$  with a spread towards the Goss orientation  $\{011\} \langle 100 \rangle$  (Fig. 21.2 (a)). After 60% reduction, the Cu component diminishes whereas the brass component and the Goss component become stronger (Fig. 21.2 (b)). Also, at this stage, a scatter around the twin Cu orientation  $\{554\} \langle 225 \rangle$  can be noted. ODF of the 95% cold rolled sample shows two major components: the brass orientation  $\{110\} \langle 112 \rangle$  along with a scatter towards the Goss orientation  $\{011\} \langle 100 \rangle$  and the S orientation  $\{123\} \langle 634 \rangle$  (Fig. 21.2 (c)). Presence of the Cu component  $\{112\} \langle 111 \rangle$  can also be seen with a little volume fraction. The overall texture can be represented as Brass-type texture. A key graph indicating the position of the texture components is represented in Fig. 21.2 (d) [8].

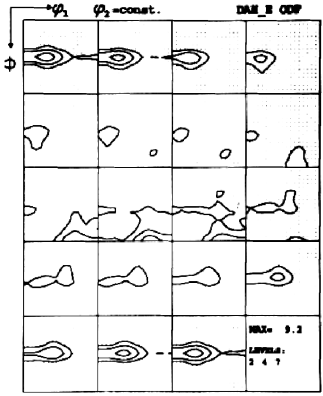
Fig. 21.1 ODF of the hot rolled and annealed AISI 316L sample.



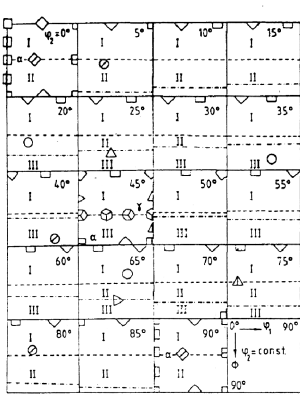
(a)



(b)



(c)



(d)

symbol- {hkl} <uvw> - name

△	{112}	{111}	- C
○	{123}	{634}	- S
◇	{011}	{211}	- B
□	{011}	{100}	- G
△	{255}	{511}	- TC
△	{111}	{112}	- Y
△	{111}	{110}	- Z
◇	{001}	{110}	- rotW
□	{011}	{011}	- rotG
◇	{168}	{211}	- S/B
◇	{025}	{100}	- WRD
□	{001}	{100}	- W
◇	{112}	{110}	- A

Fig. 21.2 ODFs of samples after cold rolling (a) 40%, (b) 60%, (c) 95% and (d) ideal ODF.

To elucidate more into the textural evolution with the degree of cold reduction, various fibers are plotted and presented in Fig. 21.3. Figure 21.3 (a) representing  $\alpha$ -fiber shows slow increase in the intensity of the Goss  $\{011\} \langle 100 \rangle$  upto 90% reduction. After 60% reduction, the orientation near  $\{110\} \langle 112 \rangle$  becomes prominent and it becomes strongest after 90% reduction. The brass component is very much anisotropic with a scatter towards Goss. It can be seen that there is shift of the brass component from its ideal position at  $\phi_1 = 35^\circ$ . The corresponding orientation changes can be visualized by plotting the densities of orientations with a common  $\langle 110 \rangle$  transverse direction i.e.  $\tau$ -fiber (Fig. 21.3 (b)). The Cu orientation, at  $\phi = 35^\circ$ , in this fiber shows a gradual decrease with the degree of cold reduction.

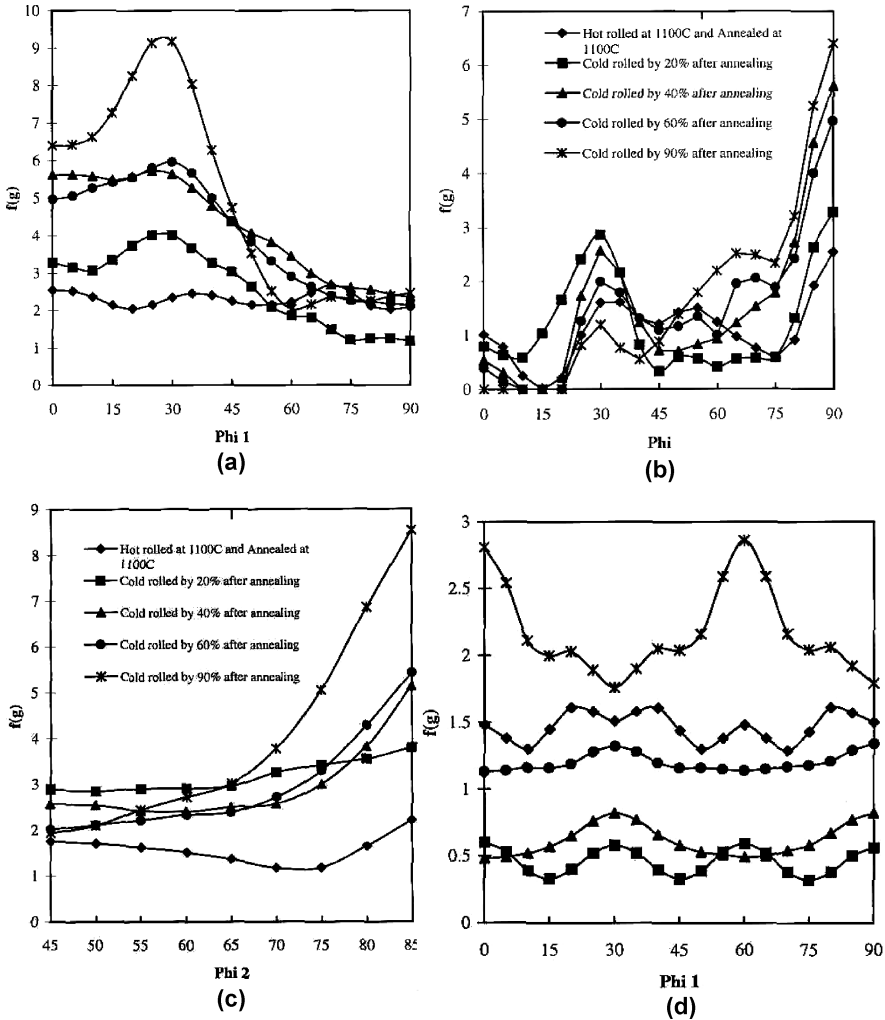
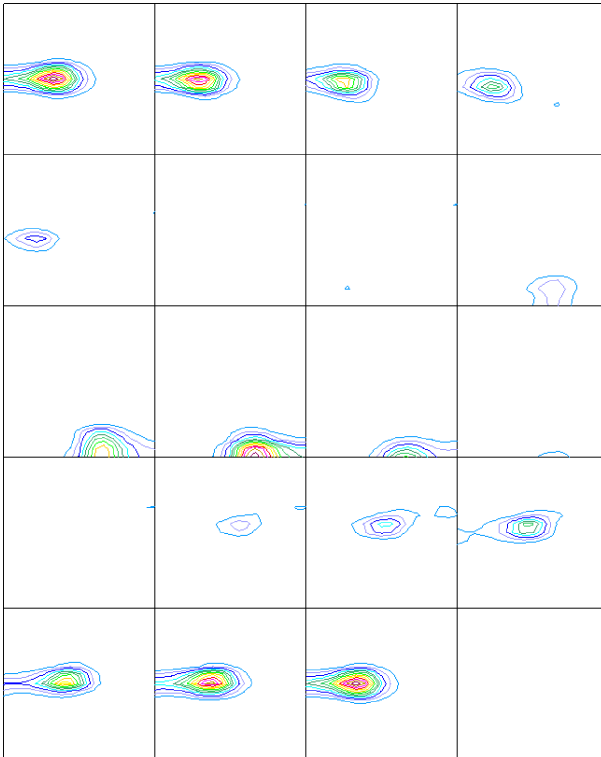


Fig. 21.3 Fibers developed during rolling (a)  $\alpha$ -fiber; (b)  $\tau$ -fiber, (c)  $\beta$ -fiber and (d)  $\{111\}$  fiber.



The  $\{111\} \langle 112 \rangle$  orientation which is a characteristic intermediate orientation lies at  $\varphi = 55^\circ$  and can be seen after 40% cold reduction. The twin Cu orientation which lies at  $\varphi = 75^\circ$  shows its prominence from 40% cold reduction onwards. The  $\beta$ -fiber plot shown in Fig. 21.3 (c) shows that the ratio of copper to brass components decreases drastically from 1:2 after 40% reduction to 1:4 after 90% reduction. The reduction in the intensity of the Cu orientation which initiates the formation of the brass-type texture is known to be caused by mechanical twinning by which copper orientation is transformed to a position near the Goss orientation [9]. This apparently contributes to the further increase of the Goss orientation. These new orientations as well as the orientations that develop due to twinning on further deformation lie outside the  $\alpha$  and  $\beta$  tubes. They are situated on a so-called  $\gamma$ -fiber corresponding to  $\langle 111 \rangle$  parallel ND and stretching along  $\varphi_1$  at  $\varphi = 55^\circ$  and  $\varphi_2 = 45^\circ$  from  $\{111\} \langle 112 \rangle$  ( $\varphi_1 = 30^\circ/90^\circ$ ) to  $\{111\} \langle 110 \rangle$  ( $\varphi_1 = 0^\circ/60^\circ$ ) (Fig. 21.3 (d)). A close look on the  $\{111\}$  fiber shows presence of a weak fiber upto 60% cold reduction. Initially, the intensity along the fiber decreased quite a lot; however, after 90% reduction, some other orientation is formed i.e.  $\{111\} \langle 110 \rangle$  along with the  $\{111\} \langle 112 \rangle$ . From the  $\tau$ -fiber it can be pointed out that Goss orientation increases with the degree of cold reduction. The formation of this Goss component coincides with the evolution of the  $\{111\}$  fiber at this deformation level.



**Fig. 21.4** ODF of 95% cold rolled AISI 304L steel.

### 21.3.1.2 304L

ODF of the austenite phase after 95% cold rolling has been presented in Fig. 21.4. The major components are brass orientation  $\{110\} \langle 112 \rangle$  along with a scatter towards the Goss orientation  $\{011\} \langle 100 \rangle$  and the S orientation  $\{123\} \langle 634 \rangle$ . The overall texture can be represented as Brass-type texture.

### 21.3.2 Microstructure

316L Samples after 20% cold rolling show inhomogeneous presence of slip bands in some of the grains. With the increase in rolling reduction, formation of bands is pronounced. After 90% reduction and onwards, the grains are elongated to such an extent that it becomes a fibrous structure indicating extensive homogeneous deformation (Fig. 21.5 (a)). Figure 21.5 (b) and 21.5 (c) show presence of shear bands within this fibrous structure. The darkly etched shear bands signify localized non-homogenized deformation. The length of these bands remains within the level of grain scale in few cases. Extension of these bands over several grains can also be seen in few cases (marked with arrow in Fig. 21.5 (c)).

Deformation after 40% cold reduction shows accumulation of dislocations in the form of bands. It might be the beginning of the formation of lamellar structure. After 60% deformation, proficiency of twinning increases (Fig. 21.6). Twinning as primary deformation mechanism leads to nanoscale layered structures, because of the small thickness of the twins ( $\sim 100$  nm). At large strains it is difficult to observe the active deformation mechanisms in the grains because of the elongation and the fragmentation of the grains.

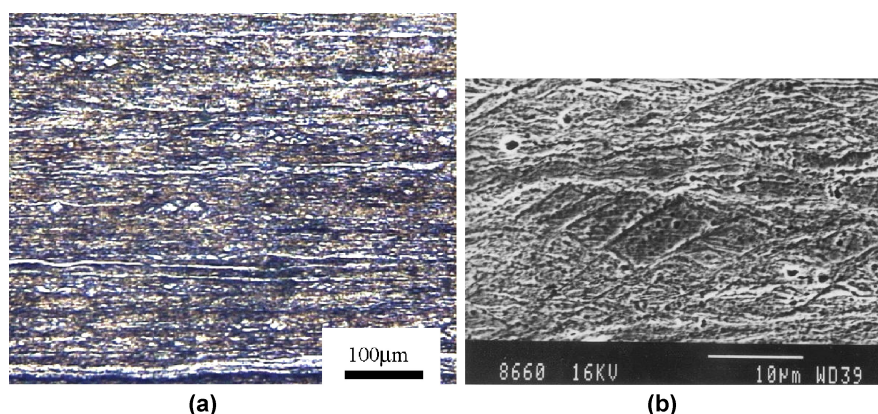


**Fig. 21.5 (a), (b)** (a) Lamellar structure after 95% cold rolling; (b) formation of copper-type shear bands within grains.

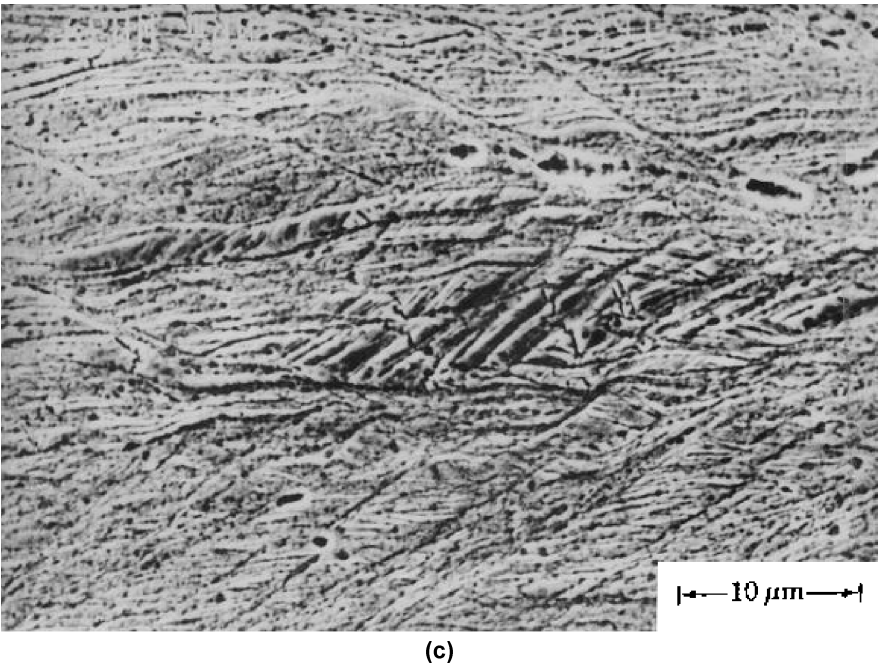


**Fig. 21.5 (c)** Formation of brass-type shear bands across the grains.

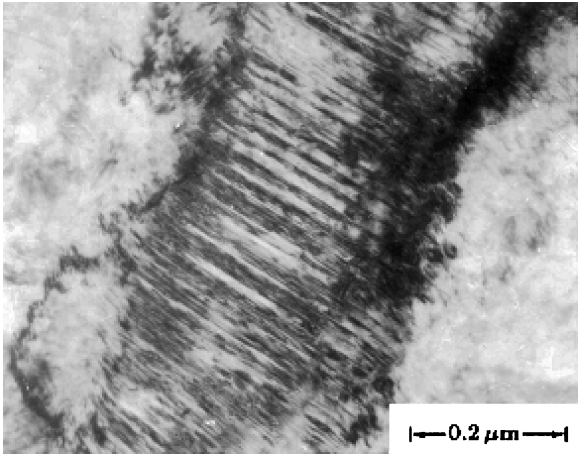


**Fig. 21.6** Formation of twins after 95% cold rolling.

### 21.3.3 Recrystallization

#### 21.3.3.1 316L

ODFs of samples annealed isothermally at various temperatures are presented in Fig. 21.7. In comparison to the cold rolled state, there is not much change in the texture components even after annealing at 700°C (Fig. 21.7 (a)). The rolling texture is retained as annealing texture. The intensity of the texture components is also similar in nature. Evolution of new texture components is observed only after annealing at 800°C (Fig. 21.7 (b)). There is a drastic change in the evolution of textural components at this stage along with the drop in the overall intensity of the texture (nearly half compared to that of the previous). There is no existence of the brass component and S component at this stage. Major components are centered around Goss orientation and ideal Cu component  $\{4\ 4\ 11\} \langle 11\ 11\ 8 \rangle$  as well as the BR component  $\{236\} \langle 385 \rangle$  at  $\phi_1, \phi, \phi_2 = 80^\circ, 31^\circ, 35^\circ$ , the typical recrystallization texture component observed in materials with low SFE. Also, there are intensity maxima at various few points in the ODF: one orientation at  $\phi_1, \phi, \phi_2 = 35^\circ, 68^\circ, 15^\circ$  which is equivalent to  $\{142\} \langle 2\ -1\ 1 \rangle$ . In addition to those components, there are other components i.e.  $\sim \{011\} \langle 2\ -2\ 1 \rangle$  and  $\{213\} \langle -1\ -1\ 1 \rangle$  at  $\phi_1, \phi, \phi_2 = 80^\circ, 34^\circ, 65^\circ$  which are little deviated from the ideal texture components. The orientation  $\{011\} \langle 2\ -2\ 1 \rangle$  is the P orientation which is related to the S orientation through a  $40^\circ \langle 111 \rangle$  relationship.  $\{142\} \langle 2\ -1\ 1 \rangle$  or  $\sim \{114\} \langle 211 \rangle$  component is the first order twin of Goss orientation. Such orientations have also been described as minority components in the recrystallization textures of other Cu alloys, especially in Cu alloys with medium contents of Zn, Al or Ge [10, 11–16]. Later with increase in annealing temperature, the sharpness of these orientations increases relatively; however, the overall texture intensity remains same. These components can be seen in Fig. 21.7 (c), which is the ODF of the sample annealed at 1000°C for 1 hr. In this figure, apart from the other orientations, there is a component  $\sim \{197\} \langle 211 \rangle$  at  $\phi_1, \phi, \phi_2 = 20^\circ, 45^\circ, 80^\circ$ . Therefore, with increase in annealing temperature, the textural evolution shows emergence of weak texture with a few new components.

To elucidate more about the emergence of new textural components during isothermal annealing, fibers are plotted in Fig. 21.8.  $\alpha$ -fiber presented in Fig. 21.8 (a) shows strengthening of the brass component after annealing at 700°C. This might be due to recovery of the deformed structure, which in turn reduces the scatter around the ideal component at these orientated regions. After annealing at 800°C, there is disappearance of brass component after recrystallization and a gradual decrease in the intensity of Goss component. It can be better represented as Bs/G component after annealing at 800°C.  $\tau$ -fiber plot (Fig. 21.8 (b)) shows some unusual changes. Component  $\{4\ 4\ 11\} \langle 11\ 11\ 8 \rangle$  at  $\phi_1, \phi, \phi_2 = 90^\circ, 27^\circ, 45^\circ$  appears after annealing at 800°C. This component is  $8^\circ$  away from the Cu orientation  $\{112\} \langle 111 \rangle$ . After annealing at 1000°C, this component rotated around TD and is found at nearly exact Cu orientation i.e.  $\phi_1, \phi, \phi_2 = 90^\circ, 35^\circ, 45^\circ$ . This component was observed in the deformed state with a very limited intensity. One component  $\{111\} \langle 112 \rangle$ , which was present at the 95% deformed texture disappears after annealing at 700°C whereas the

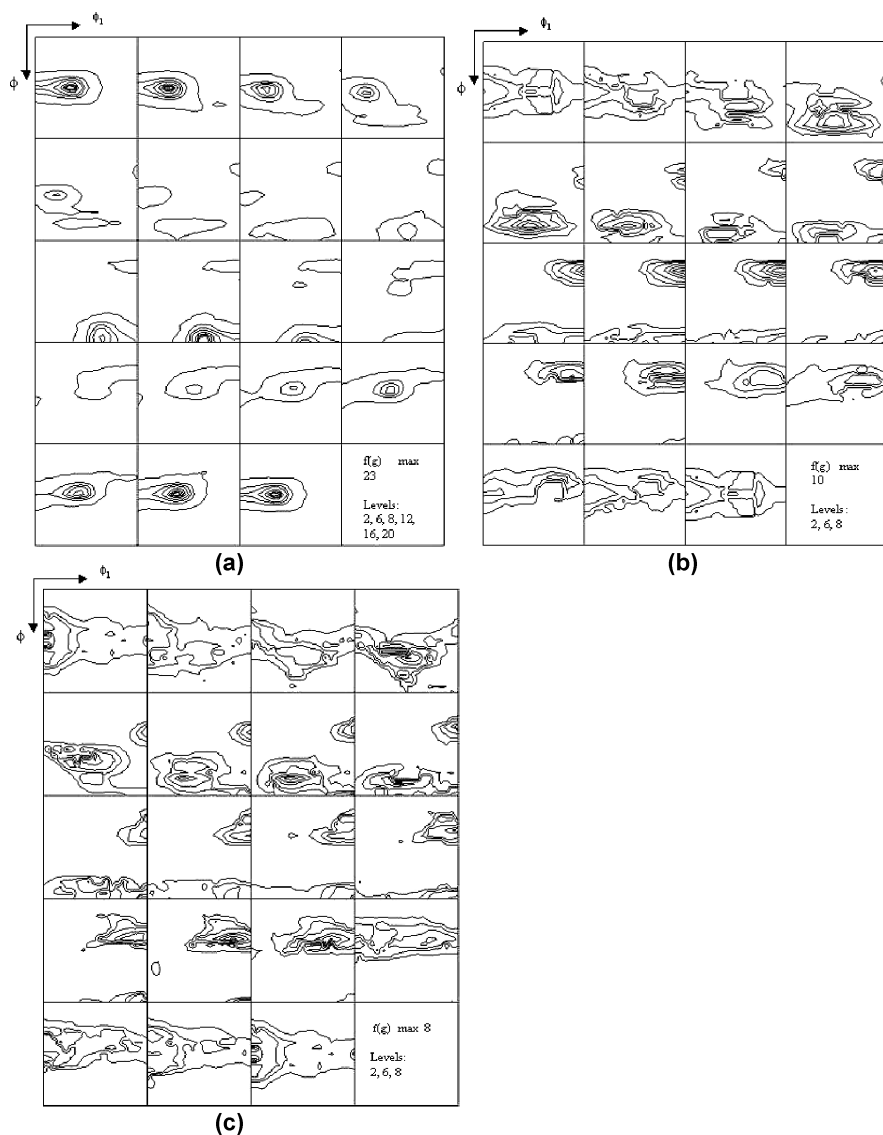


**Fig. 21.7** ODFs of 95% cold rolled and annealed samples of 316L: (a) 700°, (b) 800° and (c) 1000°C.

intensity of the Goss component gradually decreases with the increase in annealing temperature. The  $\{111\}$  fiber plot shows complete dissolution of this fiber after recrystallization. The  $\beta$ -fiber plot presented in Fig. 21.8 (c) shows that samples annealed upto 700°C are having nearly similar nature to that of the rolled sample. After annealing at 800°C, the  $\beta$ -fiber becomes nearly homogeneous; however, after annealing at 1000°C, there are orientations at  $\phi_1, \phi, \phi_2 = 70^\circ, 35^\circ, 60^\circ$  i.e.

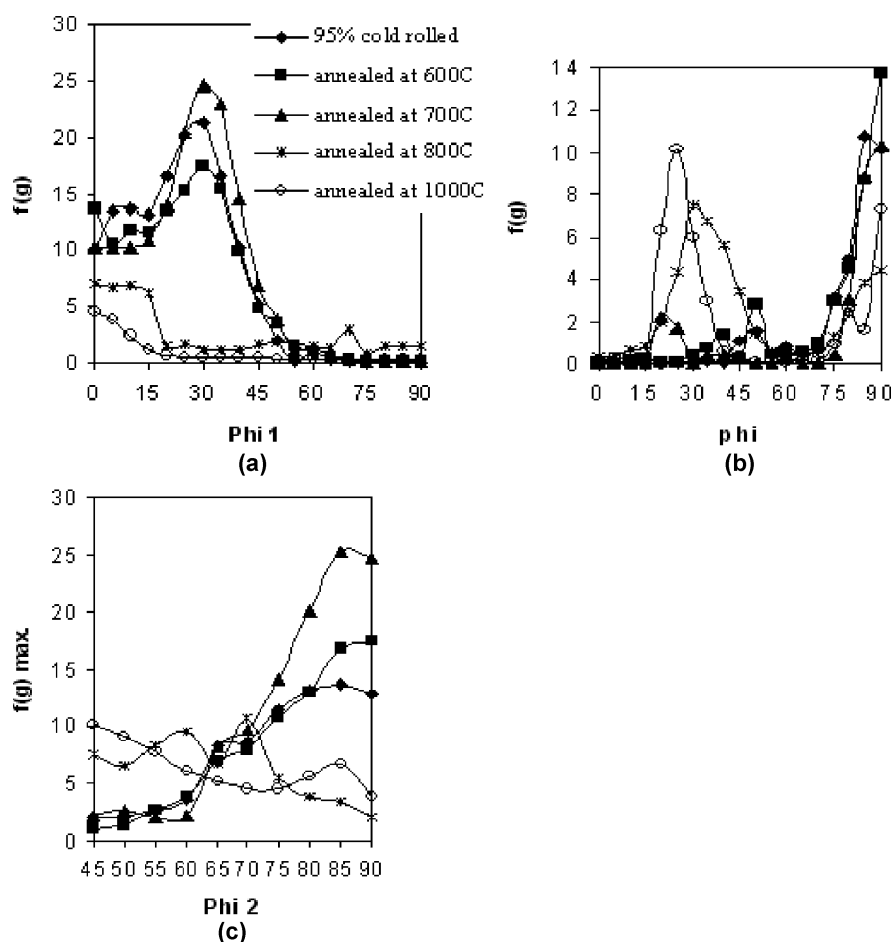


Fig. 21.8 Evolution of fibers during annealing : (a)  $\alpha$ -fiber; (b)  $\tau$ -fiber and (c)  $\beta$ -fiber.

$\sim \{213\} \langle -1 -1 1 \rangle$  along with orientation near Cu orientation. There is some intensity at the brass position; however these are due to presence of near  $\alpha$ -fiber orientation.

Hence, from the above analysis it can be pointed out that there is a continuous evolution of the texture components depending upon the temperature of annealing as well as the extent of recrystallization and thereafter.

### 21.3.3.2 304L

The temperature of annealing is varied from 600°C to 1000°C; these temperatures were chosen to differentiate the textural evolution in retained austenite and reverted austenite from martensite. At lower temperatures, the martensite phase is transform-

**Fig. 21.9** Microstructure showing formation of twins in the recrystallized grain.



ing to austenite phase and it has been observed that reversion is nearly complete within 700°C [17]. Recrystallization of austenite phase takes place at 800°C. A typical microstructure of a recrystallized grain with twins can be seen within the recovered bands with subgrains after annealing at 700°C (Fig. 21.9). The evolution of texture during annealing of the 95% cold rolled samples is presented in Fig. 21.10. Figure 21.10 (a) shows that there is no change in the texture components after annealing upto 700°C. After annealing at 800°C, there are changes in the texture components as well as there is a drop in the overall texture intensity (nearly half compared to that of the previous) (Fig. 21.10 (b)). There is large scatter and smearing of the brass component and S component. Major components are centered on Goss orientation and ideal Cu component  $\{4\ 4\ 11\} \langle 11\ 11\ 8 \rangle$  as well as the BR component  $\{236\} \langle 385 \rangle$  at  $\phi_1, \phi, \phi_2 \equiv 80^\circ, 31^\circ, 35^\circ$ , the typical recrystallization texture component observed in materials with low SFE. Also, there are intensity maxima at various

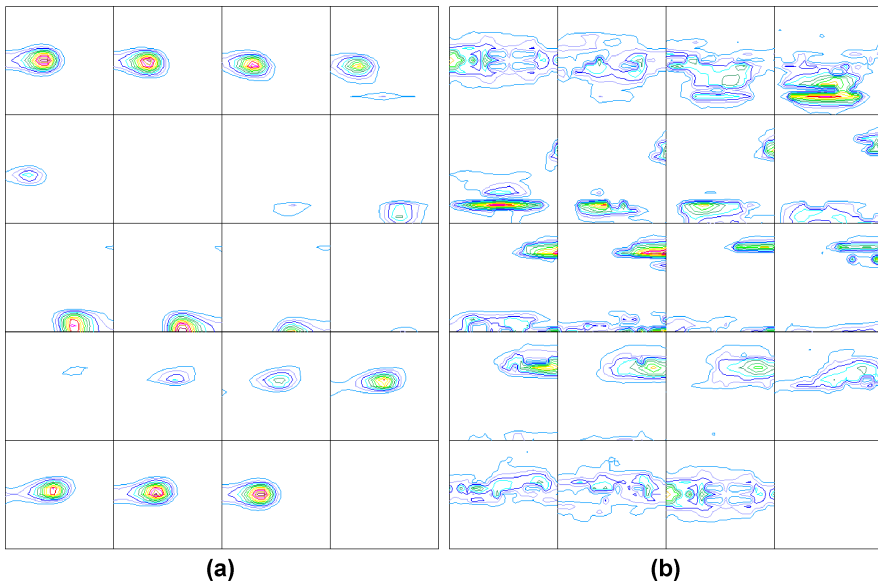
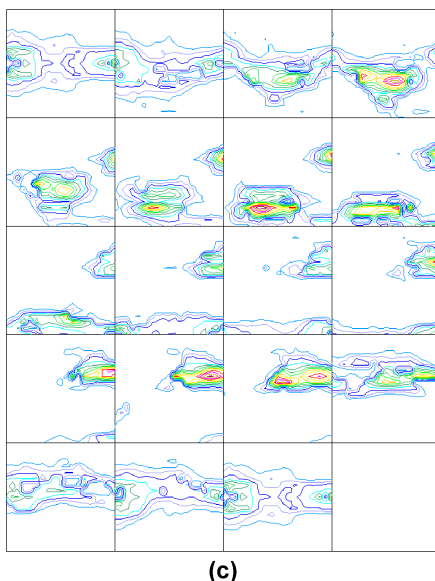


**Fig. 21.10 (a), (b)** ODFs after annealing 95% cold rolled sample: (a) 700°, (b) 800°C.

**Fig. 21.10 (c)** ODFs after annealing 95% cold rolled sample: (c) 1000°C.



few points in the ODF: one orientation at  $\phi_1, \phi, \phi_2 \equiv 45^\circ, 70^\circ, 15^\circ$ , which is equivalent to  $\{142\} \langle 2 -1 1 \rangle$ . In addition to those components, there are other components i.e.  $\sim \{011\} \langle 2 -2 1 \rangle$  and  $\{213\} \langle -1 -1 1 \rangle$  at  $\phi_1, \phi, \phi_2 \equiv 80^\circ, 35^\circ, 65^\circ$  which are little deviated from the ideal texture components. There is evidence of rotated Goss component along with a scatter around P component along the  $\alpha$ -fiber. Later with increase in annealing temperature, the sharpness of these orientations increases relatively; however, the overall texture intensity remains weak. These components can also be seen in Fig. 21.10 (c), which represents the ODF of the sample annealed at 1000°C for 1 hr. The  $\{4 4 11\} \langle 11 11 8 \rangle$  component is observed to be shifted towards the Cu orientation  $\{112\} \langle 111 \rangle$ . In this figure, apart from the other orientations, there is a component at  $\phi_1, \phi, \phi_2 \equiv 30^\circ, 80^\circ, 30^\circ$ , which lies within the scatter of Cu component  $\{112\} \langle 111 \rangle$ . Therefore, with increase in annealing temperature, the textural evolution shows emergence of weak texture with a few new components.

## 21.4 Discussion

As evident above, the textural evolution after recrystallization is quite different compared to that of the deformed texture. In both the materials, the deformation texture is similar. In 304L, there was formation of martensite ( $\alpha'$ ) after cold rolling and that gets transformed back to austenite in the course of reverse transformation.

Donadille et al. [18] observed retainment of rolling texture components after recrystallization; although they observed preferential recrystallization at the shear band region. This behaviour is unusual in a sense that generally depending on the SFE of the material, evolution of annealing texture from the rolling texture be-



haves differently. In high SFE material, Cube texture  $\{100\} \langle 001 \rangle$  develops after annealing from the Cu-type rolling texture. In medium and low SFE materials, the brass-type rolling texture transforms to a complex pattern of orientations, which are centered on brass recrystallization texture (BR)  $\{236\} \langle 385 \rangle$  [8]. With continuous changes in rolling texture with decreasing SFE, the corresponding recrystallization texture changes drastically [15]. In most cases, a good twin relationship exists to the rolling texture components (Fig. 21.11 (a)). The recrystallization texture can be interpreted as a random nucleation process in the inhomogeneous structure with a few new orientations through recrystallization twinning; and the resulting change in rolling texture from the copper to the brass type results a different condition for the growth process. The resulting texture may evolve by a widely scattered Brass/R (BR) component. It has a preferred  $40^\circ \langle 111 \rangle$ -orientation relationship to the main rolling texture components (Fig. 21.11 (b)). It forms by a twinning process out of the available spectrum of rolling texture orientations between Goss and Brass orientation.

BR orientation is known to develop by second order twinning if it is assumed that the starting orientation is  $\sim \{110\} \langle 115 \rangle$  [8]. This orientation,  $\{110\} \langle 115 \rangle$  lies in the rolling texture spread of Brass and Goss components. Therefore, the emergence of this BR component may be due to micro growth selectivity. This observation is also in line with other observations in 70:30 brass [19,20] and 78:22 brass [21]. In highly alloyed brass the complete recrystallization texture i.e. the BR orientation along with the minor components of the  $\alpha$ -fiber orientations, can be explained in terms of a  $40^\circ \langle 111 \rangle$  growth selection out of a spectrum of nuclei being formed by recrystallization twinning i.e. by  $60^\circ \langle 111 \rangle$  rotations with respect to the rolling texture orientations [11]. In the present investigation, nucleation of recrystallization was observed at the bands and BR orientation emerges as the major recrystallization texture component. Hence, it can be concluded that

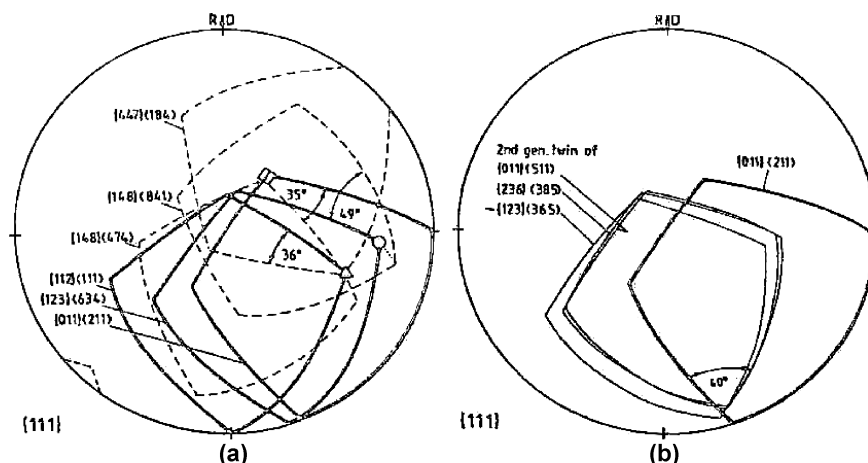


**Fig. 21.11** (a) Twin relationship between the rolling and recrystallization texture components. (b)  $40^\circ \langle 111 \rangle$  relationship between BR component with Brass component.

they form by similar mechanisms as in brass, i.e. nucleation in the bands and a subsequent preferred growth into the deformed matrix. It must be emphasized here, that in comparison to that of Brass, the propensity of shear bands was much smaller and hence, the contribution of the recrystallization textures was limited.

The other investigators have reasoned that due to presence of twinning in the deformed microstructure, the next generation of twins may possess the BR orientation  $\{236\} \langle 385 \rangle$  and/or  $\{526\} \langle -2 \ -4 \ 3 \rangle$  and this can grow very fast due to its compromise character leading to this as a characteristic recrystallization texture [21–23].

These recrystallization textures are considerably different from other low to medium SFE materials, even though they all have brass-type rolling texture. It can be noted that a different  $[111]$  axis may have been selected as the rotation axis and that may be the reason for having different texture from a common rolling texture. It is to be mentioned here that if twins were to form on all four systems of each variant, there would be fourteen different twin orientations contributing to the texture. There is no evidence that all twin orientations develop uniformly.

It was reported by Gottstein [23] that the evolution of twin chains leads to the occurrence of orientations entirely different from the rolling texture. The twins can develop from the scatter of the orientations present in the deformed state. However, it can be pointed out here that even though the rolling texture was similar in various AISI 316L steels, the resulting recrystallization texture is found to be quite different. It may be due to restriction of twin formation. Twinning to high generations leads only to a random texture evolution owing to the scattered recurrence of the origin in higher generation.

In order to avoid random texture evolution during recrystallization, composition of 304L steel has been modified to have ferrite of 8–10% within the microstructure. The material was cold rolled to 95% reduction without any difficulty. The ODFs corresponding to austenite and martensite phases has been evaluated and presented in Fig. 21.12. The austenite phase shows evolution of brass-texture and the martensite phase shows evolution of  $\{111\} + \{110\}$  fiber texture. The 95% cold rolled material was annealed at the temperatures from 600° to 1000° at an interval of 100°C. At 600°C, the austenite texture gets sharpened due to recovery induced rearrangement of defects within the material (Fig. 21.13 (a)). After annealing at 800°C, the texture is nearly as that of the rolled austenite. Although there is a scatter around the brass and Goss components till annealing at 900°C (Fig. 21.13 (b)); the texture after annealing at 1000°C shows retained rolling texture without any scatter (Fig. 21.13 (c)). The retention of the rolling texture with annealing at different temperatures generally results due to recrystallization through extensive recovery or recrystallization in situ. In the present case, there are evidence of recovery prior to the onset of recrystallization. The scatter around the brass orientation extended towards the  $\phi_1 = 90^\circ$  indicates the emergence of B/P orientation. However, with increase in annealing temperature, scatter decreases and it is the retention of rolling texture. It might be due to presence of ferrites along the austenite grain boundaries. The surface tension between ferrite and austenite might be hindering the migration of the austenite grain boundaries and that leads to the retention of the grain boundaries. The detailed description has been presented elsewhere [24].

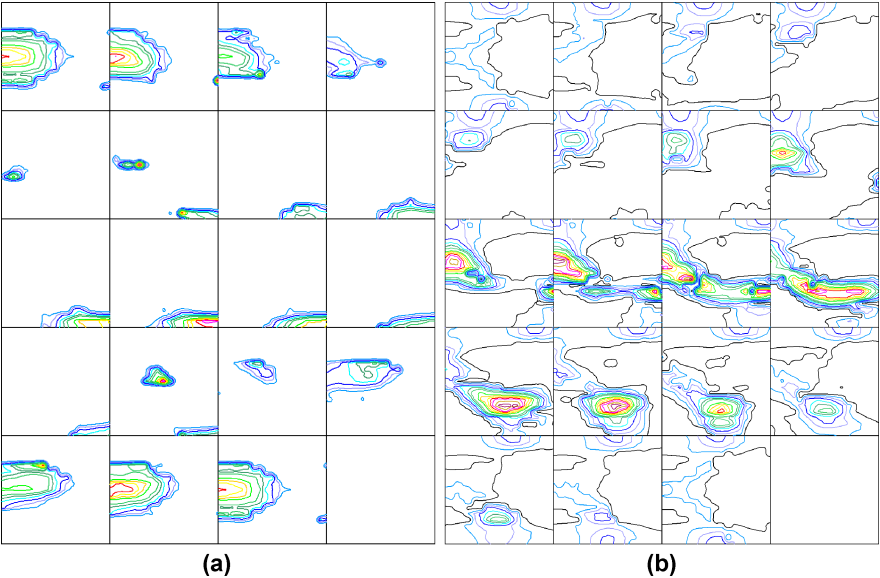


**Fig. 21.12** ODFs (a) Austenite and (b) martensite after 95% cold rolling.

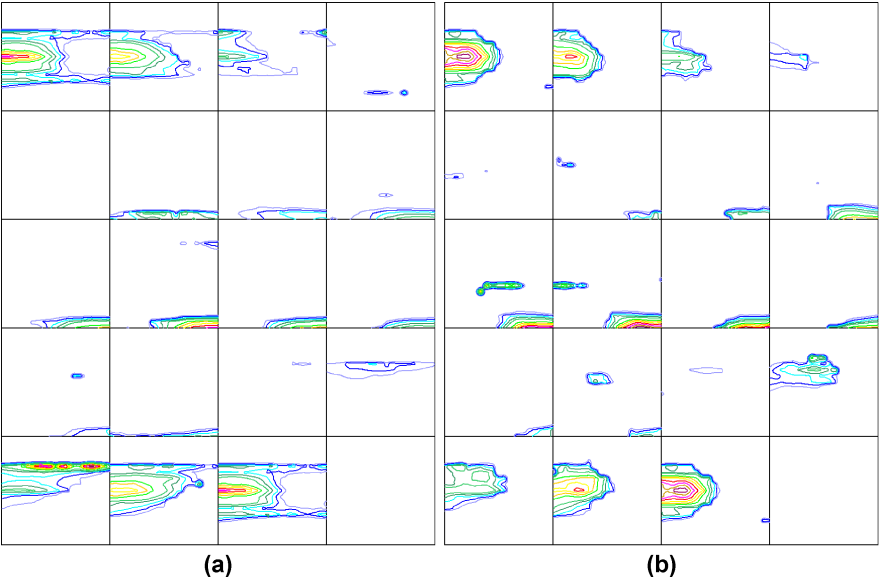
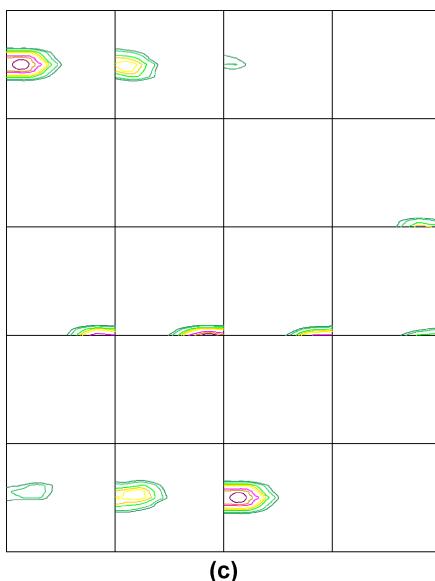


**Fig. 21.13 (a), (b)** ODF after annealing of a 95% cold rolled austenite: (a) 600°, (b) 800°C.

**Fig. 21.13 (c)** ODF after annealing of a 95% cold rolled austenite: (c) 1000°C.



## 21.5 Conclusions

The textural evolution was characterized overall weak texture. There were several new orientations after recrystallization; prominent among them are BR orientation  $\{236\} \langle 385 \rangle$ ,  $\{4\ 4\ 11\} \langle 11\ 11\ 8 \rangle$ ,  $\{213\} \langle 1\ 1\ 1 \rangle$  as well as the Goss orientation. The orientation can be correlated well with the deformation texture by twin relationship. After annealing at higher temperature, there are formation of  $\{197\} \langle 211 \rangle$  which has 2nd order twin relationship with BR orientation.

The recrystallization texture cannot be interpreted exclusively in terms of  $40^\circ \langle 111 \rangle$  rotations. Some of the very first components to emerge during recrystallization were related to the diminishing rolling texture components. Other deformation texture components were related to the fading rolling texture components by 2nd order twinning relationships. It was concluded that only a selective with favourable growth criteria could be taken into account for the evolution of recrystallization texture in the presence multiple twinning. The precipitation of carbides as observed did not play a role in the recrystallization behaviour and the associated texture evolution.

In presence of ferrite (8–10%), the recrystallization texture is basically the retained rolling texture even after annealing at higher annealing temperatures. The ferrites present along the austenite grain boundaries put a drag force in hindering the migration of the grain boundaries and that lead to retention of rolling texture.

## References

- [1] F.B. Pickering, Physical Metallurgical development of stainless steels, in Proc. Conf. Stainless Steels 84, Gothenburg, 1984, p2–281.
- [2] J.W. Christian, S. Mahajan, Deformation Twinning, Prog. Mater. Sci., 1995, 39, 1–157.
- [3] C. Donadille, R. Valle, P. Dervin and R. Penelle, Acta Metall., 1989, 37(6), 1547–71.
- [4] P.H. Alder, G.B. Olson and W.S. Owen, Metall. Trans. A, 1986, 17A, 1725–37.
- [5] S. Vercammen, B. Blanpan, B.C. De Cooman and P.Wollants, Acta Metall., 2004, 52, 2005–12.
- [6] R.E. Smallman and D. Green, Acta Metall., 1964, 12, 145.
- [7] K. Pawlik, Phys. Stat. Sol. (b), 1986, 134, 477.
- [8] J. Hirsch and K. Luecke, Acta Mater., 1988, 36, 2863.
- [9] G. Wassermann, Z. Metallk., 1963, 54, 61.
- [10] U. Schmidt and K. Lucke, Textures Cryst. Sol., 1979, 3, 85.
- [11] O. Engler, J. Hirsch and K. Luecke, Z. Metallk., 1995, 86, 475.
- [12] H. Eichelkraut, J. Hirsch and K. Lucke, Z. Metallk., 1984, 75, 113.
- [13] R.H. Richman and Y.C. Liu, Trans. AIME, 1961, 221, 720.
- [14] K.H. Virnich and K. Lucke, ICOTOM 5, 1978, p397.
- [15] J. Hirsch, 7th Riso Intl. Symp., Eds. N.Hansen et al., 1986, p349.
- [16] J. Savoie and K. Luecke, Textures and Microstructures, 1991, 14/18, 897.
- [17] V.I. Yushkov, R.A. Adamescu, Y.S. Machnev, T.M. Gapeka and P.V. Geld, Mater. Sci. Engg., 1984, 64, 157.
- [18] C. Donadille, R. Valle, P. Dervin and R. Penelle, Acta Metall., 1989, 37(6), 1547–71.
- [19] J. Huber and M. Hatherly, Z. Metallkd., 1980, 71, 15.
- [20] T. Noda, B. Plege and J. Grewen, ICOTOM 5, 1978, p443.
- [21] K.H. Virnich and K. Lucke, ICOTOM 5, 1978, p397.
- [22] B. Plege, 7th Riso Intl. Symp. Eds. N.Hansen et al., 1986, p493.
- [23] G. Gottstein, Acta Metall., 1984, 32, 1117.
- [24] Sandip Ghosh Chowdhury, Arpan Das, B. Mahato and P. Sahu, unpublished research.



Sandip Ghosh Chowdhury  
Materials Science and Technology Division  
National Metallurgical Laboratory  
Jamshedpur 831007  
India

## Chapter 22

# Deformation and Recrystallization Textures in Iron Aluminides

W. Skrotzki, R. Tamm, K. Kegler, and C.-G. Oertel

**Abstract.** Iron aluminides of different composition were deformed at high temperatures by extrusion through a round and rectangular die, approximating tension and plane strain deformation, respectively. Depending on temperature and composition dynamic recrystallization takes place. To investigate post-deformational recrystallization annealing treatments have been applied. Global and local textures were measured by neutron and electron back scatter diffraction (EBSD), respectively. The EBSD method allows the separation of deformation and recrystallization texture components. Moreover, the texture development is correlated with the microstructure evolution derived from EBSD mappings. The development of the deformation and recrystallization textures is discussed by means of different models on polycrystal deformation and recrystallization, respectively. Conclusions concerning the anisotropy of the elastic and plastic properties are drawn.

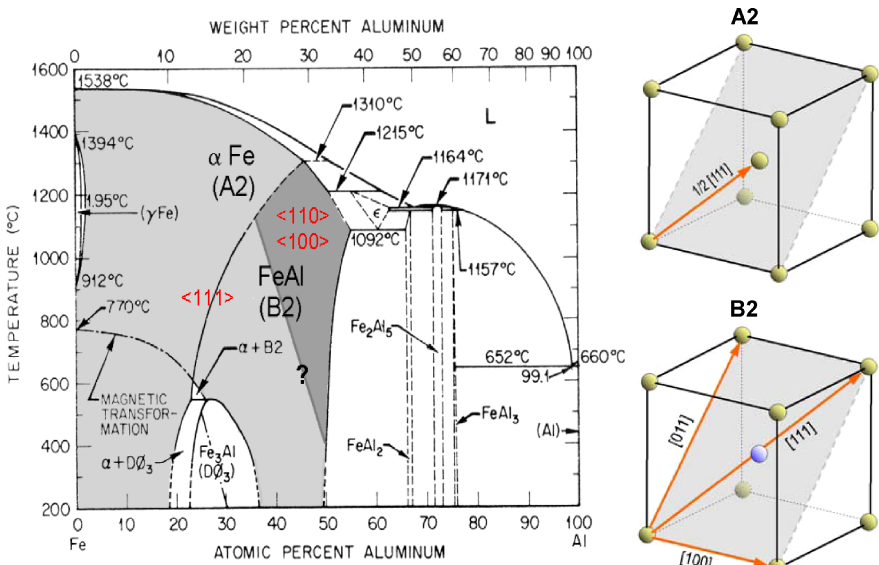
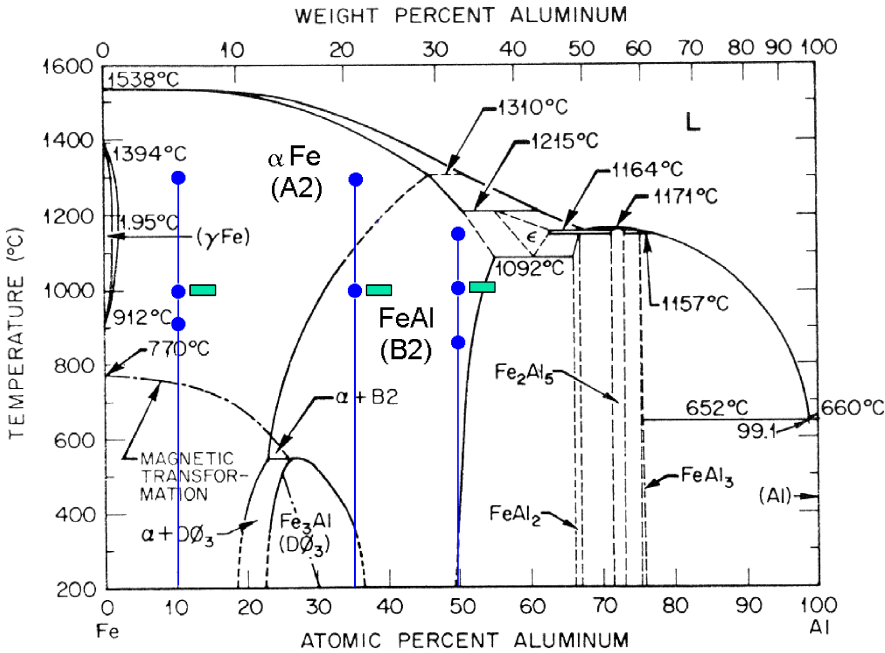
**Keywords:** FeAl, extrusion, microstructure, texture, simulations

## 22.1 Introduction

B2 structured intermetallic FeAl alloys offer a variety of advantages, some of which are low raw material cost, low density, high electrical resistivity and excellent resistance to oxidation and sulfidation [1, 2]. These properties make these alloys attractive for high temperature applications. However, so far the low ductility at low temperatures and the low creep resistance limit their use as structural materials. To eliminate these disadvantages, previous research was focused on the influence of ternary alloying elements, hydrogen embrittlement and grain structure. Systematic investigations of the influence of texture on the mechanical properties

---

W. Skrotzki, R. Tamm, K. Kegler, and C.-G. Oertel  
Institute of Structural Physics, Dresden University of Technology, D-01062 Dresden, Germany



are still missing. This is surprising because the elastic and plastic behavior of these materials is quite anisotropic and therefore texture is of major concern.

To shed more light on the texture development, in the present study Fe-Al alloys of different compositions have been deformed by extrusion. The deviation from stoichiometry and the degree of order of FeAl changes with composition and temperature (Fig. 22.1). Correlated with this is a change of the slip systems (Fig. 22.2) and the grain boundary mobility which strongly determines the deformation and recrystallization behavior, respectively.

## 22.2 Experimental

Cast polycrystalline Fe-Al cylindrical ingots (30 mm diameter) of three compositions (Fe-10Al, Fe-35Al and Fe-50Al, confirmed by electron beam microprobe analysis, error  $\pm 1$  at.%) were extruded at high temperatures (850°C–1300°C) through a round (13 mm diameter) and rectangular (18 mm  $\times$  7 mm) die (Fig. 22.1), yielding an extrusion ratio of 5.3 and 5.6, respectively. The strain rate was of the order of  $1 \text{ s}^{-1}$ . To diminish friction, the samples were sealed using copper and steel cans for extrusions below and above 1000°C, respectively. After extrusion the rods were air-cooled.

The microstructure was investigated on mechanically and electrolytically well-polished sections in the scanning electron microscope (SEM, Zeiss DSM 962) using electron back-scatter electron (BSE) contrast.

Complete pole figures for  $\{100\}$ ,  $\{110\}$  and  $\{111\}$  reflections of the global texture were measured by neutron diffraction using cylindrical samples with a height and diameter of 10 mm. Orientation distribution functions (ODF) were calculated using the series expansion method up to a series expansion degree of 22 and axial or orthorhombic sample symmetry [3]. In addition, electron back-scatter diffraction (EBSD) measurements of the local texture were carried out on in the SEM in order to correlate texture components with the microstructure shown by orientation contrast.

Texture simulations were done with the relaxed constraints (RC) Taylor theory [4] applied on a random distribution of 1000 grains. In the case of extrusion through the round die, relaxation of  $\epsilon_{yy}$ – $\epsilon_{zz}$  and  $\epsilon_{zy}$  allows for “curling” around the extrusion axis  $x$  [5], while for extrusions through the rectangular die the shear components  $\epsilon_{zx}$  and  $\epsilon_{zy}$  are relaxed (“pancake model”), with  $x$ ,  $y$  and  $z$  being the extrusion, transverse and normal direction, respectively (Fig. 22.3). In all simulations the strain was achieved in steps of 5%. The slip systems used are  $\{110\}\langle 111 \rangle$ ,  $\{110\}\langle 100 \rangle$  and  $\{110\}\langle 110 \rangle$ , their activity changing with composition and temperature (Fig. 22.2). These slip systems yield 5, 3 and 2 independent systems, respectively. For Fe-10Al and Fe-35Al only slip along  $\langle 111 \rangle$  was used, while for Fe-50Al  $\langle 100 \rangle$  and  $\langle 110 \rangle$  slip on  $\{110\}$  with equal critical resolved shear stresses was assumed.



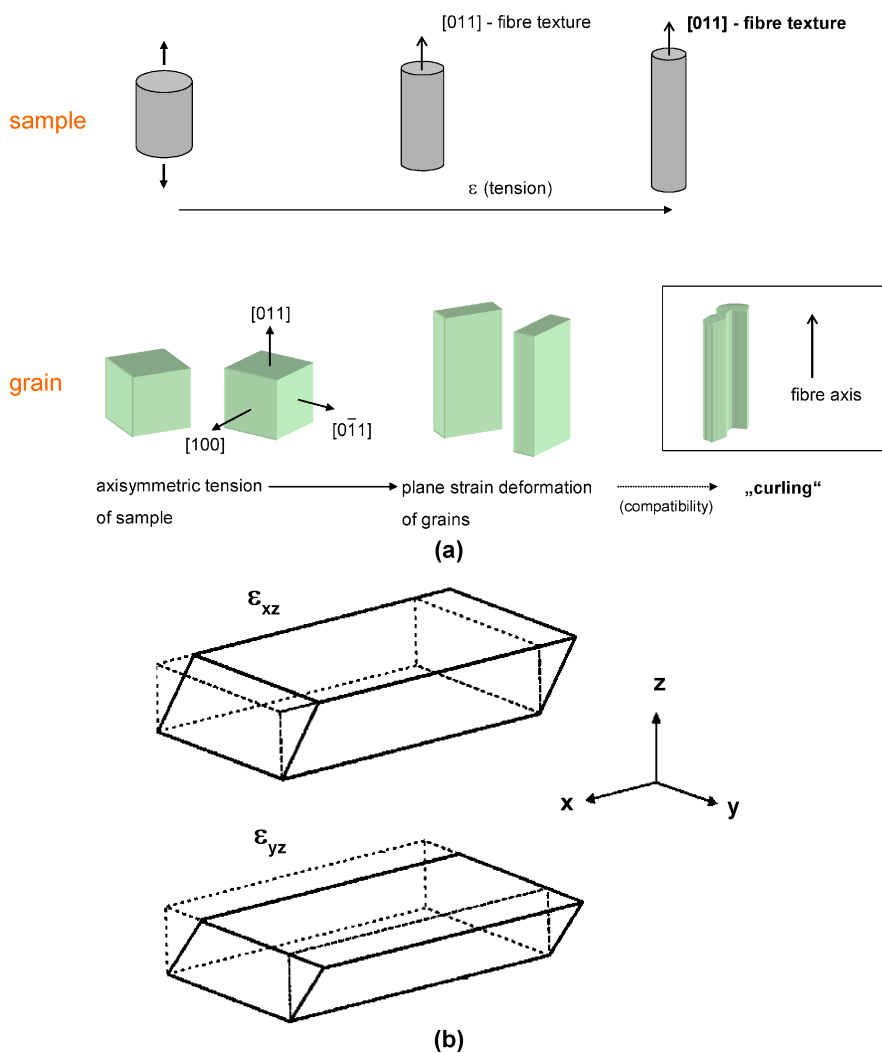


**Fig. 22.3** Principle of "curling" in axisymmetric tension along the  $\langle 110 \rangle$  fibre axis (a) and relaxations used in the "pancake" model of plane strain deformation (b). ( $x$ =extrusion direction,  $y$ =transverse direction,  $z$ =normal direction).

## 22.3 Results and Discussion

The microstructure of the extruded Fe-Al rods shown in orientation contrast (Fig. 22.4) is characterized by a banded structure most likely representing the elongated original grains. The microstructure varies from band to band in the degree of recovery (subgrain structure) and recrystallization (grain structure, i.e. area

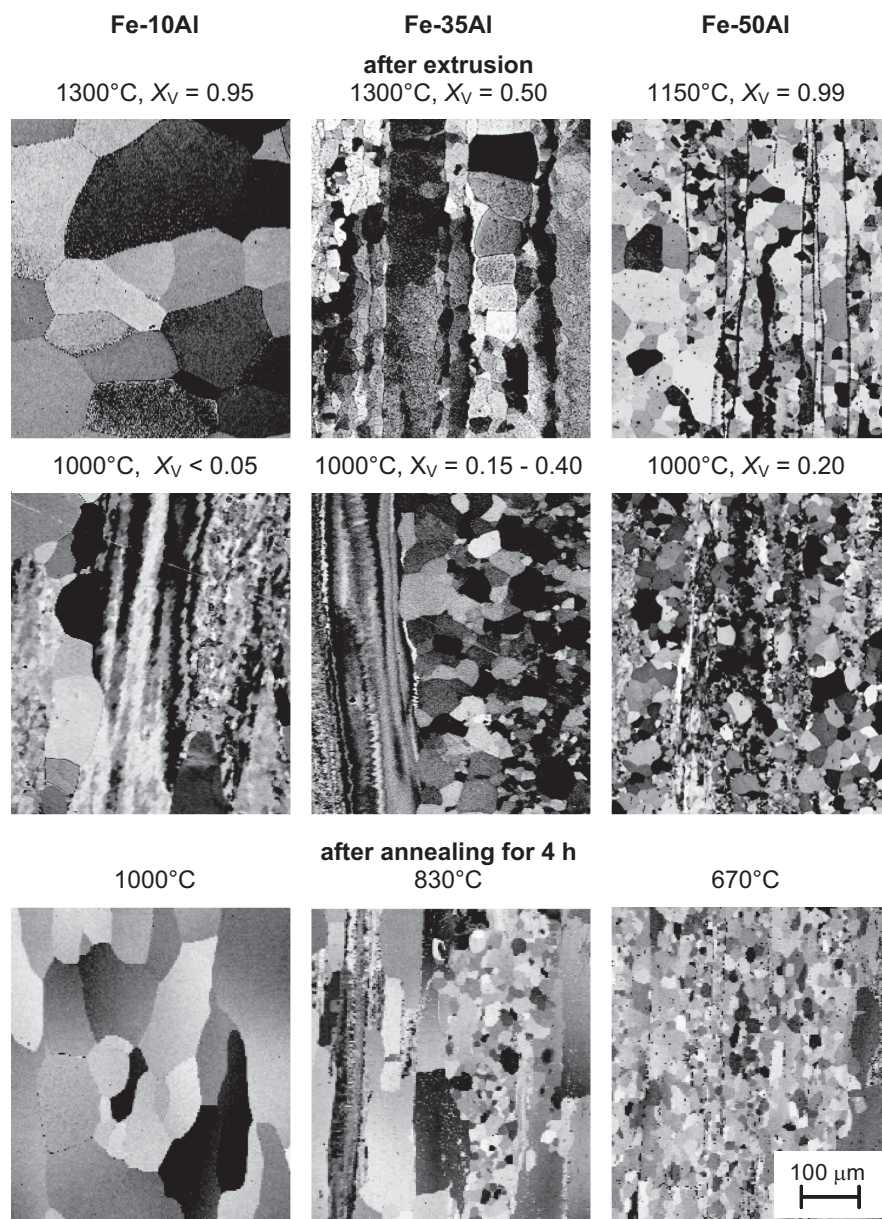


**Fig. 22.4** Orientation contrast images of the microstructure of Fe-Al samples extruded through a round die at different temperatures as well as after annealing for 4 h at the temperatures given (longitudinal section, extrusion axis vertical). The volume fractions recrystallized  $X_V$  are given.

recrystallized and grain size). The largest inhomogeneity is observed for Fe-35Al (Fig. 22.5). The fraction recrystallized depends on temperature and Al content. The subgrain size is about 5  $\mu\text{m}$ , the recrystallized grain size about 50–200  $\mu\text{m}$  [6]

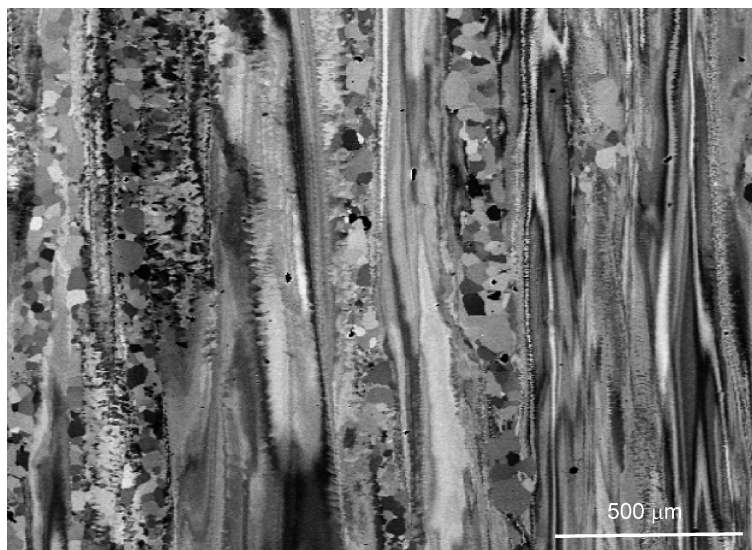


**Fig. 22.5** Orientation contrast image of the inhomogeneous microstructure of the Fe-35Al sample extruded through a round die at 1000°C (longitudinal section, extrusion axis vertical).

compared to the ingot grain size of about 1–2 mm [7]. After annealing for 4 h at the temperatures given in Fig. 22.4 all alloys are fully recrystallized and the grain structure compares well with that after extrusion at high temperatures.

The textures shown in Fig. 22.6 change both with composition and temperature. Extrusions through a round die between 850°C and 1000°C with increasing Al content show a change from a  $\langle 110 \rangle$  fibre texture to a  $\langle 100 \rangle$ – $\langle 110 \rangle$  double fibre texture. Samples extruded at higher temperatures exhibiting a higher degree of recrystallization develop weak texture components extending from  $\langle 110 \rangle$  via  $\langle 102 \rangle$  to  $\langle 114 \rangle$  in the case of Fe-10Al and a  $\langle 111 \rangle$  fibre in Fe-35Al and Fe-50Al, which in the latter alloy primarily goes at the cost of the  $\langle 110 \rangle$  fibre texture. To correlate the texture components with the grain structure, orientation imaging microscopy (OIM) has been applied. Figure 22.7 shows that the  $\langle 100 \rangle$  and  $\langle 110 \rangle$  fibres of FeAl are deformation induced, while the  $\langle 111 \rangle$  fibre is clearly related to the small recrystallized grains. Moreover, the deformed microstructure consists of a subgrain structure with the density of subgrain boundaries increasing from the center to the mantle of the grains, which represents the area for the onset of recrystallization.

To distinguish deformation and recrystallization texture components, OIM has been applied. Figure 22.8 shows the texture belonging to the recrystallized fraction. The inverse pole figures clearly show that in the case of the A2 structure the dynamically recrystallized grains have orientations ranging from  $\langle 100 \rangle$  to  $\langle 102 \rangle$ . The B2 structured samples show an increased intensity close to  $\langle 111 \rangle$  and  $\langle 112 \rangle$ . During recrystallization, the texture strength decreases markedly. The weak textures after static recrystallization agree more or less with those observed for dynamic recrystallization.

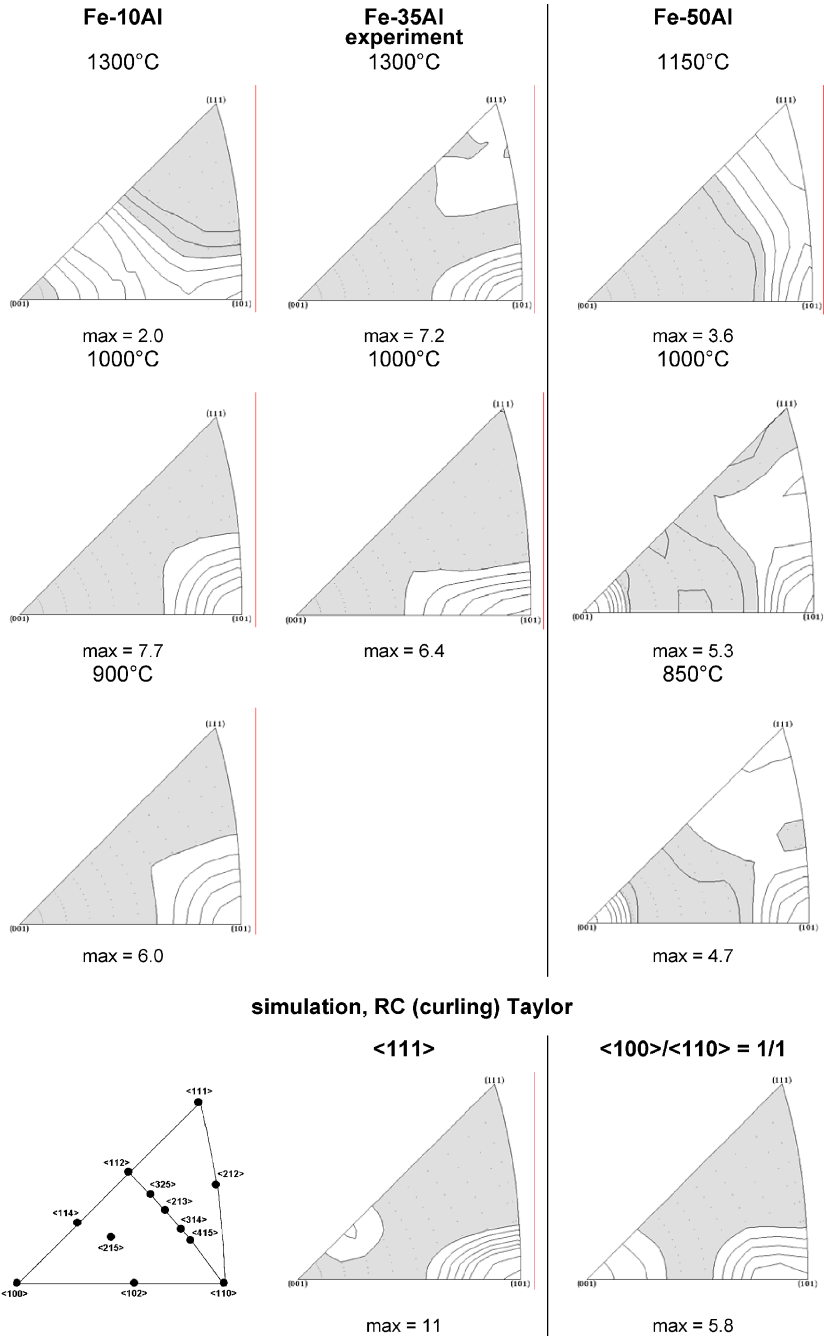


**Fig. 22.6** Inverse pole figures of the extrusion direction of Fe-Al alloys extruded through a round die. The simulated textures may be compared with the experimental ones of 1000°C and below (grey areas are below the level of 1.0 m.r.d. (=multiples of a random distribution)).

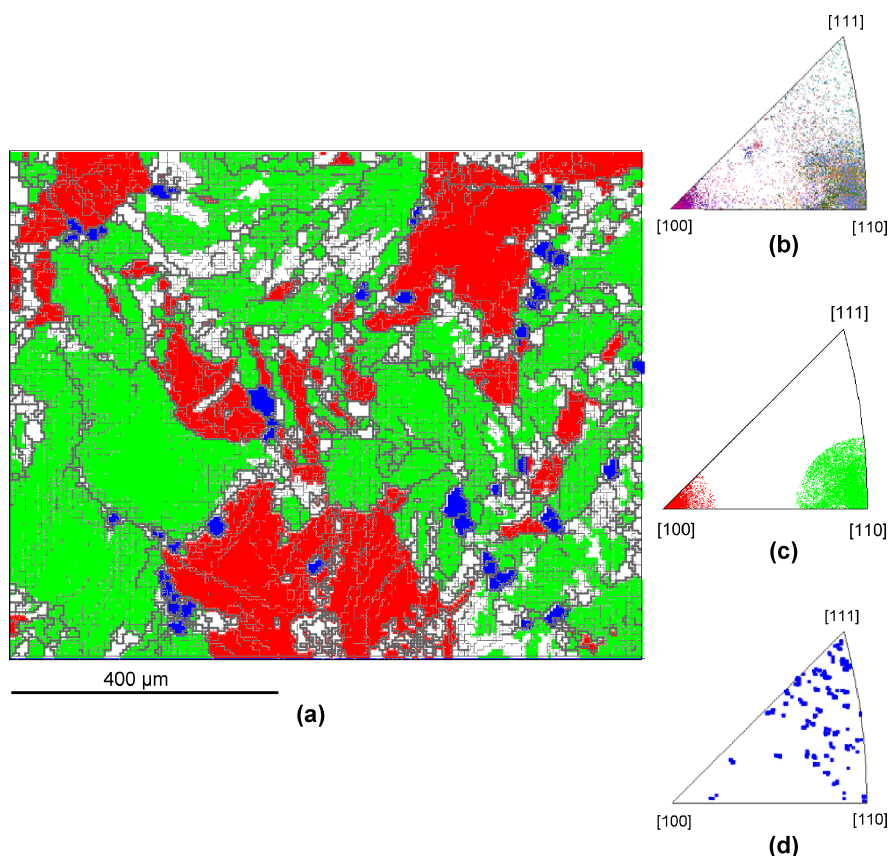


**Fig. 22.7** OIM of a cross section of Fe-50Al extruded at 1000°C through a round die (a). Thin and thick lines represent low and high angle grain boundaries with misorientation angles between 2 and 15° and larger than 15°, respectively. The texture of this section (b) is displayed as inverse pole figure of the extrusion direction. Grains of the main fibres marked in the inverse pole figure of (c) are displayed in (a) as red (<100>) and green (<110>). Recrystallized grains displayed blue in (a) are preferentially aligned with <111> parallel to the extrusion direction as shown in (d).

These results may be compared with textures published previously. Cast Fe-38Al extruded at 1000°C with an extrusion ratio of 16:1 shows a <110>-<111> double fibre texture with <110> dominating. Annealing for 24 h at the same temperature yields a change to a <112> fibre [8]. Similarly, extruded Fe-40Al powder shows a <110>-<111> double fibre texture, but now <111> is dominating and strengthens by annealing [8,9]. In contrast, extrusion of intensively ball-milled Y<sub>2</sub>O<sub>3</sub> strengthened Fe-40Al between 1000°C and 1100°C for extrusion ratios of 14:1 and 28:1 only leads to a <110> fibre [10–13]. There is a change to a <111> fibre by annealing above 1200°C.

The textures of the samples extruded through the rectangular die, because of the pure shear deformation, have orthorhombic symmetry. They exhibit components

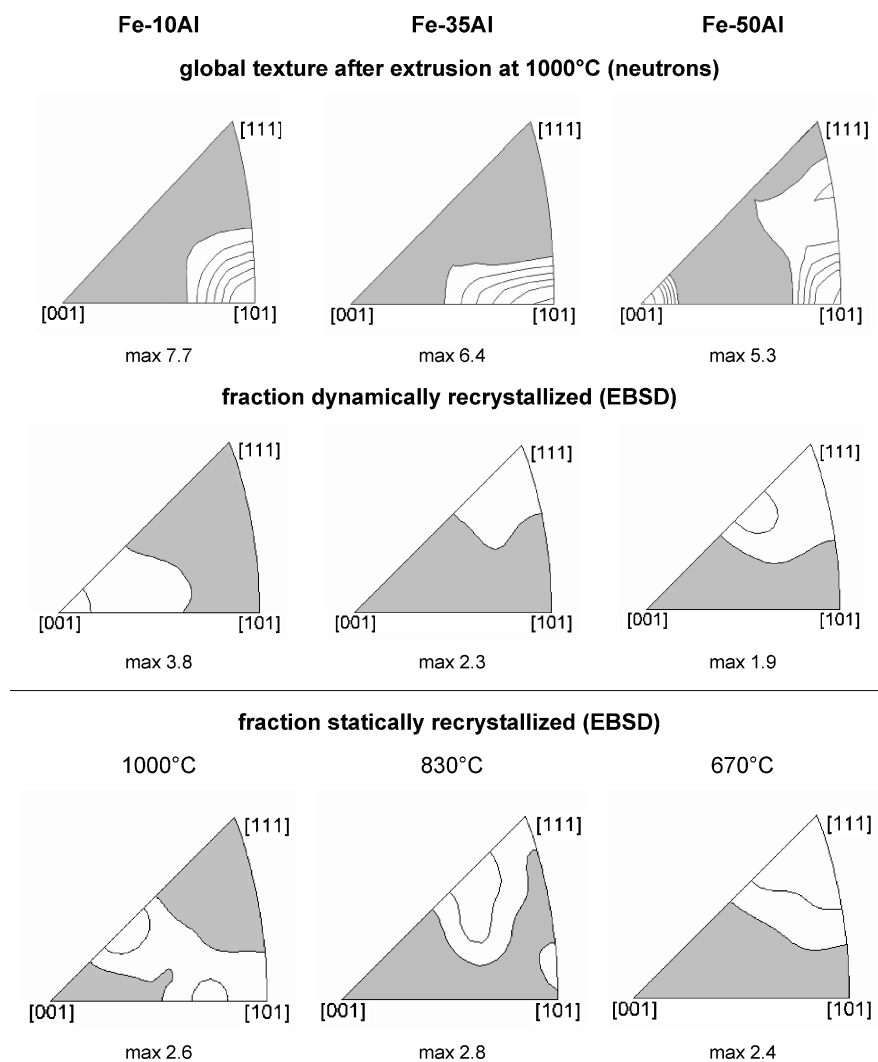


**Fig. 22.8** Global texture of the Fe-Al alloys extruded through the round die measured by neutron diffraction and texture of the dynamically and statically recrystallized volume fraction measured by EBSD.

typical of plane strain textures of body-centered cubic metals, i.e. partial coverage of the  $\alpha$ - and  $\gamma$ -fibre characterized by an alignment of the  $\langle 110 \rangle$  and  $\langle 111 \rangle$  direction parallel to the extrusion and normal axis, respectively (Fig. 22.9). These fibres can be best seen in the  $\varphi_2 = 45^\circ$  section of the ODF representation. With decreasing Al content the texture changes from a  $\gamma$ -fibre with predominant  $\{111\}\langle 110 \rangle$  component plus  $\{100\}\langle 100 \rangle$  cube component to a  $\gamma$ - and  $\alpha$ -fibre with predominant  $\{100\}\langle 110 \rangle$  rotated cube component.

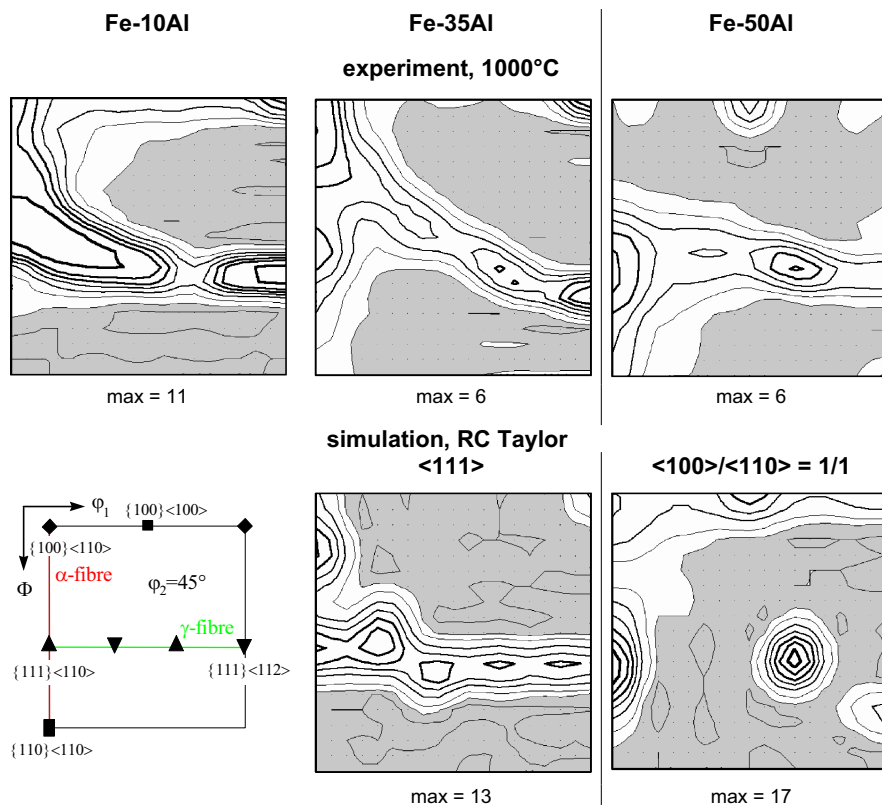


**Fig. 22.9** Textures of Fe-Al alloys extruded through a rectangular die represented by  $\varphi_2 = 45^\circ$  ODF sections in comparison with simulated textures. The main texture components are indicated in the key figure.

The main texture components can be well simulated with the RC Taylor model taking into account the change of slip system operation with decreasing Al content. Thus, there is a change of the deformation behavior with ordering energy. Stoichiometric FeAl at high temperatures behaves similar to NiAl [14], but an easier activation of the  $\{110\}<110>$  slip system may be responsible for the additional  $<100>$  fibre and cube component in tension and plane strain deformation, respectively (Figs. 22.6 and 22.9).

In axisymmetric tension in all cases a  $<110>$  fibre develops. Therefore, grains with a  $[011]$  tensile axis have a  $[100]$  and  $[0\bar{1}1]$  direction normal to it (Fig. 22.3 (a)). These orthogonal directions in general mechanically behave differently. Thus, grains with  $<110>$  fibre axis will preferentially deform in pure shear, i.e. in the extreme case in plane strain. However, as the overall deformation of the aggregate is axisymmetric, in order to relax strain incompatibilities folding around the tensile axis, so-called “curling”, may take place. As shown in the next section,

the main component developing in plane strain deformation is  $(111)[0-11]$ . Folding of grains with such an orientation around  $[0-11]$  leads to a  $[0-11]$  fibre texture.

In plane strain deformation the main texture components are well reproduced with the RC Taylor model allowing shears not producing too large strain incompatibilities (Fig. 22.3 (b)). At higher temperatures such incompatibilities may be reduced by diffusional processes and grain boundary sliding. However, compared with experiment the simulated textures are too strong. This is a generally observed phenomenon which may mainly be attributed to the fact that grain fragmentation has not been taken into account.

The stored strain energy determines the stability of particular orientations. Highly strained grains have the tendency to nucleate new grains and those with low stored energy (less deformed) have the tendency to grow at the expense of their neighbors. Therefore, the texture developing during recrystallization will depend on the balance between nucleation (defined by the probability and “critical strain” for nucleation) and the boundary mobility. Iron aluminides at all temperatures in tension develop a  $\langle 110 \rangle$  fibre texture. During recrystallization in the ordered state, there is a change to  $\langle 111 \rangle$  extending towards  $\langle 112 \rangle$ . The observation of recrystallized grains in highly strained regions along grain boundaries shows that recrystallization in FeAl is nucleation dominated in line with the low boundary mobility typical for ordered structures [15]. Moreover, in copper it has been found that nucleation starts first in grains with the highest density of stored dislocations [16]. In the case of a higher boundary mobility of Fe-10Al a  $\langle 100 \rangle$  recrystallization fibre texture would be expected for tension deformed samples as the  $\langle 100 \rangle$  oriented grains are stable when deformed by  $\{110\}\langle 111 \rangle$  slip. Indeed such an orientation and/or those close to it are observed as main recrystallization components. However, it should be mentioned that the recrystallization textures are very weak so that the arguments favoring one or the other mechanism may not be too conclusive.

Concerning the elastic and plastic properties of single crystals, it should be mentioned that in the B2 structured iron aluminides the Young's modulus and the yield stress are strongly anisotropic, i.e. they decrease with orientation in the sequence  $\langle 111 \rangle$ ,  $\langle 110 \rangle$ ,  $\langle 100 \rangle$  [17, 18]. Thus, for strength increase, textures containing the  $\langle 111 \rangle$  component in loading direction are desirable. This may be achieved by recrystallization.

## 22.4 Conclusions

- 1) Extrusion of Fe-Al alloys leads to specific deformation textures. With increasing Al content in tension the texture changes from a  $\langle 110 \rangle$  to a  $\langle 100 \rangle$ – $\langle 110 \rangle$  double fibre texture. In plane strain deformation the change is from a  $\alpha + \gamma$  to a  $\gamma$ -fibre texture.



- 2) Dynamic and static recrystallization produces new weak texture components which with increasing Al content in tension are extending from  $\langle 110 \rangle \leftrightarrow \langle 102 \rangle \leftrightarrow \langle 114 \rangle$  to  $\langle 111 \rangle \leftrightarrow \langle 112 \rangle$ .
- 3) The microstructure and texture depend on the degree of order and deviation from stoichiometry.
- 4) The deformation textures with regard to the main texture components can be simulated well with the RC Taylor model.
- 5) The recrystallization mechanism changes with ordering. In the disordered state the recrystallization texture seems to be controlled by the grain boundary mobility while in the ordered state it is controlled by nucleation.

**Acknowledgements** The authors thank Prof. Dr. G. Frommeyer (Max-Planck-Institut für Eisenforschung, Düsseldorf) for providing the cast Fe-Al alloys. Extrusions were done by R. Opitz (Leibniz-Institut für Festkörper und Werkstoffforschung, Dresden). Neutron texture measurements have been done at the TOF-diffractometer SKAT at IBR-2 (JINR Dubna) under the guidance of Dr. K. Ullemeyer. The work has been supported by the Bundesministerium für Bildung und Forschung under contract 03DUODRE/7.

## References

- [1] C.G. McKamey, in: *Physical Metallurgy and Processing of Intermetallic Compounds*, eds.: N.S. Stoloff and V.K. Sikka (Chapman & Hall, New York 1996), p. 351.
- [2] S.C. Deevi, D.H. Sastry and V.K. Sikka, in: *Structural Intermetallics 2001*, eds.: K.J. Hemker, D.M. Dimiduk, H. Clemens, R. Darolia, H. Inui, J.M. Larsen, V.K. Sikka, M. Thomas and J.D. Whittenberger, (The Minerals, Metals & Materials Society, Warrendale 2001), p. 111.
- [3] M. Dahms: *J. Appl. Cryst.* 25 (1992), p. 258.
- [4] P. van Houtte: *Textures Microstruct.* Vols. 8–9 (1988), p. 313.
- [5] H.-R. Wenk, in: *Preferred Orientation in Deformed Metals and Rocks: An Introduction to Modern Texture Analysis*, ed. H.-R. Wenk (Academic Press, Inc., New York), p. 361.
- [6] W. Skrotzki, K. Kegler, R. Tamm, and C.-G. Oertel, 2004. Recrystallization of iron aluminides. *Mater. Sci. Forum*, 467–470: 525–530.
- [7] W. Skrotzki, K. Kegler, R. Tamm, and C.-G. Oertel, 2005. Grain structure and texture of cast iron aluminides. *Cryst. Res. Technol.*, 40: 90–94.
- [8] P.S. Khadkikar, G.M. Michal and K. Vedula: *Met. Trans. A21* (1990), p. 279.
- [9] J.J. Stout and M.A. Crimp: *Mater. Sci. Eng. A152* (1992), p. 335.
- [10] V.E. Pirov, B. Verlinden, L. Delaey and E. Aernoudt: *Rev. Met.* A96 (1996), p. 220.
- [11] R. Baccino, K. Wolski, F. Thevenot, J. Le Coze and F. Moret: *Ann. Chim. Sci. Mat.* 22 (1997), p. 423.
- [12] S. Lenhard, F. Wagner and T. Grosdidier, in: *Proc. ICOTOM 12*, ed. J.A. Szpunar (NRC Research Press, Ottawa 1999), p. 683.
- [13] S. Lenhard: Ph.D. Thesis, University Metz (2001).
- [14] R. Tamm, M. Lemke, C.-G. Oertel and W. Skrotzki, in: *Texture and Anisotropy of Polycrystals*, ed.: R.A. Schwarzer (Trans Tech Publications, Switzerland 1998), p. 411.
- [15] F.J. Humphreys, M. Hatherly, *Recrystallization and Related Annealing Phenomena*, Elsevier, Oxford (2004).

- [16] G. Mohamed, B. Bacroix, *Acta Mater.* 48 (2000) 395.
- [17] K. Yoshimi, S. Hanada and M.H. Yoo: *Intermetallics* 4 (1996), p. S159.
- [18] K. Yoshimi, S. Hanada and M.H. Yoo: *Acta Metall. Mater.* 43 (1995), p. 4141.



Werner Skrotzki  
Institute of Structural Physics  
Zum Turmberg 24  
Division of Metal Physics 01328 Dresden  
Dresden University of Technology  
Germany



## Chapter 23

# Effect of Nanocrystallization on the Phase Stability of Al-Cu-Ti and Al-Cu-Nb Metallic Systems

S. Bera and I. Manna

**Abstract.** The model proposed by Miedema is widely used to calculate the enthalpy and Gibbs energy of formation under non-equilibrium conditions, but ignores the possible effect of interfacial component of Gibbs energy change on phase evolution. The latter may be significant in aggregates with ultrafine or nanometric grain size. In the present study, Miedema model is extended to calculate enthalpy and Gibbs energy of ternary Al-Cu-Ti and Al-Cu-Nb systems after incorporating interfacial energy component as a function of grain size. This exercise allows determination of probable composition range of solid state amorphization operative below a critical grain/crystallite size for a given solid solution.

**Keywords:** Amorphous material, nanostructures, mechanical alloying, thermodynamics, grain boundaries, Al-ternary alloys

### 23.1 Introduction

Age hardenable Al alloys are time tested materials for structural application in aviation and transportation. However, strength of these crystalline alloys is limited to about 500–550 MPa. It is known that the amorphous phase or partially crystallised amorphous alloys can offer 2–3 times superior yield strength, hardness and modulus than their crystalline counterparts [1–2]. Several attempts have been made to develop binary and multi-component amorphous Al alloys through different non-equilibrium routes [3–5]. Mechanical alloying is one such possibility to synthesize amorphous

---

S. Bera and I. Manna  
Department of Metallurgical and Materials Engineering, Indian Institute of Technology,  
Kharagpur, W.B. 721302, India,  
phone: +91 3222 283266, Fax: +91 3222 282280  
e-mail: imanna@metal.iitkgp.ernet.in

alloys from appropriate elemental powder blend [3–4]. However, suitable thermodynamic explanation for solid state amorphization by mechanical alloying incorporating the possible influence of crystalline size reduction has not been established.

It is known that a large negative heat of mixing (thermodynamic basis) and wide difference in diffusion coefficients (kinetic constraint) of the constituent elements constitute the most favourable conditions for solid state amorphization of a solid solution [6]. On the other hand, adequate strain energy and grain refinement induced by mechanical attrition alone can account for the necessary driving force for amorphization of intermetallic phases/compounds [7]. The enthalpy of formation of different products (solid solution, amorphous, intermetallic) in a binary system, especially when one of the constituents is a transition metal, can be calculated using the models of Miedema [8] and Alonso and Lopez [9]. However, a model suitable for calculating the Gibbs energy of a solid solution with different grain size levels is not available.

Thus, an attempt has been made in the present work to calculate the Gibbs energy of the concerned phases of Al-Cu-Ti and Al-Cu-Nb ternary alloys subjected to mechanical alloying using modified Miedema model to predict the phase equilibrium considering both chemical and interfacial contributions. The modification to Miedema model is necessitated to extend this approach for calculating enthalpy of ternary systems as this model is otherwise applicable only to dilute binary alloys. It may be noted that Al-Cu-Ti and Al-Cu-Nb are chosen as model systems for calculation as extensive amount of experimental data on kinetics and mechanism of solid state amorphization by mechanical alloying from our group is available for comparison and validation.

## 23.2 Thermodynamic Model

Gibbs energy ( $\Delta G$ ) is expressed as

$$\Delta G = \Delta H - T\Delta S \quad (23.1)$$

where  $\Delta H$  and  $\Delta S$  are the enthalpy and entropy of mixing, respectively. The entropy of mixing for an ideal solution with components  $A$  and  $B$  is

$$\Delta S = -R(X_A \ln X_A + X_B \ln X_B) \quad (23.2)$$

where  $X_A$  and  $X_B$  represent the respective atomic fraction of the components  $A$  and  $B$  and  $R$  is the gas constant.  $\Delta H$ , as per Miedema model [8] is expressed as

$$\Delta H = \Delta H_C + \Delta H_E + \Delta H_S \quad (23.3)$$

where  $\Delta H_C$ ,  $\Delta H_E$  and  $\Delta H_S$  are the chemical, elastic and structural contributions respectively. Compared to the first two terms, the structural contribution has no significant effect [10]. Thus,

$$\Delta H \cong \Delta H_C + \Delta H_E \quad (23.4)$$

Now,  $\Delta H_C$  can be estimated as

$$\Delta H_C = X_A X_B \left( f_B^A \Delta H_{\text{Sol}}^{A \text{ in } B} + f_A^B \Delta H_{\text{Sol}}^{B \text{ in } A} \right) \quad (23.5)$$

$$\Delta H_{\text{Sol}}^{A \text{ in } B} = \left[ \frac{V_A^{2/3}}{\left( n_{\text{WS}}^{-1/3} \right)_{\text{av}}} \right] \left[ -P (\Delta \Phi)^2 + Q \left( n_{\text{WS}}^{-1/3} \right)^2 \right] \quad (23.6)$$

$$\Delta H_{\text{Sol}}^{B \text{ in } A} = \left[ \frac{V_B^{2/3}}{\left( n_{\text{WS}}^{-1/3} \right)_{\text{av}}} \right] \left[ -P (\Delta \Phi)^2 + Q \left( n_{\text{WS}}^{-1/3} \right)^2 \right] \quad (23.7)$$

where  $\Phi$  is the effective chemical potential,  $\Delta n_{\text{WS}}$  represents the electron density at the boundary of the Wigner-Seitz (WS) cell,  $V$  expresses the molar volume and  $P$ ,  $Q$  are empirical constants. Furthermore

$$f_B^A = C_B \left[ 1 + y (C_A C_B) \right] \quad (23.8)$$

$$f_A^B = C_A \left[ 1 + y (C_A C_B) \right] \quad (23.9)$$

Here,  $y$  is taken to be 0 for amorphous and 5 for solid solution, respectively. The concerned coefficients ( $C_A$  or  $C_B$ ), say  $C_B$  can be expressed as

$$C_B = \frac{X_B V_B^{2/3}}{X_B V_B^{2/3} + X_A V_A^{2/3}} \quad (23.10)$$

In order to estimate  $\Delta H$  as per Eq. 23.4,  $\Delta H_E$  may be calculated as,

$$\Delta H_E = X_A X_B \left( f_B^A \Delta E_e^{A \text{ in } B} + f_A^B \Delta E_e^{B \text{ in } A} \right) \quad (23.11)$$

where  $\Delta E_e^{A \text{ in } B}$  is the size mismatch contribution to the enthalpy of solution of  $A$  in  $B$  per mol of  $A$ , which can be estimated as,

$$\Delta E_e^{A \text{ in } B} = \frac{2K_A \mu_A (V_A - V_B)}{3K_A V_B + 4\mu_A V_A} \quad (23.12)$$

where  $K$  and  $\mu$  are bulk and shear modulus, respectively. Thus,  $\Delta G$  of the amorphous state is expressed as,

$$\Delta G_a = \Delta H_C - T \Delta S + X_A \Delta G_A^{\text{a-c}}(T) + X_B \Delta G_B^{\text{a-c}}(T) \quad (23.13)$$

Here  $\Delta G_A^{\text{a-c}}(T)$  is the difference in Gibbs energy between amorphous and crystalline phase of the pure element at room temperature.  $\Delta G_A^{\text{a-c}}(T)$  can be estimated from

$$\Delta G_A^{\text{a-c}}(T) = \frac{\Delta H_f (T_m - T)}{T_m} \quad (23.14)$$

where  $T_m$  is the melting point and  $\Delta H_f$  is enthalpy of fusion.  $\Delta G$  of the crystalline state is expressed as

$$\Delta G_{\text{cryst}} = \Delta H - T\Delta S - \Delta G_\gamma \quad (23.15)$$

where the subscript  $\gamma$  to  $\Delta G$  terms refers to interfacial contribution, which is expressed as,

$$\Delta G_\gamma = \frac{4\gamma V_m}{d_c} \quad (23.16)$$

where  $d_c$  represents average grain size (or minimum coherence length) and  $\gamma$  is the interfacial energy [11]. Thus,  $\Delta G$  of a ternary system ( $ABC$ ) can be expressed as

$$\Delta G_{ABC} = \frac{1}{2(X_A + X_B + X_C)} \left[ (X_A + X_B)\Delta G^{(AB)} + (X_B + X_C)\Delta G^{(BC)} + (X_A + X_C)\Delta G^{(AC)} \right] \quad (23.17)$$

Here  $X_A$ ,  $X_B$  and  $X_C$  represent the atomic fraction of the components  $A$ ,  $B$ ,  $C$ , respectively.

### 23.3 Results and Discussion

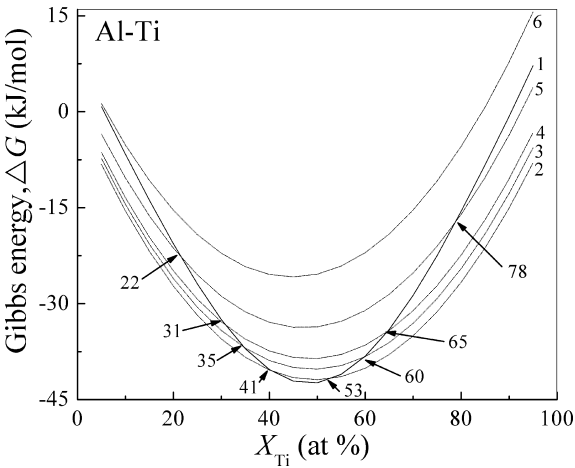
Al-Cu-Ti and Al-Cu-Nb are taken as two model systems to study the effect of grain size reduction on phase equilibrium solid state amorphization when subjected to mechanical alloying as a large volume of relevant experimental data on phase/microstructure evolution in these systems are available from earlier studies reported by us [12–15]. Furthermore, interfacial energy data of the concerned components are available in the literature [11]. The present exercise involves prediction of the  $\Delta G$ -composition curves for the three concerned Al-based binary alloys (Al-Cu, Al-Ti and Al-Nb), and subsequently, extending the same initially to pseudo-binary (Al,Cu)-Ti and (Al,Cu)-Nb alloys and finally to the Al-Cu-Ti and Al-Cu-Nb systems in the entire composition range as a function of grain size. Thus, the present approach is useful to consider both the effect of composition (binary to pseudo-binary to ternary) as well as crystallite/grain size on phase equilibrium in binary and ternary alloys.

Gibbs energy change ( $\Delta G$ ) of the binary alloys between Al and Ti and Nb and Cu as a function solute content in amorphous and crystalline state is calculated using the Eq. 23.13 and Eq. 23.15, respectively. Results are summarized in Table 23.1 and compared with the experimentally observed composition range for amorphization [4]. The predicted composition range (in terms of atomic fraction of solute element) for complete amorphous phase field at different levels of average crystallite size ( $d_c$ ) for the respective binary alloys are also listed in Table 23.1.

**Table 23.1** Comparison of the predicted (this study) and observed (from literature) ranges for solid state amorphization by mechanical alloying in Al-rich binary system [4].

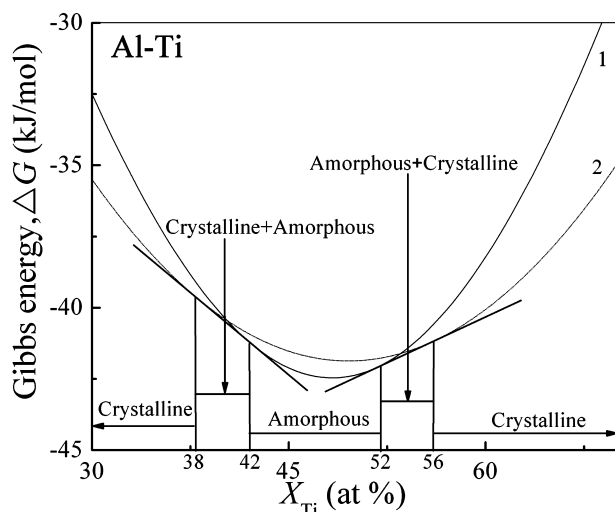
Systems	Grain size $d_c$ (nm)	Composition range (at %) for complete amorphization (this study)	Composition range (at %) for amorphization reported in the literature
Al-Cu	1 $\mu\text{m}$	—	
	20	—	
	15	49-56 Cu	
	10	40-65 Cu	
	5	Entire composition	
Al-Ti	1 $\mu\text{m}$	42-52 Ti	40-90 Ti [14]
	50	39-56 Ti	
	25	35-60 Ti	
	10	28-74 Ti	
	5	Entire composition	
Al-Nb	1 $\mu\text{m}$	—	15-75 Nb [15]
	50	—	
	25	—	
	10	33-63 Nb	
	5	Entire composition	

Figure 23.1 shows the variation of  $\Delta G$  as a function of composition ( $X_{\text{Ti}}$ ) for the Al-Ti system for both amorphous (curve 1) and crystalline solid solutions curve (2 to 6) having different values of  $d_c$  and hence different levels of  $\Delta G_\gamma$  contributions.  $\Delta G$  curves for amorphous and crystalline solid solution with coarse grain ( $d_c \sim 1 \mu\text{m}$ ) intersect at  $X_{\text{Ti}} = 41$  and 53 at%, respectively. As  $d_c$  decreases,  $\Delta G_\gamma$  and  $\Delta G$  of crystalline solid solution increases raising the  $\Delta G$ - $X_{\text{Ti}}$  curve to more positive values and expanding the composition range of stability for single-phase amorphous solid solution. In fact, the smaller the  $d_c$ , the wider the composition range for solid state amorphization.



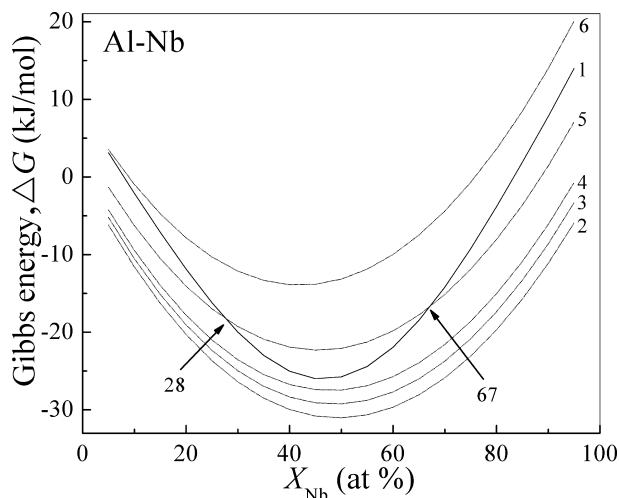
**Fig. 23.1** Variation of  $\Delta G$  as a function of Ti concentration ( $X_{\text{Ti}}$ ) in Al-Ti system for amorphous (curve 1), and nanocrystalline solid solutions (curves 2 to 6 with  $d_c = 1 \mu\text{m}$ , 50 nm, 25 nm, 10 nm and 5 nm respectively).





**Fig. 23.2**  $\Delta G$ - $X_{Ti}$  curves in Al-Ti system for amorphous (curve 1), and crystalline solid solution (curves 2 with  $d_c = 1 \mu\text{m}$ ). The common tangents demarcate various phase fields as a function of  $X_{Ti}$ .

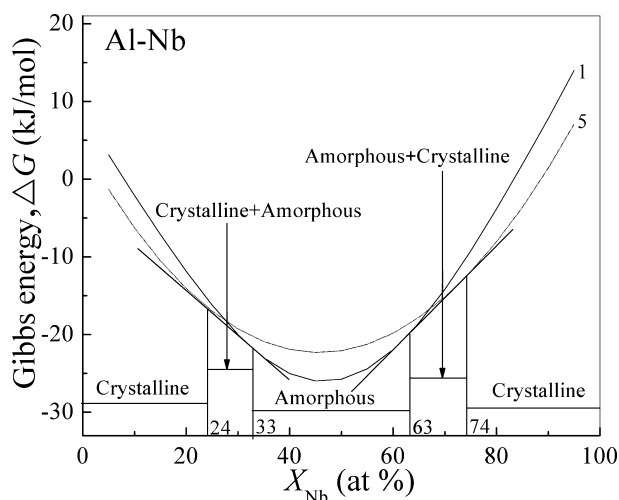
If common tangents between the concerned  $\Delta G$ -curves are drawn around these two points of intersection, single-phase amorphous solid solution is predicted in the range  $42 < X_{Ti} < 52 \text{ at}\%$ , and  $X_{Ti} < 38 \text{ at}\%$  and single phase crystalline alloys are predicted at  $X_{Ti} > 56 \text{ at}\%$ , respectively (Fig. 23.2). In other words, the pair of



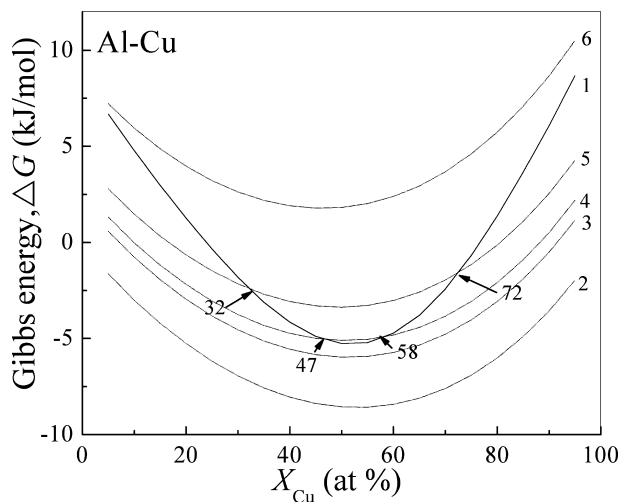
**Fig. 23.3** Variation of  $\Delta G$  as a function of Nb concentration ( $X_{Nb}$ ) in Al-Nb system for amorphous (curve 1), and nanocrystalline solid solutions (curves 2 to 6 with  $d_c = 1 \mu\text{m}$ , 50 nm, 25 nm, 10 nm and 5 nm respectively).

tangential points from Al rich to Ti-rich end composition domains for pure crystalline (Al-rich), mixture of crystalline and amorphous, completely amorphous, again mixture of amorphous and crystalline and finally pure crystalline (Ti-rich) solid solutions, respectively. Indeed, the available experimental data confirm and validate the predicted composition range for solid state amorphization in the Al-Ti system [4]. The predicted amorphous phase field at  $d_c = 10$  nm of the Al-Ti crystalline solid solution is in good agreement with that observed by experimental study (Table 23.1) [4, 16]. It is apparent that reduction in grain size increases  $\Delta G$  of the system such that curve 6 (for  $d_c = 5$  nm) is above curve 1 in the entire composition range with no mutual intersection. Thus, reduction in grain size below a critical level appears to introduce sufficient metastability so that the amorphous phase is more stable than the nanocrystalline solid solution.

Figure 23.3 shows the similar type of  $\Delta G$ - $X_{Nb}$  curves for the of Al-Nb system. Unlike the Al-Ti system,  $\Delta G$ - $X_{Nb}$  curves for amorphous and coarse-grained crystalline solid solution ( $d_c = 1 \mu\text{m}$ ) do not intersect. With reduction in  $d_c$ ,  $\Delta G$ - $X_{Nb}$  curves of crystalline solid solution move upward and intersect the  $\Delta G$ - $X_{Nb}$  curve for amorphous phase at  $d_c = 10$  nm. It is calculated that intersection between the concerned curves first occur exactly at  $d_c = 19$  nm. At  $d_c \leq 10$  nm the nature of the  $\Delta G$ - $X_{Nb}$  (Fig. 23.3) and  $\Delta G$ - $X_{Ti}$  (Fig. 23.1) curves and their respective intersections with that for amorphous solid solution appear very similar. Furthermore, the common tangents between the concerned  $\Delta G$ - $X_{Ti}$ -curves are drawn around these two points of intersection in order to determine composition range for the occurrence of single-phase amorphous and crystalline solid solutions as  $33 < X_{Ti} < 63$  at%, and  $X_{Ti} < 24$  at% and  $X_{Ti} > 74$  at%, respectively (Fig. 23.4). The composition ranges for solid state amorphization predicted in this study are comparable with that ob-

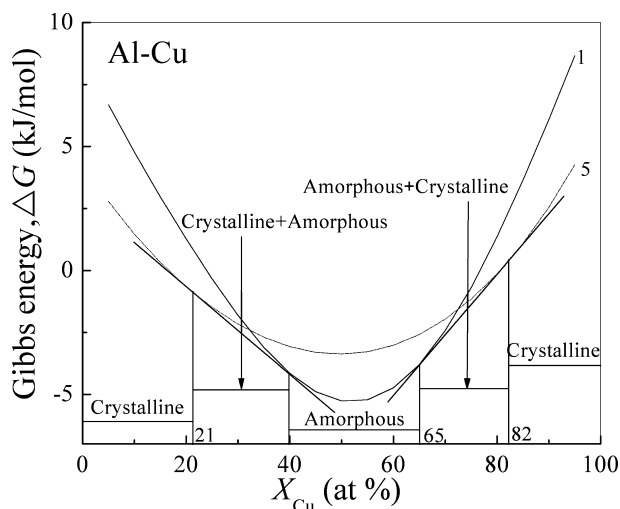


**Fig. 23.4**  $\Delta G$ - $X_{Nb}$  curves in Al-Nb system for amorphous (curve 1), and crystalline solid solution (curves 5 with  $d_c = 10$  nm). The common tangents demarcate various phase fields as a function of  $X_{Nb}$ .



**Fig. 23.5** Variation of  $\Delta G$  as a function of Cu concentration ( $X_{\text{Cu}}$ ) in Al-Cu system for amorphous (curve 1), and nanocrystalline solid solutions (curves 2 to 6 with  $d_c = 1 \mu\text{m}$ , 20 nm, 15 nm, 10 nm and 5 nm respectively).

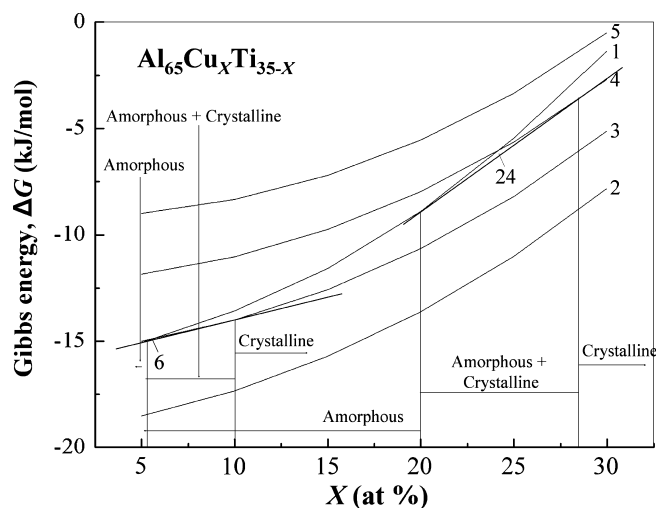
tained from experimental studies (Table 23.1). It is interesting to note that curve 6 in Fig. 23.3 (a) moves above curve 1 at  $d_c = 5 \text{ nm}$ , just like the results in Fig. 23.1 for Al-Ti system indicating that amorphous state is more stable than crystalline solid solution at  $d_c < 5 \text{ nm}$  level.



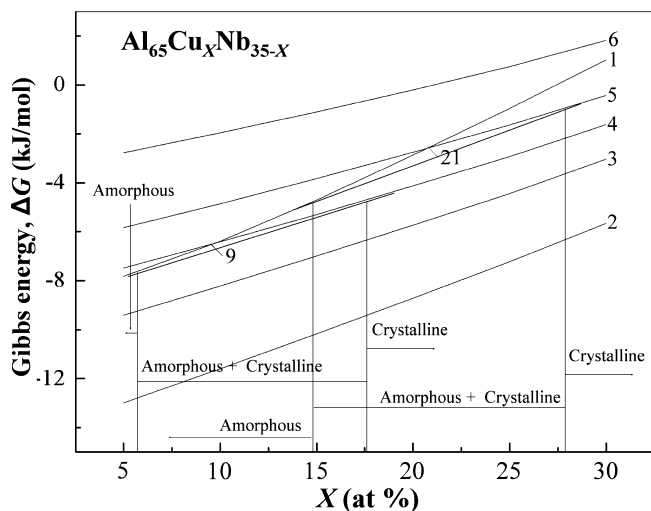
**Fig. 23.6**  $\Delta G$ - $X_{\text{Cu}}$  curves in Al-Cu system for amorphous (curve 1), and crystalline solid solution (curves 5 with  $d_c = 10 \text{ nm}$ ). The common tangents demarcate various phase fields as a function of  $X_{\text{Cu}}$ .

Figure 23.5 shows the results of similar studies on the effect of  $d_c$  on crystalline to amorphous transition due to grain size reduction. Like Al-Nb (Fig. 23.3),  $\Delta G$ - $X_{Cu}$  curves for amorphous and crystalline solid solution with coarse grain size ( $d_c = 1 \mu m$ ) do not intersect. With the gradual reduction in  $d_c$ ,  $\Delta G$ - $X_{Cu}$  curves of crystalline solid solutions rise upwards and intersect the  $\Delta G$ - $X_{Cu}$  curve for amorphous phase at  $d_c = 15$  nm. The common tangents, drawn between the concerned  $\Delta G$ -curves around the two points of intersection, show the predicted phase fields as a function of  $X_{Cu}$  (Fig. 23.6). Here also, for  $d_c = 5$  nm, curve 6 is above curve 1 in the entire composition range suggesting that the amorphous state is more stable than the nanocrystalline solid solution at  $d_c \leq 5$  nm.

Figures 23.7 and 23.8 show the results of the effect of crystallite size on crystalline to amorphous transition due to crystallite size reduction for the pseudo-binary system of  $Al_{65}Cu_XTi_{35-X}$  and  $Al_{65}Cu_XNb_{35-X}$  systems, respectively. In both the systems,  $\Delta G$ -composition curves for the amorphous and crystalline solid solutions (coarse grain,  $d_c = 1 \mu m$ ) do not intersect until  $d_c$  reduces below a critical level. As  $d_c$  reduces,  $\Delta G$  curves of crystalline solid solution goes upward and intersects the  $\Delta G$  curve of amorphous phase at  $d_c = 19$  nm and 13 nm for  $Al_{65}Cu_XTi_{35-X}$  and  $Al_{65}Cu_XNb_{35-X}$  systems, respectively. At  $d_c = 10$  nm, the common tangent to the concerned  $\Delta G$ - $X$  curves predicts that the amorphous phase is more stable than the crystalline solid solution for  $Al_{65}Cu_XTi_{35-X}$  in the composition range of Cu = 6 to 20 at% (Fig. 23.7). Above 28 at% Cu, the crystalline phase seems to be more stable. This is also in good agreement with the earlier experimental results obtained by mechanical alloying [12, 13]. Like  $Al_{65}Cu_XTi_{35-X}$



**Fig. 23.7** Variation of  $\Delta G$  as a function of concentration of the second element Cu in  $Al_{65}Cu_XTi_{35-X}$  pseudo-binary alloy for amorphous (curve 1), and nanocrystalline solid solutions (curves 2 to 5 with  $d_c = 1 \mu m$ , 19 nm, 10 nm and 7 nm, respectively). The common tangents between curves 1 and 3 ( $d_c = 19$  nm) and curves 1 and 4 ( $d_c = 10$  nm) define the probable composition ranges for pure amorphous or crystalline phase or their mixture.



**Fig. 23.8** Variation of  $\Delta G$  as a function of concentration of the second element Cu in  $\text{Al}_{65}\text{Cu}_X\text{Nb}_{35-X}$  pseudo-binary alloy for amorphous (curve 1), and nanocrystalline solid solutions (curves 2 to 6 with  $d_c = 1 \mu\text{m}$ , 20 nm, 13 nm, 10 nm and 7 nm, respectively). The common tangents between curves 1 and 4 ( $d_c = 13 \text{ nm}$ ) and curves 1 and 5 ( $d_c = 10 \text{ nm}$ ) define the probable composition ranges for pure amorphous or crystalline phase or their mixture.

pseudo-binary system,  $\text{Al}_{65}\text{Cu}_X\text{Nb}_{35-X}$  pseudo-binary system shows a very similar trend of the experimental results of mechanical alloying of Al-Cu-Nb system [14, 15]. For  $d_c = 7 \text{ nm}$  amorphous curve is above curve 1 for both the pseudo-binary systems, indicating that the amorphous phase is stabler than the nanocrystalline solid solution with identical composition. Unlike the binary systems, complete amorphization occurs at relatively higher crystalline size for these two pseudo-binary systems.

Figures 23.9 and 23.10 show the favourable composition contour for amorphous phase transformation at different values of  $d_c$  (crystalline solid solution) for Al-Cu-Ti and Al-Cu-Nb ternary systems, respectively. The predicted results show that formation of amorphous phase at some composition is possible even for coarse crystalline structure in Al-Cu-Ti system. This trend is not present in Al-Cu-Nb system. This is also in good agreement with the earlier predicted results (Fig. 23.1, Fig. 23.3 and Fig. 23.5) where Al-Ti binary system is found to be the most favourable system for solid-state amorphization among all three binary systems. Amorphous phase formation is predicted to start at 37 nm for Al-Cu-Nb system. However with gradual decrease in crystalline size both the systems follow the similar trend of increasing composition zone of amorphous phase stability.

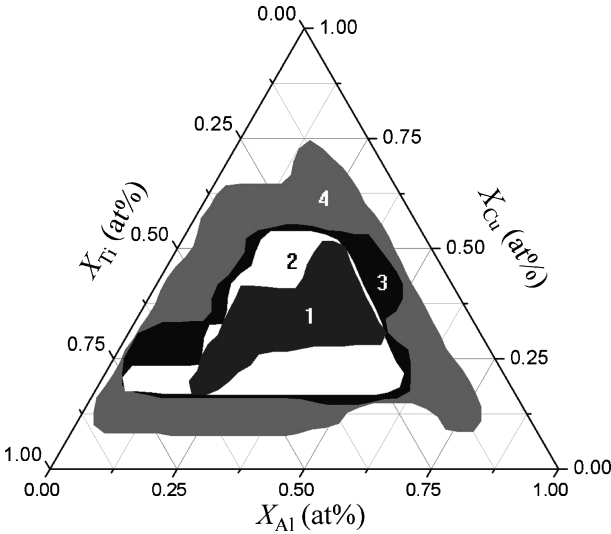


**Fig. 23.9** Favourable composition (at%) zones in Al-Cu-Ti ternary alloy for amorphous phase formation with different  $d_c$  values (contour 1 to 4 are for crystallite sizes of 1  $\mu\text{m}$ , 50 nm, 25 nm, 10 nm, respectively).

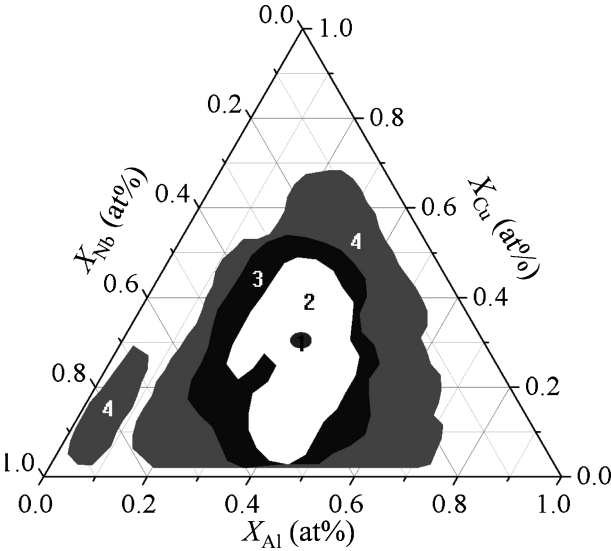


**Fig. 23.10** Favourable composition (at%) zones in Al-Cu-Nb ternary alloy for amorphous phase formation with different  $d_c$  values (contour 1 to 4 are for crystallite sizes of 37 nm, 25 nm, 20 nm, 10 nm, respectively).

## 23.4 Conclusion

Enthalpy ( $\Delta H$ ) and Gibbs energy change ( $\Delta G$ ) as a function of composition and crystalline size of some binary, pseudo-binary and ternary alloys in crystalline and amorphous state have been calculated using modified Miedema approach.  $\Delta G$  of crystalline solid solution increases with decreasing crystallite size and expands the composition range for solid state amorphization by mechanical alloying. The predicted results have been validated by suitable comparison with experimental data reported in the literature. Thus, the present analytical study predicts for the first time that complete amorphization of the binary, pseudo-binary and ternary Al-alloys considered in this investigation can be achieved below a critical crystallite size (say 5–8 nm).

**Acknowledgement** The authors would like to acknowledge the partial financial support provided for this research work by CSIR, New Delhi (project no. 70(0048)/03-EMR-II) and DST, New Delhi (NSTI grant SR/S5/NM-04/2005). Useful technical discussion with Prof. S. Ranganathan and Prof. H J. Fecht is deeply appreciated.

## References

- [1] A. Inoue, K. Ohtera, A.P. Tsai and T. Matsumoto. Jpn. J. Appl. Phys. 27 (1988), L479
- [2] A. Inoue, K. Ohtera and T. Matsumoto. Jpn. J. Appl. Phys. 27 (1988), L1796
- [3] P. Nandi, P.P. Chattopadhyay, S.K. Pabi and I. Manna, Mater. Sci. and Engg. A359 (2003) pp. 11–17
- [4] C. Suryanarayana, Progress in Mater. Science 46 (2001) 1–184
- [5] K. Chattopadhyay, R. Ramachandrarao, S. Lele and T. R. Anantharaman, Proc. 2nd Int. Conf. on Rapidly Quenched Metals, ed. By N. J. Grant and B. C. Giessen (MIT Press, Massachusetts, 1976) Section I, p. 157
- [6] E. Hellstern, and L. Schultz, Mater. Sci. Eng., 93 (1987) 213
- [7] J.S.C. Jang, and C.C. Koch, Mater. Res., 5 (1990) 498
- [8] F.R. deBoer, R. Boom, W.C.M. Mattens, A.R. Miedema, and A.K. Niessen, Cohesion in Metals, 2nd ed., (Eds. F.R. deBoer, and D.G. Pettifor), (1989) North Holland Physics Publishing, Amsterdam
- [9] J.A. Alonso, and J.M. Lopez, Phys. Status Solidi, A85 (1984) 423
- [10] J.M. López, J.A. Alonso, L.J. Gallego, Phys. Rev. B36 (1987) 3716
- [11] L.E. Murr, in Interfacial Phenomena in Metals and Alloys, (Addison-Wesley Publishing Company; 1975)
- [12] P. P. Chattopadhyay, R. N. R. Gannabattula, S. K. Pabi, I. Manna, Scripta Mater., 45 (2001) 1191–1196.
- [13] P. P. Chattopadhyay and I. Manna, Materials and Manufacturing Processes, 17 (2002) 583–594
- [14] P. Nandi, P. P. Chattopadhyay, S. K. Pabi, I. Manna, Mater. Sci. and Engg. A, 359 (2003) 11–17.
- [15] P. Nandi, P. P. Chattopadhyay, S. K. Pabi and I. Manna, Mater. Phys. Mech. 4 (2001) 116–120
- [16] B.S. Murty, M.D. Naik, M. Mohan Rao, S. Ranganathan, Mater Forum, 16 (1992) 19–26
- [17] Z. Peng, C. Suryanarayana, F.H. Froes, In: J.J. deBarbadillo, et al., editors, Mechanical alloying for structural applications, Materials Park, OH: ASM International, (1993) 335–341.



Dr Indranil Manna  
Professor  
Department of Metallurgical  
and Materials Engineering  
Chairman  
Central Research Facility  
Indian Institute of Technology  
Kharagpur,  
WB 721302  
India





**Part VI**  
**Contributory Papers**



## Chapter 24

# Investigation of Microstructure Development During $\alpha$ - $\gamma$ - $\alpha$ Phase Transformation in Steel by Using High Temperature in situ EBSD

I. Lischewski, D.M. Kirch, A. Ziemons, and G. Gottstein

**Abstract.** A newly developed laser powered heating stage for commercial SEMs in combination with automated EBSD-data acquisition was used to investigate the  $\alpha$ - $\gamma$ - $\alpha$  phase transformation in steel. This novel experimental setup can be used to achieve more information about microstructure and orientation changes. First, the results on the  $\alpha$ - $\gamma$ - $\alpha$  phase transformation in a microalloyed steel are presented.

**Keywords:**  $\alpha$ - $\gamma$ - $\alpha$  phase transformation, transformation texture, low carbon steel, orientation relationship, heating stage, in situ EBSD

## 24.1 Introduction

Most investigations into microstructure and texture evolution are limited to post-mortem analysis. Due to this limitation there is a need for experimental setups permitting the in situ observation of microstructural changes of polycrystalline materials. Besides in situ deformation, the main focus lies on the in situ observation of temperature influenced processes like grain growth, recrystallization, recovery and phase transformations. An example is the  $\alpha$ - $\gamma$  phase transformation in low carbon steels [1–3]. The observation of this phase transformation by using the EBSD technique is limited to the low temperature regime since it is a reversible process and cooling down instantaneously leads to a back transformation to the low temperature phase.

Due to this fact, a new laser powered heating stage was developed for commercial SEMs with the capacity to heat specimens up to a temperature of 1000°C. By using a combination of a heating stage with the automated EBSD technique

---

I. Lischewski, D.M. Kirch, A. Ziemons, and G. Gottstein  
Institut für Metallkunde und Metallphysik, RWTH Aachen, 52056 Aachen, Germany  
e-mail: lischewski@imm.rwth-aachen.de

we achieved a powerful tool for in situ observations of microstructural changes at elevated temperatures.

## 24.2 Experimental Results

A Jeol JSM-6100 SEM was used for the measurements. More detailed information about the experimental setup is given elsewhere [4].

A ferritic hot band was cold rolled down to 80% thickness reduction in a reverse manner. After recrystallization annealing the center part of the sample was investigated subsequent to metallographic preparation. The sample was heated up, respectively cooled down in 1°C steps in the temperature range between 880°C and 920°C. The temperature was directly measured by a thermocouple placed inside the sample. The exact chemical composition of the investigated material is given in Table 24.1. All data were collected using beam controlled measurements and the commercial Channel 5 software by HKL technology.

Figure 24.1 (a)–(b) shows acquired EBSD data maps of identical positions of the sample surface at two different temperatures between 897°C and 900°C for the  $\alpha$ - $\gamma$  phase transformation. The thick black lines mark the grain boundaries of misorientation angles larger than 10° and the light grey lines inside the fcc  $\gamma$ -phase indicate  $\Sigma 3$ -twin boundaries. The light grey shaded area corresponds to the low temperature bcc  $\alpha$ -phase and the dark grey shaded grains are the high temperature fcc  $\gamma$ -phase. The phase boundaries between the  $\alpha$ - and  $\gamma$ -phase are colored in reference to the Kurdjumov-Sachs (K-S) orientation relationship [5]. Disorientations from K-S between 0° and 10° are marked with white lines, larger than 10° black lines.

The  $\alpha$ - $\gamma$  phase transformation can be seen to start with nucleation and growth in the temperature range of 897°C (Fig. 24.1 (a)) (5,3%  $\gamma$ -phase). With increasing temperature, further growth of the already formed nuclei as well as the formation of new fcc  $\gamma$ -nuclei occur. Besides that, new  $\gamma$ -grains with twin-relationships to the already formed neighbouring fcc  $\gamma$ -grains appear. At 900°C already 50% of the area has been turned into  $\gamma$ -phase (Fig. 24.1 (b)). As expected from former ex situ experiments the nucleation sites are predominantly at grain boundaries and triple junctions (Fig. 24.1 (a)–(b)) [1, 2]. Further, it can be seen that the growth of the

**Table 24.1** Chemical composition in wt% of the investigated microalloyed ferritic low carbon steel.

C	Si	Mn	Al	N	Cr	V	Mo	Ti	Nb
0.065	0.05	0.99	0.042	0.003	0.027	0.006	0.005	0.07	0.003

new  $\gamma$ -grains is mainly homogeneous and isotropic. Also a grain refinement can be observed (bcc 5.3  $\mu\text{m}$ , fcc 3.1  $\mu\text{m}$ ).

The K-S correspondence holds for the majority of the newly formed  $\gamma$ -grains in relation to mostly one neighbouring bcc mother grain.

The reverse process, the  $\gamma$ - $\alpha$ -phase transformation is shown in Fig. 24.2 (a)–(d). The EBSD-maps reflect the microstructural evolution of the surface area between 893°C and 890°C, respectively, after two complete transformation cycles. The marking of the lines and the colours of the grains are the same as in Fig. 24.1.

In comparison to the forward transformation the back transformation of the newly formed  $\alpha$ -phase occurs also by nucleation mainly at triple junctions and its growth. The  $\gamma$ - $\alpha$  phase transformation can be seen to start at the temperature of 893°C (Fig. 24.2 (a)) (1.4%  $\alpha$ -phase). With decreasing temperature further growth of the already formed nuclei as well as the formation of new  $\alpha$ -bcc nuclei occur. But there are obvious differences to the  $\alpha$ - $\gamma$  phase transformation. The main difference is the inhomogeneous growth of the bcc grains. The white and light grey lines indicate a good K-S relationship between the two phases; at these K-S boundaries no further phase transformation was observed (see the marked lines). The marked bcc grains which show no significant growth during transformation are bordered by more K-S boundaries with less deviation from the perfect relationship. These bcc grains have a good K-S relationship with two or three of the surrounding fcc grains, and no further growth of such grains takes place. In contrast to the  $\alpha$ - $\gamma$  phase transformation no grain refinement occurred, rather during the  $\gamma$ - $\alpha$  phase transformation a grain coarsening (fcc 9.3  $\mu\text{m}$ , bcc 24.2  $\mu\text{m}$ ) was observed.

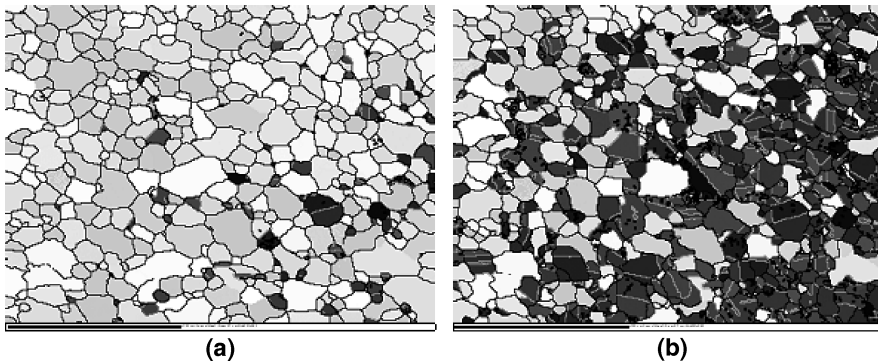


**Fig. 24.1** (a)–(b)  $\alpha$ - $\gamma$  phase transformation from 897°C (5.3% fcc) to 900°C (49.4% fcc) during heating up. Thick black lines mark grain boundaries of misorientation angles larger 10°, light grey lines inside the fcc  $\gamma$ -phase indicate  $\Sigma 3$ -twin boundaries, light grey shaded grains identify the bcc  $\alpha$ -phase, dark grey shaded grains are the fcc  $\gamma$ -phase. Disorientation from K-S between 0° and 10° are marked with white lines, larger than 10° with black lines, the length of the black bar (bottom left corner) corresponds to 100  $\mu\text{m}$ .

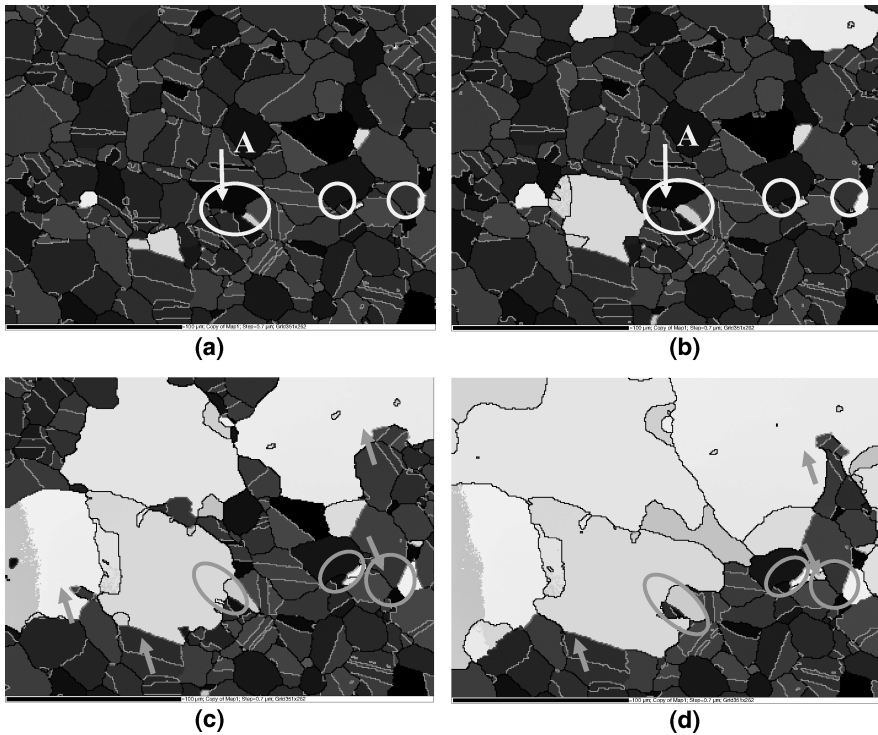


**Fig. 24.2** (a)–(d)  $\gamma$ - $\alpha$  phase transformation from 893°C (1,4% bcc) to 890°C (71,8% bcc) during cooling down. The marking of the lines and the colours of the grains are the same as in Fig. 24.1. Some grains without or less growth are marked with white circles. Some K-S phase boundaries are marked with white arrows.

### 24.3 Discussion

The results of the high temperature in situ EBSD measurements for the  $\alpha$ - $\gamma$  phase transformation demonstrate that the nucleation of the newly formed phase occurs mainly at triple junctions. Also, a good K-S correspondence in relation to mostly one neighbouring bcc mother grain was found for the majority of the newly formed  $\gamma$ -grains.

During the  $\gamma$ - $\alpha$  phase transformation the nucleation occurs also mainly at triple junctions and large ferrite grains develop. In contrast to the  $\alpha$ - $\gamma$  phase transformation several ferrite grains exhibit a good K-S relationship not only to one but two or three of the surrounding austenite grains, and virtually no growth of such grains takes place. Therefore, the microstructure during the  $\gamma$ - $\alpha$  phase transformation consists of small bcc grains surrounded by K-S boundaries and large bcc grains

with less K-S boundaries. Some of the small bcc grains develop an elongated shape during the  $\gamma$ - $\alpha$  phase transformation. This can be attributed to the fact that the phase transformation to ferrite is only feasible in a direction free of K-S boundaries (see grain A).

## 24.4 Summary

A new laser induced heating stage for commercial SEMs was used to acquire microstructural and crystallographic data by means of the EBSD-technique. The in situ investigations into the high temperature  $\alpha$ - $\gamma$ - $\alpha$  phase transformation in a microalloyed low carbon steel demonstrate the excellent performance of this laser powered heating stage and its potential for other high temperature applications. The following preliminary results were obtained:

- Nucleation occurred mainly at triple junctions
- The microstructure development during the  $\gamma$ - $\alpha$  phase transformation is inhomogeneous
- The mobility of the transformation front depends on its proximity to a K-S relationship

**Acknowledgements** The authors would like to thank the Deutsche Forschungsgemeinschaft for financial support through the research project “Investigation of variant selection during  $\alpha$ - $\gamma$ - $\alpha$  phase transformation in steel by using high temperature in situ EBSD in a high resolution SEM” (Go 335/33-1).

## References

- [1] I. Lischewski and G. Gottstein: Mat. Sci. Forum Vol. 495–497 (2005), p. 447
- [2] I. Lischewski and G. Gottstein: PTM 05 Conf. Proceedings (2005), p. 577
- [3] G. Brückner and G. Gottstein: ISIJ International Vol. 41 (2001), p. 468
- [4] I. Lischewski, D. M. Kirch, A. Ziemons, G. Gottstein: Texture, Stress, and Microstructure, (in press)
- [5] G. Kurdjumov and G. Sachs: Z.Phys., 64 (1930), 225





## Chapter 25

# A New Flow Function to Model Texture Evolution in Symmetric and Asymmetric Rolling

Benoît Beausir and László S. Tóth

**Abstract.** Using a new analytic flow function, an analysis of the deformation field in symmetrical and asymmetrical rolling has been carried out. The asymmetry concerns the differences in the angular speeds of the rolling cylinders. The flow function describes the trajectory of the material flow from which the velocity field and the velocity gradient is obtained by partial derivations. The new flow function takes also into account the “discontinuity” at the entry of the material into the die. By introducing a non-homogeneous velocity distribution at the end of the flow line, the shear component in the rolling plane and in the rolling direction that is characteristic to the asymmetric rolling is naturally introduced into the deformation process. The varying velocity gradient along selected flow lines is incorporated into the viscoplastic self-consistent polycrystal plasticity model to simulate the development of the deformation texture. The effect of multiple passes as well as the asymmetries on the evolution of the deformation textures is studied for bcc iron.

### 25.1 Introduction

Several descriptions of the deformation by streamlines in symmetric rolling are proposed in the literature [D00, SAC07]. Most of the time they describe only the deformation zone with a discontinuity at the entry point. Concerning asymmetric rolling, the difference between the roll speeds induces a shear component in the rolling plane and in the rolling direction which is taken into account by simply adding an arbitrary chosen constant shear to get the appropriate texture evolution [JL07, LL01, LL07, ZVS03]. In this work, a new flow function is proposed; it is able to describe the discontinuity at the entry point of the plastic flow and a vary-

---

B. Beausir and L.S. Tóth

Laboratoire de Physique et Mécanique des Matériaux, Université de Metz, Ile du Saulcy,  
57045 Metz Cedex 1, France

ing shear component is naturally generated by introducing a non-uniform output velocity profile. The velocity gradient is obtained by partial derivation of the streamline function and implemented into a viscoplastic self-consistent polycrystal plasticity model to simulate the development of the deformation texture in the cases of symmetric and asymmetric rolling.

## 25.2 Flow Modelling

Figure 25.1 shows the geometrical parameters of the rolling process; the entry half thickness  $e$ , the half exit thickness  $s$ , the roll radius  $R$ , the angle  $\theta$  corresponding to the contact zone between the sheet and the roll, the x-coordinate  $d$  of the exit flow, the top and bottom roll angular velocities  $\omega_{roll}^t$  and  $\omega_{roll}^b$  (rad/s), respectively, the top and bottom contact sheet velocities  $v_0^t$  and  $v_0^b$ , respectively, and the deviation part  $v_n$  of the speed at the exit of the deformation zone in the centre of the sheet. The  $z_s$  parameter defines the position of the streamline at the end of the deformation zone.

The proposed streamline is defined by:

$$\phi(x, z) = z \left[ 1 + \left( \alpha + (1 - \alpha)(x - d)^2 / d^2 \right)^{-n} \right]^{1/n} = z_s / \alpha, \quad (25.1)$$

with  $\alpha = s/e$ ;  $d = R \sin(\theta)$ ;  $\cos(\theta) = (R + s - e)/R$ .

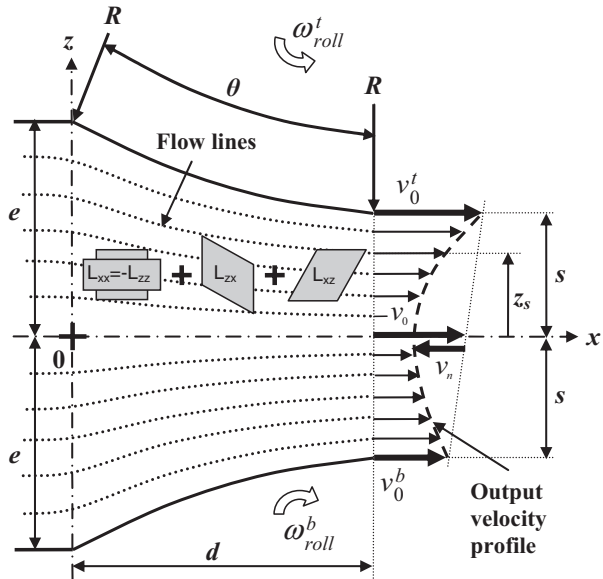


Fig. 25.1 Rolling schema.

By supposing a steady state flow, a kinematically acceptable velocity field can be defined as follows:

$$\begin{aligned} v_x &= \lambda(x, z) \partial \phi(x, z) / \partial z = \lambda(x, z) \zeta, \\ v_z &= -\lambda(x, z) \partial \phi(x, z) / \partial x = 2\lambda(x, z) z(1-\alpha)(x-d) \zeta d^{-2} \xi^{-(n+1)} \kappa^{-1}, \\ \text{with } \xi &= \alpha + (1-\alpha)(x-d)^2 / d^2, \quad \kappa = 1 + 1/\xi^n, \quad \zeta = \kappa^{1/n}. \end{aligned} \quad (25.2)$$

The function  $\lambda(x, z)$  is obtained from the velocity at the exit of the deformation zone ( $x = d$ ):  $v_z|_{x=d} = 0$  and  $v_x|_{x=d} = \lambda(x, z)(\alpha^{-n} + 1)^{1/n}$ . Then by replacing  $\lambda(x, z)$  into Eq. 25.2, the velocity field is fully expressed. The output velocity distribution (at  $x = d$ ) is supposed to be parabolic (see Fig. 25.1) and given by:

$$\begin{aligned} v_x|_{x=d} &= Az_s^2 + Bz_s + C \\ \text{with } A &= v_0' + v_0^b - 2(v_0 + v_n)/2s^2; \quad B = (v_0' - v_0^b)/2s; \quad C = v_0 + v_n. \\ \text{and } v_0' &= \omega_{roll}' R; \quad v_0^b = \omega_{roll}^b R; \quad v_0 = R(\omega_{roll}' + \omega_{roll}^b)/2; \quad v_n = -pv_0; \end{aligned} \quad (25.3)$$

Here  $p$  is a parameter that specifies the exact shape of the parabolic output velocity field; it can be affected by the friction conditions. Note that  $v_x|_{x=d}$  is a function of  $z_s$ , thus, in order to derive the velocity gradient, the velocity field has to be fully expressed in terms of the  $x$  and  $z$  variables using the flow function before further derivation. For this purpose, we express  $z_s$  from the flow function as:  $z_s = \alpha z \zeta$ . Then by replacing first  $z_s$  in  $v_x|_{x=d}$ , the velocity gradient is finally expressed by:

$$\begin{aligned} L_{xx} &= \partial v_x / \partial x = 2\zeta(\alpha-1)(x-d)(3Az_s^2 + 2Bz_s + C) / d^2 \kappa(\alpha^{-n} + 1)^{1/n} \xi^{(n+1)}, \\ L_{xz} &= \partial v_x / \partial z = \alpha \zeta^2 (2Az_s + B) / (\alpha^{-n} + 1)^{1/n}, \\ L_{zx} &= \frac{4z_s(1-\alpha)^2(d-x)^2 v_x|_{x=d}}{\alpha d^4 \kappa^2 (\alpha^{-n} + 1)^{1/n}} \\ &\quad \left( \frac{(n-1)}{\xi^{2(n+1)}} + \frac{\xi^{-(n+1)} d^2 \kappa}{2(1-\alpha)(d-x)^2} - \frac{z_s(2Az_s + B)}{v_x|_{x=d} \xi^{2(n+1)}} - \frac{\kappa(n+1)}{\xi^{(n+2)}} \right), \\ L_{zz} &= \partial v_z / \partial z = -L_{xx}, \quad L_{yy} = L_{xy} = L_{yx} = L_{yz} = L_{zy} = 0. \end{aligned} \quad (25.4)$$

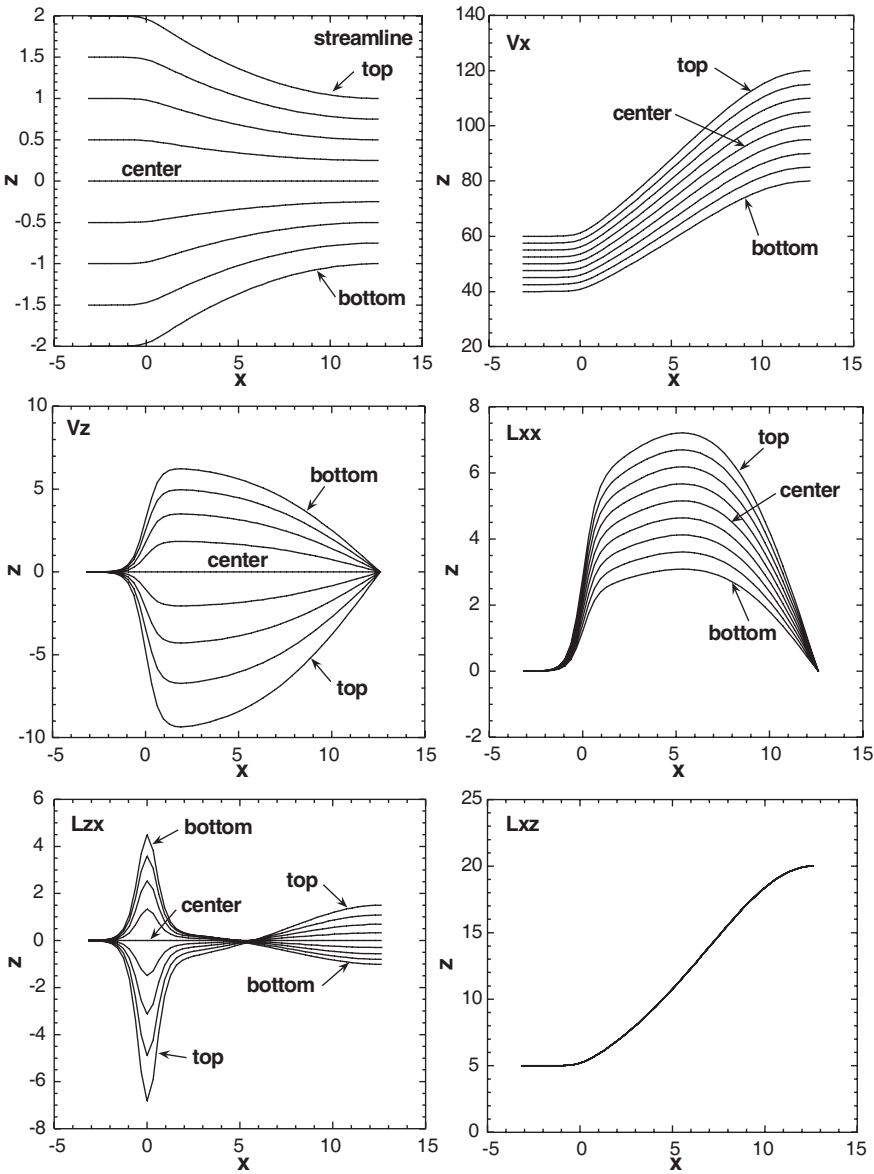
This varying velocity gradient can be incorporated into the viscoplastic self-consistent polycrystal plasticity model to simulate the evolution of the deformation texture.

### 25.3 Velocity Field, Velocity Gradient and Texture Results

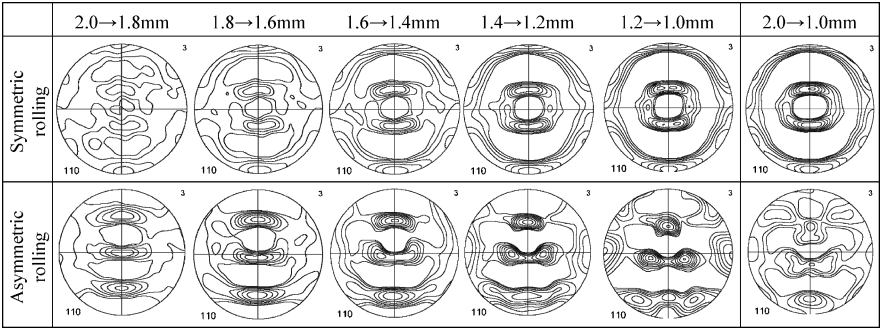
Variations of the velocity and the velocity gradient in the plastic deformation zone are first analyzed. The following combination of the parameters were chosen:  $e = 2 \text{ mm}$ ,  $s = 1 \text{ mm}$ ,  $R = 80 \text{ mm}$ ,  $\omega_{roll}^f = 1.5 \text{ rad.s}^{-1}$ ,  $\omega_{roll}^b = 1.0 \text{ rad.s}^{-1}$  and  $p = 0$  (that means a linear distribution of the velocity at the exit,  $v_n = 0$ ). From Fig. 25.2 it can be seen that the discontinuity is conveniently described by the streamline function at the entry point of the flow line. The  $L_{zx}$  component of the deformation shows large variations near the entry point, at  $x = 0$ . The  $v_x$  component of the velocity continuously increases along the flow line (a consequence of the incompressibility condition). As the output velocity field is supposed to be linear,  $L_{xz}$  is independent of the flow lines position but varies along the  $x$  coordinate; at the exit point it can be about 4 times larger than  $L_{xx}$ .

Figure 25.3 presents the texture evolution results obtained for bcc iron for a reduction of 2 mm to 1 mm obtained in one or five passes in symmetric or asymmetric rolling (the angular velocity ratio of the rolls is 1.5) on the upper flow line (near to the faster roll) using the self consistent viscoplastic polycrystal plasticity model [MCA87]. The pencil glide mode was approached by using the  $(110)\langle 111 \rangle$  and  $(112)\langle 111 \rangle$  slip system families with equal strengths. 2000 randomly oriented grains represented the initial texture. The  $n$  exponent was 35. The power law of Asaro and Needleman [AN85] with a strain rate sensitivity of 0.05 was employed for the slip process.

As can be seen, the texture evolution in asymmetric rolling is very different from the symmetric rolled case. This is due to the shear component which can be about 4 times larger than the compression component. The texture in asymmetric rolling tends towards a shear type deformation texture of bcc metals, especially at increasing pass numbers.



**Fig. 25.2** Streamlines and values of  $v_x, v_z, L_{xx}, L_{zx}, L_{xz}$  in the thickness of the sheet (along 9 lines; top,  $3/4, 1/2, 1/4$ , centre,  $-1/4, -1/2, -3/4$ , bottom).



**Fig. 25.3** Simulated texture evolution in Fe for symmetric and asymmetric rolling on the upper surface. ND is in the middle and RD is pointing down in all figures.

25.4 Conclusion

A new flow line function is proposed to describe symmetric or asymmetric rolling processes in multiple passes. The model predicts shear type textures in asymmetric rolling near to the surface region of the rolled plate. A comparative experimental study is needed to explore the performance of the present flow line approach.

References

[LL07] Lee JK, Lee DN, 2007. Texture control and grain refinement of AA1050 Al alloy sheets by asymmetric rolling. *International Journal of Mechanical Sciences*, in press

[ZVS03] Zhang F, Vincent G, Sha YH, Zuo L, Fundenberger JJ, Esling C, 2004. Experimental and simulation textures in an asymmetrically rolled zinc alloy sheet. *Scripta Materialia* 50, 1011–1015

[LL01] Lee SH, Lee DN, 2001. Analysis of deformation textures of asymmetrically rolled steel sheets. *International Journal of Mechanical Sciences* 43, 1997–2015

[JL07] Jin H, Lloyd DJ, 2007. Evolution of texture in AA6111 aluminum alloy after asymmetric rolling with various velocity ratios between top and bottom rolls. *Materials Science and Engineering A* 465, 267–273

[D00] Dođruoğlu AN, 2001. On constructing kinematically admissible velocity fields in cold sheet rolling. *Journal of Materials Processing Technology* 110, 287–299

[SAC07] Sezek S, Aksakal B, Can Y, 2007. Analysis of cold and hot plate rolling using dual stream functions. *Materials and Design*, in press

[AN85] Asaro RJ, Needleman A, 1985. Texture development and strain hardening in rate dependent polycrystals. *Acta Metallurgica* 33, 923–953

[MCA87] Molinari A, Canova G, Ahzi S, 1987. A self consistent approach of the large deformation polycrystal viscoplasticity. *Acta Metallurgica* 35, 2983–2994.

# Chapter 26

## Microstructure and Texture Evolution During the Accumulative Roll Bonding of Pure Ni

P.P. Bhattacharjee, D. Terada, and N. Tsuji

**Abstract.** Evolution of microstructure and texture was studied in severely plastically deformed (up to an equivalent strain of 6.4) high purity (99.99%) Ni sheets processed through Accumulative Roll Bonding (ARB). As received Ni plates ( $\sim 10$  mm in thickness) were cold rolled to  $\sim 80\%$  reduction in thickness ( $\sim 2$  mm) and vacuum annealed at  $600^\circ\text{C}$  for one hour and these were used as the starting materials (average grain size  $\sim 25\text{ }\mu\text{m}$ ) for the subsequent ARB processing. ND and TD plane normal sections of the ARB processed sheets were subjected to Electron Back Scatter Diffraction (EBSD) and Transmission Electron Microscope (TEM) studies. The ARB processed Ni sheets were found to be filled with ultrafine grains (average grain size  $\sim 400$  nm) after 8 cycles of ARB. Extensive shear band formation was observed particularly in the high cycle ARBed materials. The deformation textures were found to be quite inhomogeneous at the low cycle regime of the ARB. However, the deformation texture achieved remarkable homogeneity after 6 and 8 cycles of ARB and S ( $\{123\} < 634 >$ ) component of the deformation texture was found to be quite strong.

### 26.1 Introduction

Ultrafine grained (UFG) materials with average grain size smaller than  $1\text{ }\mu\text{m}$  show outstanding mechanical properties such as high strength, toughness and often room temperature superplastic properties. Severe plastic deformation (SPD) is one of the most effective means of achieving such ultrafine grain sizes in a wide variety of materials.

---

P.P. Bhattacharjee, D. Terada, and N. Tsuji

Department of Adaptive Machine Systems, Graduate School of Engineering, Osaka University,  
2-1 Yamadaoka, Suita, Osaka, 565-0871, Japan,  
phone: + 81 6 6879 4173, Fax: + 81 6 6879 4174  
e-mail: pinaki@ams.eng.osaka-u.ac.jp



Several different kinds of SPD processes such as equal channel angular pressing/extrusion (ECAP) [1, 2], high pressure torsion (HPT) [3] and accumulative roll bonding (ARB) [4] have been developed to produce ultrafine grained materials in bulk scale. Amongst these processes the ARB process is very attractive due to the fact that it is the only SPD process based upon rolling deformation i.e. an already established industrial fabrication process.

A number of different material systems have so far been subjected to ARB processing such as pure Al, different Al alloys, pure Cu and interstitial free (IF) steels and the subject has recently been reviewed by Tsuji et al. [5].

The current work investigates the microstructural and textural changes in pure Ni subjected to ARB processing. Pure Ni is one of the most studied materials for understanding the evolution of deformation structure and textures subjected to normal cold rolled condition. Additionally, Ni is a f.c.c. metal having intermediate stacking fault energy value between pure Al and pure Cu. Thus the results from Ni could be very helpful in understanding the mechanism of formation of ultrafine grains and characteristic deformation textures during ARB processing.

## 26.2 Experimental

### 26.2.1 *ARB Process*

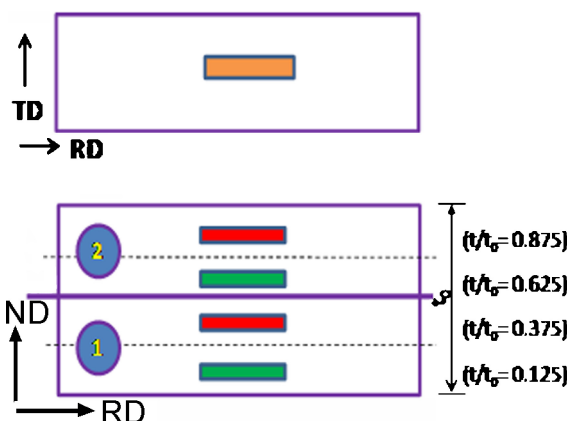
As received Ni plates ( $\sim 160 \text{ mm}^L \times 60 \text{ mm}^W \times 10 \text{ mm}^T$ ) of  $\sim 99.99\%$  purity were first cold rolled to  $\sim 80\%$  reduction in thickness ( $\sim 2 \text{ mm}$  in thickness). The cold rolled sheets were then annealed at  $600^\circ\text{C}$  for one hour in vacuum. These annealed sheets were used as the starting materials for the subsequent ARB process.

In the first cycle of the ARB process an annealed sheet of pure Ni of thickness  $\sim 2 \text{ mm}$  was cold rolled in a single pass to  $\sim 1 \text{ mm}$  in thickness corresponding to  $50\%$  reduction in thickness. This cold rolled sheet was then cut into halves, degreased with acetone and subjected to wire brushing to achieve suitable bonding surfaces. And then the two sheets were stacked and roll-bonded by  $\sim 50\%$  reduction in thickness in a single pass at ambient temperature. A two-high rolling mill with well lubricated rolls and having a roll diameter of  $310 \text{ mm}$  was used for this work. The rolling speed was maintained constant at  $17.5 \text{ m min}^{-1}$ . The rolled sheets coming out from the exit side were immediately quenched with cold water. The procedures described above were repeated for each cycle of the ARB. The ARB process was carried out at room temperature and up to 8 cycles corresponding to a true strain of 6.4.

### 26.2.2 *Microstructural Investigation*

The ARBed sheets were subjected to thorough Electron Back Scatter Diffraction (EBSD) and Transmission Electron Microscopy (TEM) studies to figure out the

**Fig. 26.1** Schematic diagram of various thickness locations from where EBSD measurements were taken. (1) and (2) as marked in the figure indicates the two stacked sheets.



microstructural and textural changes occurring during the ARB process. EBSD data were acquired from the rolling plane section as well as in the longitudinal section at various thickness locations to understand the through thickness microstructural and textural variation. Figure 26.1 depicts a schematic diagram of various locations from where the EBSD measurements were taken. The measurements were carried out in a fully computer controlled automated EBSD (TSL-OIM) attached with a field emission gun FEI scanning electron microscope (model:) operated at 15 kV. A constant working distance of 15 mm was used through out this work.

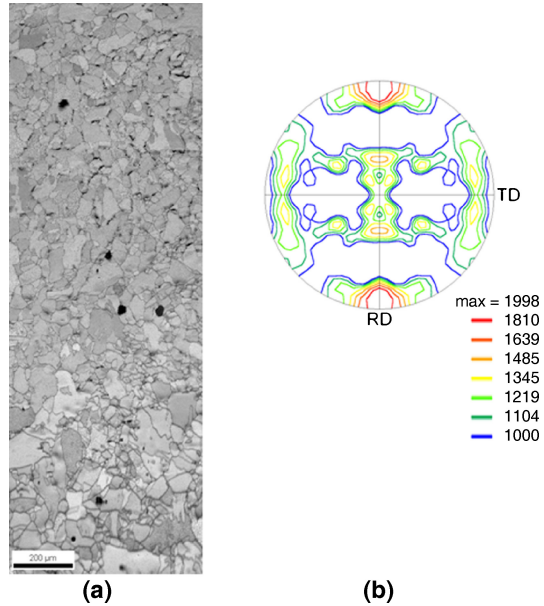
## 26.3 Results and Discussion

Figure 26.2 shows the image quality (IQ) map and the (111) pole figure of the starting material for the ARB process. The starting sheet of Ni had a fully recrystallized microstructure. The average grain size determined from the EBSD scan at this condition was found to be  $\sim 25 \mu\text{m}$ .

Figure 26.3 (a)–(e) show the image quality with overlaid grain boundaries for the 2 cycle ARB processed material measured at various thickness locations. The low ( $2^\circ \leq \theta_{\text{mis}} \leq 15^\circ$ ) and high angle ( $\theta_{\text{mis}} \geq 15^\circ$ ) boundaries have been depicted in red and blue lines in these maps, respectively. The fraction of high angle boundaries and the average misorientation angle are found to depend strongly on the thickness location as is shown in Fig. 26.4. Figure 26.4 also includes the results for the successive ARB cycles and will be referred in subsequent discussions. The distribution of high angle boundaries and average misorientation angles after two cycles of processing reveals in homogeneity through the thickness of the sheet. A large fraction of low angle boundaries are found to be present across all thickness locations in this condition.

The (111) pole figures corresponding to the various thickness locations in the 2-cycle ARB processed materials have been shown in Fig. 26.5(a)–(e). The vol-

**Fig. 26.2** (a) Image quality map and (b) (111) pole figure of the starting material for the ARB process.



ume fractions of typical texture components in cold rolled fcc materials have been determined from the EBSD scan and those have been plotted against the thickness locations in the sheet as shown in Fig. 26.5 (f). It may be easily seen that there is pronounced through thickness texture variation in the 2-cycle ARB processed material resulting in very inhomogeneous deformation texture in this condition.

The through thickness microstructural variation after 4 cycles of ARB processing has been shown in Fig. 26.6 (a)–(e). The microstructural evolution in this condition is characterized by the clear presence of macroscopic shear bands. Dis-

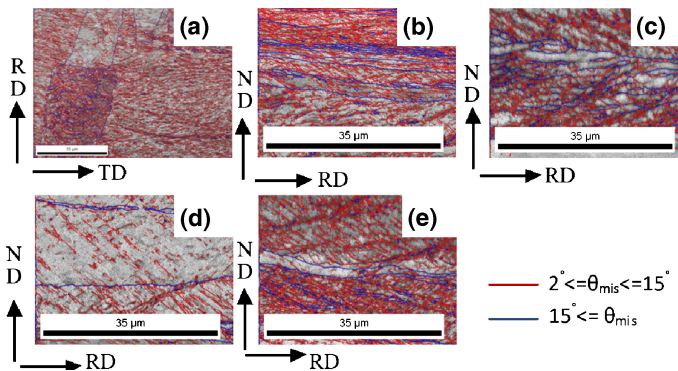


**Fig. 26.3** EBSD image quality maps with overlaid boundaries for the 2-cycle processed materials. The different thickness location corresponds to (a) surface ( $t/t_0=0$ ), (b)  $t/t_0=0.125$ , (c)  $t/t_0=0.375$ , (d)  $t/t_0=0.625$  and (e)  $t/t_0=0.875$ .

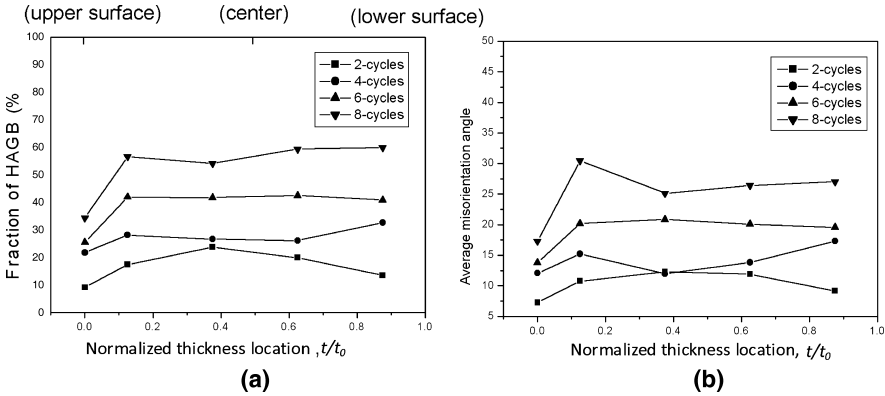


**Fig. 26.4** Through thickness variation in (a) HAGB fraction and (b) average misorientation angles in pure Ni processed to different ARB cycles.

tribution of high angle boundaries across the thickness of the sheet reveals inhomogeneity but the fraction of HAGBs and average misorientation angle increases as compared to 2-cycle processed material (Fig. 26.4).

The (111) pole figures corresponding to the various thickness locations in the 4-cycle processed materials have been shown in Fig. 26.7 (a)–(e). Although, the plot of volume fractions of the texture components vs. thickness location (Fig. 26.7 (f)) in the 4-cycle ARB processed material reveals the presence of through thickness texture heterogeneity, a clear pattern evolves at this stage and the S-component ( $\{123\} < 634 \rangle$ ) of the deformation texture becomes quite strong.

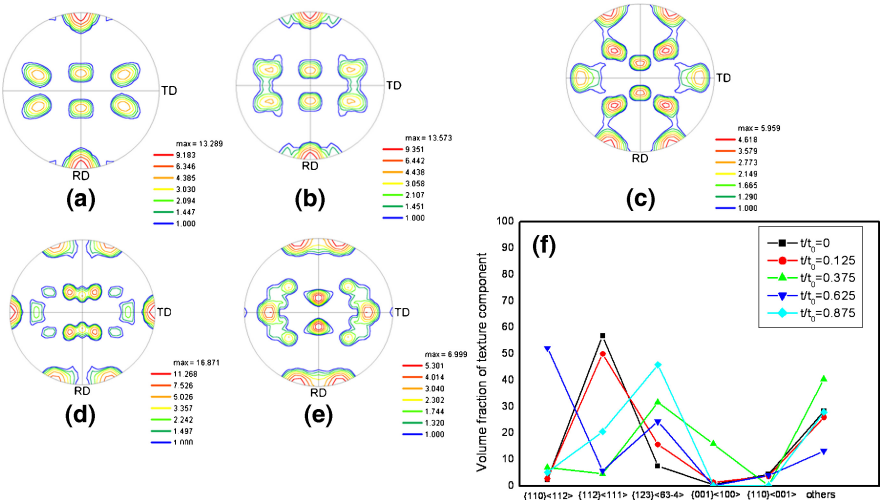


**Fig. 26.5** (111) pole figures of 2-cycle processed material at different thickness locations; (a)  $t/t_0=0$ , (b)  $t/t_0=0.125$ , (c)  $t/t_0=0.375$ , (d)  $t/t_0=0.625$  and (e)  $t/t_0=0.875$ ; the volume fraction of rolling texture components at various thickness locations is shown in (f).

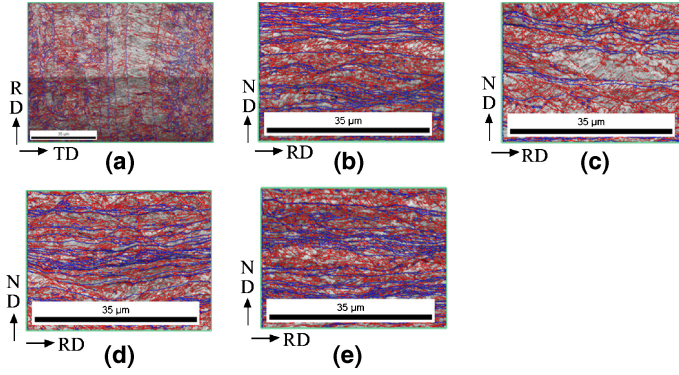


**Fig. 26.6** EBSD image quality maps with overlaid grain boundaries for the 4-cycle processed material. The different thickness location corresponds to (a) surface ( $t/t_0=0$ ), (b)  $t/t_0=0.125$ , (c)  $t/t_0=0.375$ , (d)  $t/t_0=0.625$  and (e)  $t/t_0=0.875$ . The color key for grain boundaries is same as in Fig. 26.3.

The IQ maps in Fig. 26.8 (a)–(e) show the microstructure evolution in 6-cycle processed material at various thickness locations. Intense shear band formation is observed across all thickness locations in this condition. The distribution of HAGBs and average misorientation angle (Fig. 26.4) shows that the variation in these two microstructural parameters has diminished dramatically as compared to the 4-cycles process material and a through thickness homogeneity has been established. Although, the fraction of HAGBs and average misorientation at the rolling surface greatly differs with those at other thickness locations but this could be due to the two different observed planes.

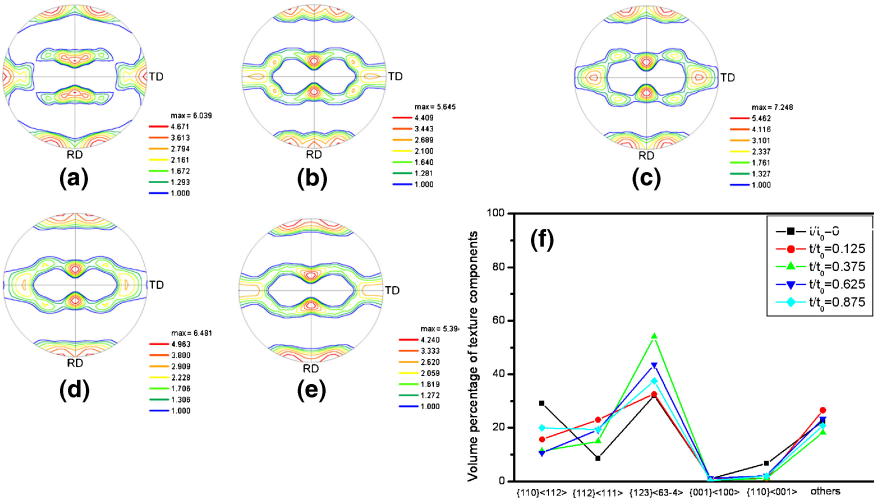


**Fig. 26.7** (111) pole figures of 4-cycle processed material at different thickness locations; (a)  $t/t_0=0$ , (b)  $t/t_0=0.125$ , (c)  $t/t_0=0.375$ , (d)  $t/t_0=0.625$  and (e)  $t/t_0=0.875$ . The volume fraction of rolling texture components at various thickness locations is shown in (f).

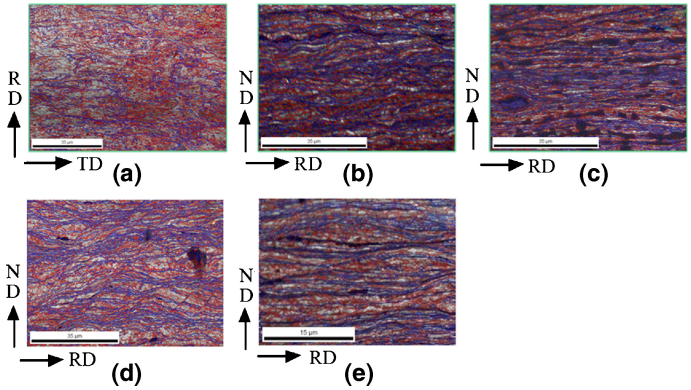


**Fig. 26.8** EBSD image quality maps with overlaid grain boundaries for the 6-cycles processed materials. The different thickness location corresponds to (a) surface ( $t/t_0=0$ ), (b)  $t/t_0=0.125$ , (c)  $t/t_0=0.375$ , (d)  $t/t_0=0.625$  and (e)  $t/t_0=0.875$ . The color key for grain boundaries is same as in Fig. 26.3.

The (111) pole figures corresponding to the various thickness locations in the 6-cycle processed material have been shown in Fig. 26.9 (a)–(e). The deformation texture is characterized by the presence of a large volume fraction of S-component which was also witnessed in the 4-cycle processed material.

Microstructural evolution in 8-cycles processed material has been shown in Fig. 26.10 (a)–(e). The distribution of HAGB and average misorientation angle (Fig. 26.4) across different thickness location reveals that there is little through thickness variation which also indicates that the ultrafine microstructure at this

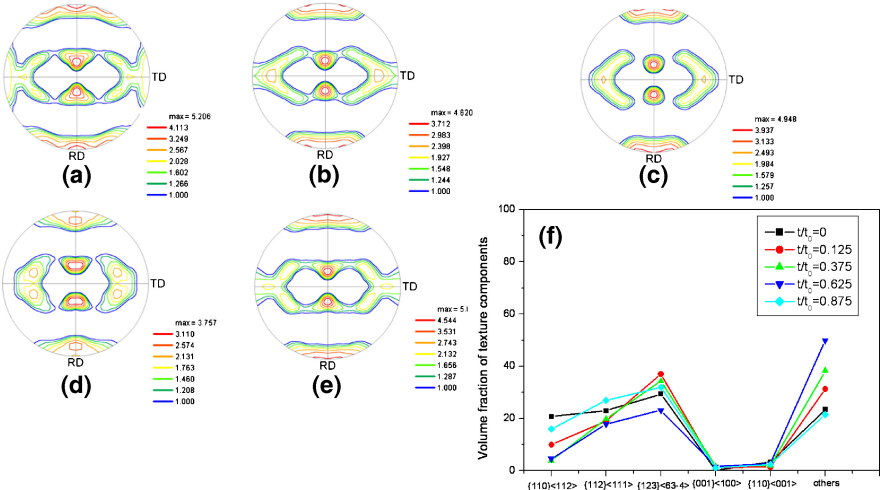


**Fig. 26.9** (111) pole figures of 6-cycle processed material at different thickness locations; (a)  $t/t_0=0$ , (b)  $t/t_0=0.125$ , (c)  $t/t_0=0.375$ , (d)  $t/t_0=0.625$  and (e)  $t/t_0=0.875$ . The volume fraction of rolling texture components at various thickness locations is shown in (f).



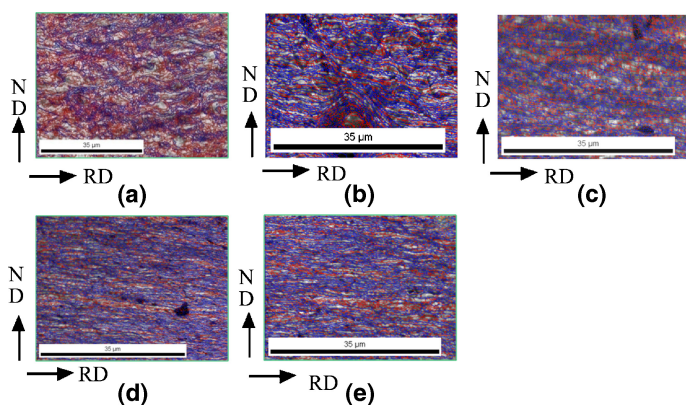


**Fig. 26.10** EBSD image quality with overlaid grain boundaries for the 8-cycles processed materials. The different thickness location corresponds to (a) surface ( $t/t_0=0$ ), (b)  $t/t_0=0.125$ , (c)  $t/t_0=0.375$ , (d)  $t/t_0=0.625$  and (e)  $t/t_0=0.875$ . The color key for grain boundaries is same as in Fig. 26.3.

stage is quite homogenous. The average interval of HAGB along ND in this condition is found to be  $\sim 400$  nm.

Remarkable homogeneity in deformation textures is achieved in this condition as may be seen clearly from the (111) pole figures (Fig. 26.11 (a)–(e)) and the plot of volume fraction of texture component vs. thickness locations.

The microstructure evolution during the ARB processing of pure Ni is such that a typical lamellar boundary structure evolves with increasing ARB cycles. The de-

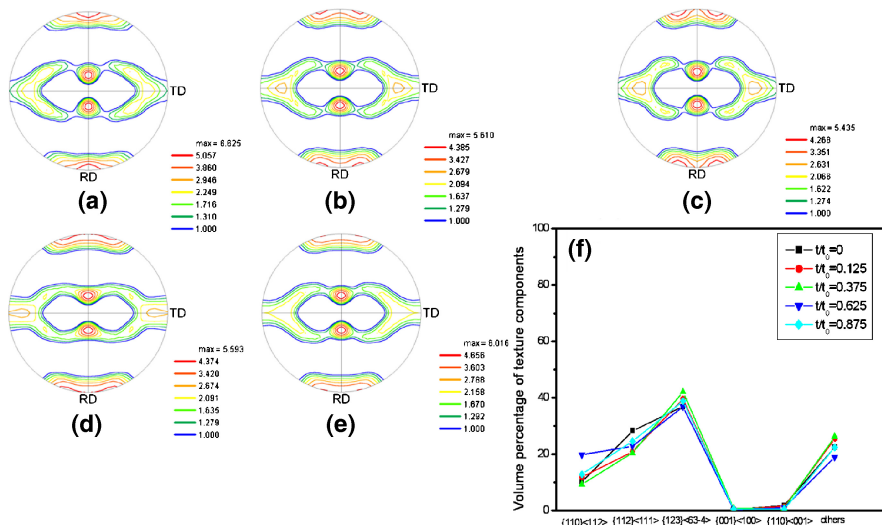


**Fig. 26.11** (111) pole figures of 8-cycle processed material at different thickness locations; (a)  $t/t_0=0$ , (b)  $t/t_0=0.125$ , (c)  $t/t_0=0.375$ , (d)  $t/t_0=0.625$  and (e)  $t/t_0=0.875$ . The volume fraction of rolling texture components at various thickness locations is shown in (f).

formation microstructure and texture remain quite inhomogeneous at low processing cycles. However, at high cycle regime both the deformation microstructure and texture becomes homogenous. It may be noted that, the fraction of high angle boundaries even after 8-cycles of ARB processing is quite low ( $\sim 60\%$ ). The fraction of high angle boundaries was also found to be quite low after 6-cycle of ARB in OFHC-Cu [6]. Li et al. [6] has reported that low proportion of high angle boundary in OFHC-Cu could be due to room temperature recovery and recrystallization during ARB processing. The formation of new grains has been attributed to the accumulated strain, which drives recovery and recrystallization, the adiabatic heating caused by large deformation in a single pass and very high purity of the material. The new recrystallized grains are deformed in next ARB cycles generating substructure consisting of low angle boundaries and thus increasing the low angle boundary fraction. In pure Ni, however, such recrystallized grains have not been identified in the microstructure even at high ARB cycles and this must be investigated further.

## 26.4 Conclusions

The microstructural and textural evolution in pure Ni during ARB processing is quite inhomogeneous at lower ARB cycles which results in the through thickness variation of relevant microstructural parameters and volume fraction of textural components. With increasing ARB cycles both microstructure and texture achieves remarkable homogeneity. The deformation behavior in the high cycle regime of the ARB process is characterized by appearance of large shear bands. Through thickness variation in HAGB fraction and average grain boundary misorientation indicate that the 8-cycle processed material possesses quite homogenous ultrafine grain structure having an average grain size of  $\sim 400$  nm. The deformation texture of ARB processed material at high cycle regime is characterized by the presence of a strong S-component.

**Acknowledgement** The authors gratefully acknowledge the support from the JSPS Postdoctoral Fellowship for Young Foreign Researchers and the Global CoE Program (Center of Excellence for Advanced Structural and Functional Materials Design) from the Ministry of Education, Culture, Sports, Science and Technology (MEXT), Japan.

## References

- [1] Segal VM, Mater. Sci. Eng. A 1995;197:157.
- [2] Iwahashi Y, Wang J, Horita Z, Nemoto M, Langdon TG, Scripta Mater 1996;35:143.
- [3] Abdulov RZ, Valiev RZ, Krasilinikov NA, J Mat Sci Lett 1990;9:1445.
- [4] Saito Y, Tsuji N, Utsunomiya H, Sakai T, Hong RG, Scripta Mater 1998;39:1221.
- [5] Tsuji N, Saito Y, Lee S-H, Minamino Y, Adv Eng Mater 2003;5:338.
- [6] Li BL, Tsuji N, Kamikawa N, Mater Sci Eng A 2006; 423:331.





## Chapter 27

# Microstructure of the Rust Formed on Si-Al Bearing Ultrafine-Grained Weathering Steel

V. Raman and T. Nishimura

**Abstract.** In the Ultra-steel project in NIMS, high-Si and Al type ultrafine-grained (UFG) weathering steel was created by the multi-pass warm rolling method, and the corrosion resistance and microstructure of the rust were estimated. The Si and Al-bearing UFG steels exhibited excellent corrosion resistance than carbon steel (SM). The EPMA and TEM analyses showed that Si and Al were mainly existing as nano-oxides in the inner rust layer formed on the UFG steels. The Al  $K_{\alpha}$  X-ray spectrum of the test sample exhibited the peak at the same position as that of  $Al_2O_3$ , which suggests that Al is present in the inner rust in  $Al^{3+}$  state. In the same way, Si was identified as  $Si^{2+}$  in the complex Iron oxides of inner rust using EPMA.

The EIS (Electrochemical Impedance Spectroscopy) measurement was conducted for the corrosion test samples to find that the corrosion resistance ( $R_t$ ) of Si and Al-bearing UFG steel was much larger than that of SM. In the developed steel, the nano-complex oxides were made in the lower layer of iron rust, that increased  $R_t$  and suppressed the corrosion. Finally, it was found that High-Si and Al type UFG weathering steel showed excellent properties in strength, toughness and corrosion resistance.

**Keywords:** Rust, Al, Si, weathering steel, ultrafine grain, EIS, EPMA

## 27.1 Introduction

Recently, it has become highly essential to use weathering steel to reduce the maintenance cost of infrastructure facilities. In addition, there are number of steel

---

V. Raman and T. Nishimura  
Structural Metals Center, National Institute for Material Science (NIMS), 1-2-1 Sengen,  
Tsukuba, Ibaraki, 305-0047, Japan, Tel.: +81-29-859-2127, Fax: +81-29-859-2101  
e-mail: Raman.Vedrajan@nims.go.jp

structures being constructed in coastal areas, it is necessary to use high resistant steels against the corrosion caused by air-borne salt particles [1]. Thus, Ni-bearing weathering steels [2] that can be used in coastal environments have been proposed in Japan. However, Ni is a rare metal and hard to use for the recycle of steels. While, there have been many analyses of rust on the steels in mild environments [4–10], there are many problems that remain unclear regarding the basic mechanisms of the rust formation [11] and the effect of alloy elements [12–14] in saline environments. Therefore, in order to obtain the corrosion guidance for weathering steels that can be used in coastal environment, the thermodynamic stability of various rusts (Fe-X system) were investigated using a binary-phase potential-pH diagram [15]. Finally, it was concluded that Al and Si had the possibility to form stable complex-oxides with Fe. Moreover, Si and Al do not prevent the recycle-use of steels that will be necessary in the future to take into consideration of LCA (Life Cycle Assessment). However, there have been a few reports about the effect of Si or Al [16, 17] on the atmospheric corrosion of steels in saline environment. In this study, the process of rust formation and their electrochemical behavior were investigated on Si and Al-bearing steels in a wet/dry condition. Specially, the chemical state of Si and Al in the rust for the developed steel was examined using EPMA and TEM. Moreover, the electrochemical behavior of the rust was investigated by the electrochemical impedance spectroscopy (EIS) method after corrosion test. Finally, the relation between the formation and electrochemical behavior during the formation of rust over Si and Al-bearing steel was discussed.

## 27.2 Experiments

Slabs of high Si and Al type low alloy steel were quenched from 1373 K and subjected to the multi-pass warm caliber-rolling with accumulated area reduction of 95% at a temperature between 773 K and 873 K. The grain size of steel rolled at 873 K was about 1  $\mu\text{m}$ , which was almost similar to that of Si-Mn carbon steel

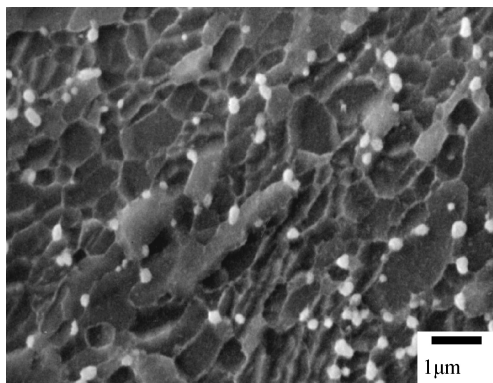


**Fig. 27.1** Structure of UFG weathering steel.

(SM) rolled at the same temperature (Fig. 27.1). However, yield strength (YS) was 130 MPa higher than that of SM by the solid-solution hardening of Si and Al. In general, high Si and Al steels shows worse toughness property than SM, however, samples showed very excellent one by the grain refinement. Thus, we are newly able to develop high corrosion resistant steels with high Si and Al using the refinement method. Corrosion resistance of sample was estimated by wet/dry accelerated corrosion test and the exposure test. After corrosion test, the iron rust was investigated by EPMA, TEM and EIS.

## 27.3 Results and Discussions

Corrosion-stress (YS) map was created in Fig. 27.2. Corrosion ratios of samples were estimated by assuming that the content of corrosion of SM was 100% in accelerated test. Corrosion ratios of samples were shown between that of 1%Ni and 3%Ni steel, which means that the developed steels are thought to be able be used in the coastal area of 0.2 mdd ( $\text{mg}/\text{dm}^2/\text{day}$ ). YS of samples were obtained between 700 and 1000 MPa according to the rolling temperature. There are few reports about weathering steels which have more strength than 600 MPa in YS, thus the developed steel is very unique as structural steels. Corrosion ratios of samples were shown as a function of the rolling temperature in Fig. 27.3. Samples rolled at 550 to 600°C showed high corrosion resistance. Corrosion ratio depended mainly on the chemical composition (content of Si and Al), and secondly on the ultrafine grained structure.

Distributions of Si, Al and oxygen in the rust were shown in Fig. 27.4 using EPMA after 20 cycles of corrosion test. Al and Si were enriched at the same position in the lower layer of the rust. Thus, they were thought to make a complex oxide with iron in the lower layer. The states of Si and Al in the rust were analyzed by EPMA. Si  $K_{\alpha}$  X-ray analyses were performed on two standard reference samples,  $\text{SiO}_2$  and metallic Si as shown in Fig. 27.5. The Si  $K_{\alpha}$  X-ray spectra of  $\text{SiO}_2$  and metallic Si have different peak positions, and that of the test sample were at a point in between these two peaks. This result suggests that Si is present in

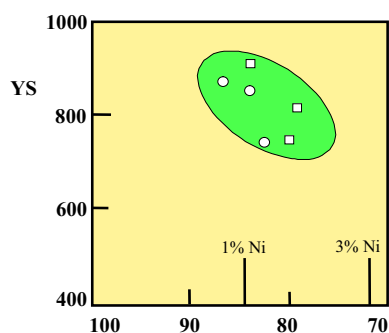


Fig. 27.2 Corrosion – yield stress (Mpa) map.

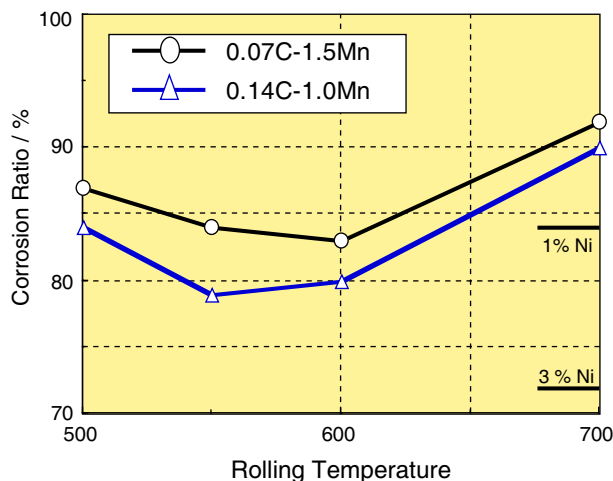


Fig. 27.3 Corrosion mechanism of developed steels.

inner rust layer as  $\text{Si}^{2+}$  state, and has an intermediate chemical bonding state different from that of  $\text{SiO}_2$ . Similarly, Al  $K_{\alpha}$  X-ray analyses were performed and are presented in Fig. 27.6. The Al  $K_{\alpha}$  X-ray spectra of  $\text{Al}_2\text{O}_3$  and metallic Al have different peak positions, and that of the test sample overlapped with  $\text{Al}_2\text{O}_3$ . This result suggests that Al is present in the inner rust as  $\text{Al}^{3+}$  state.

In order to determine the structure of the inner rust, TEM analysis was conducted. The inner rust layer was cut by FIB, and the rust containing Si and Al was selected by EDXS analysis. Figure 27.7 shows the TEM image of the rust. The result showed that the rust was made by the nano-scale oxides. From EPMA, Si was thought to be present as  $\text{Si}^{2+}$ , and Al was  $\text{Al}^{3+}$  in the inner rust. Thus, Si and Al were involved in complex oxides which showed the nano-scale crystal structure in Fig. 27.6. We could understand that Ni increases the corrosion resistance of weathering steel by making the complex oxides with the iron in the inner layer. In the case of the developed steel, complex nano-scale oxides containing Si and Al

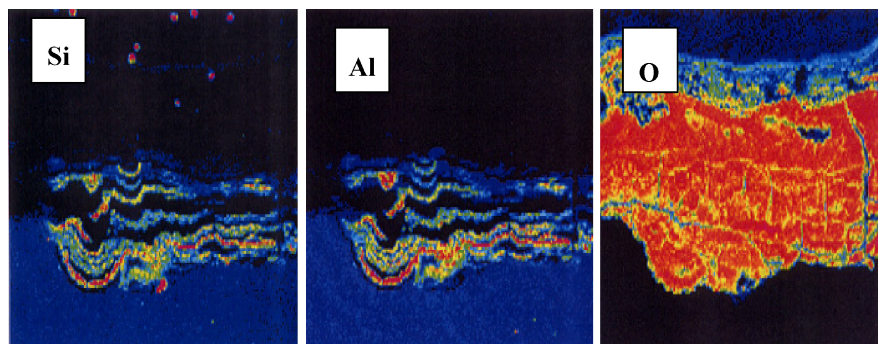
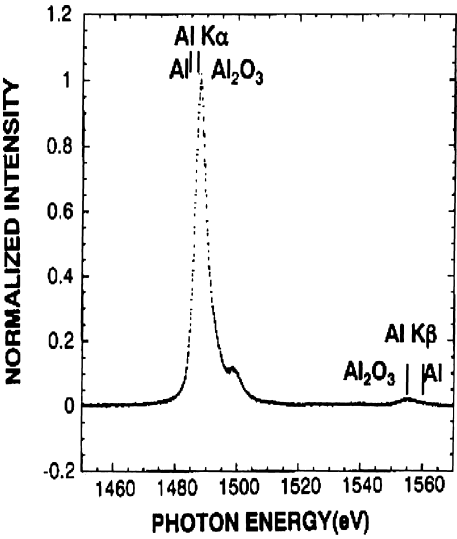


Fig. 27.4 Distribution of Si, Al, O in the rust of UFG Weathering steel by EPMA.

**Fig. 27.5** Al K spectra from the rust by EPMA.



was made, and it would increase the corrosion resistance of the steels by preventing the Cl ions penetrating into the rust.

Exposure test was conducted at coastal area in Japan for advanced weathering steels which contained high Si and Al. The corrosion resistance was estimated by EIS (Electrochemical Impedance Spectroscopy) after the exposure test. The impedance spectra of high Si and Al steel of test sample (100×50×3 mm) showed much higher value than those of conventional weathering steel (SMA) and carbon steel (SM) at wide frequency region in Fig. 27.8. From the previous research, it was investigated that the resistance at high frequency region was shown the rust resistance ( $R_{\text{rust}}$ ) and that of low frequency region was corrosion resistance ( $R_t$ ). In the case of this work it was found that  $R_{\text{rust}}$  and  $R_t$  of developed steel were higher than those of SMA. Thus

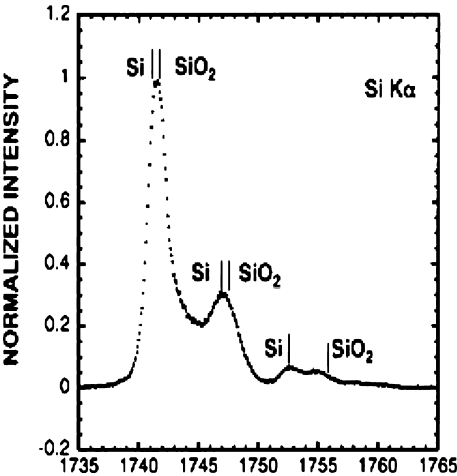


**Fig. 27.6** Si K spectra from the rust by EPMA.

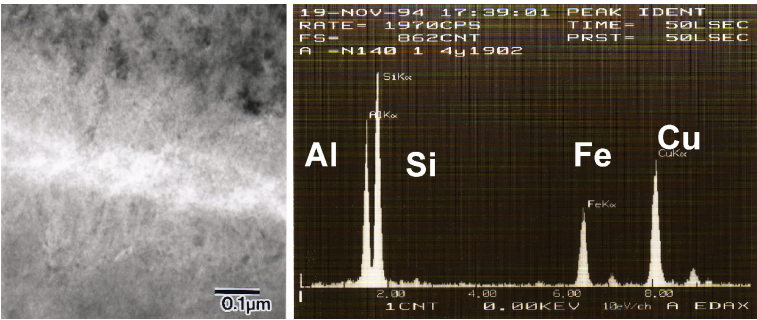


Fig. 27.7 FIB-TEM results of inner rust of UFG weathering steel.

high Si and Al steel was thought to have higher corrosion resistance than SMA. The main reason for this fact is considered that nano-scale complex oxide containing Si and Al is formed in inner rust, which suppresses the anodic reaction. As the formation of the rust proceeds, the value of  $R_{rust}$  and  $R_t$  of Si and Al-bearing steel show larger than those of SM, which depends on the fineness of the rust. Figure 27.9 shows the schematic diagram of the corrosion mechanism of the rust of Si and Al-bearing steel. In general, the rust has many micro-defects (pores) through which the chloride ( $Cl^-$ ) ions can penetrate to the base metal. However, the Si and Al-bearing steel makes

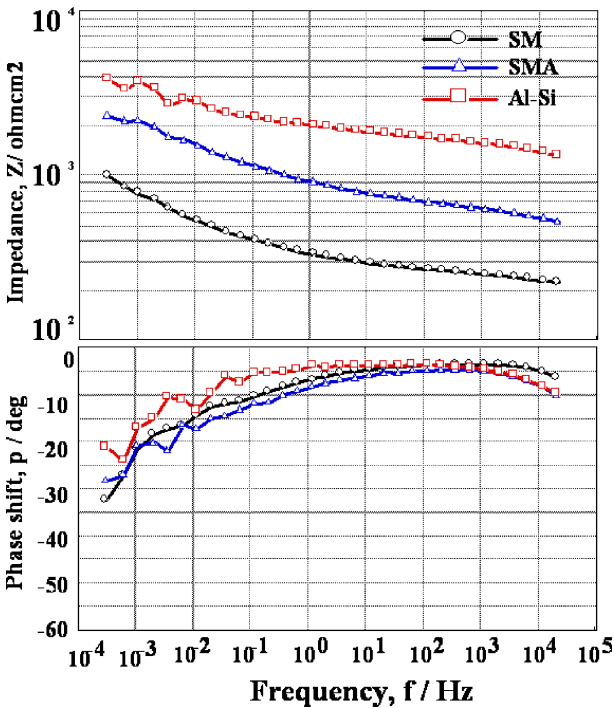


Fig. 27.8 Impedance spectra of test samples after exposure test at coastal area in Japan.

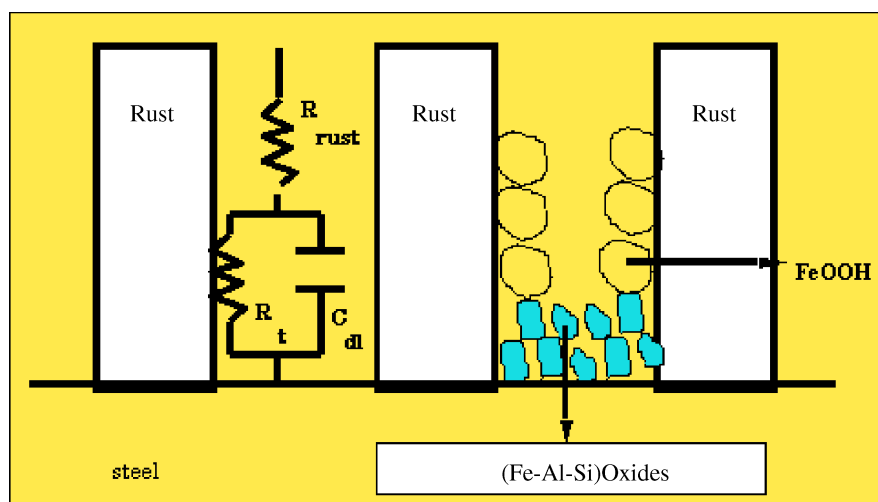


Fig. 27.9 Corrosion mechanism of developed steels.

nano-scale complex oxides containing Si and Al in inner rust at micro-defects, then increases the  $R_{rust}$  and  $R_t$  by the physical protection of the fine rust. Finally the Si and Al-bearing steel could suppress the corrosion in saline environment.

## 27.4 Conclusions

High-Si and Al type ultrafine-grained (UFG) weathering steel was created by the multi-pass warm rolling, and it was found that this steel showed excellent properties in strength, toughness and corrosion resistance. The main results were as follows,

1. The corrosion tests confirmed that the Si and Al-bearing UFG steels exhibited excellent corrosion resistance than carbon steel (SM).
2. The EPMA and TEM analyses showed that Si and Al were mainly existing in the inner rust layer formed on the Si and Al-bearing UFG steels. Si and Al were identified as  $Si^{2+}$  and  $Al^{3+}$  in the nano-scale complex iron oxides of inner rust.
3. The EIS measurement was conducted for the corrosion test samples to find that the rust resistance ( $R_{rust}$ ) of Si and Al-bearing UFG steel was much larger than that of SM. In the developed steel, the nano-scale complex oxides were made in the lower layer of iron rust, and increased rust and suppressed the corrosion.

## References

- [1] T. Kodama: Zairyo-to-Kankyo 49 (2000) 3–9.
- [2] M. Yamamoto and T. Kodama: Bull. ISIJ 4 (1999) 155–162.



- [3] U.R. Evans: Corrosion Science 9 (1969) 813–821.
- [4] T. Misawa, K. Asami, K. Hashimoto and Shimodaira: Corrosion Science 14 (1974) 279–289.
- [5] I. Suzuki, Y. Hisamatsu and N. Masuko: J. Electrochem. Soc. 127 (1980) 2210–2215.
- [6] M. Stratmann, K. Bohnenkamp and T. Ramchandran: Corrosion Science 27 (1987) 905–926.
- [7] J. Dunnwald and A. Otto: Corrosion Science 29 (1989) 1167–1176.
- [8] H.E. Townsend: Corrosion 57, (2001) 497–501.
- [9] M. Yamashita, H. Miyuki, Y. Mastuda, H. Nagano and T. Misawa: Corrosion Science 36 (1994) 283–299.
- [10] H. Konishi, M. Yamashita, H. Uchida and J. Mizuki: Mater. Trans. 46 (2005) 329–336.
- [11] T. Nishimura, H. Katayama, K. Noda and T. Kodama: Corrosion 56 (2000) 935–941.
- [12] T. Nishimura, H. Katayama, K. Noda and T. Kodama: Corrosion Science 42 (2000) 1611–1621.
- [13] T. Nishimura, K. Noda and T. Kodama: Corrosion 57 (2001) 753–758.
- [14] T. Nishimura, A. Tahara and T. Kodama: Materials Transactions 42 (2001) 478–483.
- [15] T. Nishimura and T. Kodama: Corrosion Science 45 (2003) 1073–1084.
- [16] K.Y. Kim, Y.H. Hwang and J.Y. Yoo: Corrosion 58 (2002) 570–583.
- [17] K. Asami and M. Kikuchi: J. Japan Inst. Metals 66 (2002) 649–656.

# Chapter 28

## Microstructure Evolution in Three FCC Materials During Limited Dome Height Test

S. Mishra, P. Pant, K. Narasimhan, and I. Samajdar

**Abstract.** AA 1050 Aluminium, AISI 304L and AISI 316L austenitic stainless steel were deformed at different strain and strain path. Deformed microstructure in AISI 304L and AISI 316L austenitic stainless steel shows significant amount of deformation twin and Strain Induced Martensite (SIM). AA 1050 Aluminium shows grain interaction between neighbouring grains. In this study effort has been made to understand these microstructural developments. It has been found that biaxial strain path and high strain shows higher amount of deformation twins in AISI 316L stainless steel, strain induced martensite in AISI 304L stainless steel and grain interaction in AA 1050 Aluminium.

**Keywords:** Deformation twin, Strain Induced Martensite, Stainless Steel, Grain Interaction, Strain Path, Microstructure, EBSD

### 28.1 Introduction

With increasing renovation in both materials and design, greater demands are being placed on the formability of sheet metals [1–2]. Sheet metal formability is represented as forming limit diagrams or FLD [3–4]. FLD can be generated by different experimental setup [2–4]. Or given the availability of good computational resources it can be generated using FEM based simulation technique thus saving both material and time. This predicated FLD takes into account all material parameters which affect formability. These material parameters change during deformation, which is in general, assumed to be constant (properties of undeformed sample) during FLD predication. In this study effort has been made to understand the microstructural development of AA1050 Al, AISI 304L SS and AISI 316L SS during deformation.

---

S. Mishra, P. Pant, K. Narasimhan, and I. Samajdar  
Department of Metallurgical Engineering and Materials Science, IIT Bombay, Mumbai-76, India

Stacking fault energy (SFE) of AA 1050 is approximately  $200 \text{ mJ/m}^2$ , AISI 316L austenitic stainless steel is  $60 \text{ mJ/m}^2$  and AISI 304L austenitic stainless steel is approximately  $20 \text{ mJ/m}^2$  [5]. Due to difference in stacking fault energy these material shows different microstructural features during deformation. Sheets were deformed at different strain and strain path by limiting dome height (LDH) [3] tests. The deformed structures were extensively studied to understand & outline structural developments associated with forming – especially the effects of strain and strain path on Strain induced martensite.

## 28.2 Experimental Details

Fully annealed sheets of Aluminium, 304L stainless steel and 316L Stainless steel sheets 1 mm in thickness were subjected to limiting dome height (LDH) [3–4] tests in a 200 ton double-action hydraulic press. From such estimates, the FLD was plotted as shown in Fig. 28.1. Three different strain and stain paths were selected for subsequent microstructural characterization. Strain paths were generalized as biaxial (BS), uniaxial (US) and plane strain (PS), while strains were classified as low (LS), intermediate (IS) and high (HS). The different strain and strain paths selected are outlined in Fig. 28.1.

Bulk texture studies were done using a Panalytical MRD System for all the strains and strain paths [6]. EBSD samples were prepared using the standard electropolishing technique [6]. A TSL OIM (orientation imaging microscopy) or EBSD system on a FEI Quanta 200HV SEM (scanning electron microscope) was

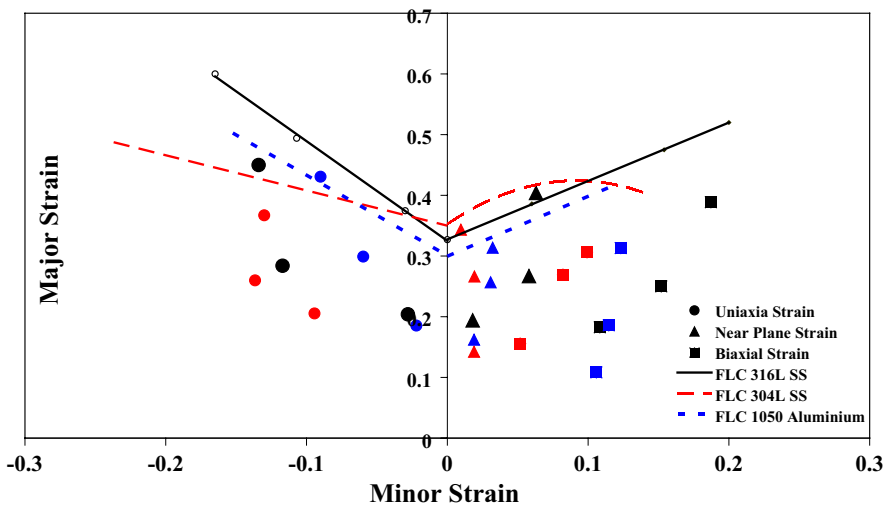


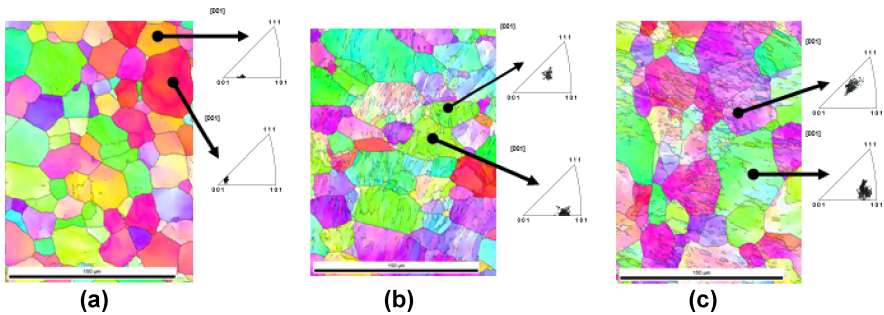
**Fig. 28.1** Experimental Forming limit diagram of Aluminium, 304L Stainless steel and 316L Stainless steel.

used. When misorientation between two neighboring point exceeded  $2^\circ$ , a grain boundary was assumed to be present. For identifying coincident site lattice (CSL) boundaries [6] standard Brandon's criteria [7] was used. The EBSD data was also used for estimating the developments misorientation. Vibrating sample magnetometer (VSM – Lake shore, Model-7410) measurements (operated at 82 Mhz and at 3 tesla) were used to estimate the relative presence of martensite phase at different strain/strain path in stainless steels.

### 28.3 Results and Discussions

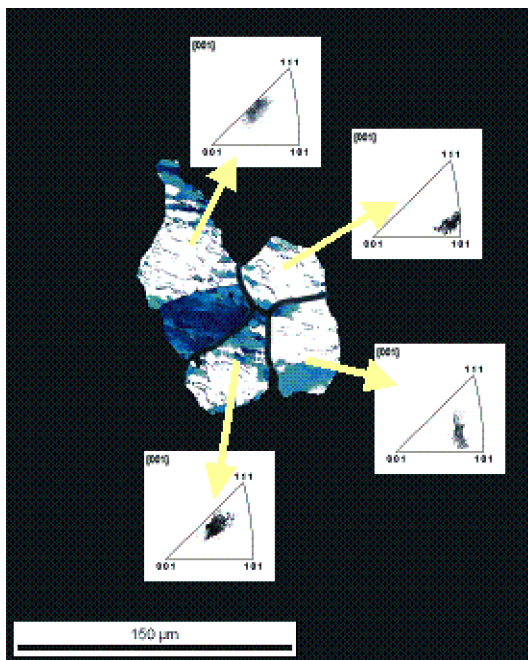
As shown in Fig. 28.2, deformation did bring strong in-grain misorientation developments. The misorientation development observed at all the strain and strain path but at the grain interior low angle boundaries ( $1\text{--}15^\circ$  misorientation) were observed only at or beyond intermediate strains. In-grain misorientation development during plastic deformation is a complex but fascinating problem. Any misorientation development is expected to depend on the deforming grain as well as on its immediate neighbors. As shown in Fig. 28.3, near grain boundary regions often show large deviations from grain average orientation – possibly indicating regions with considerable influence or interactions with the neighboring grains. Complete accounting for the grain interactions through relatively simple microstructural or microtextural parameters was not successful so far. More rigorous deformation modelling appears to be in order.

Figure 28.4 (a) and (b) shows the twin fraction with effective strain for different strain paths for 304L SS and 316L SS. Undeformed 304L SS has more twin fraction (0.39) than 316LSS (0.28) due to its lower SFE. It can be seen from figure that twin fraction was decreased with increase in effective strain for 316L SS (see Fig. 28.4 (b)) for uniaxial and plane strain conditions but for biaxial strain path twin fraction was marginally increased with effective strain. For 304L SS twin



**Fig. 28.2** EBSD images of the near plane strain deformed material after (a) low (L), (b) intermediate (I) and (c) high (H) strain as in Fig. 28.1. For few of the grains inverse pole figures are used to indicate orientation developments.

**Fig. 28.3** EBSD image of 4 randomly selected neighboring grains subjected to the highest strain in biaxial strain path. The orientations corresponding to the grains are indicated by inverse pole figures. 1–15° and above 15° grain boundaries are drawn respectively as thin and thick lines. Regions of the respective grains with large deviations from average grain orientations are shaded in grey levels. It is to be noted that all such large deviations were restricted to near grain boundary regions.



fraction was increasing with effective strain for biaxial and near plane strain but it is decreasing only for uniaxial strain path (see Fig. 28.4 (a)).

304L SS and 316L SS are austenitic stainless steel. However, austenitic phase is not stable when it is subjected to deformation and it transforms to martensite [5]. In this study martensite fraction in deformed samples were measured by OIM, X-ray Diffraction and VSM techniques. It has been found that martensite percentage for 316L SS is very less (<3%) which can not be measured either by

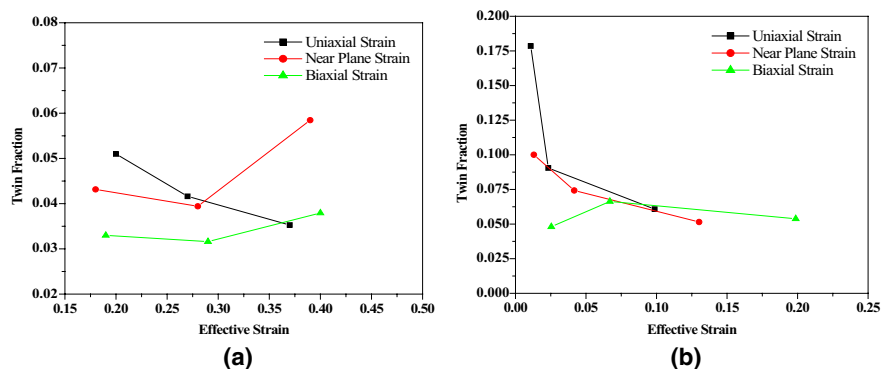


**Fig. 28.4** Graph between twin fraction and effective strain at different strain and strain paths for (a) 304L SS and (b) 316L SS.

**Table 28.1** Strain induced martensite formation at different strain and strain path for 304L SS. The extent of martensite formation was measured from VSM estimated saturation magnetization ( $4\pi M_s$ ) values in emu/gm.  $4\pi M_s$  values were converted to % Martensite using a methodology described elsewhere [5].

Uniaxial strain			Near plane strain			Biaxial strain		
Effective strain, $\bar{\epsilon}$	$4\pi M_s$	% Martensite	Effective strain, $\bar{\epsilon}$	$4\pi M_s$	% Martensite	Effective strain, $\bar{\epsilon}$	$4\pi M_s$	% Martensite
0.22	6.5	6.915	0.23	13.6	10.76	0.29	14.3	19.226
0.29	13.2	11.715	0.34	17.0	12.6	0.40	18.5	25.128
0.46	25.0	17.365	0.50	30.0	26.14	0.58	35.0	25.311

OIM or X-ray diffraction techniques. But it is observed that in 316L SS formation of martensite is strain path dependent and it is more in biaxial strain path (measured by VSM technique). For 304L stainless steel formation of martensite is quite substantial, as shown in Table 28.1 measured by all three techniques, due to low stacking fault energy.

## 28.4 Conclusions

- Extent of martensite and twin fraction did strongly depend on the strain and strain path. Biaxial strain path, in general, was associated with higher percent of martensite.
- In general, high deformed grains had more grain interaction. The role of strain and strain path on grain interaction has been observed, though grain interaction is more significant at higher strains.

## References

- [1] H.W. Wagener: J. Mater. Proc. Technol., 1997, 72, 342–357.
- [2] S.S. Hecker: Mech. Eng. Q., 1974, 14, 30–36.
- [3] S.P. Keeler: Sheet Met. Industr., 1965, 42, 683–691.
- [4] G.M Goodwin: Trans. SAE, 1968, 77, 380–387.
- [5] D.N. Wasnik, I.K. Gopalkrishnan, J.V. Yakhmi, V. Kain and I. Samajdar: ISIJ Int., 2003, 43, 1581–1589.
- [6] S. Mishra, K. Narashiman, and I Samajdar, Mats. Sci. and Tech., 2007, 23, 1118–1126.
- [7] D.G. Brandon: Acta Metall., 1966, 14, 1479–1484.



## Chapter 29

# The Facet Method for the Description of Yield Loci of Textured Materials

Sampath Kumar Yerra, Albert Van Bael, and Paul Van Houtte

**Abstract.** A new approach, the *Facet* method, to describe the yield loci of textured materials is proposed. It is based on an analytical expression of plastic potentials in strain rate space of which the parameters are identified by fitting to the predictions of multilevel micromechanical models. The chief advantage of this new formulation is that it automatically ensures convexity of the anisotropic yield loci. Furthermore, the approach can be easily extended to formulate stress-space based plastic potentials. This is quite an efficient property especially for the implementation in finite element codes that are used for simulation of industrial metal forming processes because it offers a significant reduction in computation time needed for yield checks compared to that of strain rate space based plastic potential expression. In our work, the *Facet* method is applied in combination with the Taylor-Bishop-Hill micromechanical model, with both strain rate as well as stress space formulations, to various model textures and industrial materials. In this paper, the equipotential surfaces and the corresponding yield loci will be presented for a sharp rotated-cube model texture and a moderately sharp industrial grade IF steel sheet texture. A brief quantitative assessment of the new method with respect to the original model data will be presented.

**Keywords:** anisotropic material, yield criterion, convex loci, metal forming

---

S.K. Yerra

Department MTM, K.U.Leuven, Kasteelpark Arenberg 44, BE-3001 Leuven, Belgium  
e-mail: SampathKumar.Yerra@mtm.kuleuven.be

A. Van Bael

Department MTM, K.U.Leuven, Kasteelpark Arenberg 44, BE-3001 Leuven, Belgium, and  
IWT, KHLim, Campus Diepenbeek, Agoralaan Gebouw B, bus 3, BE-3590 Diepenbeek, Belgium

P. Van Houtte

Department MTM, K.U.Leuven, Kasteelpark Arenberg 44, BE-3001 Leuven, Belgium



## 29.1 Introduction

Predominantly two systems of thought prevail in the field of plasticity to formulate anisotropic yield loci. In one system [1], the parameters of the yield locus expression are identified practically from the results of real-time mechanical tests. In the other system [2], the parameters are obtained based on the theory of dual plastic potentials using a multilevel modelling scheme, where the anisotropic response of material is calculated by a micromechanical model, provided the crystallographic texture of the material in the form of orientation distribution function is known. The important advantages of the theoretical approach are its capability to embody complex deformation modes (which are otherwise almost impossible to apply in the laboratory testing environment), its quick ability to acquire the material response and its less work-intensive nature compared to the practical route.

In the lines of the latter approach, Van Houtte and Van Bael [3] developed an analytical expression which makes use of average Taylor factors calculated by the multilevel model for several thousands of deformation modes. This is called the *Quantic* method hereafter. Despite its successful implementation in FE codes, the *Quantic* method, however, featured non-convexity for very sharp textured materials in some vertices of the stress space leading to divergence of the FE solution. It needs an additional modification of the parameters to surpass this problem. The other drawback of *Quantic* method is that it was defined in strain rate space but not in stress space which makes it computationally intensive for determining the onset of yielding in both implicit and explicit FE simulations [4]. The novel expression proposed in this paper not only overcomes these limitations but also is well-suited for materials with stress differential effect [5].

## 29.2 The Facet Method

In strain rate space, for a given macroscopic strain rate tensor  $\mathbf{D}$ , the new expression for rate of plastic work per unit volume  $\psi(\mathbf{D})$  is defined as:

$$\psi(\mathbf{D}) = \left[ \sum_{k=1}^K \lambda_k (S_{kp} D_p)^n \right]^{1/n} \quad \text{with } n \geq 2, \lambda_k \geq 0 \quad (29.1)$$

$D_p$  are the components of strain rate tensor for incompressible materials with contracted index  $p=1.5$ .  $S_{kp}$  and  $\lambda_k$  are the parameters. The identification of parameters in Eq. 29.1 proceeds as follows. The multilevel model is applied on the known crystallographic texture for a set of  $K$ -directions in strain rate space, and the deviatoric stresses  $\mathbf{S}_k$  are calculated for each of the imposed strain rate directions  $a_k$ . The components of those deviatoric stress tensors are then treated as parameters  $S_{kp}$ . They are kept fixed here on. The parameters  $\lambda_k$  are then obtained by fitting the rates of plastic work obtained by the multilevel model for the set of

$K$ -directions in strain rate space. Details on the choice of these  $K$ -directions as well as the fitting procedure for  $\lambda_k$  are given in [5].

However, as mentioned earlier, the *Facet* method can be easily adopted in deviatoric stress space. The plastic potential in stress space can be simply mirrored as:

$$\phi(\mathbf{S}) = \left[ \sum_{k=1}^K \lambda'_k (D_{kp} S_p)^n \right]^{1/n} \quad \text{with } n \geq 2, \lambda'_k \geq 0 \quad (29.2)$$

In this case, the parameters are  $\lambda'_k$  and  $D_{kp}$ . The identification procedure of parameters is similar as above but this time using the solutions obtained with the plastic potential given by Eq. 29.1 for  $K$  deviatoric stress modes [6]. Once the parameters are identified, Eq. 29.2 enables to perform quick yield checks when implemented in FE simulations. The strength of the Facet method lies in the fact that it automatically ensures convex yield surfaces. Van Houtte et al. [5] used the mathematical theory of convexity [7] to show that Eqs. 29.1 and 29.2 always render a convex surface if the coefficients of those expressions,  $\lambda_k$  or  $\lambda'_k$ , are greater than or equal to zero.

### 29.3 Results and Discussion

The power of the new method is examined, both qualitatively and quantitatively, for two examples in this paper viz., one is ferrite single crystal with a strong rotated-cube texture component, (001)[110], which is very commonly observed in BCC steels. It is a model texture with a Gaussian spread of  $11^\circ$  and a high texture (sharpness) index of 30.0. The second example is an industrial grade IF steel sheet with texture sharpness index of 4.84. The crystallographic texture of this sample was calculated from the measured XRD pole figures according to the standard procedure [8]. The new Facet method with  $n=6$  is then applied on their discretised orientation distribution function using 5000 crystals. The multilevel model considered here is conventional Taylor-Bishop-Hill theory with 24 slip systems:  $\{110\}$  and  $\{112\}$  slip planes and  $\langle 111 \rangle$  slip directions. In our study, a set of 402 directions which are nearly equidistant in nature were chosen.

Figure 29.1 below shows a section of the equipotential surfaces in the  $\pi$ -plane section: all strain rates are zero except  $D_{11}$ ,  $D_{22}$  and  $D_{33}$  while maintaining the constancy of volume. The figure shows the projections of these axes on the  $\pi$ -plane section. It can be seen that the Facet curve (thick line) passes almost right through all the original model data (superimposed points), except those at the vertices for very sharp texture in Fig. 29.1 (a). However in both examples, the Facet method (thick line) and the previous method (thin line) almost overlap on each other.

The yield locus sections calculated using the *Facet* method and the *Quantic* method are shown in Fig. 29.2. It is clear that both the strain rate and stress space based Facet potentials produced nearly similar surface to that of the *Quantic*

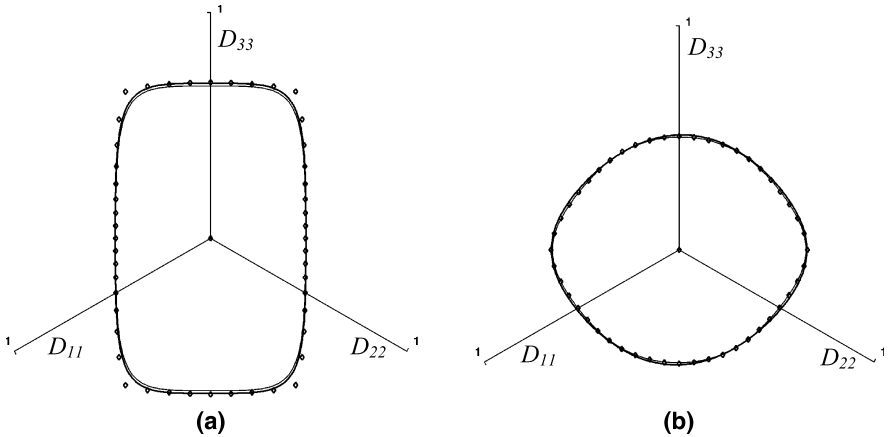


**Fig. 29.1** Equipotential surfaces in  $\pi$ -plane section. (a) Rotated-cube model texture (b) Industrial grade IF steel. Thin lines correspond to the surface calculated using the *Quantic* method [3] and thick lines correspond to the surface calculated by the Facet method in strain rate space, Eq. 29.1 after 4 iterations. Superimposed points are obtained from the average Taylor factors computed directly by the multilevel model.

method for as low as 402 directions as opposed to 35,000 directions of the latter, except in case of Fig. 29.2 (b) (very sharp texture) where the stress space based Facet formulation is not able to reproduce the curvature at the vertices. For assessing the method quantitatively, the relative difference of Taylor factors and yield stresses between those calculated by Facet method and the original multilevel model is computed for all chosen 402 directions, see Table 29.1. It is evident that the reproducibility of Taylor factor and yield stress length by Facet method, barring the case of stress space based potential for very sharp texture, is within a maximum error of 3.5% which is comparable with that of the *Quantic* method – thus indicating its efficiency over the previous method.

From Figs. 29.1 (a) and 29.2 (b), and Table 29.1 it follows that for very sharp textures, the 6th order analytical expression ( $n=6$ ) does not allow to reproduce the high curvature. A higher order ( $n=8$  or higher) would indeed allow for smaller radii of curvature; however, this should be done with care, as the use of higher values of  $n$  may require a parameter identification using a larger set of directions with a higher angular resolution. Nonetheless, it can be seen that the Facet curves are always perfectly convex in all figures – thus paving the way to its implementation in FE codes.

**Table 29.1** Taylor factors and yield stresses obtained by Facet method

Maximum Relative Differences	Facet method in strain rate space		Facet method in stress space	
	Rotated cube	IF Steel	Rotated cube	IF Steel
Taylor factor	2.31%	3.27%	12%	3.51%
Yield stress	3.65%	3.24%	7%	3.49%

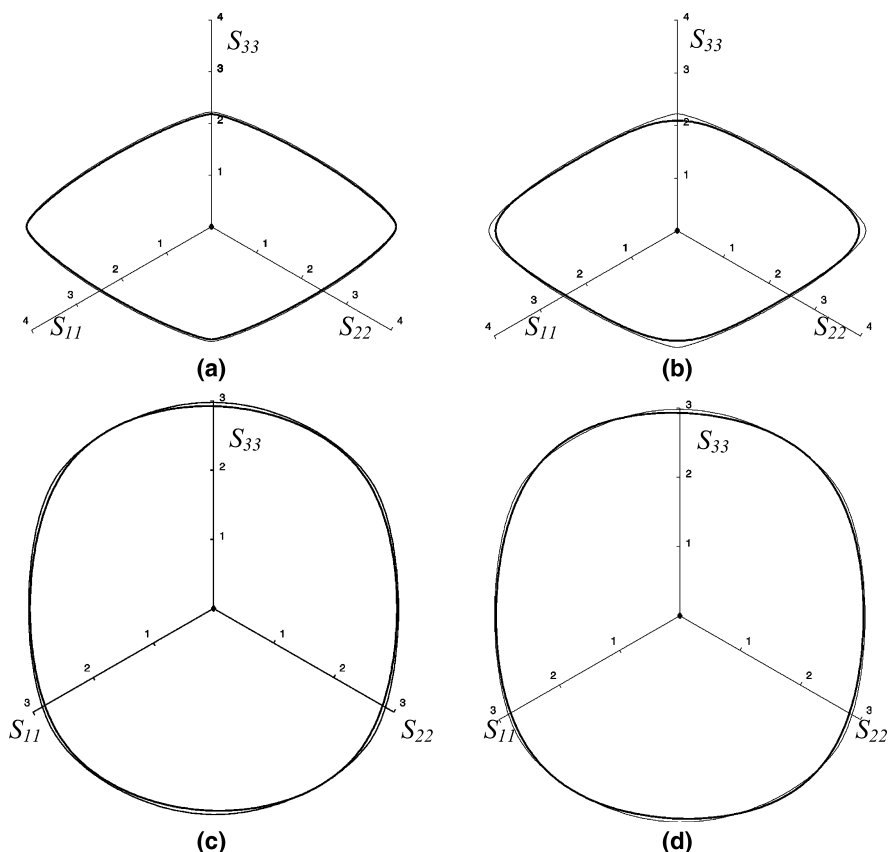


**Fig. 29.2** Yield locus in  $\pi$ -plane section (a, b) Rotated-cube model texture (c, d) Industrial grade IF steel. Thin lines correspond to the surface calculated using the *Qunic* method [3] and thick lines correspond to the surface calculated by the Facet method after 4 iterations: in (a, c) according to strain rate space formulation, Eq. 29.1 and in (b, d) according to stress space formulation, Eq. 29.2.

**Acknowledgement** The authors are grateful to the financial support offered by the Belgian Science Policy in the framework of IUAP project P6/24.

## References

- [1] Życzkowski, M., 2001. Anisotropic Yield Conditions. In: J. Lemaitre (Ed.), *Handbook of Materials Properties*, vol. I: Deformation of Materials. Academic Press, New York, pp. 155–165.
- [2] Van Houtte, P., 1994. Application of Plastic Potentials to Strain Rate Sensitive and Insensitive Anisotropic Materials. *Int. J. Plasticity* 10, 719–748.
- [3] Van Houtte, P., Van Bael, A., 2004. Convex Plastic Potentials of 4th and 6th Rank for Anisotropic Materials, *Int. J. Plasticity* 20, 1505–1524.

- [4] Ristic, S., He, S., Van Bael, A., Van Houtte, P., Texture-based explicit finite-element analysis of sheet metal forming, *Materials Science Forum* 495–497, 1535–1540 (2005).
- [5] Van Houtte, P., Yerra, S.K., Van Bael, A., 2007, The Facet method: a hierarchical multi-level modelling scheme for anisotropic convex plastic potentials, Full length journal paper submitted to *International Journal of Plasticity*.
- [6] Van Bael, A., Yerra, S.K., Van Houtte, P., 2008, Texture-Based Plastic Potentials in Stress Space for Finite Element Simulations, Being communicated to ICOTOM-15 conference, Pittsburgh, USA.
- [7] Rockafellar, R.T., 1972. *Convex analysis* (Second Printing). Princeton University Press, USA.
- [8] Van Houtte, P., 2004. The “MTM-FHM” software system manual, Version 2, Department MTM, K.U. Leuven, Belgium.

## Chapter 30

# The Hall-Petch Relationship in Interstitial-Free Steel Processed by Equal Channel Angular Extrusion

Azdiar A. Gazder, Christopher H.J. Davies, and Elena V. Pereloma

**Abstract.** The Hall-Petch relationship was studied in interstitial-free steel subjected to  $\Phi=90^\circ$  Equal Channel Angular Extrusion for up to  $N=8$  passes via route B<sub>C</sub> processing. The composite equation indicates that although low-angle grain boundaries provide the maximum strengthening up to  $N=8$  passes, the contribution from high-angle boundaries also increases with greater pass number. Alternatively, the evolution of boundary misorientation in as-ECAE microstructures and its effect on mechanical properties up to  $N=3$  passes is also understood by using a misorientation scaling factor within the original Hall-Petch equation.

### 30.1 Introduction

It is accepted that mechanical strength in pure polycrystalline metals is attributed to grain refinement as described by the Hall-Petch (H-P) equation [1, 2]. Accurate understanding of mechanical behaviour requires delineation between “grains” in the undeformed state or “subgrains”, “cell-block boundaries” (comprising parallel microbands and/or lamellar boundaries also defined as geometrically necessary boundaries, GNBs) and “cell boundaries” (incidental dislocation boundaries, IDBs for mixed tilt and twist walls) in as-deformed substructures. To account for the

---

A.A. Gazder and E.V. Pereloma  
School of Mechanical Materials & Mechatronics Engineering, University of Wollongong,  
New South Wales 2522, Australia

C.H.J. Davies  
Department of Materials Engineering, Monash University, Victoria 3800, Australia

linear additive contributions of GNBs and IDBs in deformation substructures, Hughes et al. [3] suggested a composite H-P equation:

$$\sigma = \sigma_0 + \sigma_{LAGBs} + \sigma_{HAGBs} = \sigma_0 + M\alpha Gb \left[ \sqrt{\frac{1.5S_{V_{1^\circ-15^\circ}} \theta_{1^\circ-15^\circ}}{b}} \right]_{IDB} + \left[ \frac{k_{HP}}{\sqrt{d_{15^\circ-62.8^\circ}}} \right]_{GNB} \quad (30.1)$$

where,  $\sigma_0$  is the friction stress and has been defined as either: (i) the internal resistance to the motion of a dislocation through the crystal lattice [4] or, (ii) the flow stress of an undeformed single crystal oriented for multiple slip or, (iii) the approximate yield stress of a coarse, untextured polycrystal [5]. In the present study  $\sigma_0$  is regarded as the grain size independent term and includes strengthening contributions from solutes and particles but not dislocations.  $M$  is the average Taylor factor from texture data [6],  $\alpha$  is a constant ( $=0.24$ ),  $G$  is the shear modulus (in MPa),  $b$  is the Burgers vector ( $=2.48 \times 10^{-10}$  m) and  $S_v$  is the boundary area per unit volume of IDBs ( $\approx \pi/2d_{1^\circ-15^\circ}$ ).  $k_{HP}$  is the strain hardening parameter (or grain size dependent term) related to the additional resistance to dislocation motion caused by the dislocation source density at grain boundaries [5, 7] and  $d_{15^\circ-62.8^\circ}$  is the effective diameter of high-angle GNBs. Thus as deformation proceeds, low-angled grain boundaries (LAGBs) gradually transform into high-angled boundaries (HAGBs) and are rendered indistinguishable from original grain boundaries [5]. In this respect, the second term uses the misorientation ( $\theta_{1^\circ-15^\circ}$ ) of LAGBs while the last term accounts for HAGB strengthening.

In contrast a simplified stress dependence in relation to the smallest observable microstructural feature (in this case, the subgrain size ( $d_{1^\circ-15^\circ}$ )) has also been suggested for deformation substructures [8]. Since a grain boundary is modelled as an array of dislocations in the lattice, the spacing between dislocations is inversely proportional to the boundary misorientation [9]. Previous reports also indicated no misorientation effects on the flow stress when the average misorientation is above a critical saturation angle (usually  $15^\circ$ ) [10].

Accordingly, Li et al. [8] suggested that a scaling factor can be utilised in the H-P equation such that:

$$\begin{aligned} \sigma_{0.2} &= \sigma_0 + k' \sqrt{\frac{(\theta_{AVG}/15^\circ)}{d_{1^\circ-15^\circ}}} \quad \text{when } \theta_{AVG} \leq 15^\circ \text{ or,} \\ \sigma_{0.2} &= \sigma_0 + \frac{k'}{\sqrt{d_{1^\circ-15^\circ}}} \quad \text{when } \theta_{AVG} > 15^\circ \end{aligned} \quad (30.2)$$

where,  $\sigma_{0.2}$  is the 0.2% proof stress and  $\theta_{AVG}$  is the average misorientation for the entire range.

In the present study, the efficacy of both methodologies is compared using interstitial-free (IF) steel subjected to Equal Channel Angular Extrusion (ECAE) for up to  $N=8$  passes via route B<sub>C</sub> processing. Mechanical data is obtained via uniax-

ial tensile testing and correlated to microstructural information calculated from Electron Back-Scattered Diffraction (EBSD) mapping.

## 30.2 Experimental Procedure

Commercially available hot-rolled Ti IF-steel plate from BlueScope Steel Limited was machined into  $20 \times 20 \times 80 \text{ mm}^3$  billets and annealed at 1023 K for one hour. Optical microscopy returned an average grain size of  $140 \pm 10 \mu\text{m}$  for  $N=0$  pass condition. Thereafter room temperature ECAE via route B<sub>C</sub> for up to  $N=8$  passes was undertaken on a  $\Phi=90^\circ$ ,  $\Psi=0^\circ$  sharp cornered die-set.

Room temperature uniaxial tensile testing was undertaken using a screw-driven Instron 4505 at  $0.5 \text{ mm min}^{-1}$  crosshead speed and a 10 mm extensometer on round samples of  $\varnothing 4 \text{ mm}$  diameter. The 0.1% and 0.2% proof stress ( $\sigma_{0.1}$  and  $\sigma_{0.2}$ ) and ultimate tensile strength ( $\sigma_{UTS}$ ) were calculated using a purpose-written MATLAB<sup>®</sup> subroutine.

EBSD was performed on a LEO-1530 FEG-SEM fitted with a Nordlys-II<sup>™</sup> detector operating at 20 kV,  $\times 15 \text{ k}$  magnification and 80 nm step size on samples cut perpendicular to the extrusion direction from the centre of the stable billet length. Post-processing was undertaken using VMAP and HKL – Channel 5<sup>™</sup> software packages. In order to reduce the effects of noise, the average misorientation ( $\theta_{AVG}$ ) was calculated using the  $> 1^\circ$  lower cut-off criterion. The equivalent circle diameter (ECD, denoted as  $d_{ECD}$ ), effective average ( $d_{AVG}$ ), subgrain ( $d_{1^\circ-15^\circ}$ ) and grain ( $d_{15^\circ-62.8^\circ}$ ) diameters were calculated using the misorientation definition of the various boundary types [11].

## 30.3 Results and Discussion

A brief summary of mechanical property – deformation substructure evolution is as follows. Beyond  $N \geq 4$  passes, the  $\theta_{AVG}$ -value exceeds  $15^\circ$  (Table 30.1) and the  $\Delta\sigma_{0.2}$  between passes reduces (Fig. 30.1 (a)). As the percentage fraction of HAGBs increases with pass number, further substructure refinement also occurs as the effective grain size ( $d_{15^\circ-62.8^\circ}$ ) rapidly approaches the subgrain diameter (Fig. 30.1 (b)).

**Table 30.1** Change in the average misorientation ( $\theta_{AVG}$ ) and HAGB area fraction after multiple passes.

	N=1	N=2	N=3	N=4	N=5	N=6	N=7	N=8
$\theta_{AVG}$ (°)	$6.2 \pm 1.3$	$7.4 \pm 1.6$	$10.4 \pm 3.9$	$16.6 \pm 0.5$	$20.8 \pm 1.2$	$24.5 \pm 1.2$	$25.3 \pm 0.6$	$24.5 \pm 0.9$
HAGBs (%)	$5.9 \pm 4.5$	$10.2 \pm 4.8$	$19.2 \pm 9.1$	$37.8 \pm 1.1$	$48.4 \pm 6.1$	$57.1 \pm 3.4$	$56.7 \pm 1.6$	$53.7 \pm 2.7$



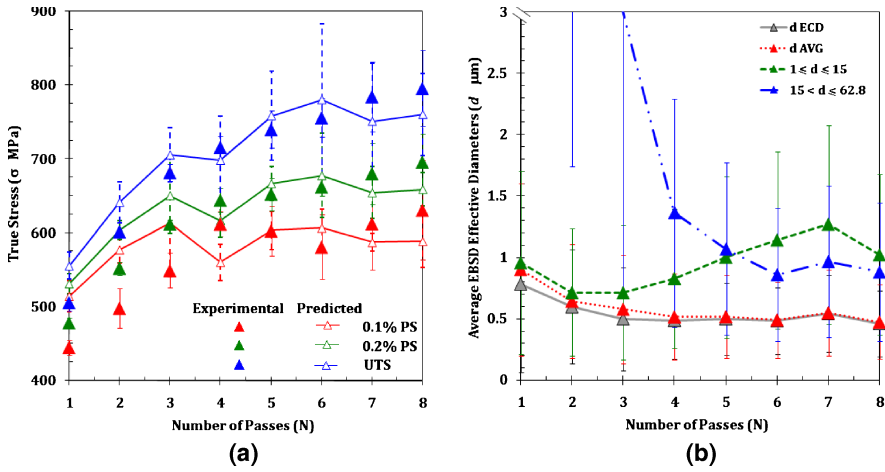


**Fig. 30.1** (a) Experimental and Eq. 30.1 predicted 0.1% proof, ( $\sigma_{0.1}$ ), 0.2% proof ( $\sigma_{0.2}$ ) and ultimate tensile ( $\sigma_{UTS}$ ) stresses and, (b) A magnified view of the close correlation between the EBSD-returned effective diameters  $d_{1^\circ-15^\circ}$  and  $d_{15^\circ-62.8^\circ}$ .

During application of Eq. 30.1, optimised values of  $\sigma_0 = 99.33$  MPa and  $k_{HP} = 0.09, 0.16$  and  $0.25 \text{ MPa} \cdot \text{m}^{0.5}$  for the  $\sigma_{0.1}$ ,  $\sigma_{0.2}$  and  $\sigma_{UTS}$  ranges were calculated by minimising the sum of the squared difference between the experimental and predicted data. The latter values are small but agree with published IF-steel data [12]. As seen in Fig. 30.2 (a), the unstable LAGBs behave as loose dislocations and provide the maximum strengthening via entanglement for up to  $N=8$  passes. The approximately constant subgrain strength with increasing pass number can be attributed to misorientation increase and subgrain refinement within the LAGB class interval remaining low ( $\Delta\theta_{1^\circ-15^\circ} = 1.5^\circ$ ). Such behaviour results in a similitude relationship ( $(d\cdot\theta)_{1^\circ-15^\circ}/b \approx \text{constant}$ ) for the IDBs between  $N=1$  to 8 passes [3].

For any given pass the increase in  $k_{HP}$ -values from  $\sigma_{0.1}$  through to  $\sigma_{UTS}$  is evidence of work hardening. The averaged strengthening effect of HAGBs ( $= k_{HP}/(Gb)$ ) was  $5.2 \pm 0.6, 9.1 \pm 1.1$  and  $14.6 \pm 1.7 \times 10^3 \text{ m}^{-0.5}$  for  $\sigma_{0.1}$  through to  $\sigma_{UTS}$  and is of the same order as nanocrystalline Al, Ni and Cu compacted powders [5]. Beyond  $\geq 4$  passes, increasing area fractions comprise similarly sized high-angled grains and low-angled subgrains. The refinement of the former also produces the slightly enhanced HAGB strengthening effect between passes.

Alternatively the H-P relationship can also be derived using  $d_{1^\circ-15^\circ}$  and accounting for  $\theta_{\text{AVG}}$  effects via scaling for up to  $N=3$  passes (Fig. 30.2 (b)). Optimised values of  $\sigma_0 = 99.33$  MPa and  $k' = 0.57 \text{ MPa} \cdot \text{m}^{0.5}$  (or  $564.49 \text{ MPa} \cdot \mu\text{m}^{0.5}$ ) are used and agree with published data [13, 14]. The Eq. 30.2 best-fit line is also compared to cold-rolled IF-steel [8], and re-iterates that at least up to  $N=3$  passes,

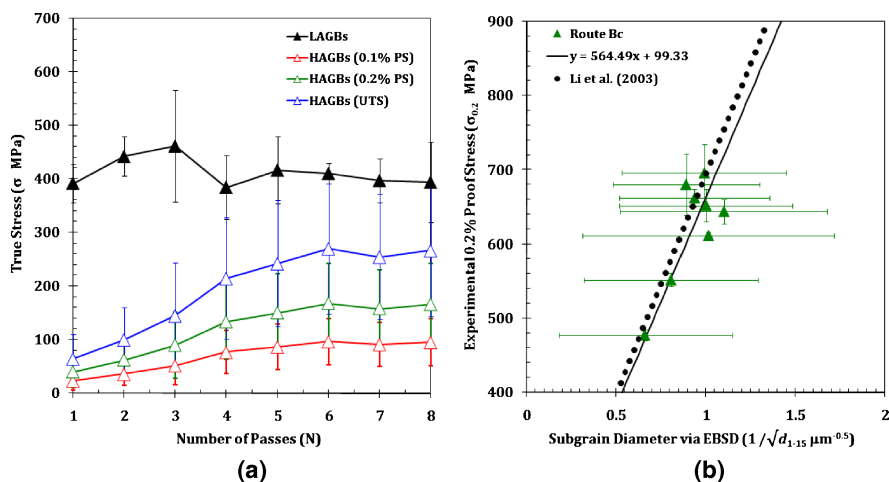


**Fig. 30.2** (a) The strengthening contributions from LAGBs and HAGBs after multiple passes predicted by Eq. 30.1 and, (b) The relationship between the experimental 0.2% proof stress ( $\sigma_{0.2}$ ) and the EBSD-returned average subgrain diameter ( $d_{1^\circ-15^\circ}$ ) according to Eq. 30.2. The terms ‘y’ and ‘x’ in the equation of best-fit denote the  $\sigma_{0.2}$  and  $1/\sqrt{d_{1^\circ-15^\circ}}$ , respectively.

strengthening is dictated by subgrain structures. This agrees with previous conclusions [15] that low-angled subgrain size controls mechanical behaviour when it is significantly smaller than the grain size.

Thus at low to medium strains and in agreement with Eq. 30.1, the resistance of LAGBs is proportional to the square root of misorientation [12]. But Eq. 30.2 also suggests that for  $N \geq 4$  passes the strengthening mechanism shifts to HAGBs as it reverts to the original H-P formulation via removal of the scaling factor. The latter negates subgrain contributions entirely and treats *all* boundaries as HAGBs. In contrast, EBSD data indicates that even up to  $N=8$  passes LAGBs still constitute a significant area fraction (Table 30.1). Thus Eq. 30.2 simply fits mechanical data by increasing the H-P slope during the initial deformation stages when substructures enclose low misorientation angles [5]. Correspondingly  $k'$  can only be considered an ‘approximation’ as boundary character is not considered over all passes [16].

### 30.4 Conclusions

The H-P relationship estimated using the composite equation accounts for a ‘mixed’ LAGB+HAGB deformation substructure. Both Eqs. (30.1 and 30.2) are reasonable for up to  $N=3$  passes when the deformation substructure comprises predominantly LAGBs and its mechanical properties correspond to the subgrain

size. Beyond  $N \geq 4$  passes the increases in strength can be attributed to the sub-grain and grain diameters. The analyses underline the importance of the misorientation angle as the single-most significant parameter with which to correlate microstructural observations and mechanical property information.

**Acknowledgements** The authors are grateful to Prof. F.J. Humphreys (University of Manchester, United Kingdom) for the use of the VMAP software package.

## References

- [1] E.O. Hall, Proc. Phy. Soc., Ser. B 64 (1951) 747.
- [2] N.J. Petch, J. Iron Steel Inst. 174 (1953) 25.
- [3] D.A. Hughes, N. Hansen, Acta Mater. 48 (2000) 2985.
- [4] S.G. Tresvyatskii, Prob. Proch. 11 (1971) 60.
- [5] N. Hansen, Scr. Mater. 51 (2004) 801.
- [6] W.F. Hosford, The Mechanics of Crystals and Textured Polycrystals, 1st ed., Oxford University Press, New York, 1993.
- [7] J.-P. Baille, A. Loyer, J.-M. Dorlot, Mat. Sci. Eng. 8 (1971) 288.
- [8] B.L. Li, W.Q. Cao, Q. Liu, W. Liu, Mat. Sci. Eng. A 356 (2003) 37.
- [9] J.D. Messemaker, B. Verlinden, J.V. Humbeeck, Mat. Let. 58 (2004) 3782.
- [10] J.C. M. Li, Trans. Metall. Soc. AIME 227 (1963) 239.
- [11] F.B. Pickering, The Basis of Quantitative Metallography, 1st ed., Institute of Metallurgical Technicians, London, 1976.
- [12] N. Hansen, Mat. Sci. Eng. A 409 (2005) 39.
- [13] S. Takaki, K. Kawasaki, Y. Kimura, J. Mat. Pro. Tech. 117 (2001) 359.
- [14] B.Q. Han, S. Yue, J. Mat. Pro. Tech. 136 (2003) 100.
- [15] Y.J. Li, X. H. Zeng, W. Blum, Acta Mater. 52 (2004) 5009.
- [16] D.J. Abson, J.J. Jonas, Met. Sci. 4 (1970) 24.

# Chapter 31

## Evolution of Crystallographic Texture During Equal Channel Angular Extrusion (ECAE) of ( $\alpha+\beta$ ) Brass

Satyaveer Singh D., Ayan Bhowmik, Somjeet Biswas, Satyam Suwas  
and K. Chattopadhyay

*Dedicated to Prof. Ranjit Kumar Ray for his invaluable  
teaching and guidance to the scientific community working  
on texture of materials*

**Abstract.** Equal channel angular extrusion is now a well know process to generate ultra-fine grain microstructure in bulk materials. Since the material undergoes a large deformation, the process is also associated with evolution of characteristic texture. Most of the studies carried out on this subject aim at studying single phase materials. However, such a study is very relevant for two-phase materials owing to the possible enhancement of super-plastic properties. In the present work, a thorough investigation of evolution of microstructure and texture has been carried out to elucidate the deformation mechanisms and subsequent texture evolution in a model two-phase material, namely ( $\alpha+\beta$ ) brass. A detailed analysis of texture evolution in both  $\alpha$  and  $\beta$  (B2) phases will be presented.

### 31.1 Introduction

Over the last few years, with the rising expectation of enhanced materials performance, there has been a growing demand for ultra-fine grain sized material which results in higher strength without deteriorating the ductility of the material. Amongst the several types of severe plastic deformations, equal channel angular extrusion (ECAE) is regarded as a promising technique to develop ultra-fine grained microstructures in bulk samples. As defined by Segal [1, 2], under ideal conditions, the deformation in ECAE can be approximated by simple shear (SS) occur-

---

S. Singh D., A. Bhowmik, S. Biswas, S. Suwas, and K. Chattopadhyay  
Department of Materials Engineering, Indian Institute of Science, Bangalore-560012

ring on the die intersection plane. While the magnitude of strain imparted to the billet in a single extrusion passage depends on the die angle ( $\Phi$ ); billet re-insertion after varying the magnitude of rotation around its longitudinal axis (or 'route'2) between successive passes allows for a sequence of strain path changes to be introduced in the bulk material. Consequently, in multipass ECAE, the evolution of crystallographic texture and the resultant anisotropy in end physical and mechanical properties are influenced by the various strain path changes instigated by the prescribed processing route. On the characteristics of ECAE textures, a large number of studies have shown that they are comparable with those developed in fixed-end torsion, as both processes are characterized by simple shear (SS) deformation [3–12]. This observation has been found to hold good for all types of crystal structures viz. fcc [3–10], bcc [11, 12] and hcp [20] crystal structure. An adequate number of papers have been published on texture that evolves in fcc pure copper during equal channel angular extrusion [6, 9, 13–15]. Most of these studies are limited to single phase materials. However, many useful engineering alloys have two-phase structure. It is therefore desirable to study the microstructure and texture evolution during ECAE processing of two-phase materials. The alloy Cu-40 Zn consists of two phases,  $\alpha$  (fcc) and  $\beta$  (B2) and is an important engineering alloy. In the current work, the step-wise evolution of texture in a Cu-40Zn alloy through four passes of Equal Channel Angular Extrusion following route A. The  $\alpha$ -phase has fcc crystal structure based on copper lattice and  $\beta$ -phase has an ordered B2 (CsCl-type) structure with zinc atom occupying the body center position or vice versa. The texture have been measured individually in the two phases,  $\alpha$  and  $\beta$  after extrusion.

## 31.2 Experimental Procedures

The experiments were conducted using a commercially available 60Cu-40Zn alloy. The initial billet was a bar with cross-section  $10\text{ mm} \times 10\text{ mm}$  and length 100 mm. The initial grain size was  $3\text{ }\mu\text{m}$ . The die used for the experiments was similar to the one designed by Mathieu et al. [16] with sharp inner and outer corners with  $\Phi = 90^\circ$ . Before extruding the samples, they were annealed at a temperature of about  $400^\circ\text{C}$ . The extrusions were carried out at a temperature of

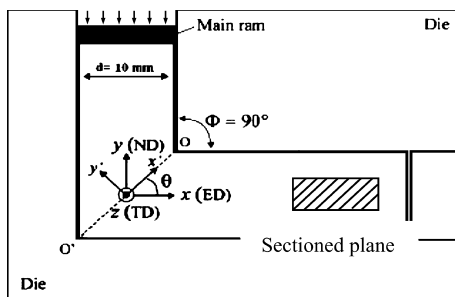


**Fig. 31.1** Schematic representation of cross section of the ECAE die.

$300 \pm 10^\circ\text{C}$  using a constant cross- head speed of  $1 \text{ mms}^{-1}$  on a hydraulic press. Route A of ECAE was followed where the billet after every pass was fed in for the next pass without any rotation about its longitudinal axis.

The corresponding von Mises equivalent strain per pass is 1.15 [17]. For microstructural and texture characterization, the specimens were sectioned as shown in Fig. 31.1. The observations were made on the TD-plane, the surface of which was electropolished. After electropolishing, the samples were subjected to microstructural investigation using Electron Back Scatter Diffraction. These experiments were carried out using a field emission gun scanning electron microscope. The texture analysis was done using TSL software.

### 31.3 Results and Discussions

The inverse pole figure maps for the overall microstructure, and individually the  $\alpha$ -phase and  $\beta$ -phase are shown in Fig. 31.3, for the starting material and after four passes. After four passes, there is a uniform distribution of fine equiaxed grains.

Although, the distribution of the grain size is fairly uniform for the B2 ordered  $\beta$ -phase with the average grain size being more than that in the  $\alpha$ -phase. This can be attributed to the higher hardness of  $\beta$ -phase. In Fig. 31.2, the variation in the grain size with number of ECAE passes has been plotted. It can be seen that the

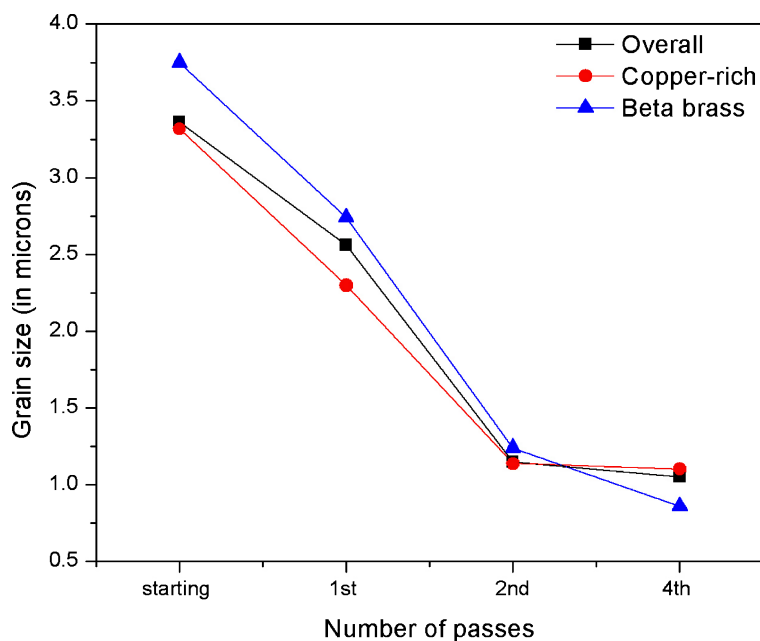
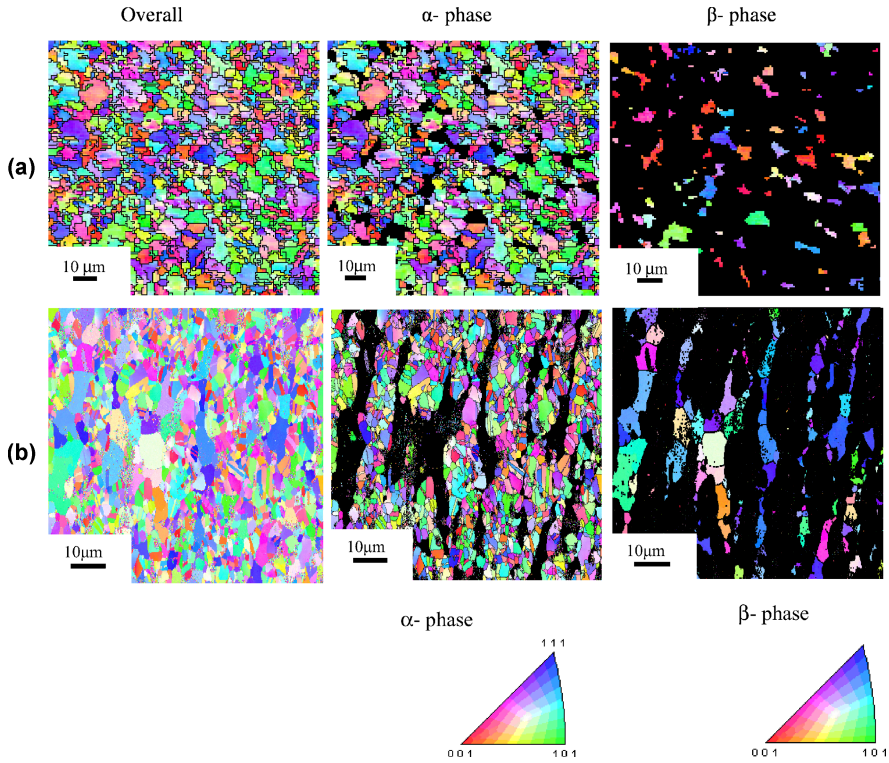


Fig. 31.2 Variation of grain size with ECAE passes.



**Fig. 31.3** The IPF maps for (a) starting material, (b) 4th pass.

reduction in grain size is not as expected during a severe plastic deformation process as ECAE. The grain size reduced from  $\sim 3.5 \mu\text{m}$  in the starting material to  $\sim 1 \mu\text{m}$  after four passes. A similar level of grain refinement was reported by Neishi et al. [18] in two phase brass processed by ECAE.

The grain boundary character distribution shows a gradual increase in the high angle grain boundaries at the expense of low angle ones, as depicted in Fig. 31.4, an observation that is quite as expected given the fact that with increasing number of ECAE passes the density of dislocations evolve from within the grains and move towards the low-angle sub-grain boundaries increasing the misorientation angle and hence resulting in the formation of high-angle boundaries. However, this does not accurately reflect the GBCD as the grain and phase boundaries do not get distinguished. Therefore, the measured data was filtered to separate the  $\alpha$  and  $\beta$  grains although Neishi et al. [18] reported  $\alpha$  and  $\beta$  phases separated by high angle grain boundaries. A similar trend in the fraction of low and high angle boundaries is seen in the  $\alpha$ -phase. Moreover, in the grain boundary character distribution the fraction of special CSL boundaries increases in the overall microstructure with passes, most of which is contributed by the  $\alpha$ -phase by generation of twins and hence  $\Sigma 3$  boundaries in profusion. The amount of CSL boundaries in the  $\beta$ -phase is negligible.

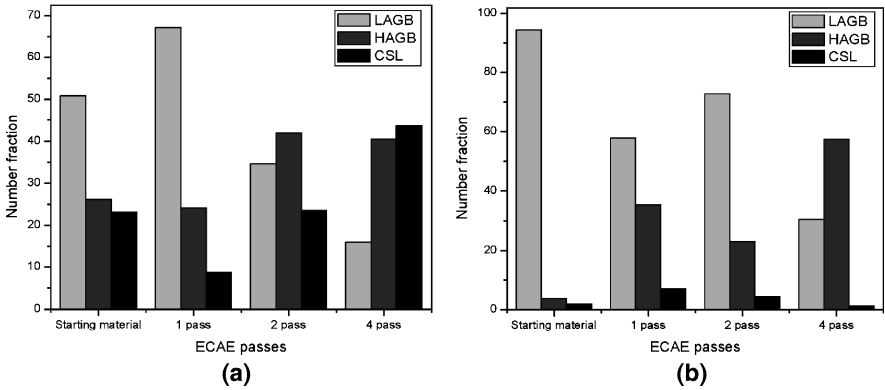


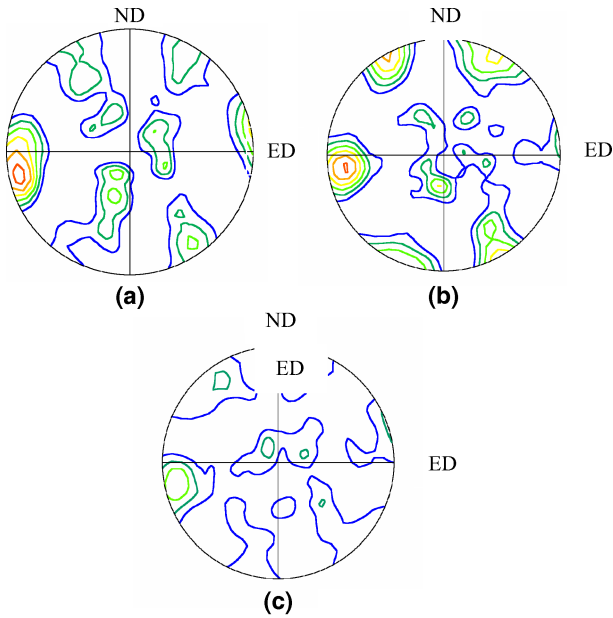
**Fig. 31.4** The distribution of low-angle grain boundaries (LAGB), high-angle grain boundaries (HAGB) and coincident site lattice (CSL) boundaries as a function of passes for (a)  $\alpha$ -phase, and (b)  $\beta$ -phase.

Separate pole figures obtained for the two phases  $\alpha$  and  $\beta$  are given in Figs. 31.5 and 31.6. The common feature of all the pole figures is that they are all found to resemble very closely to negative simple shear as produced during torsion test except that ECAE textures are rotated about the TD axis by an angle which is half the inter-channel die-angle, which in this case is  $45^\circ$ . Comparing the experimentally obtained pole figure for the  $\alpha$ -phase with the simulated key figure [19] reveals the clear presence of the  $A_{1E}$ ,  $A_{2E}$ ,  $C_E$  and  $B_E$  after the first pass. Both  $\{111\}_0$  and  $\langle 110 \rangle_0$  fibres are found to be present in the pole figures. Table 31.1 documents the miller indices for the ideal orientation of fcc metal. There occur subtle shifts in the texture components from the ideal position with increasing number of passes. It is evident, that the intensity of the components also decreases with passes which may be due to the randomization of grain orientation as a result of grain fragmentation in the softer  $\alpha$ -phase. Texture of the B2 phase was analyzed with the simulated pole figure of Li et al. [12]. For the ordered B2 phase the components that were identified from the pole figures are  $D_{10}$ ,  $D_{20}$  and  $J_0$  along the  $\{110\}_0$  and  $\langle 111 \rangle_0$  fibres, again with certain shifts from the ideal bcc orientation. Table 31.2 depicts the position of the ideal ECAE texture components for bcc material. In Fig. 31.6, gradual evolution of the shear type texture can be seen from the 1st pass to the 4th pass sample.

**Table 31.1** Ideal orientation components for copper [19].

Notation	Miller indices		
	ND	ED	TD
$A_{2E}$	[6 25-25]	[25-3 3]	[011]
$A_{1E}$	[25 3-3]	[6 25-25]	[011]
$C_E$	[100-71 71]	[-100-71 71]	[011]
$B_E$	[-73-27 100]	[73-100 27]	[111]





Texture Name: Binned: Size=5.0, HW=5.0  
Calculation Method: Discrete Binning  
Bin Size: 5.0°  
Gaussian Smoothing: 5.0°

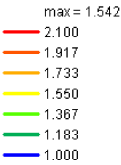
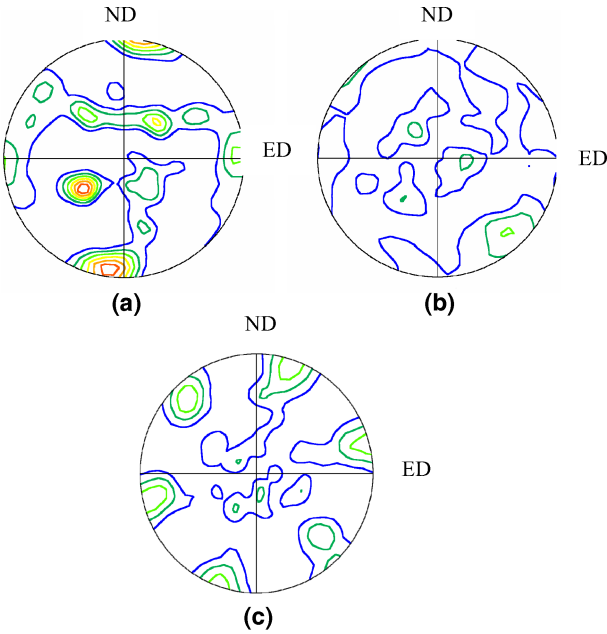


**Fig. 31.5** Experimental (111) pole figures of the fcc  $\alpha$ -phase obtained for the (a) starting material, (b) 1st, (c) 4th pass samples.

**Table 31.2** Ideal orientation components for IF steel [12].

Notation	Miller indices		
	ND	ED	TD
$D_{10}$	[118]	[4-41]	[1-10]
$D_{20}$	[44-1]	[118]	[-110]
$J_0$	[15 4 11]	[7 26 11]	[111]



Texture Name: Binned: Size=5.0, HW=5.0  
Calculation Method: Discrete Binning  
Bin Size: 5.0°  
Gaussian Smoothing: 5.0°

**Fig. 31.6** Experimental (110) pole figures of the ordered B2  $\beta$ -phase obtained for the (a) starting material, (b) 1st, (c) 4th pass samples.

The shift from the ideal position may be accounted for various reasons such as the discontinuous nature of shear during the ECAE process, variation in the composition of the experimental material with the one for which the key pole figures are plotted, viz. pure fcc copper and Interstitial Free (IF) steel having a bcc crystal structure. Comparing the pole figures of both the phases, it can be concluded that in either cases the crystallographic slip plane and the slip directions tend to align themselves to the macroscopic shear plane and direction respectively.

## 31.4 Conclusions

Two-phase ( $\alpha + \beta$ ) brass was processed by Equal Channel Angular Extrusion and an average grain size of the order of  $1\ \mu\text{m}$  was achieved. The crystallographic texture of  $\alpha$  and  $\beta$  phase measured individually indicate characteristic shear texture formation. Texture weakens after ECAE in the  $\alpha$ -phase while it strengthens with number of passes in the  $\beta$ -phase.

**Acknowledgement** This work was carried out under IISc-DRDO Collaboration Programme. The authors duly acknowledge the financial support from Defense Research and Development Organization, Ministry of Defense, Govt. of India. The work also uses the facility set up under Institute Nanoscience Initiative sponsored by DST-FIST program.

## References

- [1] Segal V.M., Mater. Sci. Eng. A 197 (1995) 157.
- [2] Segal V.M., Mater. Sci. Eng. A 271 (1999) 322.
- [3] Arrufat-Masion R., Suwas S., Toth L.S., Mat. Sci. Forum Part 1 & 2 2005 839.
- [4] Suwas S., Toth L.S., Fundenberger, Solid State Phenomena 105 (2005) 357.
- [5] Suwas S., Toth L.S., Fundenberger J.J., Scripta Materialia 49 (2003) 1203.
- [6] Toth L.S., Massion R.A., Germain L., Acta Mater 52 (7) (2004) 1885.
- [7] Gholinia A., Bate P., Prangnell P.B., Acta Mater. 50 (2002) 2121.
- [8] Suwas S., Toth L.S., Fundenberger J.J., Solid State Phenomena 105 (2005) 345.
- [9] Li S., Beyerlein I.J., Bourke M.A.M., Mater. Sci. Eng. A 394 (2005) 66.
- [10] Li S., Beyerlein I.J., Alexander D.J., Vogel S.C., Acta Mater. 53 (2005) 2111.
- [11] J. De Messemaeker, B. Verlinden, J. Van Humbeeck, Acta Mater. 53 (2005) 4245.
- [12] Li S., Gazder A.A., Beyerlein I.J., Pereloma E.V., Davies C.H.J., Acta Mater. 54 (2006) 1087.
- [13] Gazder A.A., Li S., Dalla Tore F.H., Beyerline I.J., Gu C.F., Davies C.H.J., Pereloma E.V., Mater Sci Eng A 437 (2006) 259.
- [14] Suwas S., Singh A.K., Rao K.N., Z. Metall, 94 (12) (2003) 1313.
- [15] S. Li, I.J. Beyerline, D.J. Alexander, Mater Sci Eng A 431 (2006) 339.
- [16] Mathieu J.-P., Suwas S., Ebarhardt A., Toth L.S., Moll P., Journal of Mater. Proc.Tech. 173 (2006) 29.
- [17] Yoshinori Iwahashi, Jingtao Wang, Zenji Horita, Minoru Nemoto and Terence G. Langdon, Scripta Mater. 35 (1996) 143.
- [18] Neishi. K., Horita. Z., Langdon. T.G., Scripta Materialia, 45 (2001) 965.
- [19] Suwas S., Arruffat-Massion R., Toth L.S., Fundenburger J.J., Ebarhardt A., Skrotzki W., Met. and Materials Transactions A, 37A, (2006) 739.
- [20] Suwas S., Gottstein G., Kumar R., Mat Sci and Engg A 471 (2007) 1.

## Chapter 32

# Grain Growth in ECAE Processed Pure Magnesium

Somjeet Biswas, Satyaveer Singh D. and Satyam Suwas

*Dedicated to Prof. Ranjit Kumar Ray for his invaluable teaching and guidance to the scientific community working on texture of materials*

**Abstract.** Grain growth kinetics was studied for commercially pure magnesium subjected to equal channel angular extrusion (ECAE). The specimens were ECAE processed upto 4 passes at 523 K following all the three important routes, namely A, B<sub>c</sub> and C. Texture and microstructures of the samples were studied using Electron Back Scattered Diffraction (EBSD) technique in a Field Emission Gun – Scanning Electron Microscope (FEG-SEM). It was observed that the grain size significantly reduces after ECAE. ECAE process produces a slightly rotated B and C<sub>2</sub> fiber. Static annealing leads to normal grain growth with unimodal distribution of grains through out the temperature range. Average activation energy for grain growth in the temperature range studied is found to be less than the activation energy for lattice diffusion and grain boundary diffusion of magnesium. No significant change in texture during isochronal annealing for 1 hour i.e., the predominant deformation texture remains same.

**Keywords:** Magnesium, ECAE, EBSD, DRX, Texture

### 32.1 Introduction

Magnesium and its alloys are important materials to be used in automobile, aerospace and electronics industries, due to superior specific stiffness and strength [1].

---

S. Biswas, S. Singh D., and S. Suwas  
Laboratory for Texture and Related Studies, Department of Materials Engineering,  
Indian Institute of Science, Bangalore-12

However, poor formability and limited ductility at room temperature are obstacles for its industrial use. Hexagonal crystal structure and therefore limited operating slip systems are the major hurdle. For wide spread application strength and ductility needs to be improved. The ECAE process is very effective in enhancing the workability and strength of Mg alloys by grain refinement [2–4] and suitable crystallographic texture [5–8]. The present study has been carried out to understand changes that can take place during subsequent annealing after ECAE of commercially pure magnesium. Efforts were made to characterize the texture evolution during deformation. Mechanical properties of magnesium alloys are improved by ECAE by producing smaller grain sizes and optimum texture [9–11].

## 32.2 Experimental Methods

Hot forged pure magnesium of 99.92% purity was processed by ECAE following the routes A, B<sub>c</sub> and C in a 90° die upto 4 passes at 523 K. The route A involves no rotation around the billet axis, in B<sub>c</sub> the sample is rotated by 90° in one direction (clockwise or anti-clockwise) between each pass, and in route C the sample is rotated by 180° between the passes [12]. The stability of grain structure at elevated temperatures was investigated by isochronal annealing for 1 hr in the range of 373 K–773 K in argon atmosphere for all the samples. Optical microscope was used to see the microstructure of the ECAE processed and the annealed samples. The samples were prepared by metallographic method followed by etching with a mixture of 100 ml Ethanol, 10 ml acetic acid, 6 ml picric acid and 20 ml distilled water. Grain size was measured and analyzed using Sigma scan pro software. The grain size was calculated using linear intercept method using Sigma Scan-pro software, where the average grain size is:

$$d = 1.74 L \quad (32.1)$$

where,  $d$  is the average grain size and  $L$  is the linear intercept grain size measurement [13] that are obtained by optical microscope. Activation energy for grain growth was calculated. Texture analyses were carried out by electron back scatter diffraction (EBSD) using scanning electron microscope (SEM). Measurements were done on the TD plane keeping account of the reference system i.e., ED, ND and TD to be same for all the samples.

## 32.3 Results and Discussions

Figure 32.1 shows the respective linear intercept grain size variation with temperature, the curves are parabolic in nature. The optical microstructures of pure Mg for ECAE route B<sub>c</sub> 4 passes and annealed are shown in Fig. 32.2.

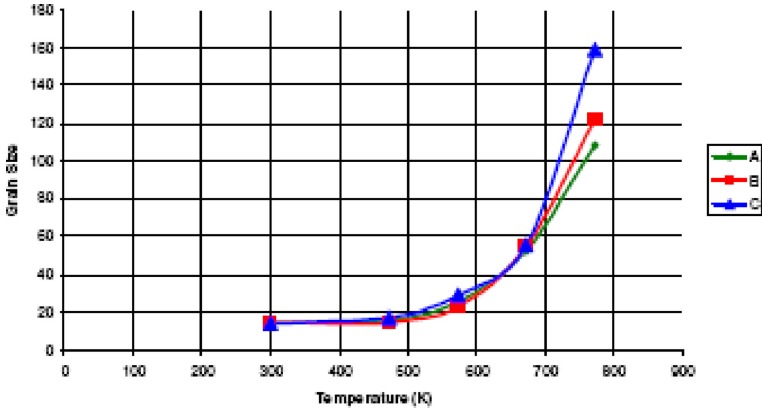


**Fig. 32.1** Average grain size against annealing temperature for annealing time of 1 hr for the samples ECAE'd by A, B<sub>C</sub> and C route.

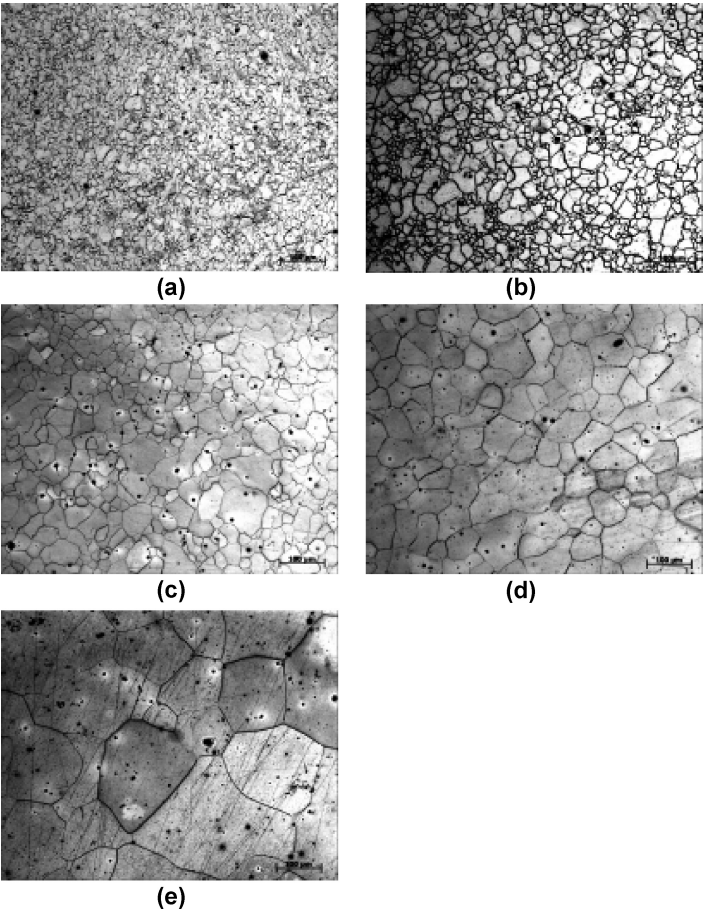


**Fig. 32.2** Optical micrographs of (a) Mg ECAP Bc 4 pass, (b) annealed at 473 K, (c) annealed at 573 K, (d) annealed at 673 K and (e) annealed at 773 K.

### 32.3.1 Grain Growth Statistics

Microstructural observations of the ECAE processed samples by both optical microscope and SEM based EBSD shows equiaxed grains with serrated grain boundaries. EBSD analysis also shows a large fraction ( $\sim 50\%$ ) of low angle grain boundaries. It can be said that although dynamic recrystallization (DRX) has taken place, large amount of cold work still persisted in the ECAE processed samples. It can be said that deformation at 523 K favours dynamic recrystallization. Further deformation of dynamically recrystallized grains and DRX leads to the formation of equiaxed grains with high concentration of low angle grain boundaries. The microstructure consists of grain with average size  $\sim 14 \mu\text{m}$ . No significant grain growth was observed when the material is annealed at 473 K for 1 hr. On annealing at 573 K, the grain size increases to  $\sim 30 \mu\text{m}$ , and after annealing at 673 K, new bigger polygonal grains of  $\sim 54 \mu\text{m}$  size observed. Further annealing at 773 K the grain size increases tremendously to  $\sim 130 \mu\text{m}$ . Jäger et al. [14] have observed that for AZ31 magnesium alloy static recrystallization occurs at above 423 K.

### 32.3.2 Activation Energy

In order to investigate the grain growth mechanisms, it is necessary to determine the activation energy for grain growth. Grain growth behavior in the investigated temperature range was assumed to follow the general equation:

$$L^n - L_o^n = K_o t \exp(-Q_g / RT)$$

where  $L$  is the linear intercept grain size at a given annealing time,  $L_o$  is the initial linear intercept grain size,  $K_o$  is a constant,  $t$  is the annealing time,  $Q_g$  is the activation energy for grain growth,  $R$  is the molar gas constant and  $T$  is the temperature. Assuming parabolic relationship for grain growth,  $n = 2$ . Based on the above equation,  $Q_g$  can be obtained by plotting  $(L_2 - L_{2o})$  against  $(1/T)$  in a semi-logarithmic scale for the same annealing time. Such a plot has been obtained for all the pass ECAE processed samples, annealed at different temperature as shown in Fig. 32.3.

From Fig. 32.3 the measured average activation energy ( $Q_g$ ) values for the grain growth in the ECAE processed by route A, Bc and C up to 4 passes for the temperature range of 473 K to 773 K are 58.3, 75.9 and 55.8 kJ/mole, respectively. The activation energy is much lower than that of lattice self diffusion ( $Q_L$ ) ( $= 135 \text{ kJ/mole}$ ) [15] and that for grain boundary diffusion ( $Q_{gb}$ ) in pure magnesium ( $= 92 \text{ kJ/mole}$ ) [16]. The average value of  $Q_g$  for route A and C 4 passes (57 kJ/mole) corresponds to  $\sim 0.45 Q_L$ . The average value of  $Q_g$  for route Bc 4 pass sample is  $\sim 75.9 \text{ kJ/mole}$ , which corresponds to  $\sim 0.55 Q_L$ , which is always lower than that of grain boundary diffusion ( $Q_{gb}$ ). Kim [17] suggested that if activation energy for grain growth ( $Q_g$ ) is less than lattice self diffusion ( $Q_L$ ) and grain boundary diffusion ( $Q_{gb}$ ), grain growth occurs in the unrecrystallized condition.

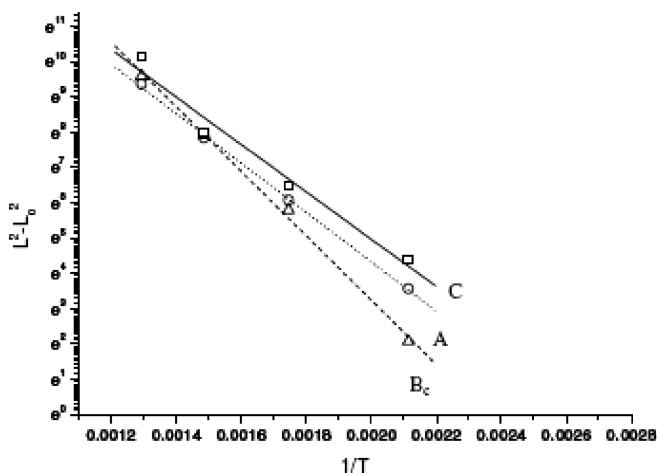


Fig. 32.3 Semilog plot of  $(L_2-L_{20})$  vs.  $(1/T)$ .

Thus it was observed that after 4 passes ECAE and annealing  $Q_g$  for A is 58.3 KJ/mole, Bc is 75.9 KJ/mole and C is 55.8 KJ/mole, which are less than the  $Q_{gb}$  and  $Q_L$ . Therefore, the grain growth occurs in the unrecrystallized condition.

From the above observation it can be said that as the initial samples which were ECAE processed at higher deformation temperature of 523 K, though about 150 K higher than the minimum recrystallization temperature of magnesium, contains equiaxed grains with serrated grain boundaries. The structure is not strain free; therefore, the activation energy required for grain growth is less than that for lattice and grain boundary diffusion. The grains grow at the expense of the accumulated strain energy apart from the heat supplied.

### 32.3.3 Texture Analysis

Figure 32.4 shows the IPF maps of samples processed by ECAE Route A up to 4 passes and annealed at 373 K and 773 K. It can be seen from the figure that grain color for the as ECAE processed and the annealed samples are same, owing to the fact that there is no alteration in the orientation of the grains. Figure 32.5 shows the  $\langle 0002 \rangle$ ,  $\langle 1010 \rangle$  and  $\langle 1120 \rangle$  pole figures for the same sample. ECAE process produces  $\langle 0002 \rangle$  texture fiber which is with B and  $C_2$  component most prominent, a detailed analysis of texture evolution of magnesium during ECAE is given by Beausir et al. [18]. It can be attributed that DRX occurred during ECAE at 523 K will not alter the ECAE texture of magnesium. It was found that, the deformation texture was not only retained after annealing, but strength of the basal fiber also increases from 8 MRD to 27 MRD from the as ECAE processed to post annealing at 773 K. The same trend was also observed for the Bc and C route. The misorientation angle distribution (Fig. 32.6) shows that the fraction of low angle grain boundaries



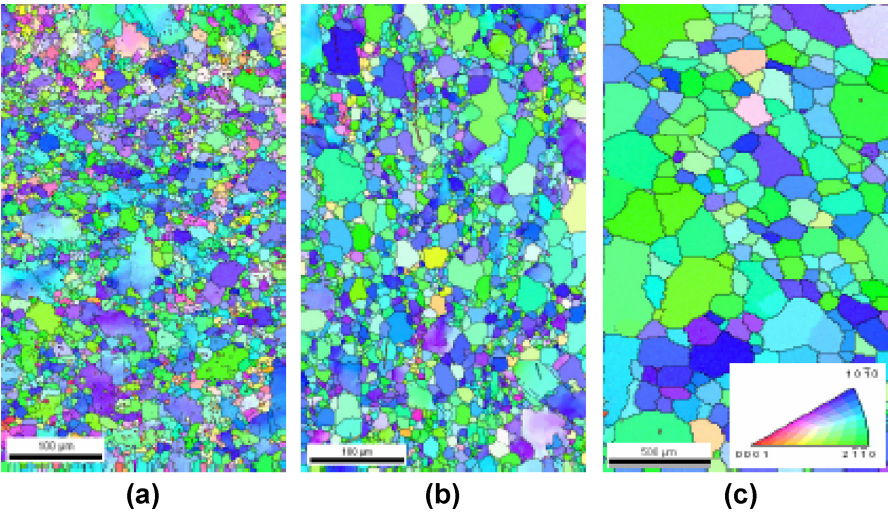


Fig. 32.4 IPF Map of (a) ECAE Route A 4 pass, (b) annealed at 473 K and (c) annealed at 773 K.

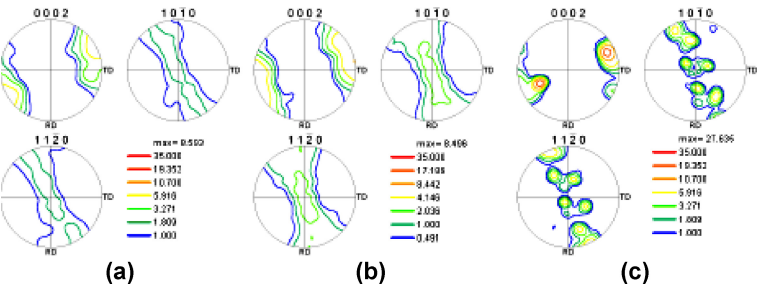


Fig. 32.5 Pole figures of (a) ECAE Route A 4 pass, (b) annealed at 473 K and (c) annealed at 773 K.

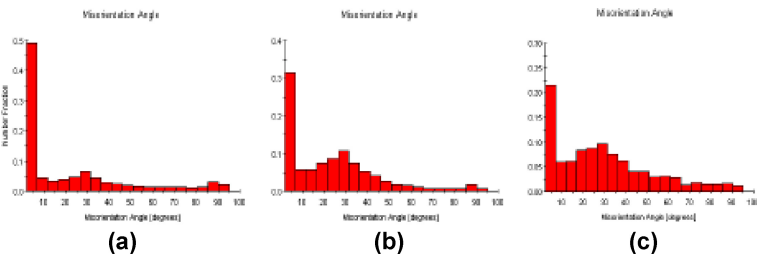
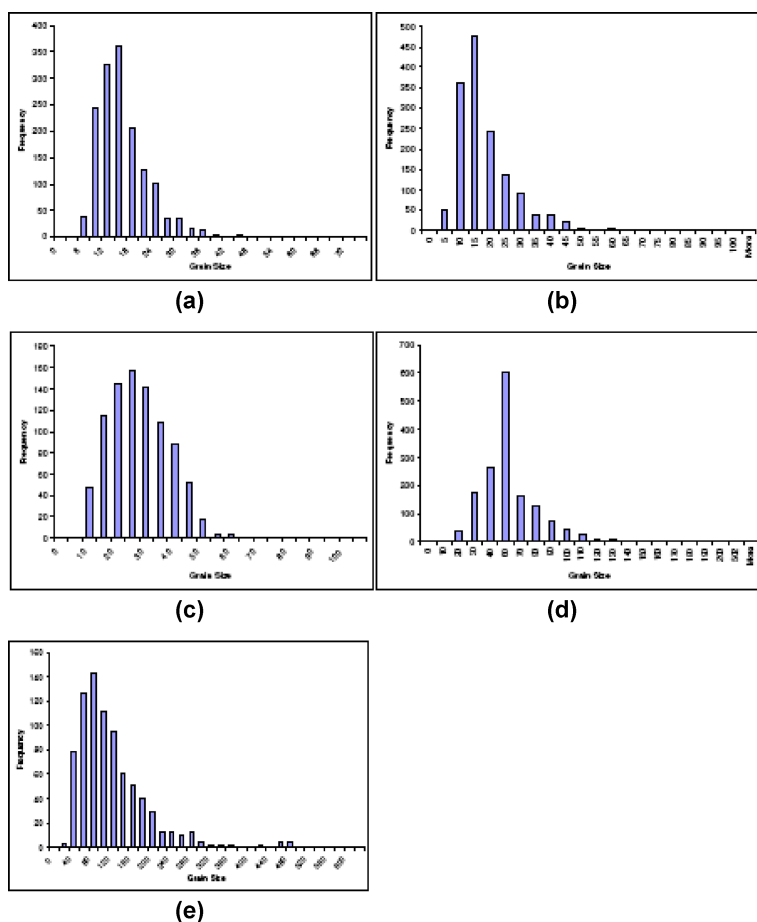


Fig. 32.6 Misorientation angle distribution of (a) ECAE Route A 4 pass, (b) annealed at 473 K and (c) annealed at 773 K.

was decreased with the annealing temperature. Texture evolution during annealing of Magnesium AZ-31 and AZ-61 alloy was studied by Ruano et al. [19, 20], it was concluded that normal grain growth takes place upon moderate annealing without changing the initial deformation texture. The deformation texture of the as received mater-



**Fig. 32.7** Grain size distribution of (a) Mg ECAP Bc 4 pass, (b) annealed at 473 K, (c) annealed at 573 K, (d) annealed at 673 K and (e) annealed at 773 K.

ials are basal and prismatic ( $\langle 1010 \rangle$  and  $\langle 1120 \rangle$ ) fiber texture component. Moderate annealing increases the basal texture intensity. Abnormal grain occurs if extensive annealing is carried out for many hours. In such case  $\langle 1010 \rangle$  and  $\langle 1120 \rangle$  planes parallel to the sheet planes are observed and bimodal distribution of grains formed. Gottstein et al. [21, 22] have shown that recrystallization texture is identical to the deformation texture of the sample, though sometimes there is a growth preference for  $30^\circ$  rotation along  $\{0002\}$  axis from  $\langle 1120 \rangle$  to  $\langle 1010 \rangle$ . If annealed more than 673 K some more components developed although predominant texture do not change. Wagner et al. [23] also reported a similar observation on titanium, where the texture evolution was sluggish during static recrystallization with respect to deformation texture. From the above observation, it can be concluded that annealing of the ECAE processed samples in the range 473–773 K for 1 hr., does not lead to abnormal grain growth. Figure 32.7 shows the grain size distribution of the ECAE processed

as well as annealed samples for ECAE route A. Samples processed by all the routes results in singular peak, which shows the occurrence of primary recrystallization and normal grain growth. Texture evolution during isochronal annealing in the range of 473–773 K for 1 hr., shows that the predominant deformation texture remains the same, and recrystallization does not alter the deformation texture, rather it strengthens it.

## 32.4 Conclusions

Commercially pure magnesium was ECAE processed upto 4 pass by route A, Bc and C at 523 K and annealed in the range of 473 K–773 K. Grain size calculations, activation energies and texture evolution during grain growth were studied. The main conclusions of the studies are as follows:

1. ECAE processed samples have equiaxed grains with serrated grain boundaries and singular peak grain size distribution. Low angle grain boundaries (LAGBs) are observed at high fraction. Even if some dynamic recrystallization during ECAE and static recrystallization in the intermediate passes has occurred, then also there was lots of strain energy accumulated in the grains. It was also observed that dynamic recrystallization does not alter the deformation texture, this can be observed from the  $\langle 0002 \rangle$  pole figure, which shows B and C2 (shear texture) fiber.
2. Static annealing between 473–773 K for 1 hour shows normal grain growth with the activation energy for A, Bc and C almost constant throughout and less than the activation energy for lattice ( $Q_L$ ) and grain boundary diffusion ( $Q_{gb}$ ) for pure magnesium. Grain growth takes place in the unrecrystallized condition in all the cases. A lower  $Q_g$  also represents the presence of high fraction of stored energy in the initial material.
3. It was observed that deformation texture of the ECAE processed samples does not get altered up on static annealing, rather it strengthens it up to a temperature of 773 K for 1 hr i.e., the predominant deformation texture remains same. Grain size distribution for all the annealed samples at different temperature shows a singular peak, which shows that only primary recrystallization has taken place. Decrease in the low angle grain boundary shows that the amount of strain energy decreased with the annealing.

**Acknowledgement** The authors would like to acknowledge Department of Science and Technology (DST) for the financial support. The work also uses the facility set up under Institute Nanoscience Initiative, IISc sponsored by DST-FIST program.

## References

- [1] A. Stalman, W. Sebastian, H. Friedrich, S. Schumann and K. Dröder, *Adv. Engg. Mat.*, 2001, 3, 969–974.
- [2] M. Mabuchi, K. Ymeyama, H. Iwasaki, K. Higashi, *Acta Mater*, 47, 1999, 2047.
- [3] S. Komodo, T. Ashie, H. Yamada, K. Sanbun, Y. Kojima, *Material Science Forum*, 65, 2000, 350–351.
- [4] S.R. Agnew, G.M. Stoica, Li Chen, T.M. Lillo, J. Macheset, P.K. Liaw, In: Y.T. Zhu et al. Editors, *Ultra fine grain Materials II*, Warrendale, PA: TMS, 2002, 643–652.
- [5] T. Mukai, M. Yananoi, H. Watanabe, K. Higashi, *Scripta Mater*, 45, 2001, 89.
- [6] W.J. Kim, C.W. An, Y.S. Kim, S.I. Hong, *Scripta Materialia*, 47, 2002, 39.
- [7] T. Mukai, Y. Masashi, K. Iigashi, *Material Trans. JIM*, 42, 2001, 2652.
- [8] S. Suwas, G. Gottstein, R. Kumar, *Mater. Sci. Engg. A* 2007
- [9] S.R. Agnew, P. Mehrotra, T.M. Lillo, G.M. Stoica, P.K. Liaw, *Mater. Sci. Engg. A*, 408, 2005, 72.
- [10] S.R. Agnew, J.A. Horton, T.M. Lillo, D.W. Brown, *Scripta mater*, 50, 2003, 377.
- [11] S.R. Agnew, P. Mehrotra, T.M. Lillo, G.M. Stoica, P.K. Liaw, *Acta Mater.*, 53, 2005, 3135.
- [12] M. farukawa, Y. Iwashashi, Z. Horita, M. Nemoto, T.G. Langdon, *Mater. Sci. Engg. A*, 257, 1998, 328.
- [13] S. Mukai, *Philosophical Magazine letters*, vol. 86, no.3, march 2006, 195–204
- [14] A. Jäger, P. Lukáč, V. Gärtnerová, J. Haloda, M. Dopita, *Materials Science and Engineering A*, 432, 2006, 20–25.
- [15] P.G. Shewman, *Trans. AIME* 206, 1956, 918.
- [16] H.J. Frost, M.E. Ashby, *Deformation Mechanism Maps*, Pergamon Press, Oxford, 1982, 44.
- [17] H.-K. Kim, *J. Mater. Sci.*, 39, 2004, 7107–7109.
- [18] B. Beausir, S. Suwas, L.S. Tóth, K.W. Neale, J.-J. Fundenberger, *Acta Mater.*, 56, 2, 2008, 200.
- [19] M.T. Pérez-Prado, O.A. Ruano, *Scripta Mat.*, 46, 2002, 149–157.
- [20] M.T. Pérez-Prado, O.A. Ruano, *Scripta Mat.*, 48, 2003, 59–64.
- [21] R.K. Nadella, I. Samajdar, G. Gottstein, *Static recrystallization and texture changes in warm rolled pure magnesium. ICOTOM Proceedings 2002.*
- [22] R. Gehrman and G. Gottstein, *Proc. 12th International conference on texture of materials, ICOTOM 12* (ed.: J.A. Szpuner) Aug. 9–13, 1999, Montreal Canada, NRC Research Press, Vol. 1, 665–670.
- [23] F. Wagner, N. Bozzolo, O. Van Landuyt, T. Grosdidier, *Acta Mat.*, 50, 2002, 1245–1254.



## Chapter 33

# Solidification Microstructure and Texture in Grain-Refined Titanium Alloys

Segolene de Waziers, Shibayan Roy, Satyam Suwas, S. Tamirisakandala, R. Srinivasan, and D.B. Miracle

**Abstract.** In the present study, solidification microstructure and texture evolution in grain-refined Ti-6Al-4V and  $\gamma$ -TiAl alloys via trace boron addition are compared with their baseline counterparts. Boron addition resulted in dramatic grain refinement by almost an order of magnitude. The texture developed in these alloys is also markedly different from the baseline alloys.

### 33.1 Introduction

Since the introduction of titanium and titanium alloys in the early 1950s, these materials have become backbone materials for the aerospace, energy, and chemical industries. They are very useful light materials and exhibit high specific strength and fracture toughness combined with good corrosion resistance at tem-

---

S. de Waziers  
Ingenierie des Materiaux, ENSIACET, Institut National Polytechnique de Toulouse,  
Toulouse, France

S. Roy and S. Suwas  
Laboratory for Texture and Related Studies, Department of Materials Engineering,  
Indian Institute of Science, Bangalore, INDIA

S. Tamirisakandala  
FMW Composite Systems, Inc., Bridgeport, WV, USA

R. Srinivasan  
Mechanical and Material Engineering Department, Wright State University, Dayton, USA

D.B. Miracle  
Air Force Research Laboratory, Materials and Manufacturing Directorate,  
Wright-Patterson AFB, USA

peratures up to 550–800 K [1]. The most widely used titanium alloy is the Ti-6Al-4V ( $\alpha + \beta$ ) alloy which is most commonly used in the annealed condition [1]. Microstructure and texture evolution in this alloy was studied in great details by many researchers. Kobryn et al. [2] have found that metal-mold-cast Ti-6Al-4V tends to have equiaxed prior  $\beta$  grain morphology, while direct-laser-fabricated Ti-6Al-4V usually has a columnar morphology. The alpha-phase texture in direct-laser-fabricated Ti-6Al-4V was found to be fairly weak (i.e. maximum IPF intensity of  $\sim 1.6$  times random). In another study, Kalinyuk et al. [3] showed that the microstructure of two electron beam melted Ti-6Al-4V ingots at all locations are identical and characterized by coarse beta grains decorated by a layer of grain-boundary  $\alpha$ . The texture of both the ingots is found to be completely random suggesting the possibility that the orientation distribution is not affected by anisotropy in grain growth during solidification.

TiAl-based materials are pursued mainly because of their high thrust-to-weight ratio of high-performance aircraft engines. The microstructure of these alloys can be controlled by heat treatment. The optimum desirable properties in this class of alloys could be achieved only with ( $\alpha_2 + \gamma$ ) microstructure, which corresponds to the composition Ti-48Al. When an alloy, Ti-48Al, is cooled from the  $\alpha$ -phase field ( $T \sim 1400^\circ\text{C}$ ) the final microstructure is lamellar. On the other hand, if the alloy is cooled from two phase field ( $\alpha_2 + \gamma$ ), a microstructure with lamellar grains and  $\gamma$  grains is expected [4].

The primary problem in wrought processing of titanium and its alloys is the coarse grain size (often in the millimeter range) after solidification due to its poor thermal conductivity. Extensive deformation processing above and below the  $\beta$ -transus is a standard industrial practice for refining the coarse as-cast microstructure. This process, popularly known as ‘ingot breakdown’ increases the production cost of the finished titanium products, which limits their extensive use.

Zhu et al. [5] observed that small amount ( $\sim 0.086$  to  $0.14$  mass%) of boron addition induces a significant refinement of as-cast structure and improvement of mechanical properties such as tensile ductility, strength and hardness for cast CP Titanium and Ti-0.5Si alloys. Similar observations are reported by other researchers [6–8] for ( $\alpha + \beta$ ) alloys like Ti-6Al-4V. On the other hand, the use of boron as a grain refiner is quite common in ( $\alpha_2 + \gamma$ ) titanium aluminides. Boron addition can strongly influence the microstructure of these alloys. Wherein large amounts of boron (generally more than  $0.5$  at%) results in grain refinement in the cast material, small amounts (less than  $0.2$  at%) refines the lamellar structure in the grain [9, 10]. The texture evolution of as cast boron modified titanium alloys (both Ti-6Al-4V and titanium aluminides) are, however, still lacking, which is the *prima facie* of the present work.

## 33.2 Experimental

The materials used in this present study are,

1. Ti-6Al-4V and Ti-6Al-4V-0.1B, (hereafter referred to as Ti64 and Ti64-B, respectively). The cast ingot dimensions were 70 mm diameter  $\times$  500 mm length.
2. Ti-48Al-2V and Ti-48Al-2V-0.2B (in wt%) (hereafter referred to as Ti482 and Ti482-B, respectively). The samples are “plane parallel” with 8 mm  $\times$  8 mm  $\times$  12 mm dimension.

For both the materials, boron was added in the elemental form that completely dissolved in the liquid melt. For the Ti64 and Ti64-B, as shown in Fig. 33.1 (a), a thin strip of 35 mm length  $\times$  7 mm width  $\times$  5 mm thickness was cut from the periphery to the center of the as-cast ingot. The thin strip was divided into six equal pieces. For Ti482 and Ti482-B, the samples were parallelepipeds of 8 mm  $\times$  8 mm  $\times$  12 mm (see Fig. 33.1 (b)).

The microstructure and texture of the samples were characterized using scanning electron microscopy[1]<sup>1</sup>. The samples were first metallographically polished up to 2500 grit sized silicon carbide paper and finally electro-polished using Struers<sup>®</sup> Lectropol-5<sup>2</sup>. The samples were etched with a custom made etchant containing 5% HF, 10% HNO<sub>3</sub> and rest water for 30 seconds.

For the Ti64 and Ti64-B, each of the pieces from the original thin strip was subjected to microstructural characterization using a Field Emission Gun Scanning Electron Microscope<sup>3</sup> with Electron Backscattered Diffraction (EBSD) attachment. From each of the samples, an area of 1 mm  $\times$  4 mm was scanned with a step size of 5  $\mu$ m. For Ti482 and Ti482-B, from the parallelepiped samples, an area of 1.5 mm  $\times$  1.5 mm was scanned with a step size of 2  $\mu$ m. All the samples were prepared in the same way as described above. The accelerating voltage used was 20 kV and minimum boundary misorientation was taken to be 2°. Texture analysis (pole figures, inverse pole figures, IPF maps etc.) was done using OIM<sup>™</sup> Analysis Software<sup>4</sup>.

## 33.3 Results and Discussions

Figure 33.2 (a) shows the microstructure of the as-cast starting material Ti64-B. The microstructure is homogenous and uniform from the periphery towards the center of the ingot in terms of all length scales. This observation is quite consistent with the earlier reports [9, 10] and can be attributed to the faster solidification rate which

<sup>1</sup> QUANTA 200, FEI, The Netherlands

<sup>2</sup> Struers A/S, Germany

<sup>3</sup> FEG-SEM, Sirion XL-40, FEI, The Netherlands

<sup>4</sup> TSL Crystallography, AMETEK Inc., USA



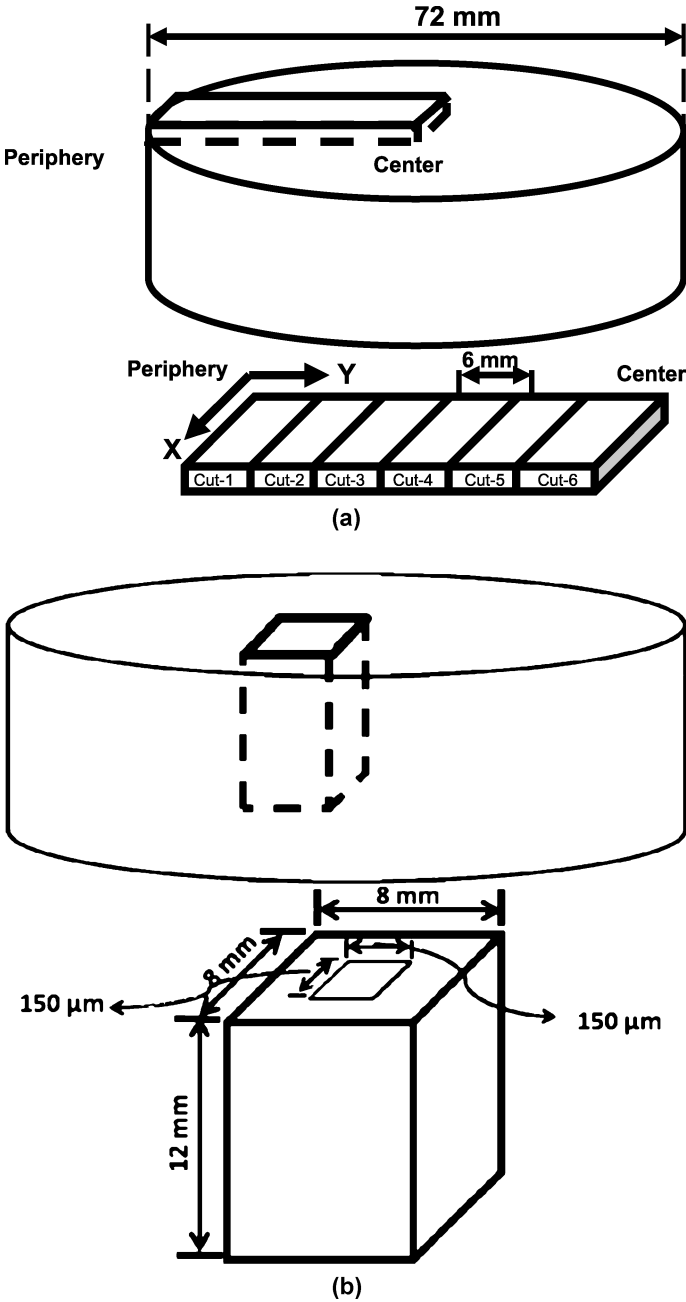


**Fig. 33.1** Experimental procedure showing (a) a bar is cut from the as-cast ingot and (b) the bar is divided into six equal pieces for texture measurement. This method is applied for both Ti64 and Ti64-B.

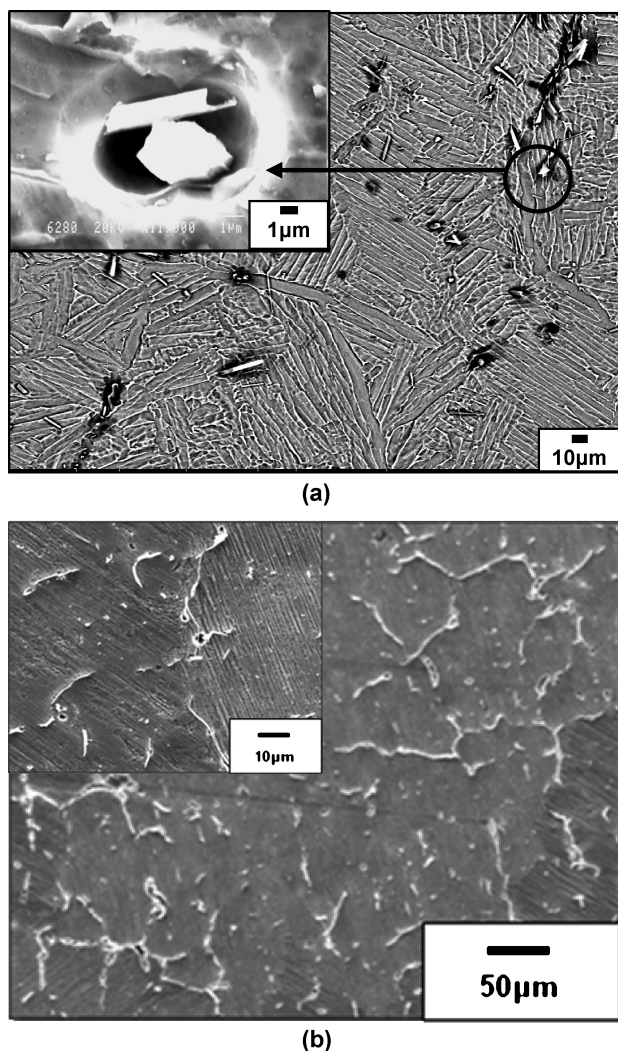


**Fig. 33.2** Microstructure of the as-cast (a) Ti64-B, and (b) Ti482-B samples.

ensures the formation of equiaxed beta grains instead of columnar grains [11]. Hexagonal TiB whisker cross-sections can be seen at the grain boundary (see Fig. 33.2 (a) inset) forming a 'necklace' structure.

Microstructure of the alloy Ti482, with and without boron, shows lamellar structure resulting from a cooling of the alloy from  $\sim 1400^{\circ}\text{C}$ , (in the single  $\alpha$  phase) [12]. The grain size is  $\sim 120\text{ }\mu\text{m}$  without boron addition and  $\sim 52\text{ }\mu\text{m}$  with boron. The boride particles, which are identified as  $\text{TiB}_2$  in this case, are randomly distributed within the microstructure, and do not present any obvious preference for grain interior or boundary region.

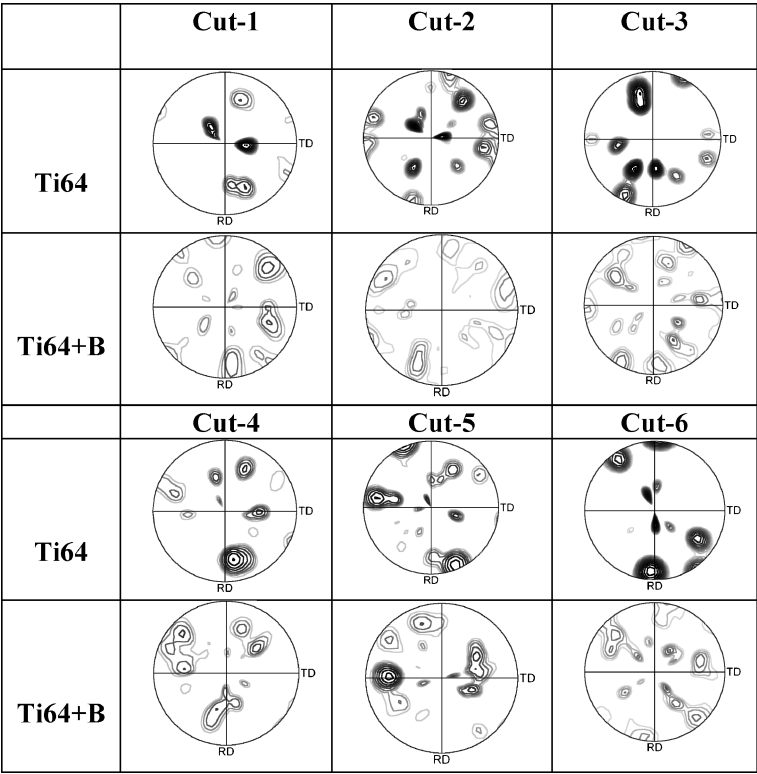


**Fig. 33.3** (0001) pole figures of  $\alpha$ -phase for as-cast Ti64-B vis-à-vis as-cast Ti64. Both types of pole figures are expressed in terms of similar intensity levels.

Large area scan for EBSD has been carried out in order to get statistically significant data. When brought to the same level of m.r.i. (maximum random intensity), the pole figure for Ti64-B reveals less number of contour lines than that of Ti64. Also, the total number of intensity maxima is more for Ti64-B indicating that this material does not have sharp texture consisting of a few well defined components. Texture rather consists of many clusters of orientations; therefore overall sharpness of texture is less in the case of Ti64-B. This randomness in the solidification texture of the as-cast material can be attributed to the basic grain refinement mechanism by boron addition in titanium alloys. As mentioned earlier, boron addition increases  $\beta$  nucleation and suppresses its growth. This process, not only reduces the prior  $\beta$  grain size, but also increases the number of  $\alpha$  colonies in a given sampling area as compared to Ti64. Since, from a single  $\beta$  orientation, 12 different  $\alpha$  orientations can be generated in accordance with the Burger's orientation relationship [13], the refinement in the prior  $\beta$  grain size may lead to the randomization in the  $\alpha$  phase texture unless a variant selection process takes place during the solidification through the transformation temperature.

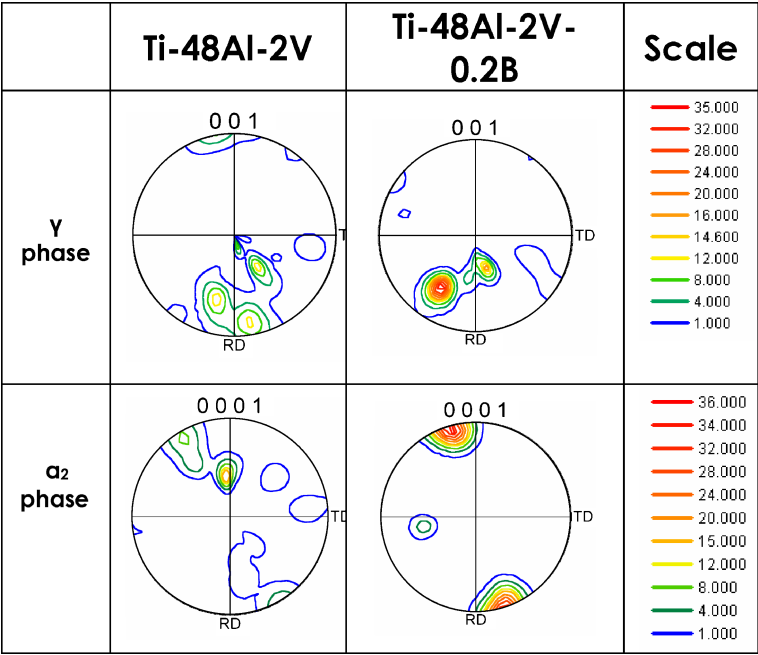


**Fig. 33.4** (001) Pole figures of  $\gamma$  phase and (0001) pole figures of  $\alpha_2$  phase of Ti-48Al-2V and Ti-48Al-2V-0.2B.

In order to study texture of the alloys Ti482 and Ti482-B, the (001) pole figure for the  $\gamma$  phase and the (0001) pole figure for the  $\alpha_2$  phase are calculated (see Fig. 33.4). The pole figures have plotted with the same intensity level for both the phases. For the  $\gamma$  phase as well as for the  $\alpha_2$  phase, the maxima intensity for the alloy Ti482-B is much larger than the Ti482 alloy. Thus the texture of the both phases increases with addition of boron. Further investigation is underway to explore the reasons for the differences in the response of boron addition to both types of alloys.

**33.4 Conclusion**

The solidification microstructure and texture of titanium alloy and titanium aluminide with and without boron addition was studied. It is concluded that

- i) Addition of boron refines the microstructure as well as modifies/weakens the texture of the solidified ingot for Ti64 and Ti64-B alloys.
- ii) Microstructure of Ti482 and Ti482-B showed lamellar structure. The alloy with boron shows  $TiB_2$  flakes either at the grain boundaries or inside the grain. Intensity of texture of titanium aluminide increases with the addition of boron.

**Acknowledgement** The authors cordially acknowledge the Asian Office of Aerospace Research and Development (AOARD) for the financial support and Institute Nanoscience Initiative (INI), Indian Institute of Science, Bangalore, India for providing the required research facilities to carry out the present investigation.

## References

- [1] ASM Metals Handbook Volume 2, "Properties and selection of nonferrous alloys and special purpose materials," ASM International, Tenth Edition
- [2] P.A. Kobryn, S.L. Semiatin, "Microstructure and texture evolution during solidification processing of Ti-6Al-4V," *Journal of Materials Processing Technology*, 135, 330–339 (2003)
- [3] N. Kalinyuk, N.P. Trigu, V.N. Zamkov, O.M. Ivasishin, P.E. Markovsky, R.V. Teliovich, and S.L. Semiatin, "Microstructure, texture, and mechanical properties of electron-beam melted Ti-6Al-4V," *Materials Science and Engineering A*, 346, 178–188 (2003)
- [4] R.M. Imayev, V.M. Imayev, M. Oehring, and F. Appel, "Microstructural evolution during hot working of Ti aluminide alloys: Influence of phase constitution and initial casting texture," *Met. & Mat. Trans. A*, 36A, 859–867 (2005)
- [5] J. Zhu, A. Kamiya, T. Yamada, W. Shi, and K. Naganuma, "Influence of boron addition on microstructure and mechanical properties of dental cast titanium alloys," *Materials Science and Engineering A*, 339, 53–62 (2003)
- [6] S. Tamirisakandala, R.B. Bhat, J.S. Tiley, and D.B. Miracle, "Grain refinement of cast titanium alloys via trace boron addition," *Scripta Materialia*, 53, 1421–1426 (2005)
- [7] S. Tamirisakandala, R.B. Bhat, D.B. Miracle, S. Boddapati, R. Bordia, R. Vanover, and V.K. Vasudevan, "Effect of boron on the beta transus of Ti-6Al-4V alloy," *Scripta Materialia*, 53, 217–222 (2005)
- [8] Sen, S. Tamirisakandala, D.B. Miracle, and U. Ramamurty, "Microstructural effects on the mechanical behavior of B-modified Ti-6Al-4V alloys," *Acta Materialia*, 55, 4983–4993 (2007)
- [9] D. Hu, A.J. Huang, D. Novovic, and X. Wu, "The effect of boron and alpha grain size on the massive transformation in Ti-46Al-8Nb-xB alloys," *Intermetallics*, 14, 818–825 (2006)
- [10] Z.X. Li, and C.C. Cao, "Effects of minor boron addition on phase transformation and properties of Ti-47.5Al-2Cr-2Nb alloy" *Intermetallics*, 13, 251–256 (2005)
- [11] J.P. Kuang, R.A. Harding, and J. Campbell, "Microstructures and properties of investment castings of  $\gamma$ -titanium Aluminide," *Materials Science and Engineering A*, 329–331, 31–37 (2002)
- [12] Y.W. Kim, "Intermetallic alloys based on gamma titanium aluminide," *JOM*, 41(7), 24–30 (1989)
- [13] L. Zeng, T.R. Bieler, "Effects of working, heat treatment, and aging on microstructural evolution and crystallographic texture of  $\alpha$ ,  $\alpha'$ ,  $\alpha''$  and  $\beta$  phases in Ti-6Al-4V wire," *Materials Science and Engineering A*, 392, 403–414 (2005)

## Chapter 34

# Effect of Intercritical Heat Treatment on the Abrasive Wear Behaviour of Plain Carbon Dual Phase Steel

M.K. Manoj, V. Pancholi, and S.K. Nath

**Abstract.** Dual phase (DP) steels have been prepared from low carbon steel (0.14% C) at intercritical temperature 740°C and time is varied from 1 minute to 30 minutes followed by water quenching. These steels have been characterized by optical microscopy, FE-SEM, hardness measurements, tensile properties and electron backscattered diffraction (EBSD) studies. Tensile properties of a typical dual phase steel are found to be 805 MPa ultimate tensile strength with 18% total elongation. Martensite volume fraction of D P steel (determined by EBSD technique) prepared at 740°C for 6 minutes is found to be 10.2% and the grain size of ferrite and martensite found to be 14.39 micron and 1.05 microns respectively. Abrasive wear resistance of dual phase steels has been determined by pin on drum wear testing machine. DP steels have been found to be 25% more wear resistant than that of normalized steel. Short intercritical heating time followed by water quenching gives higher wear resistance by virtue of smaller and well dispersed martensite island in the matrix of ferrite.

**Keywords:** DP steel, Abrasive wear, Martensite

### 34.1 Introduction

The properties which make dual phase (DP) steels most popular and versatile includes high strength to weight ratio, absence of yield point phenomena, high uniform and total elongation, good formability and weldability. Currently these steels are most commonly used in automobile and structural applications, where they have replaced more conventional HSLA steels. DP steels combine high

---

M.K. Manoj, V. Pancholi, and S.K. Nath  
Department of Metallurgical & Materials Engg, I.I.T Roorkee.  
e-mail: manojmkm123@rediffmail.com.

strength of conventional HSLA steels with formability approaching that of plain carbon steel and therefore have emerged as a potential alternative.

The microstructure of dual phase steel primarily consists of ferrite and martensite. Ferrite is soft and tough whereas martensite is hard. Wear resistance of a material depends on hardness of material as well as toughness to absorb energy. Dual phase steel fulfills these requirements as martensite provides hardness and ferrite provides soft and tough matrix. Martensite islands also reduce the real contact area which further improves wear resistance of the material.

Dry sliding wear of DP steel have been studied systematically by researchers [1–8]. Very few literatures are available on the abrasive wear behavior of DP steels. The contributions of Modi et al. are significant in this direction [9–10]. However, it is observed in this work that sample does not move always on fresh emery paper as compared to present work where sample always moves on fresh emery paper on the drum.

In the present work a detailed investigation on dual phase steels has been undertaken using plain low carbon steel. Intercritical heat treatment has been carried out at 740°C and heating time is varied from 1 minute to 30 minutes. Abrasive wear resistance of DP steels having varying martensite volume fraction is studied using pin on drum.

## 34.2 Experimental

DP Steels have been prepared from low carbon steel. Samples in the form of tensile specimens of gauge length 20 mm have been prepared which are used for intercritical heat treatment. The chemical composition of the steel is given in Table 34.1. Intercritical heat treatments have been done at 740°C for 1, 3, 6, 9, 15 &

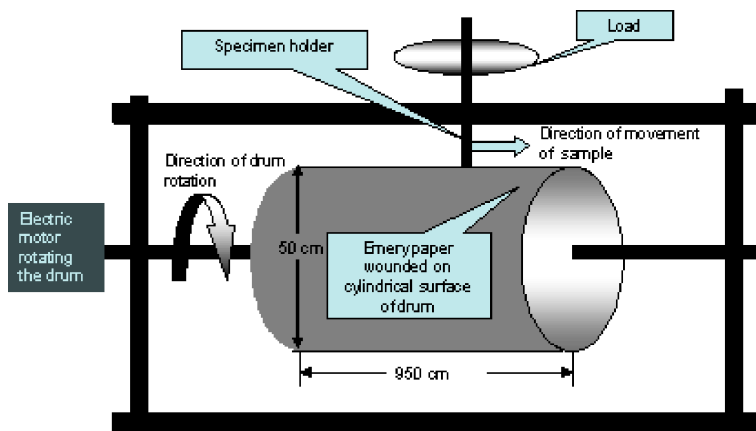


Fig. 34.1 A schematic diagram of pin-on-drum abrasive wear tester.

**Table 34.1** Chemical composition of as received steel in wt%.

C	Mn	Si	S	P
0.14	0.56	0.04	0.014	0.034

30 minutes followed by water quenching (WQ). DP steels have been characterized by optical microscopy, FE-SEM, hardness measurements, tensile properties and EBSD studies. Abrasive wear test of these DP steels have been carried out by using pin-on-drum abrasive wear tester (Fig. 34.1). After the tensile test, the broken sample from the grip region has been used as pin sample for abrasive wear test. The test has been performed at 1.2 Kg normal load and rotation of the drum is kept at 2 rpm (Dia of drum – 0.5 m). Emery paper used has abrasive particles of grit size 220.

**34.3 Results and Discussion**

Chemical analysis of low carbon steel used for preparation of DP steels has been done by emission spectroscopy and is shown in Table 34.1. Vickers hardness of DP steels has been determined at 30 kg load. Five readings have been taken for each samples and average have been reported. Figure 34.2 show (a) optical micrograph and (b) SEM picture of DP steels prepared at 740°C, 3 min, WQ.

EBSD technique has been used to determine distribution and volume fraction of martensite phase. The step size of 0.2 micron has been selected for EBSD studies. Figure 34.3 shows step wise determination of grain size and volume fraction of different phases in DP steel prepared at 740°C for 6 minutes followed by WQ. There are two peaks in image quality chart (Fig. 34.3 (a)). The first peak which has lower image quality (<545), represents martensite phase where as the second peak having higher image quality (>545) represents ferrite phase. Average grain size of ferrite (Fig. 34.3 (b)) and martensite (Fig. 34.3 (c)) found to be 14.39 micron and

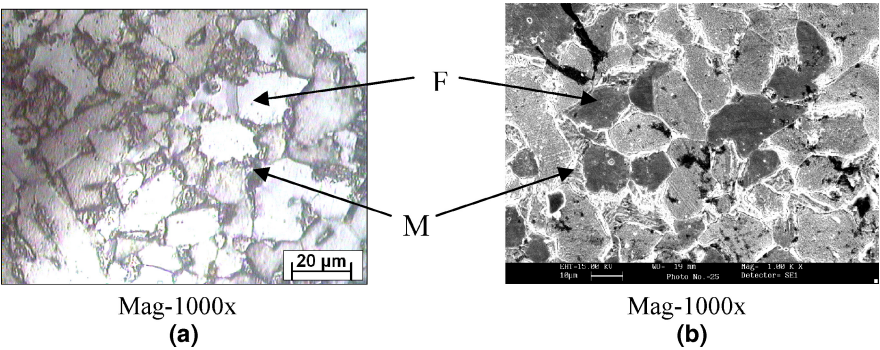


**Fig. 34.2** (a) Optical microstructure and (b) SEM picture of DP steel prepared at 740°C, 3 min, WQ. F-Ferrite, M-Martensite.



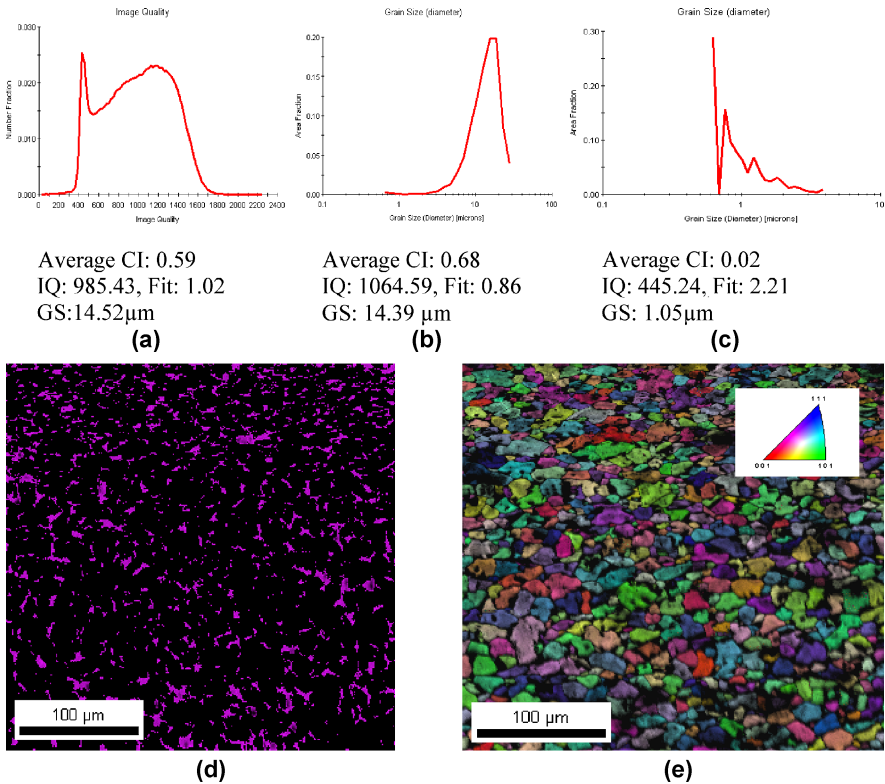


**Fig. 34.3** EBSD study of DP steel prepared at 740°C, 6 min, WQ (a) Image quality chart (b) Grain size distribution of ferrite (c) Grain size distribution of martensite (d) Image quality map showing distribution of martensite phase (e) Inverse pole figure map of ferrite phase. CI – Confindex Index, IQ – Image Quality, GS – Grain Size.

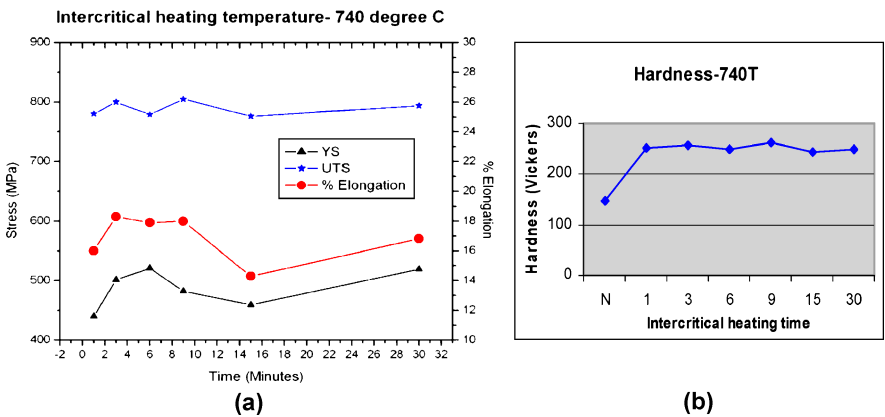


**Fig. 34.4** Tensile properties (a) and hardness (b) of DP steels prepared at 740°C for different intercritical heating time.

**Abrasive Wear test of DP Steels prepared at 740 degree  
C for different time.**

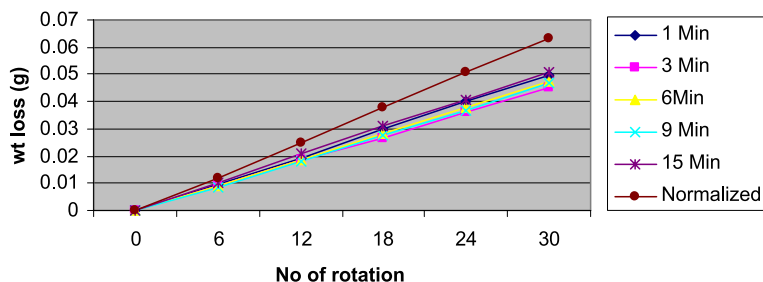


**Fig. 34.5** Abrasive wear of DP Steels intercritically heated at 740°C for different intercritical time.

1.05 microns respectively. Distribution of martensite phase is shown in Fig. 34.3 (d), and inverse pole figure map of ferrite grains are shown in Fig. 34.3 (e). DP steels prepared at 740°C for different austenitisation time show martensite volume fraction varying from 8 to 15%.

Figure 34.4 (a) shows tensile properties of DP steels prepared at 740°C for different intercritical heating time. The figure shows that at intercritical heating temperature 740°C, variations in UTS is less. Figure 34.4 (b) shows variation of hardness with increasing intercritical heating time. Hardness of normalized steel is found to be 147 HV where as hardness of DP steels varied from 243 to 262 HV. This variation in hardness is due to variation in the volume fraction of martensite in DP steel. At 740°C intercritical temperature variation of intercritical heating time for 1, 3, 6, 9, 15 & 30 minutes form varying amounts of austenite which on water quenching transforms to martensite.

Abrasive wear test of DP steels have been carried out by using pin-on-drum abrasive wear tester. The variation of weight loss with increasing number of rotation of abrasive drum is found to be linear (Fig. 34.5). It is observed DP steel prepared at 740°C for 3 minute of intercritical heating time shows lowest wear and normalized steel shows maximum wear. DP steels prepared from 1, 6, 9 and 15 minute of intercritical heating time show wear resistance close to DP steel prepared from 3 minute of intercritical heating time. Smaller and well dispersed martensite islands in the matrix of ferrite shows relatively higher wear resistance property than interconnected martensite islands in ferrite matrix. It is also observed that DP steels have considerably higher wear resistance than that of normalized steel of same chemical composition.

## 34.4 Conclusion

Plain carbon DP steels have been successfully prepared by intercritical heat treatment followed by water quenching. DP steels prepared at 740°C for different aus-

tenitisation time show martensite volume fraction varying from 8 to 15% as determined by EBSD technique. UTS of DP steels have been found to be nearly two times more than that of normalized steel with little decrease in ductility. Abrasive wear resistance of DP steels has been found to be approximately 25% more than that of normalized steel. DP steels with well dispersed martensite islands in the matrix of ferrite show better mechanical and tribological properties than DP steels with interconnected martensite islands.

## References

- [1] A. Wang and H.J. Rack, Dry sliding wear in 2124 Al-Si Cw/17-4PH stainless steel systems, *Wear*, 147 (1991) 355–374.
- [2] A. Gocke, I. Schmit and M. Wilhelm Goring and sliding abrasion of austenitic manganese steels reinforced by hard phases, *Wear*, 119 (1987) 313–327.
- [3] Rajnesh Tyagi, S.K. Nath, S. Ray, “Dry sliding friction and wear in plain carbon dual phase steel”, *Metallurgical and Materials Transactions*, Vol. 32A, Feb. 2001, pp. 359–367.
- [4] Rajnesh Tyagi, S.K. Nath, S. Ray, “Effect of martensite content on friction and oxidative wear behavior of 0.42 pct carbon dual phase steel”, *Metallurgical and Materials Transactions, A*, Vol. 33A, 2002, pp. 1–10.
- [5] Rajnesh Tyagi, S.K. Nath and S. Ray, “Oxidative wear in multi-phase materials”, *Metals Materials and Processes*, Meshap Science, April–June, Vol. 14, No. 2, 2002, pp. 103–114.
- [6] Rajnesh Tyagi, S.K.Nath, S.Ray, Modelling of dry sliding oxidation-modified wear in two phase materials, *wear*, 255 (2003) 237–332.
- [7] M. Aksoy, M.B. Karamis, and E. Evin, An evaluation of the wear behavior of a dual-phase low carbon steel, *Wear*, 193 (1996) 248–252.
- [8] You Wang, Tingquan Lei, JiaJum Liu, Tribo-metallographic behaviour of high carbon steels in dry sliding II. Microstructure and wear, *wear* 231 (1991) 12–19.
- [9] Anand Prakash Modi, Effects of microstructure and experimental parameters on high stress abrasive wear behavior of a 0.19% C dual phase steel, *Tribology International*, 40 (2007) 490–497.
- [10] O.P. Modi, Pallavi Pandit, D.P. Mondal, B.K. Prasad, High stress abrasive wear response of 0.2% carbon dual phase steel: Effects of microstructural features and experimental conditions, *Materials science and engineering A*, 458 (2007) 303–311.